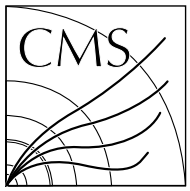

CERN-LHCC-2017-012
CMS-TDR-016
12 September 2017

The Phase-2 Upgrade of the CMS Muon Detectors

Technical Design Report

CMS Collaboration

CERN-LHCC-2017-012 / CMS-TDR-016
22/10/2018

Editors

T. Hebbeker, A. Korytov

Chapter editors

P. Azzi, C. Calabria, C. Carrillo, A. Colaleo, M. Franco Sevilla, L. Guiducci, J. Hauser, T. Hebbeker, M. Hohlmann, A. Korytov, M. Narain, P. Paolucci, I. Pedraza, D. Piccolo, I. Redondo, A. Safonov, S. Ventura, D. Wood

Cover Design

S. Cittolin

Acknowledgements

This document would not exist without the devoted efforts of many colleagues, too many to be named explicitly, who contributed text, figures, etc.

The very useful feedback from all readers from the muon groups, the CMS internal reviewers (P. Bloch, T. Cox, M. Dallavalle, G. Iaselli, D. Kovalskyi, D. Loveless, J. Olsen, G. Rakness, and G. Rolandi), and the chair of the CMS Phase-2 TDRs editorial board (C. Lourenço) helped to improve the quality of this document.

We would also like to emphasise the support of the CMS management and upgrade teams, as well as the many contributions from the offline, computing, and physics groups in the development of the physics performance studies.

We would like to thank the technical staff from the various institutions for the excellent work during the design and R&D phase of this upgrade.

We also wish to thank the LHCC for their oversight and crucial advice during the development of the Phase-2 muon upgrade project.

Contents

Part I

Overview of the CMS Phase-2 Muon Detector Upgrade

Chapter 1

The CMS Phase-2 muon detector

1.1 Motivation for the upgrade of the CMS muon system

CMS is a general purpose experiment measuring proton-proton and heavy-ion collisions at the Large Hadron Collider (LHC) at CERN [1]. It has already produced many excellent scientific results. By mid 2017 CMS has published more than 600 papers in refereed journals. The highlight was the discovery of the 125 GeV Higgs boson by the ATLAS and CMS experiments in 2012. CMS is looking for answers to fundamental questions in particle physics and beyond: Are there more particles than the well established fermions and gauge bosons of the Standard Model (SM)? Are all properties of the 125 GeV neutral boson consistent with the SM Higgs particle? Is nature supersymmetric? Can we explain the Dark Matter in the universe by particles that can be produced at the LHC?

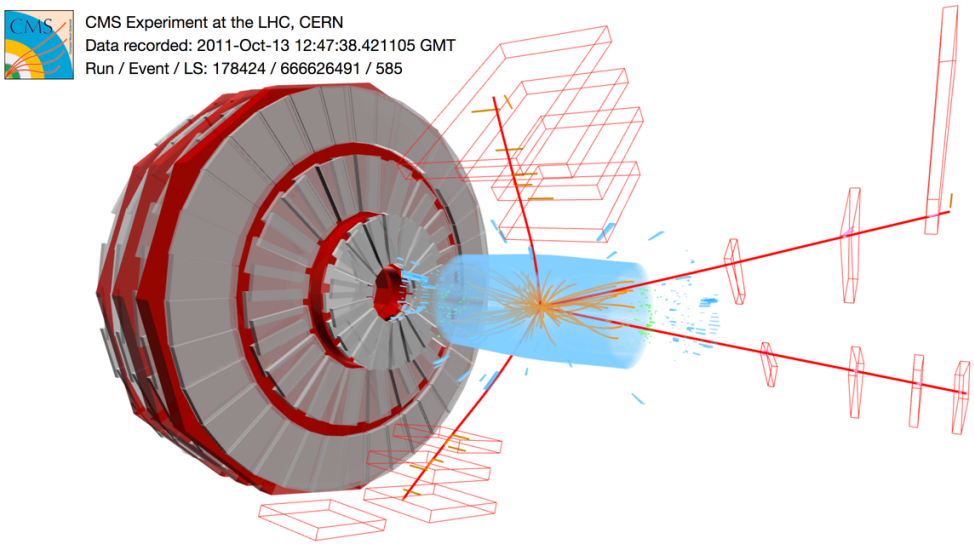

Figure 1.1: CMS event display with four muons (red lines), probably stemming from a Higgs boson decay.

The CMS experiment has been very successful. The detector has been running smoothly at world-record proton-proton center-of-mass energies up to 13 TeV, with an LHC luminosity exceeding 10^{34} cm^{-2}s^{-1}. The SM was tested in an unprecedented energy regime and with high precision. The missing key particle of the SM, the Higgs boson, was discovered through its two-photon and four-lepton decay modes [2, 3]. Figure 1.1 shows a four-muon event measured by CMS in 2011, with an invariant mass close to 125 GeV. Also extremely rare decays such as $B_s^0 \to \mu\mu$ were observed [4], as shown in Fig. 1.2. They are very sensitive to new

physics contributions. New 'Beyond the SM' (BSM) particles have been searched for in many channels, and stringent limits have been set, but so far no new physics was found.

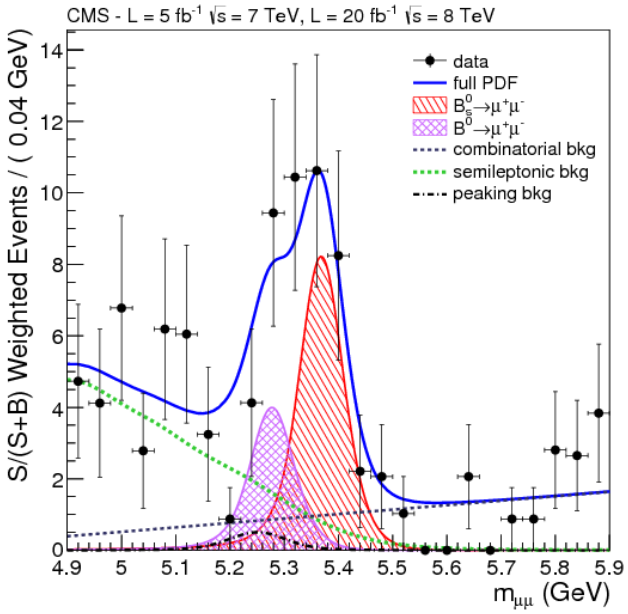

Figure 1.2: The dimuon mass spectrum measured in neutral B decays. The peak corresponds to B_s^0 decays to two muons, and the shoulder marks the position of the B^0 mass [4].

To extend the sensitivity for new physics searches, a major upgrade of the LHC has been decided and is being prepared, the High Luminosity LHC (HL-LHC). The integrated luminosity will increase tenfold with respect to the original design values, as shown in Table 1.1, which summarizes some key parameters at LHC and HL-LHC for proton-proton running [5, 6]. The projected evolution of instantaneous and integrated luminosity with time is shown in Fig. 1.3, for the design scheme and also for an ultimate scenario, which can possibly be reached by exploiting all LHC margins. The center-of-mass energy for proton-proton collisions is expected to be raised from the current 13 up to 14 TeV. The current 'Phase-1' data taking period will end in the year 2023, followed by a shutdown for the HL-LHC upgrade ending in 2026. The high luminosity data taking period with the upgraded LHC is called 'Phase-2' and is expected to last from 2026 till 2038. The HL-LHC will increase the projected integrated luminosity of 300 fb^{-1} for 'Phase-1', the current LHC period, by an order of magnitude to 3000 fb^{-1} in the coming two decades, for both the CMS and ATLAS detectors.

This upgrade programme is necessary to fully exploit the physics potential of the LHC. Many search channels are statistics limited and their sensitivity increases in proportion to the integrated luminosity. For many proposed scenarios, including Supersymmetry and new heavy gauge bosons, the attainable mass range can be improved at HL-LHC by at least one TeV. The properties of the discovered Higgs boson will be measured with higher precision, which will allow searches for new physics associated with the Higgs sector. Also the accuracy for many SM tests will improve dramatically; in particular, the sensitivity to rare processes increases linearly with luminosity. The searches for new physics will be extended to exotic models, with challenging signatures from the experimental point of view: long-lived particles decaying leptonically, final states with low p_{T} muons, heavy slowly moving charged particles, or highly boosted dimuons, requiring improved muon detection and trigger capabilities.

The HL-LHC upgrade of the accelerators and of the LHC detectors will be implemented mainly

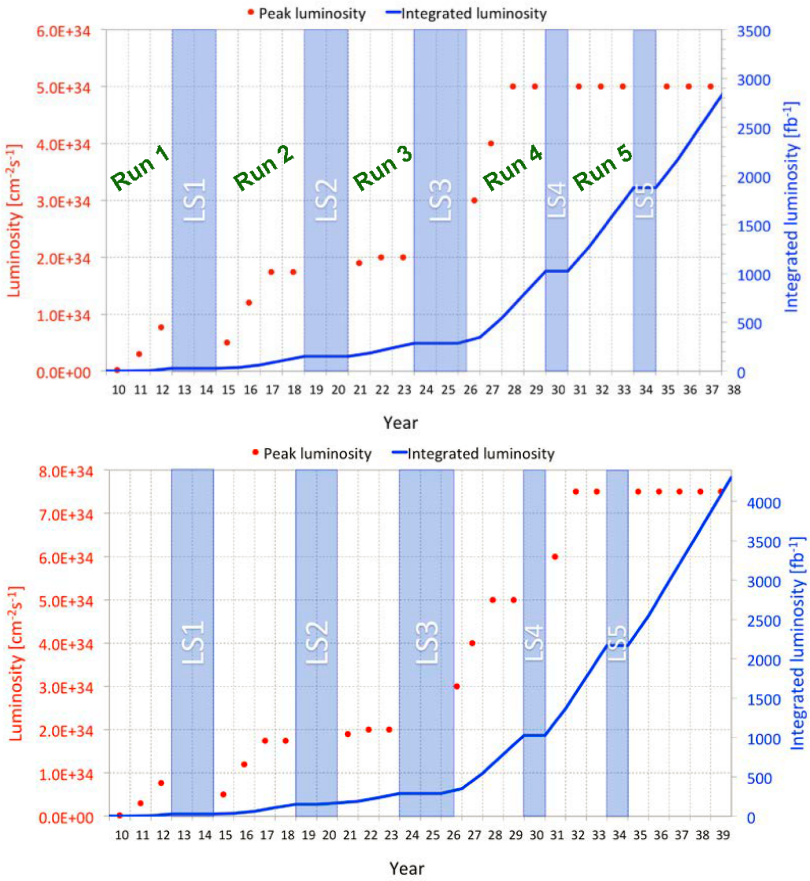

Figure 1.3: The LHC schedule and the design values (top) and ultimate figures (bottom) for instantaneous and integrated luminosity [5, 6]. The data taking periods in between the long shutdowns (LS) are labeled Run 1, Run 2, etc.

during the 'Long Shutdown 3' (LS3), see Fig. 1.3, but some installation will take place during earlier LHC shutdowns. After the LS3 the high luminosity proton-proton data taking will begin. The upgrade of the CMS detector has already started, with the insertion of 'demonstrator' GEM (Gas Electron Multiplier) muon chambers of type GE1/1 [7] in the 2016/17 winter shutdown.

Table 1.1: Characteristic parameters for HL-LHC data taking [6] in comparison to original design values [8]. The ultimate performance values of 7.5×10^{34} cm^{-2}s^{-1} and 4000 fb^{-1} might be reached by exploiting the margins of the LHC parameters.

	LHC design	HL-LHC design	HL-LHC ultimate
Peak luminosity (10^{34} cm^{-2}s^{-1})	1.0	5.0	7.5
Integrated luminosity (fb^{-1})	300	3000	4000
Number of pileup events	∼30	∼140	∼200

The CMS 13 TeV data sample of about 40 fb^{-1} recorded by the end of 2016 will thus be multiplied by a factor of more than 50. To cope with the much higher collision rate, which will go up by a factor of 5, and to fully profit from it, the CMS experiment and the muon detectors in particular need major upgrades.

The muon detectors play a central role in CMS, as stressed already by its name, Compact Muon

Solenoid. Muons can be identified and measured individually and accurately, and they stand out from the large hadronic background typical of hadron colliders. In the historic discoveries of the W and Z bosons at the CERN Sp$\bar{p}$S [9–12], the top quark at the Tevatron proton-antiproton collider at Fermilab [13, 14], and the Higgs boson at the LHC, muons played a crucial role. The most sensitive signatures of the production of new particles often include one or more muons. Therefore, CMS was built with several complementary subdetectors to identify muons, already at trigger level, and to measure their momentum and charge over a broad range of kinematics. Examples for breakthrough analyses with muons are given above (Higgs boson decay $H \to 4\,\mu$, B meson decay $B \to \mu\mu$). The forward region is particularly challenging for muon detection: on one hand, relatively light particles to be studied or searched for are produced predominantly with high pseudorapidities; on the other hand, backgrounds here are the highest.

To maintain the present excellent performance of the CMS muon system within a large geometrical acceptance, several measures must be undertaken:

- **Electronics.** The HL-LHC will produce well above 100 proton-proton interactions for every bunch crossing (pileup), taking place every 25 ns, yielding billions of secondary particles each second. Such a high rate is a major challenge for the particle detectors; it had not been envisaged as possible in the planning phase of the LHC in the 1990s. Now detector and electronics must be upgraded to handle this rate, using the latest technology such as high bandwidth optical data transfer. In addition, new requirements on the Level-1 trigger and the data acquisition in terms of latency can only be met with new electronics with deeper buffering and faster processing.
- **Longevity.** All present gaseous detectors and a large fraction of their electronics are expected to stay also for HL-LHC, so their longevity must be validated. Aging electronics parts need to be replaced by new components, if possible exploiting technology advancements. Aging of high-tech components over the long lifetime of the CMS detector of about 30 years (2008–2038) is clearly expected, as for any technical product. In addition, the high particle flux causes radiation damage to detectors as well as electronics, shortening the life expectancy even further.
- **Resolution and Redundancy.** In Phase-2 the background induced by neutrons and low energy gammas, and the large number of particles crossing the CMS detector quasi simultaneously, will be very high. This makes the association of individual hits to tracks and thus the event reconstruction a major challenge, both for the muon trigger and the offline analysis. It can be met only if the number of hits recorded for a single particle is sufficiently large, and if both the spatial resolution and the time resolution are very good. Most backgrounds and most muons are produced in the forward direction at high pseudorapidity. Currently this region in CMS is not yet fully equipped with all the muon chambers foreseen for Phase-1. In addition, the magnetic bending is reduced due to their trajectories being nearly parallel to the magnetic field lines, so that muon momentum measurement is particularly challenging here. Therefore, the forward region must be completed with the missing muon chambers, and complemented by additional muon detectors to enhance the redundancy and to resolve the track reconstruction ambiguities, already at trigger level. A precise momentum measurement by the Level-1 muon trigger is necessary to allow for a rejection of unwanted soft background muons, mismeasured as having a high momentum. In this way the trigger rate can be kept at a manageable level without an increase in p_{T} threshold, preventing a loss of new physics signatures with low momentum muons. The addition of GE1/1 detectors (already approved

for construction) during the Long Shutdown 2 is the first step in this direction. Also, if muon detectors of one type will show an unexpected problem at HL-LHC, it is essential to back them up with other muon chambers of a different type.

- **Standalone Triggering.** Standalone muon trigger capabilites are important for reconstructing long-lived BSM particles decaying into muons outside the inner tracker. In these scenarios neither a vertex constraint nor the trigger information from the tracker can be exploited. Standalone muon triggering requires a good measurement of the track bending to determine the momentum, which is possible only with several independent direction measurements, for which the additional muon chambers in the endcap regions are essential.
- **Acceptance.** The extended coverage of the Phase-2 inner tracker in the very forward region reaches to $|\eta| = 4$, well beyond the current muon detector acceptance of $|\eta| < 2.4$. The enlarged η range of the new tracker needs to be matched by a muon detector, since the silicon tracker alone cannot identify muons. The increase in acceptance is particularly rewarding for multi-lepton final states, for example in Higgs boson decays to four muons.

Another challenge to be addressed in the muon upgrade is the set of new environmental restrictions on the use of fluorine based gases. In order to comply with these constraints, the gas mixtures of some CMS muon subdetectors must be adapted, or the release of greenhouse gases into the atmosphere must be substantially reduced.

This Technical Design Report (TDR) describes the planned upgrades to the CMS muon detectors for the proton-proton runs at HL-LHC. In the following introductory sections, forming Part I of the TDR, the current CMS experiment and in particular the different muon subdetectors are briefly outlined, and the required upgrade steps for the HL-LHC phase are motivated and presented. The resulting performance is demonstrated for some physics cases in the following Section1.6. Finally the needed resources are summarized.

The subsequent chapters, forming Part II of this TDR, describe all these aspects in detail, starting from Chapter 2 dealing with the detector longevity studies. Chapters 3 through 6 are devoted to the four muon subdetectors, DT (Drift Tubes), CSC (Cathode Strip Chambers), RPC (Resistive Plate Chambers), and GEM. Muon trigger and reconstruction performance studies are the subject of Chapter 7. The physics examples presented in Chapter 8 illustrate the capabilities of the proposed muon detector upgrades. Resources and schedule are the topics of Chapter 9.

1.2 The current CMS detector

1.2.1 Overview of the CMS detector

A schematic view of one R-z quadrant of the CMS detector after Phase-2 upgrades is shown in Fig. 1.4, where the location of the muon chambers is highlighted. A detailed description can be found in Ref. [1]. CMS has a cylindrical geometry, with coordinates ϕ, θ and z. The azimuthal angle ϕ is measured in the transverse plane perpendicular to the beam, the polar angle θ defines the pseudorapidity $\eta = -\ln(\tan(\theta/2))$, and the z coordinate runs along the beam. The radius R denotes the distance from the beam axis. At the heart of the experiment is a superconducting solenoid magnet with a field of 3.8 T oriented along the beam axis, providing strong bending power for momentum measurements. The magnetic flux is returned by a large steel return yoke.

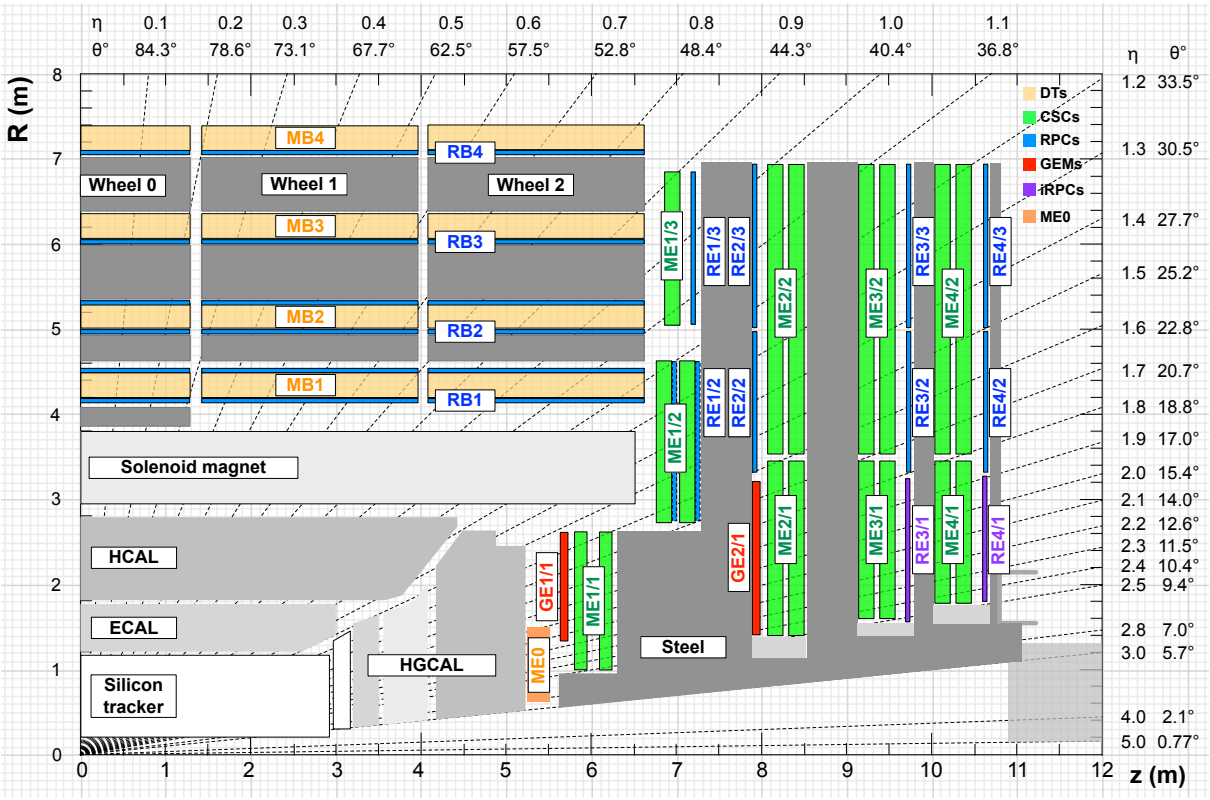

Figure 1.4: An *R*-*z* cross section of a quadrant of the CMS detector, including the Phase-2 upgrades (RE3/1, RE4/1, GE1/1, GE2/1, ME0). The acronym iRPCs in the legend refers to the new improved RPC chambers RE3/1 and RE4/1. The interaction point is at the lower left corner. The locations of the various muon stations are shown in color (MB = DT = Drift Tubes, ME = CSC = Cathode Strip Chambers, RB and RE = RPC = Resistive Plate Chambers, GE and ME0 = GEM = Gas Electron Multiplier). M denotes Muon, B stands for Barrel and E for Endcap. Labelling details are given in Section 1.2.2. The magnet yoke is represented by the dark gray areas.

Near the interaction region a silicon tracker, composed of an inner pixel detector surrounded by a silicon strip detector, measures vertices and momenta of charged particles. The electromagnetic calorimeter (ECAL) and the hadronic calorimeter (HCAL) are located inside the solenoid, measuring electromagnetic and hadronic showers with lead tungstate crystals and a scintillator-brass sampling detector, respectively.

The current silicon tracker must be replaced before the start of Phase-2, since it will suffer significant radiation damage by the end of Run 3. To maintain excellent track reconstruction at high pileup, the granularity of both the inner pixel tracker and the outer tracker will be increased, by decreasing the pixel size and by shortening the strip lengths. For the first time at CMS a momentum measurement will become possible within a few microseconds, and this information can be used in the Level-1 (L1) trigger. The track trigger will greatly sharpen the L1 p_{T} resolution, which will reduce the trigger rate at a given transverse momentum. Thus by combining input from the tracker and muon systems the p_{T} threshold for the single muon trigger can be kept low despite the high rate at HL-LHC.

The endcap calorimeters will also suffer significant radiation damage. The replacement planned for Phase-2, the High Granularity Calorimeter (HGCAL), will have an electromagnetic and a

hadronic section. It will consist of a sampling calorimeter with silicon detectors in the inner region, and scintillators as active part in the outer region. The HGCAL will allow for a three-dimensional shower reconstruction. Given its high granularity the HGCAL can also identify tracks and discriminate between charged pions and muons [15]. The efficiency and purity depends on the track length and its isolation. At trigger level the use of this information is not envisaged, while in the offline analysis muon reconstruction in the ME0 can be helped by the corresponding HGCAL hits.

The Phase-2 upgrade plans of these subdetectors are documented in separate Technical Design Reports [15–17]. In the Phase-2 simulations presented in this muon TDR the new tracker and the new calorimeters, influencing the material budget, are included. The improvements in the Level-1 trigger system are the subject of an interim report [18].

Muons are detected with multi-layer gas-ionization detectors positioned outside the solenoid. As of 2017, three types of chambers make up the CMS muon system, Drift Tube chambers (DT), Cathode Strip Chambers (CSC) and Resistive Plate Chambers (RPC). They are highlighted in Fig. 1.4 and described in detail in the original CMS muon TDR [19]. The GE1/1 installation will be completed in LS2. The chambers are sandwiched between the steel plates of the return yoke. There are four muon stations, both in the barrel and in each endcap, see Fig. 1.4. Thus a muon track is measured at many well-separated points along its trajectory. The bending angle reaches its maximum in the innermost stations, where momentum determination is most effective. Since the magnetic field directions inside the solenoid and in the return yoke are opposite, the bending decreases in subsequent muon stations.

The CMS trigger system has two stages: The hardware based Level-1 trigger (L1) uses partial information from subdetectors and makes a preselection of events at an output rate of up to 100 kHz (Phase-1). The L1 muon trigger finds tracks by combining 'trigger primitives' (track segments) as obtained by the trigger electronics of the DT, CSC, and RPC chambers. It is subdivided into a barrel muon track finder (BMTF), an endcap muon track finder (EMTF), and the track finder for the barrel-endcap overlap region around $|\eta| = 1$ (OMTF), which uses input from all three muon subdetector types. The subsequent high-level trigger stage (HLT), subdivided further into Level-2 (L2) and Level-3 (L3), uses a large computer farm to perform a full analysis of the L1-accepted events, using similar algorithms as in the offline data processing. The average HLT output rate reached 1 kHz in 2017, with an average event size of the order of 1 MB. The overall average dead time of the trigger and DAQ is below 5%.

1.2.2 The current CMS muon system

The barrel yoke and, with it, the DT and barrel RPC muon chambers are subdivided in 5 wheels, complemented by the two endcaps hosting CSCs and endcap RPCs, where the particle rate is particularly high. The different detector technologies have been chosen to optimize the CMS detector with respect to performance and cost. Most muon detectors have been operating since the start of the LHC, in the year 2008 [19, 20]. Notable exceptions are the ME4/2 CSC stations and the RE4/2 and RE4/3 RPC chambers, which have been installed during the Long Shutdown LS1, which took place in the years 2013 and 2014. The very first GEM chambers (demonstrator, of type GE1/1) were inserted in the forward region in the beginning of 2017. The Phase-2 upgrade will be a major enhancement of the current muon system.

All muon subsystems work with high efficiency and resolution, well within specifications [20–22], even at $1.7 \times 10^{34}\,\mathrm{cm^{-2}s^{-1}}$, the highest instantaneous luminosities reached by the summer of 2017. Up to 2017, in the different subdetectors no or only minor aging effects have been observed, with no impact on the overall performance.

The DT and CSC chambers are located in the $|\eta| < 1.2$ and $0.9 < |\eta| < 2.4$ regions, respectively, and are complemented by the RPC detectors in both barrel and endcaps, with a maximum pseudorapidity reaching $|\eta| = 1.9$. The use of these different technologies approximately aligns with the three regions of CMS, referred to as barrel ($|\eta| < 0.9$), overlap ($0.9 < |\eta| < 1.2$), and endcap ($|\eta| > 1.2$). The active chamber areas are arranged to overlap, avoiding gaps in the η coverage. The CSC and RPC chambers overlap also in ϕ.

The DTs are segmented in long aluminum drift cells. The position of a traversing muon is determined by measuring the drift time to the anode wire in the center of each cell, with an optimally shaped electric field. The spatial resolution per cell is 250 μm or better, which translates into about 100 μm resolution per 8-layer chamber. A DT chamber consists of three 'SuperLayers', each of them comprising four staggered layers of parallel drift cells. The wires are oriented so that two of the SuperLayers measure the muon position in the bending plane ($R - \phi$) and the third one measures the position in the longitudinal plane ($R - z$), except for the outer chambers, which have only the two $R - \phi$ SuperLayers. Because of the staggering by half cells, the trajectory of the muon and the time at which it traverses the chamber can be derived from sums and differences of drift times. Since the drift time is measured, the cell size can be relatively big, and a large detector area is built up with a modest number of readout channels. Figure 1.5 shows the layout of a single drift cell and a photo of several DT muon chambers, inside the CMS magnet yoke.

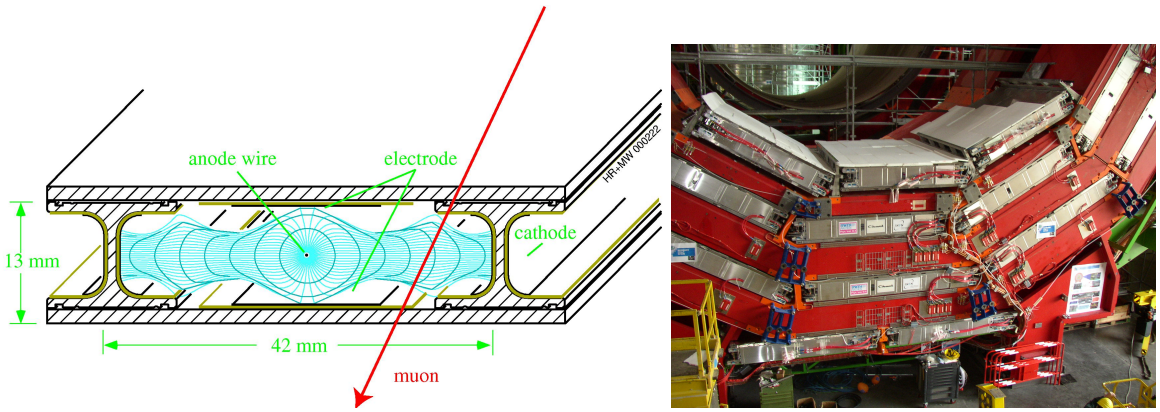

Figure 1.5: Left: Single DT cell. Right: DT chambers (aluminum) sandwiched between steel plates of the yoke (red), during installation.

The CSCs operate as standard multi-wire proportional counters with a finely segmented cathode strip readout. The strips run radially outward to measure the muon position in the bending plane, while the anode wires provide a measurement in R. The precise position in the dimension orthogonal to the strips can be reconstructed by interpolating the charges read out on the strips. Figure 1.6 illustrates the operation of the cathode strip chambers and shows some of the trapezoidal CSC chambers during installation in the CMS detector. The CSC detection technology was chosen because it provides good position and time resolution of hits along a muon trajectory, can handle high particle rates, and is able to operate in strong non-uniform magnetic fields. Each CSC chamber is made of six layers. Typical resolution figures for position and time are 50–140 μm (depending on chamber type) and 3 ns per chamber, respectively.

The RPCs are double-gap chambers operated in avalanche mode, at high electric field. They use High Pressure Laminate (HPL, commonly known as Bakelite) electrodes with a high bulk resistivity. RPCs are mainly used for accurate timing and fast triggering, with an excellent intrinsic resolution of about 1.5 ns for a double-gap chamber. This allows in particular the

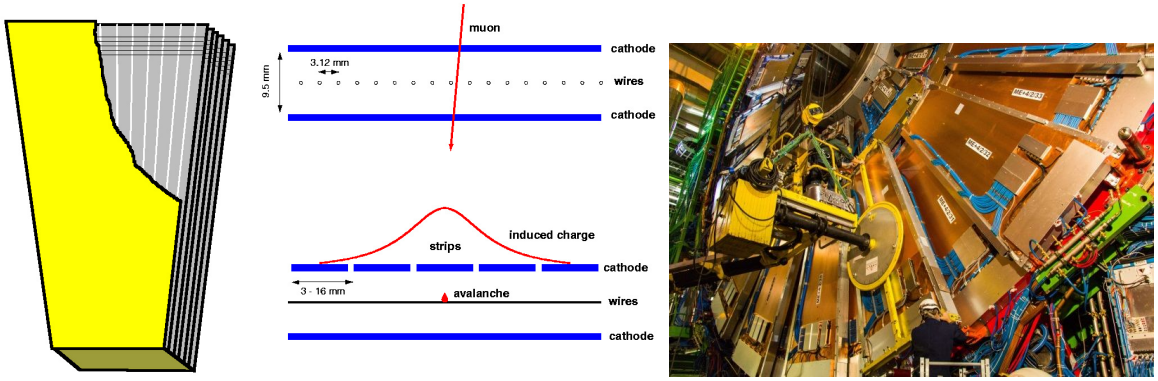

Figure 1.6: Left: Geometry of CSCs in CMS. Middle: Working principle of CSCs. Right: Outer CSC chambers ME4/2 during installation.

identification of the corresponding bunch crossing. In Fig. 1.7 the schematic layout and a photo of endcap RPCs are shown.

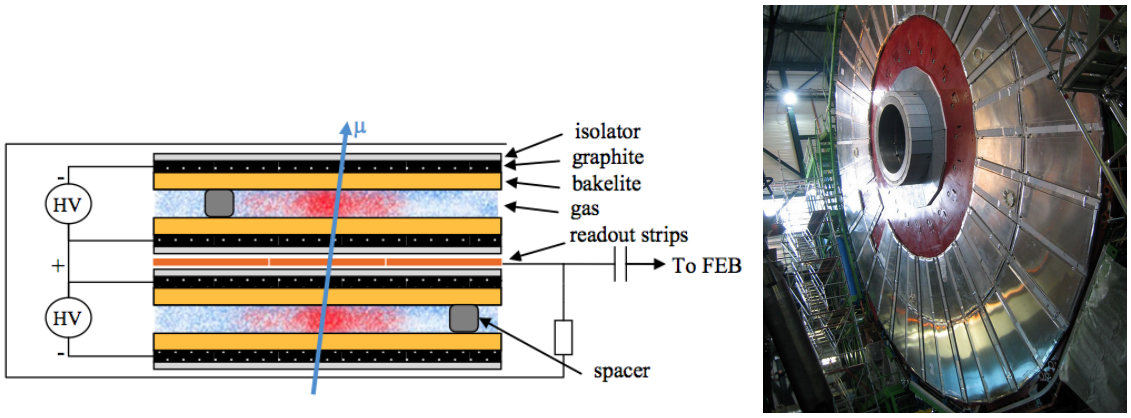

Figure 1.7: Left: Working principle of the double gap RPCs in CMS [23]. Right: RPC endcap chambers RE1/2 and RE1/3 after installation. The iron yoke is shown in red.

In the barrel, a 'station' is a group of chambers around a fixed value of R. There are four DT and RPC stations in the barrel, labeled MB1–MB4 and RB1–RB4, respectively (Fig. 1.4). The segmentation in ϕ is twelve-fold, as indicated in Fig. 1.5 (right). For the RPC system, the innermost barrel stations, RB1 and RB2, are instrumented with two RPC chambers per ϕ sector, one on each side of the corresponding DT chamber, while the outer ones, RB3 and RB4, have one chamber.

In the endcap, a station is an assembly of chambers at a similar value of z. There are four CSC and RPC stations in each endcap, labeled ME1–ME4 and RE1–RE4, respectively. A CSC station consists of six staggered layers, each of which measures the muon position in two coordinates. In the inner rings of stations 2, 3, and 4, a CSC subtends a ϕ angle of 20°; all other CSCs subtend an angle of 10°.

Using these conventions, the DTs are specified according to chamber position using the label "MBn ±w", where n is the barrel station (increasing with R) and w is the wheel (increasing with $|z|$, with w = 0 centered at z = 0). Similarly, the barrel RPCs are labeled "RBn ±w". The CSCs are labeled "ME ±n/m", where n is the station (increasing with $|z|$) and m is the ring (increasing

with R). Finally, the endcap RPCs are labeled "RE $\pm$n/m". The number of chambers per type, the number of readout channels, the achieved spatial and time resolution, and the number of active channels in 2016 are summarized in Table 1.2. All CMS muon chamber layers together have a total surface area of 28 000 m^2.

Table 1.2: Properties of the CMS muon system in the year 2016. The intrinsic spatial and time resolutions refer to a full chamber (bending projection), the value depends on chamber type.

Muon subsystem	Drift Tubes (DT)	Cathode Strip Chambers (CSC)	Resistive Plate Chambers (RPC)
$\|\eta\|$ range	0.0–1.2	0.9–2.4	0.0–1.9
Number of chambers	250	540	Barrel 480 Endcap 576
Number of layers/chamber	r-ϕ: 8; z: 4	6	2 in RB1 and RB2 1 elsewhere
Surface area of all layers	18 000 m^2	7000 m^2	Barrel 2300 m^2 Endcap 900 m^2
Number of channels	172 000	Strips 266 112 Anodes 210 816	Barrel 68 136 Endcap 55 296
Spatial resolution	100 μm	50–140 μm	0.8–1.3 cm
Time resolution	2 ns	3 ns	1.5 ns*
Fraction of working channels	98.4%	99.0%	98.3%

*The intrinsic RPC time resolution is currently not fully exploited, since the DAQ system records the hit time in steps of 25 ns. Section 1.4.3 proposes upgrades to exploit it.

1.3 Operational conditions and longevity at the HL-LHC

1.3.1 Data and trigger rates

The LHC was originally designed for an instantaneous luminosity of $10^{34}\,cm^{-2}s^{-1}$ [8] and an integrated luminosity of the order of 300 fb^{-1}. With the 25 ns time interval between subsequent bunch crossings, the average pileup (pp collisions per bunch crossing) is close to 30. Already in the years 2015–2017 the peak luminosity exceeded the design value by a factor of more than 1.7, bringing some CMS subsystems close to their rate capability limits.

The increase in luminosity at the HL-LHC, as summarized in Table 1.1, has many implications on the CMS subdetectors. It leads to more pileup, which leads to worse background conditions, higher trigger rates, more difficult event reconstruction, and accelerated aging of components.

Some important requirements on the CMS muon detectors to be fulfilled at HL-LHC running are shown in Table 1.3. They are compared to the maximum values that the current CMS detector can handle or is certified for, and to the performance parameters expected from the upgraded muon detectors. The higher L1 accept rate is necessary to cope with the HL-LHC luminosity without raising the trigger thresholds [24]. The increase in latency (the time during which the raw data information must be stored awaiting for a Level-1 trigger decision) from 3.6 to 12.5 μs is a direct consequence of the new Level-1 track trigger envisioned for the upgraded silicon tracker [18]. Table 1.3 shows that the current DT and CSC detector electronics systems (in their entirety or partially) are not designed to handle the new requirements, while the upgraded electronics can cope with the HL-LHC conditions. The current RPC system is able to operate also at HL-LHC rates.

Table 1.3: HL-LHC CMS requirements (design values) on the detector performance compared to the upper limits of the current and Phase-2 upgraded DT and CSC systems. The numbers given do not include any safety factor.

	HL-LHC needs	CMS 2017	CMS upgraded
Level-1 trigger accept rate (kHz)	500	DT: <300 CSC: <250	DT: $\gg 500$ CSC: 4000
Level-1 latency (μs)	12.5	DT: 20 CSC: 3.6	DT: $\gg 12.5$ CSC: 28.8
Total DAQ data transfer rate (Gbit/s)	DT: 1082 CSC: 1026	DT: 42 CSC: 230	DT: 3600 CSC: 2764

1.3.2 Aging and longevity tests

Aging, in particular in the presence of radiation, affects both the gaseous detectors and electronic components. For example, deposits on the anode wires can result in a decrease of gas gain and hit-efficiency losses. Background hit rates can rise as well, eventually leading to a high voltage breakdown inside the detector. Radiation damage of the silicon substrate in electronic chips can lead to noisier electronics performance and even fatal failures of entire electronics boards. The phenomena are complex, but in general the performance of gaseous detectors deteriorates with an increase of the integrated charge released in the gas volume, expressed in either C/cm for wires or C/cm^2 for surfaces. For the electronics longevity, the relevant quantities are the integrated neutron flux, or fluence, measured by the number of neutrons per cm^2, and the total ionization dose (TID), measured in Gray (Gy) or Rad units.

Catastrophic interactions of a single particle (usually a neutron) with the electronic chip material, so-called single-event effects (SEE), can cause electronic circuits to fail temporarily or permanently because of severe damage in the crystal lattice triggered by such an interaction. Temporary failures are associated with memory or communication signal bit flips and can be restored by reloading those memory chips or recycling power on electronics, neither of which can be done too frequently without disruption to the data-taking activities.

Table 1.4 summarizes the integral doses expected in the CMS muon detectors at the end of the HL-LHC running. These numbers follow either from the recent HL-LHC CMS background simulation (for electronics and new GEM detectors) or from extrapolating hit rates, which are also listed, and currents measured during recent running periods (for DTs, CSCs, and RPCs). The table does not include any safety factor.

Due to the complex physics and chemistry of the aging phenomena, it is known that the accelerated aging tests are indicative, but not exactly quantitatively predictive. Hence, in the tests that were performed, the detectors and electronics are subject to radiation doses at least a factor of three larger (safety factor) than what can be presently expected to integrate over the HL-LHC lifetime (3000 fb^{-1}).

For the current components of the CMS muon detectors, many irradiation tests were performed at the time of development and prior to installation. It was shown that the present-day detectors and their electronics would function well for more than 10 years at the nominal LHC operation conditions.

In order to study the longevity of detector components in the context of HL-LHC radiation doses, the GIF++ test zone (Gamma Irradiation Facility) started user operation at CERN in 2015 [25], replacing its predecessor GIF [26]. It consists of an intense 14 TBq (in 2015) ^{137}Cs

Table 1.4: Integral radiation dose, hit rate and accumulated charge for the CMS muon detectors after Phase-2 upgrades, at the end of HL-LHC running, assuming an instantaneous luminosity of $5 \times 10^{34}\,\mathrm{cm}^{-2}\mathrm{s}^{-1}$. Only the worst-case values are given. The neutron fluences are given with no cuts on the neutron kinetic energy. Neutron fluences and total ionization doses are relevant for electronics. Charges expected to be accumulated in the chamber gas volume are relevant for the detector longevity. The numbers shown do not include safety factors. The new improved RPC chambers are referred to as iRPCs, to be installed next to ME3/1 and ME4/1 CSC chambers. The column 'RPC' refers to the RPC chambers already present in the year 2017.

	DT	CSC	RPC	iRPC	GE1/1	GE2/1	ME0
$\lvert\eta\rvert$ range	0-1.2	0.9-2.4	0-1.9	1.8-2.4	1.6-2.15	1.6-2.4	2.0-2.8
neutron fluence (10^{12} n/cm^2)	0.4	40	1	7	20	12	200
total ionization dose (kRad)	0.12	10	2	3	3	7	490
hit rate (Hz/cm^2)	50	4500	200	700	1500	700	48000
charge per wire (mC/cm)	20	110	-	-	-	-	-
charge per area (mC/cm^2)	-	-	280	330	6	3	280

source emitting 662 keV photons. The main source of background hits in the muon detectors are neutron-induced photons with an energy in the range 0.1–10 MeV. Thus, GIF++ provides a fairly realistic simulation of the HL-LHC conditions. The cesium source is complemented by a 100 GeV muon beam produced with the SPS. These muons provide excellent probes for detector performance studies in the presence of high radiation.

The ongoing longevity tests show that most of the existing chambers are expected to operate until the end of Phase-2 with no or little, and therefore acceptable, losses in efficiency. Only in the outermost DT chambers (MB1 chambers in the large-z wheels and the MB4 chambers, see Fig.1.4) a significant deterioration is predicted; mitigation measures are being actively explored, as discussed below and in Section 3.2. On the other hand, several electronics components are predicted to fail, or their survival cannot be guaranteed until the end of Phase-2. Thus, they need to be replaced, as detailed in the following chapters.

The new muon detectors that are to be installed as part of the detector upgrades (GEMs and iRPCs) are designed to maintain excellent performance throughout the HL-LHC operation. To verify their radiation hardness at the required level, tests of prototype detectors are being made at the GIF++ facility, and they will be continued over the next years. The preliminary results obtained so far are reassuring.

To project the long term deterioration of the present muon detectors and electronics for the next 20 years, an aging model has been developed, based on measured and estimated failure rates as a function of radiation dose and time. In the following chapters the performance of the 'aged Phase-1 detector' is compared to the Phase-2 muon system, clearly demonstrating that the proposed upgrades are required to retain the present performance of the muon system.

1.3.3 Environmentally-friendly chamber gases

The CSC and RPC detectors use gas mixtures with a fluorine component (F-gases). For example, 40% Ar + 50% CO_2 + 10% CF_4 is the present CSC chamber gas. The CSC and RPC gas compositions were optimized with respect to gas gain, drift time, quenching, aging, and they have proven to work very well. However, the European regulations of 2014 [27] call for restricting the use of fluorine-based gases to one-fifth of their consumption in 2014 by 2030. The regulation is due to the undesired environmental impact of such gases, notably because of their

greenhouse effect, leading to global warming. Studies of CSC and RPC detector operation with alternative, ecologically friendlier gas compositions are underway. In case a complete elimination of F-gases is not feasible, several measures to stop the release of these components into the atmosphere are being explored: preventing leakage, efficient recuperation, and burning of the exhaust gas into harmless compounds. Thus, the new environmental regulations can be handled, and a significant performance loss of the CMS muon chambers will be avoided.

1.4 Upgrade of the existing muon detectors

The existing DT, CSC, and RPC detectors are all essential for identifying and measuring muons at the required precision and accuracy needed to fulfill the CMS physics program. Therefore, it must be guaranteed that their performance will be sustained at high luminosity. This requires several upgrades of their electronics, which are described in the following three Sections (DTs, CSCs, and RPCs).

1.4.1 Drift Tube chambers

The DT chambers and on-chamber electronics should continue to work at the HL-LHC. However, the 'Minicrate' electronics attached to each chamber will need to be replaced for several reasons. A detailed description of all tests and studies performed, and more thorough explanations of the DT system upgrade scope are given in Chapter 3.

1.4.1.1 Longevity tests of the present DT detectors

The hit rates in the DT chambers at the HL-LHC will be up to about 50 kHz per drift cell. The highest rates are expected for the MB1 chambers in the large-z wheels (these DTs receive the highest photon and charged particle rate within the DT system) and for the MB4 chambers, exposed to a high neutron-induced background coming back from the cavern. The highest integrated charge in DTs per unit of wire length is estimated to be of the order of 20 mC/cm.

Measurements performed on a MB1 spare detector at the GIF++ radiation facility show that the DT chambers can handle the hit rate expected during Phase-2. The GIF++ longevity tests demonstrate that all MB2 and MB3 chambers, as well as the MB1 chambers of the three low-z wheels will maintain their current level of performance during Phase-2. Only in the MB1 stations in the outer wheels and in the MB4 detectors, a significant drop of the hit efficiency is predicted. The loss of efficiency is due to a decrease of the gas gain caused by deposits forming on the anode wires. The main culprit is believed to be outgassing of DT materials.

The hit efficiency of the MB1 chambers in the two outer wheels ($\sim$10% of the chambers) is expected to drop below 50% during HL-LHC operation, if the expected radiation dose is scaled up by a safety factor of three (87% if no safety factor is applied) and only conservative mitigation measures are taken, which touch the DT system only a little. However, since for each muon track, a large number of hits is measured (more than 40 in the pseudorapidity range covered by the DT system), even a 50% per-layer loss in DT efficiency translates into a small reduction in the track reconstruction efficiency, which will remain above 90 (95)% in the barrel (barrel-endcap overlap) pseudorapidity range. Therefore, we conclude that the current DT chamber system should be able to work throughout the Phase-2 operation period and a replacement is not needed.

Furthermore, possible mitigation measures of the aging effects are being actively studied. They include an increase of high voltage, lowering of front-end electronic thresholds, an increase

of the gas flow, etc. For MB4 chambers, background rates can be reduced by improving the neutron shielding of these detectors.

The DT front-end electronics and high voltage boards are sufficiently radiation hard and do not need to be replaced.

1.4.1.2 Motivation for DT upgrades

The Minicrate electronics (MiC) are attached to each chamber, hosting readout and trigger electronics. The current version (MiC1) needs to be replaced for HL-LHC operation by improved Minicrates (MiC2) for the following reasons:

- The maximum Level-1 trigger rate that the present DT electronics can handle is 300 kHz, while the Phase-2 CMS requirement is 500 kHz for the HL-LHC design parameters and 750 kHz for the ultimate scenario.
- Some of the electronics components are not sufficiently radiation hard as tests at the PSI in Switzerland have shown. Given the accumulated DT operation experience, the longevity of some other Minicrate parts cannot be guaranteed either. Figure 1.8 illustrates the projected degradation of the current DT system because of aging of the MiC1. Depending on the assumptions made, 19–46% of all channels will fail after about one third of the expected HL-LHC luminosity. Note that a failure of a single Minicrate board turns off many neighboring cells simultaneously, up to a full chamber. This is much worse than failures of individual cells randomly distributed over the muon system.

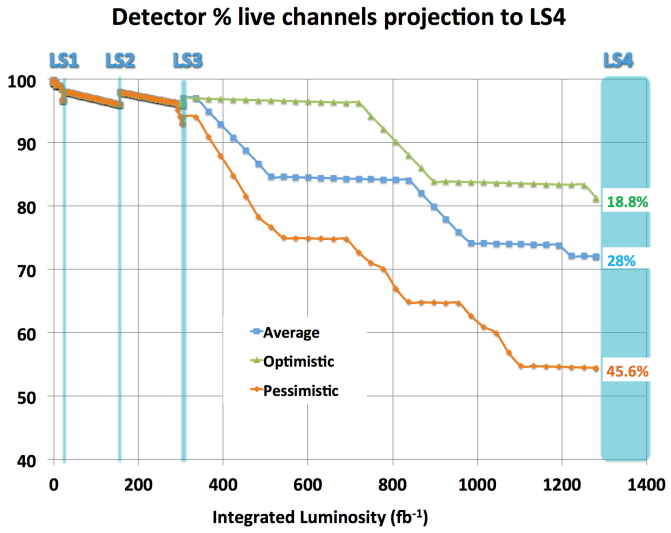

Figure 1.8: Extrapolated fraction of live channels as a function of integrated luminosity if the MiCs would not be replaced in LS3. Note that the horizontal scale covers only 1/3 of the HL-LHC luminosity, up to the first LS in the HL-LHC running period. The three aging scenarios shown (optimistic, pessimistic, average) result from different assumptions on the uncertainties coming from irradiation tests and on the expected dose profile.

In the new DT system the complex trigger logic will be moved to the CMS underground control room and will become accessible all the time. The Minicrate functionality will be reduced; the trigger and event building logic will be transfered to the back-end electronics. The MiC2 will send the DT time digitization (TDC) data to the back-end, located outside the experimental cavern, via fast optical links. Advantages of this new architecture are as follows:

- The current system severely constrains the 'trigger primitive' algorithms that can form patterns only from hits in a small region inside a single SuperLayer, and are thus limited in complexity and connectivity. The new electronics architecture will allow the trigger primitive algorithms to use much more information, from SuperLayers in different stations.
- The Minicrates are only accessible when the barrel iron yoke wheels are moved apart, implying that maintenance is possible only every few years, during long shutdowns. By relocating the trigger functionality out of the cavern, fewer Minicrate interventions will be necessary.
- The Minicrate power consumption is much reduced and the associated cooling requirements are lowered.

1.4.1.3 Upgrades of the DT system

In LS3 the MiC1 must be replaced by new Minicrates MiC2, which will be able to cope with the Phase-2 conditions in terms of latency, readout rate and trigger rules. The new back-end electronics, located outside the experimental cavern, will contain all trigger and event building logic. This has two advantages: (a) the trigger algorithms can be developed to become more powerful, (b) constraints on the CMS DAQ conditions (readout rate, latency) are removed from the front-end, and (c) the accessibility to the complex decision-making hardware is no longer a problem.

The new On-Board electronics for DT boards (OBDT, described in more detail in Section 3.3) are the heart of the MiC2. The OBDT receives signals from each anode wire and assigns a digital timestamp. It hosts a multi-channel TDC implemented in four radiation hard FPGAs and its associated services. The data are transfered out of the experimental cavern using CERN-developed high bandwidth optical link technology. Figure 1.9 compares the current and the Phase-2 DT electronics schemes. The MiC2 design also brings the advantage of reducing the power consumption, and so requires fewer low voltage power supplies and reduces the needed cooling system capacity. While the 250 rather big MiC1 each read out a full chamber, the MiC2 will be smaller, one MiC2 corresponds to one DT SuperLayer, except in the ϕ SuperLayers of the large MB3 and MB4 detectors, requiring two MiC2 per SuperLayer, making a total of 940 MiC2 and OBDTs in the DT system. This greatly facilitates the Minicrate exchange during LS3 and maintenance operations in the following years.

The 'trigger primitive' algorithms currently run in the relatively power-demanding BTI ASIC (Bunch and Track Identifier, inside MiC1), which runs at 80 MHz with 400 ns deadtime. It calculates track segments from hits generated in collisions spread along several bunch crossings, from only a small group of neighboring cells in one SuperLayer. In the proposed upgrade, the trigger primitive generation will be performed outside the experimental cavern, in the service cavern, using the latest commercial FPGAs. Full chamber information with the best Drift Tube time resolution of about 2 ns will be available to improve the current DT trigger primitives in terms of more precise and robust bunch crossing identification, better spatial resolution (almost as good as at the offline level), and better ghost track rejection. The number of primitives per event will no longer be limited as during Phase-1. As the information from the full DT system will be sent to the service cavern, the trigger primitive generation is no longer physically constrained to a single chamber, sector, or wheel. It will be able to combine information from several chambers, which will greatly help in the regions with weaker acceptance such as the wheel interfaces, for tracks close to an eventual local hardware failure, and where the background conditions are more stringent. The trigger and readout algorithms for the ϕ view

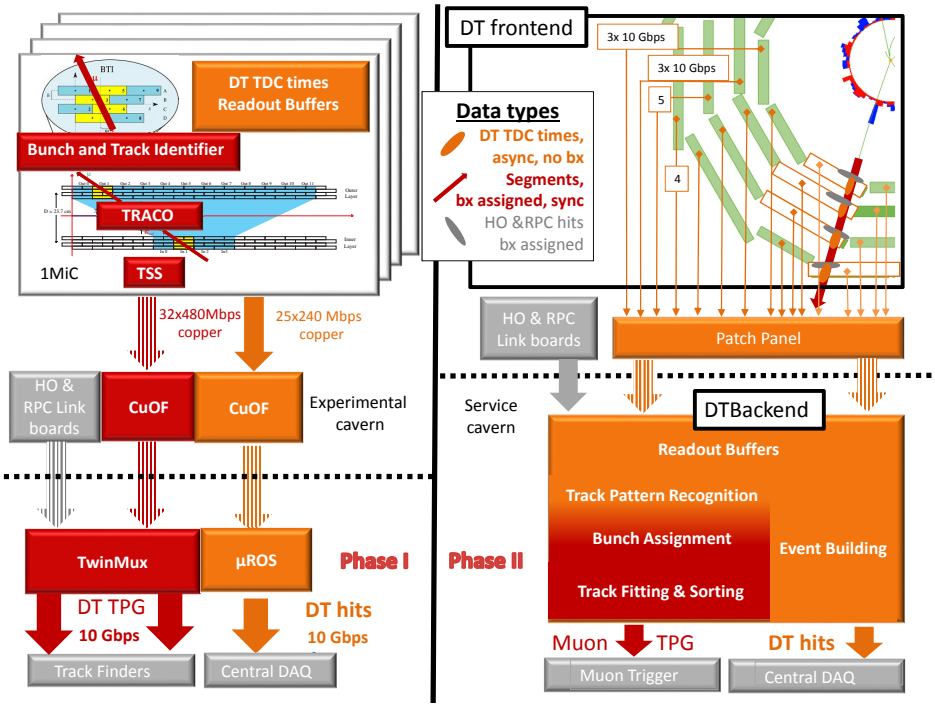

Figure 1.9: Current (left) and upgraded (right) DT electronics. In the Phase-1 version each Minicrate MiC1 sends the data via copper-to-optical-fiber translators (CuOF) to the service cavern, where the TwinMux system combines and transmits the trigger primitives (TPG), including data from the RPCs and outer hadron calorimeter HO. The μROS modules collect the TDC data and send the events to the CMS data acquisition system. In Phase-2 (right part of figure) the new Minicrates (MiC2) send TDC data from the chambers via optical links to a patch panel inside the experimental cavern, from where they are transfered to the back-end, which performs triggering and event building.

of one sector (out of $5 \times 12 = 60$) can fit in one FPGA-board, while the less numerous θ view SuperLayers can fit in altogether 24 such boards, see diagram in Fig. 1.9. The new back-end system will combine also muon data from the RPC chambers and the Hadron Outer scintillators. In addition, a final layer for cleaning duplicates and data concentration with 12 boards will be needed, giving a total of 96 boards. The slow-control links and the logic for the DT front-ends can be accommodated in 30 more cards, 6 per wheel, based on lower-power and lower-cost FPGAs.

Table 1.5 summarizes the main new hardware components needed for the DT upgrade. The installation of the new Minicrates MiC2 will have to be accomplished in LS3. The best way is to keep the old MiC1, and to put three small boxes with the new MiC2 on top of one old one. The required space is available.

1.4.2 Cathode Strip Chambers

1.4.2.1 Longevity tests of present CSC detectors

The cathode strip chambers (CSCs) cover the CMS endcap regions corresponding to $0.9 < |\eta| < 2.4$, as shown in Fig. 1.4, and, as a result, the radiation dose they are subjected to is significantly larger than for the muon chambers located in the barrel (DTs and RPCs). The highest neutron

Table 1.5: Main hardware components needed for the DT Phase-2 upgrade, excluding spares.

Component	Number
Minicrate MiC2	940
Back-end boards	96
Data links	3616
Slow-control links	30

fluence and total ionization dose, corresponding to 10 years of HL-LHC running, will reach about 4×10^{13} neutrons/cm^2 and 10 kRad, respectively. The total charge released in the gas volume per unit of wire length will be ~ 0.2 C/cm for the CSCs closest to the beam line.

Longevity tests at the GIF++ facility of chambers of both ME2/1 and ME1/1 types (the latter with thinner wires, smaller gas gaps, and different materials than the chambers from other stations) have been performed since 2015. The integrated dose achieved by the fall of 2017, equivalent to a charge of 0.36 C/cm, corresponds to about twice the amount of charge expected for 10 years of HL-LHC running. No significant deterioration of key chamber parameters such as gas gain, detection efficiency, spurious signal rates, strip-to-strip resistance, or dark currents has been observed. Thus, it is expected that the CSCs themselves can be used until the end of the HL-LHC operation.

EU regulations of greenhouse gases will severely restrict, or even ban the use of CF_4, a gas that currently makes up 10% of the CSC gas mixture and has a critical role in the longevity of CSCs by etching away harmful deposits on the anode wires. Tests with a reduced amount of CF_4 and the search for more ecologically-friendly substitutes are ongoing. These tests are being carried out in small CSC prototypes, approximately 30 cm $\times$ 30 cm in size. If an adequate substitute gas is found, larger size chambers will be prepared for tests at the GIF++ in 2018.

A program of radiation testing was carried out to identify electronic components that are sufficiently robust to function reliably in the radiation environment of the endcap muon system. It was found that all the components used in both the old and the upgraded read-out boards can withstand the expected HL-LHC doses with safety factors of more than three, except for the PROMs used in the front-end boards installed in the ME1/1 chambers, which have safety factors of only 1–1.5, and have to be replaced by radiation hard FPGAs.

1.4.2.2 Motivation for CSC upgrades

While the CSC modules are expected to provide satisfactory performance throughout the HL-LHC program, some CSC read-out electronic boards will need to be replaced in order to handle the more stringent trigger requirements. In general, the new boards will cope with higher L1 trigger rates and chamber occupancies by employing high-speed output optical links and faster processors. Similarly, the extended trigger latency requirement can be met with deeper (digital) buffers.

The current cathode front-end boards (CFEBs) use analog charge storage, realized as switched capacitor arrays, to store the signal waveforms produced on the cathode strips. These capacitor arrays are capable of storing 96 charge measurements during the Level-1 trigger latency corresponding to a total of six events worth of data. Upon receiving a L1 accept signal, CFEBs set aside and digitize the charge measurements around the L1 time and the digital output is transferred to the data acquisition mother boards (DMBs). In parallel, fast trigger information is sent to the trigger mother boards (TMBs). These CFEBs are used on all CSCs except for those in the ME1/1 ring. This ring was equipped with digital cathode front-end boards (DCFEBs) in

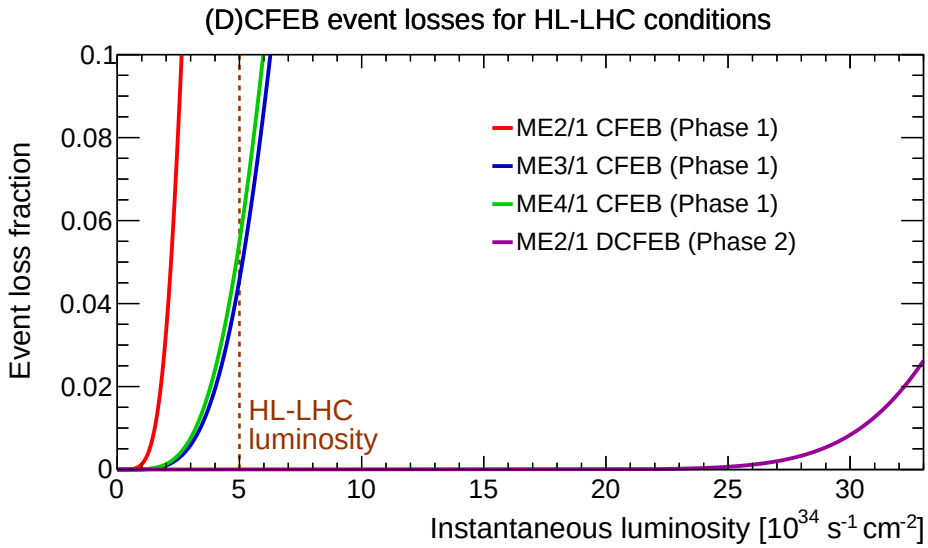

Figure 1.10: CFEB (Phase-1) and DCFEB (Phase-2) event loss fractions for HL-LHC conditions in the inner CSC rings ME2/1, ME3/1, and ME4/1 as a function of instantaneous luminosity. The design HL-LHC luminosity of 5×10^{34} cm^{-2}s^{-1} is marked by the dashed brown vertical line. The event loss fraction for the upgraded electronics, the curve in magenta, is negligible for all CSC stations at the HL-LHC luminosity.

2013–2014 to improve rate capability. In the ME2/1, ME3/1, and ME4/1 rings, which are also close to the beam, the HL-LHC trigger latency of 12.5 μs and the L1 trigger rate of 750 kHz will cause frequent memory overflows and large readout inefficiencies. Figure 1.10 shows the average event loss fraction for those stations as a function of the instantaneous luminosity. These curves are based on a statistical model that has been verified by measuring the loss rates in bench tests that emulate expected background and L1 trigger rates. Neither a safety factor nor uncertainties pertaining to the extrapolation to high luminosity are included. The figure shows that the data loss rate would increase dramatically at the HL-LHC if the current CFEBs were maintained.

The anode local charged track boards (ALCTs) detect the charge deposits on the CSC anode wires, form the corresponding trigger primitives, and send all this information to the DAQ upon receiving a L1 accept signal. With an increased L1 trigger latency time, these boards will not have sufficient FPGA memory resources to keep all the raw hit information. Moreover, the output bandwidth for the boards in the rings closest to the beamline (ME1/1, ME2/1, ME3/1 and ME4/1) will be insufficient for the expected HL-LHC data rates. Thus, all ALCT mezzanine boards will need to be replaced as well, except those in ME1/1 and ME4/2 chambers that were upgraded during LS1. In addition, the radiation hardness of the ALCT boards currently in ME1/1 is a concern, so they will be moved to ME3/1 and new radiation-hard ALCTs will be installed in ME1/1.

The low voltage (LV) and high voltage (HV) systems will also need to be upgraded to ensure the reliable operation of the CSCs at the HL-LHC. The new electronics will consume more power, which will require the redesign of the LV system with higher maximum currents and appropriate voltage levels. Higher background rates and the need for a more accurate monitoring of CSC currents will also imply an incremental upgrade for the present HV system.

Finally, the L1 trigger rates will be too high for the current output bandwidth of the DMBs, so these boards, together with the back-end modules that collect the CSC data and send it to the

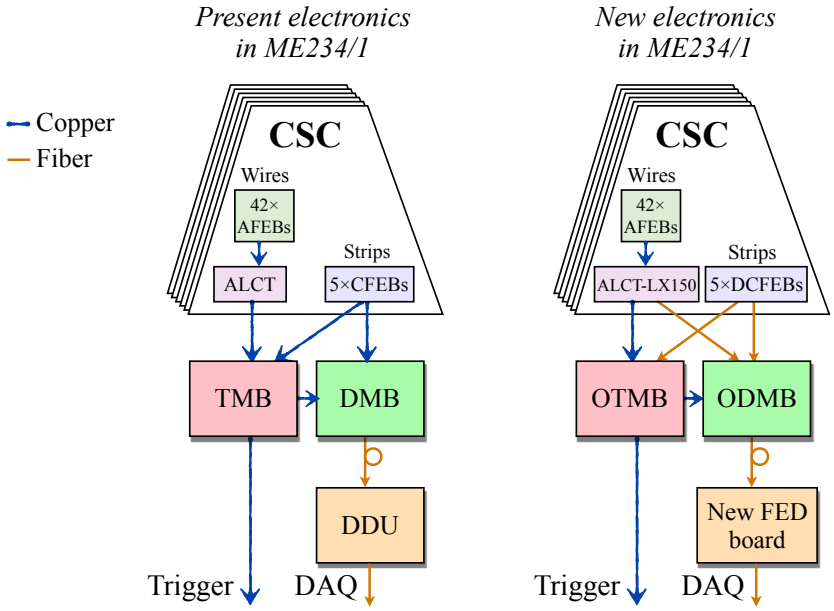

Figure 1.11: Simplified schematic of the current (left) and of the new (right) CSC electronics for the inner rings formed by ME2/1, ME3/1 and ME4/1. The orange lines mark optical data transfer, the blue lines represent copper cables.

CMS DAQ, will need to be upgraded as well.

In summary, the CSC upgrades are needed for the following principal reasons:

- The increase of the trigger latency from 3.6 to 12.5 μs would overflow the pipelines of the CSC front-end boards.
- The Level-1 trigger rates would be too high for the current output bandwidth of the data acquisition boards.

1.4.2.3 Upgrades of the CSC system

Figure 1.11 shows a simplified overview of the CSC electronics upgrade. Given that the installation schedule in LS3 is driven by the replacement of various detectors elements in the barrel region, most of the CSC replacements that require chamber access will be performed ahead of that, during LS2.

All the CFEBs in the radially innermost CSCs will be equipped with slightly modified DCFEBs to cope with the HL-LHC requirements. The DCFEBs use 12-bit 20 MHz flash ADCs and powerful Virtex-6 FPGAs with large internal memory resources. The resulting digital pipeline can hold up to 700 events, which leads to negligible dead time at the HL-LHC (Fig. 1.10). Additionally, radiation tests of the XCF128X PROMs employed in the current DCFEBs show that they may not withstand the radiation doses expected at the HL-LHC. Thus, the new DCFEBs are being designed with an option that employs the CERN-designed GBTx ASIC to allow for the remote programming of their FPGAs. These new boards will be installed in the ME1/1 chambers, thus mitigating any risks associated with the longevity of their PROMs, and the DCFEBs currently in the ME1/1 ring will be moved to other chambers in the ME2/1, ME3/1, and ME4/1 rings subject to much lower levels of radiation.

The DCFEBs send the trigger data via 3.2 Gb/s optical links, so the TMBs servicing the inner

rings will be upgraded to optical TMBs (OTMBs). The low voltage distribution boards (LVDB) that supply power to the DCFEBs will be upgraded as well.

The mezzanine boards for the ALCTs in both the inner and outer CSC rings (396 chambers in total), not including the already upgraded ME1/1 and ME4/2 rings, will be upgraded with more powerful Spartan-6 FPGAs. The inner ring boards will also incorporate optical links to cope with the HL-LHC data rates that will provide an output bandwidth of up to 6.4 Gb/s, ten times higher than previously. Finally, the boards to be installed in ME1/1 will be outfitted with the same remote FPGA programming option that the new DCFEBs will have, thus mitigating any risks associated with the aging of the PROMs in that ring.

Similarly, the DMBs in the inner rings will be upgraded with new optical DMBs (ODMBs) to handle the HL-LHC data rates. These boards will have output bandwidths of up to 25.6 Gb/s, achieved with multiple 6.4 Gb/s links. The back-end electronics collecting all the CSC data will be upgraded accordingly.

Altogether, a total of 1044 on-chamber electronics boards and 302 trigger and DAQ modules will be replaced in the CSC system. Table 1.6 summarizes the main new hardware components needed for this upgrade.

Table 1.6: Main hardware components needed for the Phase-2 upgrade of the CSC system, excluding spares.

Component	Number
DCFEB	540
ALCT	396
OTMB	108
ODMB	180
LVDB	108

1.4.3 Resistive Plate Chambers

For the RPC system two upgrade measures are foreseen. The current RPC chambers can operate until the end of Phase-2, but the link system, which connects the front-end board to the trigger processors, must be exchanged, as developed below in this Section. In addition, new detectors for the forward region, RE3/1 and RE4/1 are proposed, see Section 1.5.1 below.

1.4.3.1 Longevity of present RPC system

Figure 1.12 shows the rate (frequency of hits per area) as measured in 2016 in RPC regions with the highest background, as a function of instantaneous luminosity. The fits show a linear behavior. Extrapolating to the ultimate HL-LHC luminosity, and including a safety factor of three, gives a maximum rate of $3 \times 200 = 600\,\mathrm{Hz/cm^2}$ for the present RPC chambers, and $3 \times 700 \approx 2000\,\mathrm{Hz/cm^2}$ is predicted for the new RE3/1 and RE4/1 detectors. The corresponding maximum integrated charge in the hottest areas of the current RPC system is $3 \times 0.28 = 0.84\,\mathrm{C/cm^2}$ for the full Phase-2 running period. In the past, long-term irradiation tests were carried out, certifying the RPC performance up to an integrated charge of $0.05\,\mathrm{C/cm^2}$ for full chambers. Extensive tests with spare RPC chambers at the GIF++ zone are being performed with the plan to reach $0.84\,\mathrm{C/cm^2}$, by the middle of 2018. In these studies no degradation in efficiency as a function of integrated charge has been observed so far (summer 2017, $0.21\,\mathrm{C/cm^2}$). During Run 1 the RPC system did not show any aging symptoms. Tests at the GIF++ with muon beam also show that the efficiency for the present RPC chambers decreases

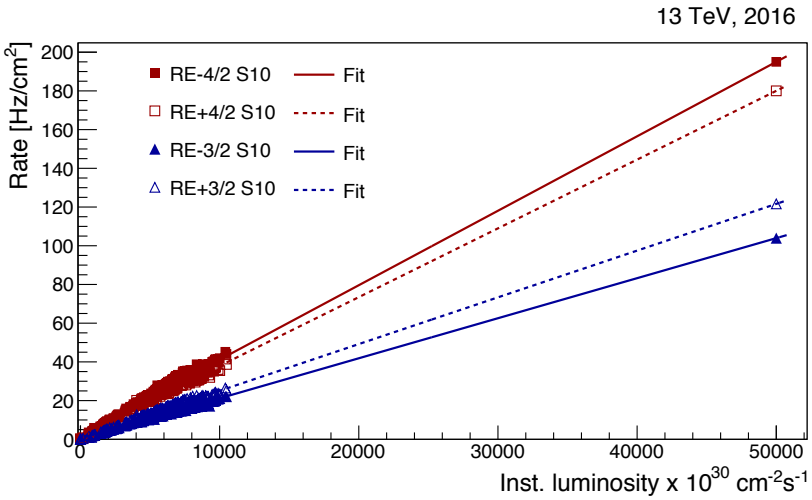

Figure 1.12: Measured hit rate for RE3/2 and RE4/2 chambers as a function of instantaneous luminosity. Both positive and negative sides (+z and −z) are shown. S10 refers to ϕ sector 10 (top of the detector), where the rate is highest.

only slightly with rate, from about 97% at low rates to 95% at 600 Hz/cm^2, thus the RPC performance remains good and the chambers do not need to be replaced.

All other RPC electronics boards including front-end electronics are evaluated to be radiation hard and can stay for the Phase-2 running.

1.4.3.2 Motivation for upgrade of RPC link system

The data from the RPC front-end boards are sent to trigger and readout via a link system. The current link system is made of electronic boards using obsolete IC components, most of them not available anymore on the market. In addition, the amount of spare boards of the present link system is quite limited. These boards have also weak electronics components, which can be disturbed by electromagnetic noise and that are not certified for the full HL-LHC lifecycle. The upgrade of the link system will make the RPC system robust against such effects. In addition, the upgraded system will exploit fully the intrinsic time resolution of the RPC chambers, which is of the order of 1.5 ns. The present link system records the hit time in steps of 25 ns, synchronized with the LHC bunch crossings. This limitation can only be removed by exchanging the existing link system by an upgraded one. An improvement of the RPC time resolution by more than one order of magnitude has several advantages:

- background hits arriving out of time can be identified and removed,
- triggering on slow heavy stable charged particles becomes possible, and
- the synchronization of the RPC system is facilitated.

Figure 1.13 illustrates the gain in timing accuracy by the upgraded link system. The resolution achievable is about a factor of two better than the DT and CSC detectors alone can provide.

1.4.3.3 Upgrade of the RPC link system

The new link system consists of 1376 Link Boards, in addition new Control Boards and optical links will be built. The old Link Boards use ASICs that are to be replaced by fast FPGAs. The new FPGAs can process several signals from many RPC detectors in parallel, so that the

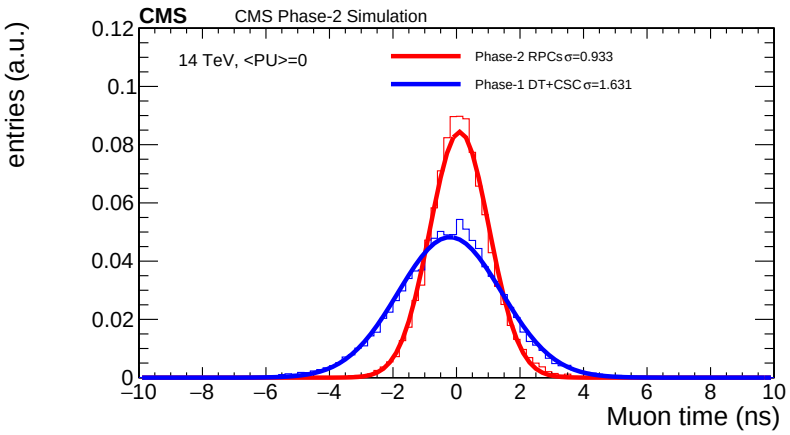

Figure 1.13: Simulated time residuals between reconstructed and true times associated to a muon, once without (blue) and once with (red) the upgraded RPC link system.

required speed can be reached easily. The new Control Boards will send data in parallel to the main computer via Ethernet, replacing the current token ring logic. The Link Boxes, the crates that house the Link and Control Boards, will stay. The long term resistance to radiation is guaranteed, since the total ionization dose in the link boards at HL-LHC is expected to be below 100 Rad, well below the tolerated dose of few kRad. However, single event upsets (SEU) in FPGAs cannot be avoided and their effect must be mitigated; this can be achieved by error correction code and/or by regularly reloading the configuration data.

Table 1.7 summarizes the main hardware components needed for the new RPC link system (not including the components needed for RE3/1 and RE4/1).

Table 1.7: Main hardware components needed for the RPC link system upgrade of the present RPC system, excluding spares.

Component	Number
Link boards	1376
Control boards	216

1.5 Enhancing muon measurement in the very forward region

Both the muon trigger and the offline muon identification and reconstruction can only work well if a sufficient number of detector hits is measured for each muon track. The two endcap regions suffer from high muon and background rates and reduced magnetic bending.

A major challenge at the HL-LHC is the reliable triggering on muons in the very forward regions. The number of hits measured per track must be increased to enhance the redundancy of the muon system and to obtain a robust track reconstruction, including rejection of wrongly reconstructed tracks, already at the Level-1 trigger. The Phase-2 muon detector upgrade must recover an effective muon system in the forward region by adding new forward muon detectors, GE1/1, GE2/1, RE3/1, and RE4/1, see Fig. 1.4, covering the pseudorapidity range up to 2.4. They provide further high resolution measurement points and significantly increase the lever arm for track reconstruction. The required space for installation and also some services already exist in CMS. So far these high rate regions have not been instrumented with RPCs,

since the previous generation of RPC detectors was not able to handle the high hit rate.

The existing muon stations ME1/1 and ME2/1, where the bending angles are largest and thus momentum determination is most effective, will be equipped with GEM detectors denoted GE1/1 and GE2/1. In the third and fourth muon stations, improved RPC (iRPC) detectors, RE3/1 and RE4/1, will provide the needed redundancy at relatively modest cost. The ME0 chambers, also using GEM technology, extend the acceptance of the muon system further to $|\eta| = 2.8$, by providing hits for triggering and for offline muon reconstruction.

The technologies of the new detectors can handle the particle hit rates at maximum HL-LHC luminosity without problem. The following sections motivate and detail the upgrades to the muon system in the forward region.

1.5.1 RPC detectors RE3/1 and RE4/1

The muon RPC upgrade extends the geometrical acceptance of the RPCs from $|\eta| = 1.9$ to 2.4, as envisaged already in the original CMS muon TDR [19]. As shown in Fig. 1.4, the new rings RE3/1 and RE4/1 constitute the so far missing partner chambers for the corresponding CSC stations ME3/1 and ME4/1.

1.5.1.1 Motivation of RE3/1, RE4/1 upgrades

The reasons for complementing the RPC forward system by the RE3/1 and RE4/1 chambers are:

- The RE3/1 and RE4/1 chambers complement the CSC stations ME3/1 and ME4/1 and enhance the local muon measurement by adding track hits and by increasing the lever arm. These RPC chambers have always been foreseen to be part of the CMS detector, but are still missing. The older RPC detectors are not able to cope with the HL-LHC rates, the new improved RPC type (iRPC) will have no problem. Thus RE3/1 and RE4/1 complement the CMS forward muon system following the original plans.
- The intrinsic time resolution is improved by about a factor just over two when the measurements of RE3/1 and RE4/1 are combined with those of the the existing CSC chambers, as Fig. 1.13 demonstrates. This improves background hit rejection and indentification and reconstruction of slowly moving Heavy Stable Charged Particles (HSCP), see Section 1.6.
- The new iRPCs will feature a better spatial resolution of the order of a few cm along the strip direction (non-bending projection), by measuring the time difference between the signals at both ends of the readout strips. This helps in resolving ambiguities in the endcap trigger for multiple tracks.
- The Level-1 muon trigger must be able to suppress low-p_T tracks, which are abundant and saturate the trigger rate if too many of them are mis-measured as having a high transverse momentum. Here the additional iRPCs play a major role, by improving the time and spatial resolution and thus the p_T assignment if RPC and CSC data are combined. In particular in the border regions of two adjacent CSC chambers where the number of layers crossed by a muon is lower, the additional iRPC hits mitigate the issue of low p_T tracks being misidentified as having high transverse momentum.
- The new RPC detectors RE3/1 and RE4/1 increase the redundancy in the difficult endcap region. In the case of a problem with the associated CSC chambers ME3/1

and ME4/1, muons can still be identified and reconstructed.

1.5.1.2 RE3/1 and RE4/1 upgrades

The new stations RE3/1 and RE4/1 for Phase-2 will use an *improved* version of RPC, iRPC for short, to sustain the high expected rates of up to 2 kHz/cm^2, including a safety factor of three, with a hit efficiency well above 95%. The higher rate capability with respect to the current RPC detectors will be achieved by shortening the recovery time of the electrodes and reducing the total charge produced in a discharge. To this purpose the iRPCs use thinner electrodes and a narrower gas gap, both reduced from a thickness of 2 mm in the current design to 1.4 mm. Furthermore, the operational high voltage is lowered. The resulting loss in gas gain will be compensated by the higher signal amplification of improved front-end electronics. The lower charge produced per traversing particle will also reduce the integrated charge deposited and slow down aging.

Since the double-gap design proved to be highly performant, it will be kept for the iRPCs. Also the new RE3/1 and RE4/1 endcap stations have one layer. The electrode resistivity will be maintained in the range from 0.9 to $3.0 \times 10^{10}\,\Omega\,\text{cm}$ (the resistivity of the present system ranges from 1 to $6.0 \times 10^{10}\,\Omega\,\text{cm}$). The baseline choice of material is HPL (Bakelite), as for the present RPCs.

Several prototype RPC chambers were built and extensive tests have been performed, in order to verify the production technology as well as performance and longevity.

New low-noise front-end electronics are needed for the iRPC readout. The corresponding ASIC, the CMS RPCROC, is developed to the needs of CMS. Each channel provides a time measurement being sent to the trigger and DAQ. The new chambers are read out by a large trapezoidal printed circuit readout board which contains 96 strips. This board will be inserted in between the two RPC gaps, as in the current RPCs. On the readout board a mezzanine hosts the ASICs and other electronic components. Each strip will be read from both sides to determine the coordinate along the strip by a measurement of the difference in arrival time of the two signals. There are 192 channels per chamber. The RPC Data Acquisition System, consisting of Data Concentrator Cards and optical links, will transmit the signals from the front-end to the Endcap Muon Track Finder board in the service cavern.

The high voltage system will be a copy of the current system, using commercial modules. The low voltage power system extension will also use commercial modules, like the present one. In the current system not all channels are needed; these spare channels will be used to power the new system, thus reducing the cost of the power system.

Table 1.8 summarizes the main hardware components needed for the new RE3/1 and RE4/1 detectors.

1.5.2 GEM detectors GE2/1

The GEM (Gas Electron Multiplier) technology has been employed in many particle physics experiments, for example COMPASS [28] and LHCb [29], and it has proven to operate reliably at hit rates of the order of a few MHz/cm^2, easily adequate for CMS at the HL-LHC. Aging problems have not been reported. The detection principle is illustrated in Fig. 1.14. A gas amplification by a factor of typically 20–25 is achieved by the high electric field between two copper layers coated on both faces of a thin polyimide foil, which is perforated by many biconical holes. A passing electron triggers an avalanche. By combining three foils to a triple-GEM chamber the gas gain reaches a value of the order of 10^4. The electrical signals are read

Table 1.8: Main hardware components needed for the new RE3/1 and RE4/1 chambers, excluding spares.

Component	Number
chambers	72
PCBs	72
concentrator boards	12
back-end board	1
HV crates	4
LV crates	4
HV boards	12
LV boards	8

out by a PCB with electrodes in form of strips.

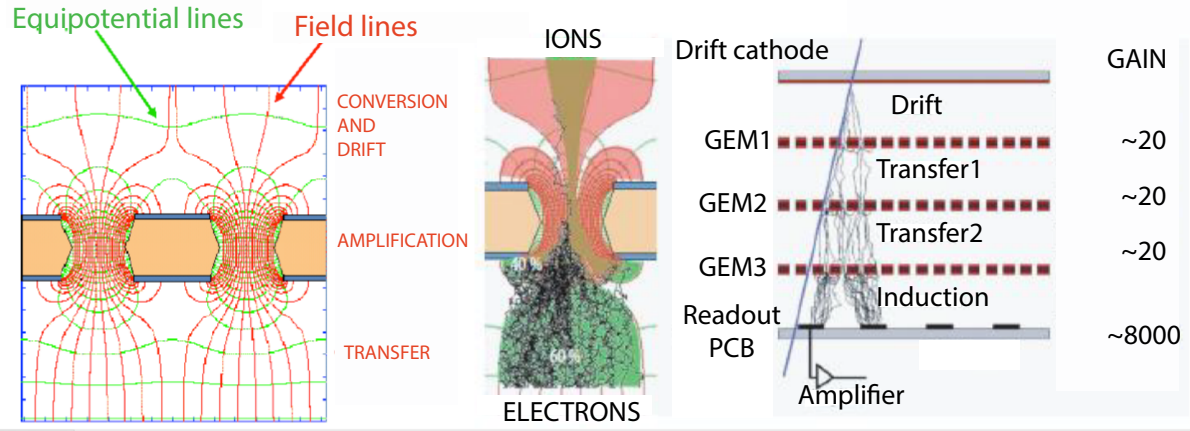

Figure 1.14: Left: electric fields and equipotential lines across the GEM foil. Within the holes the amplifying field ranges from 50–80 kV/cm. Center: a simulation of electron multiplication in the vicinity of the hole in a GEM foil. Right: arrangement of the triple-GEM chamber with three foils; the drift electrode on the top and the readout electrode at the bottom define drift and induction fields. Combining three stages with a gas gain of 20 each results in a total amplification factor of 8000.

Three sets of GEM detectors are to be used in CMS. During LS2 the CMS endcaps will be fitted with a first ring of two-layer GEM detectors, GE1/1, see Fig. 1.4. They are placed close to the ME1/1 CSC chambers. Their acceptance in pseudorapidity reaches up to $|\eta| = 2.15$. The increased path length within the first station allows for a better measurement of the track bending, which significantly reduces the Level-1 standalone muon trigger rate by rejecting mismeasured tracks. The GE1/1 chambers can also provide a backup for any problems that might arise in the ME1/1 system. This project has been approved and documented in the corresponding TDR [7] submitted in the year 2015. It is a first step to improve the muon measurements in the very forward region. The GE1/1 system is currently undergoing construction. A demonstrator, consisting of five superchambers of type GE1/1, has already been installed in CMS during the year-end technical stop 2016/2017.

The GE2/1 upgrade, consisting of a second ring of GEM muon detectors in the endcap regions, next to the ME2/1 chambers, is proposed in this TDR. Similarly to how the GE1/1 chambers complement the ME1/1 stations, the GE2/1 detectors complement the ME2/1 system. However, the GE2/1 chamber surface is considerably larger than the area of the GE1/1 detectors.

The GE2/1 chambers partly overlap in pseudorapidity with the GE1/1 chambers, and extend the GEM detector acceptance in the pseudorapidity range $2.15 < |\eta| < 2.4$, which is not covered by GE1/1. The GE2/1 chambers play the same role in triggering in the second endcap station that GE1/1 does in the first station. The GE2/1 project takes advantage of the experience gained with GE1/1, as the triple-GEM modules comprising the chambers of the GE2/1 detector system use the same basic design as the modules of the GE1/1 system. Similarly, the GE2/1 data acquisition system design is based on the same front-end ASIC and uses a similar readout architecture. The GE2/1 detectors will be installed in LS3.

Also the ME0 detectors described in Section 1.5.3 employ the triple-GEM technology as baseline, but use six layers, while GE1/1 and GE2/1 have two layers.

1.5.2.1 Motivation for new GE2/1 detectors

So far, only CSC chambers cover the pseudorapidity range up to 2.4. By complementing them with GE1/1 (matched with ME1/1) and GE2/1 (matched with ME2/1) detectors, see Fig. 1.4, the number of hits for a traversing muon is increased from six to eight. The motivation for GE2/1 is very similar to the rationale for GE1/1.

The advantages brought by the GE2/1 chambers are:

- The momentum measurement at trigger level 1 is based on the known vertex position in the $r - \phi$ plane and the measured positions of the track segments in the CSCs. Adding GEM chambers significantly increases the local lever arm for the segment reconstruction with respect to the CSC-only system, by more than a factor of two. Since there are no iron yoke elements in between the GE2/1 and ME2/1 chambers, the multiple scattering is small. Therefore, this combination of GEM and CSC detectors gives a precise measurement of the muon direction within a single station, as illustrated in Fig. 1.15. The measured direction is strongly correlated with the muon momentum. Since this is reconstructed more precisely than in the current system, the fraction of soft muons with overestimated momentum and the trigger rate for a given p_T threshold are largely reduced, while maintaining a high trigger efficiency.
- The increased number of hits measured per muon in the endcaps is essential to obtain a robust track reconstruction already at the Level-1 trigger. The GE2/1 chambers enhance the overall redundancy of the muon sytem.
- The additional local lever arm is very important also for displaced vertices, for which the vertex constraint cannot be exploited. Here two independent direction measurements, in endcap stations 1 and 2, allow a standalone momentum measurement in the muon system in the Level-1 trigger.

1.5.2.2 The GE2/1 upgrade

Each GE2/1 "superchamber" consists of a pair of triple-GEM layers of trapezoidal shape, covering 20° in ϕ, as shown in Fig. 1.16. Due to lack of space it is not possible to install more than two layers of chambers. In total $2 \times 18 = 36$ superchambers are needed. The pseudorapidity coverage extends from $|\eta| = 1.6$ to $|\eta| = 2.4$, partially overlapping with the GE1/1 chambers which reach down to $|\eta| = 2.15$, see Fig. 1.4. Short readout strips along the radial coordinate allow a precise measurement of the ϕ coordinate (in the bending plane, as shown in Table 1.11) and a crude determination of R.

A novel spacer-less stretching technique has been developed already for GE1/1, which facilitates mounting the three GEM foils into a single stack, where they are kept together with a

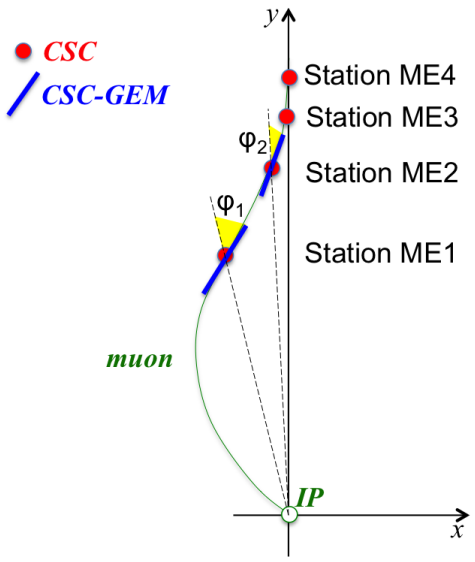

Figure 1.15: A schematic view of a muon trajectory from the axial point of view. Adding GEM detectors (GE1/1 and ME0 in Station ME1, and GE2/1 in Station 2) allows one to use them in tandem with the CSC chambers and obtain accurate measurements of muon "local bending" angles ϕ_1 and ϕ_2, and, hence, improve the muon momentum measurement.

segmented frame, guaranteeing also the required inter-foil spacing. This glue-less assembly method saves production time and allows for easy reopening of a chamber.

Each GE2/1 chamber covers an area of 1.45 m^2. The drift gap is 3 mm wide, while transfer gaps and the induction/collection gap are 2 mm thick. The GE2/1 chambers are segmented in four modules in R, each containing 12 sectors, and each sector is composed of 128 radial strips. Therefore, each chamber has about six thousand strips. The strip pitch varies from 0.5 mm to 1.2 mm. The expected spatial resolution with binary readout varies from 200 to 410 μm from inner to outer radius. The gas mixture employed is the non-flammable and environmentally-friendly Ar/CO_2 (70:30%). The typical voltage across each GEM foil is 370 V, with a total voltage across a triple-GEM chamber of 3200 V.

To verify the performance and longevity of the GEM detectors, different prototypes have been tested with X-rays and with test beams over several years. These tests have demonstrated an intrinsic spatial resolution as good as 100 μm, and a time resolution of 8 ns for the CMS GEM chambers. These studies show that a triple-GEM chamber reaches its efficiency plateau well above 95%. Tests of gain uniformity and rate capability over the surface of a full-scale GE1/1 prototype show a gain variation of the order of 10% with X-ray induced hit rates as high as 1 MHz/cm^2 (far beyond HL-LHC expectations).

The main electronics components for the readout of a single chamber are outlined in the block diagram of Fig. 1.17. Visible in the on-detector part is the four-fold η segmentation of the GEM chamber. The strips are read out by the front-end ASIC chip VFAT3. It features 128 channels, each containing a charge sensitive preamplifier and shaper, followed by a constant-fraction discriminator. Its time resolution is better than 7.5 ns (with detector). It supports a readout latency up to 25 μs. More details on the VFAT3 chip are given in Chapter 6. The link to the off-detector electronics is provided by an Opto-Hybrid board (OH), which contains a CERN-designed GigaBit Transceiver (GBT), an FPGA, and the optical receivers and transmitters.

The off-detector GEM electronics provide the interfaces from the detector and its VFAT3 front-

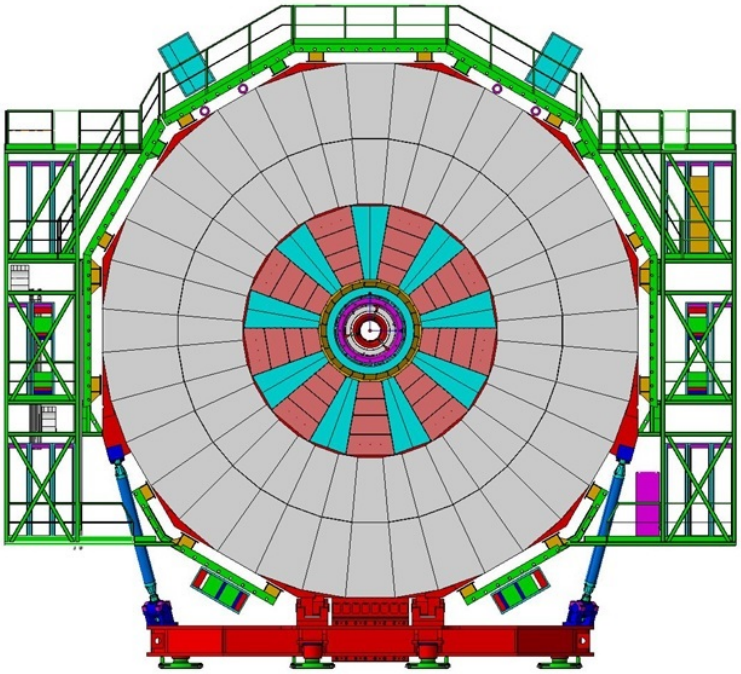

Figure 1.16: Location of the 18 GE2/1 detectors (blue and red) on the back of the yoke disks YE±1. The two chambers of neighboring superchambers overlap in ϕ, to avoid acceptance holes.

end electronics to the CMS DAQ and trigger systems. The design is based on the xTCA standard. It uses FPGAs and Multi-Gbit/s links.

The back-end electronics will use the Calorimeter Trigger Processor card CTP7 [30] or an equivalent board; it sends the data to the endcap muon track finder (EMTF) and to the CMS DAQ system.

While the trigger and tracking data are sent from the detectors to the xTCA electronics, the trigger data are also sent directly to the CSC Optical Trigger Mother Board (OTMB) located in the CMS peripheral crates. There the GEM trigger data are combined with the CSC data to improve the Level-1 trigger efficiency and the precision of the CSC system at an early stage of the trigger processing.

The precise alignment of the GEM chambers is important to ensure the required spatial resolution. The alignment between adjacent chambers in the $R - \phi$ view is measured by a position monitoring system based on capacitive sensors. It has already been built for GE1/1 and has been selected also for GE2/1 and ME0. These position measurements will be the basis for the geometric reconstruction of the full GE2/1 ring.

Irradiation tests at the GIF++ facility at CERN using the ^{137}Cs gamma source have exposed GEM prototype chambers with a hit rate of 1 kHz/cm^2, a rate expected at the HL-LHC for GE1/1 and GE2/1. The accumulated charge is 9 mC/cm^2. No aging effects have been observed. A few hundred discharges per cm^2 have been observed and are predicted for the full Phase-2 lifetime, but the chamber performance was not affected. Neutron backgrounds up to 10^{14}/year/cm^2 are expected for the CMS GEM chambers, and several corresponding irradiation tests have been performed in the framework of the RD51 collaboration. Detailed discharge studies have been done with GEM detectors exposed to neutrons and highly ionizing alpha

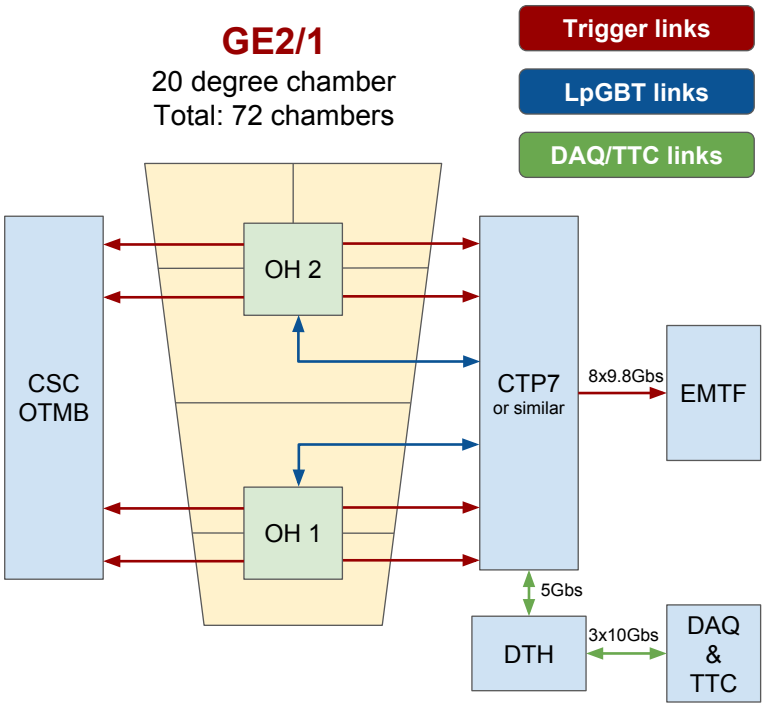

Figure 1.17: A diagram of the GE2/1 electronics readout system for CMS. For explanations see text.

particles, showing no degradation. Nevertheless further detailed cyclotron tests are planned.

Table 1.9 summarizes the main hardware components needed for the new GE2/1 chambers.

Table 1.9: Main hardware components needed for the GE2/1 system, excluding spare modules. Optical links are included in the corresponding boards.

Component	Number
triple-GEM chambers	72
GEM electronics boards (GEB)	288
Optohybrid boards	144
VFAT3 readout chips	3456
HV boards	36
LV boards	24

1.5.3 Extending muon coverage to $|\eta| = 2.8$: the ME0 detector

The ME0 chambers increase the acceptance of the muon system to $|\eta| = 2.8$, 7.0° with respect to the beam axis. They will provide a muon trigger signal in the very forward region, and the ME0 hits will be used in the offline muon reconstruction. GEM detectors are fast and are able to handle hit rates up to a few MHz/cm^2, which is five times more than needed in this region for Phase-2. Therefore triple-GEM chambers, which form the basis for GE1/1 and GE2/1, will also be used for ME0.

The ME0 station will be installed behind the new endcap calorimeter HGCAL, as shown in Fig. 1.4. The coverage extends from $|\eta| = 2.0$ to 2.8, which is the maximum possible range allowed by mechanical constraints. The ME0 chambers partially overlap (up to $|\eta| = 2.4$) with

the existing CSC endcap muon chambers and the new RE3/1 and RE4/1 iRPC chambers. The ME0 detector extends the muon acceptance into the pseudorapidity range $2.4 < |\eta| < 2.8$, which, because of the aforementioned mechanical constraints, is beyond the reach of any other CMS muon detector. The increased muon acceptance is fully covered by the new Phase-2 inner silicon tracker. Each ME0 detector consists of six layers of triple-GEM chambers, compared to the two-layer design of GE1/1 and GE2/1. An ME0 provides up to six track points and therefore enough redundancy to reject neutron-induced backgrounds and to form muon track segments in the L1 trigger. Figure 1.18 shows the layout of the ME0 chambers.

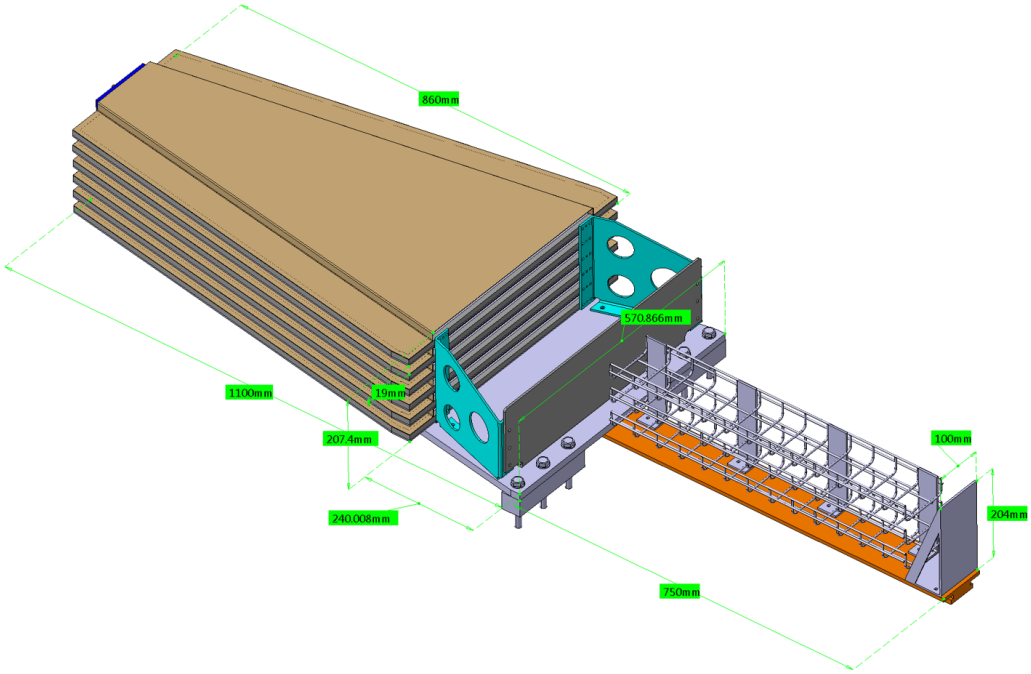

Figure 1.18: Layout of ME0 stack with six triple-GEM layers including cable trays shown in the lower right part of the figure. The six layers are staggered such that the active areas of adjacent stacks overlap in ϕ.

1.5.3.1 Motivation for the new ME0 detectors

The main motivation for the new ME0 detectors is the increase of the geometrical acceptance for muons, which is most relevant for multi-muon final states such as $H \to 4\,\mu$, and for forward particle production. This is illustrated by the physics performance examples given in Section 1.6 and in more detail in Chapter 8. In particular, the ME0 system will improve the CMS performance in the following ways:

- In the $2.15 < |\eta| < 2.4$ region, which is covered by CSCs, RPCs, and GE2/1, but not by GE1/1, the muon identification and trigger capabilites can be maintained even for high background rates. The ME0 detectors improve muon measurements by adding up to six hits per track and increase the lever arm for momentum determination, in a way similar to that shown in Fig. 1.15. This suppresses the Level-1 trigger rate due to mismeasured low p_{T} muons by an order of magnitude in this pseudorapidity window.
- In the pseudorapidity window $2.15 < |\eta| < 2.4$, ME0 together with CSC ME1/1 provides the second needed muon direction measurement (the other one is provided

by the GE2/1 - ME2/1 tandem), enabling standalone triggering on muons arising from the decays of long-lived particles.

- In the very high rapidity region, ME0 enlarges the acceptance of the current muon system to $|\eta| = 2.8$. Only the ME0 chambers cover the $2.4 < |\eta| < 2.8$ range. Since six triple-GEM layers are used, an efficient tagging of muon tracks with little background contamination is possible. Even for transverse momenta down to $p_T = 3\,\text{GeV}$ the identification efficiency is simulated to be approximately 95%. ME0 enables muon triggering capabilities in the forward-most region, $2.4 < |\eta| < 2.8$. A L1 standalone ME0 based trigger is not feasible, but Level-1 cross-triggers, in particular those with low p_T very forward muons, and the HLT will make use of the ME0 trigger data.
- ME0 takes advantage of the extended geometrical acceptance and L1 trigger capabilites of the inner tracker added for Phase-2. Since the tracker cannot identify charged particles as muons, muon detectors are needed to make full use of the new tracker capabilities. In the High Level Trigger, ME0 allows performing track reconstruction regionally, enabling the use of very forward going muons of near-offline quality in the trigger algorithms.

1.5.3.2 Description of the new ME0 detectors

Each trapezoidal ME0 detector covers an azimuthal angular window of 20°. Thus altogether $18 \times 6 \times 2 = 216$ triple-GEM chambers are needed. The chambers are 3.34 cm thick and in total a space of about 30 cm is occupied by a six-layer stack, including shielding. The inner and outer radii are $R = 0.6\,\text{m}$ and 1.5 m, respectively. The segmentation of each ME0 chamber layer is 8 rings in η and 3 sectors in ϕ; each ϕ sector is in its turn subdivided into 128 radial strips.

The chamber gas is the same as for GE2/1, Ar-CO_2 (70:30). The applied high voltage is 3200 V, leading to a gas gain of the order of 10^4. The electronics will be based on the same architecture used also for GE1/1 and GE1/2, as shown in Fig. 1.19. Also the DAQ layout is a copy of the GE2/1 system. The alignment with muon tracks exploits the overlap with the nearby ME1/1 chambers. Both the HV and LV power supply systems follow that of the GE2/1 detector, using commercial modules.

Longevity tests of GEM chambers at the GIF++ zone are ongoing and will be performed also with a ME0 prototype in the near future. It should be noted that the triple-GEM technology, on which GE2/1 and ME0 are based, has been extensively tested at GIF++ and elsewhere and proven radiation hard, as described in Chapter 6.

Table 1.10 summarizes the main hardware components needed for the new ME0 chambers, to be installed during long shutdown LS3.

Table 1.10: Main hardware components needed for the ME0 chambers, excluding spare modules. Optical links are included in the corresponding boards.

Component	Number
triple ME0 modules	216
GEM electronics boards (GEB)	216
Optohybrid boards	216
VFAT3 readout chips	5184
HV boards	36
LV boards	36

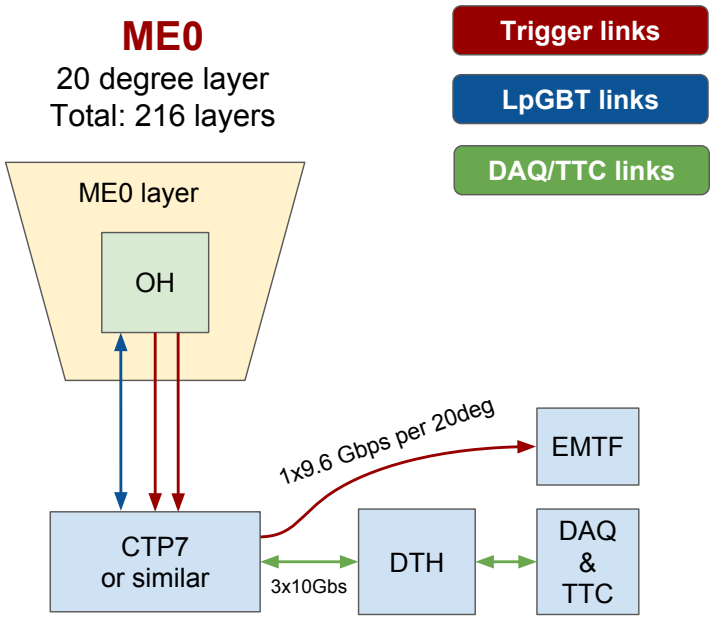

Figure 1.19: A diagram of the ME0 electronics readout system. Links between different boards are color-coded according to their functionality, as defined in the legend. For details see text.

1.5.4 Summary of properties of new CMS muon detectors

Table 1.11 summarizes the main parameters for the new detectors including key resolution figures.

Table 1.11: Properties of the new CMS muon detectors installed as part of the HL-LHC upgrade. The RE3/1 and RE4/1 detectors are double-gap iRPC chambers. The GE1/1 and GE2/1 detectors comprise two layers of triple-GEM chambers, referred to as superchambers. The ME0 detectors are made of six layers of triple-GEM chambers, referred to as stacks. The quoted intrinsic spatial and time resolutions refer to a chamber for RPCs, to a superchamber for GE1/1 and GE2/1, and to a stack for ME0. Note that GE1/1 is not part of this TDR.

Muon subsystem	RE3/1 + RE4/1	GE1/1	GE2/1	ME0
Detector technology	iRPC	GEM	GEM	GEM
$\|\eta\|$ range	1.8–2.4	1.6–2.15	1.6–2.4	2.0–2.8
Number of chambers	36 + 36	144	72	216
Number of channels	13 824	442 368	442 368	663 552
Number of layers/station	1	2	2	6
Surface area of all layers	93 m^2	54 m^2	105 m^2	64 m^2
spatial resolution	$\sim$ 0.3 cm	200–340 μm	200–410 μm	160–390 μm
time resolution	1.5 ns	8 ns	8 ns	8 ns

1.6 Performance of the upgraded CMS muon system

The Phase-2 upgrades of the existing DT, CSC and RPC systems and the addition of GEM and iRPC muon chambers will preserve and enhance the performance of the CMS muon system despite much higher pileup and neutron-induced backgrounds. In Section 1.6.1, we compare

the capabilities of the muon system before and after the upgrade, and demonstrate how the upgrades successfully address the HL-LHC challenges. Section 1.6.2 briefly describes a few representative physics analyses, whose measurement and search sensitivities are expected to be enhanced by the muon system upgrades.

1.6.1 Muon trigger and reconstruction

For a muon system to perform reliably, it must have redundancy for a number of reasons. Tracks can be reconstructed unambiguously and efficiently only if the number of hits measured along the trajectory is sufficiently large. However, due to large background rates, individual detector layers can fail to identify a muon. Also, if an unexpected degradation of some muon detectors occurs in the coming 20 years, it is essential to back them up with other detectors, preferentially of a different type that may not suffer a similar degradation.

Figure 1.20 illustrates qualitatively the need to have additional chambers in the forward region, which is exposed to very high background rates. The black histogram shows the average number of ϕ-measuring muon layers (bending projection) with reconstructed hits in the current CMS detector. While in the barrel region there are typically 25 hits per track, the more challenging endcap regions yield only around 20 hits per muon. Also displayed in the figure is the neutron flux as a function of pseudorapidity, which is almost three orders of magnitude higher at $|\eta| = 2.4$ than at $|\eta| < 0.5$. With two additional hits in both GE1/1 and GE2/1, six hits in ME0, and one hit per iRPC chamber, the number of hits per track in the forward regions will increase by six to ten, depending on the muon's η.

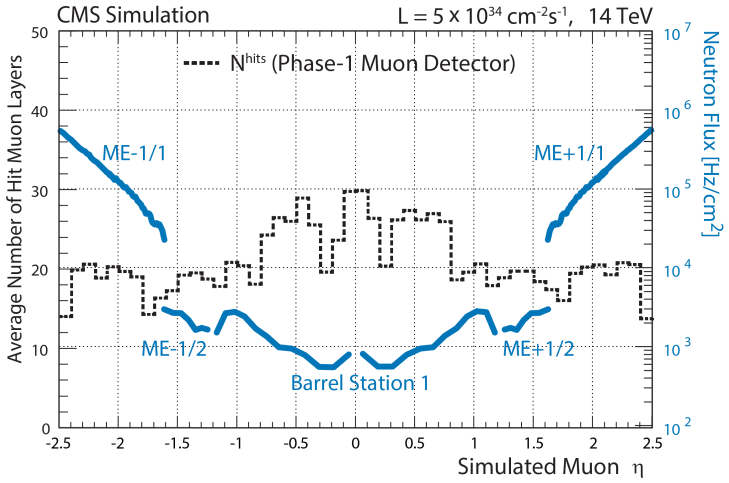

Figure 1.20: Average number of ϕ-measuring muon layers with reconstructed hits as a function of pseudorapidity (black dashed line) for the Phase-1 muon system, in comparison to the neutron flux expected at HL-LHC, on a logarithmic scale [24].

1.6.1.1 Muon trigger performance

The HL-LHC conditions are particularly challenging for the Level-1 trigger that has to take a decision on a time scale of a few microseconds. The Phase-2 L1 Muon trigger [18] will have several important advantages compared to the current system, as demonstrated by the following examples.

Higher efficiency There will be more hits produced along a muon's trajectory in the forward muon system due to the added GEM (GE1/1, GE2/1, ME0) and iRPC chambers. The

different detector subsystems (DTs, CSCs, RPCs, GEMs) will be better integrated for identifying local muon "super-segments" within each muon station. Due to the new electronics architecture in the barrel, signals from multiple stations will reach the same processor in the back-end where they will be combined. Additionally, in the barrel, the deadtime in the trigger due to background hits is substantially reduced by a factor more than 40 in the new electronics. As a result, the trigger efficiency/robustness even in presence of high background or intermittent/deteriorating operation of detectors will be much improved. The impact of the current RPCs and the new iRPCs on the L1 trigger efficiency as a function of pseudorapidity is illustrated in Fig. 1.21. A clear improvement can be seen with respect to the CSC-only trigger efficiency. Figure 1.22 (left) shows the gain in trigger efficiency for muons with $p_{\mathrm{T}} > 15\,\mathrm{GeV}$ in the endcap forward region $2.1 < |\eta| < 2.4$ (where GE2/1 and ME0 overlap) due to adding GEM detectors. The upgraded muon system will increase the trigger efficiency for forward muons from about 80% to 90%. Being able to measure muon directions in the first and second stations will also allow one to trigger on highly "displaced" muons, i.e. muons displaced from the interaction point by as much as $\mathcal{O}(1)$ m. Inclusion of GE2/1 and ME0 chambers also improves the displaced muon trigger efficiency by about 12% in this region, as shown in Fig. 1.22 (right).

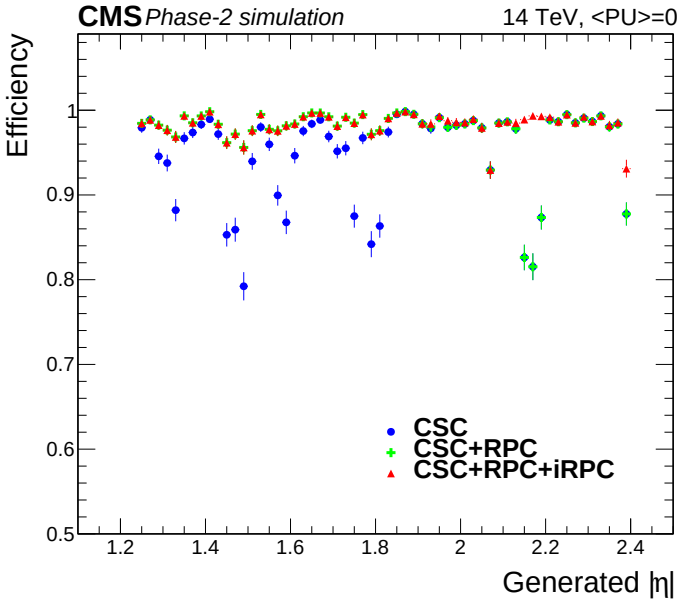

Figure 1.21: Comparison of the simulated L1 single muon trigger efficiencies with and without the RPC information, as a function of $|\eta|$. The contribution of iRPC starts above $|\eta|$ =1.8.

Lower rate The GEM-CSC chamber tandems will allow one to measure a local muon direction in a single station with a far better accuracy, thanks to the large lever arm (distance between the chambers). This will improve the muon identification and momentum measurement, which directly translates into a much purer muon sample and, hence, much lower trigger rates. Figure 1.23 (left) shows the L1 prompt muon trigger rate as a function of muon p_{T} for the current and the upgraded muon systems in the $|\eta|$ range 2.1–2.4. By adding GEM chambers, the trigger rate is expected to be reduced by a factor of 5–10, which will allow CMS to maintain a single muon trigger with a p_{T} threshold as low as 15 GeV. Figure 1.23 (right) shows the rate of a special L1 trigger (in the forward region) not requiring that a muon originates from the interaction point, which allows one to trigger on displaced muons. As in the case of prompt

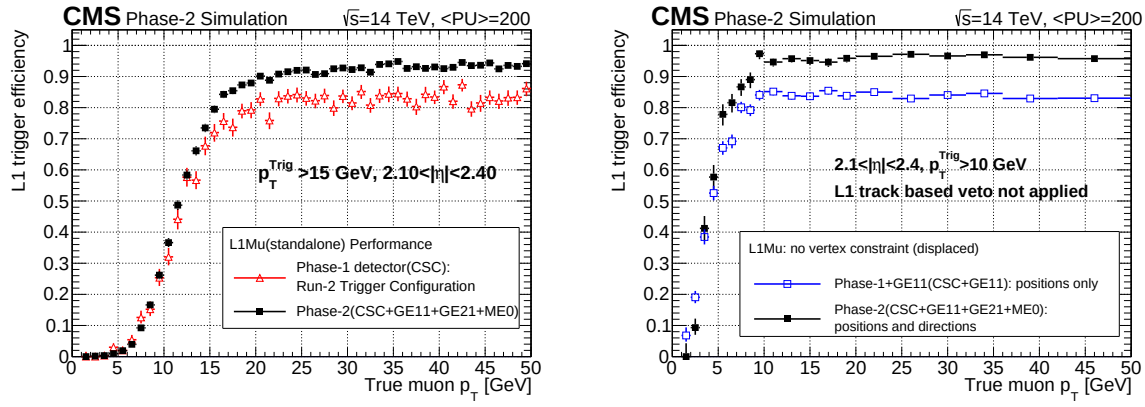

Figure 1.22: L1 Muon trigger efficiency for the prompt muon trigger (left) and displaced muon trigger algorithm (right), as a function of a true muon p_{T} in the region $2.1 < |\eta| < 2.4$. The L1 trigger p_{T} threshold is 15 GeV (left) and 10 GeV (right).

muons, the inclusion of GEM chambers will significantly reduce the trigger rate.

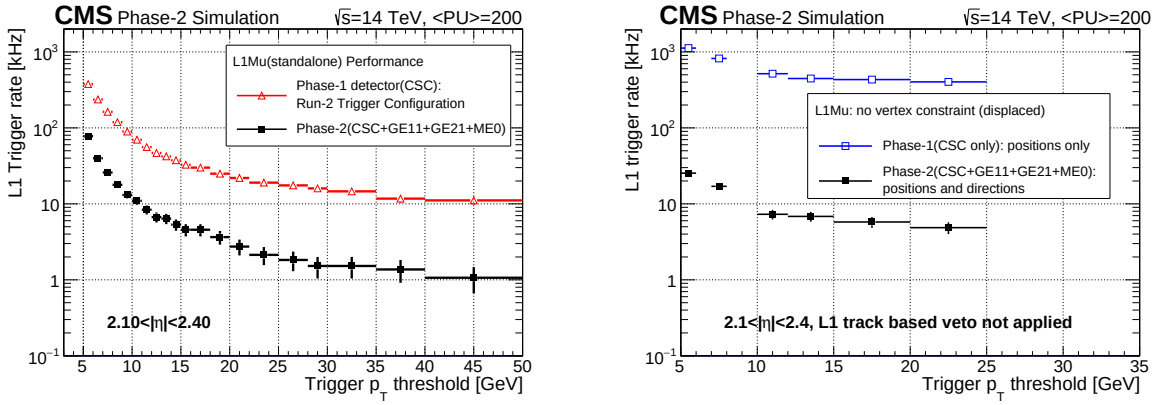

Figure 1.23: L1 *prompt* (left) and *displaced* (right) muon trigger rates, with and without GEM chambers, as a function of muon trigger p_{T} threshold in the region $2.1 < |\eta| < 2.4$. The L1 track based veto is expected to further reduce the displaced muon trigger rate by a factor of 3–8.

Better timing The time resolution of the RPC link system, affecting all the present RPCs as well as the new iRPCs, will be much improved by the upgrade of the link system, which will help suppress out-of-time background and improve muon beam crossing (BX) identification throughout the entire muon system. The time precision of the DT trigger system will also improve, from the 12.5 ns of the old electronics to about 1 ns in the upgraded system, translating in a better resolution of the trigger primitives (position, bending angle/momentum, BX). These timing improvements also enable efficient triggering on heavy "muon-like" stable charged particles (HSCP) that, should they exist, would emerge from the interaction point with velocities substantially smaller than the speed of light. Figure 1.24 shows that a special HSCP-targeting L1 muon trigger, fully exploiting the improved timing of the upgraded RPC link system, can be efficient to HSCPs with velocities as low as $\beta \sim 0.2$, which would not be possible without the upgrade.

Benefit of a L1 Track Trigger The new L1 Track Trigger will be combined with the muon trigger, which will dramatically sharpen muon trigger efficiency turn-on curves. By matching

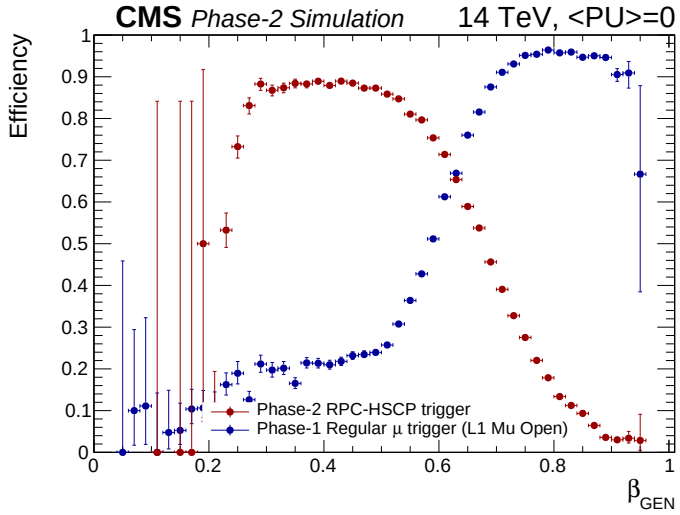

Figure 1.24: L1 Trigger efficiency as a function of an HSCP velocity β for the 'regular' trigger (assuming the muon to come from the primary vertex, blue points) and a dedicated HSCP trigger, fully exploiting the improved timing of the upgraded RPC link system (red points).

a track identified by the Track Trigger to a muon found by the Muon Trigger, one will reduce the prompt muon trigger rates. Matching to the tracker will be greatly helped in the barrel by the much higher η precision available at L1: from 32 cm to the $\sim$1 mm provided by the DT TDC hits. On the other hand, a track veto will help suppress false displaced muon triggers by a factor of about 10, as is shown in the studies of the barrel-region displaced muon trigger, see Section 7.1.4.1. The purity of an HSCP muon trigger will be significantly improved by complementing it with dE/dx data from the Tracker (e.g, a charged particle moving with $\beta \sim 0.3$ will produce 10 times denser ionization).

Extended pseudorapidity coverage The pseudorapidity coverage of the first endcap muon station is increased from $|\eta| = 2.4$ to 2.8. A standalone L1 trigger cannot be realized in the extended range due to unsustainably high rates in this very forward region. However, muon segments identified in this region can be used as a part of multi-object topological L1 triggers dedicated to specific physics analyses. An example is the four-muon decay channel of the Higgs boson.

1.6.1.2 Offline standalone muon measurement

In physics analyses involving prompt muons, one is concerned with reconstructing such muons with a high efficiency, while keeping the rate of background-muons as low as possible. A background-muon refers to any "reconstructed muon" that is actually not associated with a true prompt muon. It can simply be a reconstructed non-prompt muon (e.g., a muon from a b-quark decay or from a π/K decay-in-flight), a punch-through hadron or a hadron whose track accidentally matches to "spurious" hits in the muon chambers. The high pileup conditions naturally tend to reduce the reconstruction efficiency for prompt muons and cause a higher rate of background-muons.

Prompt muon reconstruction efficiency Figure 1.25 shows the prompt muon reconstruction efficiency in the endcap muon system as a function of muon pseudorapidity. Solid points are for different muon detector configurations; they assume HL-LHC neutron-induced background, average pileup $\langle \text{PU} \rangle = 200$, and include a model of the muon system deteriora-

tion/failures. For a reference, the open squares represent the complete muon system upgrade without any hardware deterioration/failures and without neutron-induced background. One can see the effiency of the upgraded muon system is expected to be remarkably resilient to the HL-LHC adverse conditions. Muon reconstruction in the extended pseudorapidity range, $2.4 < |\eta| < 2.8$, is also highly efficient and robust.

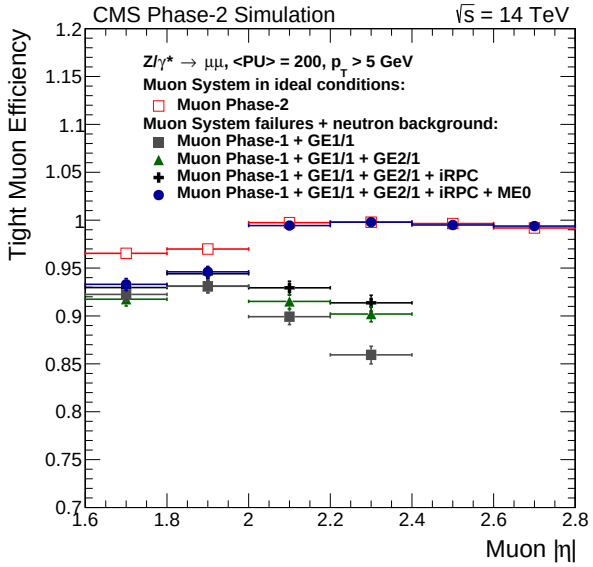

Figure 1.25: Muon reconstruction and identification efficiency with statistical uncertainty in DY events as a function of a simulated muon's $|\eta|$, for tight muon selection cuts. Results for different detector configurations are shown. Solid points assume an average pileup of 200, HL-LHC neutron background, and a model of Muon System aging. Open squares show results for the not-aged muon system and without neutron-induced background.

Background-muon multiplicity Figure 1.26 shows the average background-muon multiplicity as a function of muon $|\eta|$ for the Phase-2 detector in three pileup scenarios, compared to the performance of the Phase-1 detector. One can see that the rate of background-muons in the full pseudorapidity range (including $2.4 < |\eta| < 2.8$) remains fairly independent of the pileup conditions.

1.6.2 Physics performance

To illustrate how the proposed muon system upgrade enhances the CMS physics program, a set of representative physics analyses is briefly presented in this section (for details, see Section 8):

- The first five analyses directly benefit from the increased muon system acceptance, better trigger, and higher reconstruction efficiency, which help to increase the signal acceptance and improve the sensitivity of the measurements or search:
  - Measurements of Higgs boson properties in the decay $H \to ZZ \to 4\mu$,
  - top quark mass measurement in $t \to \mathrm{J}/\psi(\mu\mu)\,\mu + X$ decays,
  - studies of double parton scattering in the pp $\to W^+W^+$ process,
  - search for lepton flavor violating decays $\tau \to 3\mu$,
  - precision measurement of the electroweak mixing angle with $\mu^+\mu^-$ events.
- The next search example illustrates how the increased muon system acceptance helps reduce the main background to the search by a large factor:

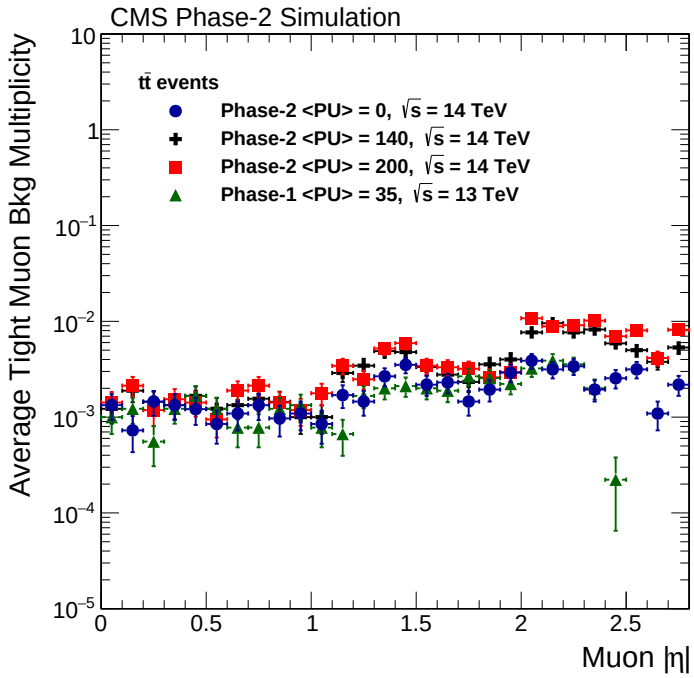

Figure 1.26: Average background-muon multiplicity in $t\bar{t}$ events as a function of muon $|\eta|$ for the Phase-2 detector in three pileup scenarios, compared to the performance of the Phase-1 detector.

  - search for BSM physics with two same-sign leptons in the final state.
- The last two analyses present examples of searches whose sensitivities become greatly enhanced thanks to the new capabilities of the upgraded muon system to trigger on "unconventional" muons:
  - search for BSM physics with highly displaced muons,
  - search for production of heavy stable charged particles.

Four-muon Higgs boson decays $H \to ZZ \to 4\mu$ Measurements of the Higgs boson properties are one of the major physics goals of the HL-LHC program. The Higgs boson decay to four muons, $H \to ZZ \to 4\mu$, allows for precise measurements of the Higgs boson production rate, mass (a fundamental parameter of the SM), spin-parity properties, and width (via an analysis of off-shell production). Differential measurements, such as the Higgs boson p_{T}, can shed more light on the nature of the Higgs boson and will become much more accurate with the large HL-LHC data set. Since all $H \to ZZ \to 4\mu$ analyses are statistics limited, the largest possible muon acceptance is highly desirable. Muons with low transverse momentum down to a few GeV are frequent and must be included in the analyses. With four muons in the final state, a high muon reconstruction efficiency is required. The upgraded muon system extends the muon acceptance and improves the muon reconstruction. The extended tracker acceptance accompanied by the presence of forward muon chambers allows for a good muon identification of low momentum muons, while keeping the misidentification rate under control. The upgraded muon system increases the signal acceptance by 17%. Figure 1.27 shows the expected four-muon invariant mass distributions for signal and background, obtained in the $\langle \mathrm{PU} \rangle$=200 conditions for an integrated luminosity of 3000 fb^{-1}.

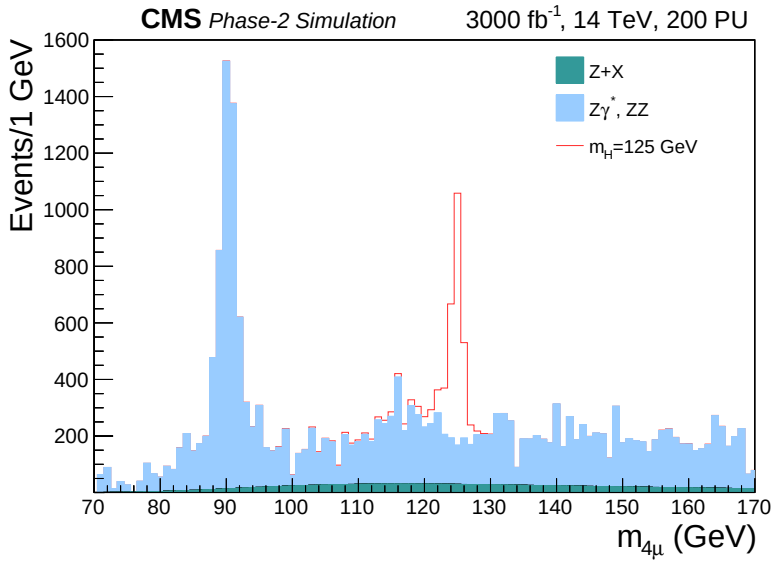

Figure 1.27: Four-muon invariant mass distribution for $H \to ZZ \to 4\mu$ signal, and for irreducible ($Z\gamma^*, ZZ$) and reducible backgrounds ($Z + X$). The peak near 90 GeV comes from rare $Z \to 4\mu$ decays.

Top quark mass measurement in $t \to J/\psi(\mu\mu)\,\mu + X$ decays The top quark mass is a fundamental parameter of the standard model and its precise measurement is one of the goals of the HL-LHC program. The main challenge of this measurement is systematic uncertainties that already limit the precision of the present measurements. One interesting method to address the issue of systematic uncertainties is to use $t\bar{t}$ events with $W \to \mu\nu$ and rare $B \to J/\psi(\mu\mu) + X$ decays [31, 32]. The invariant mass distribution for the trimuon system $J/\psi(\mu\mu)\,\mu$ is shown in Fig. 1.28. Since not all particles from the top decay are included, this invariant mass is smaller than the top mass. The known relation between these two masses allows one to perform a top quark mass measurement not affected by jet reconstruction uncertainties, which are the dominant source of systematic uncertainties in the "standard" lepton+jets, dilepton, and all-hadronic analyses. Moreover, studies of $t \to J/\psi(\mu\mu)\,\mu + X$ decays will help improve the knowledge of the b-quark fragmentation process, which should further the "standard" analyses as well. Studies of $t \to J/\psi(\mu\mu)\,\mu + X$ decays with three final state muons, none of which is of particularly high momentum, will benefit from the improved muon reconstruction and trigger of the upgraded muon system.

Double-parton scattering in $pp \to W^+W^+$ process Studies of double parton scattering (DPS) occurring in a collision of two protons shed light on the inter-parton interactions inside the proton. The process pp $\to W^+W^+$, with subsequent decay of the W bosons to muons and neutrinos, is particularly clean and, given the large HL-LHC data sample, will provide a quantitative probe for testing various models for such interactions. Figure 1.29 shows the distribution of events as a function of the product of pseudorapidities of the two muons. One can see that events with both muons in the most forward directions are the best in discriminating between different theoretical models. Hence, this analysis will greatly benefit from the muon system upgrade extending the muon acceptance toward high pseudorapidity and improving the trigger and reconstruction for muons in the forward direction.

Lepton flavor violating decays $\tau \to 3\mu$ In the standard model, the $\tau \to 3\mu$ decay is possible only via higher order contributions involving neutrino oscillations and $\mathcal{B}(\tau \to 3\mu)$

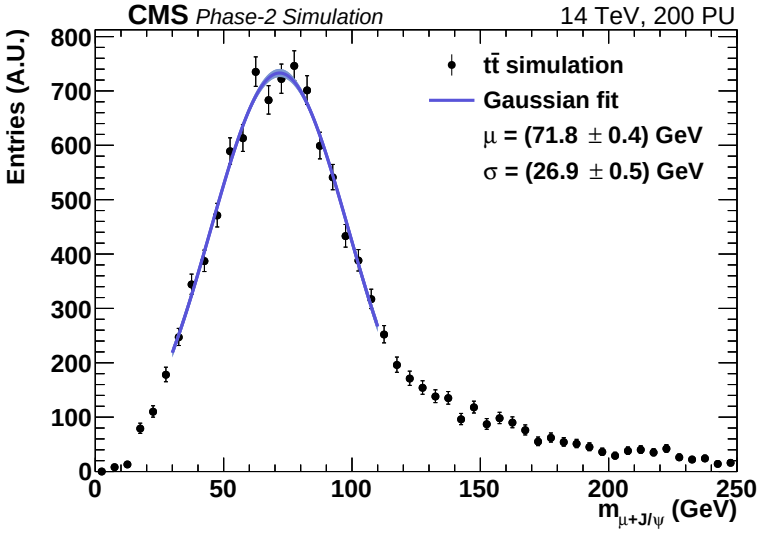

Figure 1.28: Trimuon invariant mass $m_{\mu+J/\psi}$ reconstructed in $t\bar{t}$ events by the Phase-2 upgraded CMS detector.

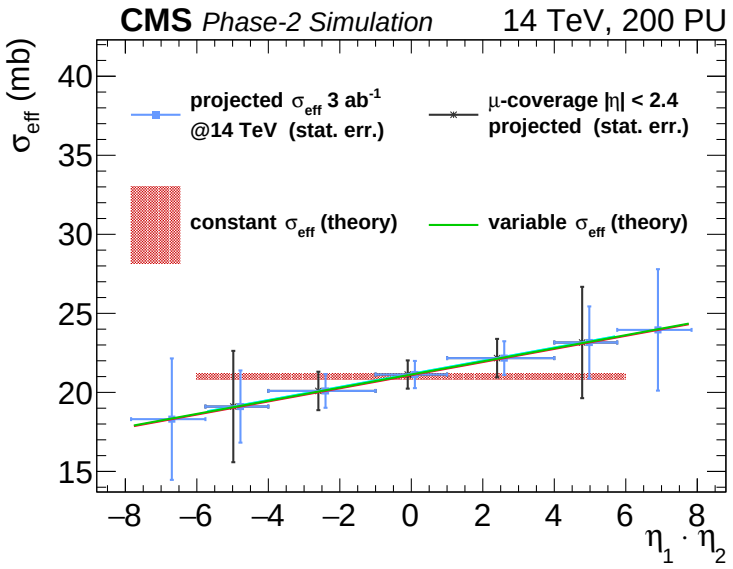

Figure 1.29: Predicted dependence of σ_{eff} on $\eta_1 \cdot \eta_2$ for the cases of complete factorization and non-factorization compared to the projected differential cross section measurement. The black and blue symbols indicate the expected sensitivity of the measurement; their central values are set to the prediction for nonfactorizable σ_{eff}. The black symbols show the expected measurements with muon system coverage up to $|\eta| = 2.8$, the blue symbols — up to $|\eta| = 2.4$.

is immeasurably small. However, many new physics scenarios predict decay rates that could be within experimental reach (the present best 90% CL limit is $\mathcal{B}(\tau \to 3\mu) = 2.1 \times 10^{-8}$ [33]). During the HL-LHC running period, about 10^{15} τ leptons will be produced mostly in D_s meson decays. Muons arising from decays of such τ leptons tend to have low momenta and large pseudorapidities, which makes their reconstruction a challenge. This also immediately implies that this search will benefit greatly from the extended coverage of the upgraded muon system and from the system's strongly enhanced capabilities to trigger on and reconstruct low mo-

mentum muons. In fact, the extension of the muon coverage from $|\eta| = 2.4$ to 2.8 increases the signal fiducial acceptance by a factor of two. Figure 1.30 presents the trimuon mass distributions for signal and background in the event category with at least one muon reconstructed by the ME0 detectors of the upgraded muon system. All event selection cuts are applied. The absence of tails in the signal distribution shows that, despite the high pileup ($\langle \text{PU} \rangle = 200$), muons from $\tau \to 3\mu$ decays are picked correctly. The trimuon mass resolution is also found to not be affected by the pileup. The projected exclusion sensitivity in the absence of a signal is $\mathcal{B}(\tau \to 3\mu) < 3.7 \times 10^{-9}$ at 90% CL, while the expected 5σ-observation sensitivity is $\mathcal{B}(\tau \to 3\mu) = 1.1 \times 10^{-8}$. To reach the same sensitivity without the ME0 chambers, CMS would need a dataset corresponding to 4000 fb^{-1}.

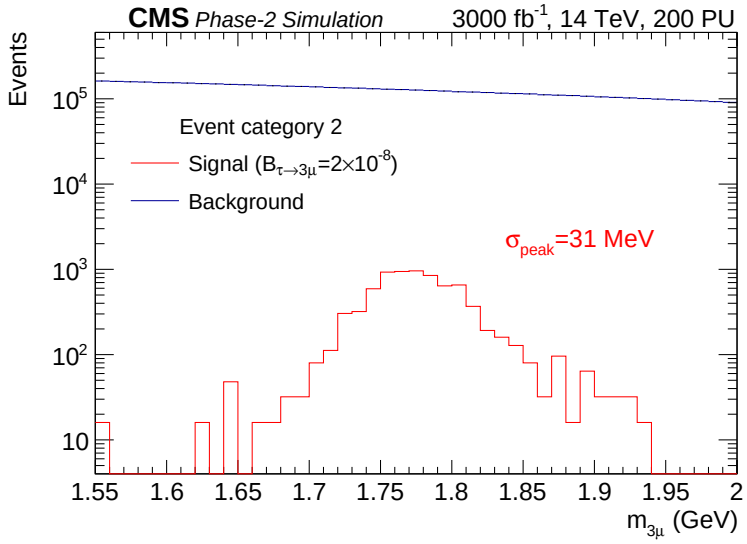

Figure 1.30: Trimuon invariant mass $m_{3\mu}$ for a $\tau \to 3\mu$ signal (red) and background (blue) after all event selection cuts, in the event category 2, defined as containing at least one muon reconstructed by the ME0 detectors. The signal is shown for $\mathcal{B}(\tau \to 3\mu) = 2 \times 10^{-8}$.

Precision measurement of the electroweak mixing angle with Drell–Yan events The electroweak mixing angle is a fundamental parameter of the standard model. A precise determination of $\sin^2\theta^{\text{lept}}_{\text{eff}}$ tests the model and constraints BSM physics. So far the most precise measurements have been obtained at LEP, SLD, at the Tevatron and at the LHC. The best published LHC results have an absolute uncertainty in $\delta\sin^2\theta^{\text{lept}}_{\text{eff}}$ of about 10^{-3} [34–37]. At the HL-LHC we will be able to improve this accuracy by one order of magnitude, exploiting the extended $|\eta|$ coverage of the upgraded CMS detector. This is a significant improvement even with respect to the precise results obtained at LEP and SLD, with an uncertainty of 2.6×10^{-4} on the combination of their $\sin^2\theta^{\text{lept}}_{\text{eff}}$ measurements [38].

Dimuon pairs are produced mainly through the annihilation of a quark and an antiquark, $q\bar{q} \to Z/\gamma^* \to \mu^+\mu^-$. The corresponding forward backward asymmetry A_{FB} is sensitive to $\sin^2\theta^{\text{lept}}_{\text{eff}}$. It is defined as

$$A_{\text{FB}} = \frac{\sigma_{\text{F}} - \sigma_{\text{B}}}{\sigma_{\text{F}} + \sigma_{\text{B}}},$$

where σ_{F} and σ_{B} are the cross sections in the forward ($\cos\theta^* > 0$) and backward ($\cos\theta^* < 0$) hemispheres, respectively, and θ^* is the polar angle of the μ^- flight direction in the Collins–Soper frame.

The total uncertainty on $\sin^2\theta^{\text{lept}}_{\text{eff}}$ is limited by the knowledge of the parton distribution functions (PDF). By measuring A_{FB} as a function of invariant mass $m_{\mu\mu}$ and rapidity $y_{\mu\mu}$ of the dimuon system the PDFs can be strongly constrained. Since $\sin^2\theta^{\text{lept}}_{\text{eff}}$ and the PDFs are affecting the two-dimensional $A_{\text{FB}}\,(m_{\mu\mu}, y_{\mu\mu})$ distribution in different ways, the measurement of the weak mixing angle is not biased by this method. Figure 1.31 shows the expected uncertainties of the CMS measurement as a function of luminosity, for both the current muon acceptance of $|\eta| < 2.4$, and for $|\eta| < 2.8$ in the upgraded muon detector. The uncertainties shrink by 20% to 30% due to the enlarged $|\eta|$ range, resulting in a total uncertainty of $\delta\sin^2\theta^{\text{lept}}_{\text{eff}} \approx 10^{-4}$ at 3000 fb^{-1}.

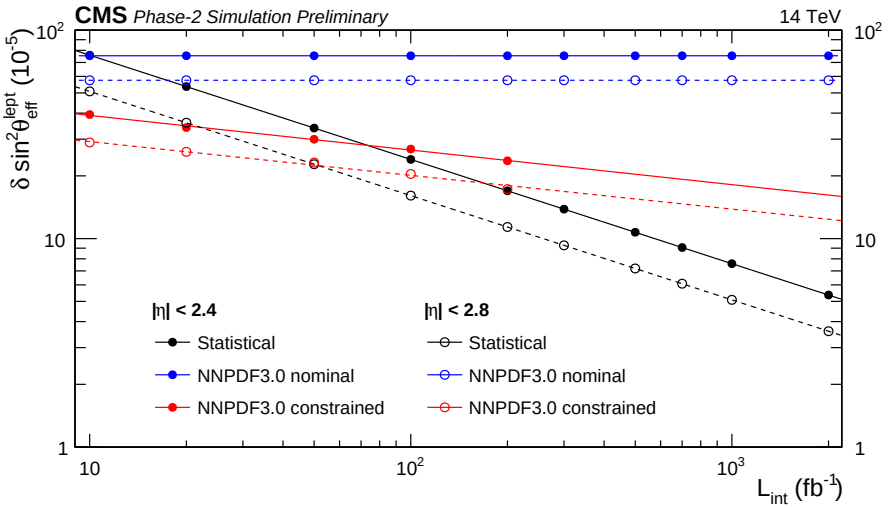

Figure 1.31: Expected uncertainties in $\sin^2\theta^{\text{lept}}_{\text{eff}}$ extracted by fitting the $A_{\text{FB}}(m_{\mu\mu}, y_{\mu\mu})$ distributions at $\sqrt{s} = 14\,\text{TeV}$ as a function of integrated luminosity for $|\eta| < 2.4$ and for $|\eta| < 2.8$ acceptance selections for the muons. The figure shows that the total uncertainty on $\sin^2\theta^{\text{lept}}_{\text{eff}}$, given by the combination of the constrained PDF error and the statistical uncertainty, can be reduced by 20% exploiting the extended pseudorapidity acceptance.

BSM physics with two same-sign leptons in the final state Besides increasing the acceptance of a signal, the extended muon system can also be of great help in suppressing background. A search for new physics using a signature of two same-sign leptons and missing transverse momentum is one such case. This final state signature arises in many BSM models, including SUSY. The dominant background for this search is WZ production, with both bosons decaying leptonically. To suppress this background, one uses a veto on the presence of a third lepton in an event. The background that remains is still the WZ process, with one of the leptons being "lost" due to either reconstruction inefficiency or being outside of the detector acceptance. Figure 1.32 shows the number of WZ background events passing all selection criteria as a function of a "lost" muon's $|\eta|$ for three different muon system acceptance ranges: $|\eta| < 2.8$ (upgraded muon system), $|\eta| < 2.4$ (upgrade without ME0 chambers), and $|\eta| < 1.6$ (no upgrades to electronics of ME1234/1 chambers and no GEM detectors). From one scenario to the next, the background rate changes by approximately a factor of two.

BSM physics giving rise to highly displaced muons It is possible that BSM particles with a mass scale well below $\mathcal{O}(1)$ TeV can be produced at the LHC/HL-LHC and nevertheless evade detection if they are sufficiently long-lived that their decay products, e.g. muons, appear displaced from the interaction point. A displacement by as much as 10–100 cm is large

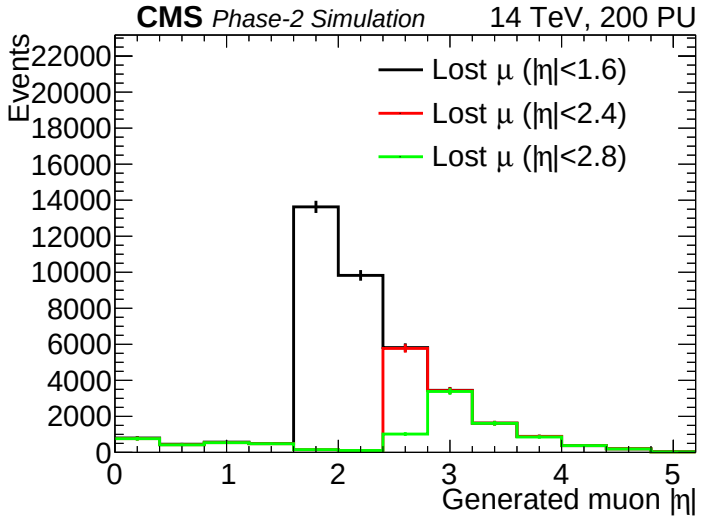

Figure 1.32: Number of WZ background events passing all selection criteria in a search for new physics with two same-sign leptons and missing transverse momentum, as a function of a "lost" muon's $|\eta|$ for three different muon system acceptance ranges: $|\eta| < 2.8$ (green), $|\eta| < 2.4$ (red), and $|\eta| < 1.6$ (black). The event numbers are for 3000 fb^{-1}.

enough to fail the endcap muon trigger that uses the beam spot as a built-in constraint. Without such a constraint, L1 trigger momentum measurements in the forward direction are not accurate enough to allow for sustainable trigger rates. The GEM detectors added to enhance conventional muon trigger/reconstruction at high pseudorapidity will also enable triggering on highly displaced muons in the forward direction.[1] With the help of dedicated trigger and reconstruction algorithms developed for the upgraded endcap muon system, CMS will improve its sensitivity for measuring, or setting limits on, the production cross section of such events by a factor of three, as can be seen in Fig. 1.33.

BSM physics with heavy stable charged particles If BSM particles have masses larger than $\mathcal{O}(1)$ TeV, they are mostly produced with velocities well below the speed of light, e.g. with $\beta \sim 0.3$–0.5. If such particles are electrically charged (heavy stable charged particles, or HSCP), have no color charge, and are extremely long lived, they would therefore look like slow muons propagating through the CMS detector volume over a time as long as a few BXs and failing the present muon trigger whose efficiency sharply drops for particles with $\beta < 0.6$, as shown in Fig. 1.24. The upgraded RPC link system will allow one to register particles crossing different muon stations with a precision of $\mathcal{O}(1)$ ns at the L1 trigger. With this system CMS will be able to identify patterns of delayed hits from one station to the next and trigger on such an event, should the observed pattern of hits be consistent with a slow moving particle. Figure 1.34 shows the efficiency of such a trigger in the (β, η) plane in the pseudorapidity range where an HSCP would cross four muon stations with RPC detectors. The CMS HSCP trigger capabilities will be extended from the present limitation of $\beta \sim 0.6$ down to $\beta \sim 0.2$. The trigger purity is expected to be high and can be improved even further by combining the HSCP muon system trigger with dE/dx measurements in the inner silicon track detectors (see CMS Tracker Upgrade TDR [16]).

Table 1.12 summarizes the sensitivity gains in the five presented physics analyses particularly benefiting from the acceptance extension provided by the ME0 chambers. The gain can be as

[1] The barrel muon system already can trigger on such highly displaced muons.

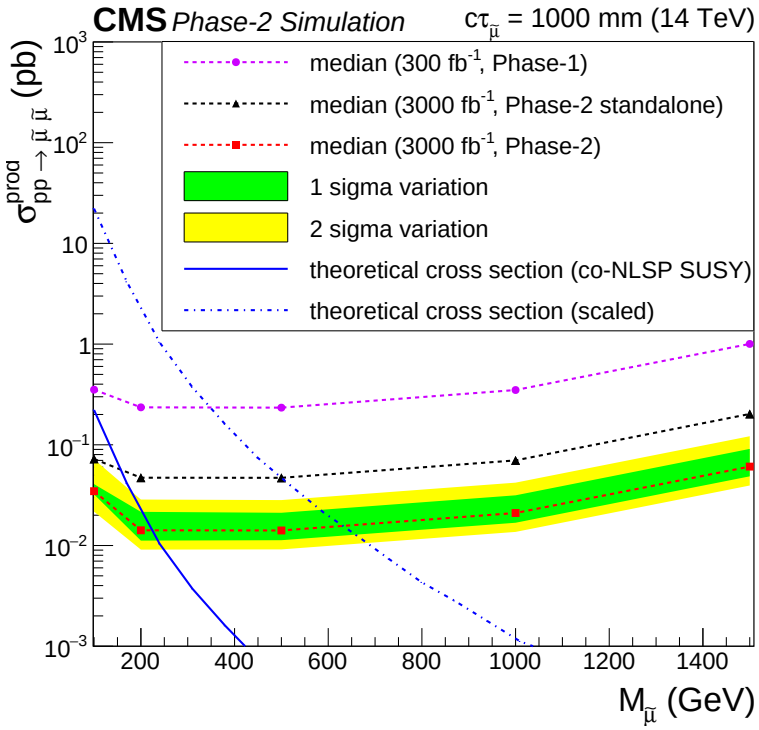

Figure 1.33: Upper limits on pair production of hypothetical $\widetilde{\mu}$-particles, decaying $\widetilde{\mu} \to \mu + X$ with lifetime distance $c\tau = 100$ cm, as a function of the $\widetilde{\mu}$-particle mass. The expected limits for the Phase-1 detector at 300 fb^{-1} are shown as dotted magenta line. The expected limits for the Phase-2 detector are shown in red. The black dottted line shows the sensitivity without applying the special algorithm for displaced tracks. The theoretical cross section for a specific SUSY model is represented by the solid blue line. Modifications of the model parameters can change this cross section by as much as a factor of 100, which is indicated by the dash-dotted blue line.

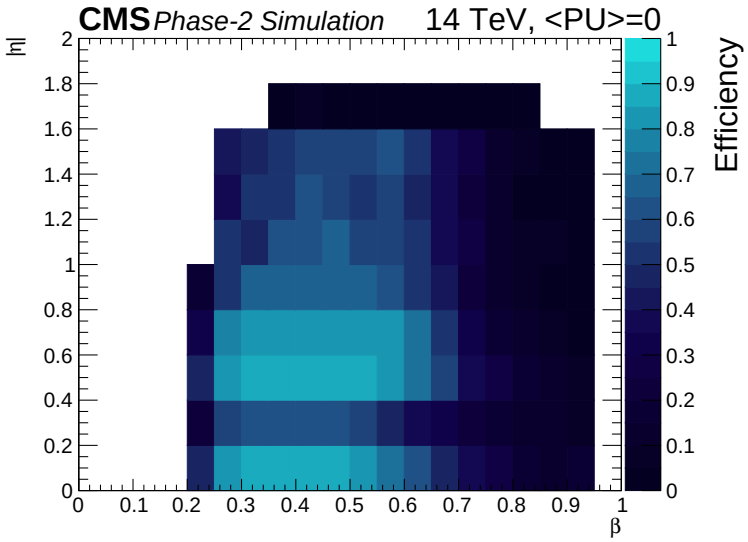

Figure 1.34: HSCP trigger efficiency as a function of HSCP velocity β and pseudorapidity η.

large as a factor of 1.5.

Table 1.12: Sensitivity gains due to extending the muon pseudorapidity coverage from 2.4 to 2.8 provided by the ME0 chambers.

analysis topic	parameter of interest (POI)	sensitivity gain in POI
$H \to ZZ \to 4\mu$	signal strength	7 %
Double-parton scattering	slope of $d\sigma/d(\eta_1\eta_2)$	factor 1.5
$\tau \to 3\,\mu$	$B(\tau \to 3\mu)$	17 %
Drell-Yan FB asymmetry	$\sin^2\theta^{lept}_{eff}$	factor 1.3
BSM same-sign dilepton search	BSM cross section	15 %

1.7 Resources and schedule

The current CMS muon system, comprising CSC, DT and RPC chambers, was completed in time and has been fully operational in the CMS cavern since 2008.

The Phase-2 upgrades to the CMS muon system require another big effort in manpower, and additional CORE costs, about 25 MCHF, as outlined in Table 1.13 and detailed in Chapter 9. For comparison, the CORE costs for the current muon system were about 100 MCHF. The Muon system upgrade amounts to about 10% of the total CMS Phase-2 upgrade CORE cost. CORE costs represent the value of the equipment installed in the experiment, without contingency. They include costs for fabrication and construction, and for installation and integration. They do not include R&D and prototype costs, costs for infrastructure and facilities at CMS institutions, nor institution personnel costs. The CORE cost estimates include spare parts to cover production losses, while spares to support long term maintenance and operation are paid separately from the CMS M&O budget. Costs are reported here in 2016 CHF, with no correction for inflation to future years.

More than seventy CMS institutions will share the muon upgrade work, according to their expertise and areas of interest. Most of them already participated in the construction of the present muon system and in the R&D for Phase-2. The tasks have been identified and assigned, as shown in Chapter 9.

The design choices and cost figures result from an extensive R&D effort optimizing the performance, as needed to exploit the HL-LHC discovery potential, and the resources, in terms of manpower and core cost, under the constraints of the HL-LHC schedule. The cost estimates are reliable, since they are based on extrapolations from the original chamber and electronics production, known electronics technology costs, or the prices of pre-production components.

The schedule is driven by the HL-LHC schedule, and summarized in Fig. 1.35. Given the detailed R&D upgrade studies performed in the last years this plan is realistic. Before production can start, Electronics System Reviews (ESR) will validate the proposed electronics upgrades for the existing detectors, while both the RPC and GEM projects, which use new chamber types, must undergo also an Engineering Design Review (EDR). These milestones are also marked in the schedule in Fig. 1.35. The environmental plan for CSC and RPC gas usage will be made well before LS3.

Table 1.13: CORE Cost estimates for the Phase-2 Upgrades of the Muon System. The table includes also the GE1/1 system, which is subject of a separate TDR [7].

Estimated CORE cost in MCHF (2016)		
DT System Upgrade	On-detector electronics	3.289
	Back-end electronics	1.609
	Optical links	0.784
	Total DT Upgrade cost	**5.682**
CSC System Upgrade	On-detector electronics and OTMBs	2.690
	FED system and ODMBs	0.887
	High Voltage modules	0.209
	Total CSC Upgrade cost	**3.785**
RPC System Upgrade	RE3/1 and RE4/1 chambers	0.764
	RE3/1 and RE4/1 power system and on-detector electronics	1.084
	RE3/1 and RE4/1 service and installation	0.406
	Link System Upgrade	1.380
	Total RPC Upgrade cost	**3.634**
GE1/1 System	**Total GE1/1 System cost**	**3.750**
GE2/1 System	Chambers	1.606
	DAQ system	1.099
	Power system	0.920
	Services, installation, test bench	0.470
	Total GE2/1 System cost	**4.095**
ME0 System	Chambers	1.336
	DAQ system	1.343
	Power system	1.106
	Services, installation, test bench	0.456
	Total ME0 System cost	**4.241**
Muon System Upgrade cost (excluding GE1/1)		**21.437**
Total Muon System Upgrade cost (including GE1/1)		**25.187**

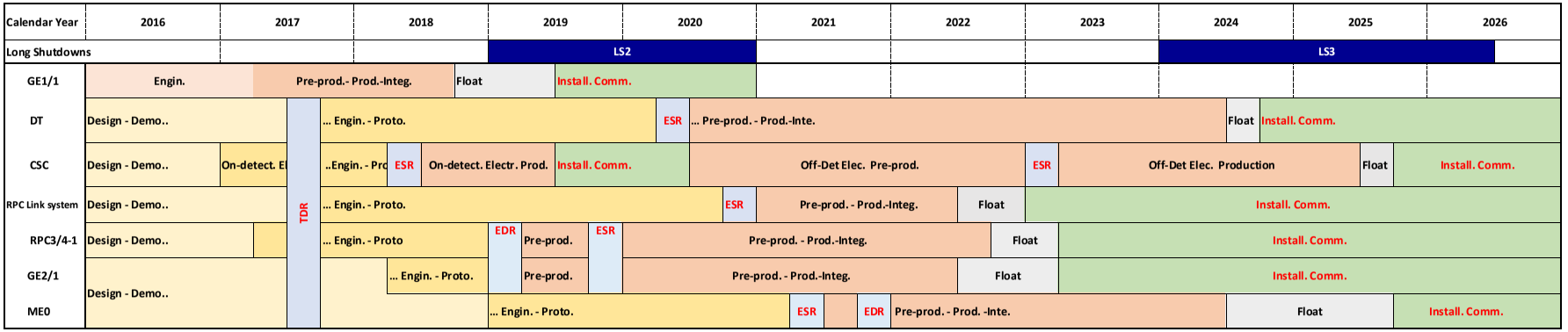

Figure 1.35: Schedule for the CMS Phase-2 muon detector upgrades. The GE1/1 project is the subject of a separate TDR [7].

1.8 Synopsis

The CMS detector at the Large Hadron Collider has shown excellent performance. A remarkable wealth of physics results has been published, notably the discovery of the Higgs particle. The CMS research programme is aimed at fundamental questions in particle physics: Are there particles and forces beyond the SM? Can dark matter particles be detected at the LHC? Has the Higgs boson all the properties as predicted by the SM?

After a major machine upgrade to be completed in 2026, the High luminosity LHC will provide CMS with an integrated luminosity of 3000 fb^{-1} for proton-proton running, at a center of mass energy of 13 or 14 TeV. This represents a fifty-fold increase with respect to the high energy data set accumulated by end of 2016. This upgrade is necessary to explore the full physics potential of the LHC, since most analyses are statistics limited.

To cope with the much higher rate CMS and the other LHC detectors need to be upgraded, too. Some detector parts in CMS have come to age and need to be replaced by new radiation hard components. Many electronic circuits in readout and trigger must be exchanged by faster versions that can handle the high data rates. Additional subdetectors must be installed in CMS to guarantee a geometrical acceptance close to 4π, and to provide reliable triggering and precise measurements also under very demanding conditions with huge track and hit densities. The searches for new physics must cover challenging experimental signatures, such as heavy particles decaying outside the inner tracker or slowly moving heavy charged particles.

CMS has carried out an extensive research and development programme to optimize the detector upgrades needed to fully exploit the physics potential at LHC, while keeping the cost under control.

Muons play a crucial role for precision measurements and discoveries in a hadron collider environment, since they can be separated easily from the large hadronic background, and their direction and momentum can be measured accurately. A fine physics example is the Higgs boson decay into four muons.

This Technical Design Report motivates and specifies the CMS Phase-2 upgrade programme for the muon system. It updates the less-detailed muon chapter of the CMS Phase-2 Upgrade Technical Proposal [24]. Presently, three types of muon detectors are used, Drift Tube chambers (DT), Cathode Strip Chambers (CSC) and Resistive Plate Chambers (RPC), covering the pseudorapidity range up to 2.4 (translating into an angle of 10.4° with respect to the beam axis).

High dose longevity tests in the CERN GIF++ facility have shown that the chambers will survive and function also at HL-LHC, but various electronics components must be replaced for reasons of aging and to allow for much increased rates. Without the proposed upgrades to the DT and CSC systems many muon detectors will cease to work properly, so that major physics goals cannot be reached, thus the whole CERN LHC upgrade would be severely compromised. Plans for the usage of environmentally friendly gases in RPC and CSC chambers will be developed in due time.

To maintain the present excellent performance of the CMS muon system within a large geometrical acceptance, several measures must be undertaken. Most challenging for muon triggering and measurement are the forward regions, with a high track density, huge background rate, and reduced magnetic bending power. To recover the performance of the existing CSC and RPC detectors in the endcap regions, additional fast GEM and RPC detectors will be added. Further GEM detectors will extend the pseudorapidity range to $|\eta| = 2.8$ (angle 7.0° with respect to beam), following the increased acceptance of the Phase-2 inner tracker. This is relevant

for example for the “golden” Higgs boson decay into four muons.

The muon upgrade task is shared by more than seventy CMS institutions, which have all the expertise and manpower needed. First demonstrator GEM chambers have already been successfully inserted at the beginning of the year 2017. Most of the new components will be installed in the CMS detector during the Long LHC Shutdown LS3 (2024–2026), some items will be set up already in LS2 (2019–2020). The end of LS3 marks the beginning of the LHC high luminosity Phase-2. The total core cost for the CMS Phase-2 muon upgrade is calculated to 25 MCHF (2016 prices).

Part II

Details of the CMS Phase-2 Muon Detector Upgrade

Chapter 2

Detector and electronics longevity at HL-LHC

All muon system detectors—DTs, CSCs, RPCs, GEMs—and a large part of their electronics are presumed to last through 10 HL-LHC years (3000 fb^{-1}), even though the original designs of the DT, CSC, and RPC systems were specified and validated for 10 LHC years (500 fb^{-1}, Ref. [39]). The results of those old aging studies for DTs, CSCs, and RPCs obtained at the time when these CMS detectors were designed can be found in Refs. [40], [41], and [42, 43], respectively. The past longevity studies of the present-day DT, CSC, and RPC electronics are described in Refs. [44], [45, 46], and [47], respectively. As the part of the muon upgrade program, the longevity of all detectors and electronics, both the original ones and the new upgraded systems must be re-certified/certified for 10 years of operation at the *High Luminosity* LHC.

In this chapter, we address the common aspects of detector and electronics aging R&D, including the description of the irradiation facilities used in such studies. In addition, we discuss the strategy addressing the new greenhouse gas regulations adopted by the European Commission in 2014. These new regulations demand us finding ways to significantly reduce the exhaust of greenhouse gases presently used in CSCs and RPCs.

The actual results of the muon detector and electronics longevity studies are presented in the corresponding subsystem Chapters 3–6. We find that the upgraded CMS muon system should be able to withstand 10 years of operation at HL-LHC, while also satisfying the new greenhouse gas use regulations.

2.1 Radiation in the muon system

HL-LHC background in the muon system is simulated as follows. Minbias pp collisions with the average pileup of 200 are generated with PYTHIA. Then, FLUKA is used to propagate particle through the detector and surrounding material, cavern, etc. Besides the material in the CMS detector itself, simulation takes into account the following elements (see Fig. 2.1):

- the cavern walls modeled with an ellipsoidal shape (although the actual CMS cavern is not exactly elliptical, the lengths of the ellipse axes correctly reproduce the distances between the detector and the cavern ceiling and side walls);
- the 100-meter-high cylindrical shaft;
- the cavern floor, including air gaps for cables and stainless steel insertions;
- two stainless steel cuboids placed at the near and far sides of the barrel represent a simplified model for the electronics racks on the balconies;
- the forward hadron calorimeter raisers are described as a set of 4 stainless steel cuboids at each endcap;

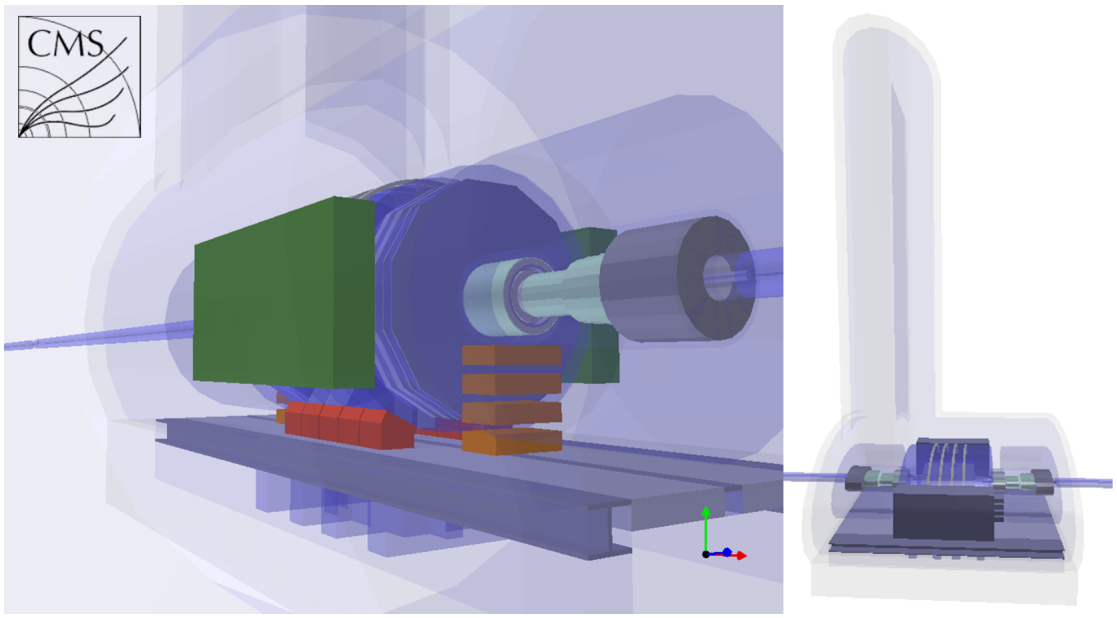

Figure 2.1: Geometry of the CMS detector and its surroundings used in the simulation of background. Besides the material in the CMS detector itself, the simulation takes into account the cavern/shaft walls, the experimental hall floor, the main electronic racks (green), the forward hadron calorimeter raisers (brown), and the barrel return yoke feet (red).

- a simplified model of the iron feet that support the barrel yoke.

Neutrons are tracked in the simulation down to the 10^{-5} eV energy (well below the thermal limit of 0.025 eV). The tracking threshold for photons and charged particles is 100 keV. Fluxes of all particles to be shown below are calculated at the surfaces of the muon chambers.

The main sources of background in the muon system are:

- neutrons produced in the wake of hadronic showers; directly, neutrons do not contribute significantly to signal rates in gaseous detectors, but they do affect considerably the electronics longevity;
- photons produced in de-excitation of nuclei, the excitation of which goes via a capture of low energy neutrons; photons are the main source of background hits in muon detectors (primarily caused by Compton electrons and some electrons/positrons born via pair production); photons are also the main source of ionization-related damage to electronics;
- collision muons and punchthrough hadrons;
- accelerator background (mostly muons).

The contribution of collision muons, punchthrough hadrons, and accelerator background to single hit rates in muon chambers and their damaging effect to electronics are generally small in comparison to the photon-induced hits. However, they are the main source of multi-layer hit segments in muon chambers and, hence, are of concern in the context of muon segment reconstruction.

The simulated energy spectrum of neutrons in ME1/1 chambers at HL-LHC is shown in Fig. 2.2 (left). The neutron energy spectrum ranges from the thermal limit (a bump near 0.025 eV) to $\mathcal{O}(100)$ MeV. The energy spectrum on the right hand side exhibits two pronounced "peaks",

one near 1 MeV (mostly due to back scattering albedo neutrons) and the other near 70 MeV, where the neutron-nucleus cross section is the smallest (and so is neutron absorption by the calorimeters and the iron yoke). The long tail (in the log(E)-scale) of near-thermal neutrons stems from the fact that non-thermal neutrons mostly scatter elastically and slowly lose energy without disappearing from the overall pool of neutrons.

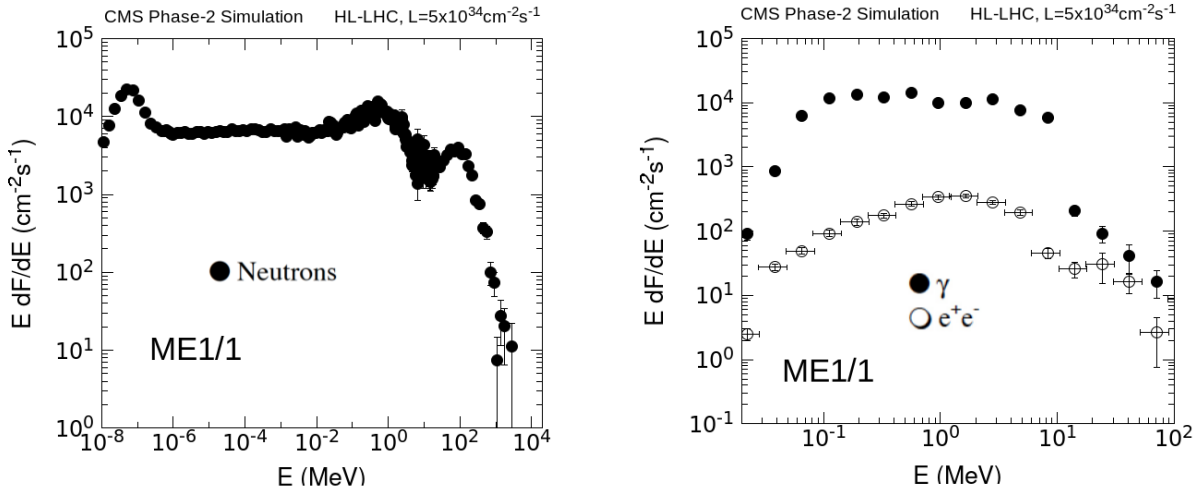

Figure 2.2: Left: Simulated energy spectrum of neutrons entering ME1/1 chambers at HL-LHC. Right: Simulated energy spectrum of photons and electrons/positrons entering ME1/1 chambers at HL-LHC. The energy spectra shapes in the other muon detectors are similar.

The energy spectrum of photons is in the range 0.1–10 MeV energy (Fig. 2.2 (right)), which corresponds to the typical nuclear de-excitation levels. Photons in this energy range passing through gaseous detectors have a probability of $\mathcal{O}(1\%)$ to convert/scatter in the material in front of the gaseous volume so that resulting electrons/positrons could enter the gas volume, produce ionization, and give rise to signals.

The fluxes of neutrons and photons vary considerably with pseudorapidity and distance from the interaction point, as can be seen in Figs. 2.3 and 2.4, respectively. The highest rates are in the high pseudorapidity region. It is worthwhile noting that the outermost detectors are not the quietest; they are affected by the flux of backscattered neutrons (albedo) or thermalized neutrons present in abundance in the cavern. The simulated fluxes of electrons and positrons and of muons and charged hadrons are displayed in Figs. 2.5 and 2.6. Figure 2.7 shows the total ionization dose in the muon system expected for 3000 fb^{-1} at HL-LHC.

2.2 Longevity and operational stability of gaseous detectors

When exposed to prolonged radiation, all gaseous detectors suffer aging [48], whose typical operational manifestations are:

- a loss of gas gain,
- a rise in spurious signal rates ("dark rate"),
- an increase in leakage currents ("dark current"),
- and development of self-sustained discharges set off at high radiation rates, a phenomenon known as the Malter effect [49].

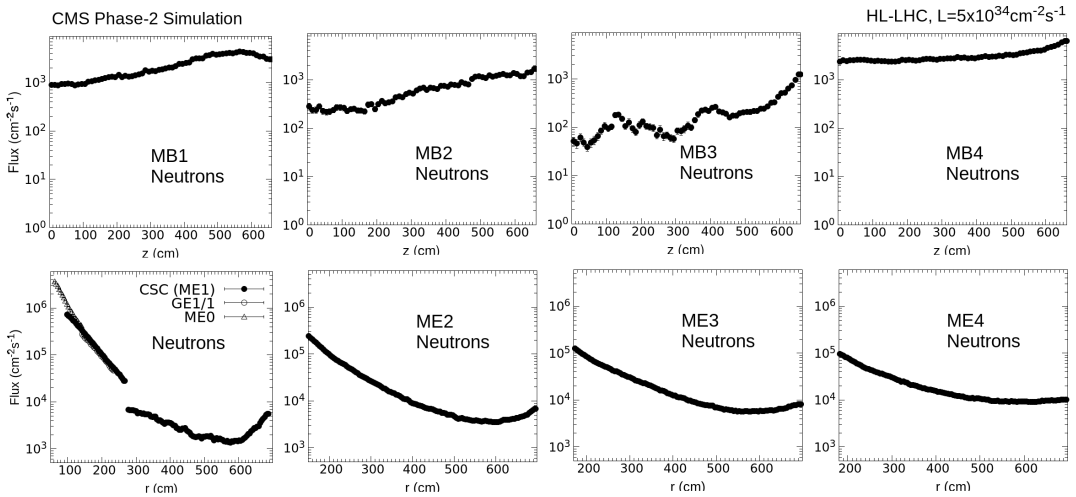

Figure 2.3: Simulated flux of neutrons in the muon system at HL-LHC for the barrel muon system (top) and endcaps (bottom).

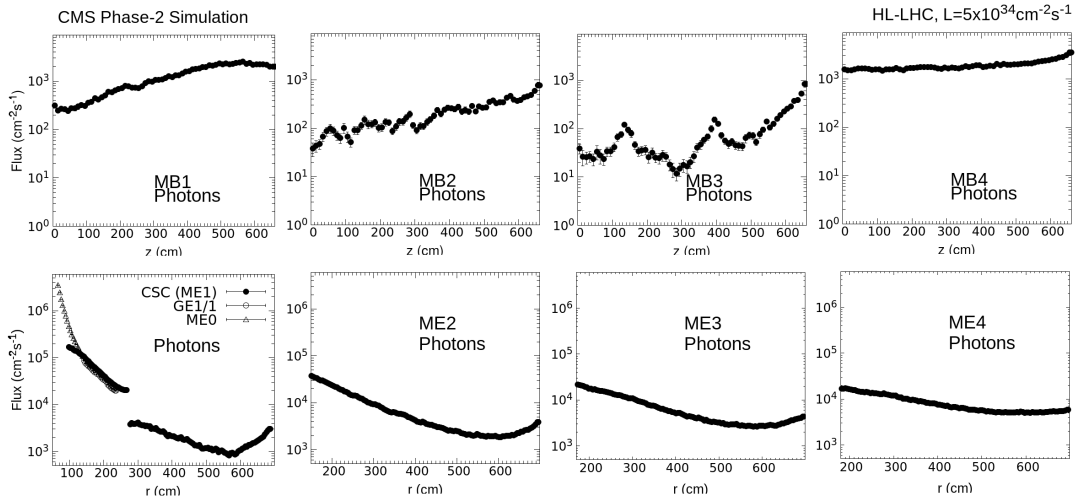

Figure 2.4: Simulated flux of photons in the muon system at HL-LHC for the barrel muon system (top) and endcaps (bottom).

The main causes behind the detector performance deterioration are chemical processes largely occurring in the hot plasma inside electron multiplication avalanches. Gas molecule fragments produced inside avalanches may form polymers growing on anode wires, cathode surfaces, and anode-cathode insulating elements. Polymerization builds up with increasing integral of a radiation exposure at a rate that depends on a myriad of factors, such as detector geometrical design, materials used for cathode and anode, operational gas gain, gas mixture used, impurities in the gas itself and/or outgassing from the detector material (including such auxiliary elements as gas supply lines), gas flow rate, primary ionization, etc. The deterioration of performance can be homogeneous on non-homogeneous over the detector volume.

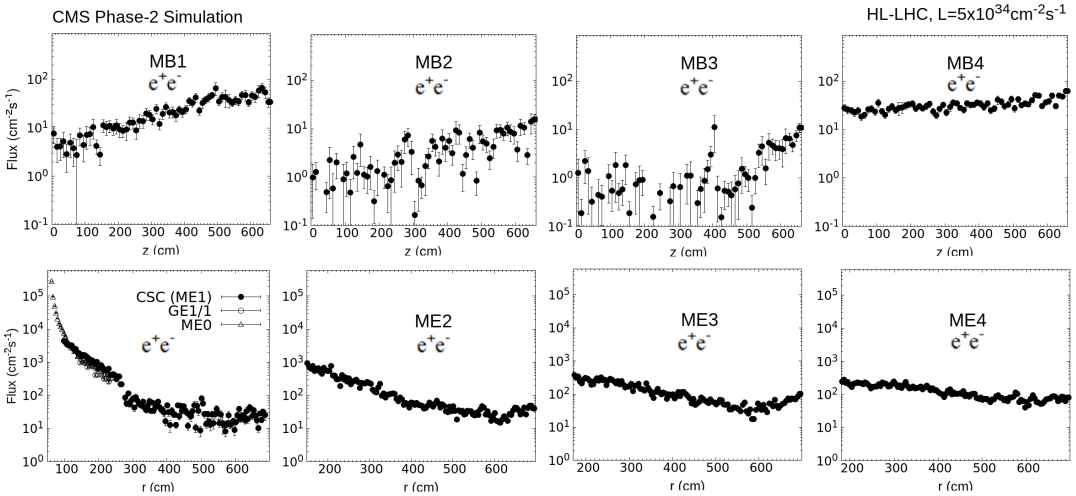

Figure 2.5: Simulated flux of electrons and positrons in the muon system at HL-LHC for the barrel muon system (top) and endcaps (bottom).

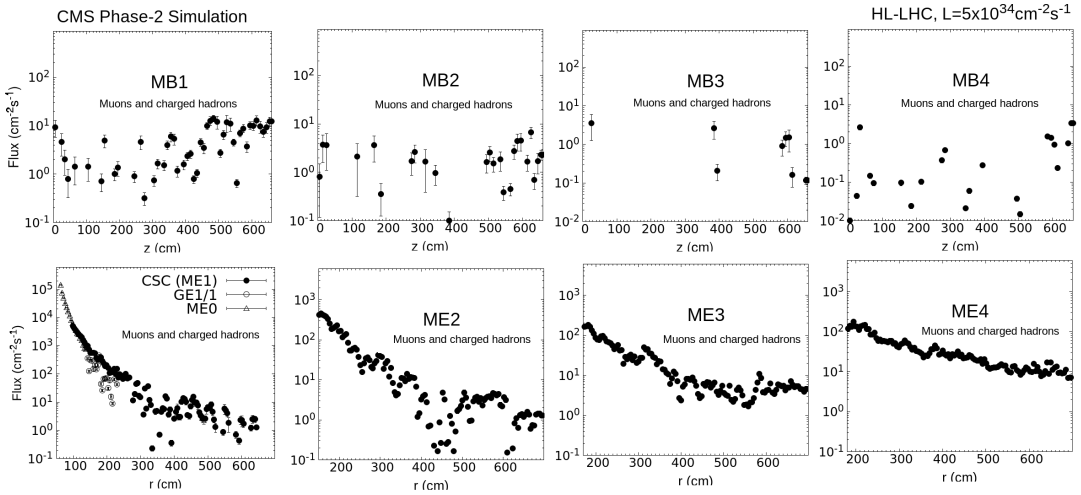

Figure 2.6: Simulated flux of muons and charged hadrons in the muon system at HL-LHC for the barrel muon system (top) and endcaps (bottom).

Aging is driven by a complicated chemistry and depends on many factors, many of which are hard to account for (e.g., gas impurities and material outgassing). To evaluate the potential detector performance deterioration over the lifetime of an experiment, detector prototypes are subject to accelerated aging tests performed at a higher instantaneous radiation rate, while keeping all other operation parameters such as gas gain and gas flow as close to the nominal as possible. It is prudent to use the exact same materials and their vendors in construction of prototypes as those envisioned for the ultimate detector. To project the results of such accelerated tests toward many years of operation at the expected nominal radiation, one assumes that the aging depends on the integral accumulated charge per unit of a wire length (C/cm) or per unit of detector area (C/cm^2). However, such a simple scaling is obviously an approximation

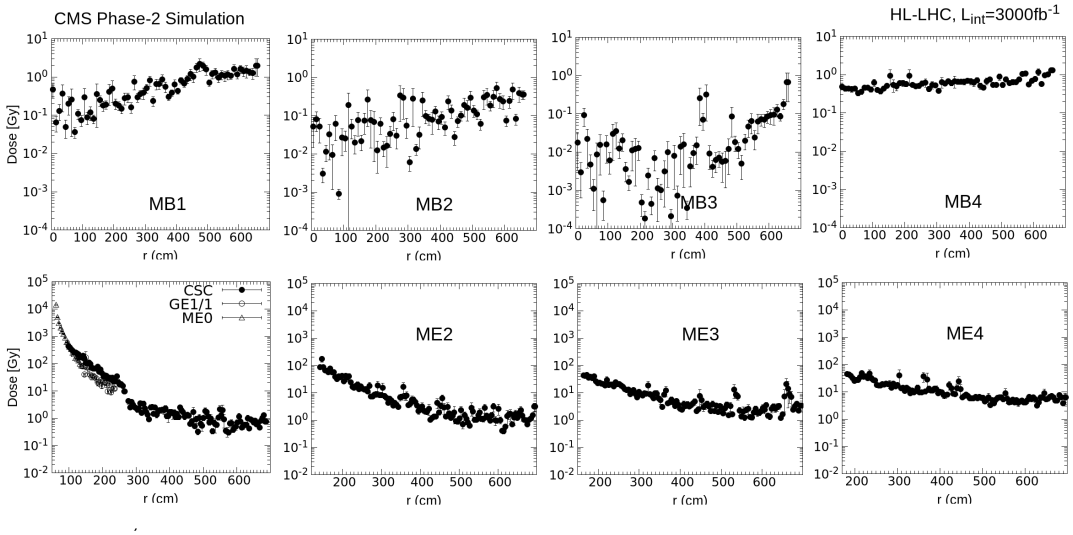

Figure 2.7: Simulated total ionization dose (TID) in the muon system for 3000 fb^{-1} at HL-LHC for the barrel muon system (top) and endcaps (bottom).

at best; hence, one should regard projections derived from such accelerated aging tests as indicative, not quantitatively predictive. Therefore, large safety margins of a factor of 3 or more are commonly required in the amount of radiation to be accumulated in the accelerated tests.

CSCs and DTs use 50 μm thin gold-plated anode wires made of tungsten and stainless steel, respectively. Polymerization on anode wires makes the wires effectively thicker, which naturally results in decreasing of the gas gain. Irradiation was seen to cause oxidation of the tungsten wire core; this makes wires swell, which also reduces the gas gain. Under the pressure of such swelling, the outer layer of gold may start cracking and flaking. Sharp flakes in their turn can cause local discharge instabilities or complete electrical breakdown, making a large detector element corresponding to one high voltage channel inoperable.

Should polymer blemishes formed on cathode surfaces be non-conductive, they can become significantly charged under an intense radiation, so much that the resulting strong electric field could cause an emission of electrons from the cathode. Such electrons proceed to make their own avalanches and the positively charged ions produced in these avalanches, after drifting back to the cathode, can stuck on the same non-conductive spots and, thus, help maintain them charged. With such a positive feedback (so-called Malter effect), a self-sustained local discharge can be ignited that can then persist indefinitely even if the external radiation is removed. Malter discharges avalanches, if large enough, can lead to "hot" local spots of high rate signals; they also may can be below the signal detection threshold. Either way, Malter currents, being very local, can lead to current densities thousands of times larger than those associated with the nominal radiation.

Should deposits formed on CSC cathode surfaces be conductive, they could cause signal current leaks between nearby cathode strips, which would result in induced signal shape variations and a loss of a spatial resolution. In DTs, conductive deposits between drift field shaping electrodes could result in a significant distortion of the drift electric field, causing losses in the signal hit efficiency and deterioration of the hit spatial resolution. Polymerization of conductive material separating anode and cathode elements in all gas-ionization detectors can cause leakage currents, a decrease of the effective difference of potentials between the anode and the

cathode (and, hence, a reduction of the gas gain), and a complete electrical breakdown.

The RPC and GEM detectors do not have thin wires, but they can be affected by polymerization on plate or foil surfaces as much as any other gaseous detectors. Changes of RPC surface resistivity or surface flatness due to a build-up of deposits can lead to gas gain modifications, Malter currents, and overall operation instabilities. Non-conductive deposits on GEM foils can lead to electric field distortions between foils and inside foil pinholes, which again can affect both GEM gas gain and general operational stability of a detector.

2.3 Reduction of greenhouse gas usage/emission

In 2014, the European Commission adopted the new "F-gas regulation" [27] limiting the total amount of the most important fluorinated greenhouse gases (F-gases) that can be sold in the EU from 2015 onward and phasing them down in steps to one-fifth of 2014 sales in 2030. CERN is committed to follow the EC regulations, and so is the CMS Experiment.

In the CMS muon system, the detectors using fluorinated gases are CSCs and RPCs (DTs and GEMs uses Ar/CO_2-based mixtures). The gases used by CSCs and RPCs, and their global warming impact in the present modus operandi, are summarized in Table 2.1. The presence of these specific greenhouse gases in the CSC and RPC gas mixtures is not accidental; they all play very specific roles. CF_4 is added to enhance the CSC longevity. This gas also makes electron drift velocity fast and is an efficient non-flammable photon quencher. In RPCs, $C_2H_2F_4$ is used as an efficient photon quencher, while SF_6 is a strongly electronegative gas; both components are needed to ensure a stable operation of RPCs.

Table 2.1: Greenhouse gases used in CMS muon system and their global warming impact. The Global Warming Potential (GWP) is given for a 100-year time horizon [50]. The CF_4 recuperation system for the CSC detectors is in operation since 2013.

	CSC	RPC
Greenhouse gases used	CF_4	$C_2H_2F_4$ and SF_6
Greenhouse gases fraction in the gas mixture	10%	95.2% and 0.3%
Global Warming Potential (relative to CO_2)	6500	1300 and 23 900
Gas mixture re-circulation	Yes, 90%	Yes, 85%
Gas mixture replenishing rate (l/hr)	700	1100
F-gas recuperation	Yes, $\sim$40%	No
F-gas venting rate (l/hr)	42	1047 + 3.3
CO_2-equivalent rate (m^3/h)	273	1440
Relative impact (entire muon system = 100%)	16%	84%

To reduce the greenhouse gas emission, the following options are being considered:

- *Reducing the amount of F-gases vented out into the atmosphere without changes in the operating gas mixture.* This will be achieved by means of the following measures. For CSCs, we plan to upgrade the present CF_4 recuperation system and improve its efficiency from the current 40% to 70%. For RPCs, we will first repair gas leaks where possible (about half of the 47 leaking chambers), shut off the remaining leaking RPCs (the impact of which on the muon system performance was studied in detail and found to be marginal), and then add a high-efficiency F-gas recuperation system with the quoted efficiency of 80%. In addition, CMS is committed to buy an abatement system to burn F-gases into considerably less harmful states before venting the

gas into the atmosphere. The abatement efficiency is quoted to be 90% for the CSC gas mixture and 95% for the RPC gas mixture. Table 2.2 shows the effect of each mitigation measure and the net reduction in the F-gas exhaust. In addition, CSCs are now being tested for aging with a much reduced amount of CF_4 in the gas mixture.

Table 2.2: Mitigation measures and their impact on reducing the amount of greenhouse gases vented into the atmosphere. The impact is shown as the ratio of the new exhaust rate and the current one.

	CSC	RPC
CSC: upgrade of the current recuperation system	0.5	n/a
RPC: leak fix and adding a recuperation system	n/a	0.2
Abatement system	0.1	0.05
Net rate reduction per sub-system: (new rate)/(current rate)	0.05	0.01
Net reduction in the CO_2-equivalent rate for the muon system	0.016	

- *Eliminating F-gases in the gas mixtures.* We are conducting preemptive studies for the worst-case scenario, in which usage of F-gases would be completely banned. This scenario requires an R&D on detector performance and detector longevity with alternative gas mixtures. The first steps in this direction are presented in the CSC and RPC chapters 4 and 5, respectively. It is not yet clear, if such alternative gas mixtures can be found. Should greenhouse-friendly and aging-preemptive mixtures are not found, CSCs will be switched to operate with the Ar+CO_2 mixture and RPCs will operate with a gas mixture based on the eco-friendly HFO-1234ze gas. Both CSCs and RPCs are shown to provide the adequate "instantaneous" performance with these mixtures, but may suffer long-term aging. CSCs are expected to drop gas gain by about 20% at the highest pseudorapidity range [51]. The RPC aging properties with the HFO-based mixture are under the ongoing studies. The high redundancy of the overall CMS muon system, which is considerably enhanced in the forward direction by the upgrades presented in this TDR, will insure the adequate muon trigger and reconstruction performance even in this worst-case scenario.

2.4 Longevity and operation stability of electronics

Besides the gaseous detectors themselves, their electronics are also susceptible to radiation damage, with semiconductor chips being the most vulnerable element. In the context of semiconductor electronics, there are two distinct radiation damage mechanisms: ionization caused by charged particles and photons and displacement of atoms' nuclei (including nuclear reactions) primarily caused by neutrons. Both mechanisms contribute to electronics aging, whose manifestations can be a permanent steady worsening of performance (e.g., an increase of noise in front-end amplifiers, a deformation of response characteristics, growing leakage currents, etc.) and functional unrecoverable failures.

The principal ionizing-based damage effects are an increasing conductivity in the bulk of the semiconductor material and a surface damage, created when the positively charged holes, generated by the passage of an ionizing particle, get trapped in a silicon oxide layer. Displaced nuclei create defects in the semiconductor crystal, which act as a recombination and charge trap centers and may have a strong impact on electric property of the material (including the chip substrate). All these effects exert influence on the electric characteristics of electronic components. The endured damage simply scales with the absorbed ionization radiation dose (Gy) and neutron fluence (integral number of neutrons passing per unit of area).

In addition, one must be wary of single event effects (SEE), the frequency of which depends on the instantaneous radiation rate. These include single event upsets (SEU, a bit flip in programmable electronic elements such as FPGAs and EEPROMs), single event transients (SET, voltage or current spurious pulses), and potentially destructive single event latch-up (SEL, a type of short circuit that can occur in semiconductor p-n-p-n structures). Upon an SEE occurrence, the electronics can typically be reset by reloading the FPGAs/EEPROMs or cycling the power; however, such operations are very disruptive and can be tolerated only if their rate does not exceed a few per hour. SELs can also result in a permanent damage of electronics.

2.5 Detector and electronics irradiation facilities

2.5.1 Detector irradiation

Initial (probe) aging tests of gaseous detectors are routinely done with small scale prototypes with small radioactive sources like ^{90}Sr, ^{55}Fe, ^{137}Cs, etc. These tests can be done fairly quickly allowing for a quick turn-around in a search for promising gas mixtures and testing chamber design and materials. However, to get more realistic results, tests with full scale chambers of the final design (including all materials and using the final assembly technological steps) must be conducted. In the past, such full scale aging studies were done at the dedicated Gamma Irradiation Facility (GIF) [26] at CERN and now are carried out at the new Gamma Irradiation Facility (GIF++) [25] that has replaced its predecessor in 2015.

GIF++ features an intense ^{137}Cs source of 662 keV photons with a set of filters of various attenuation factors. The GIF++ photons have an energy fairly representative of the energy of LHC/HL-LHC photons seen by the muon detectors, 0.1-10 MeV (see Fig. 2.2 (right)). The source provides continuous irradiation over large areas and has sufficient room in the bunker for testing several full-size muon detectors at the same time, as can be seen in Fig. 2.8. As of March 2016, the source intensity was about 13.5 TBq (the half-life of ^{137}Cs is 30.1 years). The open source photon flux is by far greater than the photon flux expected in the muon detectors at HL-LHC and, hence, GIF++ provides an excellent facility for accelerated aging tests of full/large-size detectors.

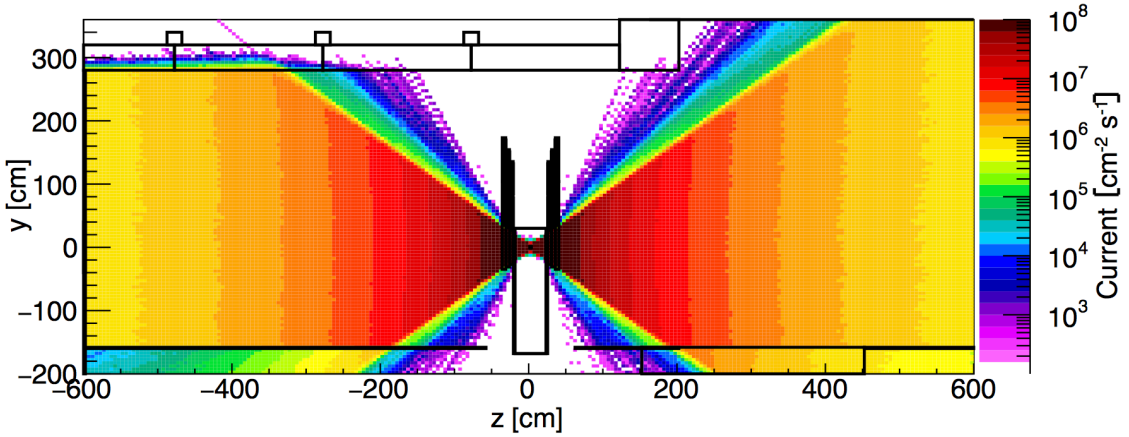

Figure 2.8: The GIF++ floor plan in the (y, z)-plane, and the photon current map for the open source [25]. Correction filters make the flux uniform in planes transverse to the z-axis.

2.5.2 Electronics irradiation

The damage to individual chips due to ionization radiation can be investigated with radioactive sources readily available at various labs. Aging of entire boards subject to photon-induced ionization is de facto probed in the detector longevity studies at GIF++ (see Section 2.5.1).

Thermal nuclear reactors produce neutrons with an energy spectrum from the thermal energy to $\mathcal{O}(1)$ MeV, with characteristic bumps at both ends of the spectrum. Therefore, nuclear reactors are perfect facilities for studying the damage to electronics due to neutrons with $\lesssim 1$ MeV energy, which constitute a large fraction of all neutrons at LHC (see Fig. 2.2 (left)). Neutrons in this energy range cause both ionization aging and nuclear displacement defects.

Neutrons in the energy range 10–100 MeV, besides contributing to aging of electronics, are the main cause of SEEs (sec Section 2.4). Until recently, there have not been too many convenient sources of neutrons in the this energy range; therefore, one had to opt for low energy cyclotron protons as a proxy for such neutrons. The limitation of such tests is represented by the fact that, in addition to neutron-like scatterings on nuclei, low energy protons also produce very dense ionization, orders of magnitude denser than that induced by relativistic charged particles.

The CERN High-energy AcceleRator Mixed field (CHARM) facility [52, 53], commissioned in late 2014, provides a unique irradiation environment with a mixture of neutrons, photons, electrons/positrons, and charged hadrons, whose energy spectra and relative fluxes are shown in Fig. 2.9. The mixed composition background is achieved by colliding 24 GeV protons from the CERN PS with a copper target. One can see that the neutron energy spectrum closely resembles that in the muon system (cf. Fig. 2.2). Therefore, the CHARM facility has been used to perform a large number of LHC electronic aging studies.

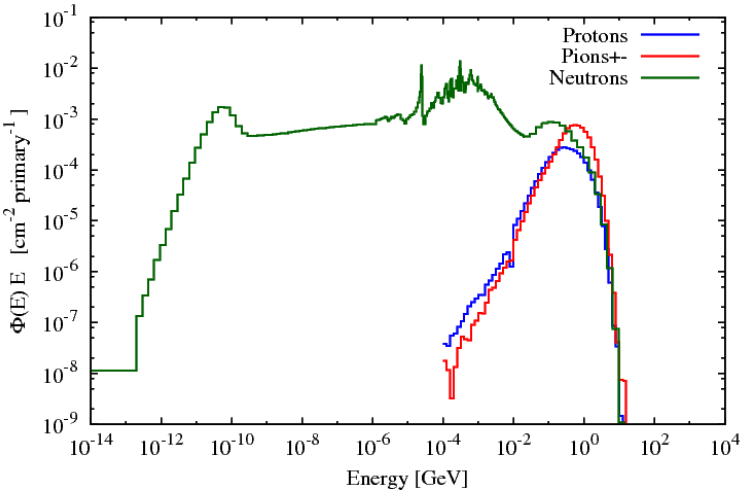

Figure 2.9: The energy spectra for different background components produced at the CHARM facility at CERN [53].

2.5.3 System performance in the HL-LHC-like environment

The GIF++ source (see Section 2.5.1) is located in the H4 beam line, with a muon beam being available a few times a year.[1] Therefore, with properly adjusted GIF++ filters, one can

[1] The H4 beam delivers $\mathcal{O}(10^4)$ muons per 4.8 s spill over about 1 m^2 area. Muon momenta are distributed approximately uniformly in the range 0–140 GeV.

imitate the HL-LHC background and study the performance of muon detectors with their trigger/readout electronics in a HL-LHC-like environment. Such studies include an efficiency to trigger on and reconstruct muon track segments, rates of fake triggers and fake reconstructed (offline) muon track segments, and an overall operational stability of detectors (e.g., appearance of Malter currents) and electronics.

Chapter 3

DT upgrades

3.1 Overview and motivation

The Drift Tube (DT) chambers are located in the barrel region of CMS ($|\eta| < 1.2$) [19]. DTs are responsible for muon identification and momentum measurement over a wide range of muon momenta. The role of the muon system is particularly important in measuring momenta of high-p_{T} muons, that are kinematically favoured to have a central η. The DT system also provides a robust standalone muon trigger with precise bunch crossing assignment. The future barrel muon trigger output will need to be combined optimally with the Phase-2 Tracker Track trigger to reach the best p_{T} resolution. At the same time, the standalone functionality must be maintained to ensure efficient triggering on tracks with large impact parameters, for which the Tracker Track trigger will be inefficient.

The use of DT technology in the CMS barrel has been possible due to the low hit rate and the relatively small strength of the local magnetic field. By the time of the HL-LHC start-up, the DT system will be more than 20 years old and will need to operate for another 10 years integrating $\sim$10 times more luminosity than it was designed for.

The goal of the DT upgrade is to maintain the present system performance, trigger, and reconstruction, at the HL-LHC background rates (instant and integrated) and under the HL-LHC CMS Trigger/DAQ conditions (500–750 kHz L1 trigger rate and 12.5 μs L1 trigger latency).

The present DT detectors will stay for HL-LHC operation. Preliminary studies show that the most exposed of them may risk suffering detector aging at the end of HL-LHC. An extensive R&D upgrade program is underway to mitigate the potential aging-associated problems. The results of aging studies and the discussion of possible mitigation measures are presented in Section 3.2.

The rate of failures of DT on-detector electronics, the so-called Minicrates (MiC), is projected to be unsustainably high at HL-LHC. The new HL-LHC CMS Trigger/DAQ requirements exceed the present MiC capabilities in terms of Level 1 trigger accept rate. Therefore, as a consequence of the higher L1A rate set by CMS, as well as MiC maintainability and chamber aging mitigation arguments, all MiCs together with the associated back-end electronics will be replaced by the Phase-2 Minicrates (MiC2) and a new back-end.

The new electronics are described in Sections 3.3–3.5. Section 3.6 presents the cost of the upgrade, production and installation schedule, and institutional responsibilities.

3.1.1 The DT system

The DT system is made of 250 DT gas wire chambers (85/15% Ar/CO_2 mixture) that instrument the return yoke of the CMS solenoid, see Fig. 1.4 in Section 1.2, each providing up to 8 hits in

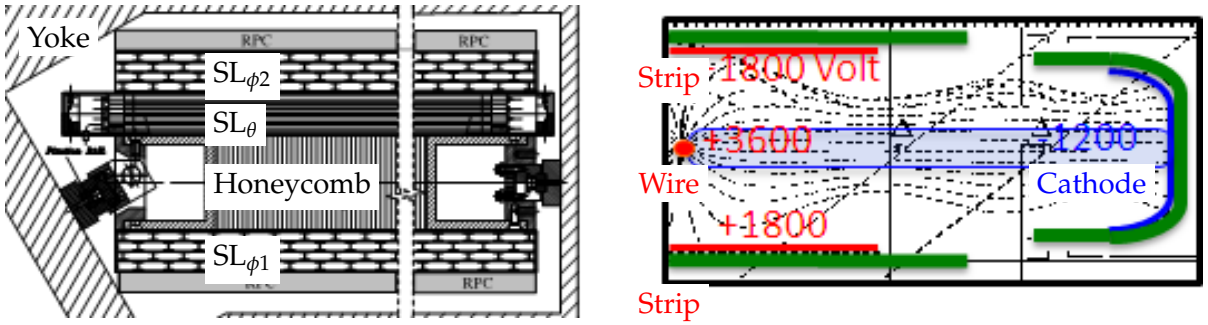

Figure 3.1: Left: Drawing of a transverse view of a DT chamber made of three SuperLayers and a honeycomb plate in between; the RPC chambers of the same station are also shown. Right: Sketch of a half-cell section of 2.1 $\times$ 1.3 cm^2 showing the three electrode types (wire and strip in red; cathode in blue) with the voltages applied at LHC start. Also indicated are the drift lines.

the bending plane (ϕ) and up to 4 in the axial one (θ). The basic element of the DT chamber is the drift tube, which has cross section dimensions of 13 mm $\times$ 42 mm, with length varying from 2 to 4 m for the larger chambers. The total number of sensitive cells is around 172 000. A DT chamber is typically composed of three separated gas volumes called SuperLayers (SL), segmented in four layers, each consisting of 50 to 100 drift tubes. The front-end electronics and the HV distribution to the three electrodes of each cell (anode, cathode and strip) are hosted inside the gas volume (see Fig. 3.1).

The MiC (see Fig. 3.2) is a complex electronics system; each DT chamber has one MiC attached to it. The MiC houses the Level 1 trigger and readout electronics, a design choice driven at the time to reduce the total amount of copper cables in the system. These electronics boards are located outside the gas volume in a special aluminum C profile, which is 10 cm deep, nearly as long as the chamber width. It is attached to the chamber, inserted on its most accessible side, in a shallow volume free from the honeycomb structure, which separates the SuperLayers to increase the lever arm (see Fig. 3.1).

Alhtough the MiC concentrates most of the functionality of the DT detector, it is deeply buried inside the yoke and, to a large fraction, covered by cables and services belonging to other detectors.

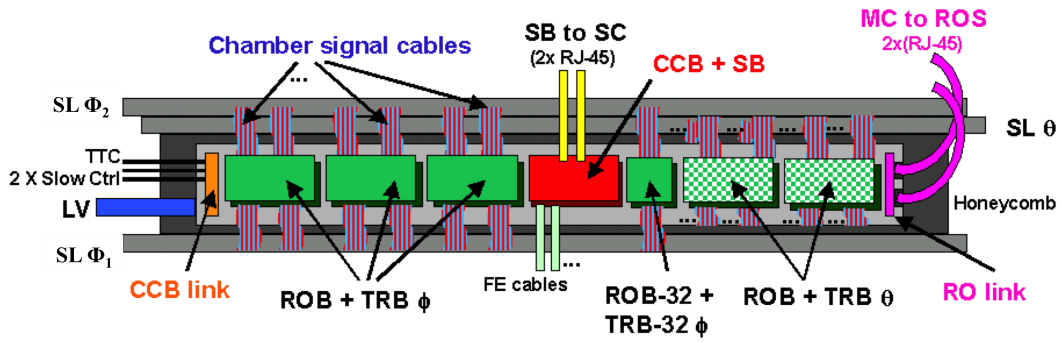

Figure 3.2: A schematic drawing of the DT MiC boards and connections superposed to the DT chamber.

A MiC, see Fig. 3.2, contains on average six pairs of Read Out (ROB) and Trigger Boards (TRB), and a single pair composeed by a Clock and Control Board (CCB) and a Server Board (SB), plus a CCB link board and a RO link board. The ROB and TRB have 128 channels each and

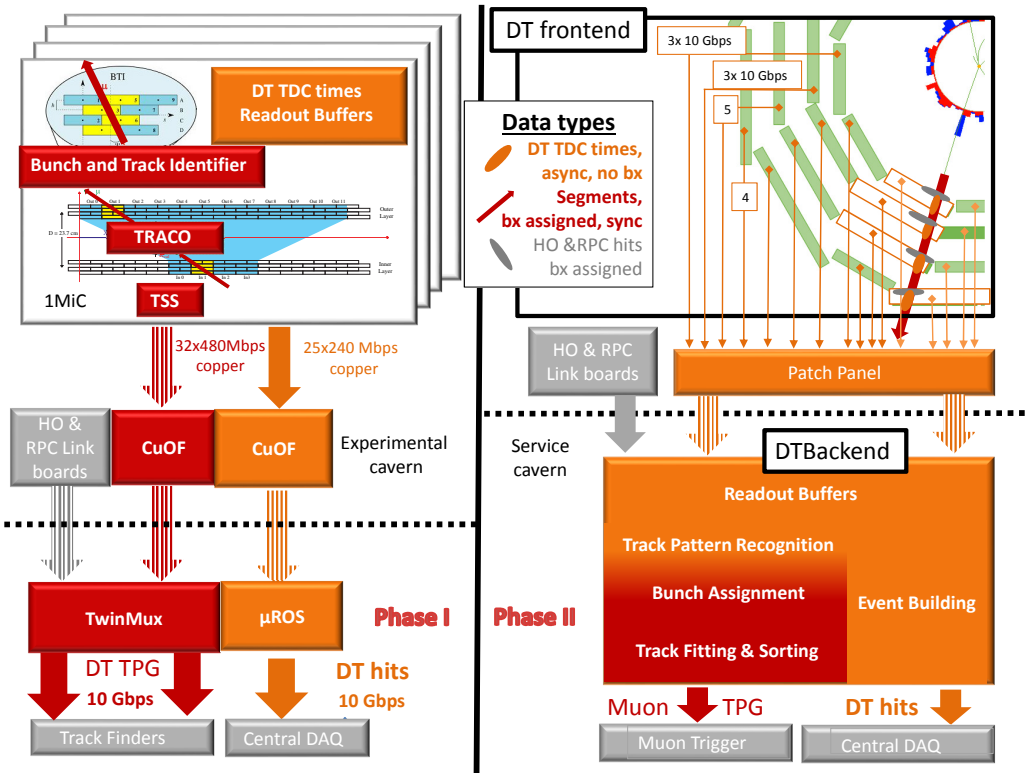

Figure 3.3: Current (left) and upgraded (right) DT electronics. In the Phase-1 version each Minicrate MiC sends the data via copper-to-optical-fiber translators (CuOF) to the service cavern, where the TwinMux system combines and transmits the trigger primitives (TPG), including data from the RPCs and outer hadron calorimeter HO. The μROS modules collect the TDC data and send the events to the CMS data acquisition system. In Phase-2 (right part of figure) the new Minicrates (MiC2) send TDC data from the chambers via optical links to a patch panel inside the experimental cavern, from where they are transfered to the back-end, which performs triggering and event building.

are physically coupled together. The MiC is a very dense and sophisticated system with lots of interconnecting cables and multiple connectors. Its power consumption is about 100 W, which is dissipated exclusively through conduction into a water circuit, keeping the internal temperature below 34 °C (maximum value). Without cooling the system cannot be operated, reaching 45 °C in a few minutes; protection systems are in place on the CCB to avoid overheating.

The back-end electronics, relocated from the experimental cavern, UXC, to the service cavern (USC) during LS1, and upgraded recently to the μTCA standard, are accessible during collisions. The present system features two parallel data paths coming from the MiC, which are interfaced to the central DAQ and L1 Trigger systems. The present back-end electronics has two roles: data concentration, converting slow optical legacy links into 8 Gbps links, and fanout of trigger primitives information to neighboring sectors for subsequent track finding in the trigger.

A schematic of the Phase-1 DT system and of the proposed upgrade can be seen in Fig. 3.3.

The legacy DT electronics design had to deal with limits on the throughput of data links over

relatively long copper lines between the on-detector electronics and the tower racks in UXC. Its architecture was a chosen to reduce as much as possible the data transfer and thus the number of cables: trigger primitives are generated locally on the MiC combining aligned hits within four adjacent layers. With the same purpose, readout pipeline is achieved on local FIFOs with a O(μs) long time window covering the maximum drift time and being transmitted only on L1A signal reception.

The scope of the Phase-2 DT upgrade is the replacement of the MiCs and its receiving back-end electronics, reorganizing the role of both parts in the trigger and readout chain. The partitioning of the electronics components between UXC and USC will be re-optimized making use of the higher bandwidth optical link technologies available at low cost now.

In addition, as will be described later in section 3.5, the MiC replacement opens new interesting opportunities for a more performing DT trigger algorithm that mitigates chamber aging effects, and that matches better with the new information made available in Phase-2 from other detectors, such as the new tracker. Thus already at Level 1 the maximum resolution available from the chambers can be attained; in Phase-1 this resolution can be exploited only at the Level 2 of the software based HLT. Deadtime will be reduced to the minimum achievable without replacing the chamber.

3.1.2 Limitations of the DT system in the Phase-2 environment

Operation of the DT system during HL-LHC needs to take into account the expected signal and background rates at the increased instantaneous luminosity. Extrapolations have been made and, since the DT chambers are located in a relatively low occupancy region, the results show no major concern for the operation of the detector with the expected hit rates in the order of 50 Hz/cm^2 (see Fig. 3.4). An important concern is the long term operation of the system and the impact of accumulated dose and aging of the different parts. In order to assess the performance of the DT system under these conditions, the impact of the failure of each part in the overall system performance has been considered.

First of all, the impact of a lower efficiency from the DT chambers themselves was studied. DT chambers present failure modes affecting very small regions of the detector. Dead channels can be treated as randomly distributed loss of hit efficiency, i.e. one expects to loose only single hits, which has a very modest impact on the segment efficiency since there are 8–12 sensitive layers in each DT chamber. Aging should be accounted for all the materials that build the chamber as well as the mechanical degradation of its own structure and the gas quality. Ongoing radiation tests aiming to evaluate its impact on the system performance will be discussed in Section 3.2, including available interim conclusions by the time of this writing.

The MiC electronics is a weak point for HL-LHC operation and needs to be replaced. As mentioned before, the main limitation of present MiCs for operating in Phase-2 is the available bandwidth, which cannot follow the larger CMS Level 1 trigger rate in Phase-2, between 500 kHz and 750 KHz. Tests at the laboratory show that at the HL-LHC luminosity, the ROB limit is between 300 kHz and 500 kHz L1A rate, depending on the detector region occupancy. Hence, the ROB would need to be redesigned for all the 250 MiC, even if the expected Level 1 latency increase and buffer occupancy in Phase-2 is within the ROB limits. Moreover, in order to avoid a 5% deadtime at 1 MHz, CMS plans to remove the present L1A rule of minimum trigger spacing of three bunch crossings, which implies the replacement of all the CCB and SB boards, since they host a TTCRx ASIC that have this requirement.

The MiC is a complex electronics system with altogether more than 3000 boards and several

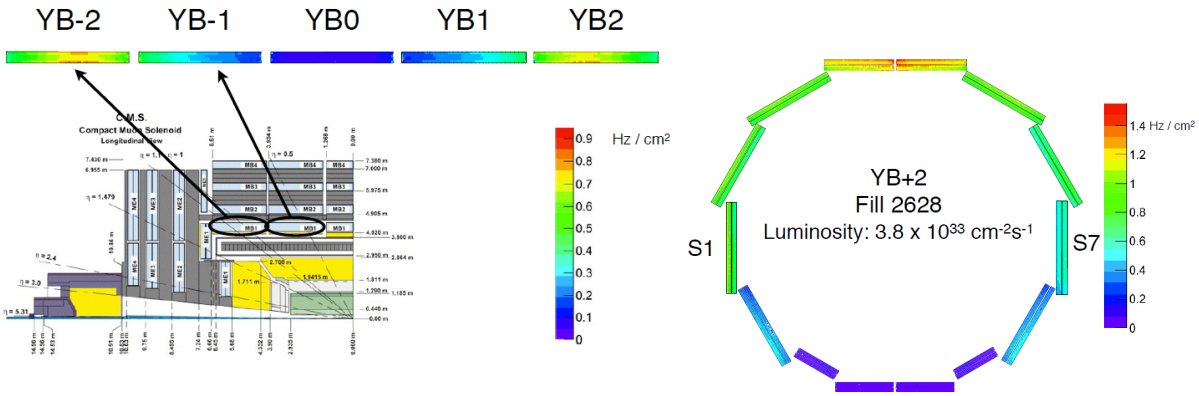

Figure 3.4: Left: Distribution of the single hit background rate in the MB1 chambers as a function of η. Right: Distribution of the single hit background rate in the MB4 chambers as a function of ϕ.

types of custom ASICs that date back to the late 90s. They will have operated for more than 20 years at the beginning of LS3. Determining the lifetime of electronic devices is an arduous task which brings unavoidably large uncertainties. Reliability cannot be guaranteed when approaching the wear-out phase of the system, since then maintenance is no longer possible: custom parts cannot be rebuilt and installed fast enough. Also, spare parts were foreseen for 10 years of LHC operation only.

Experience during operation showed some reliability issues both in the TRBs and ROBs that were mitigated by reducing the number of power on/off cycles that produced large temperature changes. Furthermore, a significant effort took place in LS1 to migrate one of the ASICs algorithms into an FPGA in order to be able to rebuild TRB spares whose stock had suffered from a high, unforeseen mortality.

The MiCs are accessible only when the barrel wheels are open and, even in that case, the maintenance effort is very large. As an example, about 50 MiC boards were replaced in LS1 (1.5% of the boards in the detector) but to substitute them it was necessary to open and access 25% of the MiC in the detector. These numbers illustrate the present maintenance effort, which will become more difficult in the much harsher radiation environment of HL-LHC, as accessibility will be considerably harder.

During the tests to certify the MiC radiation resistance to 10 years of nominal LHC operation in 2003 [44], all the components and boards were irradiated up to half the doses expected at HL-LHC (a bit more in the case of the TRBs) without damage. However, the SB/CCB pack was found to fail, with two components failing in a non recoverable way after an exposure by 60 MeV protons (10^{11} cm^{-2}) in the tests performed at PSI. Radiation tests found in the literature confirm the sensitivity of the mentioned components to radiation [54].

In contrast with the chamber failure modes, problems in one MiC lead to lose full segments from regions of the chamber acceptance, which has serious consequences for the trigger generation in the current architecture. Assuming no limitation was given by the Level 1 rate, the knowledge accumulated during the operation of the system in Run 1 was used to model the evolution of the number of dead channels due to foreseen problems in the legacy MiC up to LS4 (see Fig. 1.8). As can be seen, the loss of channels is relevant, the performance impact is very significant, as already pointed out in the CMS Phase-2 Technical Proposal [24].

Summarizing, MiC replacement is necessary for Phase-2 operation, our aim is to redesign a more robust and less expensive system, leaving in UXC a minimal and highly resistant new electronics system and moving to USC all the trigger functionality nowadays located inside the MiC. This solution builds up on the DT Phase-1 upgrades in which the back-end electronics was moved to USC and the optical fibers were already installed.

The DT system depends on the power supply system and the gas and cooling infrastructures to operate reliably through HL-LHC.

The DT HV and LV power system is one of the largest power supply systems in CMS, with about 10000 HV channels for wires, strips and cathodes, and 4000 LV channels for front-end, trigger, and read-out electronics. The system includes 240 HV and 250 LV modules exposed to radiation, being localized in the barrel tower racks in the experimental cavern, an area of relatively easy access. The modules have a clear maintenance model through a CERN frame contract. Thus we expect to keep minimal impact on operation through routine maintenance tasks and adiabatic replacements, keeping the main system structure in place. The LV system in the new MiC design will have also a lower power requirement, which will translate into longer lifetime expectations.

Demineralized water cooling and a gas system with a 85/15% Ar/CO_2 mixture share are centrally managed by CERN groups and have radiation tolerant technologies. The cooling system has large granularity with each circuit covering two DT chambers from neighboring sectors. Cooling water circulates through stainless steel, aluminum and flexible (plastic) pipes. Status of the flexibles is monitored regularly during shutdowns. Gas circulates through copper pipes. Cooling fluid and gas quality are monitored and recorded; the drift time is measured by an independent monitoring system [55]. Alignment of the DT chambers (dominant effect in $\sigma(p_T)$ at hight-p_T) is performed by a laser alignment network (the Barrel Alignment) and by using muon tracks. Major limitations in the operation of these systems through HL-LHC are not expected, provided maintenance and monitoring take place.

3.2 DT system longevity in Phase-2

The expected performance of the DT system at HL-LHC luminosity will depend on the background and muon rates expected in the DT chambers, but also on the failure rate of the electronics and on the aging of the different parts of the system, notably those that are not being upgraded, as the DT chambers and the infrastructure. The background dominates the deposited dose, thus being the most relevant to determine the radiation related aging.

To estimate an aging scenario, the maximum hit rates (background), chamber trigger rates and currents have been extrapolated to an instantaneous luminosity of 5×10^{34} $cm^{-2}s^{-1}$, making use of the linear luminosity relation observed so far. The maximum hit rates are of the order of 50 kHz/cell (or $\sim$ 50 Hz/cm^2), and the trigger segment rate is about 500 kHz per chamber. As can be seen in right side of Fig. 3.4 (background rate) and in Fig. 3.6 (HV currents), the measured distribution of the background is not uniform throughout the detector. At the end of this section we will take into account all the factors affecting efficiency, including this geographical dependence, i.e. as a function of the chamber location, to assess the impact of the detector degradation on the muon object reconstruction by the end of HL-LHC running, considering a safety factor three.

3.2.1 Electronics aging scenario in Phase-2

Since the Phase-1 MiC will be replaced by simpler on-detector electronics, the electronics failure rates at the HL-LHC are expected to be small:

- We estimate the effect on hit efficiency to be <1%, taking into account the experience of the ROB failures (<1 board/year out of 1500). The ROB shares functionality and environment with the new on-detector boards to be described later. This is a conservative number considering that the failed boards in the external wheels can most probably be replaced at the end of the year LHC shutdowns.
- The impact of the increased occupancy on efficiency will be negligible since the Phase-2 TDC can be designed with the required specification.

The DT system is one of the largest power supply systems in CMS with a total amount of 240 HV and 250 LV modules. The HV power supplies were built by industry (CAEN) specifically designed to meet DT requirements, and they were extensively tested against radiation damage. LV power supplies, on the other hand, are a commercial product (CAEN EASY system), commonly used in LHC experiments. The LV modules were tested by the CERN electronics pool. Their tolerance to HL-LHC radiation levels will be verified. A maintenance contract has been signed for the LHC and must be renegotiated for the HL-LHC.

In the first six years of operation of the DT detector no effect from radiation was observed in the power supply system. The failure rate has been stable, showing no signs of aging, with an average of about five faults every year. The failure rate is similar to what other LHC users observed for the same system.

The HV system was extensively tested by the DT collaboration against radiation damage at similar levels to the EASY system. The fault rates observed for the A876 HV boards (60+6 spares, localized in USC), and for the A877 HV boards (240+20 spares, in the UXC cavern) average to roughly 10 per year in total. The main cause of the A877 failures has been identified as dust. Therefore we experienced a surge of faults after LS1, when more dust was moved inside UXC. As mitigation, dusting campaigns are performed during long shutdowns. The aging of the HV system is expected to be accelerated by the increase in the currents due to the higher instantaneous luminosity in HL-LHC. The HV currents measured in the DT chambers closely follow the background noise rate measurement in the detector and exhibit a linear dependence on instantaneous luminosity, as can be seen in Fig. 3.5 for the most heavily loaded modules. A linear fit is performed to the LHC data and extrapolated to estimate the HV current values at HL-LHC luminosity, which are sizable but within the HV module specification: the worst case corresponds to the MB4 channels from S4, which, servicing two chambers, will reach almost half of the maximum current deliverable by the module (about 10 μA out of 20 μA), if operated at 3600 V. Tests at GIF++ have shown that we can safely operate with these high values of current.

Taking into account that both the HV and LV systems were developed in the early 2000s, it is clear maintenance will become challenging during HL-LHC. Even though spare supplies of the electronics components have been stocked, they are being phased out from the market. Thus neither the LV nor the HV system can survive up to the end of HL-LHC by a simple replacement of failed modules, since spare modules of the current type will stop to be available before the end of HL-LHC. Both systems are covered by the maintenance contract signed by CERN with CAEN, that will end in 2019, and must be renegotiated every five years.

The strategy for maintenance of the LV and HV power supply systems is described in Section 3.4.3. Hereafter we consider that failures in both systems will keep having a negligible

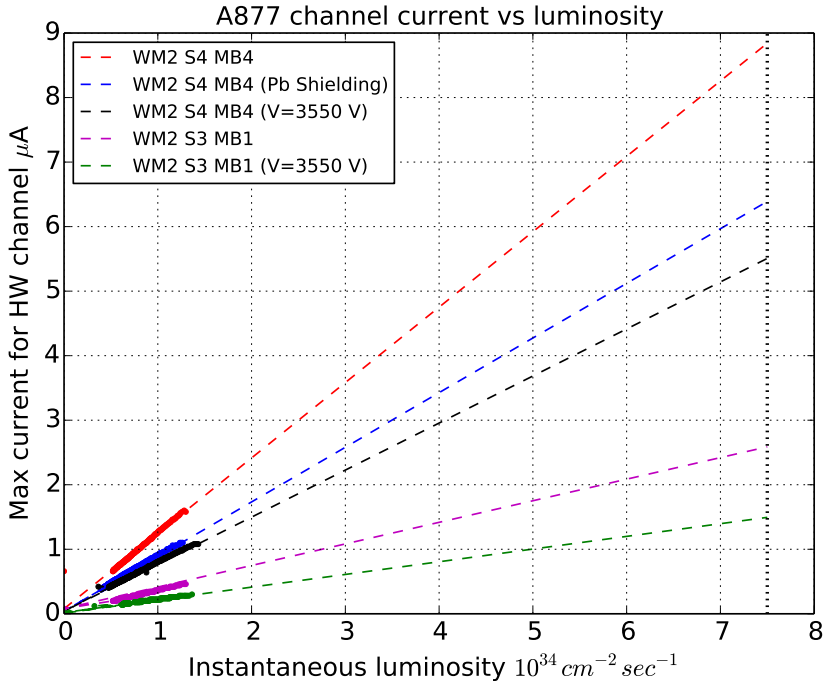

Figure 3.5: HV channel current (A877 module) in MB4 top sector and MB1 (external wheel), extrapolated to the maximum (ultimate) expected instantaneous luminosity at HL-LHC of $5\,(7.5) \times 10^{34}$ cm^{-2} s^{-1}. Measurements with different aging mitigation strategies (shielding, lowering HV set-point to 3550 V) are also shown.

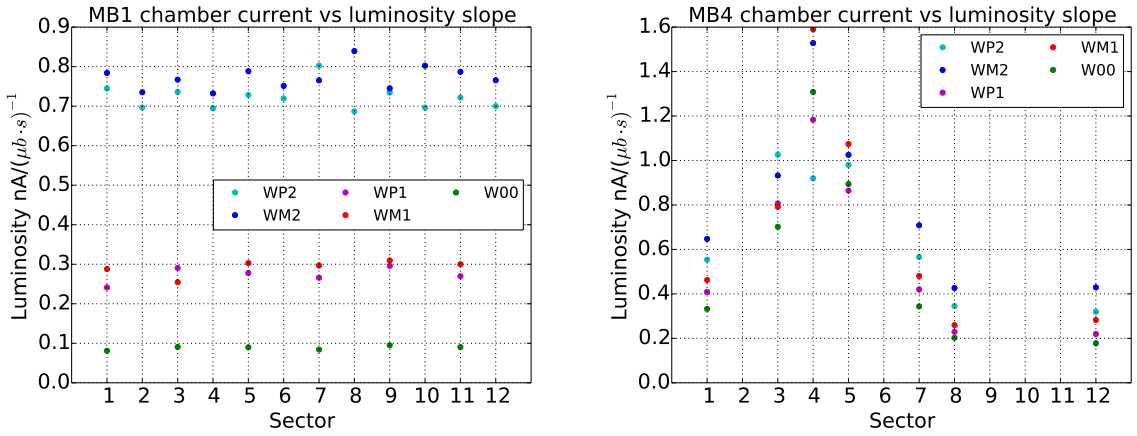

Figure 3.6: HV current dependence on instantaneous luminosity in MB1 (left) and MB4 (right) as a function of the sector number, i.e. azimuthal angle, where 4 and 10 correspond to the top and bottom sectors, respectively.

impact on the detector performance thanks to the high granularity of the system and its accessibilty.

3.2.2 DT chambers aging scenario in Phase-2

3.2.2.1 Expected irradiation of the DT chambers during Phase-2

The measured HV current vs instantaneous luminosity slopes for chambers in MB1 and MB4 stations are shown in Fig. 3.6, illustrating the wheel and azimuthal angle dependence of the irradiation. The channels with larger currents are the inner SL of the MB1 chambers in the external wheels (due to punch-through) and the outer MB4 SL in the top sectors (due to neutron background leaking from the inner detector into the cavern).

Table 3.1: Estimated integrated charge in mC/cm up to the end of HL-LHC operations (3000 fb^{-1}) based on measured currents as a function of instantaneous luminosity corrected for the effect of the MB4 top shielding and of operating at 3550 V. No safety factor was included. The quoted uncertainty includes instantaneous luminosity measurement (5%) and stability among fills (3%).

	Wheel-2	Wheel-1	Wheel 0	Wheel +1	Wheel+2
MB4 S4	3.6 ± 0.3	3.7 ± 0.3	3.1 ± 0.2	3.4 ± 0.2	4.3 ± 0.4
MB4 S3-S5	3.4 ± 0.4	2.1 ± 0.2	2.7 ± 0.2	3.0 ± 0.2	3.5 ± 0.3
MB4 S1-S7	7.0 ± 0.4	5.0 ± 0.3	3.8 ± 0.2	4.6 ± 0.3	6.0 ± 0.2
MB4 S12-S8	4.8 ± 0.3	3.0 ± 0.2	2.2 ± 0.2	2.6 ± 0.2	3.7 ± 0.2
MB1	9.9 ± 0.6 17.0 ± 0.7 (3600 V)	4.4 ± 0.3	1.6 ± 0.2	4.2 ± 0.3	10.0 ± 0.6 16.0 ± 1 (3600 V)
MB2	2.1 ± 0.2	0.90 ± 0.05	0.50 ± 0.03	0.80 ± 0.05	2.0 ± 0.2
MB3	0.4 ± 0.1				

The expected integrated charge per unit length for an integrated luminosity of 3000 fb^{-1} has been calculated from extrapolating a linear fit to the instantaneous luminosity dependence, and by integrating the charge during collisions for a particular fill. Both methods agree to better than 2%. Different strategies are being considered to reduce the accumulated charge collected by the detectors as this is beneficial to their lifetime. Shielding of the upper MB4s by a factor of three is achievable, as shown by tests with shield prototypes in situ. Apart from this shielding, the values quoted in Table 3.1 assume 3550 V are applied to the anode, the expected operation set-point through HL-LHC, which gives 1.6 times lower charge than 3600 V, the operating value up to 2017, when it was reduced. The effects on the expected currents of these mitigations are also indicated in Fig. 3.5.

The use of data taken during LHC to estimate HL-LHC backgrounds is a solid strategy but has the caveat that the detector geometry, notably the beam-pipe near the interaction point, the inner detector and the endcap calorimeter will change. Present Fluka simulations [56, 57] predict lower fluences in the region of the DT chambers than in the current configuration, so the estimations derived from using values in Table 3.1 can be considered as conservative.

The conversion from the dose (or integrated charge) measured at accelerated tests in GIF++ to the CMS luminosity is done exploiting the close HV current-luminosity correlation observed, see Fig. 3.5 above.

3.2.2.2 Expected efficiency evolution of the DT chambers during Phase-2

DT chamber construction is extensively described in Ref. [19]. Studies regarding the chamber longevity have been performed in the construction phase and results are summarized in what follows. A DT chamber is a glued structure of about 700 tubes (4.2×1.3 cm^2 cross section,

see Fig. 3.1) made from aluminum plates and I-beams glued together. The glued surface inside a SuperLayer is $\sim$ 70% of the total area. SuperLayers are glued together and to the Honeycomb. DTs are operated slightly above the atmospheric pressure (+1 hPa). A breakdown of the mechanical chamber structure could be possible only in case of a gas over-pressure $>$ 50 hPa, which is considered a catastrophic event, prevented by the gas system protections. Inside the gas volume of each SuperLayer there are aluminum strips (four per tube) that shape the drift field, HV Boards (HVB) that distribute the voltage to the wires and the strips, and FEBs. The strips are insulated with respect to ground by a 100 μm thick Mylar ribbon. Two strips (S) face the wire (W) and two additional strips (C) are located along the sides of the cell acting as cathode. The gain of the wire is determined to first approximation by the voltage difference ($V_W - V_S$), while the drift field depends on ($V_W - V_S - V_C$).

Tests of system lifetime against insulation breakdown in a tube have been performed in the laboratory. They suggest that, at the typical field of 2 kV/mm, the drift tube lifetime is in the order of 10^8 years, which translates into a 4% probability of failure of one out of the 172 000 tubes of the full Drift Tube system in 20 years [19]. This probability can be reduced by one order of magnitude by reducing the strip voltage by 300–400 V while keeping the wire gain constant. The HVB is a multilayer FR4 structure that hosts passive components only. Failures are highly improbable and not expected if safely operated. Only one HVB out of $\sim$ 11 000 has been substituted (in LS1) and it was due to a problem that appeared during an intervention in that chamber. A lower chamber operating voltage would certainly increase the HVB lifetime even further.

FEBs were tested up to a radiation dose and a neutron flux almost one order of magnitude larger than expected at HL-LHC and no damage was detected [58]. Extensive accelerated aging tests were also performed on 20 FEBs at high temperature (125 °C) for 3200 h and no degradation was observed, which corresponds to a MTBF (mean time between failures) better than one board per LHC year, limited by statistics. Actually this provides a less strict test than what has been observed during operation so far, namely four FEB failures in 10 years, and implies a negligible contribution by the end of HL-LHC. However, interventions to cope with a possible failure of one of the above items require opening the front or the back cover of a SuperLayer. This is a risky and time consuming intervention which is only possible during long shutdowns. The "splitter board", located on top of the MiC, is responsible for distributing power to the FEBs in the three SuperLayers. As a key part of the grounding system, its replacement can potentially affect noise conditions and thus imply long commissioning times. Its components are mostly passive; the weakest point is the electrolytic capacitor, which has a MTBF specified to $\sim$ 28 years. No failure has been observed so far. The opportunity of its replacement will be revisited in situ during LS2.

The DT chamber gas is a safe Ar/CO_2 mixture (85/15%). Currently the gas is recirculated, with a fresh gas intake of 15%. It takes about one day to replace the whole gas volume. Gas leaks, changes in the gas mixture, gas contamination with oxygen, water or even pollutants from outgassing of chamber materials will degrade the system behavior. All these aspects are important for the optimal performance of the chambers and are carefully monitored [55] to minimize contamination that can degrade chamber operation.

Wire aging induced by irradiation and out-gassing from all the components present inside a chamber (glue, O-rings, plastic parts) has been studied at construction time for LHC conditions [40] and is being studied at the GIF++ facility for HL-LHC conditions. Only interim conclusions can be given, as irradiation tests are still ongoing. Contrary to the initial expectations for an Ar/CO_2 mixture, accelerated aging tests at the GIF++ facility [59] show sensitivity

Table 3.2: Estimated average hit efficiency loss in the DT detector at the end of HL-LHC run, including a safety factor of three in the integrated irradiation.

Source of inefficiency	inefficiency
Lifetime of the tubes	1%
FEB failure rate	<0.1%
HVB failure rate	<0.1%
Inefficiency due to radiation averaged over chambers	18%
OBDT failure rate	1%
TOTAL Chamber hit efficiency loss	20%

of the performance of a spare DT chamber to irradiation. The requirement of a relatively low dose rate compared to those available at GIF++ has delayed the integration of enough charge to cover the expected dose in the most exposed chambers during HL-LHC. Only $\sim$ 15 % HL-LHC at reasonable acceleration factors $\sim$ 10 has been reached until July 2017, but the available data already allow us to:

1. observe a deterioration of the gain and hit efficiency;
2. identify the coating of the wire as source of this decrease;
3. make a first estimation of the speed of the gain reduction.

To further investigate these effects, small models of a DT chamber consisting of two DT cells only (bicells) [60] were built using the same materials as the DT chamber and are under irradiation at GIF++.

These measurements and other data are used in Section 3.2.3 to estimate the hit efficiency drop until the end of HL-LHC, to about 20% averaged over the full DT system, including a safety factor of three, as detailed in Table 3.2. However, the deterioration is worse in the hottest regions of the DT detector, which correspond to 15% of all DT chambers, see Table 3.3, being negligible otherwise. Indeed, the GIF++ irradiation already amounts to the expected irradiation during HL-LHC for the majority of the DT chambers. The radiation distribution being known from the HV currents, we have taken into account this geometrical distribution of the inefficiency to estimate the reduction of the system performance with aging as discussed below in Section 3.2.3.

Summarizing, from past tests and operational experience so far, the chamber structure and its internal electronics (HVB, FEB) are considered safe for being operated throughout HL-LHC, assuming the chambers are not extracted from the yoke, which is not needed for the maintenance of the chambers. The mechanical stresses associated to the removal of chambers aged under irradiation pose a risk to be avoided.

In Table 3.2 we list the different expected contributions to the total inefficiency; to first approximation they are independent from each other and distributed throughout the detector. In total, a hit efficiency loss of about 20% is expected in the DT detector at the end of HL-LHC run (including a safety factor of three in the integrated irradiation). This is considered safe given the system redundancy and the new trigger architecture; a more quantitative study of its impact on the muon object performance is discussed below in Section 3.2.3. Actions are being taken at present to maximize the lifetime of the different parts, such as lowering the HV working point.

3.2.3 Estimation of the evolution of the Phase-2 DT system performance

Simulations in CMSSW have been used to study the impact of a reduced single hit efficiency on the muon object performance by removing hits according to an aging scenario parameterized in terms of the expected hit efficiency per chamber. The TDC hits were removed from the CMSSW event with a probability given by the expected inefficiency in each DT chamber, which includes all the aging factors listed in Table 3.2. In order to extrapolate the effect of the observed gain drop from the limited integrated dose accumulated at GIF++ to HL-LHC conditions, a model was built using the available hit efficiency vs. wire HV scans and inverting gain vs. wire HV measurements. Explicitly, the estimation is built as:

$$\text{Hit Efficiency}\,(\mathcal{L}) = \text{Hit Efficiency}\,(\text{HV}\,(\text{Gain}\,(\mathcal{L}))),$$

where $\mathcal{L}$ stands for the integrated luminosity.

- Hit Efficiency(HV): Taking as input MB2 GIF test beam data from Ref. [61] (HV down to 3 400) and the MB3 hit efficiency vs. HV measured using cosmics ray muons in Legnaro (sea level) displaced to match the MB2 (to cover low HV values), see Fig. 3.7, left.
- HV(Gain): Inverting the parametrization from Ref. [62] measured at Legnaro and CERN on a prototype of a DT chamber (Q4 prototype) and at Legnaro for the bicell, see Fig. 3.7, right.
- Gain($\mathcal{L}$): A fit to chamber current response during the GIF++ irradiation in 2016 with low acceleration factors (< 10) provides the evolution of the drop of gain vs. integrated dose at GIF++. The GIF++ dose is converted to HL-LHC integrated luminosity for each chamber location from the HV currents measured during collisions, as discussed above, in Section 3.2.2.1. The result is shown for the most exposed chambers, the MB1 of the external wheels in Fig. 3.8 right.

Table 3.3 displays the aging scenario used for the simulation. The irradiation has been increased by a factor of three with respect to that expected to give a safety factor of three. Mitigations being implemented, described in Section 3.2.4, have been assumed in the extrapolation, as well as the ability to delay the gain drop at the end of HL-LHC to preserve detector performance by moderately increasing the $V_W - V_S$ delivered from the HV module (up to 4% of initial value),

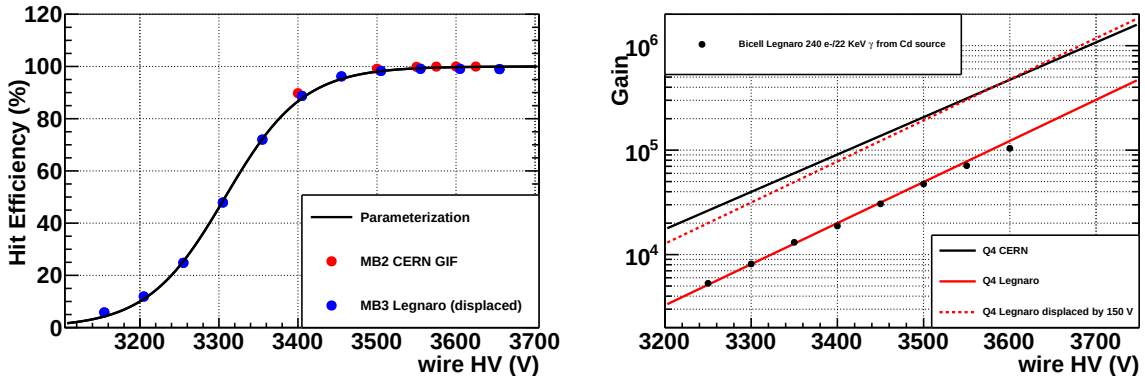

Figure 3.7: Left: Measured hit efficiency as a function of wire HV. Right: Gain as a function of HV measured at Legnaro and CERN on the Q4 prototype and bicell chambers with muons and a Cd source. The Cd source data has been normalized to the muon gain data.

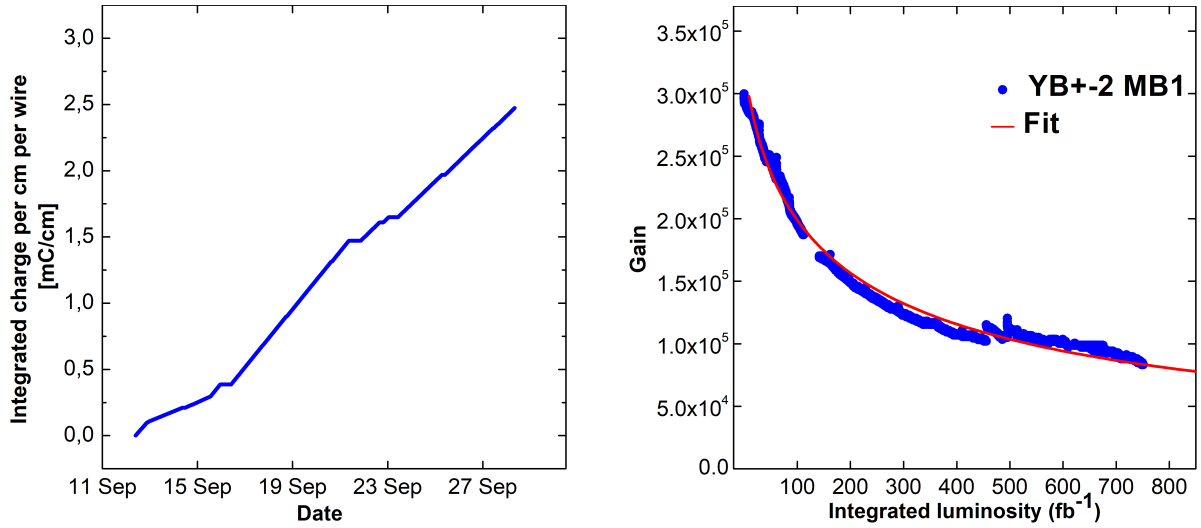

Figure 3.8: Left: Integrated charge per cm during the 2016 irradiation at GIF++ measurement assuming constant gain. Most of the irradition was performed at an acceleration factor of ~ 10, with a smaller amount integrated at three times slower rate. The HV was set at 3550 V. Right: Gain evolution, estimated from the measured response of the drift tube, as a function of integrated luminosity for a MB1 chamber of the external wheels.

Table 3.3: Extrapolation of the hit efficiency evolution as a consequence of wire aging after the full HL-LHC operation (3000 fb^{-1}) and up to LS4 (1000 fb^{-1}). The efficiency is calculated for a factor of three higher dose than expected as safety margin.

Location	Chambers	Eff(1000 fb^{-1})	Eff(3000 fb^{-1})
MB4 S1-S7 all YB	40	87%	77%
MB1 YB+2 YB-2	24	87%	43%
MB1 YB+1 YB-1	24	87%	87%
MB2 YB+2 YB-2	24	91%	87%
Other stations	143	93%	82%
Average chamber efficiency	250	92%	82%

as already tested in GIF++.

Figure 3.9 (left) shows the number of DT hits per high p_T muon track as a function of η in this aged scenario and for a perfect detector in both the ϕ and θ measurement planes. The dips correspond to the wheel cracks, where the available redundancy is lower due to acceptance. The right side shows that the p_T reconstructed using the standalone muon algorithm, which does not use the inner tracker, is rather stable against aging.

The standalone muon reconstruction efficiency as a function of muon η (left) and ϕ (right) is shown in Fig. 3.10. The efficiency remains high over the full barrel acceptance in the considered aging scenario, even though the reconstruction has not been optimized for new aged conditions and the efficiency in the MB1 of the external wheels is rather poor. It can be observed that the weakest regions with respect to aging are: i) the wheel gaps, where there is less redundancy available (see Fig. 3.9), and ii) the overlap region as expected from the background distribution in the detector. This reason also explains the lower reconstruction efficiency in the top hemisphere. It is worth mentioning that the results in Fig. 3.10 correspond to the end of HL-LHC, not to the conditions holding during the vast majority of Phase-2.

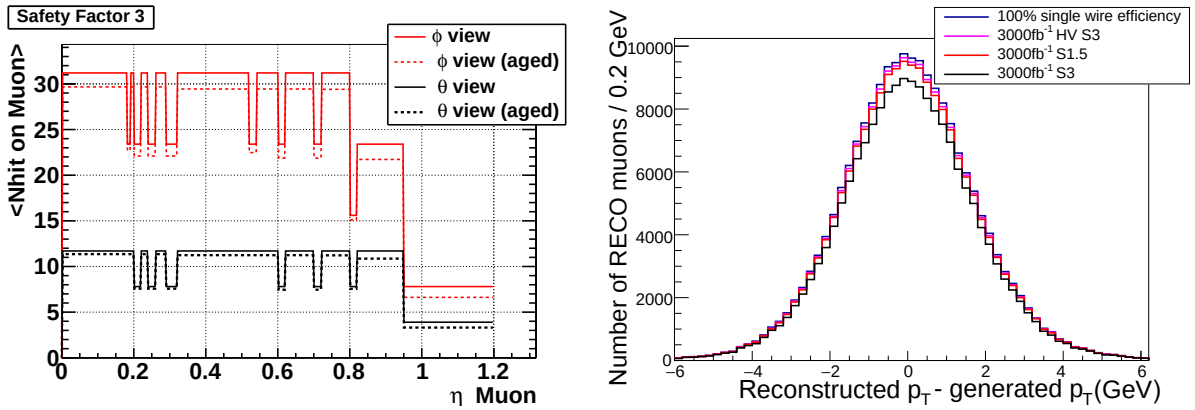

Figure 3.9: Left: Number of DT hits per high p_T muon track as a function of η for a perfect detector (full lines) in both the ϕ (red) and θ (black) measurement planes. The dash lines show the impact of aging in a scenario described in the text. Right: reconstructed p_T using the standalone muon alogorithm in a simulation of 100 GeV muons with different detector scenarios for detector aging: a perfect detector (blue line), the aging scenario described in the text (pink line), the effect of maintaining the HV constant at 3550 V (black line) and the effect of reducing the safety factor to 1.5 in the latter scenario (red line).

For what concerns the trigger performance, the current detector L2 HLT uses a reconstruction technique similar to the standalone muon reconstruction, both profi from the full resolution TDC hits. Its performance can be taken as a proxy of how an optimal trigger algorithm, which includes all the hits in the muon detector along the track, would perform. Indeed, the availability of the full detector granularity in the service cavern during Phase-2 will allow the generation of trigger primitives with similar resilience against aging as shown here for the standalone reconstruction

The aging scenario here considered will be refined as more input data (accelerated irradiation tests, hit efficiency and gain scans) become available. No account has been done for the angular dependence of the signal generated, assuming the worst case of perpendicular tracks.

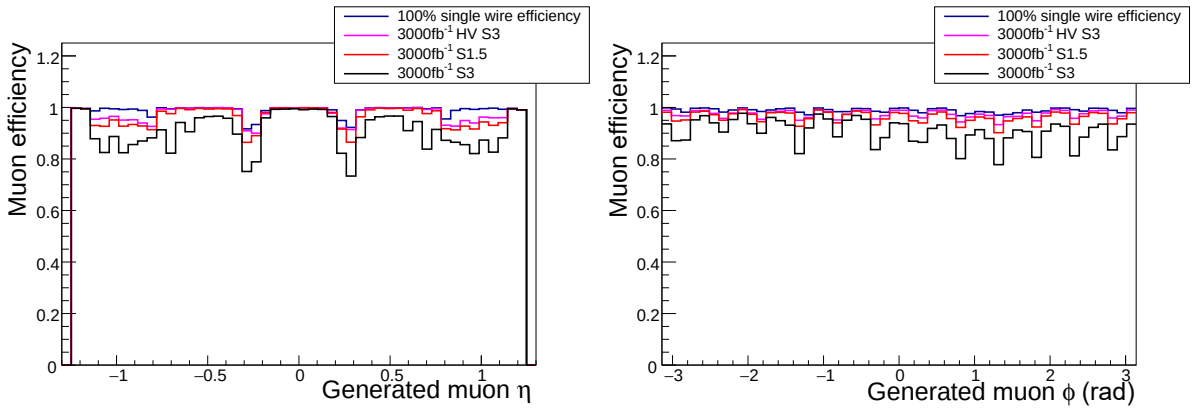

Figure 3.10: Left: Standalone muon reconstruction efficiency as a function of muon η (left) and ϕ (right) after 3000 fb^{-1} in a 100 GeV muon gun simulation with different scenarios for detector aging: a perfect detector (blue), the aging scenario described in the text (pink line), the effect of maintaining the HV constant at 3550 V (black) and the effect of reducing the safety factor to 1.5.

A caveat to be assessed is the different radiation field in CMS with respect to GIF++. During LHC operation the hit efficiency of the DT chambers in CMS will be continuously monitored to detect any degradation as early as possible, and to adjust the operation point accordingly. This will be achieved by a program of periodic HV scans, as is being done now, and by combining measurements of HV currents and background rate data, which will be included in the routine monitoring of the data quality.

3.2.4 Aging mitigation strategies

A prudent aging mitigation program is being implemented:

1. **Lower the high voltage operating point** to enhance the longevity of the wire chambers. The reduced gain of the wire results in significantly lower collected charge. In 2017 we have reduced the operation point of the DT chambers by 50 V after thorough validation of the detector performance. This will be pursued further in the MB1 external wheels, where muons from the interaction point leave considerably larger signals due to the track inclination.
2. **Changes in the gas system operation**. Currently we deliver only 15% of fresh gas and the air and water contamination from leaks cannot be independently controlled. Modifications to the gas system are being implemented so that we will be able to stop re-circulation and control independently the air and water concentrations in the gas mixture.
3. **Shielding the chambers**. Final prototypes of MB4 top sectors external shielding against neutrons/photons has been installed in the Winter shutdown 2016/2017; the ultimate system, which is being designed, can be installed in LS2 at the earliest. Improvements of shielding at the source of neutrons leaking in the cavern is being explored within CMS.

The installation of MiC2 in LS3 will have very beneficial effects on the resiliance of the DT system to aging, by increasing the number of layers that can be combined to identify the BX of the trigger primitive and by reducing the electronic failure rates of the replaced electronics. It also enables to lower the front end threshold, which is kept relativable high to suppress electronics noise fed from the legacy MiC into the chamber.

Further aging mitigation measures are under investigation in GIF++ and elsewhere:

- Investigate the effect of absolute gas flow on aging.
- Investigate the effect of anti-aging additives, particularly the effect of already existing pollutants in the gas mixture, oxygen and water, aiming to optimize their concentration.
- Investigate the out-gassing from materials that could be extracted from the gas circuit, as some flexible pipes and O-rings.

3.3 The upgraded DT electronics architecture

3.3.1 Overview and functionality

The upgraded architecture, see Fig. 3.11, relies on the continuous streaming of TDC measurements towards the back-end electronics in USC, leaving on the chamber side a minimal set of components, see Fig. 3.11, in order to provide:

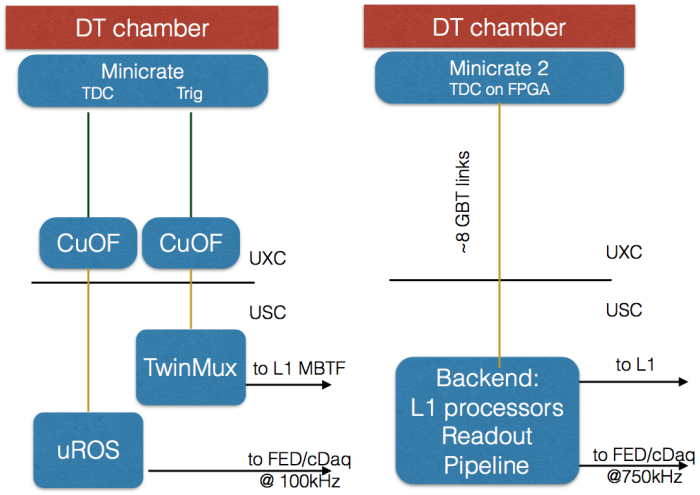

Figure 3.11: Left: Current partition of the DT system electronics. Right: Upgraded Phase-2 DT electronics. Each SuperLayer will be read by one (two in the big MB3 and MB4 SuperLayers) OBDT (On-Board Electronics for DT).

- LHC Clock and fast signal distribution (BGO commands), including Bunch Crossing Zero (BC0);
- data transfer to UXC via optical links;
- time digitization of the analog signals from the Front End Boards;
- control of the FEBs;
- test pulse generation;
- monitoring of the DT chamber sensors (temperature, pressure, etc.) ;
- slow control services for the RPC and alignment systems.

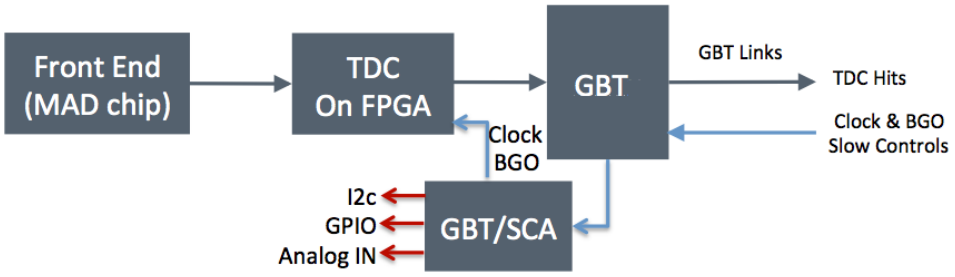

Figure 3.12: Functional block diagram of the OBDT.

Readout pipeline buffering and trigger primitive generation, formerly performed by the TRBs, SBs and ROBs, will be done in boards located outside the experimental cavern profiting from the more relaxed environmental constraints (e.g. radiation level, magnetic field, power dissipation) and introducing the possibility to intervene in case of failures. As the processing of wire hit time-stamps becomes asynchronous, equalizing the paths from the wire signal discriminators becomes unnecessary (data can be realigned through calibrated relative delays), and the cabling length from the front-end is reduced significantly. A simplified minicrate electronics will bring considerable benefits in terms of the power consumption of the DT on-detector electronics, improving the longevity not only of the minicrates but also of the FEB, and lessening the load on the whole DT LV system. The reduced functionality, implying fewer components,

and the technology evolution since the original design will also result in the shrinking of the upgraded board's size (surface needs will be mostly dominated by the front-end cable connectors): the future minicrates will hence be smaller and can be split in distinct boxes to ease installation, as later discussed in Section 3.4.1.

3.3.1.1 Time Digitization

The time resolution needed for the proper reconstruction of DT signals is around 1 ns, which makes it feasible to implement the TDC via FPGA technology, providing that the radiation hardness needed to operate in UXC under HL-LHC conditions is satisfied. In that sense, adopting radiation tolerant flash FPGAs such as the ones from Microsemi would be a good solution. A study has been carried out on a ProAsic3 flash FPGA (130 nm), with a firmware solution based on clock quadrature technique, where the internal PLL generates two 240 MHz clocks phase-shifted by 90° from the 40 MHz LHC clock, providing a final time resolution of 1.041 ns. This development has shown that it is possible to accommodate 64 TDCs of 5 bit/1 ns resolution in $\sim$ 10% of the total available FPGA area. Fig. 3.13 shows the measured non linearities of the obtained TDC channels, well contained within the least significant bit.

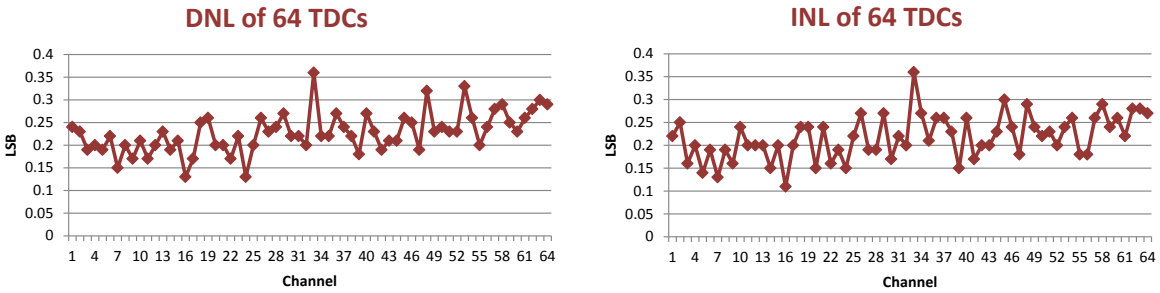

Figure 3.13: Differential and Integral Non-Linearity (DNL and INL, respectively) measured on ProAsic3 64 Channel TDC firmware.

Care for portability, through fully parameterized Register-transfer Level (RTL), scripted place& route, and avoiding to rely on specific FPGA resources, will ensure a straightforward deployment on the different future FPGA models. A key feature of this design has been to avoid gate switching when inputs are stable, thus minimising the current drawn in absence of signal.

Exploring alternative solutions, a different approach has been evaluated and deployed on a Xilinx Virtex 7 FPGA. In this case, time measurement exploits the FPGA I/O deserializers as fine grained samplers of the input signal. Relying on the provided FPGA resources, this technique inherently eliminates the clock routing complexity in the firmware itself, scales easily to hundreds of channels on a single chip, and can be pushed well below the 1 ns resolution, with better linearity (see Fig. 3.14), although slightly more demanding terms of power consumption, given that clocks on the deserializers are constantly running.

According to our requirements, both time resolution and sufficient channel integration are easily achievable with already available FPGA models, even on radiation tolerant technologies. In the present market offerings, as depicted in Fig. 3.15, the FPGA cost per channel grows rapidly when increasing the number of total I/O pads. This considered, the optimal channel aggregation factor lies at present between 50 and 150 channels per FPGA.

Nevertheless, following the rapid evolution of the market and the years before production, the final choice will be made just before the EDR (Engineering Design Review), to reach a better

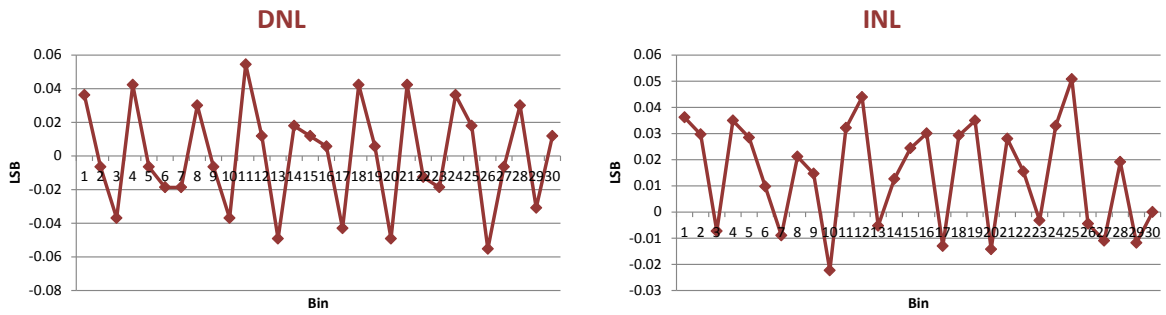

Figure 3.14: Differential and integral non linearity (left and right respectively) measured on Virtex7 138 Channel TDC firmware.

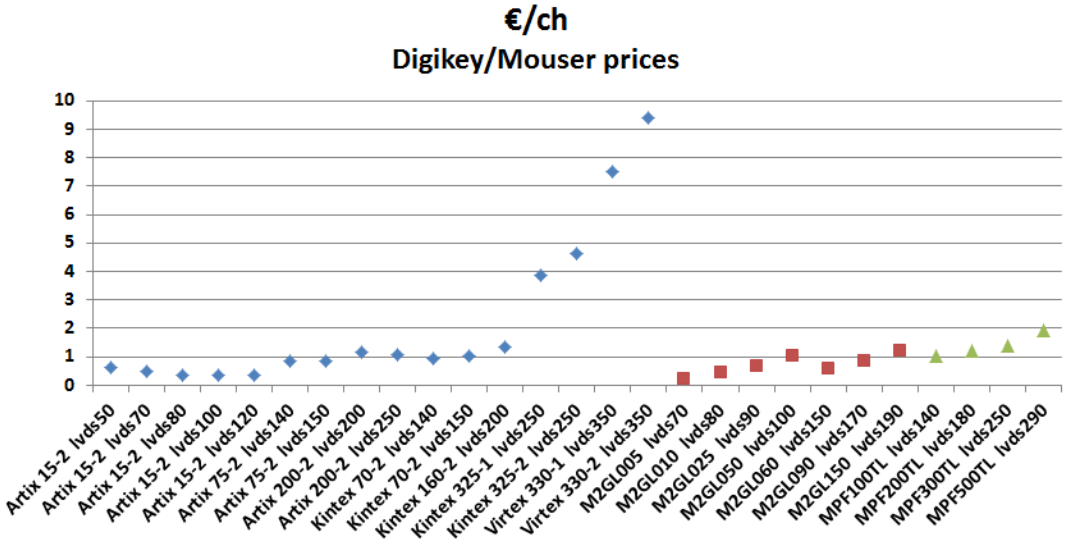

Figure 3.15: Estimated FPGA cost per channel for different I/O size models surveyed in Digikey/Mouser. Red squares and green triangles correspond to flash based FPGA, while blue are SRAM based devices.

optimization of cost and power per channel and to ensure a longer product lifetime of the chosen model.

3.3.1.2 Readout and Trigger Links, Pipeline Buffering

Each channel of the DT chamber Front End Boards (namely the MAD, Multichannel Amplifier-Discriminator, ASIC [63]) can operate up to a hit rate of $\sim$ 4 MHz/channel, with the precision on the threshold level depending on the rate. The highest precision is achieved when the rate is less than 2 MHz/channel, a value we take as an upper limit for the required bandwidth, preventing occupancy bottlenecks from internal or external instrumental noise. The expected average rate contributions from muons and collision backgrounds at HL-LHC luminosity lies comfortably within the specification ($\sim$ 50 kHz/TDC channel). In order to evaluate the total throughput required for each FPGA output we assume:

- 64 channels/FPGA;
- git time encoded with 16 bits (channel ID, BX, TDC count);
- maximum sustained rate of 2 MHz/channel.

As soon as a wire signal gets discriminated, its TDC measurement will be forwarded to the back-end processor, through the optical link. One possible implementation of the readout that works is a round robin channel exploration, the TDC hits are merged through a three-stage 6-to-1 fan-in to the output port of the FPGA. This simple fan-in introduces a variable latency

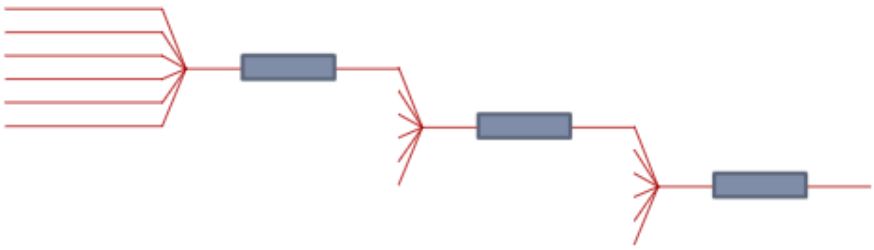

Figure 3.16: The TDC output fan-in. At each BX, one output (if any) out of six channels is moved to the next stage. If more hits are to be sent, they are queued over different BX'es.

on the hit transmission which has to be compensated before the trigger primitive generation. Although part of it will be in the shadow of the drift time (chamber cells are staggered), the final L1 latency budget might put stricter constraints: if needed, a more FPGA area consuming fan-in scheme, based on TDC time ordering, can be adopted.

Given the above specifications, the total bandwidth required for each FPGA output will top at $\sim$ 4 Gbps, well within the capacity of a single 9.13 Gbps LpGBT link (Low power GigaBit Link Transceiver). Depending on the chamber size, each ϕ superlayer (SL) will require a minimum of three (MB1 - 192 wires/SL) to six LpGBT links (MB4 - 368 wires/SL), while three LpGBT links will be enough to cover every θ SL (204 wires). These values leave margin to include monitoring information within the data stream.

On the receiving side, the hit stream from every link will be pipelined on a FIFO, whose depth complies with L1A generation latency ($>$ 5000 hits per link). For trigger primitive generation, a channel ordered buffer will keep hits belonging to the last drift from each wire.

Running the event bunch crossing identification algorithm using buffered data on back-end memories requires being able to reconstruct time correlations among TDC hits while keeping the latency within the constraints, much differently from the present electronics where a dedicated ASIC is directly sampling signals from the wire discriminator. Details on the expected improvements and the algorithms under study will be described in Section 3.5 and in Chapter 7.

3.3.1.3 Reference board design

Given the way DT chambers are structured, the three separate SuperLayers can be considered as autonomous units. The design of the upgraded minicrate will follow this separation, aiming at a single board, referred as OBDT, which fits any SuperLayer in the DT detector, providing hit time measurement, readout, control, and monitor functionality. A preliminary layout of the OBDT board is shown in Fig. 3.17. Taking into account the requirements and considerations from the previous sections, the core architecture of the OBDT board will have these elements:

- four FPGAs sized to host at least 64 TDC channels each, achieving 256 channel per OBDT;
- 384 LVDS inputs coming from 12 front-end cable connectors;
- four LpGBT outputs towards the back-end;

- two LpGBT inputs for TTC distribution and slow control channels, interfacing to local control buses.

In the choice of the board resources, a driving aspect to consider is that access for maintenance can be precluded for long periods, in particular for the internal wheels. Some redundancy and backup paths become therefore mandatory. All LVDS inputs, as well as the lines to GBTX, are to be made available to every FPGA chip, so the failure of a single FPGA chip or a specific output link can be worked around distributing the inputs over the remaining ones. The TTC and slow control links are also doubled, together with slow control local buses. Larger SuperLayers, like in the MB3 and MB4 stations, would require more than the foreseen 64 TDC/FPGA. Instead of installing larger area FPGAs, to insure the same level of redundancy achieved on the rest of the detector, those larger SL will be served by two OBDTs each.

Having redundant fiber links to distribute the TTC signals, under normal conditions the second link will be configured as a Gigabit ethernet carrier, to carry IPBus (Industry Pack Bus) traffic to the OBDT endpoints, following the same monitoring models already successfully implemented in the Phase-1 upgraded infrastructure.

As shown in Table 3.4, 940 OBDT boards are required to instrument the full DT chambers.

3.3.1.4 Legacy services: DT FE, DT Gas, barrel alignment, RPC

Each OBDT board will host two I2C interfaces needed to accommodate legacy chamber slow control interfaces. Besides local monitoring of DT chamber status (temperatures, power sup-

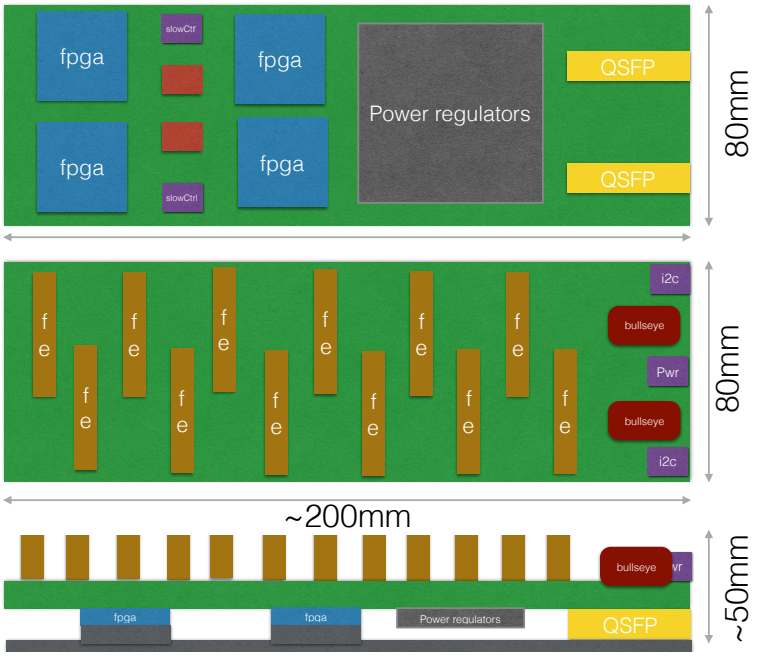

Figure 3.17: Preliminary layout of the components on a DT on-detector electronics board, OBDT, for Phase-2. The view from below (heat sink side, in gray), from above, and from the side are displayed from top to bottom. The four FPGAs, in blue, and the optical transceivers (VL+ array), in yellow, as well as other heat dissipating components will be located on the heat sink side. The accessible side will host most connections, as those to the chamber front-end, in brown, to the power source and to the legacy slow control buses (violet), as well as the bulleye connectors that bring the test pulse calibration signal to the front-end (in red).

Table 3.4: Overall DT on-detector electronics counting.

Chamber type	Number of SuperLayers	Channels per SL_ϕ	OBDT per SL_ϕ	Channels per SL_θ	OBDT per SL_θ	Total OBDT per chamber	Total OBDT per Wheel	Total chambers	Total OBDT
MB1	2 ϕ and 1 θ	196	1	224	1	3	36	60	180
MB2	2 ϕ and 1 θ	228	1	224	1	3	36	60	180
MB3	2 ϕ and 1 θ	288	2	224	1	5	60	60	300
MB4	2 ϕ	384	2			4	40	50	200
$MB4_{small}$	2 ϕ	288	2			4	16	20	80
								Total Boards	940

ply levels, etc.), this will control the FEB discrimination thresholds and will provide the line towards barrel alignment hardware, which has always relied upon the DT infrastructure. A backup communication channel to the RPC boards is also foreseen, as it exists in present system.

3.3.2 The SX5 demonstrator

As a proof of concept of the Phase-2 architecture, a spare DT MB1 chamber sitting in the CMS surface building (SX5) has been equipped with a complete chain of electronics, based on presently available boards and links, in order to model the proposed partition of the functionality between on-detector and back-end electronics (Fig. 3.18). The upgraded readout was integrated into a present CMS DAQ link. By taking cosmic muon data, this system has been used to validate TDC firmware performances, evaluate design choices and assess the final requirements.

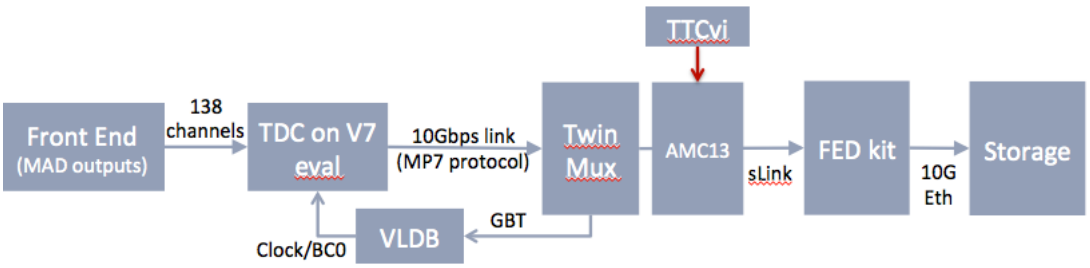

Figure 3.18: The prototype Commercial Off-The-Shelf (COTS) based Phase-2 DT readout chain. The Versatile Link Development Board (VLDB) is part of the Versatile project and provided by CERN.

On the chamber side, the emulated MiC2 relies on a Virtex7 Evaluation Board, interfaced to the front-end LVDS cables through FMC adapters. The Virtex7 FPGA hosts the multichannel TDC firmware and handles the optical links to the back-end. Those data links are using the Phase-1 MP7 8b/10b protocol, as an option to reach the 9.13 Gbps bit rate not yet available on the present GBT solution. A GBT link is instead used to carry TTC Clock and BC0 signals up to the MiC, decoded and distributed there by a Versatile Link Development Board, which also provides slow control I/O channels. Acting as the back-end, a DT TwinMux (a μTCA Virtex7 based board) receives the data links and performs readout buffering and local trigger generation (working on data from a single chamber, processing is limited to SL segments only). Following the Phase-1 upgrade μTCA based model, an AMC-13 bridges the readout to the DAQ node, a uFEDKIT equipped PC. The FEB discriminator outputs have been split, so that the legacy MiC and the upgraded electronics chain were both connected to the same channels. The original trigger logic could then be used as a reference trigger for the upgraded system.

Some runs have even been collected in parallel, allowing an explicit event by event comparison in the qualification process. By means of a specific CMS Software (CMSSW) "unpacker" able to decode the new data format, data collected both from test pulse and cosmic muon runs could be analyzed with standard DT data quality monitoring tools, following the established detector performance monitoring procedure. Standard performance plots are shown in Fig. 3.19.

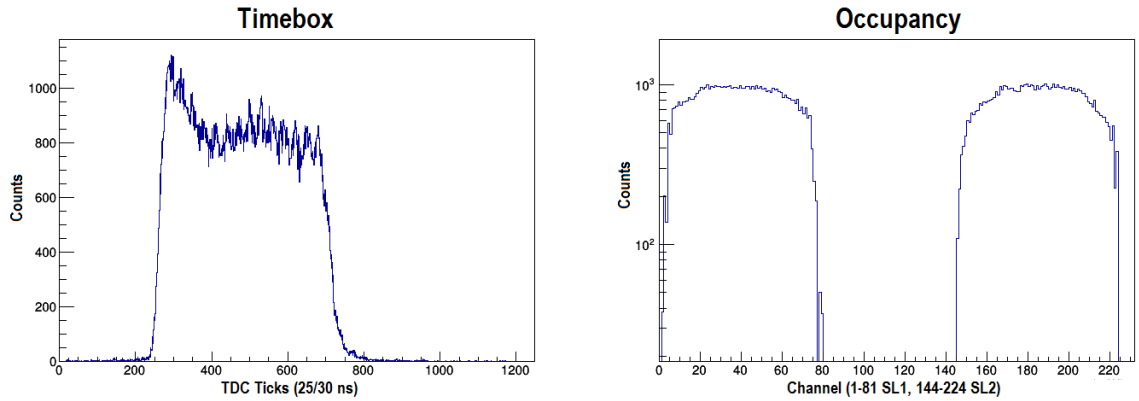

Figure 3.19: DT chamber performance plots, out of Phase-2 readout data taking. Left: TimeBox, distribution of the digitized arrival times of the hits. It is expected to have a square shape under a flat distribution of incident particles if the drift velocity is constant over the drift cell. Right: Occupancy, i.e. the number of hits per electronics channel. The shape comes from the cosmic trigger acceptance.

To evaluate the power consumption, different versions of the firmware were deployed with up to nearly 300 TDC channels integrated on the same FPGA. The measurements showed a baseline of $\sim$3 W, and less then 2 mW per TDC channel for the FPGA, plus $\sim$1 W for each optical link laser diode. This confirms, with a good margin, our assumption that the power figure for the average MiC (12 FPGA, 10 links, $\sim$ 600 TDC channels) would settle below 50 W, halving the present typical consumption.

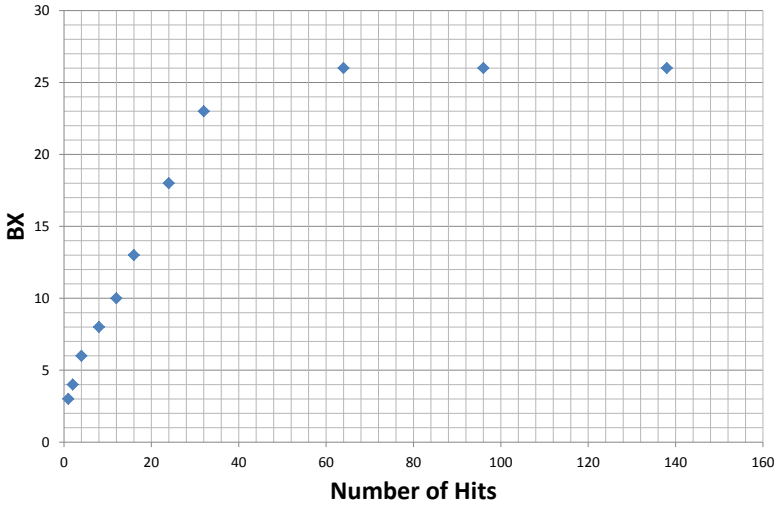

Figure 3.20: Measurement of the latency (counted in LHC bunch crossings) of the TDC output fan-in in the Phase-2 demonstrator as a function of the number of hits to be sent to the backend.

Having only one chamber, a full track finder algorithm cannot be tested in the demonstrator. This validation step is scheduled at latest during LS2, when a full DT sector in one external

wheel will be equipped with the final Phase-2 electronics prototypes. Meanwhile, the latency of the TDC hit data multiplexing to the output link in the OBDT have been measured. As shown in Fig. 3.20 the measured latency of the TDC output fan-in depends on occupancy but is bounded below 26 BX'es.

While the demonstrator infrastructure did not provide full support to the slow control functionality which is required in the MiC, the functionality of the GBT SCA available in the VLDB was tested, achieving I2C communication (e.g. FEB thresholds control) and analog I/O (e.g. test pulse generation and temperature monitoring).

3.4 Phase-2 minicrates and installation plan

3.4.1 Mechanics design and cooling

The DT on-chamber electronics is hosted in the MiC. These are boxes of extruded aluminum, up to two meters long. Two layers of electronic boards lie inside a MiC. The rear layer hosts readout boards (ROB); the front layer hosts trigger boards (TRB). An inner aluminum infrastructure supports the boards, and at the same time establishes thermic contact with the water cooling channel that is integrated in the back side of the MiC extrusion. Altogether, the boards in the MiC absorb over 100 W. The PCBs are designed to transport heat to metallic strips that are put in contact with the aluminum infrastructure. The hottest components are the BTI modules on the TRBs front face. The cooling infrastructure is completed by 2 mm thick aluminum sheets that cover the TRBs; those covers are in contact with BTIs and other TRB components via thermo-conductive rubber, and provide very efficient cooling. Since LHC start-up and all along, the MiC mechanics has proven to fulfill stringent operation requirements:

- good mechanical and electrical robustness;
- good electrical grounding;
- excellent cooling of DT on-chamber electronics.

The next generation of DT mini-crates has to fulfill the same requirements. The MiC2 will contain the electronics boards (OBDT) described in Section 3.3.1.3. The baseline assumption is that the MiC2s have SuperLayer (SL) granularity and a smaller form factor, i.e. SLs will be independent detection systems, contrary to the current system. This solution greatly improves the system robustness, a critical parameter because chambers can become less efficient with age. Each DT chamber will host three MiC2 boxes; each box will contain one OBDT board. In the current design, two OBDTs are required for each of the ϕ SuperLayers of the large MB3 and MB4 chambers. However, in those stations, because of their bigger size, the mechanical constraints are more relaxed than in the MB1 station, which is thus taken as reference for the discussion in the following.

At the current stage of R&D, the three MiC2 boxes are to be fit on-top of the MiCs, however there are concerns still to be addressed. A decision will be made in time for an installation trial of a full DT sector in an external wheel during LS2. A replacement of the legacy DT MiCs with new ones of similar form factor was initially considered. Now this possibility is only retained as fallback. The major drawback of that backup solution is that full un-cabling of DT and RPC (ECAL too in YB0) is indispensable, besides the necessity of massively opening the cooling circuit. Effort and risks are considerable. In addition, there are delicate parts that are attached on top of the MiC covers that have to be removed and reinstalled, like the splitter board that distributes low voltages to the front ends, and the gas manifold. The splitter board has been carefully designed as to provide an excellent common ground to all SLs, noise free,

and to withstand also HL-LHC operation. The un-cabling effort in the external wheels is greatly reduced if the current MiC extrusions can be preserved in situ: it mainly reduces to the DT FE cables. The small MiC2 boxes are attached to the MiC extrusions without removing the splitter board and the gas manifold. The cooling circuit remains tight.

Cooling of the MiC2 boxes is done by contact with the MiC extrusion. A stand has been built for testing the efficiency of MiC2 cooling by contact with the MiC extrusion. Water is flowed through an emptied MiC extrusion of an MB1 chamber. The cooling system runs in the same conditions of temperature, pressure and flow as in a MiC operated in CMS. In the extrusion, the cooling fluid runs along channels within the corners of the extrusion rear.

In the initial test, a MiC2 aluminum box is fit inside the MiC extrusion; its rear touches the cooling channel, and the thermic contact is made more efficient by inserting thermo-conductive rubber. Power cables run in the MiC empty space behind the rear of the MiC2 box. Sixteen bulky ceramic 0.8 Ω resistors connected in series are distributed on two PCBs; the low voltage can be regulated so that the absorbed power can vary up to and beyond 100 W. The resistors are all mounted on one PCB face. The two boards are put in the MiC2 box with the resistors facing the rear of the MiC2, in thermic contact with it via a 2 mm sheet of thermo-conductive rubber. The MiC2 rear, an aluminum sheet up to 5 mm thick, constitutes the system heat sink. The MiC2 is entirely contained within the depth of the MiC extrusion. Temperature sensors are placed in critical locations, and the temperatures are continuously monitored until they reach a plateau. Several configurations, in particular with and without thermo-conductive rubber, with a 2 mm and a 5 mm thick MiC2 rear plate have been tested. The results (Fig. 3.21) show that the electronic boards inside the MiC box can be efficiently cooled down, well within standard operating parameters.

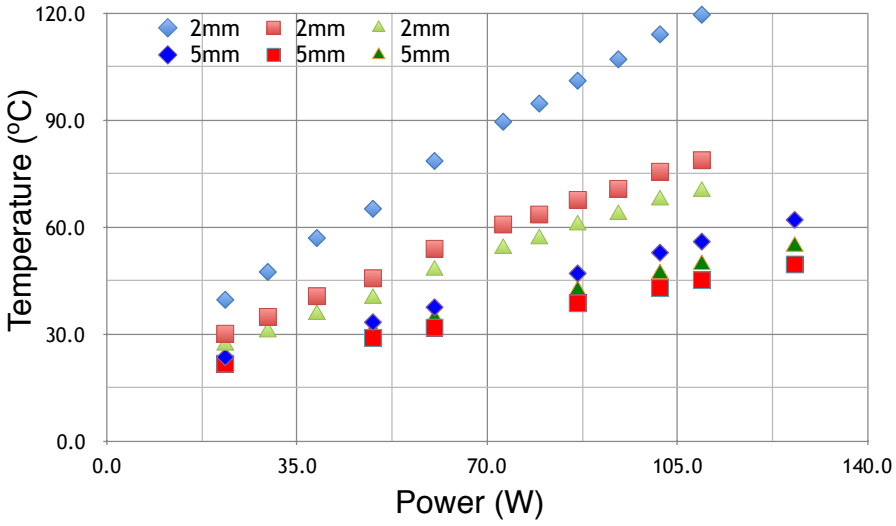

Figure 3.21: Equilibrium temperature of the hottest components in a MiC2 box cooled down by thermic contact with a MiC extrusion. The measurements are for three sensors and two configurations: MiC2 with 2 or 5 mm thick rear panel. The lowest points are for the final configuration described in this section.

However, the operation of emptying a MiC extrusion of its electronics, although conceptually simple, can take a long time because of the large number of small screws with difficult access that need to be removed. A faster destructive alternative (drilling screw, breaking stuck boards) can be potentially unsafe for CMS, since there are many small metallic parts that can fall and get lost.

Then, on the basis of the positive results of the initial test, we studied whether the small MiC2 boxes with SuperLayer granularity can be installed on top of each MiC, without emptying it of its electronic boards. Three MiC2 boxes will lie on top of each MiC, with their rear pushed against the TRB covers and in good thermic contact with those (Fig. 3.22). The covers that used to cool down the TRB components will cool down the MiC2 rear, and this is in thermic contact with OBDT components inside the MiC2 via thermo-conductive rubber. In situ measurements and design studies show that the three boxes can accomodate the OBDT boards and can fit in the available space in front of the MiC. The tests have shown that the three MiC2 boxes can be cooled down with high efficiency (Fig. 3.22).

The main difficulty is that the available space for cabling is limited. Technical drawings show that passages for all cables and fibres can be defined, that respect isolation and bending radii criteria, without compromising on the size of the surface that provides the thermic contact for cooling. To overcome the space constraints we plan to re-design the chamber covers (”carters”) in a way that is optimised for the new cabling, and/or to partially emptying the MiC extrusions.

3.4.2 On-detector power distribution

The electronics of every DT chamber is powered by four separate input channels, all equipped with a sense connection to take into account the voltage drop along the cables. The Front End Electronics for each DT chamber uses two channels from an A3009 CAEN board, giving 5.2 V and 2.6 V with currents between 1 and 3.5 A. The MiC2 is powered by one A3009 channel (5.9 V, 1.5 A) and one A3050 CAEN board channels, which gives the bulk of the power (4.10 V, up to 30 A). All these lines reach a Low Voltage Patch Connector (LVPC) above the MiC, where the current sense measurement is taken and the final distribution occurs. Front end electronics will be left unchanged by the detector upgrades, and will require to maintain the same powering. This makes convenient to keep the same LV infrastructure also for the new MiC2. The OBDT

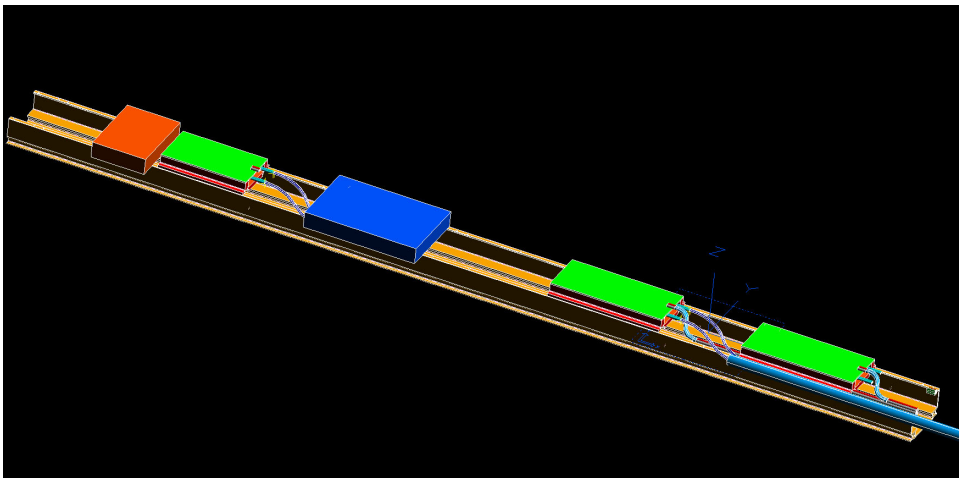

Figure 3.22: Possible arrangement of three MiC2 boxes (two for the ϕ SuperLayers, one for the θ one). Orange is the Gas Manifold; blue is the Splitter Board. The routing of the optical fibers is respecting their bending radius specifications.

is expected to be less demanding in terms of power consumption, and lower input voltages for the new FPGAs can be used. The new on-detector distribution box for the MiC2s will use the same two power supply input channels, with probably lowered voltages (the A3050 output range is 2–8 V, the A3009 delivers 1.5–8 V), and will give voltages close enough to those required by the new FPGAs such that onboard DC-DC conversion does not imply large thermal dissipation. Onboard DC-DC conversion is needed to provide the several voltages required by the FPGAs. It is to be noted that reducing the power required in the MiC2s will significantly decrease the cost for the power system maintenance. In addition, reducing power consumption of the MiC2s will also lower the FEB operating temperature, enlarging its lifetime.

3.4.3 Evolution of the DT power supply system

The proposed upgrade for the DT detector electronics will not require any change in the actual powering infrastructure. At the same time, the risks linked to aging of both the LV and HV systems suggest to have available alternative solutions, besides simple maintenance, in order to successfully operate the detector up to 2038.

Our strategy focuses on having new versions of the actual boards, from the same industrial partner (CAEN), retro-compatible with our system but made with updated electronic components. In this way a replacement of the complete powering system is avoided, just the boards actually required are to be bought, with big advantages from the economic point of view. Moreover, in case a sudden aging would require a complete substitution of the boards, we could still keep the cabling and control infrastructure.

A successful example of this strategy is given by the switch from the SY1527 to the newer SY4527 mainframes used for both LV and HV distribution, started in 2014. The new mainframes, while using updated technology, are completely backward compatible, and have been operated simultaneously in the DT system with the older version.

The industrial partner CAEN has already started the development of this kind of boards for the standard EASY system (NeoLite project [64]), in order to respond to HL-LHC requirements. We expect these boards to be suitable for our LV system, which has no peculiar requirements.

For what concerns the DT HV system, a specific system was chosen in order to keep a high granularity in the power distribution. This has the double benefit of reducing the amount of detector channels lost, both in case of a minor failure in the HV distributor and in case an electrical problem occurs inside a drift tube, without the need to access the experimental cavern. This decision greatly helped the high reliability of the DT system during operation; to maintain it at the same level we will need a custom solution able to replace the A877 HV board. For this reason we plan to ask the industrial partner to develop a dedicated prototype, and we will take care of the needed radiation tolerance test in suitable facilities.

3.4.4 Installation plan

3.4.4.1 Material readiness and storage needs for installation

Material has to be ready before installation starts in order to minimize the number of interventions. Thus storage and quality control space will be needed in the assembly facilities in building 904 at CERN.

3.4.4.2 Access strategy: scaffolding and scissor lifts

As can be seen in Fig. 3.23, scaffolding for replacing the DT MiCs is present from weeks 36 to week 76, that is 40 weeks, close to 10 months. This is compatible with our estimations of two

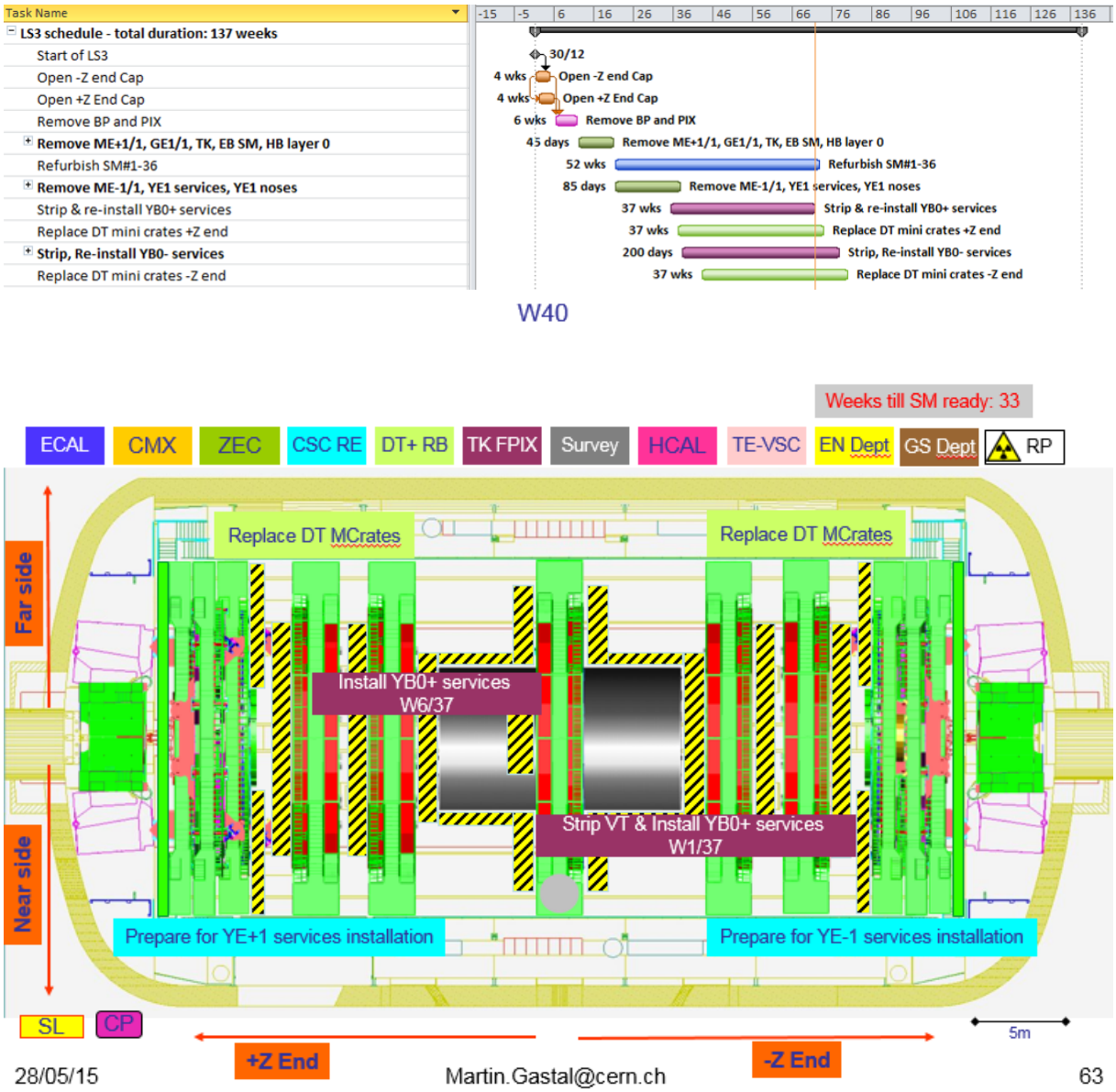

Figure 3.23: Summary of current LS3 schedule and one typical configuration during the MiC replacement.

months per wheel, which we are confident is a reasonable envelope for our intervention. All the time YB0 is accessible, scaffolding is assumed to be present due to the full replacement of services to the tracker.

There are three main factors to consider for the planning:

- MiC2 production has to be well matched to the installation schedule and availability has to be insured early on.
- Minimizing the time required for replacing each MiC on the detector. This will impose mechanical design constraints.
- Wheel accessibility will determine the level of parallelism of the intervention and thus the manpower distribution, i.e. how many installation teams can work at the same time.

We will keep working with TC to ensure enough access time is allocated but it is clear that the schedule will evolve a lot during the following years depending on other actors. On our side, we approach this dynamical process trying to minimize the impact of our intervention in LS3 with a two-fold strategy, by including this requirement during the design process (particularly the mechanics) and by being flexible on the installation strategy. While installation from scaffolding is clearly advantageous if a wheel is done one at a time and it is the only wheel available, installation from scissor lift is more efficient for the movable wheels because it allows better co-activity with other groups (YB0 services and RPC maintenance, mostly) and/or accessibility to several wheels at the same time. If several wheels are accessible at the same time, other aspects (logistics, trained manpower) will become the main limitation for the installation. With scissor lift, access to chambers in the top sectors of the YB+-1 is possible as long as it is displaced beyond the edge of the solenoid, which will be a common situation in LS3 to allow YB0 scaffolding for the new tracker service installation.

3.4.4.3 MiC Replacement Process and Access Time Estimation

The MiC replacement sequence for the baseline option ('attach') is expected to follow the listed steps, for each of the six wheel faces hosting MiCs. Apart from a commissioning team, per accessible gap a preparation team and an installation team will be switching sectors as they advance through the face of the wheel:

- Open the wheel gap and put in place the method to access the chambers: either scaffolding mounting or two scissor lifts positioning.
- Removal and safe storage of the MABs (Muon Alignment Barrel structures) at the surface. Removal and safe storage of thermal shields in UXC; 2 days/wheel
- Removal and safe storage of RPC signal cables in the periphery (as during maintenance) for all sectors or only for the sectors requiring chamber extraction loosening the rest. Extraction of legacy DT signal copper cables up to the balconies, since they are not going to be re-used to remove as much as possible copper that is not going to be used and could get otherwise activated; 6 days/wheel
- Route optical fibers from the tower racks through the wheel's periphery in its dedicated cable tray. One trunk per sector; 1 week/wheel (can be done in parallel by cabler teams)
- Per each of 12 (6 in the two YB0 faces) sectors:
  - If sector has RPC chambers which require in-situ extraction, disconnect gas and cooling, extract chambers, repair and insert back; 1 chamber/day
  - Per each of the 4(5) chambers in a sector of a given wheel:
    - Remove protections, and cables, disconnect old MiC (preparation team); 1 sector/day
      1. Open and replace the LV Patch Panel (PP).
      2. Loose cable ties from HV cables
      3. Remove, label and and store in UXC all chamber protection covers.
      4. Detach the gas manifold and the front-end (FE) splitter to ease access.
      5. Disconnect and remove ϕ cables from the chamber and the MiC (throw away).
      6. Disconnect θ cables from the MiC side and carefully protect them.

- Install new MiC2 (installation team); 2 chambers/day
  1. Remove MiC aluminum covers where needed (3-4 covers).
  2. Allow access to the CCB to remove the test pulse, FE slow control, FE threshold, RPC and alignment cables.
  3. Install the new MiC2 boxes screwed on the old MiCs aluminum profile.
  4. Route and connect the new test pulse, FE slow control, FE threshold, RPC and alignment cables.
  5. Route and connect the new ϕ FE cables to the MiC2 boxes and the chamber SuperLayers.
  6. Connect the old θ FE cables to the corresponding MiC2 box
  7. Route optical fibers from the periphery radially to the chamber.
  8. Route and connect the optical fibers to the OBDT (Trigger Control and Distribution System TCDS and data path)
  9. Route and connect the power supply cable.
- Install back chamber elements and protection covers (preparation team); 1 sector/day
  1. Fix back the gas manifold and the FE splitter.
  2. Perform DT chamber maintenance: Replace gas and cooling flexibles and O-rings as needed.
  3. Power on, perform validation tests.
  4. Put back the chamber protection covers (some of new design, adequate to new cabling) into place.
  5. Tighten the HV cables.
- Re-install RPC cables over chambers in sector. It is included in the time count, because due to 2 teams access constraints, it cannot be done in parallel. 6 days/wheel

- Put back the thermal shields. Installation of the MABs. 2 days/wheel
- Full wheel validation with cosmic ray muons and alignment of MABs and extracted chambers; 2 days/wheel
- Ready to close wheel gap.

This results in a total of 42 days/wheel ($= 2 + 6 + 24 + 2 + 2 + 6$), assuming that the installation and preparation teams work in parallel. Maintenance has not been accounted for yet. For comparison, the "replace" option with scaffolding has been estimated to need a total of 44 days/wheel. However in that estimation more teams were working in the same wheel, while here the assumption is that we can have access to more than one wheel at the same time.

3.4.4.4 Validation for HL-LHC conditions

As during construction and Phase-1 upgrades, the DT group will implement the required quality control tests to insure functionality. Although the chosen technology at the core of the OBDT, flash FPGAs, should have a good behaviour under irradiation, the board will be tested for radiation hardness in dedicated irradiation facilities. After assembly and before installation in UXC, final functionality tests and burn-in of the new Minicrates will be performed in building 904.

Trigger rates and bandwidth limitations come from the link bandwidth and memory size of

the data storing elements. The new links, as described above, will have sufficient bandwidth to read out the full detector, so we will not be limited by the trigger rate any longer. In terms of latency, the limitations are the data storage elements in the back-end electronics. The memory sizes required are the ones inside the back-end FPGAs that are large devices with no limitations like present ASICs, so we do not expect problems. The next potential bottleneck is at the interface to central DAQ, which will be designed carefully, taking into account the expected occupancy and trigger rates. The way to test it is to inject simulated data with volumes as expected in HL-LHC (with sufficient safety margin) and provide simulated trigger signals at the expected rate. First, these tests will be done on a bench at the laboratory. Later on, we can simulate test patterns in the back-end boards and test the DAQ system during the integration in CMS.

3.5 New back-end and integration in CMS

3.5.1 Present DT trigger primitives

With a drift time in the DT chambers of up to 16 bunch crossings (BX) long and the conversion between time and coordinate left-right ambiguous, the generation of DT Trigger Primitives (TPG) requires the identification of both the parent BX, i.e. the event that generated the muon, and of a track segment pattern, which are strictly inter-dependent. The DT TPG has been hosted on-detector so far, on the MiC, designed around three stages integrated in their corresponding ASICs: the Bunch and Track Identifier (BTI), the Track Correlator (TRACO) and the Trigger Server (TS) [65]. The output Trigger Primitives, up to two per chamber per BX, are track segments in the transverse projection, providing the time of the parent BX with a precision of 12.5 ns, the local bending angle ϕ_B with a resolution of O(10^{-2} rad) for the highest qualities, the local track intercept x_0 with a resolution of approximately 1.4 mm, or a track segment in the longitudinal projection identified with coarse resolution.

The core of the DT TPG is the BTI ASIC, which is a continuous track fitter operating at 80 MHz. It provides an angular resolution in $r\phi$ of about 0.06 rad and a position resolution of 1.4 mm. The angular resolution is improved by a factor 6 when correlating two BTIs at TRACO ASIC level. Each BTI inspects nine wires at a time, computing the lateral displacement between pairs of reconstructed hits for each wire pattern once a BX is assumed. The BX identification and track measurement is achieved when all the displacements in such a valid set are equal to each other. The procedure is synchronous by construction and is dependent on an equalized path for the time of arrival of the hits to the BTI.

Several lessons, which will be crucial for the HL-LHC, have been learnt from the operation of the detector: a precise reconstruction of tracks in the longitudinal projection is under-exploited so far; a good identification of the BX is obtained with the BTI when four aligned hits are found, i.e. with highest qualities; the TPG efficiency relies on a high single-hit efficiency of the Drift Tubes, as only approximately 5% of the segments output by the TRACO features less than seven aligned hits. In order to overcome the single hit efficiency requirement in the present architecture, a revision of the local trigger primitives generation is mandatory. An approach based on profiting from all the available information in USC, beyond the SuperLayer level, that exploits the longitudinal projection information will be needed.

3.5.2 Barrel muon TPG at Phase-2 and aging mitigation considerations

The proposed upgrade aims to transfer the complicated logic present nowadays in the MiCs to the counting room, where off-the-shelf high performing devices can be operated without

concerns about their radiation reliability. Therefore, the paradigm of the DT TPG, which will be then part of the back-end, is required to change: both the BX identification and track fitting will be performed by dedicated asynchronous algorithms implemented on commercial FPGA processors.

This approach opens the possibility to produce improved local trigger primitives, with only the intrinsic limitations of the DT chamber, since all chamber hits and their highest resolution time stamps will be forwarded to the off-detector electronics. In particular, the following improvements are foreseen:

- time precision is improved from the 12.5 ns of the BTI sampling to the $\approx$ 1 ns precision of TDC measurements, resulting in principle in a higher resolution of the trigger primitives (position, bending angle/momentum, BX);
- deadtime is reduced from 400 ns for the nine channels covered by a BTI every time any of the nine channels of a BTI is hit, down to $\sim$ 80 ns per single channel, determined by the width of the FEB pulses, and resulting into less influence of background signals masking muon hits by a factor of 5×9;
- the bunch crossing identification capability is not restricted to the information provided by a single SuperLayer as it is for the present BTI: although still requiring the simultaneous processing of TDC signals collected in multiple layers of the Drift Tubes, it can be extended combining together signals from all DT layers along the path of the muon.
- local track fitting, which was limited to a group of nine cells in four layers in the BTI, remains no longer a physical constraint;
- an improvement of the position resolution in θ from the current 32 cm to approximately 1 mm, and an early combination of ϕ and θ views, leads to a better estimate of the muon vertex and enhances the projection to the silicon tracker;
- the limit in the maximum number of trigger primitives per chamber will be removed.

As a consequence, BX identification will use data beyond the current SuperLayer level, which thus enables to generate trigger primitives using data from multiple DT chambers.

Furthermore, the new system will combine the three θ-SLs available along the muon trajectory, unaffected by the magnetic field in the longitudinal projection, which can be used for a relatively simple approach for BX identification and seeding of subsequent full track reconstruction.

Accordingly, the collection of TDC hits in USC from different chambers will allow us to process together signals from neighboring SuperLayers and chambers according to the capability of hardware resources available by the time of construction. This will be a clear asset to overcome any aging effect at single hit inefficiency level, as it is expected in the DT chambers.

The effect of all the mentioned improvements can be estimated by the higher performance obtained nowadays when moving from L1 trigger to L2 in the HLT, which provides an ultimate limit of what can be possible. First outcome is a rate reduction as a consequence of the higher resolution available for the standalone track reconstruction and from the higher complexity of the algorithms employed. This rate reduction and increased resolution allows a much more efficient matching with the tracker at Level 3 today, which will be particularly beneficial in Phase-2, where CMS aims to have a tracking trigger in the Level 1 hardware system.

Studies should continue to define the final algorithm that provides the best improvement while

requiring a reasonable implementation cost. One aspect that drives the design is that the DT chambers occupancy will be relatively low even at the expected Phase-2 luminosity, with hit rates in the order of 50 Hz cm^{-2} and muon rates per station below 500 kHz, making the coincidence of uncorrelated muons in the same station and event quite unlikely. At the same time, the technology improvements over the years allow merging into single devices a large fraction of the logic that was distributed in many ASICs and boards in the early 2000s, as was described above. This means that without any physical boundary, a processor that can receive the information from a large fraction of the detector will perform much more efficiently, reducing significantly the number of ghosts, the need of sorting layers and other problems related to the presence of boundaries segmenting the available information. It is worth mentioning that this line of argumentation makes very appealing a design that follows the time multiplexed architecture. That will not be the baseline design described here because the latency will be larger and until it can be proven otherwise, minimizing latency should be prioritized. Nevertheless, it may be a design choice later on.

The proposed system is designed to merge the information from the RPC detector as well, and from the HO detector, being implemented as part of the Phase-1 upgrade. The optimal use of HO information will depend on the results obtained at present in Phase-1. For the RPC detector algorithms exist and are already implemented in the Phase-1 electronics. The results from Run 2 implementation show that the BX identification is improved, resulting in an improved efficiency ($\sim$ 1%) of the BMTF (Barrel Muon Track Finder) and a reduced rate of BMTF tracks ($\sim$ 5%). It is worth reminding, that for Phase-2 the RPC link boards will be replaced and the new system should provide up to 1 ns resolution instead of the present 25 ns. This will improve even more the RPC BX identification capability, which could be beneficially used as seed for the DT BX identification, but taking into account that the system has to work efficiently without the RPC input.

3.5.3 The Phase-2 barrel muon back-end architecture

The present algorithms featured by the BTI and TRACO ASICs can be a good starting point for a first approximation of the FPGA resources needed per chamber, as such ASICs, currently hosted in the MiCs, contain the majority of the TPG logic. In order to do that, the numbers of ASIC gates from the different trigger ASICs and FPGAs used in the MiCs have been added up, obtaining approximately 20 million gates of logic required per MiC. This first rough assessment shows that it is possible to accommodate the full MiC L1 trigger algorithms in one of nowadays powerful and costly (10 keuros) SRAM FPGA like the Virtex 7 biggest part 7V2000T. In addition, we also need to take into account the logic required to perform the event matching and readout, which in principle should be a low fraction of the overall logic. And finally, the algorithm improvements will also require further needs. However, with the cost reduction of these devices in the coming years, this order of magnitude of one such FPGA per chamber can be assumed as the maximum required for the system implementation. In what follows, a four times higher integration factor is assumed.

Accordingly, a possible architecture can be drawn starting from a μTCA form factor architecture, which is the one that was used in present Phase-1 upgrades, where one board containing one powerful FPGA will receive links from several DT chamber SuperLayers.

In particular, assuming a separated ϕ and θ view processing, a single board will be able to handle the ϕ-SL links of an entire DT sector, i.e. 8 SL and 12 OBDTs for a total of 48 input links (64 input links in Sectors 4 and 10). The total number of ϕ processors is therefore 60 boards. θ SL's instead are just three per sector, giving a total count of 12 input links per sector. θ han-

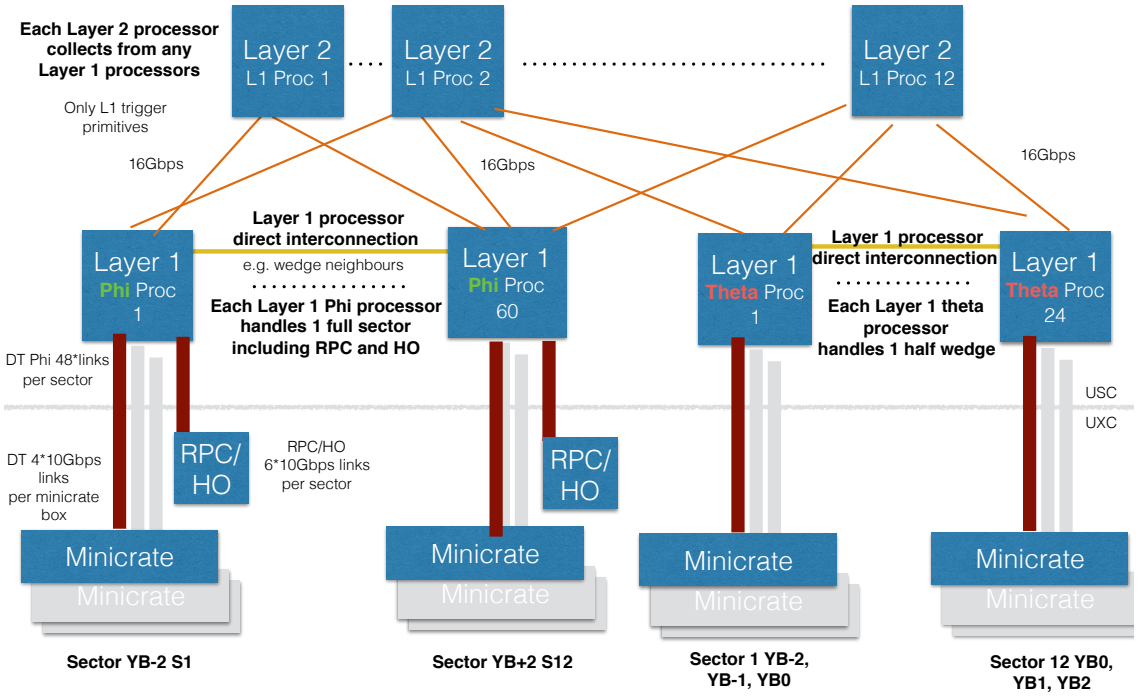

Figure 3.24: Back-End layout focusing on data interconnections.

dling processors are expected to concentrate inputs from same sectors on different wheels, with the 60 links coming from the same wedge distributed over two processors.

The total number of boards in USC receiving detector links is therefore 84 ($60\,\phi + 24\,\theta$), followed by a layer of 12 trigger processor acting as wedge sorters and routing interfaces towards the L1 trigger system. The full back-end can be arranged in 10 crates. At present an ATCA form factor is considered in the costbook, including ATCA infrastructure such as crates. This is consistent with the L1 trigger Interim Document [18].

The architecture presented should be capable of coping also with the RPC/HO input links, as it is done in Phase-1.

In addition, to fulfill slow controls and TCDS distribution needs, we consider to have another three crates hosting 30 boards (6 boards/wheel) with lower cost FPGAs, each of which controlling 22 SL.

Assuming an I/O capability similar to the Phase-1 system, we expect that both the need of interconnecting links and the interface to the Level 1 trigger system can be done smoothly from the already accounted modules. The details will depend largely on the final implementation and organization of the Phase-2 trigger architecture, including the tracking trigger.

3.5.4 Expectations about the interface to CMS DAQ and L1

As mentioned earlier the DT and presumably also the RPC readout will be done in the back-end boards located in USC. The functionality of these boards will include the event matching ca-

Table 3.5: Summary of estimated CORE costs for the DT upgrade expressed in 2016 kCHF.

Item number	Item name	Estimated Cost (kCHF)
2.2	Total DT upgrade	5682
2.2.1	DT front-end electronics	3289
2.2.1.1	OBDT electronics	2332
2.2.1.2	MiC2 mechanics&cooling	344
2.2.1.3	Cables in UXC	454
2.2.1.4	Optical patch panels in tower racks	48
2.2.1.5	Shipping	82
2.2.1.6	Testing systems	31
2.2.2	DT back-end electronics	1609
2.2.2.1	MiC2 slow control	138
2.2.2.2	Back-end boards (readout&trigger)	1471
2.2.3	Optical links	784
2.2.3.1	Optical links UXC	732
2.2.3.2	USC fiber plant	52

pability that was previously implemented in the ROB with the different characteristics of overlapping events, orbit roll over capability, etc. The logic required to implement this functionality should be relatively small and it has already been implemented in the SX5 demonstrator. From the resources available in today's FPGAs, the memory requirements are also small and are easy to accommodate on whatever device.

According to the ongoing R&D activities within the CMS TriDAS (Trigger and Data Acquisition) group [66], the Phase-2 DAQ will provide a common board as an interface to the Event Builder, the DAQ& TTC HUB (DTH). This board, through 100 Gbps crate back-plane lanes, will collect and funnel readout data from the Data and Trigger Concentrators (DTC), the subsystem specific back-end boards which handle the links from the detector and provide output links to the upstream L1 trigger system [18].

In the present scheme, the trigger and readout chains will be read simultaneously, differently from what is done in Phase-1. The trigger primitive generation might put some peculiar requirements on the processing resources of a future DT DTC, thus possibly requiring a customized sizing of the on-board FPGA processors. Nevertheless, the DT back-end layering fits well the architecture proposed by TriDAS, with bandwidth needs (we expect a typical subevent size of 130 kB) both to L1 and DAQ largely covered by the foreseen capabilities of the future DTC/DTH. This further supports the plan to rely on CMS common hardware in the DT USC infrastructure.

3.6 Cost, schedule, and institutional responsibilities

The estimates of the CORE costs of the DT upgrade are shown in Table 3.5. The costs are all converted to 2016 kCHF. The CORE costs include the production costs of all modules that are needed in the CMS experiment itself, plus any needed in test stands at CERN. Extra modules are included where production is expected to result in some fraction of modules that cannot be used for commissioning, but operational spares are not included in the CORE costs.

Although the full back-end requires 96 back-end boards, the responsibility for this part of the system is shared with the TriDAS project at an agreed fraction of 60/40 %. That is the reason why only 60 back-end boards are listed in the DT cost-book. Figure 3.25 (left) characterizes the

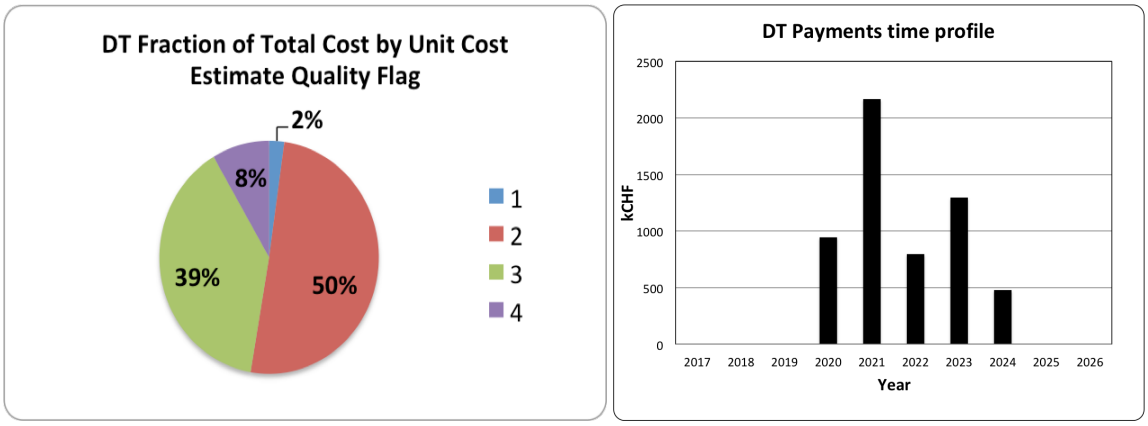

Figure 3.25: Left: Distribution of costs for the DT upgrade by cost estimate quality flag, as defined in the text. Right: Expected time profile for expenditures in the Phase-2 upgrade of the DTs expressed in 2016 kCHF.

quality of the cost estimation in terms of a flag assigned to each item: (1) is based on an vendor quote or catalog price, (2) is based on a recent similar part, (3) is based on an engineering conceptual design where sub-components are known, and (4) is based on a conceptual design or scaled from similar systems.

The schedule for prototyping, production, testing, and integration of the upgraded DT electronics is implemented and tracked with a MERLIN schedule that is common to all muon subsystems. The higher level summary tasks and some of the milestones are shown in Table 3.6 and Fig. 3.26, separated in pre-production (top) and production (bottom) by the Engineering Design Review (EDR) scheduled for summer 2020.

The DT Phase-2 upgrade schedule evolves from a design phase to a prototyping one, with the first OBDT demonstrator expected to be fully tested on a DT chamber early 2018. It will be followed by the production of the first OBDT prototype which will be used for validation during LS2 at the CMS detector. The front-end electronics mechanics and installation will be validated *in situ*. It is expected that one full DT sector of the CMS detector is instrumented with upgraded electronics during LS2 to allow evaluation of the readout and trigger algorithms performance with a extensive cosmics data taking campaign. The back-end electronics schedule follows a different time scale since it needs to accommodate to the different TriDAS project schedule and therefore, during LS2 the algorithms will be developed on testing platforms with presumably different form factor than the final system.

After LS2 validation, the project enters into a new phase with the EDR expected by mid 2020. This sets the start of the production that includes the final OBDT board fabrication and assembly submission, the mechanics and cabling manufacturing and the final MiC2 production. The MiC2 will be assembled on the different home institutes (expect roughly 3 assembly sites) and thorough quality tests are expected through adequate testing systems. The modules will be sent to CERN where final quality checks will be performed before installation on the detector. As mentioned above, the slow control and back-end electronics follows a slightly different timeline, but the full production is also expected to be completed early in LS3. The full DT electronics is expected to be ready for installation by April 2024, with a final installation targeted to start on September 2024, the date set by current TC LS3 schedule.

The resulting expected yearly expense profile is displayed in Fig. 3.25 (right). The 2021 and

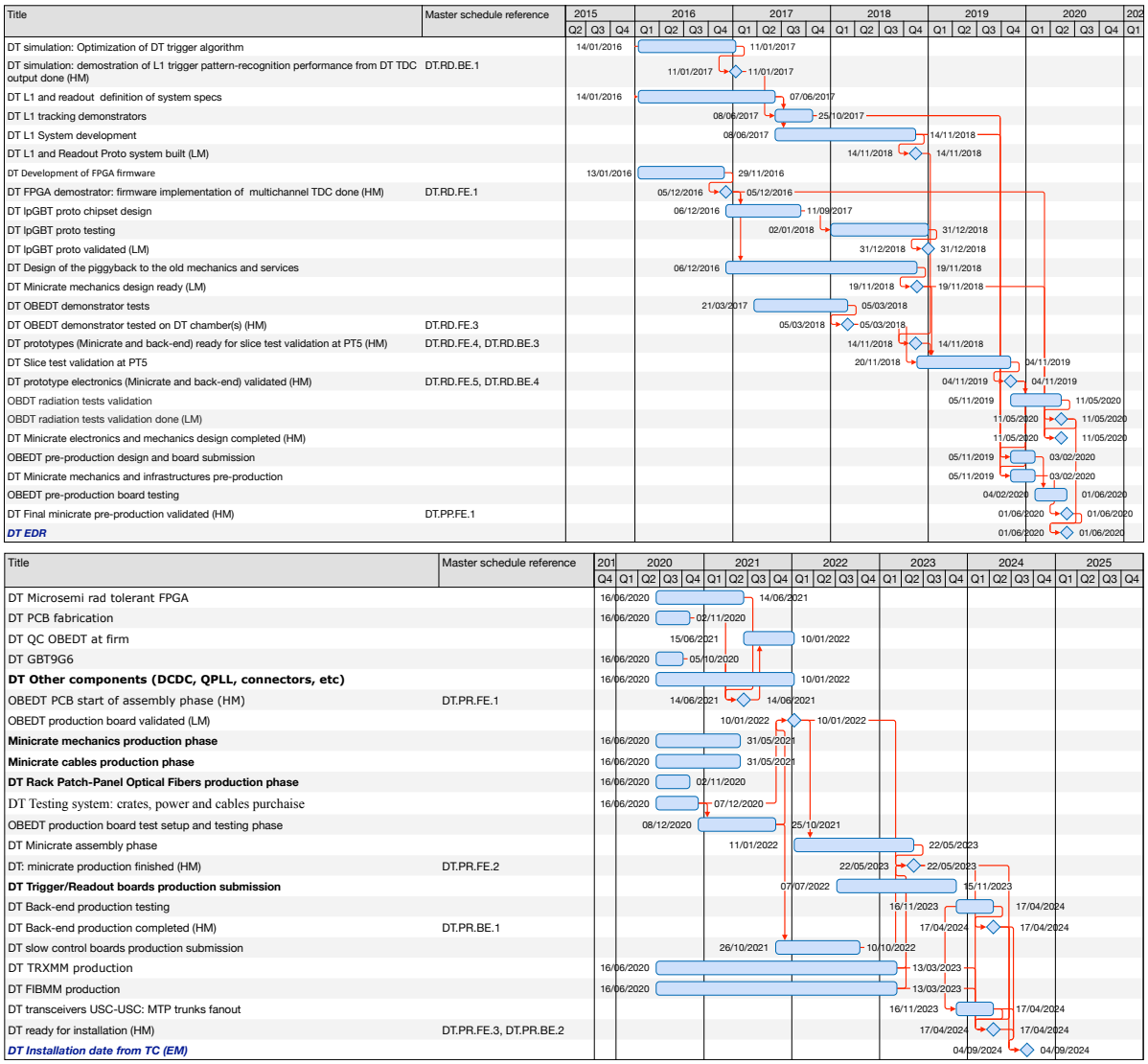

Figure 3.26: Pre-production (top) and production (bottom) schedule and milestones as extracted from MERLIN.

2023 peaks in the profile corresponds to the purchase of the bulk of the MiC2 and back-end system material, respectively.

The institutions that are expected to contribute to the DT upgrade are shown in Table 3.7. Most of them were already involved in the construction phase.

Table 3.6: High Level and External Milestones (HM and EM, respectively) for the DT upgrade.

	ID	Milestone title	Date
Design	DT.RD.FE.1	DT FPGA demonstrator: firmware implementation of multichannel TDC done (HM)	5.Dec.2016
	DT.RD.BE.1	DT simulation: demonstration of L1 trigger pattern-recognition performance from DT TDC output done (HM)	11.Jan.2017
	DT.RD.FE.2, DT.RD.BE.2	DT L1 and Readout System specification defined with demonstrator (HM)	7.Jun.2017
Prototyping	DT.RD.FE.3	OBDT demonstrator tested on DT chamber(s) (HM)	5.Mar.2018
	DT.RD.FE.4, DT.RD.BE.3	DT prototype ready for slice test validation at PT5 (HM)	14.Nov.2018
	DT.RD.FE.5, DT.RD.BE.4	DT prototype electronics (MiC2 and back-end) validated (HM)	4.Nov.2019
	DT EDR (EM)		1.Jun.2020
Production	DT.PP.FE.1	DT Final MiC2 pre-production validated (HM)	1.Jun.2020
	DT.PR.FE.1	OBDT PCB start of assembly phase (HM)	14.Jun.2021
	DT.PP.BE.1	DT Back-end pre-production system validated (HM)	6.Jul.2022
	DT.PR.FE.2	DT: MiC2 production ready (HM)	22.May.2023
	DT.PR.BE.1	DT Back-end production completed (HM)	17.Apr.2024
	DT.PR.FE.3, DT.PR.BE.2	DT ready for installation (HM)	17.Apr.2024

Table 3.7: Institutional responsibilities in DT upgrade.

Institute	Country	*Longevity*	*On-detector elec.*	*MiC2 mech.*	*Cabling &services*	*Slow Control*	*Back-end elec.*	*Installation &commiss.*
AACHEN-3A	Germany	x		x	x			x
ATOMKI DEBRECEN-IEP	Hungary		x					
BOLOGNA	Italy	x		x	x		x	x
TORINO	Italy	x	x		x	x	x	x
PADOVA	Italy	x	x			x	x	x
MADRID-CIEMAT MADRID-UNIV	Spain	x	x	x	x		x	x
OVIEDO	Spain	x					x	x

Chapter 4

CSC upgrades

4.1 Overview and motivation

The Cathode Strip Chamber (CSC) system, located in the endcap region of CMS, provides precise measurements of the position of points (hits) along the trajectories of muons in the high $|\eta|$ region ($0.9 < |\eta| < 2.4$). The CSC technology was chosen to instrument the CMS endcaps because it provides good position and time resolution, good performance in large and nonuniform magnetic fields, and the ability to handle high particle rates. A general overview of the CSC system is presented in Section 4.2.

As described in Section 4.3, CSC modules have been irradiated up to three times the nominal radiation dose corresponding to 10 years of HL-LHC data taking. These tests have shown that the performance of the detector itself is not expected to be a problem for Phase 2. However, various components of the electronic readout system do present limitations that would lead to unacceptable data losses at high values of the pseudorapidity. Specifically, the longer latency requirements in Phase 2 would fill up and overflow the storage pipelines of the front-end boards in some CSC stations. Additionally, the higher L1 trigger rates and occupancy would overwhelm the output bandwidth of the various data acquisition boards. These limitations are described in Section 4.4, together with the various upgrades that will be performed to preserve the performance of the CSC system under HL-LHC running conditions. Finally, the installation of the upgrades, institutional responsibilities and costs are detailed in Sections 4.5 and 4.6.

4.2 The CSC system

Figure 1.4 shows the geometry of the CSC system. A total of 540 trapezoidal CSC modules, placed between the iron disks, are arranged into four disks (stations). The first station, closest to the interaction point, is further segmented into three rings (ME1/1, ME1/2, and ME1/3), while stations 2 through 4 are separated into just two rings. The rings closer to the beamline (ME1/1, ME2/1, ME3/1, and ME4/1, or ME1234/1 for short) are subject to the highest particle rates. They are referred to as inner rings, while all the others are referred to as outer rings. Each of the chambers in the ME1/1 ring is further subdivided into two parts with separate readouts: ME1/1a, covering the $2.1 < |\eta| < 2.4$ range, and ME1/1b, extending from $|\eta| = 1.6$ to $|\eta| = 2.1$.

As illustrated in Fig. 4.1, all but the ME1/3 chambers overlap in ϕ and thus form seamless rings. The spaces between the chambers are not projective, and thus the coverage, defined as at least three chambers on a muon path, is close to 100% in the $1.1 < |\eta| < 2.4$ region. The $0.9 < |\eta| < 1.1$ region is covered by a combination of DT and CSC modules (overlap region), which also provide at least three position measurements along all possible muon paths

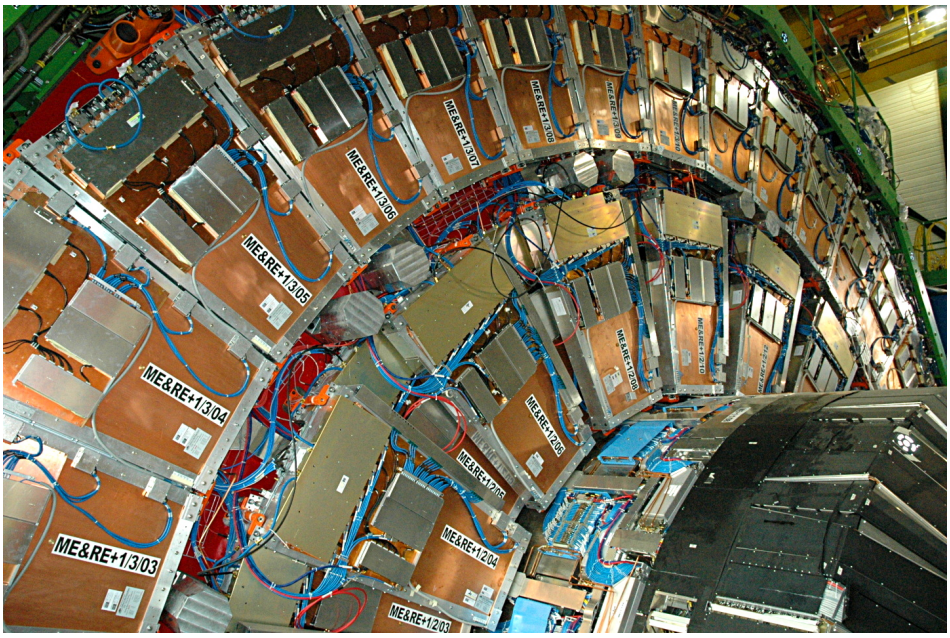

Figure 4.1: View of the CSCs installed in the ME2/1 and ME3/1 rings of the positive z endcap. The chambers in ME2/1 are alternatingly arranged at two different values in z, thus forming a seamless ring that covers all values of ϕ. All the chambers in ME3/1 lie on the same value of z, which leads to small uncovered gaps in between contiguous chambers.

in that area. Moreover, the four layers of RPCs arranged in between CSCs provide additional muon hits at the trigger level in the $0.9 < |\eta| < 1.9$ region, and the planned extension of the RPC layers and addition of GEM detectors will further extend the enhanced coverage to the $1.9 < |\eta| < 2.4$ region. The high redundancy of the muon system is a central feature of the design and is responsible for the robustness of the muon triggering and reconstruction in CMS.

Each CSC module consists of six gas layers, each layer having a plane of radial cathode strips and a plane of anode wires running perpendicular to the strips (Fig. 1.6). In total, there are 210 816 anode channels and 273 024 precision cathode channels. Hits in four layers out of a maximum of six are presently required to generate a trigger primitive or a particle stub. The spatial resolution from each chamber is typically 100 μm. A precision momentum measurement is achieved by fitting the position of successive hits in successive chambers. The signal on the wires has a fast rise time (with a time resolution of about 3 ns achieved offline) and is used in the level-1 accept (L1A) time determination, as well as providing a coarse position determination along the radial direction (1–5 cm).

Figure 4.2 shows a schematic of the different components in the CSC readout system. As explained below, the readout system of the ME1/1 chambers differs from that of the other chambers because it was upgraded during LS1. As a result, most of the ME1/1 boards are expected to be able to handle the requirements under HL-LHC running conditions.

The names and basic functions of the electronic modules on non-ME1/1 chambers are:

- **AFEB (Anode Front-End Board)**: amplifies signals from the anode wires and sends hits to the ALCT. There are 18–42 AFEBs per CSC.
- **ALCT (Anode Local Charged Track board)**: finds patterns among the six-layer anode hits sent by the AFEBs consistent with muon stubs, and sends the two with the most layer hits to the TMB. Upon receiving an L1A, it sends all wire hits and reconstructed local charged tracks to the DMB.

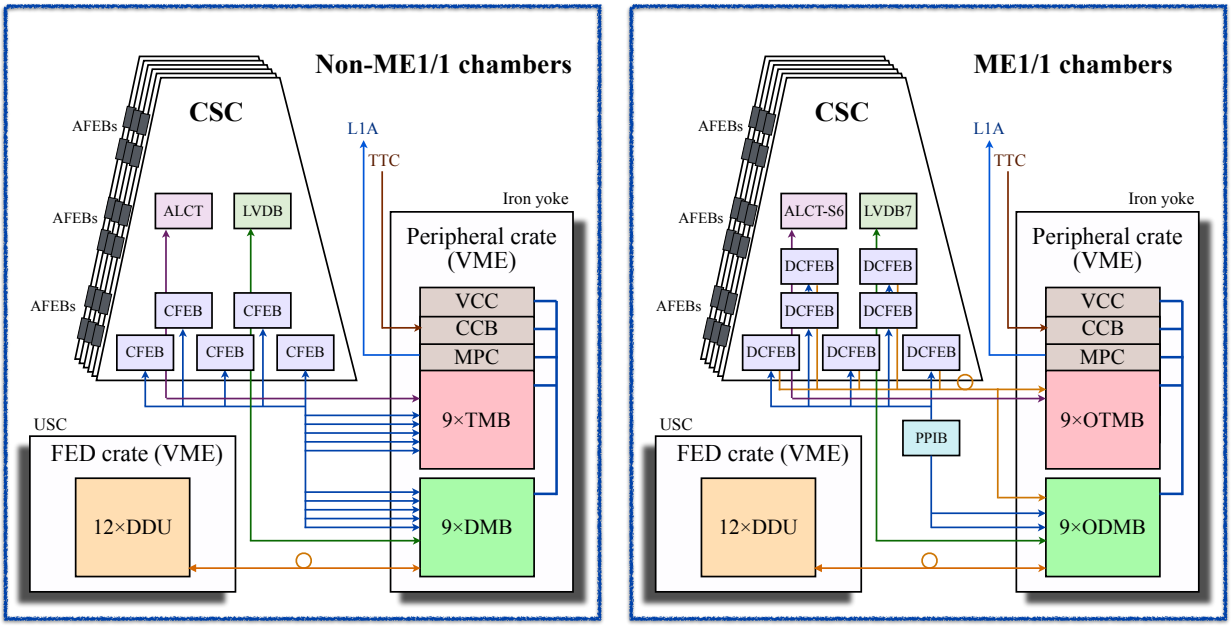

Figure 4.2: Schematic of the current CSC electronic readout system in the non-ME1/1 (left) and ME1/1 (right) chambers. The peripheral crates are shared among the ME1/1 and non-ME1/1 rings, so the TMBs/DMBs and the OTMBs/ODMBs are mixed together in some of those crates.

- **CFEB (Cathode Front-End Board)**: amplifies signals from the cathode strips, sends fast trigger information to the TMB, and, upon receiving an L1A, digitizes the strip signal waveforms and sends them to the DMB. There are typically 5 CFEBs per CSC.
- **LVDB (Low Voltage Distribution Board)**: distributes the low voltage power at the appropriate voltage levels to the on-chamber boards.

The on-chamber electronics are read out by boards situated in VME crates mounted on the edge of the endcap iron yoke (peripheral crates). In non-ME1/1 chambers, these boards are:

- **TMB (Trigger MotherBoard)**: builds cathode hit patterns and finds coincidences with anode hit patterns to form local charged track primitives (LCTs). It sends up to two LCTs to the MPC (trigger path) and, upon receiving an L1A, to the DMB.
- **DMB (Data acquisition MotherBoard)**: upon arrival of an L1A, it collects anode, cathode, and trigger information and sends it to the DDU. It also controls the CFEBs on a chamber.
- **MPC (Muon Port Card)**: collects LCTs from each of up to nine TMBs in a trigger sector, and sends them to the muon track finder system. There is one MPC per peripheral crate.
- **CCB (Clock and Control Board)**: provides the interface of the CSC system with the Trigger, Timing and Control (TTC) system of CMS. It distributes necessary signals for synchronized operation of a peripheral crate.
- **VCC (VME Crate Controller)**: receives VME commands from the control room and distributes them to the other boards in the peripheral crate via the backplane.

Finally, all the CSC data are collected by VME boards situated in the front-end driver crates (FED boards) located in the underground service cavern (USC):

- **DDU (Detector-Dependent Unit)**: upon arrival of L1A, collects data from all 15

DMBs in a CSC sector, corresponding to 30 or 60 degree ϕ slices of each endcap, and sends the information through the global DAQ path.

The readout system of ME1/1 chambers was the same as that in non-ME1/1 chambers up to the LHC Long Shutdown 1 (LS1) that occurred during 2013–2014. At that time, CSCs for the ME4/2 ring, part of the original design but descoped because of budget concerns, were constructed and installed. Since the ME4/2 installation required building new electronic boards, it was natural to move most of the ME1/1 electronics to ME4/2 and upgrade the ME1/1 readout system with new technology. This allowed us to reduce trigger rates in the high $|\eta|$ region by removing the ganging of channels in the readout of cathode strips, thus reducing the number of ghost tracks, as well as to increase the output bandwidth of CFEBs to handle the data rates expected at the HL-LHC.

The new electronics installed in the ME1/1 chambers during LS1 have functioned successfully. The various upgrades needed to maintain the performance of the CSC system at the HL-LHC follow in large measure the design already in place in the boards instrumenting the ME1/1 CSCs. Section 4.4 describes the new boards and upgrades in detail, but the main characteristics of the ME1/1 boards upgraded during LS1 are described below for reference:

- **DCFEB (Digital Cathode Front-End Board)**: upgrade of the CFEB with flash ADCs, a digital pipeline, and a 3.2 Gb/s optical output link. There are 7 DCFEBs per ME1/1 chamber.
- **ALCT-S6 (Anode Local Charged Track Spartan 6 board)**: upgrade of the old ALCT with a mezzanine based on more powerful FPGA (Xilinx Spartan 6) to reduce dead time. These were installed as well in the ME4/2 chambers during LS1 to reduce dead time.
- **LVDB7 (Low-Voltage Distribution Board)**: upgrade of the LVDB with connections to 7 DCFEBs and updated voltage levels.
- **ODMB (Optical Data acquisition MotherBoard)**: upgrade of the DMB with optical links that receive the DCFEB data.
- **PPIB (Patch-Panel Interconnecting Board)**: on-chamber patch panel that repeats the signals that are common to all DCFEBs (e.g. L1A, clock, JTAG). It is required due to constraints with front-panel space on the ODMB.
- **OTMB (Optical Trigger MotherBoard)**: upgrade of the TMB with optical links that receive trigger data from the DCFEBs and a more powerful FPGA that can handle more trigger primitives.

The present high voltage (HV) system for the CSCs comprises two independent subsystems: a subsystem providing HV to the non-ME1/1 chambers (11 016 channels) made by the University of Florida (UF) and the Petersburg Nuclear Physics Institute (PNPI) [67], and a commercial CAEN subsystem covering the ME1/1 chambers (432 channels) [68]. The voltage can be individually regulated in all channels and the currents are continuously monitored.

The custom UF/PNPI subsystem has a three-tier structure. There are 8 commercial Matsusada primary HV supplies that can provide a maximum voltage of up to 5000 V and a maximum current of 60 mA. These supplies provide HV power to 50 master boards, each of which has 8 regulated outputs with each providing a maximum current of 1.5 mA. Both the primary HV supplies and crates with master boards are located in USC. The master board outputs are routed to distribution boards located near CSCs (on the periphery of the endcap disks). There are two types of distribution boards: 216 thirty-channel boards that serve ME2/2, ME3/2, and ME4/2 chambers (one chamber per board); and 126 thirty-six-channel boards that serve

ME2/1, ME3/1, ME4/1, ME1/2, and ME1/3 chambers (two chambers per board). The total current on the outputs of each distribution board is limited by the master board outputs to be 1.5 mA, while the maximum current for each channel is 100 μA. The resolution of the current measurements in individual channels is 100 nA.

The commercial CAEN subsystem is of much smaller scope; it has sixteen 28-channel HV boards (CAEN 1733BP) housed in USC. Each channel can provide a maximum voltage of up to 4000 V and a maximum current of 2 mA. Even though the nominal resolution of current measurements in individual channels is 200 nA, the experience of operating the system at the LHC shows significant noise in the current measurements (see Section 4.4.1.3).

4.3 Longevity

As discussed in Chapter 2, the performance of both the CSCs and the readout electronics can degrade after being exposed to large doses of radiation. These doses are largest in the innermost parts of the ME1/1 chambers, as shown in Figs. 2.3, 2.4, and 2.7, and decrease with increasing distance from the beam line and from the interaction point. Table 4.1 summarizes the expected radiation doses at the HL-LHC in terms of both accumulated charge in the chambers and total irradiation dose (TID). The TIDs for the peripheral crates, situated on the periphery of the detector, are between 0.2 and 0.8 kRad.

Table 4.1: Summary of the expected radiation doses in the four CSC stations after 10 years of running at HL-LHC conditions. The accumulated charge is estimated from measurements performed during Run 1 running for the areas on the chambers subject to the highest level of radiation. The irradiation doses are estimated by FLUKA simulations of the HL-LHC normalized to the expected integrated luminosity, 3000 fb^{-1}, and taking into account the placement of the electronics on the chamber (specifically, the placement of the PROMs). The dose for ME1/1 corresponds to ME1/1a. The dose for ME1/1b is 3.0 kRad. The accumulated charge of ME1/1 is smaller than that of ME2/1, despite having higher radiation dose, because of the higher density of wires in ME1/1 chambers.

	ME1/1	ME2/1	ME3/1	ME4/1
Accumulated charge [mC/cm]	110	80	76	76
TID for DCFEBs [kRad]	10.2	0.6	0.8	1.3
TID for ALCTs [kRad]	6.5	1.8	2.0	3.4

This section describes the longevity of the CSC system under these conditions. Section 4.3.1 details past and present studies of the aging of the CSCs under the current mode of operation. Section 4.3.2 presents ongoing R&D efforts to find an alternative gas mixture with less greenhouse impact. Finally, Section 4.3.3 discusses the expected performance of the readout electronics under HL-LHC running conditions.

4.3.1 Chamber aging

The aging of CMS CSCs was first studied in 1997 by irradiating two wires of a small chamber prototype with a strong beta ray source [19]. This chamber was flushed with the current gas mixture, Ar+CO_2+CF_4 = 40%+50%+10%. After an accumulation of 2000 mC/cm, ten times more than the charge expected after 10 years of HL-LHC operation, neither gas gain nor dark current were affected.

More detailed studies were performed on two full-size chambers of ME2/1 type, also flushed with the current gas mixture. These chambers were tested at the Gamma Irradiation Facility

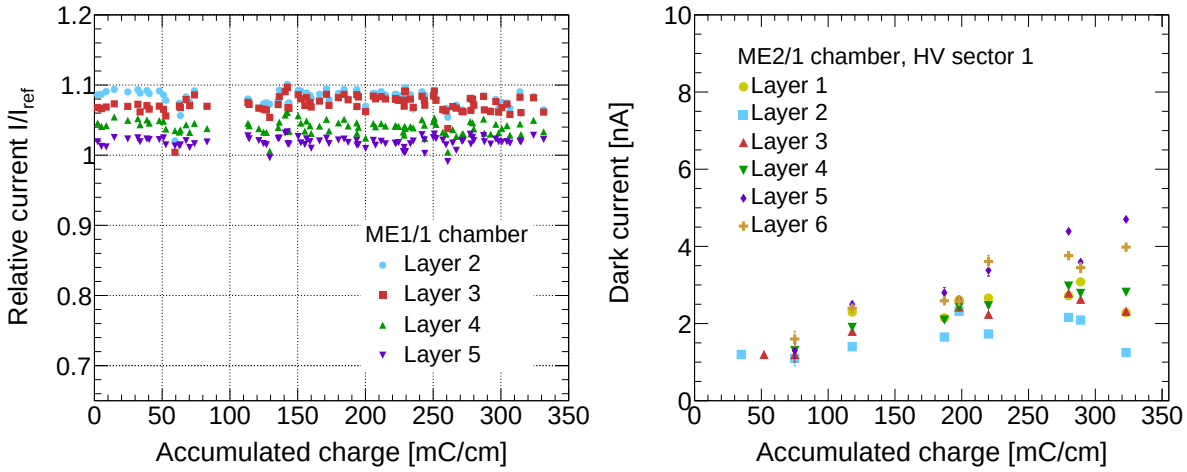

Figure 4.3: Left: relative currents normalized to the average of the first and sixth non-irradiated planes, $I_{\text{ref}} = (I_1 + I_6)/2$, as a function of the total accumulated charge for an ME1/1 CSC. Right: Leakage current (dark current) as a function of the accumulated total charge in Sector 1 of the ME2/1 CSC being tested at GIF++.

(GIF) [26] at CERN during 2000 and 2001. A total charge of 300–400 mC/cm was accumulated, and the only consistent signs of aging were a small increase in dark current of about 8 nA per wire plane and a decrease of strip-to-strip resistance from 1000 GΩ to 10–100 GΩ, neither of which is consequential. No significant changes in gas gain, chamber efficiency, and wire signal noise were observed for either of the two chambers.

These tests did not include ME1/1 chambers. The study of the longevity of this type of chamber is important, however, because the ME1/1 CSCs are subject to the highest radiation levels of all CSCs and their design presents significant differences with respect to that of other stations. These differences include thinner wires, smaller gas gaps, materials from different vendors, and others.

In preparation for the HL-LHC, tests with higher safety factors were carried out on two chambers of ME1/1 and ME2/1 types at the new GIF++ facility [25]. Between 2016 and 2017, a total of 330 and 340 mC/cm were accumulated on the ME1/1 and ME2/1 chambers, respectively, thus providing a safety factor of more than 3 with respect to 10 years of HL-LHC operations. The two chambers, equipped with the full chain of strip and anode wire readout electronics, were set up and commissioned at GIF++ in 2015. These chambers are being flushed with the current gas mixture, Ar+CO_2+CF_4 (40%+50%+10%), which reproduces closely the system used in CMS, including the gas recirculation scheme.

The key operating parameters of these chambers are being closely monitored as a function of the accumulated charge. Figure 4.3 shows that the relative gas gain, with respect to reference layers that are turned off during data taking, has so far remained stable, while the dark current has increased by a negligible 3 nA. The dark current rates shown in Fig. 4.4 have remained stable for most layers, even though two isolated wire groups in the ME1/1 chamber started showing some aging effects after about 100 mC/cm. Despite some deterioration, the performance of the overall detectors after an accumulated charge equivalent to more than 10 years of HL-LHC running remains very satisfactory.

Additionally, in situ measurements of the gas gain in the CSCs will allow us to detect early signs of aging in individual chambers and in the entire system. The early detection of the aging

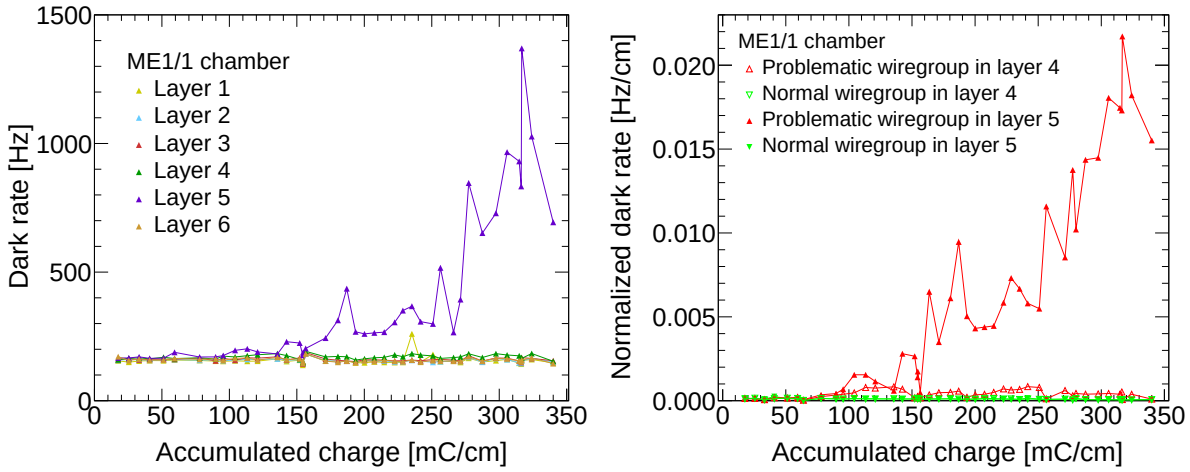

Figure 4.4: Spurious signal rates or dark rates for the different layers (left) and the two problematic wire groups (right) of the ME1/1 CSC being tested at GIF++.

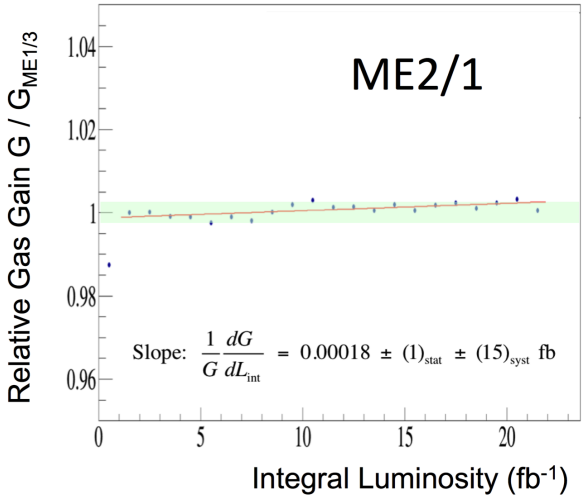

Figure 4.5: Average gas gain in ME2/1 chambers normalized to that in ME1/3 as a function of integrated luminosity. The systematic uncertainty in the slope is assessed from the range of small wiggles, indicated by the shaded area ($\pm$0.3%).

onset naturally provides time for developing corrective actions. These types of measurements have been conducted periodically since the LHC started running in 2008. Figure 4.5 illustrates the results of such an analysis with Run 1 data by showing the average gas gain in all ME2/1 chambers, normalized to the average gas gain in the ME1/3 chambers. The ME1/3 chambers see the least amount of background and thus are used as a reference. Many systematic uncertainties in gas gain stability measurements cancel nearly perfectly in such normalized gas gains. Among these systematic effects are variations in atmospheric pressure, gas mixture composition, etc. One can see from Fig. 4.5 that the gas gain in ME2/1 chambers remained stable within $\pm$0.3% over the duration of Run 1. The origin of small long-period wiggles at the level of $\pm$0.3% is being investigated. Results for the other chamber types are very similar. Using the Run 1 results, one can reliably project that the gas gain of CSCs after 300 fb^{-1} is not expected to deviate from the present gain by more than $\pm$5%. As we collect more data, the precision of the long term projections will improve. By the end of Run 2, the projections will become accurate enough to project to 3000 fb^{-1}.

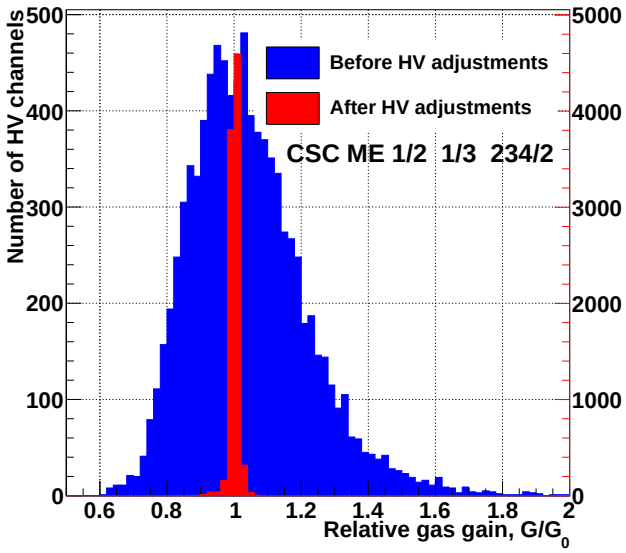

Figure 4.6: Gas gain distribution in CSCs before and after the gas gain equalization campaign in 2016.

In addition to the aggregate results shown in Fig. 4.5, analyses of the local gas gain in planes of individual chambers, as well as subsets of planes, are performed to detect local gas gain drifts. In fact, the Run 1 analysis did reveal a few chambers with drifting gas gains. After further investigation, it was found that CSC aging was not causing the observed gas gain changes; rather the gas gain was decreasing due to a drift in the high voltage that was not detected by the voltage monitoring circuits.

The following refinement of the CSC gas gains can also be used to help extend the longevity of the CSC system. Until 2016 the CSCs operated at a common high voltage that resulted in a large variation of the gas gains as shown by the blue histogram in Fig. 4.6. These gas gain variations arise from gas gap thickness non-uniformity in different parts of the chambers. The largest chambers have areas of 3.3×1.5 m^2 and keeping the panel flatness to a specification much tighter than ± 200 μm would have been too costly. Gas gap changes at the level of ± 200 μm are expected to result in a factor of two gas gain variations, which is what we observe. However, the operational range of the CMS CSCs is large enough that at the nominal HV the areas of the chambers with small gas gains operate at full efficiency, while the areas with large gas gains still operate reliably without producing signal afterpulsing or spurious signals. Nevertheless, the latter CSC areas clearly operate at too large a gas gain, which results in a decreased longevity. To reduce these effects, in 2016 the individual HV channels serving various areas of the CSCs were adjusted to produce a more uniform gain. After these HV adjustments the gas gain has become much more uniform as shown in the red histogram in Fig. 4.6. The next step will be to reduce the HV in all channels by about 50 V, which will decrease the gas gain by about 25%. The chambers will then operate uniformly just above the knee of the efficiency plateau and hence remain fully efficient, while the CSC system lifetime would be extended by about the same 25%.

4.3.2 R&D on gas mixture alternatives

It is expected that more restrictive EU regulation of greenhouse gases will severely restrict or ban the use of CF_4, a gas with a 100-year Global Warming Potential (GWP) 6500 times larger

than that of CO_2 (see Section 2.3). This gas, which currently makes up 10% of the CSC gas mixture, plays a critical role in the longevity of CSCs by etching away various harmful deposits on the anode wires. As an example, a test in 2001 on a prototype CSC operated without CF_4 showed a gas gain drop at an unacceptable rate of 20% per 100 mC/cm [51]. Moreover, CF_4 also helps to increase the electron drift velocity (important for unambiguous muon track bunch crossing tagging) and, being a quenching gas, makes the operation of CSCs more stable.

An R&D program to find a more eco-friendly substitute for CF_4 without compromising the longevity and performance of the CSCs has been started. Small CSC prototypes, approximately 30 cm $\times$ 30 cm, have been built at PNPI and at CERN. Aging tests have been performed on the PNPI prototype by irradiating it with a ^{90}Sr source for the nominal 10% CF_4-based gas mixture as a reference. After a total charge of 1360 mC/cm was accumulated on the prototype, the results were in agreement with previous studies; namely, the gas gain remained stable throughout the duration of the full test and aging of the cathode surface corresponding with the irradiation area was observed, causing higher dark current and an increase of the inter-strip conductivity.

Tests have been performed at PNPI with an Ar-CO_2 mixture plus different percentages of CF_3I: 1%, 5%, and 10%. CF_3I was chosen because of its low GWP (1–5) and for the Si and SiO_2 deposits etching properties, which are among the harmful wire deposits contributing to aging. Present results indicate that this gas is not suitable for CSC operation given its high electronegative properties. Besides continuing the investigation with smaller percentages of CF_3I (0.1%) (and addition of methane to extend the operation plateau), CSC operation with other gases with small GWPs will be explored: C_4F_6, IC_3F_6, C_3F_8, CHF_3. If a substitute gas is found, larger size chambers will be prepared for tests at GIF++ in 2018. Collecting the full exposure with detailed CSC performance monitoring will follow in 2019 and 2020 using full-size spare CSCs.

Finally, in addition to testing with low GWP gas mixtures, we plan to operate the small CSCs with increasingly lower percentages of CF_4 (5%, 2%, and 1%) in order to determine the end point of efficient CSC operation.

Should the outlined R&D program reveal no acceptable substitutes for CF_4, a two-fold mitigation strategy would be adopted. Firstly, the performance of the CF_4 recuperation and reinjection system at CMS would be maximized from the present 40% to at least 70% efficiency. Secondly, CMS would consider adopting a system for point-of-use abatement of exhaust streams, thus effectively eliminating the risk of pollution. Commercial abatement systems have shown excellent efficiency ($>$96%) in decomposing CF_4 and other high GWP gases [69].

4.3.3 Electronics radiation hardness and performance at the HL-LHC

A program of radiation testing was carried out to identify electronic components that are sufficiently robust to function reliably in the radiation environment of the endcap muon system. Before the production of new electronics boards for the ME1/1 upgrade, radiation tests were carried out at the Texas A&M cyclotron and nuclear reactor [46], as well as at the UC Davis cyclotron. As discussed in Section 2.4, single event upsets (SEUs) and single event latchups (SELs) are important concerns for digital components. In the CMS environment, the main contributors to SEUs and SELs are expected to be neutrons with energies above 20 MeV. Protons from cyclotrons can be used as a surrogate for these neutrons. During the tests at the Texas A&M cyclotron, the digital components on the test boards were operated with active data readout while being irradiated with 55 MeV protons. The components tested for SEUs and SELs included the FPGAs (Xilinx Virtex-6), the PROMs (Xilinx XCF128X and XCF32P), level adapters, and optical transmitters and receivers (Finisar and Reflex Photonics). In reactor tests, compo-

Table 4.2: Failure scenarios for the different components of the CSC system during 10 years of HL-LHC running. The number of failed components is given as an average over the 10 years. The "Total system" column indicates the total number of components of a given type in the CSC system.

Component loss	Impact	Failure scenario			Total system
		Optimistic	Realistic	Pessimistic	
DCFEB	1/7 or 1/5 of chamber	6	22	24	1044
CFEB	1/5 or 1/4 of chamber	37	40	46	1728
ALCT	Whole chamber	2	4	6	540
LVDB	Whole chamber	2	4	6	540
HV ME1/1 plane	Chamber layer	7	7	14	432
HV ME234/1 segment	1/5 of chamber layer	2	4	9	3240
HV outer ring segment	1/5 of chamber layer	2	4	8	6480

nents were exposed to neutrons with energies up to a few MeV with exposures equivalent to a TID of 30 kRad. This corresponds to levels of neutron radiation equivalent to about 50 years of that expected at the HL-LHC at the inner portion of the ME1/1 chambers, where the CSC electronics are exposed to the highest radiation flux. These tests targeted mostly non-digital components such as voltage regulators and power diodes. The results show that the components selected for the new electronics will operate reliably in the CMS radiation environment at the HL-LHC.

New radiation testing was initiated for the upgrades described here. Particular attention was paid to PROMs, which are known to have some failures after large radiation exposure [70]. The Xilinx XCF128X and XCF32P PROMs were tested at the CHARM II mixed radiation facility at CERN, the Texas A&M reactor, and the UC Davis cyclotron. The PROMs tested performed well up to an exposure of 10 kRad, but both types of PROMs showed some failures at 15–30 kRad. Since the optical receivers used in the OTMBs for ME1/1 have become obsolete, candidate optical receivers were also tested at the UC Davis cyclotron.

The combination of high gamma rates provided by the GIF++ gamma source and a muon beam periodically provided by the SPS offers a unique opportunity to study not only the longevity of the CSC system and their electronics but also their performance in an HL-LHC-like environment. The CSCs set up at GIF++ have the same chain of trigger and data acquisition electronics as the CSCs installed in CMS. Initial tests have already shown a decrease of the LCT reconstruction efficiency for the HL-LHC instantaneous luminosity of about 1% and 5% for ME1/1 and ME2/1 chambers, respectively, and a degradation of the position resolution of 20–50%. Throughout the next three years, in parallel with the aging tests, studies will be carried out to assess the performance and robustness of CSC operation in this environment. The program will include the overall tests of hardware (including a number of new electronic boards like DCFEB, OTMB, ODMB, etc.), various tunings of electronic firmware, and optimization of muon track segment reconstruction software.

4.3.4 Aging scenarios

As described above, the performance of the CSCs and their readout electronics is not expected to suffer any significant degradation at the radiation levels of the HL-LHC, except for some increase in the level of noise and a manageable deterioration in the position resolution and the hit reconstruction efficiency. Based on the experience of Run 1, however, we do expect occasional failures of a number of components in the CSC system due to the wear and tear as a result of standard operation.

Table 4.2 shows the expected failure scenarios for the CSC system running under HL-LHC conditions based on the experience accumulated during the Run 1 (2009–2012) and Run 2 (2015–2016) data taking periods. The time dependence of the number of failed components is assumed to be linear and to follow the failure rate during Run 2 of the most critical components. The extrapolation procedure also takes into account the replacement of the ME234/1 chamber electronics during LS2 and all chambers on YE1 disks being repaired during LS3. The number of failed components is given as an average over the 10 years of HL-LHC running. The optimistic scenario assumes that the problem components can be fully fixed or replaced during each technical stop. The realistic scenario assumes the replacement can only happen during long shutdowns, and in the pessimistic scenario no component is fixed or replaced for the duration of HL-LHC running.

The impact of the pessimistic scenario has been implemented in the simulation, and the results presented in Chapters 7 and 8 include these effects.

4.4 New electronics

While the present CSCs are expected to provide adequate performance throughout the HL-LHC program, several components of the CSC readout electronics will need replacement. The limitations of the present system and requirements for the upgrade are presented in Section 4.4.1.

Table 4.3 summarizes the various upgrades that will be performed to preserve the performance of the CSC system under HL-LHC running conditions. In all cases except for the HV and FED upgrades, the design of the new boards is based to a large extent on the design of the boards employed in the ME1/1 upgrade deployed during LS1. The overall layout of the CSC readout system will remain similar to the schematic shown in Fig. 4.2 (right) except for new optical links connecting the relocated DCFEBs and ALCT-LX100/LX150T boards to the new ODMBs in ME2/1, ME3/1, and ME4/1 (see Fig. 1.11). Sections 4.4.2–4.4.8 discuss the technical details of each of the upgrades individually.

Some of the upgrades are scheduled for LS2 because the inner chambers in the ME2/1, ME3/1, and ME4/1 rings will not be accessible during LS3. The detailed installation schedule is discussed in Section 4.5.

4.4.1 Limitations of the present electronics

The combination of increased CSC occupancy plus larger L1 trigger rates and latency requirements in Phase 2 (Table 1.3) will cause the pipeline storage of the front-end electronics (CFEBs and ALCTs) in certain rings to fill up and lead to unacceptable dead time. The limitations of these boards together with detailed calculations of the event losses are presented in Section 4.4.1.1. Additionally, as a result of the higher CMS readout rates, the output bandwidth of the data acquisition boards (ODMBs and DDUs) will have to be expanded, as shown in Section 4.4.1.2. Finally, the increased occupancy in the chambers will necessitate the upgrade of the high voltage system, as described in Section 4.4.1.3.

4.4.1.1 On-chamber electronics

The CFEBs, currently used on all CSC rings except ME1/1, use analog charge storage based on custom switched-capacitor array (SCA) chips that sample at 50 ns intervals and contain a depth of 96 cells (6 events worth of data) during Level 1 trigger latency and 26 μs of charge digitization (Wilkinson ADCs). As we detail below, at the HL-LHC L1 latency of 12.5 μs and rate up to 500 kHz, the CFEBs in the 108 inner CSC chambers of ME2/1, ME3/1, and ME4/1

Table 4.3: Summary of the CSC electronics boards that will be upgraded during LS2 and LS3. Boards above the horizontal line are placed on-chamber, while those below the line occur in off-chamber crates. Of the 540 new DCFEBv2s, 504 will be installed in the ME1/1 chambers, while the rest plus the DCFEBs currently in ME1/1 will be installed in ME2/1. The ALCTs in stations 2, 3, and 4 will be upgraded during LS2 while those in station 1 will be upgraded in LS3. The ALCTs in ME1/3 do not need upgrading because they will be replaced with the ALCT-S6 currently installed in ME1/1.

Board	Num.	Where	When	Main reasons for upgrade
DCFEBv2	540	ME12/1	LS2	Latency, rate, rad-hard requirements
LVDB5	108	ME234/1	LS2	Power levels of DCFEBv2s
ALCT-LX100	288	ME1/1, ME123/2	LS2/LS3	Latency, rate, rad-hard requirements
ALCT-LX150T	108	ME234/1	LS2	Latency and rate requirements
OTMBv2	108	ME234/1	LS2	Receive optical link from DCFEBv2s
ODMB7	72	ME1/1	LS3	Increased DAQ output bandwidth
ODMB5	108	ME234/1	LS3	Increased DAQ output bandwidth
HV master	40	ME1234/1	LS3	Increased current due to higher occupancy
HV distribution	12	ME1234/1	LS3	Increased current due to higher occupancy
FED	14	USC	LS3	Increased data volume, number of links

will overwrite capacitor cells in the SCAs causing large readout inefficiency. The outer CSC chambers will not suffer from these problems because trigger rates in those rings are lower than those in the inner rings by factors of more than 3.

The CFEB event loss rates depend on the chamber preCLCT and L1A$\times$LCT rates. A preCLCT is a lower quality trigger primitive generated early from the rising edges of the slowly developing cathode signals. It does not have a requirement on the pattern of hits accross different layers so that any combination of hits in four layers will satisfy it. CLCTs on the other hand use the full shape of the cathode signals and require hits to form mostly-straight patterns. Thus, the preCLCT rate is more sensitive than the CLCT to gamma and neutron backgrounds, which are expected to be large at the HL-LHC. Upon receipt of preCLCTs, events are stored in the SCAs during the L1 latency time. These events are subsequently digitized when coincidences of L1As and full LCTs, called L1A$\times$LCT, are received. LCTs are combinations of full CLCTs and anode trigger signals.

TMB counters that keep track of the relevant CSC trigger rates are read out periodically during LHC running and stored to disk. Based on these counters, the preCLCT rates have been measured to scale linearly with luminosity during the 2015–2016 LHC running for a given chamber type. In contrast, the L1A$\times$LCT rates depend on Level 1 trigger tables. These tables control which event topologies are triggered and set their prescaling rates. They vary run to run when the luminosity is low and nonrestrictive triggers are turned on. At higher luminosities, the standard physics triggers dominate and the L1A$\times$LCT rate increases roughly linearly with luminosity.

The expected data losses at the HL-LHC can then be estimated by extrapolating the occupancy rates in the CSCs to the HL-LHC conditions and modeling the response of the SCA analog storage with a simple statistical model of a Poisson distribution coupled to a 5-event queue [71]. The preCLCT rates are scaled linearly with luminosity to the HL-LHC luminosity, 5×10^{34} cm^{-2}s^{-1}, and the L1A$\times$LCT rates are scaled linearly with luminosity, and again linearly with the L1A rate (from 100 kHz to 500 kHz). Figure 4.7 (left) shows the expected event losses due to SCA overwriting in the CFEBs based on this statistical model as a funtion of luminosity for the ME2/1, ME3/1, and ME4/1 chambers operating at the HL-LHC L1 rate and latency. Data losses increase dramatically as luminosity increases. For the HL-LHC luminos-

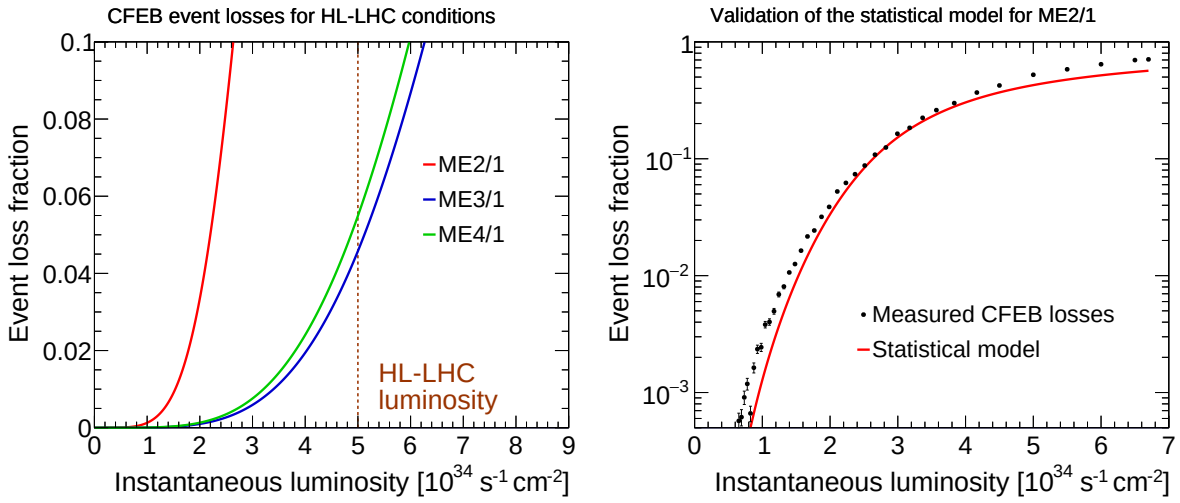

Figure 4.7: Left: event loss fraction as a function of instataneous luminosity. The dashed brown line indicates the design HL-LHC luminosity. Right: event loss rate measured in a CFEB under HL-LHC conditions for an ME2/1 chamber compared to the statistical model. Note that the y-axis scale is linear on the left and logarithmic on the right to show the agreement on the full range. The red curves on the left and right panels are the same.

ity of 5×10^{34} cm^{-2}s^{-1}, over 40% of the hits at ME2/1 and over 5% of the hits at ME3/1 and ME4/1 would be lost.

The statistical model described above was validated by measuring the actual CFEB overflow rates in December of 2015. Test triggers at the expected HL-HLC rates in ME2/1 were generated by an ODMB, and the CFEB was programmed with special firmware modified for the HL-LHC running conditions, namely 12.5 μs latency, a 3 bunch-crossing L1A$\times$LCT window, and event handling optimized for the 500 KHz L1 rate. Figure 4.7 (right) shows good agreement between our pulser tests and the statistical model for the whole luminosity range. It is important to note that these estimates are not conservative, as no HL-LHC rate uncertainty nor safety factors have been included in the calculations. Thus, the CFEBs in the inner CSC rings clearly need to be replaced.

Additionally, given the uncertainties associated with the TID values shown in Table 4.1, the radiation tests described in Section 4.3.3 indicate that the XCF128X and XCF32P PROMs employed in the DCFEBs and ALCT-S6s already installed in ME1/1 may not withstand the TID expected at the HL-LHC.

The problems outlined above can be overcome with selective replacement of CSC electronics. As detailed in Section 4.4.2, the SCA overwriting problem can be addressed by replacing the 540 CFEBs in ME2/1, ME3/1, ME4/1 with DCFEBs, together with the replacement of the 108 TMBs servicing those chambers by OTMBs. New DCFEBs are being designed with an option that will allow for the remote programming of their FPGAs. As described in Section 4.5, these new boards will be installed in the ME1/1 chambers, thus mitigating any risks associated with their longevity, and the DCFEBs currently in the ME1/1 ring will be moved to chambers in the ME234/1 rings, which are subject to much lower levels of radiation.

As it was the case with the CFEBs, some of the currently installed ALCTs will incur significant data losses at the HL-LHC running conditions due to a rather fundamental limitation with respect to the HL-LHC L1A latency. All the wire-hit data is stored in a pipeline within the

Table 4.4: Expected data rates for the CSC system at the HL-LHC and currently available output bandwidth for (D)CFEBs, ALCTs, and (O)DMBs (see Table 4.6 for the available bandwidth after the upgrade). "Util." refers to the total bandwidth utilization of the available output link. In the case of optical links, it includes the overhead used by the 8b/10b transmission encoding. The cathode strips in the ME1/1 chambers are divided into two segments, ME1/1a and ME1/1b. The ME1/1 DCFEB rate in the table corresponds to ME1/1a, the larger of the two. The (O)DMB data rate includes data from the (D)CFEBs, ALCT, and trigger.

	(D)CFEB			ALCT			(O)DMB		
Chamber	Rate [Gb/s]	Link [Gb/s]	Util. [%]	Rate [Gb/s]	Link [Gb/s]	Util. [%]	Rate [Gb/s]	Link [Gb/s]	Util. [%]
ME1/1	0.25	3.2	6	0.87	0.64	169	4.3	1.6	333
ME2/1	0.19	1.0	19	1.16	0.64	226	2.8	1.6	221
ME3/1	0.12	1.0	12	0.57	0.64	111	1.6	1.6	125
ME4/1	0.11	1.0	11	0.56	0.64	109	1.6	1.6	123
ME1/2	0.02	1.0	2	0.08	0.64	12	0.3	1.6	20
ME2/2	0.01	1.0	1	0.05	0.64	7	0.2	1.6	13
ME3/2	0.02	1.0	2	0.06	0.64	9	0.2	1.6	15
ME4/2	0.03	1.0	3	0.12	0.64	18	0.4	1.6	31
ME1/3	0.01	1.0	1	0.00	0.64	1	0.0	1.6	2

Virtex-E FPGA while the ALCT waits for an L1A. With the present latency of 3.6 μs, there is enough Block RAM (BRAM) available for this pipeline, but for the HL-LHC latency requirement of 12.5 μs there will not be enough BRAM resources to create a pipeline of sufficient depth. Therefore, all the old ALCT mezzanine boards (that is, those in all CSC rings except ME1/1 and ME4/2 which were upgraded during LS1) need to be replaced.

Additionally, the ALCT data readout for the inner rings will suffer from another limitation at HL-LHC rates. The existing boards transfer 16 time bins (25 nsec each) of data to the TMB board through copper Skewclear cables. For the HL-LHC running conditions, the bandwidth of the copper connection, 640 Mb/s, will not be enough to handle more than one time bin of data in the high-rate chambers (ME1/1, ME2/1, ME3/1, and ME4/1), as shown in Table 4.4. The solution to this limitation is relatively simple and inexpensive as the more powerful FPGAs employed in the ALCTs upgraded during LS1 can accommodate 3.2 Gb/s optical transceivers. By adding this transceiver to the mezzanine board, 16 time bins of wire data can be transferred at the HL-LHC rates, which allows the current performance to be comfortably maintained. The optical output of the upgraded ALCTs will be read by the new ODMBs when they are installed in LS3. Finally, the risks to the longevity of the XCF32P PROMs employed in the ME1/1 ALCTs will be avoided by the addition of an option to program their FPGAs remotely. The details of this upgrade are presented in Section 4.4.3.

4.4.1.2 Off-chamber electronics

The significant increase of the L1 rate at the HL-LHC presents additional challenges for the CSC readout system. The estimated total (D)CFEB data rates for each chamber under HL-LHC running conditions, based on the calculations described in Section 4.4.1.1, are shown in the first column of Table 4.4. For all CSC rings, the utilization of the output link (1 Gb/s Skewclear copper cables in the case of CFEBs and 3.2 Gb/s optical fibers in the case of DCFEBs) is less than 50%, which provides a safety factor of at least two. However, this is not the case for the (O)DMBs. These boards collect all the CSC information for each chamber and send it to the CSC FED system via a 1.6 Gb/s optical link. The (O)DMB data rates are estimated by adding up the

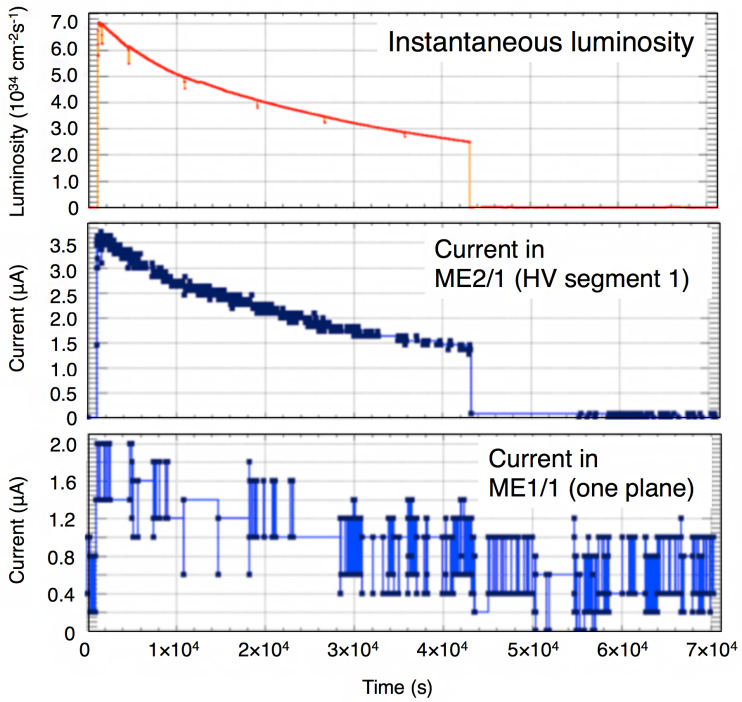

Figure 4.8: Top: Instantaneous luminosity versus time for one of the LHC fills in 2016. Middle: Current in an ME2/1 chamber (the HV segment closest to the beam) for the same run as measured with the custom UF/PNPI HV subsystem. Bottom: Current in an ME1/1 chamber (one plane) for the same run as measured with the CAEN HV subsystem.

total (D)CFEB data rate for each chamber, including an additional 20% covering the events where multiple (D)CFEBs are read, together with the anode and trigger data, which typically amount to 88% of the (D)CFEB data. These rates, shown in Table 4.4, significantly exceed the (O)DMB output bandwith in all the inner rings. This limitation would not only lead to large losses of data, but also to the DMBs going out of synch given that the external FIFO chips that buffer the CFEB data do not indicate how full they are. In principle, the creation of an output buffer in the Virtex-2 FPGA of the DMBs could theoretically fix this problem, but there are not enough resources left in the chip.

Thus, the DMBs on ME2/1, ME3/1, and ME4/1 as well the ODMBs in ME1/1 will need to be replaced with a new design based on the ODMB, but with faster output links (Section 4.4.5). The safety factors for the output bandwidth of the DMBs in the outer rings are all greater than three, so no upgrade is needed for these boards.

The CSC FED system, which collects the data from all the (O)DMBs and sends it to the CMS data acquisition system, will also need to be upgraded to handle the increased data volume and faster optical links, as well as to adapt the output to match the specifications of the upgraded central DAQ (Section 4.4.6).

4.4.1.3 High voltage system

The custom UF/PNPI subsystem needs to be upgraded because it does not have a sufficient margin to handle the current load expected at HL-LHC (5 times larger than the nominal LHC) with a comfortable safety factor. The experience so far has been that the currents in the CSCs scale linearly with the instantaneous luminosity (see the top and middle panels of Fig. 4.8).

Based on a linear extrapolation to HL-LHC conditions, the currents that are expected in a single ME2/1 chamber plane at 5×10^{34} cm^{-2}s^{-1} are as follows: $\sim$23 μA in HV segment 1, $\sim$9 μA in HV segment 2, and $\sim$5 μA in HV segment 3. The ME2/1, ME3/1, and ME4/1 chambers are closest to the beam and draw the largest currents. Therefore, one expects a total current of about 467 μA in a pair of ME2/1 chambers served by a single HV distribution board. The present limit of the HV distribution boards, set by the master HV boards, is 1.5 mA. This gives a safety factor of only three, which is uncomfortably small. Indeed, the background rates at the HL-LHC may prove to be larger than the linear extrapolation from LHC conditions. The gas gain is subject to $\pm$20% changes due to atmospheric pressure variations, and it is possible that we may want to increase the CSC gas gain by a factor of two at the HL-LHC if the electronics noise conditions become much worse (CSCs do allow for such an increase in the gas gain).

The CAEN subsystem serving ME1/1 chambers has marginal monitoring of currents (compare the middle and bottom panels of Fig. 4.8) and must be upgraded to provide more reliable current measurements. The present system fluctuations are $\mathcal{O}(1\ \mu\text{A})$ and do not provide a reliable detection of Malter currents [49], which have already been observed in ME1/1 chambers at the nominal LHC conditions and are expected to become a more frequent problem at the HL-LHC. The identification of chambers susceptible to Malter currents is critically important. Whenever Malter currents exist, they produce a rapid aging and are likely to destroy an entire CSC plane, as discussed in Chapter 2. Indeed, we expect a total accumulated charge per unit of wire length at the places with the highest background rates of the order of 110 mC/cm; however, a local Malter current of $\sim 1\ \mu$A (e.g., over 1 mm or 1 cm of wire) left not extinguished for 10^7 seconds per year over 10 years of HL-LHC operation would result in a local charge accumulation of 100 000–1 000 000 mC/cm, which is a factor of approximately a thousand times larger than the expected charge for normally operating CSCs at the highest pseudorapidity.

4.4.2 CFEB upgrade (DCFEBv2)

As Section 4.4.1.1 showed, the latency and rate requirements at the HL-LHC would lead to significant data losses in ME2/1, ME3/1, and ME4/1 due to events being overwritten in the CFEB analog storage (SCAs). Additionally, the PROMs of the DCFEBs currently in the ME1/1 chambers may not withstand the radiation doses expected at the HL-LHC. To solve these problems, all the inner rings will be outfitted with either DCFEBs, the cathode readout boards that were part of the ME1/1 upgrade installed during LS1, or DCFEBv2s, slightly modified DCFEBs that include a remote programming option for their FPGAs.

The DCFEBs incorporate the CFEB design features that will work without problems at the HL-LHC. The connection to the cathode strips and the spark protection of these inputs, the Buckeye amplifier and shaper ASICs, and the comparator ASICs are identical to those in the CFEBs. The key differences arise in the storage and digitization of the analog signals, and the transmission of the trigger and cathode data to the TMBs and DMBs.

As described in Section 4.2, the CFEBs store the cathode signals in the SCAs during the L1 latency and then digitize them upon receipt of an L1A$\times$LCT coincidence. In contrast, the DCFEBs employ fast flash hybrid 12-bit ADCs that continuously digitize the cathode signals at 20 MHz. The digitized signals are then fed into a Xilinx Virtex-6 FPGA that stores the data in a pipeline during the L1A latency. The data are trasmitted to an ODMB via a 3.2 Gb/s optical link if an L1A$\times$LCT coincidence is received within the L1A latency. If not, the pipeline storage is erased and reused. A different 3.2 Gb/s optical link transmits the fast hit information generated by the comparator ASICs to the OTMB.

Given the continuous digitization of the cathode signals, and the possibility of storing more

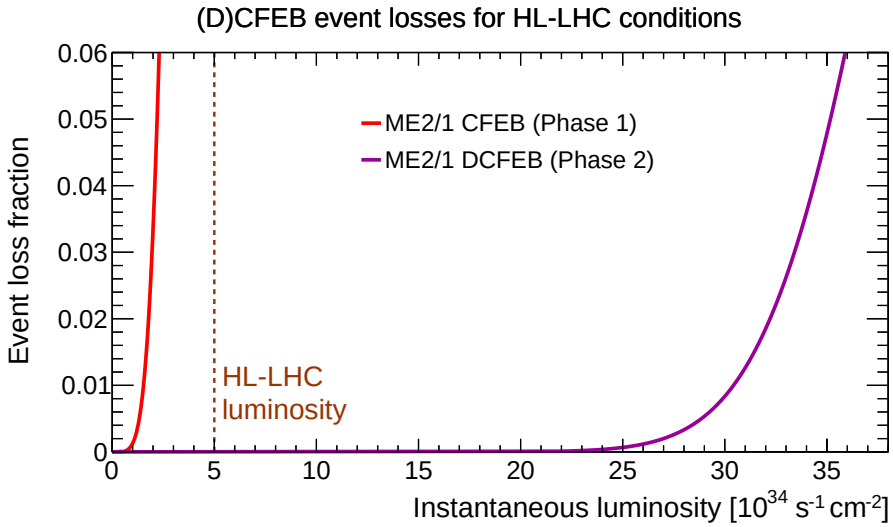

Figure 4.9: Comparison of the data losses as a function of the instataneous luminosity for an ME2/1 chamber outfitted with CFEBs and DCFEBs. The dashed brown line indicates the design HL-LHC luminosity. The losses in the CFEBs are due to event overwriting in the SCAs while for the DCFEBs are due to the 3.2 Gb/s output link.

than 700 events in the digital memory banks inside the Virtex-6 FPGA, the DCFEBs read out the cathode data with virtually no dead time for latencies much longer than that at the HL-LHC. The output rate is limited only by the 3.2 Gb/s optical output bandwidth. Figure 4.9 compares the event losses as a function of luminosity for an ME2/1 chamber outfitted with CFEBs and DCFEBs. The DCFEBs are capable of handling instantaneous luminosities more than ten times higher than the CFEBs.

Figure 4.10 shows a picture of one of the DCFEBs produced for the ME1/1 upgrade. Only minor modifications with respect to the LS1 DCFEB design are expected for the new DCFEBv2s being developed for installation during LS2. The performance of the two optical transceivers that provide the 3.2 Gb/s links to the OTMB and ODMB has been sometimes unreliable, largely due to SEUs. While software and firmware updates have now greatly reduced this problem, in the DCFEBv2s these transceivers will be replaced by the VTTx, a radiation-hard twin transmitter designed by CERN. The third optical transceiver in the LS1 DCFEBs, originally included to allow for the possibility of optical transmission of TTC, is currently unused and will be removed. The Xilinx XCF128X PROM has become obsolete, so it will be replaced by two XCF32P PROMs to store the firmware and one XCF08P chip to store the configuration parameters. Additionally, an option to program the FPGA remotely from the ODMB or the FED boards via a 4.8 Gb/s link connected to a GBTx ASIC (via a VTRx) will be included. As detailed in Section 4.5, 504 of the DCFEBv2s will be installed on the 72 chambers in the ME1/1 ring, where the radiation dose is the highest, and the DCFEBs currently in that ring will be moved to the chambers in the ME234/1 rings. Finally, an unused feature that allowed the transmission of JTAG signals via both copper and optical links will be removed, and the routing and placement of a few components will be optimized.

The new DCFEBv2s will be installed during LS2 because the access to the inner CSC rings will be restricted during LS3, but the new ODMBs will not be installed until LS3. As a result, the DCFEBv2s and the DCFEBs that will be relocated into ME234/1 will be read out between LS2 and LS3 by the DMBs currently servicing those chambers. Backwards compatibility is achieved via the HD50 port shown on Fig. 4.10, which, in addition to being used to receive TTC, can be employed to transmit the cathode data to the old DMBs. The ability to read data from LS1

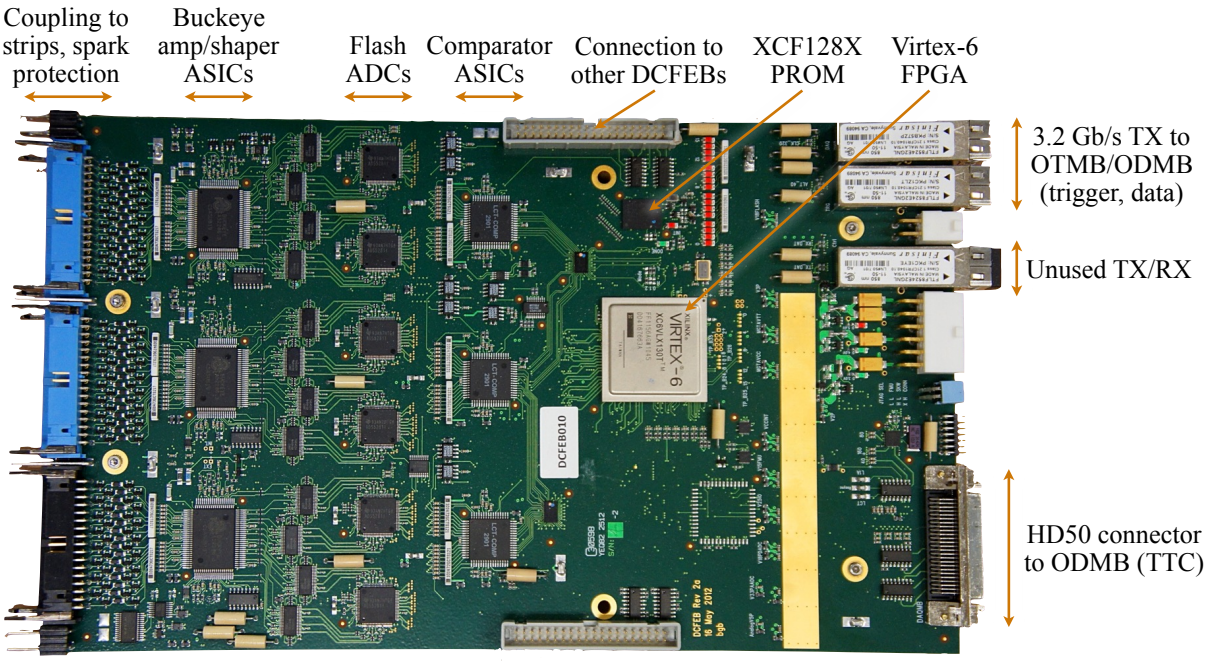

Figure 4.10: Top side of one of the DCFEBs produced for the ME1/1 upgrade. The DCFEB is about 300 mm $\times$ 175 mm in size, with chips mounted on both sides.

DCFEBs with old DMBs has been demonstrated in test stands at the Ohio State University and building 904 at CERN.

4.4.3 ALCT mezzanine upgrade (ALCT-LX150T and ALCT-LX100)

As described in Section 4.4.1.1, the ALCT mezzanine cards in all CSC rings will need to be upgraded, except for those in the ME1/1 and ME4/2 rings, which were upgraded during LS1. The limited resources in the Xilinx Virtex-E FPGAs (XCV600E and XCV1000E) powering the two types of mezzanine cards on those boards will not be able to store the anode data during the 12.5 μs latency requirement of the HL-LHC. Additionally, the copper cable used in the ALCTs to send the anode data to the TMBs does not provide enough output bandwidth in the inner rings to cope with the expected data rates at the HL-LHC.

Both of these problems are solved by replacing the mezzanine cards in the affected chambers by new boards based on the design of the ALCT-S6 developed for the LS1 upgrade (Fig. 4.11). The Spartan-6 FPGAs that will power the upgraded cards (XC6SLX100-3FGG676C and XC6SLX150T-3FGG900C) have 9–12 times more memory than the currently used Virtex-E FPGAs, which allows for the pipeline storage to be made deep enough to satisfy the HL-LHC latency requirements. Additionally, the current FPGAs are almost 100% full, whereas the Spartan-6 have 3–5 times more logic and are twice as fast. The increased logic resources allows for the impact of SEUs on the ALCTs, already a concern under the current LHC conditions, to be reduced by implementing triple voting and Xilinx's soft error mitigation. Additional hit patterns could also be included, which would improve the rejection of low-p_T multiple-scattering tracks. The timing resolution could be improved by employing both the leading and trailing edges of the discriminator output pulse (currently only the leading edge is being used).

Two similar designs for the new ALCT mezzanines will be employed. The ALCT-LX150T boards servicing the ME234/1 rings will largely follow the ALCT-S6 design except for a few minor modifications to increase the output bandwidth with two new 3.2 Gb/s optical links.

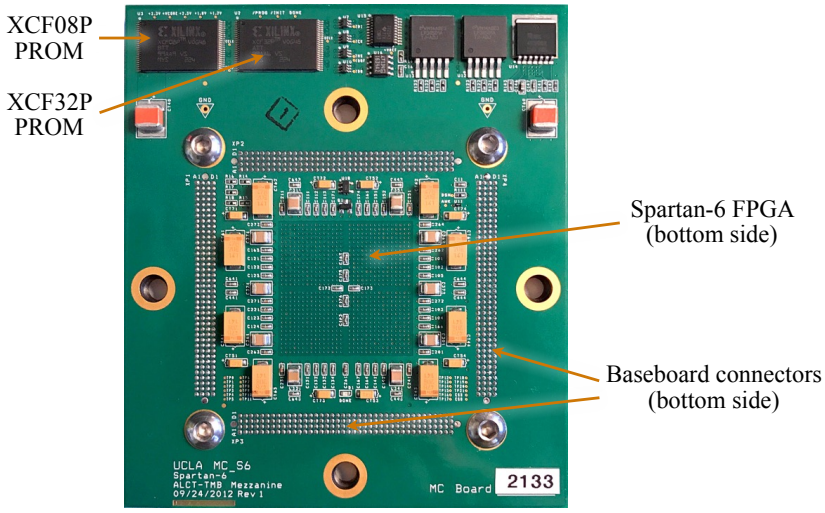

Figure 4.11: Top side of one of the Spartan-6 ALCT mezzanine boards produced for the ME1/1 upgrade. The ALCT-S6 mezzanine is about 104 mm $\times$ 118 mm in size, with chips mounted on both sides. The upgraded ALCT-LX150T/LX100 mezzanine boards will be around 104 mm $\times$ 140 mm to accommodate the new optical components.

The FPGA will be replaced with the XC6SLX150T model, which has the same footprint and almost the same resources as the XC6SLX150 model but includes eight GTP transceivers. Two of these GTP ports will be connected to a new VTTx optical transceiver with two transmitters. As shown in Table 4.6, the resulting 6.4 Gb/s bandwidth covers the expected HL-LHC data rates with a safety factor of more than three.

The smaller chambers in the ME1/1 ring and the lower-occupancy chambers in the ME123/2 rings can be serviced by ALCT-LX100s based on the cheaper XC6SLX100 FPGA with 408 I/O pins. The boards installed in ME1/1 will be outfitted with the same remote FPGA programming option (based on the GBTx ASIC) that the DCFEBv2s will have, thus mitigating any risks associated with the aging of the PROMs in that ring. A VTRx transceiver will provide an optical link to the ODMB running at 4.8 Gb/s, which translates to a bandwidth of 4.48 Gb/s for data transmission when the full-frame mode of the GBTx is employed.

The new ALCT-LX150T/LX100 mezzanine cards will be installed during LS2 and LS3 on the current ALCT baseboards for all the CSC rings except ME1/3 and ME4/2, a total of 180 chambers in the inner rings and 216 in the outer ones. The 72 ALCT-S6 boards currently in ME1/1 will be moved to ME1/3 during LS3 (see Section 4.5 for the detailed installation schedule). The optical ALCTs in the inner CSC rings will be read out by the new ODMBs, to be installed during LS3. Since the new design maintains backwards compatibility, the anode data can be transmitted to both TMBs and OTMBs via the copper path, and the new ODMBs via the optical link. The increased output bandwidth will not be necessary in the outer rings, but employing the same design as the one used for ME1/1 will simplify the R&D and production of the new boards, and will allow for the pool of spare boards to be of wider use. Initially, the VTRx optical transceiver would not be installed on the ALCT-LX100 boards intended for the outer rings, but if the amount of spare boards with optical links decreases to uncomfortable levels, additional transceivers could be acquired and easily plugged onto the corresponding socket.

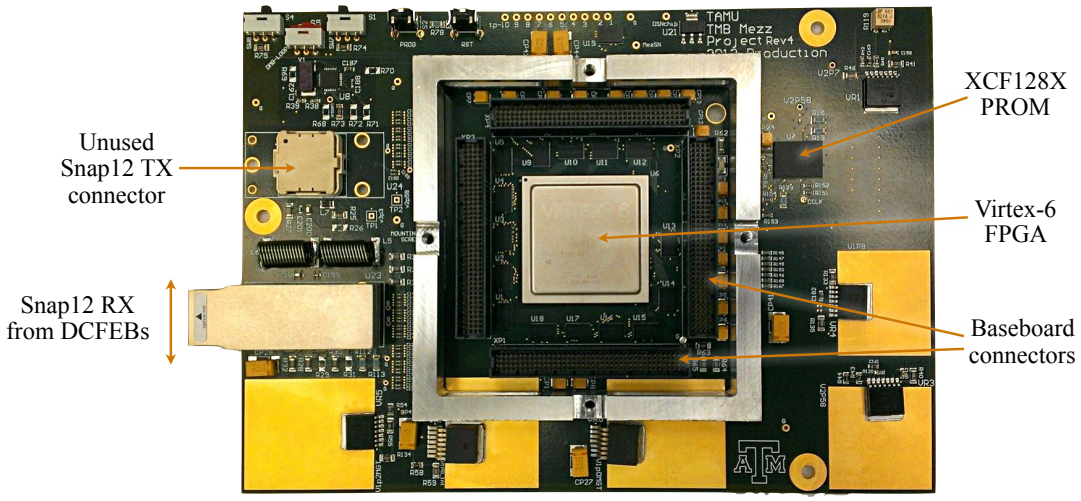

Figure 4.12: Bottom side of one of the OTMB mezzanine boards produced for the ME1/1 upgrade. The OTMB mezzanine is about 190 mm $\times$ 134 mm in size.

4.4.4 TMB upgrade (OTMBv2)

The relocated DCFEBs and the new DCFEBv2s in the ME234/1 rings will transmit trigger primitive data to the peripheral crates via 3.2 Gb/s optical links. Since the currently installed TMBs are designed to work with CFEBs, they have no optical receivers to accommodate the optical data link from the DCFEBv2s. This necessitates building 108 OTMBv2 mezzanine boards and 108 OTMBv2 main boards in LS2 for the ME2/1, ME3/1, and ME4/1 rings.

The OTMBs were designed and built during LS1 for the ME1/1 upgrade. The mezzanine boards employ a Reflex photonics Snap12 transceiver featuring 12 optical input receivers as shown in Fig. 4.12. This mezzanine board plugs into a VME OTMB baseboard. The boards also have a relatively modern Xilinx Virtex-6 FPGA with built-in high speed serial transceivers. The use of an upgraded FPGA provides the additional advantage of increased logic resources to improve the trigger algorithms in this high rate region.

The design of the new OTMBv2s will only include a few modifications with respect to the LS1 OTMBs. The Snap12 receivers are now obsolete so they will be replaced by another MTP12-type set of 12 receivers. Options from Samtec (Firefly ECUO-R12-14-030-0-1-1-2-01) and Reflex Photonics (LightABLE LHR12P4183101AA) are being considered. The LS1 design of the OTMB included a Snap12 transceiver with 12 transmitters that in the end was not needed nor installed. For the LS2 upgrade this connector will be replaced by a new MTP12 receiver that will simplify the connection to the new GE2/1 detectors being installed during LS3 (Section 6.4.2). Six fibers from GE2/1 will connect to each OTMBv2 in ME2/1 via a 12-fiber bundle, while the five fibers connecting the OTMBv2 to the DCFEBv2s will come in a different 12-fiber bundle.

4.4.5 DMB and ODMB upgrades (ODMB5 and ODMB7)

As shown in Section 4.4.1.2, the 1.6 Gb/s output link in the DMBs and ODMBs will not be able to handle the data rates in the inner CSC rings expected under HL-LHC running conditions. Two similar boards based on the ODMB design developed for the LS1 upgrade will increase the output bandwidth of the affected stations: the 72 ODMBs in ME1/1 will be replaced by ODMB7s that will connect to the seven DCFEBv2s in each ME1/1 CSC via the patch panel shown in Fig. 4.2 (right), and the 108 DMBs in ME234/1 will be replaced by ODMB5s that will connect directly to the five DCFEB(v2)s in those CSCs as shown in Fig. 4.2 (left). New optical

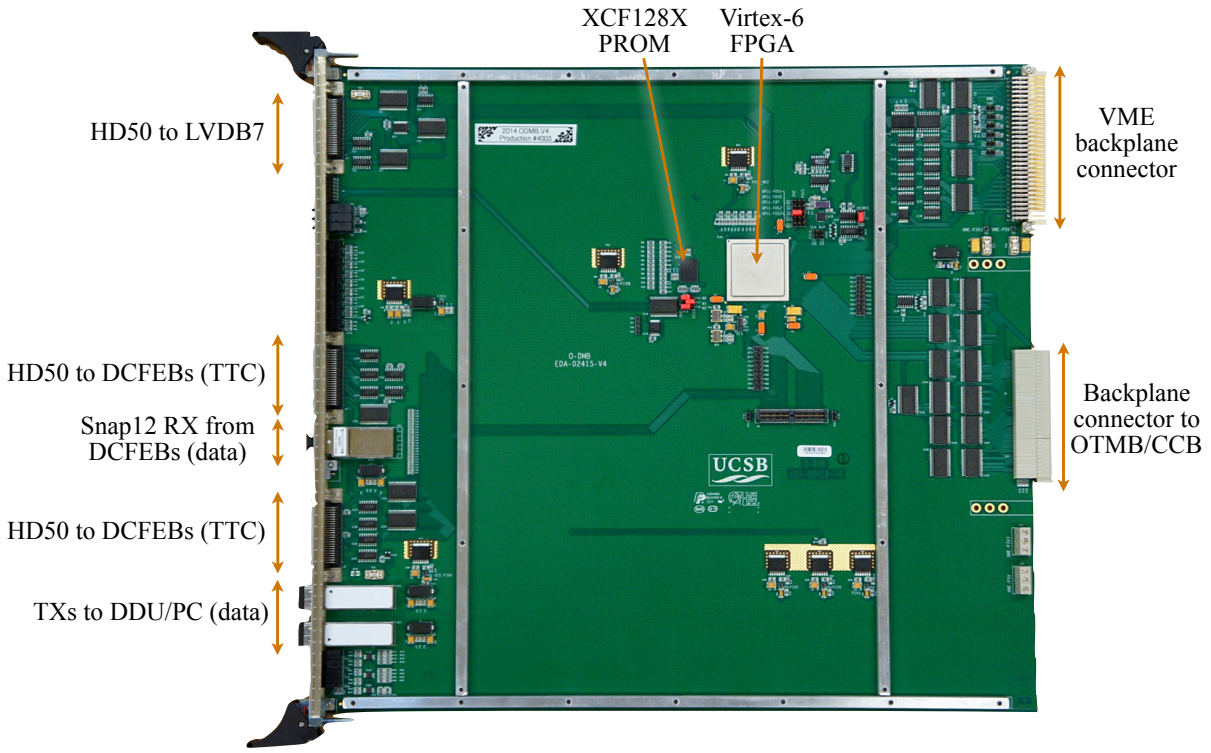

Figure 4.13: Top side of one of the ODMBs produced for the ME1/1 upgrade. The ODMB is a 9U VME board, 400 mm × 367 mm in size. The upgraded ODMB7 will be very similar to the ODMB, while the ODMB5 will have a different front panel configuration with copper connections to the five DCFEB(v2)s.

fibers connecting the DCFEB(v2)s in ME234/1 with the corresponding ODMB5s will be laid out.

The main difference between the designs of the ODMB5 and the ODMB7 lies in the front panel. For the LS1 upgrade of ME1/1, the five CFEBs on each CSC module were replaced by seven DCFEBs. Since there was not enough space on the front panel of the ODMB to fit seven HD50 connectors, a patch panel was used to reroute and fan out the signals coming from two 50-pin Skewclear cables connected to the ODMB to the seven cables going to the DCFEBs. The front panel of the ODMB7s will be largely the same as that in the current ODMBs, shown in Fig. 4.13. On the other hand, only five DCFEB(v2)s are needed to read out the cathode strips of the CSCs in the ME234/1 rings, and there is just enough space on the ODMB5 front panel for five HD50 connectors, an HD22 connector for the LVDB5, and two MTP optical connectors for the fiber links with the DCFEB(v2)s and the FED board. As a result, no patch panel will be necessary for the ME234/1 rings.

The design of the backplane connections, the clock and power distribution, and the FPGA and PROM will be the same for the ODMB5 and ODMB7, and will be very similar to the design of those parts in the existing ODMB. The main modification with respect to the ODMB corresponds to the upgrade of the FPGA from a Virtex-6 to the largest and highest speed grade Artix-7 model (Table 4.5). The new Xilinx 7-series, based on 28 nm architecture, provides higher performance at reduced cost and power consumption. Additionally, a new PROM will be added and the Snap-12 receivers will be replaced by a transceiver with full duplex connections such as the Finisar FTLD10CE3C to allow for the fast remote programming of the DCFEBv2s and ALCTs.

Table 4.5: FPGA resources currently used in the ODMB, and available in specific models of the Xilinx Virtex-6, Kintex-7, and Artix-7 FPGAs, as well as the Microsemi PolarFire flash FPGA. The ODMB uses the Virtex-6, while the upgraded ODMB5 and ODMB7 will use the new Artix-7. The Kintex-7 and PolarFire models are back-up options in case faster output links are required. The PolarFire, while an attractive alternative to the Artix-7, would require expertise with the Microsemi development tools, which are very different from those used in the Xilinx framework. The prices are list unit prices as of July 2017.

	Used in current ODMB	Virtex-6 XC6VLX130T 1FFG1156C	Artix-7 XC7A200T 3FFG1156E	Kintex-7 XC7K325T 3FFG900E	PolarFire MPF300TS FCG1152
Logic elements	52k	128k	215k	326k	300k
Total RAM	3 Mb	9.5 Mb	13 Mb	16 Mb	20.6 Mb
Clock managers	2	10	10	10	8
I/O pins	300	600	500	500	512
Opt. transceivers	8	20 @ 5 Gb/s	16 @ 6.6 Gb/s	16 @ 12.5 Gb/s	16 @ 12.5 Gb/s
Price		$1054	$389	$1940	$391

Table 4.6: Expected data rates for the CSC system at the HL-LHC and available output bandwidth for ALCTs and (O)DMBs after the Phase-2 upgrade. In the case of optical links (all but the ALCT links of the outer rings), the number of fibers and the line rate for each link are indicated. "Util." refers to the total bandwidth utilization of the available output link. Values greater than 100% indicate that the data rate exceeds the available bandwidth. The utilization of the optical links takes into account the overhead used by the transmission encoding.

	ALCT			(O)DMB			Full ring			
Chamber	Rate [Gb/s]	Link [Gb/s]	Util. [%]	Rate [Gb/s]	Link [Gb/s]	Util. [%]	CSCs	Rate [Gb/s]	Fibers to FED	Fibers from FED
ME1/1	0.87	1×4.8	19	4.3	4×6.4	21	72	306.7	288	72
ME2/1	1.16	2×3.2	23	2.8	3×6.4	18	36	102.0	108	36
ME3/1	0.57	2×3.2	11	1.6	2×6.4	16	36	57.5	72	36
ME4/1	0.56	2×3.2	11	1.6	2×6.4	15	36	56.5	72	36
ME1/2	0.08	0.64	12	0.3	1×1.6	20	72	18.4	72	72
ME2/2	0.05	0.64	7	0.2	1×1.6	13	72	11.6	72	72
ME3/2	0.06	0.64	9	0.2	1×1.6	15	72	14.2	72	72
ME4/2	0.12	0.64	18	0.4	1×1.6	31	72	28.7	72	72
ME1/3	0.01	0.64	1	0.1	1×1.6	2	72	1.9	72	72
Total CSC							540	597.5	900	540

The maximum speed of the optical transceivers in the Artix-7 models is 6.6 Gb/s. In order to meet the output bandwidth requirements at the HL-LHC, the ODMB5 and ODMB7 will include multiple optical links transmitting data to the FED boards. The current Finisar optical transceivers will be replaced by the CERN-designed VL+ transceivers with four transmitters capable of 10 Gb/s speeds and one receiver. Table 4.6 shows that with 4, 3, 2, and 2 fibers in ME1/1, ME2/1, ME3/1, and ME4/1, respectively, running at 6.4 Gb/s, the fiber utilization would be lower than 33% in all cases, thus providing appropriate safety factors. This will require laying out 540 new OM3 fibers from the peripheral crates to the FED crates in the service cavern.

The ODMB5 and ODMB7 will retain the upstream optical link with the FED board to take advantage of the large internal memories in the Artix-7 FPGA. This link can be used to signal that the FED buffers are starting to fill up (back pressure) and that the (O)DMBs should halt data transmission. By temporarily storing additional data in the (O)DMBs, the buffering capabilities

of the CSC system can be significantly increased.

4.4.6 FED upgrade

As shown in Fig. 4.2, the CSC Front-End Driver (FED) system collects the data from all the (O)DMBs and transmits them to the CMS central DAQ (cDAQ) system. The current 540 (O)DMB output links running at 1.6 Gb/s are read out by a total of 36 DDUs, each connected to 15 (O)DMBs. The data are aggregated and transmitted to cDAQ via S-links. For Phase 2, the CSC FED system will be upgraded to handle the 900 optical links at speeds up to 6.4 Gb/s, delivering a total data rate of 598 Gb/s, as shown in Table 4.6.

The bandwidth and protocols used by the CSC FEDs must be compatible with the cDAQ [66]. The cDAQ proposal for the Phase-2 upgrade allows for 20 links running at 100 Gb/s dedicated for CSC data (Table 7.2 in Ref. [24]), which corresponds to a total rate of 2000 Gb/s, thus covering the expected data rates for the CSC system.

Designs similar to those of the Master Processor board (MP7) [72] or the Calorimeter Trigger Processor card (CTP7) [30], currently in use by other CMS groups, would satisfy the requirements for the CSC system. These are μTCA boards with flexible designs based on Virtex-7 FPGAs that can handle numerous 10 Gb/s fiber links with excellent capability for high-capacity data handling. The CTP7 includes 67 receivers and 48 transmitters with speeds up to 10 Gb/s. Of these, 36 transmitters and 36 receivers use Avago CXP optical modules compatible with MPO-24 connectors. The remaining 31 receivers and 12 transmitters use Avago MiniPODs with an MPO-48 interface on the front panel. The 900 optical links coming from the (O)DMBs could thus be read out with a total of 14 CTP7s. As a proof of concept, the basic functions carried out by the DDUs have been implemented in the CTP7. Reading and buffering data from (O)DMBs, including recognizing event boundaries and merging data from multiple sources, has been achieved in cosmic ray tests at building 904 at CERN. Remote programming of a Virtex-6 FPGA has also been tested successfully.

The proposed architecture for the new CSC FED boards will likely be based on the ATCA platform, the common CMS format for Phase 2. The trigger group is designing new generic ATCA boards with different FPGA sizes. These boards would each have 80 to 104 optical links with speeds up to 16 or 30 Gb/s, and also include a Zynq processor card and large memories that could handle the remote programming of the DCFEB and ALCT FPGAs, exactly as needed for the CSC DAQ. A total of twelve of these boards would be able to handle the CSC data rates expected at the HL-LHC.

4.4.7 Low voltage system upgrade

The power needs for the upgraded boards being installed for the Phase-2 upgrade are well understood because their design is based in all cases on the boards developed for the ME1/1 upgrade. The needs for ME1/1 and the outer rings will not change much, but the total current per chamber on the 7 V digital and analog levels in ME2/1, M3/1, and ME4/1 will go from 9.8 A and 5.5 A to 22.8 A and 13.0 A, respectively, a net increase of 144 W per chamber. As in the LS1 upgrade of ME1/1, this increase is driven by the CFEBs being upgraded with DCFEBs and, as a result, the cooling requirements are well understood. There will be an additional increase of 32 W per OTMBv2-ODMB5 pair in each peripheral crate servicing the ME234/1 chambers. A global cooling solution that also takes into account the RPC and GEM upgrades for each of the yokes is being worked on.

To accommodate the increased power requirements, the low voltage system will be augmented and reconfigured as follows:

- The present systems, other than ME1/1, draw about 85% of their maximum power, and cannot accommodate the increased current needs of the new electronics. The ME2/1, ME3/1, and ME4/1 each represent a third of the total chambers in their respective stations. A total of twelve new Maraton power supplies will be added, four for each of the ME2/1, ME3/1, and ME4/1 rings. A four-fold increase in power for those rings would result in an overall increase of 100% for each station. With this addition, each station should run at about 60% of its maximum power, as ME1/1 does since the LS1 modifications.
- In addition, the junction boxes distributing low voltage power to stations 2, 3, and 4 need to be replaced to better balance the load. Some new low voltage cabling between the Maraton supplies and the junction boxes will be added, but the existing cables between the junction boxes and the chambers will be adequate. The rack space for the new Maratons is to be found.
- The LVDBs currently installed in the 108 CSCs in the ME234/1 rings provide the CFEBs with voltage levels of 3.3 V, 5 V, and 6 V, while the DCFEBs require 3 V, 4 V, and 5.4 V. New LVDB5s will be built and installed in the inner rings to provide the appropriate voltage levels to the relocated DCFEBs. The LVDB5s will be similar to the LVDB7s installed in ME1/1 during LS1 except that the former will power five DCFEBs per CSC instead of seven. The Molex connectors will be replaced with bolted lugs for greater robustness.

4.4.8 High voltage system upgrade

The CSC High Voltage System will be upgraded as described below. The technical scope of the upgrade is summarized in Table 4.7. No components need to be installed in UXC for this upgrade.

In the UF/PNPI system, the commercial Primary HV supplies will be retired and the present Master boards will be replaced with thirty-eight 9-channel Master boards of the new design. Each channel in the upgraded boards will have its own HV power source, capable of outputting voltages from 0 to 4000 V, with the maximum current of 2.5 mA (up from the present 1.5 mA). Thus, the current load safety factor will be $\sim$4, which we deem comfortably large. The design of such boards already exists and has been successfully prototyped, see Fig. 4.14.

The upgraded Master boards have somewhat larger LV power consumption than the current boards. In order to provide that power, an extra LV power supply will need to be installed. The crates that house Master boards will be replaced as well.

No other modifications to the present UF/PNPI HV subsystem are needed. For example, the control interface of the upgraded Master boards is compatible with the current Master boards, so no replacement of control boards or computers is necessary.

The CAEN subsystem used for ME1/1 chambers is small. Therefore, we will simply absorb ME1/1 chambers into the custom-made UF/PNPI HV subsystem, for which we will add two upgraded Master boards and twelve 36-channel Distribution boards of the current design. Besides ensuring reliable current measurements, such a replacement will make the entire CSC HV system homogeneous and simpler to operate and maintain.

Master and Distribution boards for ME1/1 chambers will be installed in S1A14 rack in USC, located near racks S1A11,12,13 that house the components of the existing UF/PNPI HV system. The 24 output HV cables from Distribution boards will be routed to the rack where the current ME1/1 HV system is located. That system will be replaced with a patch panel that mates

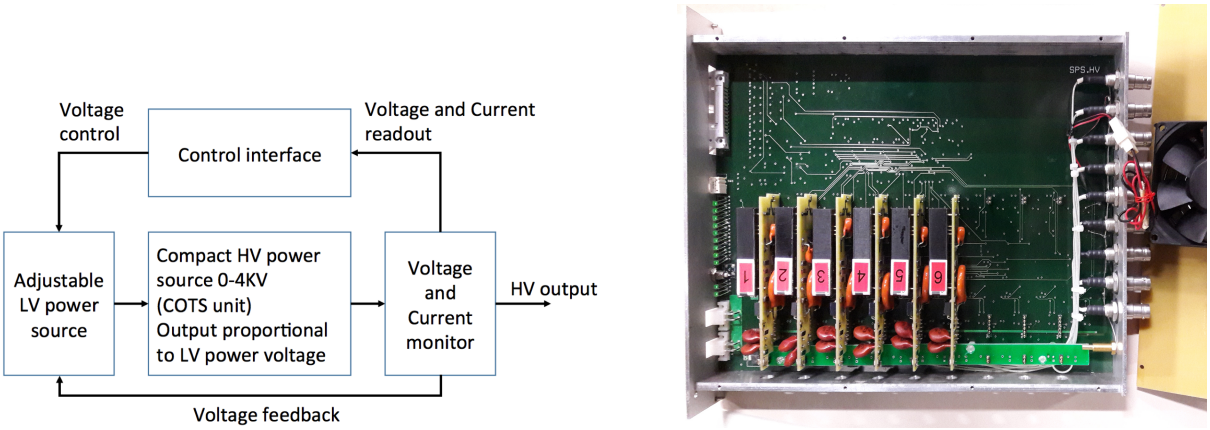

Figure 4.14: Left: A block diagram of a HV channel in the upgraded Master board. Right: A fully functional prototype of a new Master board. Six out of nine channels (mezzanine boards) are populated.

output cables from Distribution boards with HV cables to ME1/1 chambers.

Table 4.7: CSC HV System upgrade scope.

	non-ME1/1	ME1/1
HV master 9-channel boards	38	2
HV distribution 36-channel boards	–	12
Additional LV power supplies (commercial)	1	1
Euro sub-racks	8	3
HV cables: distribution to CSC patch panels	–	24
Patch panel sets	–	1

4.4.9 Quality assurance and quality control

The mechanisms to ensure that the quality requirements of this upgrade will be fulfilled (quality assurance) as well as the procedures to verify that the electronic modules satisfy these requirements (quality control) are in place and follow closely those implemented for the upgrade of the ME1/1 electronics during LS1. These are:

- The longevity of all the new boards under the challenging radiation environment expected at the HL-LHC is ensured by systematic irradiation tests of all parts to TIDs at least three times larger than the expected doses. In the cases in which a component does not satisfy this requirement (e.g., PROMs in ME1/1 front-end boards), back-up options will be implemented (e.g., remote programming of the FPGAs).
- A sufficient number of prototypes to test systematically the functionality of each board will be produced. This will allow us to identify any possible issues early and minimize the impact to the project costs and schedule.
- As described in Section 4.4.1.1, tests have been performed with CFEBs that confirm the expected data losses due to the limitations of the current boards. Similarly, we have confirmed that the bandwidth of the optical output of the existing ODMBs is the limitation for these data acquisition boards. This was measured in stress tests with increasing trigger rates where it was found that the 1.6 Gb/s output links started to overflow at the expected rates. These tests will be repeated with

the prototypes of the new boards to make sure that the new electronics is indeed compliant with the Phase-2 trigger and DAQ requirements.

- Bare PCBs are checked for electrical connectivity with a flying probe by the fabricator.
- Assembled PCBs are checked optically for correct component orientation and soldering, and connections are tested with a boundary scan tool by the vendor. Ball grid array soldering is checked with an optical system as well as 3D X-ray inspection.
- All the functionality of each board is systematically tested at each institution.
- After the boards are shipped to CERN, the functionality is re-tested at test stands in building 904 or SX5. These tests include a burn-in period of 24 hours with constant monitoring of voltages and temperatures.

4.5 Installation and integration

The proposed upgrade to the CSC system can only be fully carried out during the long shutdown periods before the HL-LHC running starts, namely LS2 and LS3. During LS3, the present installation schedule is driven by the replacement of the tracker and other detector elements of the CMS barrel region, such as the barrel ECAL and the DT front-end electronics, and by the replacement of the forward calorimeters on the YE1 disks. In order to fulfill these tasks, extended access to the barrel inner region and to the YE1 disks will be required. Thus, during most of LS3, CMS will be in a configuration with all endcap disks open and away from the barrel yokes, which will allow little opportunity to access the CSCs in stations 2, 3, and 4. To overcome this limitation, the CSC upgrade has been factorized into an early installation sequence that will take place in LS2, where most of the on-detector work will occur, and a later sequence in LS3, where only access to the racks located at the periphery of CMS will be needed.

4.5.1 Activities during LS2

During LS2, the 180 CSC chambers making up the ME1/1, ME2/1, ME3/1, and ME4/1 rings will be extracted from the CMS cavern and brought to the surface for their refurbishment with upgraded DCFEBs and ALCT mezzanine boards, as well as LVDB5s in the case of ME234/1 chambers. The surface facility in SX5 will contain storage cradles and movable tables which will allow for in situ refurbishment. The facility is already equipped with two test stands which allows for board connectivity and functionality testing, as well as for long-term (burn-in) testing for early detection of potential electronics failure before reinstallation and final commissioning in CMS.

Based on the experience with the installation of the ME4/2 chambers and the refurbishment of the ME1/1 chamber electronics during LS1, it is estimated that equipping the ME1234/1 rings with the new electronics will require about 19 weeks of access to the YE1 endcap disks (for ME1/1), 25 weeks of access to the YE2 disks (for ME2/1 and ME3/1), and about 17 weeks to the YE3 disks (for ME4/1), where the removal and reinstallation of the RPCs in the RE4 rings must also be done. These activities will be carried out simultaneously on both endcaps by taking advantage of the availability of a second crane in the experimental cavern during LS2, thus reducing substantially the overall access time.

The total time estimate for the full refurbishment of the 180 chambers is about 41 weeks, as shown in Fig. 4.15. This schedule begins by replacing the ME1/1 DCFEBs with DCFEBv2s to allow the subsequent refurbishing of the CSCs in the ME234/1 rings with the DCFEBs extracted from ME1/1. The installation sequence aims at performing uninterrupted parallel work in UXC

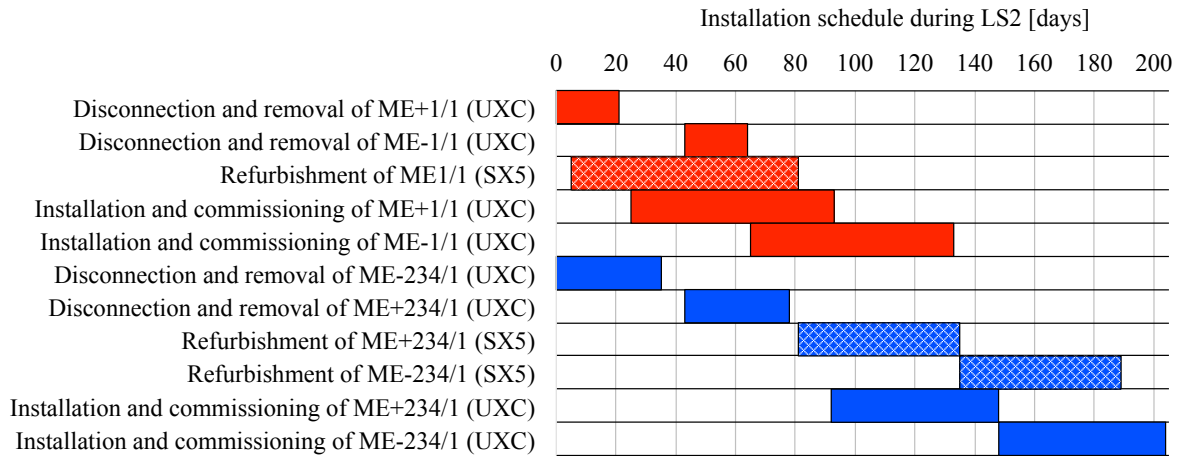

Figure 4.15: Timeline of the installation sequence for the inner CSC (MEx/1, where x = 1, 2, 3, 4) electronics upgrade. The chamber refurbishment in the surface building (SX5) is the main task driving the schedule and is highlighted with cross hatching. The activity in the underground cavern (UXC) is highly parallelized between the two endcaps. The label "ME-234/1" refers to these rings on the negative z endcap and "ME+234/1" to the positive z endcap.

employing both overhead cranes and maintaining a constant rate of electronics refurbishment in the surface facility.

The rate for removal and reinstallation of ME1/1 and ME234/1 chambers is estimated to be two and five chambers per day, respectively. This rate is slower for ME1/1 than for ME234/1 chambers because the former are located inside the YE1 "nose", and are thus more difficult to access. The full refurbishment of the 72 ME1/1 chambers is estimated to take a total of 21 weeks. Disconnecting the services and extracting the 108 ME234/1 chambers is estimated to take 16 weeks, while their refurbishment, reinstallation and commissioning is expected to last about 25 weeks. Overall, the upgrade of the ME234/1 on-chamber electronics should take 41 weeks, 40% of which would be done in parallel with the ME1/1 upgrade. The upgrade of the ALCT mezzanine boards for the ME123/2 and ME1/3 rings will happen in the shadow of the removal, installation, or commissioning of the inner chambers, whenever access to a particular CSC station is possible for an extended duration. This rather aggressive schedule benefits from past experience and takes advantage of complementary activities on both endcaps to parallelize work in the most efficient manner. The integration into the official CMS LS2 activity schedule is in progress.

The DCFEB upgrade requires specific back-end electronics to be upgraded as well. The 36 crates located on the periphery of the YE2 and YE3 disks, servicing the 108 ME2/1, ME3/1 and ME4/1 chambers will be equipped with the optical version of the TMBs (OTMB), as already done in LS1 for ME1/1 chambers. This task is independent on the particular disk location and does not require access to the chambers. Thus, it will be performed as expertise is available. In order to communicate with the OTMBs and future ODMBs in the peripheral crates, a bundle of 12 optical fibers will need to be routed from each ME234/1 chamber to the peripheral crate. This work will take place as part of the reinstallation effort described above. In order to provide the DCFEBs with adequate power, additional Wiener Maraton LV power supplies and new low voltage distribution boxes will be installed on the YE2 and YE3 tower racks to service the ME234/1 chambers. Similar to the OTMBs, this work is independent of the accessibility to any particular disk.

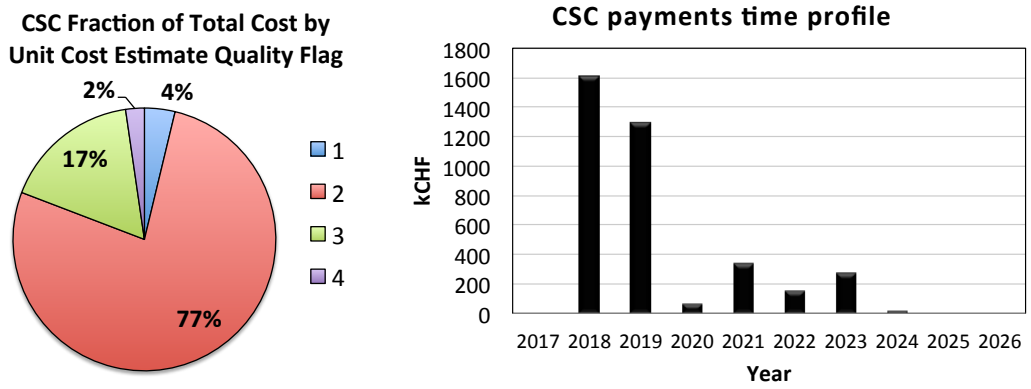

Figure 4.16: Left: Distribution of costs for the CSC upgrade by cost estimate quality flag. Right: Expected time profile for expenditures in the Phase-2 upgrade of the CSCs expressed in 2016 kCHF.

4.5.2 Activities during LS3

Work performed in LS3, in general, is less dependent on the CMS access schedule. Most upgrades will be off-detector, with the one exception being the ME1 disks. All 216 CSC chambers from the ME1 disks will be extracted to the surface for the majority of LS3 to allow for upgrade of the CMS forward calorimetry. These chambers will be stored under closely-monitored conditions for an extended period. During this surface storage, all chambers will undergo various maintenance testing.

Also during LS3, all 108 ME2/1, ME3/1, and ME4/1 chambers will receive upgraded ODMBs and the new HV system will be installed. This work is not dependent on disk movement or access. Fibers from chambers to the ODMBs will already be in place from the LS2 upgrade. All FED upgrades including crates and optical fibers are likewise not affected by major CMS access or scheduling issues.

4.6 Cost, schedule and institutional responsibilities

The current estimates of the CORE costs of the CSC upgrade are shown in Table 4.8. The CORE costs include the production costs of all modules that are needed for the CMS experiment itself, plus any needed in test stands at CERN, as well as extra modules in cases where the production is expected to result in some fraction of faulty modules that cannot be used for commissioning. Operational spares are not included in the CORE costs.

As many of the electronics boards are very similar to those produced for the ME1/1 electronics replacement in LS1, the estimates in most cases are based on the actual production costs of the ME1/1 electronics. If these costs were invoiced before 2016, a scaling of 2% per year is applied to escalate the expected costs. The distribution of the quality factors for the costs is shown in Fig. 4.16, left, where where (1) is based on an vendor quote or catalog price, (2) is based on a recent similar part, (3) is based on engineering seeding where sub-components are known, and (4) is based on a conceptual design of scaled from similar systems. The anticipated time profile for the costs is shown in Fig. 4.16, right.

The institutions that are expected to contribute to the CSC upgrade are shown in Table 4.9. Many of these institutions have been involved with the CSC system since its initial construction

Table 4.8: Summary of estimated CORE costs, scaled to 2016 kCHF, for the phase-2 CSC upgrade.

Item number	Item name	Estimated cost [2016 kCHF]
2.3	**CSC TOTAL**	**3785**
2.3.1.1	*On-chamber and OTMB boards*	*2280*
2.3.1.1.1	DCFEB boards	1588
2.3.1.1.2	OTMB mezzanine boards	300
2.3.1.1.3	OTMB baseboards	126
2.3.1.1.4	Optical ALCT boards	152
2.3.1.1.5	Copper ALCT boards	99
2.3.1.1.6–9	Shipping of on-chamber and OTMB boards	15
2.3.1.2	*Low voltage system*	*278*
2.3.1.2.1	Maraton power supplies	142
2.3.1.2.2	LV junction boxes	60
2.3.1.2.3	LVDB boards	61
2.3.1.2.4	LVDB test stands	15
2.3.1.3	*On-chamber optical fibers*	*80*
2.3.4	*On-chamber mechanics*	*52*
2.3.4.1	DCFEB board covers	17
2.3.4.2	DCFEB common covers	13
2.3.4.3	Flow restrictors	3
2.3.4.4	Chamber storage cradles	10
2.3.4.5	Fixtures for refurbishment area	10
2.3.2	*ODMBs and FED system*	*887*
2.3.2.1.1	ODMB boards	456
2.3.3.1.1	ODMB shipping	7
2.3.3.8	ODMB radiation testing	25
2.3.2.2.1	DDU replacements	234
2.3.2.2.2	FED crates	49
2.3.2.2.3	xTCA DAQ interface modules	20
2.3.2.2.4–5	FED system shipping	3
2.3.2.3	FED optical fibers	94
2.3.3	*High voltage system*	*209*
2.3.3.1.1	HV master boards	127
2.3.3.1.1	HV distribution boards	57
2.3.3.2.1	HV cables	12
2.3.3.2.2	LV power supplies, crates	13

and thus provide significant continuity and expertise.

The schedule for prototyping, production, testing, and integration of the upgraded CSC electronics is implemented and tracked with a MERLIN schedule that is common to all muon subsystems. The CSC schedule contains approximately 150 individual tasks that are linked with causal dependencies. The higher level summary tasks and some of the milestones are shown in Fig. 4.17 for the on-chamber and trigger boards to be installed during LS2, and in Fig. 4.18 for the readout boards to be installed during LS3. A list of high level milestones is shown in Table 4.10.

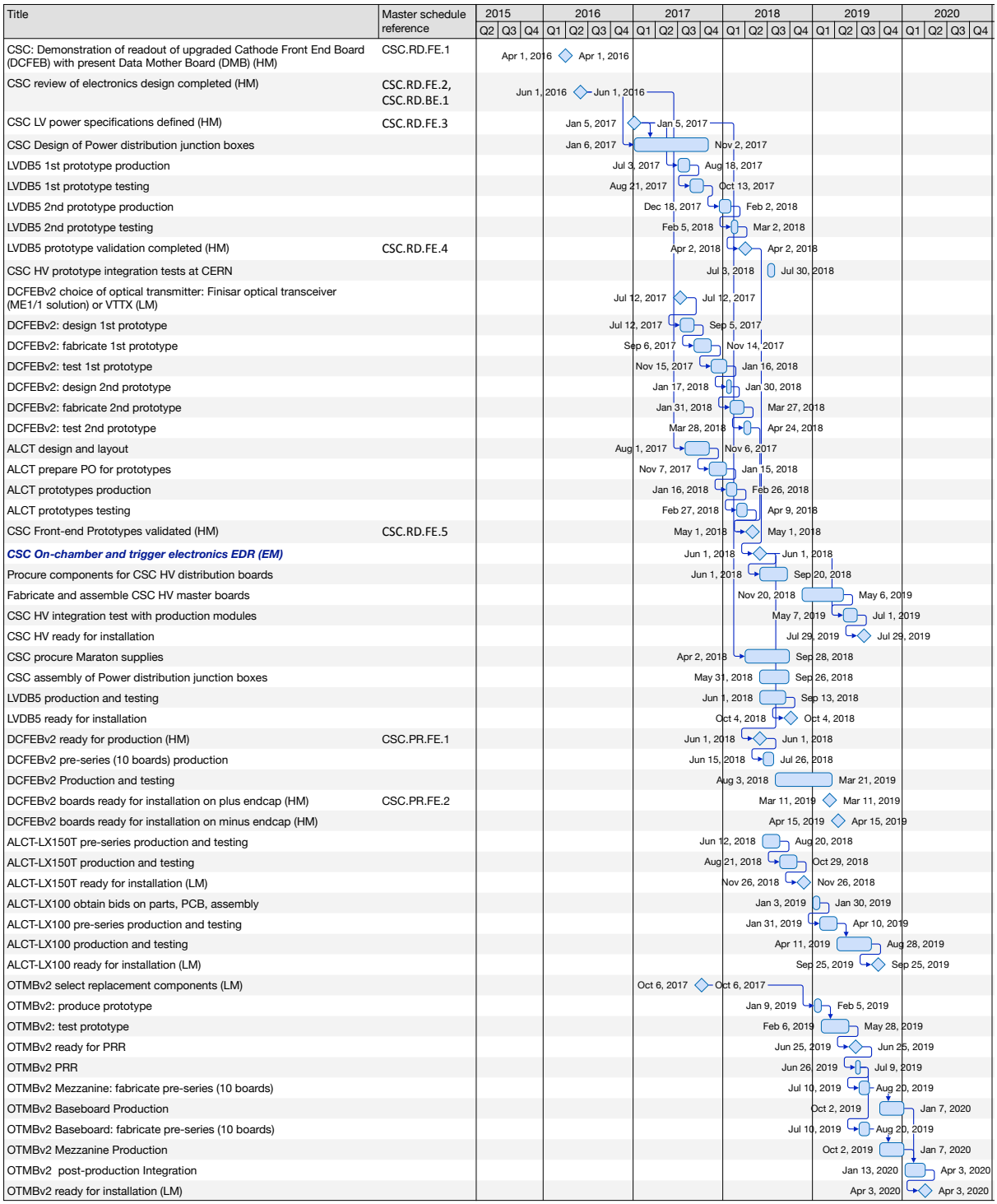

Figure 4.17: Expected schedule of the main tasks and milestones for the design and production of the CSC on-chamber and trigger boards, which will be installed in LS2 as part of the Phase-2 upgrade.

Table 4.9: Institutional responsibilities for the Phase-2 CSC upgrade.

Institution	DCFEB boards	ALCT boards	OTMB boards	ODMB boards	LVDB boards	FED system	Cables and fibers	Electronics rad. testing	Chamber aging and gas	High voltage	LV infrastructure	System engineering	Integration, installation, commissioning	Online software
UC Davis								X					X	
UCLA		X						X	X				X	
UC Riverside									X				X	
UCSB				X				X					X	
Dubna					X			X	X				X	
U. Florida									X	X			X	
Northeastern U.							X		X				X	
Ohio State U.	X			X		X		X					X	
PNPI								X	X	X			X	
Rice U.												X	X	X
Texas A&M			X			X		X					X	X
U. Wisconsin									X		X		X	

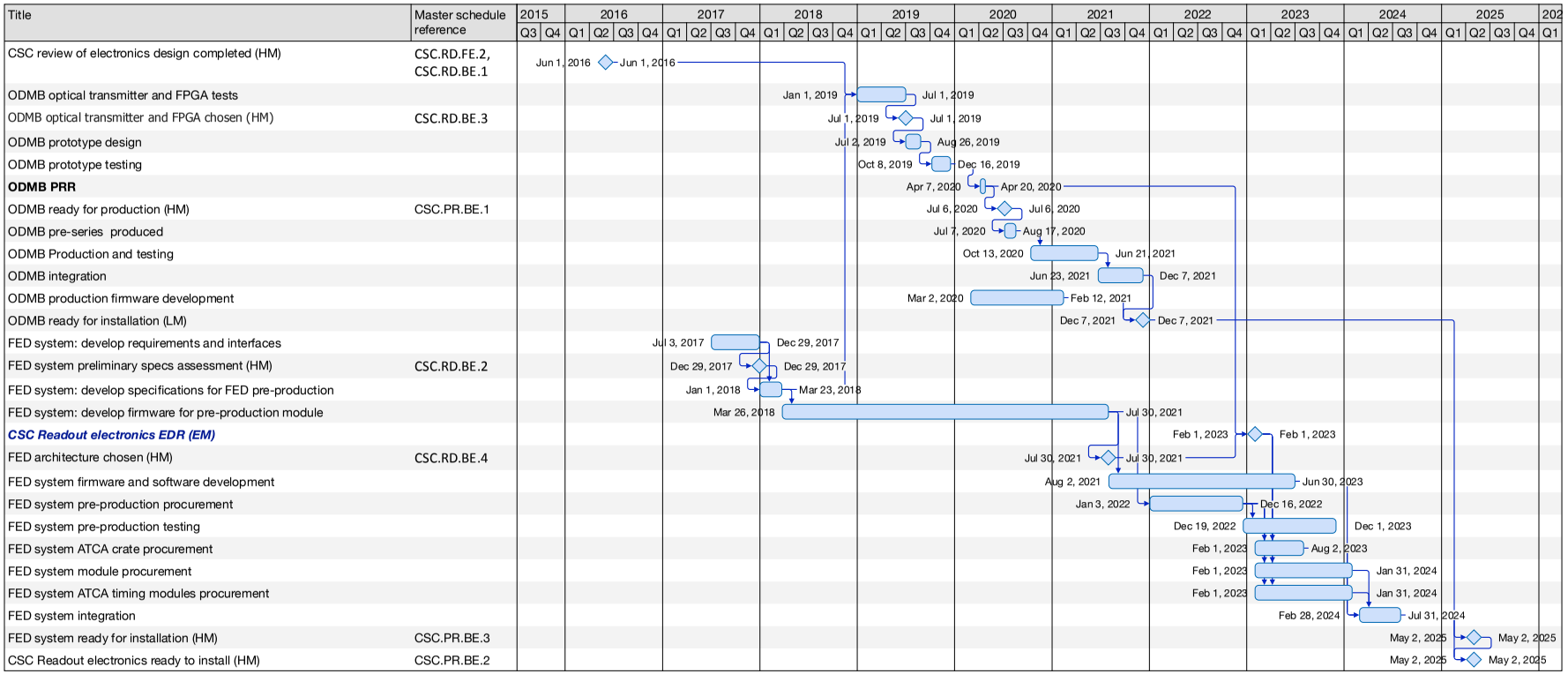

Figure 4.18: Expected schedule of the main tasks and milestones for the design and production of the CSC readout boards, which will be installed in LS3 as part of the Phase-2 upgrade.

Table 4.10: Summary of most important milestones for the CSC upgrade.

	ID	Milestone title	Date
Design	CSC.RD.FE.1	CSC demonstration of readout of upgraded DCFEB with present DMB	1.Apr.2016
	CSC.RD.FE.2, CSC.RD.BE.1	CSC review of electronics design completed	1.Jun.2016
	CSC.RD.FE.3	CSC LV power specifications defined	5.Jan.2017
	CSC.RD.BE.2	CSC FED system preliminary specifications assessment	29.Dec.2017
	CSC.RD.BE.3	CSC ODMB optical transmitter and FPGA chosen	1.Jul.2019
	CSC.RD.BE.4	CSC FED architecture chosen	30.Jul.2021
Prototyping	CSC.RD.FE.4	CSC LVDB prototype validation completed	2.Apr.2018
	CSC.RD.FE.5	CSC front-end Prototypes validated	1.May.2018
		CSC on-chamber & trigger electronics EDR	1.Jun.2018
		CSC readout electronics EDR	1.Feb.2023
Production	CSC.PR.FE.1	CSC DCFEB ready for production	1.Jun.2018
	CSC.PR.FE.2	CSC DCFEB ready for installation on plus endcap	11.Mar.2019
	CSC.PR.BE.1	CSC ODMB ready for production	6.Jul.2020
	CSC.PR.BE.2	CSC readout electronics ready to install	2.May.2025
	CSC.PR.BE.3	CSC FED ready for installation	2.May.2025

Chapter 5

RPC upgrades and new RPC detectors

5.1 Overview and motivation

The Resistive Plate Chamber (RPC) system covers both barrel and endcap regions, contributing to the trigger, reconstruction and identification of muons, in particular in the small regions not instrumented by the other muon sub-systems, CSC in the endcaps and DT in the barrel.

During the HL-LHC operation, the expected conditions in terms of background and pile-up and the probable aging of the present detectors will make the muon identification and correct p_{T} assignment a challenge for the muon system. In order to ensure redundancy of the muon system also under the HL-LHC conditions, the present RPC system has to be improved.

Two important upgrades are planned: the RPC off-detector electronics (called link system) will be replaced and the RPC coverage will be extended from $|\eta| = 1.9$ up to 2.4. Figure 5.1 shows the region where new RPCs will be placed to extend the coverage (inside the red box) and the region affected by the link system upgrade (purple box).

The link system, described in Section 5.2, has the function to process, synchronize and zero-suppress the signals coming from the RPC Front-End Boards (FEB) providing RPC hits with a time resolution of one bunch crossing (25 ns). The new link system will improve the precision in the timing readout allowing the RPC intrinsic time resolution ($\sim$1.5 ns) to be fully exploited. Furthermore it will overcome the weaknesses and the deterioration due to aging of the present system, as will be described in Section 5.3.3.

The extension of the RPC system up to $|\eta| = 2.1$ was already planned in the CMS TDR [19] from 1997, but staged because of budget limitations and expected background rates exceeding the rate capability of the CMS RPC technology used for the present system. An extensive R&D program has been performed in order to develop an improved RPC that fulfills the CMS requirements for HL-LHC. Two new RPC layers will be added in the innermost rings of stations 3 and 4. This leads to an increase of the efficiency for both trigger and offline reconstruction in a region where the background is the highest and the magnetic field is the lowest within the muon system. The extended RPC system will improve the performance and the robustness of the muon trigger, matching the coverage of the inner tracker also in the extended η region, and opening the possibility of a new independent trigger based on tracker plus RPCs. The improved time resolution will open the window to explore new physics channels with long lived particles, as is demonstrated in Chapters 7 and 8.

Regarding the present RPC system, studies of the longevity at the CERN GIF++ facility show that it performs within specifications up to the maximum expected rate and close to the maximum integrated charges expected during the full HL-LHC life. Additional tests are in progress to collect the full charge expected, including an additional safety factor of three.

5.2 The present RPC system

The present RPC system consists of 480 chambers in the barrel and 576 chambers in the endcap, organized in 4 stations called RB1 to RB4 in the barrel region, and RE1 to RE4 in the endcap region. The innermost barrel stations, RB1 and RB2, are instrumented with RPCs on the inner and outer faces of the corresponding DT chambers. All other RPC stations in the barrel and endcaps have one RPC chamber per station (see Fig. 1.4 for the layout).

The CMS RPC is a double-gap chamber working in avalanche mode with readout strips placed in the middle between the two gas gaps: a schematic view is shown in Fig. 5.2 (left). Each RPC gap consists of two 2 mm thick resistive High Pressure Laminate (HPL, commonly known as Bakelite) electrode plates separated by a 2 mm gas gap. The outer surface of the HPL plates is coated with a thin resistive graphite layer to which the high voltage is applied. The readout plane is done with copper strips on a mylar foil positioned centrally in between the two gas gaps. The strips are aligned in η with a pitch ranging between 2.28 and 4.10 cm (1.74 and 3.63 cm) in the barrel (endcap), depending on their geographical location. The RPCs are operated in avalanche mode using a gas mixture consisting of 95.2% freon ($C_2H_2F_4$), 4.5% isobutane (i-C_4H_{10}), and 0.3% sulphur hexafluoride (SF_6) with a relative humidity of 40–50%. Details on the geometry are specified in Ref. [20]. The signals coming from the strips are asynchronously sent to the FEBs, located inside the chambers, where they are amplified, discriminated and shaped. From the FEB, LVDS signals are fed via twisted pair cables of 10–20 m length to the link system located on the balconies around the CMS detector. A schematic view of the readout is shown in Fig. 5.2 (right).

The link system receives the data from the FEB, synchronizes and compresses them, and sends them via the optical links to trigger processors: the concentrator cards in the barrel (TwinMux),

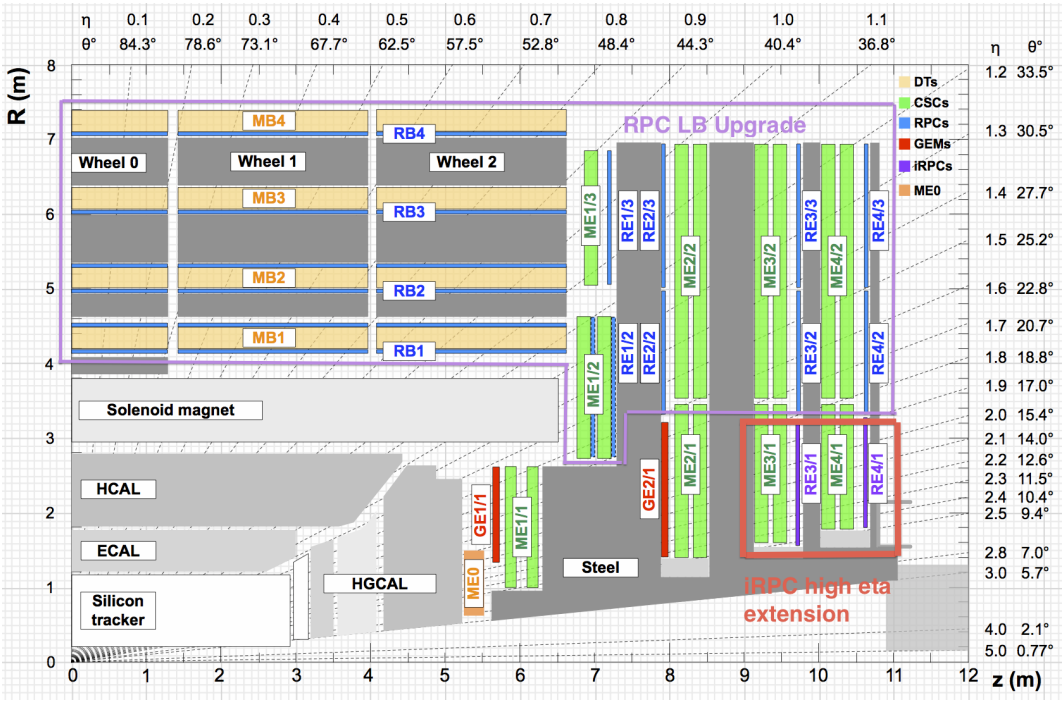

Figure 5.1: A quadrant of the CMS experiment. The red box indicates the region where additional RPCs will be placed to extend the muon coverage. The purple contour indicates the region interested by the link system upgrade.

the Overlap Muon Track Finder (OMTF) in the overlap region, and the Concentrator and Pre-Processor Fanout (CPPF) in the endcap. The link system consists of two main boards: the Link Boards (LBs) and the Control Boards (CBs). Each LB has 96 input channels (one channel corresponds to one RPC strip). The first step of LB is the synchronization, assigning the signals to the corresponding Bunch Crossing (BX: 25 ns period). Then the data are compressed with a simple zero-suppressing algorithm. The input channels are grouped into 8 bit partitions. Only the partitions with at least one nonzero bit are selected for each BX. The non-empty partitions are time-multiplexed, i.e. if there is more than one such partition in a given BX, they are sent one-by-one in consecutive BXes. The data from three neighboring LBs are concentrated by the middle LB, which contains the optical transmitter sending them to the Underground Service Cavern (USC) over a fiber, at a transfer rate of up to 1.6 Gbps. The CBs provide the communication of the control software with the LBs via the Front-End Controller (FEC) and the Communication and Control Units (CCU) system. The CBs are connected into token rings, each ring consisting of 12 CBs of one detector tower and a FEC mezzanine board placed on the Clock & Control System (CCS) board located in a VME crate in the USC. Both LB and CB boards are placed in crates called link boxes. The link box is a custom crate (6U high) with 20 slots (for two CBs and eighteen LBs). Each link box contains a custom backplane to which the cables from the chambers are connected, as well as the cables providing power to the LBs and CBs, and the FEB control cables which use an I2C protocol (through the CB). The number of components of the link system is reported in Table 5.1.

The High Voltage system is located in the USC, not exposed to radiation and easily accessible for maintenance. It provides the needed voltage of around 10 kV to the RPC chambers with A3512N boards produced by CAEN. These are 12 kV and 1 mA power supply boards. In total

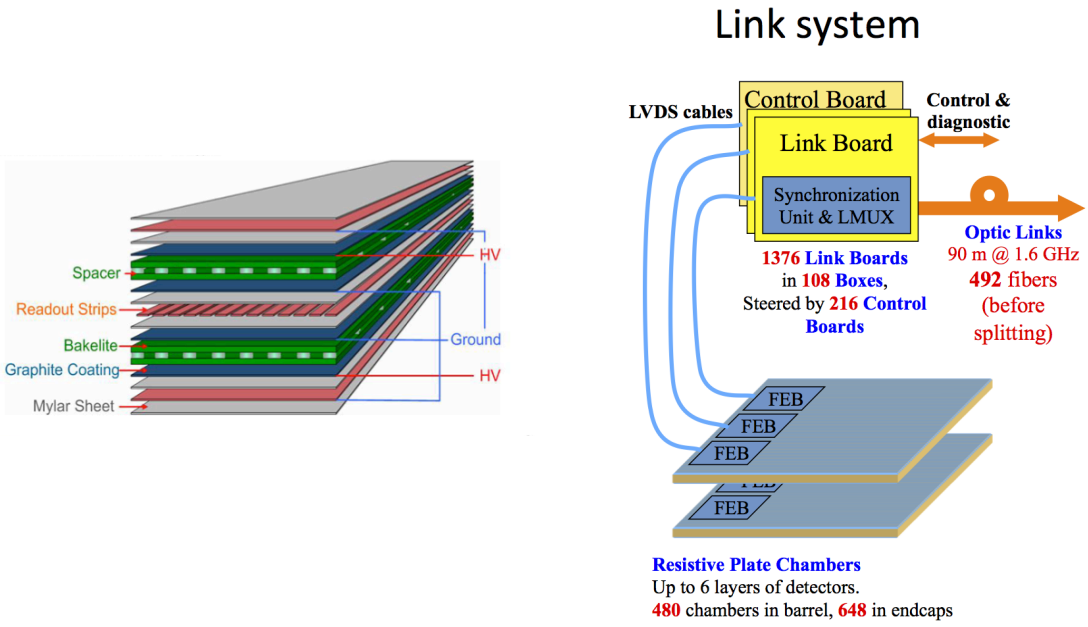

Figure 5.2: Schematic view of the double gap design of the RPC chambers (left). Schematic view of the readout and connections from and to the Link Boards and Control Boards (right). The numbers refer to the full RPC system after the upgrade.

Table 5.1: Number of components of the current link system.

Item name	Quantity
Link Boards	1376
Control Boards	216
Link boxes	108
Front planes	216
Optical links	492
12-channel fibers (from CBs to FECs)	18
TTC fibers	216

136 HV boards are used to operate the present RPC system.

The Low Voltage boards are located in the Underground eXperimental Cavern (UXC) on the balconies and provide the low voltage to the front end electronics. The system is based on A3009 CAEN boards providing 8 V and 9 A to the front-end electronics and on A3016 (8 V and 16 A) providing the voltage to the link system. Both boards have been developed to operate in a magnetic field and an environment with moderate radiation levels. In total 108 A3009 and 72 A2016 LV boards are used in the present system.

The full power system is based on CAEN Easy3000 system technology and infrastructure. It includes mainframes and branch controllers, which realize the communication between the hardware (detector) and the software (Detector Control system, DCS) via the CAEN OPC server. The branch controllers (CAEN A1676A modules) are hosted inside the mainframes (SY1527) to control up to 6 Easy crates. Up to 7 HV boards and 5 LV boards can be housed in one Easy crate to supply the HV and LV power to the RPC chambers in the CMS detector and the power to the RPC Link system. The present SY1527 mainframes are planned to be gradually replaced by the CAEN SY4527 mainframes before the year 2022. Since many of the electronic components inside CAEN HV and LV boards of type A3512N and A3009 (those used in the present system) are already obsolete, it is planned to produce new boards of the same type with new built-in components, all backward compatible with the present equipment.

5.3 Longevity

During HL-LHC operation, the instantaneous luminosity should increase to 5×10^{34} cm^{-2}s^{-1}, with a corresponding increase of the background. The experiments are expected to collect an integrated luminosity of 3000 fb^{-1}.

Run-1 and Run-2 data have shown a linear dependence of the background rates as a function of the instantaneous luminosity, over five orders of magnitude, for all barrel and endcap stations (Fig. 1.12). Assuming the same linear relationship up to a luminosity of about one order of magnitude higher, the expected rates at HL-LHC conditions are shown in Fig. 5.3 for all barrel (left) and endcap (right) chambers. A maximum rate per unit area of about 200 Hz/cm^2 is expected. Background simulations reproduce the measured rates within a factor of two. In the following we apply a safety factor of three and evaluate the performance up to a rate of 600 Hz/cm^2.

The maximum expected integrated charge on the RPC chambers can be evaluated on the basis of the expected integrated luminosity at the HL-LHC, defining an upper limit up to which the RPC system needs to be tested for aging and radiation effects. The total integrated charge, by the end of HL-LHC, will be 280 mC/cm^2 in the hottest spot of the current RPC system.

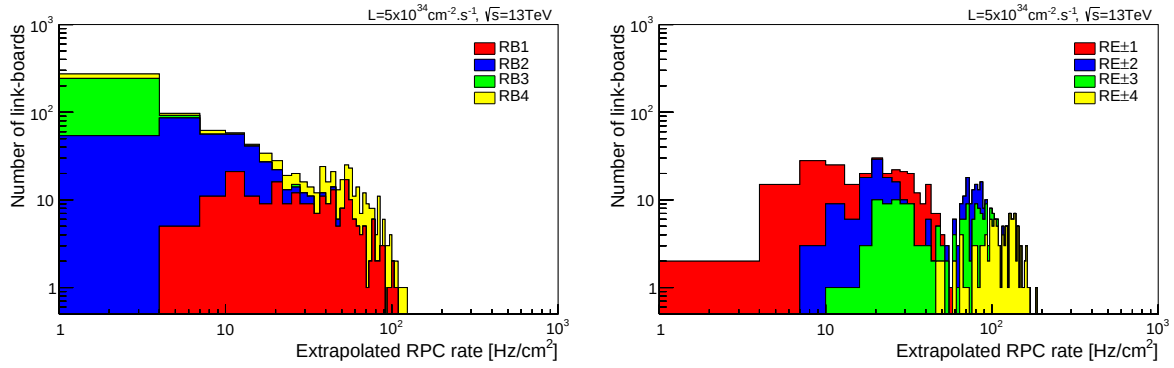

Figure 5.3: Extrapolation from 2016 data of single hit rate per unit area to HL-LHC conditions, in the barrel (left) and endcap (right) regions, for the present RPC system.

Including a safety factor of three, the chambers will be certified at GIF++ up to 840 mC/cm^2.

In the past, extensive long-term irradiation tests were carried out at several gamma and neutron facilities certifying the detector performance for ten LHC years: full size and small prototype RPCs have been irradiated with photons up to an integrated charge of ~ 50 and ~ 400 mC/cm^2, respectively [42, 43]. Recently, new tests have been performed, or are in progress, in order to certify the present RPC system up to the expected HL-LHC conditions: integrated charge of $\sim$840 mC/cm^2 and background hit rates of 600 Hz/cm^2. As reference, during Run-1, the RPC system provided stable operation and excellent performance and did not show any aging effects for an integrated charge of the order of 10 mC/cm^2.

5.3.1 Irradiation tests at GIF++

Because the maximum background rate is expected in the endcap region, in July 2016 an irradiation test was started at the CERN Gamma Irradiation Facility GIF++, using four spare endcap chambers: two RE2/2 detectors and two RE4/2 chambers. Two different types of chambers have been used for this test because the endcap RPC production has been performed in two periods: in 2005 for all RPCs in the endcap system, except the RE4/2 and RE4/3 chambers, which were made in 2013.

In order to study the longevity of the detector, two chambers (one RE2/2 and one RE4/2) are continuously operated under gamma irradiation, while the remaining two chambers are turned on only from time to time and are used as reference. The main detector parameters are monitored and periodically compared with those of the reference chambers (currents and counting rates in several background conditions, noise and dark current, electrode resistivity). Moreover, when the muon beam at GIF++ is available, the detector performance is studied with and without background. All measurements are performed under controlled environmental and gas conditions.

The integrated charge versus time is shown in Fig. 5.4 for the RE2/2 and RE4/2 chambers. At present, about 292 mC/cm^2 and 119 mC/cm^2 have been integrated in the RE2/2 and RE4/2 detectors, respectively. The detectors at GIF++ are operated with an acceleration factor of about two, and the charge already integrated on RE2/2 is about one third of the target figure. The tests will be completed in the middle of 2018.

Since July 2016, several measurements with test beams have been performed. Each time the detector performance (efficiency, cluster size, cluster multiplicity) of all four RPCs has been

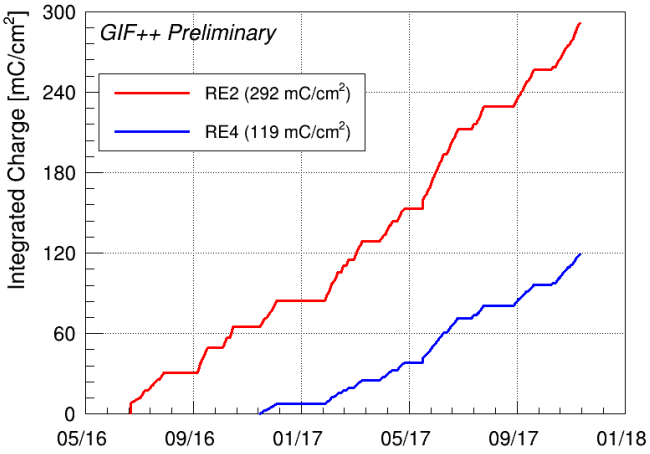

Figure 5.4: Integrated charge versus time collected during the GIF++ studies for the RE2/2 and RE4/2 chambers. The RE4/2 chamber has been turned on few months later because of total gas flow limitations. Different slopes account for different attenuation factors during data taking.

measured in several background conditions, taking advantage of the removable filters in front of the ^{137}Cs gamma source that allow us to span the background from 0 to several kHz/cm^2.

In Fig. 5.5, the hit efficiency of the RE2/2 chamber as a function of the effective HV (Voltage normalized at the standard temperature and pressure) taken with no irradiation (left) and under a gamma background rate of about 600 Hz/cm^2 (right), is reported after different periods of irradiation at GIF++. The method for the data analysis is described in Ref. [73]. The working point, defined as the voltage value at which 95% of the maximum efficiency is reached, is unchanged after different periods of irradiation, both under 600 Hz/cm^2 and without gamma background rate.

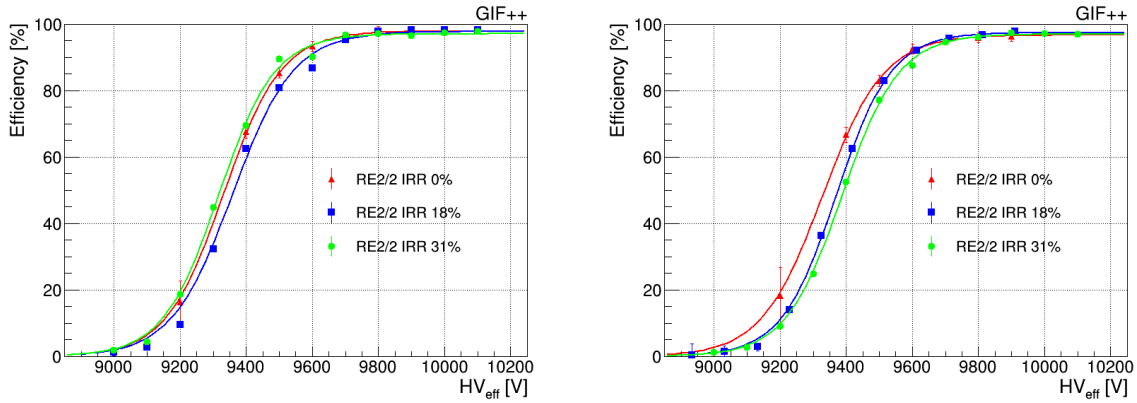

Figure 5.5: RE2/2 hit efficiency as a function of the effective HV taken with no irradiation (left) and under a gamma background rate of about 600 Hz/cm^2 (right). The efficiency of the RE2/2 chamber is measured during different Test Beams corresponding to different fractions of the target charge to integrate: 0, 153 (18%) and 257 mC/cm^2 (31%). No significant variations have been observed in the detector performance.

The hit efficiency (left) and the cluster size defined as the number of fired strips per hit (right) for the RE2/2 chambers (for the two irradiated and for the non-irradiated reference chambers)

at the working point are shown in Fig. 5.6 as a function of the background rate. For all detectors the efficiency is stable in time with a small decrease (2%) of the efficiency at the highest expected background rate of 600 Hz/cm^2. The measurements have been repeated after different periods of irradiation corresponding to 18% (153 mC/cm^2) and 31% (257 mC/cm^2) of the total integrated charge expected by the end of HL-LHC.

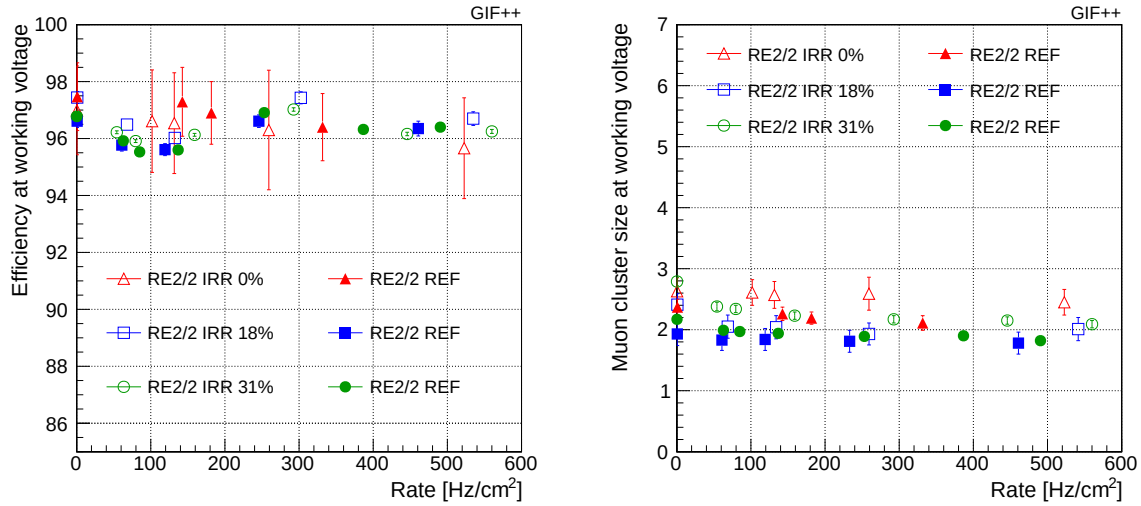

Figure 5.6: Evolution of the hit efficiency (left) and cluster size (right) at the working point, for RE2/2 chambers as a function of the γ rate per unit area. Both irradiated and non-irradiated reference chambers are shown. The measurements have been repeated after different periods of irradiation (corresponding to 18% and 31% of the total integrated charge expected by the end of HL-LHC).

To study the stability of the system, the rate and the RPC current are monitored all the time, for both irradiated and non-irradiated reference chambers. To cancel out the dependence on the environmental conditions, the ratio of irradiated and reference chambers is measured as a function of the integrated charge and reported in Fig. 5.7 (left) for the current and in Fig. 5.7 (right) for the rate. The measurements show that there is no impact of the irradiation on the performance of the detector for both RE2/2 and RE4/2 chambers. The difference in the ratio between the two chambers is due to the different relative position of RE2/2 (red circles in the figure) and RE4/2 (blue squares) chambers with respect to the reference chambers inside the GIF++ zone.

From all results presented, neither signs of performance degradation under the expected high background rates, nor aging have been observed so far. Further investigations are needed to get closer to the final integrated charge requirements proposed for the longevity study of the present CMS RPC sub-system.

5.3.2 The quest for eco-gas

In CMS the RPCs are operating in avalanche mode in order to keep the total produced charge low, which benefits aging and rate capability. In the past, an extended R&D activity has been performed to define the optimal gas mixture: $C_2H_2F_4$ (tetrafluoroethane or R134a) 95.2%, iC_4H_{10} 4.5%, and SF_6 0.3%, that allows us to prevent the transition from avalanche to streamer modes while keeping the detection efficiency above 95%. Recent European regulations de-

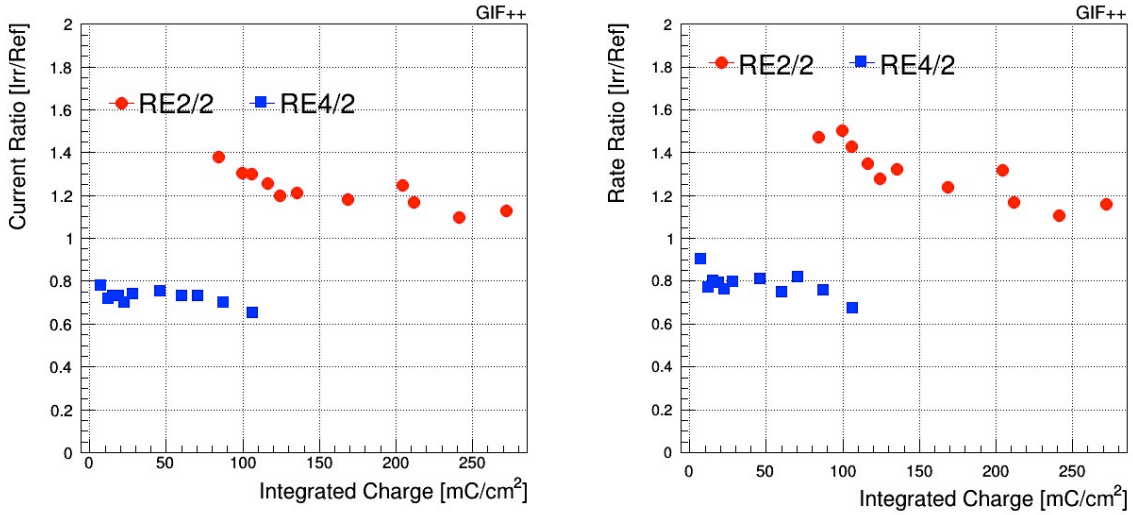

Figure 5.7: Current ratio between irradiated and non-irradiated reference chambers as a function of the integrated charge (left). Rate ratio between irradiated and reference chambers as a function of the integrated charge (right). Red circles correspond to RE2/2 chambers, blue squares to RE4/2. The difference in the ratio between RE2/2 and RE4/2 chambers is due to the different relative position of the chambers with respect to the reference chambers.

mand the use of environmentally un-friendly gases to be limited. The Global Warming Potential (GWP) of the present CMS RPC gas mixture is around 1400, mainly driven by the R134a gas. For this reason, an extensive R&D program [74] has been started inside the CMS RPC collaboration, and in collaboration with the ATLAS groups, in order to find a replacement for R134a and eventually for SF_6. For the present system, important constraints have to be considered: the front-end electronics use a discriminator threshold corresponding to about 150 fC. Lowering this value would increase the electronic noise to unacceptable levels; the high voltage boards are limited to 12 kV which is therefore the maximum possible operation voltage.

An overview of potential gas candidates can be found in Ref. [75]. Most promising gas mixtures are presented in the following sub-section.

5.3.2.1 Search for eco-friendly gas mixture for RPC operations

Two gases with low GWP have been identified as possible substitute of the $C_2H_2F_4$: Tetrafluoropropene ($C_3H_2F_4$, commonly known as HFO-1234ze with a GWP$\sim$6) and CF_3I (GWP$\leq$1). Both gases have a big impact on the reduction of the avalanche charge and, for a defined electronics threshold, move the working voltage to values above the RPC power system limits. So the approach has been to add a fraction of CO_2 to the gas mixture in order to be able to work at not so high HV values. A fine tuning of the percentage of each gas component is fundamental to reach the best performance for such gas mixtures.

Results presented in this section have been obtained with a 2 mm wide single-gap RPC; they are compared with results obtained with the current CMS RPC gas mixture in a single-gap RPC. For a double-gap RPC as used in CMS the working point is expected to be 200–300 V lower. Tests with a standard double-gap CMS RPC are in preparation to confirm the present results.

In Fig. 5.8 (top) a gas mixture in which the tetrafluorethane is replaced by different combinations of the new HFO-1234ze gas and CO_2 have been tested. Increasing the fraction of HFO-1234ze with respect to the CO_2 moves the working voltage to higher values but reduces the streamer probability (defined as the fraction of events with an induced charge above 20 pC) at the working point. The most interesting gas mixture is composed of 45% of $C_3H_2F_4$, 50% of CO_2, 4% of iC_4H_{10} and 1% of SF_6.

The results in terms of efficiency and streamer probability are more than satisfactory with a streamer probability below 10% and a working voltage just at the edge of the power system limits. Further tests fine-tuning the gas component fractions are in progress with the goal to find the best compromise between the working point and the fraction of acceptable streamers.

Very interesting results have been produced with CF_3I and CO_2 based gas mixtures as shown in Fig. 5.8 (bottom). Here the working point is below 10 kV, and efficiencies of about 90% are obtained with streamer probabilities around 1–2%, which is an acceptable value. For this gas mixture the separation between the avalanche and streamer regime is not very high, requiring further tests to fine tune the different fractions. Another drawback is the high price of CF_3I as of today. It is likely that once the industrial use of CF_3I will increase, its price will decrease on the time scale of the Phase-2 operations. More details on the results of the tests can be found in Ref. [74].

The R&D program is ongoing with the plan to define by the end of 2017 the optimal gas mixtures to be tested at GIF++. It has to be considered that in all the tested mixtures the total charge generated is larger than that generated by the standard CMS RPC gas mixture and that the plateau region with efficiency above 90% and with streamer probability below a few percent is narrowed with respect to the standard CMS RPC gas mixture. Careful validation of the RPC performance has to be carried out at GIF++ to study the aging and the rate capability.

The quest for a suitable eco-friendly replacement is a multi-parameter problem that has to take into account several aspects, flammability/toxicity/handling hazards, matching with available electronics and, last but not least, compatibility with the materials used in the muon detectors. So, in parallel to detector performance studies, the materials compatibility is also investigated.

The properties of materials used in the RPC detectors are compared before and after exposure to candidate ecogases in standard operating conditions. To expedite the aging process, materials samples are exposed to candidate gases in a pressurized detector. Preliminary results for RPC bakelite samples exposed to HFO-1234ze gas at 2 bar for 6 months show no difference in infrared spectrography analyses with respect to unused samples.

In conclusion, an ecological gas mixture reproducing the same RPC performance as that of the standard gas mixture and at the same working voltage, has not been found at this moment. Some possible replacements have been identified with performance not too far from the requirements. Further investigations and tests will be performed at GIF++. In order to work in a safe way up to the maximum HV limit of 12 kV, further extensive tests on the HV connectors have been planned.

Should the outlined R&D program reveals no acceptable ecological gas mixture, a three-fold mitigation strategy would be adopted. Firstly, reduction of the RPC leakage. Currently, the RPC system leaks about 1100 l/h (100% of the exhaust rate) due to few leaking chambers in the barrel (47 out of 480). We plan to repair some of them during the year technical LHC stops, when we will have access to the wheels. The remaining leaking chambers will be disconnected after having evaluate the impact on the trigger and reconstruction. Secondly, a recuperation system for the CF_6 and $C_2H_2F_4$ would be developed and installed allowing re-use of the RPC

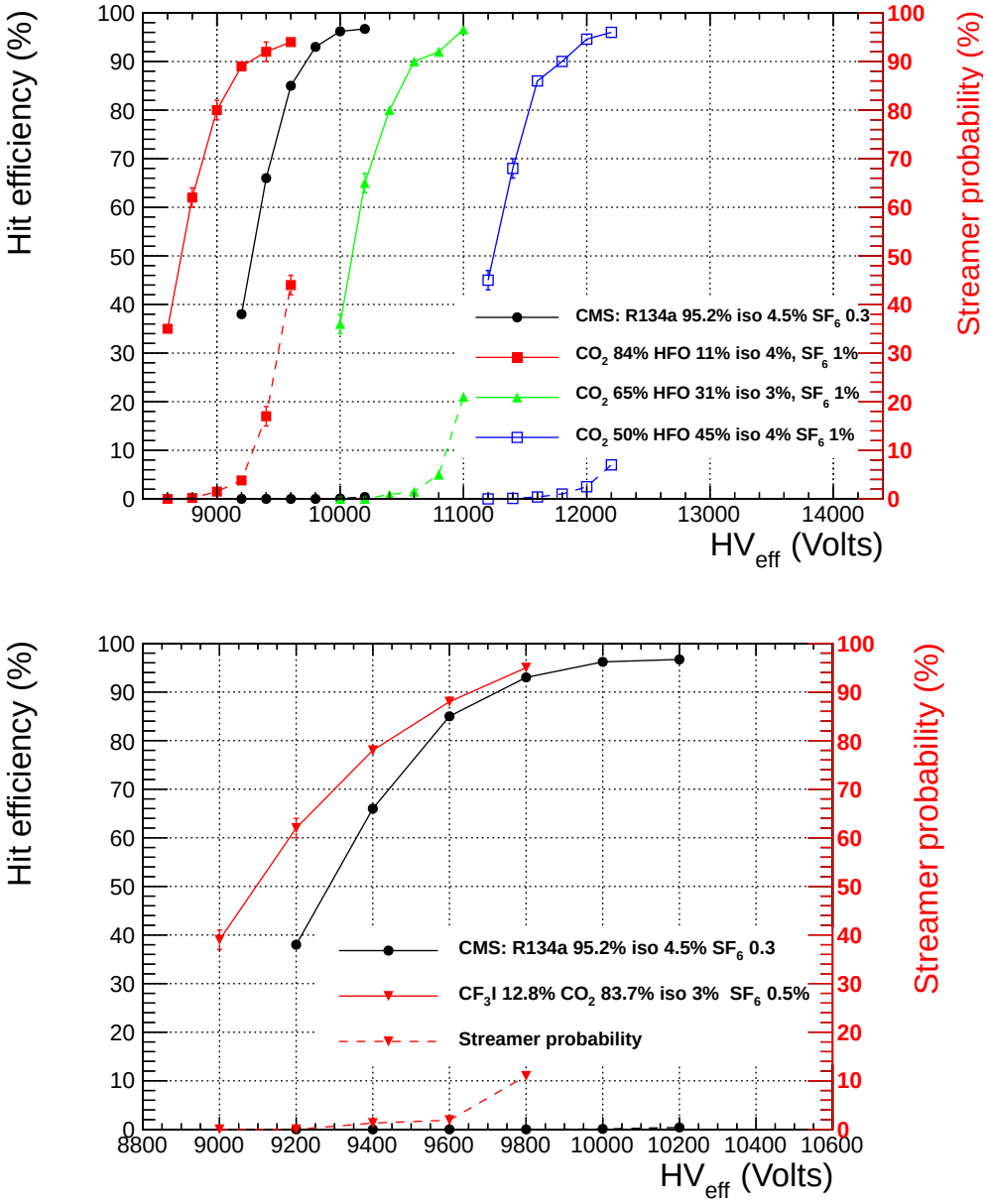

Figure 5.8: Hit Efficiency (solid line) and streamer probability (dashed line) as a function of the effective working voltage for gas mixtures with different combinations of HFO-1234ze gas and CO_2 (top), and for the mixture based on CF_3I and CO_2 (bottom). The results are compared with the present RPC CMS gas mixture. The streamer probability is defined as the fraction of events with an induced charge above 20 pC.

exhaust gas. Finally, a commercial abatement system to burn off the RPC exhaust gas will be considered. These units are commonly used in the semiconductor industry and several manufacturers are available.

5.3.3 The RPC link system

While the RPC detectors have an intrinsic time resolution [76] of the order of 1.5 ns but the link system records the RPC hits information in steps of one Bunch Crossing BX (25 ns), degrading

the full timing resolution of the detector.

The main motivations to improve the timing resolution of the link system and how it could be implemented, will be described in Section 5.4. In this section a description of the weaknesses of the hardware of the present system will be reported.

The link system was produced between 2006 and 2007, and has been working non-stop since its installation in 2008. For the RE4 station new boards were produced in 2012, with some improvements that will be described later.

The system consists of custom electronics boards containing many different devices: both Link Board (LB) and Control Board (CB) are based on the Xilinx Spartan-3 FPGAs; CB contains additionally radiation-tolerant (FLASH based) FPGA Actel ProAsicPlus. The system has worked very well during the LHC operation, causing only a small fraction of luminosity lost, but there are weak points to consider in view of the operation at the full HL-LHC luminosity for many years:

- Single Event Upsets (SEUs): during Phase-1 operations the ionizing radiation levels on the detector balconies have been relatively low, therefore it was decided to use in the LBs and CBs the SRAM based FPGAs which are vulnerable to SEUs. During operation, SEU-like problems can be detected by the online software: a frequency of one error per few days (for the full system) has been measured during Run 2. To avoid accumulation of the radiation induced SEUs the firmware is reloaded periodically (every 10–30 min). Additionally, the CB logic was implemented using the triple redundancy technique [77]. These methods worked well and we have not observed any significant impact of the SEU on the system performance. Nevertheless the vulnerability of the SRAMs to SEUs could became an issue when the luminosity will reach 5×10^{34} cm^{-2}s^{-1}.
- Spare Boards availability: with increasing age of the system we expect an increase of the board failures. A board failure can become a problem because of the limited number of spare boards available. The new RE4 boards have been produced adding an internal LV regulator to protect the board by damaging due to power on and off sequences observed during Run 1. Only few of RE4 spares are available, the old boards cannot be used for the RE4 and new boards cannot be produced because the required ASICS chips are not available anymore. For the rest of the system, about 8% spares are still available. A board failure can be caused by excess of temperature, current, or voltage. High-temperature operating Life tests have been performed by the Xilinx company in order to estimate the failure rate of the FPGA devices. From these tests, few FPGA chips failures can be expected during the next 20 years of operation of the RPC link system (it contains in total 2860 Spartan III FPGAs). For the other devices used on the LBs and CBs (FLASH memories and ASICs chips: TTCrx, GOL, QPLL, CCU25) such an estimation is not available.
- An ASIC receiver (TTCrx) has been designed and produced by the CERN electronics group in order to receive and decode the optical signal. It supplies to the front-end electronics the main signals (LHC Clock, L1A, broadcasted or individually addressed commands) with an 80 ps rms jitter and a programmable skew. Since the TTCrx jitter is greater than the maximum allowed jitter of the GOL chip (Gigabit Optical Link), a QPLL chip (Quartz Phase Locked Loop) is also used to reduce the recovered clock jitter. In the current link system, because of internal problems in the TTCrx chip, sometimes after the TTCrx hard reset, the de-skew of one of the output recovered clocks is not properly set. In this case the synchronization window in the

given link board is shorter and therefore the corresponding chamber is less efficient. Although the current online software is able to detect this problem and can fix it by resetting the affected TTCrx in the TTCrx reset period, it is not so straightforward to block these corrupted data. This problem can be more pronounced when it is necessary to reduce the timing window to improve the time resolution of the system.

- The Control Board has an additional limitation because of the CCU25 chip. Twelve CBs are connected into one token ring configuration. One ring is responsible for one detector tower, i.e. half of the barrel wheel or half of two endcap disks (18 towers in total). If one CB fails then the entire ring does not work, leading to a loss of a significant part (1/18) of the system. Moreover, the identification of the malfunctioning board is difficult and time consuming, preventing prompt repair during any short break of the LHC operation. The CBs are connected to the token rings by copper cables, some of them being over 10 meters long. Therefore, the ring operation can also be disturbed by electromagnetic interference which results in errors during the software read or write operations. In Run 2, a method for auto-recovery after token ring errors was implemented in the control software. Thereafter, the rate of CCU25 errors has been relatively low, but it can still result in a problem with the reconfiguration of the running Link System.
- In each Master Link Board the GOL chip is used for serializing data and converting them to optical signals. The rate of output optical signals is 1.6 Gb/s. This rate is slow for modern optical receiver interface and fiber optic channels. In the future, optical receivers might not be able to receive data at this rate.
- The CB and LB firmware has not been recently updated, the new VHDL compilers do not support the old chips, and the old compilers do not run on new computers.

5.4 Upgrade of the RPC link system

5.4.1 Performance motivations for a new link system

As described in the previous section, the present link system cannot be maintained in the long term. Hence, a new link system is needed in order to maintain the robustness of the RPC readout. In addition, the upgrade will provide us with an opportunity to fully exploit the excellent intrinsic timing capabilities of the RPC detectors at both trigger and reconstruction levels by changing the RPC signal sampling frequency from the present 40 MHz (25 ns) to 640 MHz (1.6 ns). The much higher accuracy in detecting RPC signals will help suppress out-of-time background. Among the main contributors to this background are neutron-induced hits (see Chapter 2), cosmic ray muons, and beam halo muons. The much better timing will also enable new BSM physics search opportunities, such as a search for slow-moving muon-like particles, to be referred to as Heavy Slow Charged Particles, or HSCP.

The gain in timing accuracy that the upgraded link system brings is illustrated in Fig. 5.9. The figure (already shown in section 1.5.1) shows that the time resolution achievable using RPCs with the upgraded link system is about a factor of two better than the DT and CSC detectors alone can provide.

The excellent timing information coming from RPCs with the upgraded link system will play critical roles in the future HSCP searches both at the trigger and reconstruction levels, as described in Sections 7.1.4.2 and 8.2.2, respectively. Here, we just note that, in Phase-1, no dedicated HSCP triggers using timing information are available, and such limitations effectively do not allows to search for particles moving with velocity smaller than $\sim$0.6 times the speed of

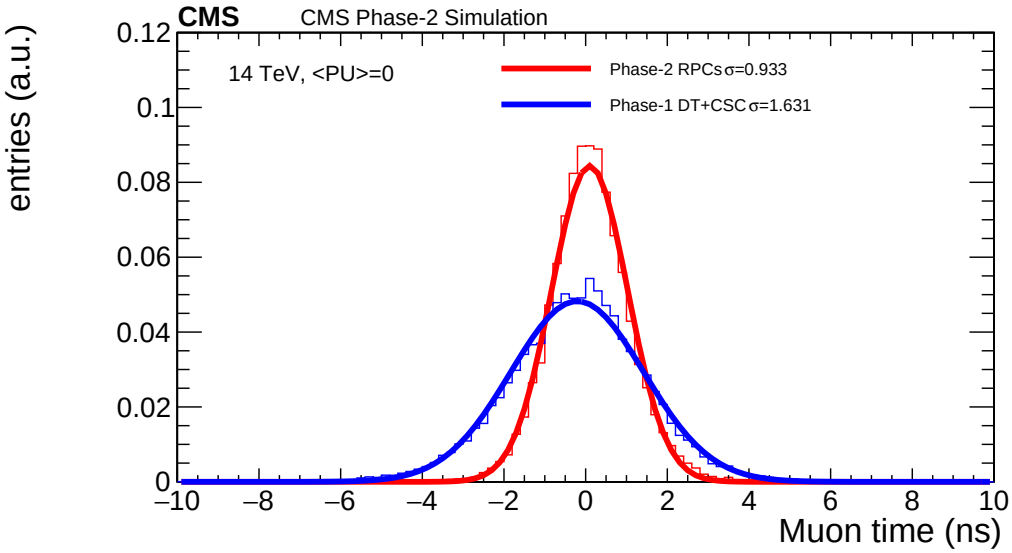

Figure 5.9: Time residuals between reconstructed and true times associated with a muon for the case when one uses the CSC and DT detectors alone (blue) and for the case of RPCs with the upgraded link system (red).

light. As shown in Section 7.1.4.2, the upgraded link system can extend the search range down to velocities of ∼0.25 times the speed of light.

5.4.2 The new link system design

The upgrade of the link system involves a replacement of LBs and CBs only. The legacy RPC Link Boxes will stay; so will all LVDS cables running from the RPC chambers to the Link Boxes. The new LBs will have the same dimensions, the same backplane connectors, and the same pin assignment on the backplane connectors (RPC strip signals, LV, and I2C channels for the FEB controls) as in the current system. The present-day technology allows one to absorb the functionality of most of the chips in the present link system (CCU, TTCrx, GOL and QPLL ASICs) into FPGAs. Moreover, FPGAs can be easily reprogrammed to accommodate future algorithmic modifications.

The functional diagram of the new link system is shown in Fig. 5.10. Each Control Board and nine Link Boards (three master and six slave LBs) are connected via a front plane board (dashed box in the figure) as in the present system. The CB communicates with the Run Control and Monitor System (RCMS) in control room through its radiation mitigated GBT link ASIC and GBT-FPGA controller located in USC. The front plane also distributes the clock to the master and slave LBs. Each master link board synchronizes its RPC signal inputs to the bunch crossing number, compresses and concentrates them with the data received from its two adjacent slave link boards (slave LB left and right) and send them out through the chain of the hardware transceiver built-in FPGA GTX and the new radiation hard SPF+ module, i.e. VTRx+, at the rate of 10 Gbps to the muon trigger system via optical splitter.

The weakest point in the current link system is the Control Board CCU chip which relies on the token ring logic. In this scheme a communication failure with a single board prevents communication with the entire system. Moreover, it is not immediately obvious which board is actually at fault. This problem will be resolved in the new system by using a high speed

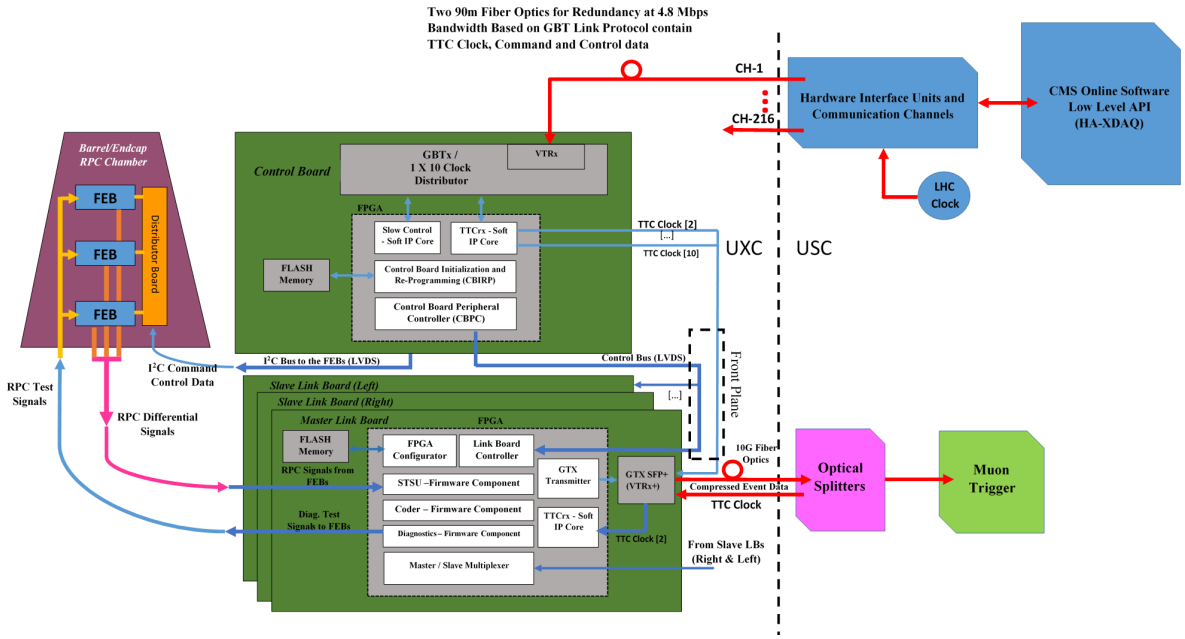

Figure 5.10: Functional diagram of the new link system.

switch board connecting each CB in parallel to the RCMS via GBT link. This will also improve the data transmission rate from 40 Mb/s to 100 or even 4800 Mb/s.

The main tasks of the GBTx chip on the CB are the following:

- Provide a robust bidirectional communication channel against noise and interference based on GBT link protocol for diagnostic, slow control command and TTC clock;
- provide a safe channel for remote programming of FPGAs;
- distribution of the TTC clocks through robust channel against jitter noise.

The entire functionality of the TTCrx chips in LB and CB will be implemented via a combination of GBTx and FPGA's firmware. The GOL chip is replaced with a high speed transceiver in FPGA.

In the new link system, many features such as timing detection, digitization of fired strips or clusterization of consecutive strips corresponding and calculation of center and width of clusters are implemented into the Link board FPGA.

The timing digitization of the fired strips is implemented making use of the state-of-art TDC techniques. The implementation of TDC based on high speed serializer built-in on each FPGA's I/O pin has many advantages such as reducing the overall logic resources and power consumption of the FPGA chip. It is noteworthy that the serializer is a built-in ASIC unit in FPGA which is more radiation tolerant relative to the other parts of FPGAs that controlled with SRAM based configuration bits. This future lead to improve the functionality of the TDC block against radiation effects like single event upsets.

The functionality of the new link system, is largely based on FPGAs (the present baseline is to use Xilinx 7 series FPGAs). Although the expected radiation dose accumulated over the lifetime of HL-LHC (3000 fb^{-1}) at the link system location is expected to be about 3 kRad, which is safely below the maximum recommended doses, we, nevertheless, foresee implementing

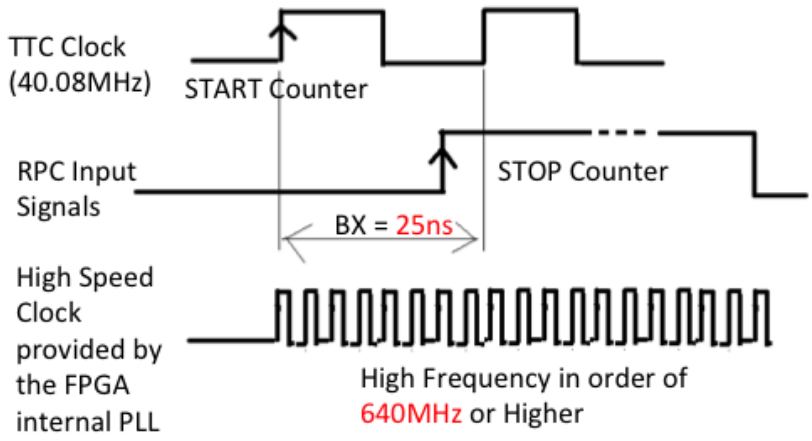

Figure 5.11: Method for achieving the 1.562 ns time resolution in the new link system.

a number of suitable SEU mitigation measures and performing extensive tests of prototype boards in the HL-LHC-like radiation environment. For SEU mitigation, the firmwares will be designed using the Triple Modular Redundancy logic and Configuration Memory Scrubbing. In addition, the built-in Error Correction Code (ECC) feature in FPGAs Block RAM memory will be used to protect data integrity.

It is worth noting that besides the above features the main handle to protect the new link system against radiation effects will be provided by remote configuration of Kintex FPGAs via online control software through optical interfaces and the GBT link system.

In summary, the upgraded link system (LBs and CBs) will resolve various operational deficiencies of the present RPC DAQ system and allow one to improve dramatically the muon reconstruction time resolution. The schedule toward the final design of the new link system is shown in Figs. 5.33 and 5.34 (Section 5.8).

5.4.2.1 Quality assurance and quality control of the link system

In order to assure that the new boards for the link system upgrade will successfully work in the harsh HL-LHC radiation environment and to guarantee their functionality for the entire period of running, the following steps are planned:

- The longevity of prototype boards is ensured by systematic exposures of all parts to TIDs at least three times larger than the expected doses. An irradiation campaign with neutrons and protons is planned at the Tehran research reactor and Karaj cyclotron (Iran), collecting an integral dose of at least 3 kRad.
- The functionality of all produced boards will be systematically verified at IPM (Tehran) performing the following tests: tests against changes of temperatures and operating voltage, noise injection tests, Electromagnetic Immunity and Compatibility tests (EMI and EMC), Electrostatic Discharge (ESD) tests; tests of linearity and maximum throughput of the boards and fiber optic outputs for increasing input signal rates.
- After the boards are shipped to CERN, the functionality will be re-tested in building 904. These tests will include a burn-in period of 24 hours with constant monitoring of voltages and temperatures.

5.5 Extension of the RPC system

5.5.1 Motivations

The high pseudorapidity region is the most challenging region for muon triggering, identification, and measurement in CMS and at all hadron colliders in general. Presently, CMS lacks redundancy in this region, where background is the highest and the magnetic field integral is low. The muon upgrade program enhances the muon system robustness in this region by installing additional detectors in the high $|\eta|$ region.

New improved RPCs (*i*RPC) chambers will be installed in stations 3 and 4 (RE3/1 and RE4/1 in Fig. 1.4), complementing the already existing CSC chambers there. This detector upgrade is driven by the necessity to increase the number of hits per muon track up to $|\eta| = 2.4$. By reading out signals from both ends of the RPC strips, excellent time resolution of ∼1.5 ns, and much improved hit localization in the radial direction (∼2 cm) can be achieved.

The CSC system can identify and trigger muons in the endcap region with a high efficiency. Nevertheless, even for a perfectly working system, there are "dips" of reduced trigger efficiency at some values of $|\eta|$, due to the presence of high-voltage spacers inside the CSC chambers. Including RPC hits into the trigger primitive stub finding algorithm helps eliminate these dips. Figure 5.12 shows the efficiency of finding trigger primitive stubs at the level of station 3 and station 4, with and without the addition of the current RPC and new *i*RPC information in the EMTF. The overall impact of the inclusion of RPC hits into the single muon trigger can be seen in Fig. 5.13 (already presented in Section 1.6.1) showing the single muon trigger efficiencies with and without the use of the RPC information. A clear improvement at the level of 15% can be seen between $|\eta|$ = 2.1 and 2.2. In case of any CSC trigger problems in ME3/1 and ME4/1, additional improvement would be expected.

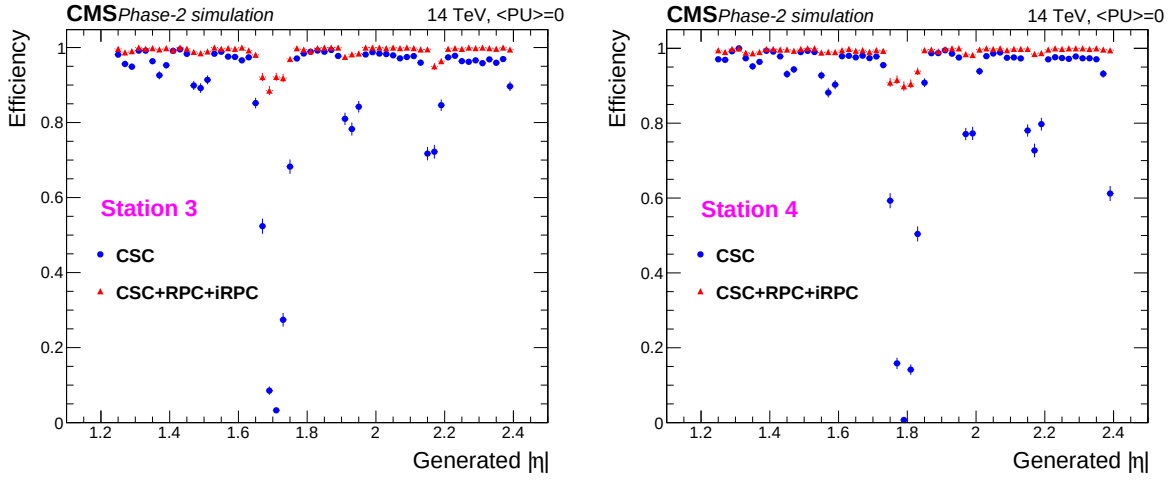

Figure 5.12: Impact of RPC hit inclusion on the local trigger primitive efficiency in station 3 (left) and station 4 (right). The contribution of *i*RPC starts above $|\eta|$=1.8.

RPC information will also be used to remove CSC ambiguities at the L1 trigger, when additional tracks are present in a CSC chamber crossed by a muon. CSCs have 1D strip and 1D wire readouts. This leads to "ghosting", a combinatorial background in presence of multiple tracks. By extrapolating the experience from the present LHC operation to the HL-LHC luminosity, we find that the chance to have a spurious Local Charged Track (LCT) inside a given ME3/1

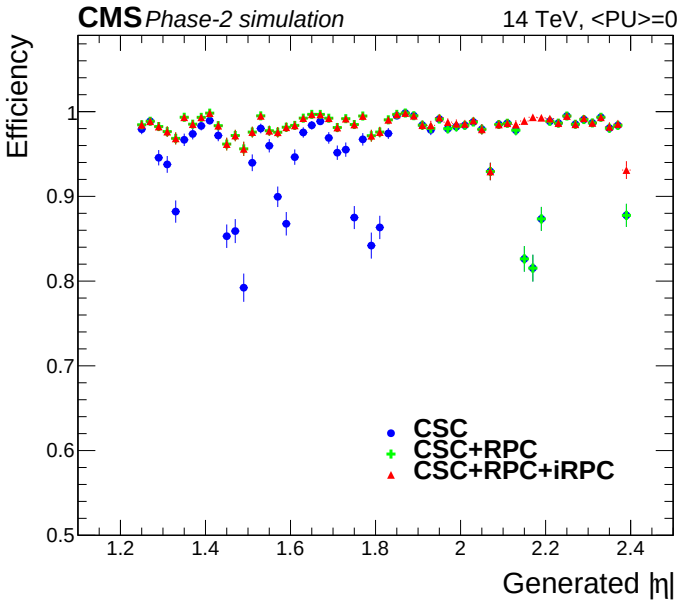

Figure 5.13: Simulated comparison between the L1 single muon trigger efficiencies with and without the RPC information, as a function of $|\eta|$. The contribution of iRPC starts above $|\eta|$=1.8.

or ME4/1 chamber, is about 13% per bunch crossing. In the presence of a real muon, these extra ghost LCTs can result in a high-p_{T} muon solution in the Endcap Muon Track Finder, even though the actual muon was low-p_{T}. The RE3/1 and RE4/1 chambers will have radial strips readout from both ends of each strip (see Section 5.5.6.2). From the time difference of these two signals, a spatial resolution of the order of a few centimeters is expected along the strip direction, which will allow one to resolve almost all of the combinatorial ambiguity in the ME3/1 and ME4/1 CSCs directly at a single-station level.

The improved timing of the RPC link system (Fig. 1.13) will be extended to the high $|\eta|$ region with RE3/1 and RE4/1. Being able to trigger on and reconstruct slow-moving particles in this region will help improve the HSCP search sensitivity as explained in more detail in Section 7.1.4.2.

5.5.2 Extended system design and overview of the requirements

The two new RPC stations, RE3/1 and RE4/1, will cover the $1.8 < |\eta| < 2.4$ region, complementing the already existing CSCs in that η range in stations ME3/1 and ME4/1, as shown in Fig. 1.4. A schematic view of the RE3/1 chamber position on the disk and a detail of the RE3/1 chamber mounted on it are shown in Fig. 5.14.

According to FLUKA simulations, the maximum hit rate of about 700 Hz/cm^2 is expected in the hottest points of the new RPC stations (Fig. 5.15). By including a safety factor of three, the requirement for the new chambers is to withstand 2 kHz/cm^2.

The resolution requirements for these two stations are similar to those of the rest of the RPC system: time resolution of the order of 1.5 ns, while for the spatial resolution a slightly finer ϕ segmentation of 0.2° is motivated by the lower bending power of the magnetic field in this region. This corresponds to strips with an average pitch of 1 cm, about a factor of two smaller than the average strip pitch of the chambers in the present endcap RPCs at $\eta \sim 1.6$–1.8. As previously mentioned, the resolution of few centimeters in the radial direction will help to

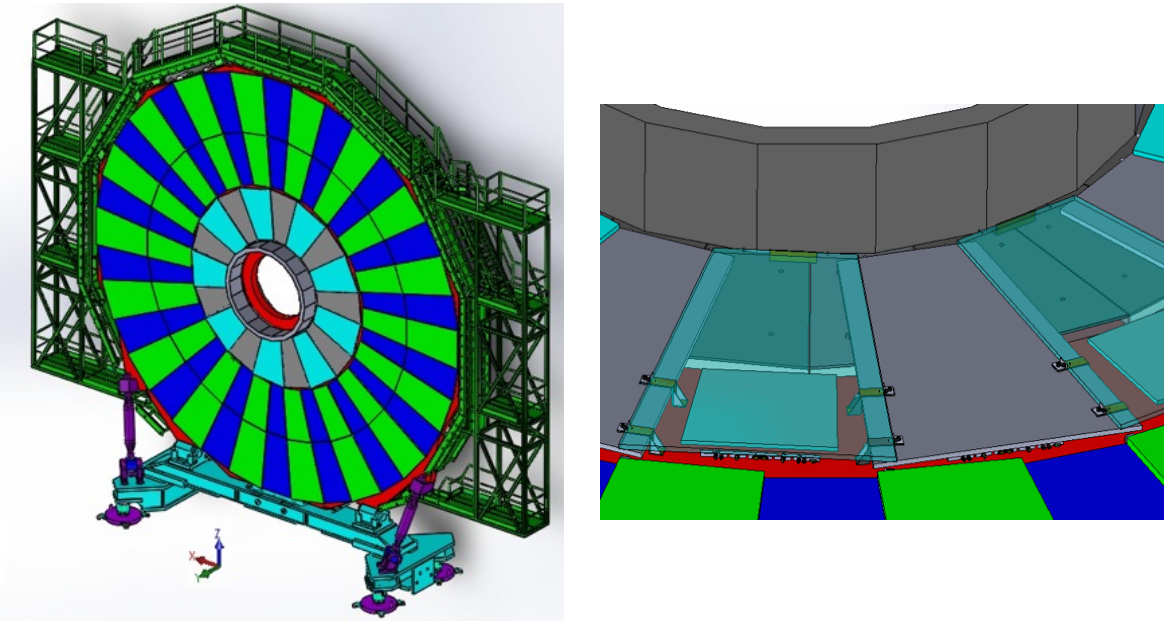

Figure 5.14: Schematic view of the RE3/1 chambers mounted on the endcap disk (left). Detail of one RE3/1 chamber mounted on the yoke (right).

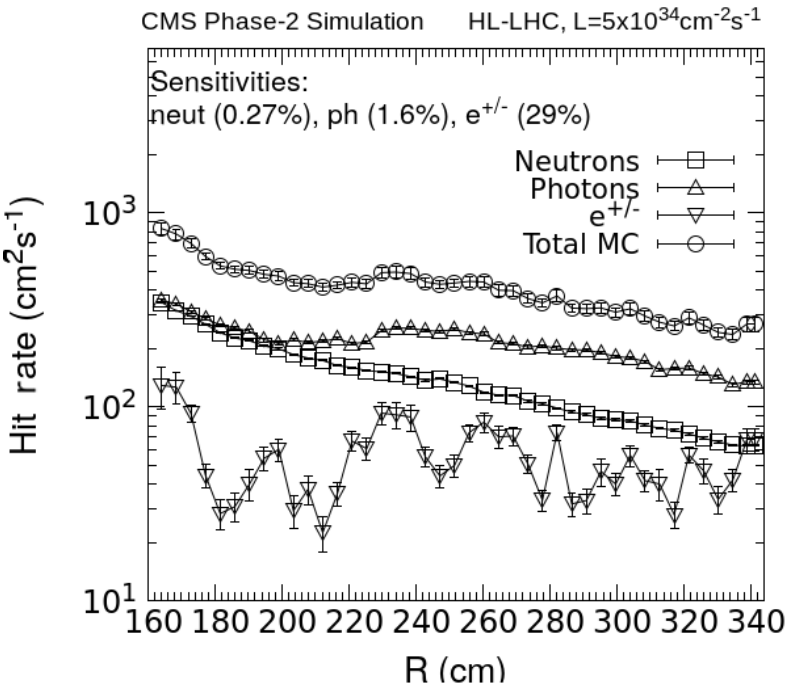

Figure 5.15: Expected hit rate due to neutrons, photons, electrons and positrons at the HL-HLC luminosity of 5×10^{34} cm^{-2}s^{-1} in the RE3/1 chambers. In the upper part of the figure the sensitivities used in the simulation for each particle are also reported. The expected hit rates in RE4/1 are similar.

resolve CSCs ambiguities when several muons cross the same chamber.

To fulfill all these requirements, while maintaining a hit efficiency above 95% in this region, an improved version of RPCs has been developed and will be described in Section 5.5.3. From the design point of view, the chambers will be similar to the existing wedge-shaped RPC detectors, each spanning 20° in φ with radially oriented readout strips. Thus, the iRPC project adds 18 new chambers per muon disk, or 72 chambers in total for the RE3/1 and RE4/1 stations in both endcaps. Each station will provide one single hit for muon reconstruction with precise time information ($\sim$1.5 ns) and spatial resolution at the level of $\sim$0.3 cm (perpendicular to strips) and $\sim$2 cm (along strips).

As in the present system, iRPCs will be double-gap detectors with signal pick-up strips in the middle. In this case, the strips are embedded in a readout board made of two parts; a large trapezoidal Printed Circuit Board (PCB), containing the signal pickup strips, and a front-end board containing front-end electronics. The PCB hosts 96 strips with a pitch of about 12.3 mm (10.9 mm) at the lowest $|\eta|$ position, and approximately 6.0 mm (5.9 mm) at the highest one, for the RE3/1 (RE4/1) chamber. Table 5.2 gives a summary of the geometrical parameters of the RE3/1 and RE4/1 chambers.

Table 5.2: Summary of the geometrical parameters of the RE3/1 and RE4/1 chambers.

Chamber	R_{in} (mm)	R_{out} (mm)	Area (m^2)	Number of strips	Average strip pitch (mm)
RE3/1	1527	3192	1.39	96	9.15
RE4/1	1770	3140	1.19	96	8.4

Dielectric layers separate strips from anode planes in each of the two RPC gaps. The thickness of the dielectric layer and its dielectric constant define the final impedance of the strips. Both ends of each strip are connected (through coaxial cables of the same impedance) to two different channels of the front-end chip located on the front-end board.

The readout strips of each chamber of the present system are split into two or three partitions (the number depends on the station position) along the strip length and are connected to an independent front-end board, giving an η resolution of about 20 cm. Each of these separated sections are called η partitions. To maintain the same η resolution also for the RE3/1 and RE4/1 chambers, five η partitions should be implemented. The new readout scheme reduces the number of electronic channels by 60%, while providing a better spatial resolution in η. This new layout scheme has the additional advantage to facilitate the cabling layout and the chamber construction as the strip signals have to be taken just from two sides of the chamber and not from several different η partitions.

The probability of a double hit on the same strip, spoiling the muon time and y-coordinate measurement, has been estimated to be about 0.6%. The main assumptions for this estimate are:

- Average rate in RE3/1 and RE4/1 about 500 Hz/cm^2;
- safety factor of 3;
- cluster size of 2 and surface of one strip 158.4 cm $\times$ 0.87 cm.

With such assumptions we expect to have 380 000 hits per second and the average time interval between them is 2600 ns. The duration of the signal is about 10 ns (this is also the maximum time for a signal to travel across the strip). The electronics introduces almost no additional dead time (lower than 1 ns). The TDC clock is 2.5 ns and a dead time of two periods is considered (5 ns).

Therefore if two signals arrive in less than 16 ns there will be confusion and the y-coordinate will be not determined adequately. This will happen in approximately only 16/2600 = 0.6% of the cases.

The RPC hits with this spatial resolution along the strip direction will be used at trigger level to improve the measurement of the θ direction of the level-1 muon candidates and to solve the ambigiuties in the CSC hits when several muons cross the same chamber (see Section 7.1.2.3).

Figure 5.16 shows a schematic view of a front-end board and on-chamber connection cables. The front-end board (green in the figure) is placed close to the larger side of the RPC. Coaxial cables, red and violet in the figure, connect both ends of strips (not shown) to the chips located on the mezzanine board. Characteristics of the front-end chip and performance of the new RPC readout are presented in Section 5.5.6.2.

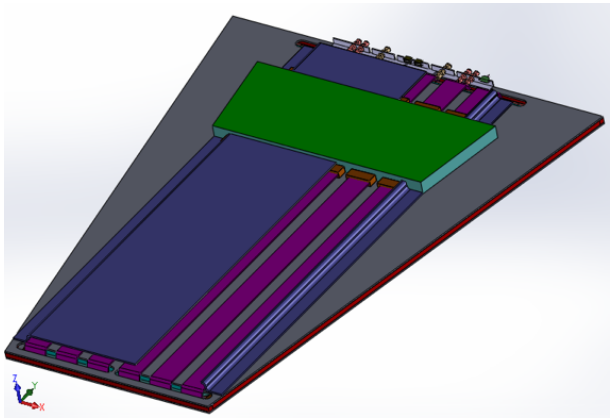

Figure 5.16: A schematic view of the new readout electronics. The front-end board is shown in green. The coaxial cables coming from the two ends of strips (violet cables) are connected to the front-end board through small matching cards (brown). The detector and the PCB with the strips are inside the mechanical structure and are not visible here.

Table 5.3 shows a breakdown of the number of components of the new RPC system (chambers, electronic boards, cables and power supplies). The numbers include all items needed for *i*RPC, adding what is needed for the test stands at CERN and taking into account the expected production yields.

5.5.3 Technology choice

The requirements presented in the previous section can be fulfilled with a double-gap RPC with HPL electrodes and with pick-up strips in the middle. This is the baseline choice for the RE3/1 and RE4/1 detectors. In order to reduce the risk of detector aging, and to improve the rate capability, both the electrode and gas gap thickness are reduced, and part of the amplification is moved to an improved front-end electronics system (described in Section 5.5.6.2).

Improving the sensitivity of the electronics is essential. It allows one to reduce the gap thickness without losing efficiency. The combined effect of improving the front-end electronics and of reducing the gas gap thickness has been shown to effectively reduce the avalanche charge, and so to enhance the rate capability [78] and the chamber longevity.

We examined the pickup charges of the avalanche pulses drawn in six double-gap RPCs, that were constructed with gap thicknesses ranging between 1.0 and 2.0 mm [79]. Figure 5.17 shows the induced charges drawn in double-gap RPCs with different gas gap thicknesses as a function

Table 5.3: Number of components for the RE3/1 and RE4/1 projects.

Item name	Quantity	Production yield	Total
Chamber Components			
Group of four electrodes	72	0.90	85
Chamber mechanics	72	0.90	85
Pair of gaps	72	0.90	85
Chamber cooling circuit	72	0.90	85
Chamber assembly components	72	0.90	85
Front-end electronics			
64-ch front-end ASICs	216	0.7	308
PCBs	72	0.95	80
FE boards	72	0.95	80
64-ch TDCs	216	0.7	308
FPGAs	72	0.7	109
Back-end electronics			
Off-detector boards	12	0.98	14
TCA crates and processing boards	1	0.98	1
Signal and DAQ cables			
Coaxial cables	13824	0.98	14106
Signal cables	288	098	310
Optical fibers	20	0.98	22
HV Power System			
HV crates	4	1	5
48V service cables	8	0.85	11
HV boards	12	1	13
HV distribution boards	8	1	9
HV cables	152	0.85	180
HV connectors	1051	0.85	1238
LV power system			
LV boards	8	1	9
LV crates	4	1	5
LV branchs	2	1	3
LV power cables	72	0.85	90
DCS control optical fibers	72	0.85	90
LV mainframes	3	1	4

of the electric field strength. Electric field values are converted to the effective ones at the reference values of pressure, $P = 990$ hPa, and temperature, $T = 293$ K. The standard CMS RPC gas mixture was used for these measurements. The thinner gap thicknesses more effectively retard the fast growth of the pickup charges of the ionization avalanches as shown in Fig. 5.17. This implies that the use of the thinner gaps will effectively preserve the size of the operational plateau when we lower the digitization threshold to enhance the detection sensitivity [80]. The reduction of the operational high voltage as the result of decreased gap thickness and of the digitization threshold will also improve the robustness of the system. In the baseline design for the *i*RPCs, a thickness of 1.4 mm for both gaps and electrodes is chosen, instead of the 2 mm used for the current CMS double-gap RPCs. Thinner gas gaps would be more sensitive to non-uniformities in the distance between electrodes, and the value of 1.4 mm is a safe compromise.

The electrode resistivity of the High Pressure Laminate plates has been specified to be in the

range from 0.9 to 3.0×10^{10} Ω·cm, which is about of a factor of two less than in the present RPC system.

5.5.3.1 iRPC performance tests: small size prototypes

In order to validate the performance of the thinner double-gap RPC baseline option, small size prototypes (65.6×35.6 cm^2) have been tested at the KOrean DEtector Laboratory (KODEL) with cosmic rays, with gamma radiation from a 5.55 GBq ^{137}Cs source, and without irradiation. In KODEL the RPC prototype has been equipped with a voltage sensitive front-end board with a threshold value of 300 μV. This value corresponds to a charge threshold of about 50 fC, which is lower than the value of the present RPC system front-end electronics by about a factor of three.

Figure 5.18 (left) shows the muon detection efficiency ε_μ and the average cluster size $\langle C_s \rangle$ as a function of the effective Voltage HV_{eff}, measured under different gamma background conditions. The right side of Fig. 5.18 displays ε_μ and the probability to have a cluster size above 6 strips, P(C_s >6). The intensity of the gamma flux impinging on the RPC was defined by adjusting the distance of the detector from the gamma source (triangles and squares in Fig. 5.18, measured at 38 and 28 cm, respectively) and by using a lead absorber (full circles measured with an absorption factor of about 2.5, at a distance of 38 cm). The Working Point (WP) for the 1.4-mm double-gap RPC is defined as the voltage at which the efficiency reaches 95%, increased by 110 V.

The rates, R_{str} (rate of strips) and R_{clus} (rate of clusters), measured at the working point with the largest gamma flux yields (at a distance of 28 cm) were found to be 4.14 and 1.85 kHz/cm^2, respectively. These values are above or close to the maximum of 2 kHz/cm^2 at HL-LHC. The shift of the WP obtained from the data labeled 'no-gamma' (open circles) to the one from the data obtained with the largest gamma flux (squares) was evaluated as 300 V (4% in $\Delta V/V$).

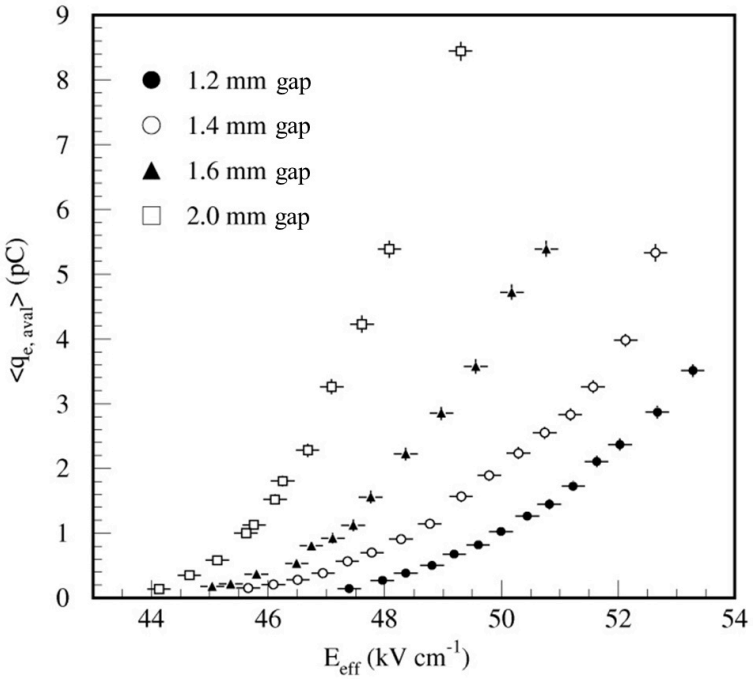

Figure 5.17: Average charge per avalanche measured on 1.20 mm (full circles), 1.40 mm (open circles), 1.60 mm (triangles), and 2.0 mm (squares) double-gap RPCs, as a function of the effective electric field strength.

Figure 5.19 shows the efficiency (left) and the average cluster size (right) at the working voltage, as a function of the cluster rate. The reduction of the efficiency at the rate of R_{clus} = 1.85 kHz/cm^2 was measured to be 2.9%.

These studies show that the impact of the maximum background rate on the RPC performance

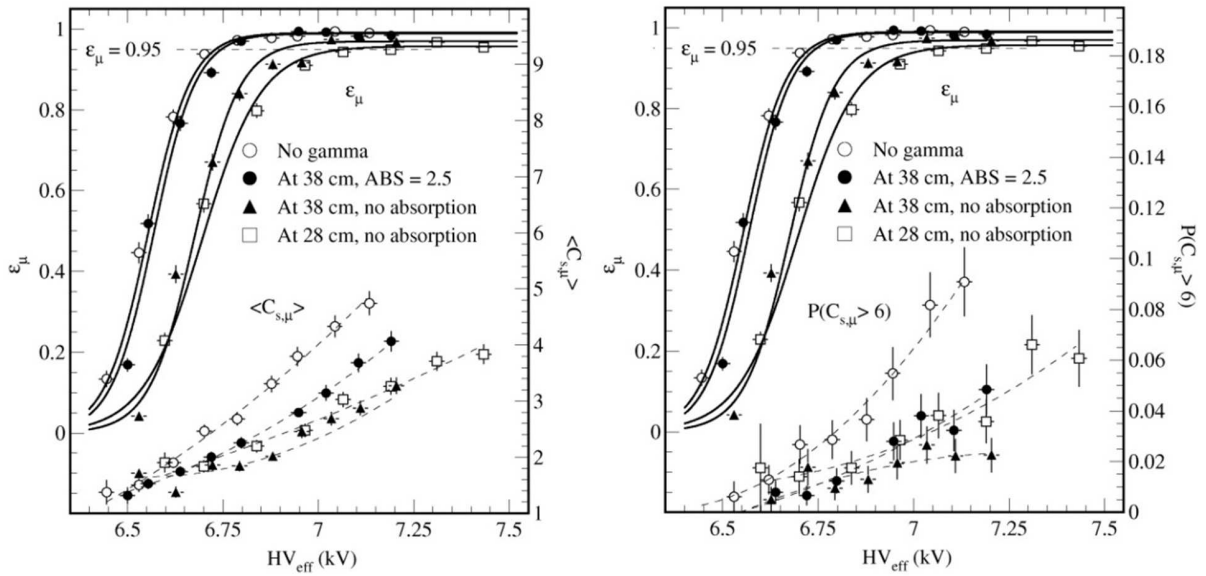

Figure 5.18: Efficiency ε_μ and average cluster size $\langle C_s \rangle$ (left) and ε_μ and P(C_s >6) (right), measured for the 1.4-mm double-gap RPC with a fixed threshold value of 300 μV and with three different gamma fluxes. The details for the data symbols are described in the text.

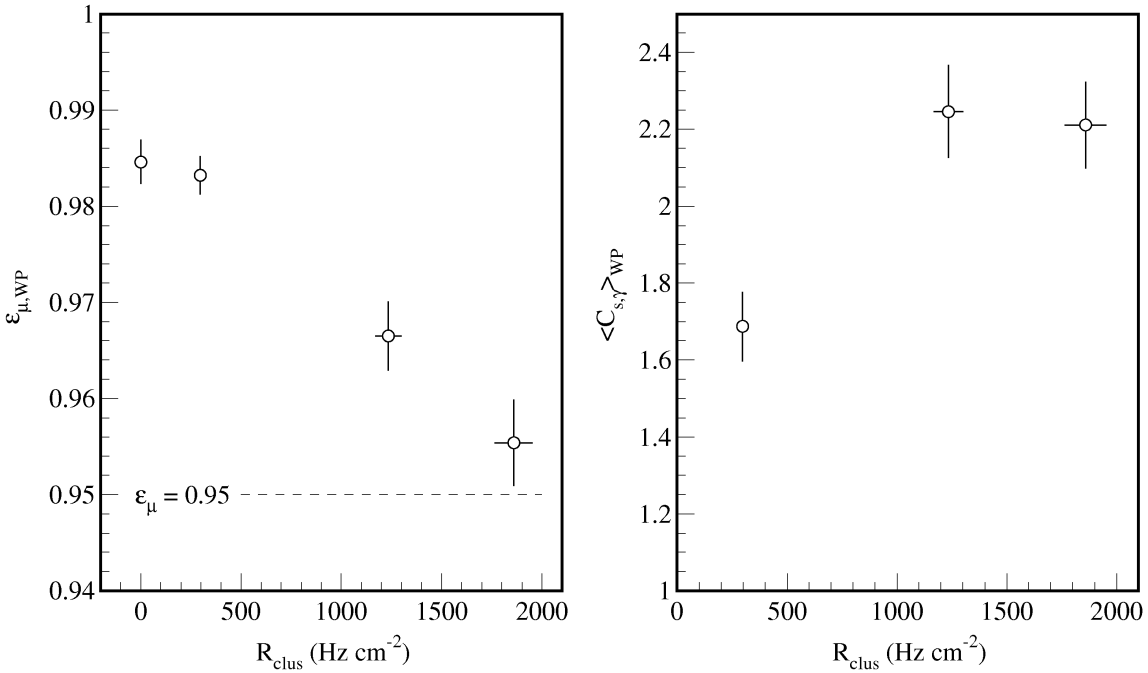

Figure 5.19: Efficiency (left) and average cluster size (right) at the working voltage, as a function of the cluster rate for the 1.4 mm double-gap RPC. The data were measured at the fixed threshold of 300 μV.

is negligible on the detection efficiency (less than 3%), while moving the working voltage by only about 4%. This voltage shift is lower than the avalanche to streamer voltage separation, and we do not expect any deterioration of the chamber performance. It should be noted that an automatic feedback control, tuning online the working voltage as a function of the measured background rate, could be implemented, making the detector operation even more stable. The residual differences in rate for different positions on the same chamber will correspond to working voltage differences below 100 V.

5.5.3.2 iRPCs performance tests: large size prototypes

A large size trapezoidal chamber (larger base 92 cm, lower base 63 cm, and height 166.3 cm) with 2 cm wide strips has been tested at GIF++ with a muon beam to validate the performance under different background conditions. The front-end electronics threshold has been fixed at the same value as in the case of the tests done in KODEL.

In Fig. 5.20 the efficiency and the average cluster size are plotted as a function of the applied effective voltage, in absence of background (left plot) and with a gamma background rate of 1.91 kHz/cm^2 (right plot). The shift in the working voltage is confirmed to be less than 300 V while the efficiency remains slightly above 95% also under the maximum background rate. In spite of the lower front-end electronics threshold, in absence of background the intrinsic noise rate has been measured to be on average about 0.2 Hz/cm^2 and the maximum efficiency is above 98%.

Aging effects of the iRPC system during the full HL-LHC program need also to be taken into account, as discussed in Section 5.3 for the existing detectors. Tests of these large size chambers at GIF++ have been planned in order to accumulate the full charge corresponding to an integrated luminosity of 3000 fb^{-1}, during the second part of 2017 and in 2018.

5.5.3.3 *i*RPC performance with ecological gas mixtures

All previous results have been carried out with the standard CMS gas mixture. In the framework of the R&D program, discussed in chapter 5.3.2, to find an eco-friendly gas mixture an iRPC prototype, approximately 100 cm$\times$50 cm, has been build at KODEL. The readout consists of 32 strips (2.5 cm pitch) equipped with a new electronics developed in the framework of the muon system upgrade of the ATLAS experiment [81]. The low noise electronics is based on Si technology (the amplifier) and SiGe Bi-CMOS technology (the discriminator). Tests comparing the performance of the iRPC with the standard CMS gas mixture and ecological gas mixture have been performed with cosmic rays and muon beam at the GIF++. Based on the previous tests the following ecological gas mixture has been tested: 50% of $C_3H_2F_4$, 4.5% of iC_4H_{10}, 0.3% of SF_6 and 45.2% of CO_2. In Fig. 5.21, the efficiency and the cluster size vs the effective High Voltage has been shown for both standard and ecological gas mixture. The efficiency at working point is consistent for both gas mixtures, with a shift of 1.3 kV as expected from the results of Section 5.3.2.1. Although we measured an increase of the cluster size in the order of one strip. Further tests are ongoing with a fine tuning of the gas composition.

5.5.4 Technological aspects of RPC detector production

In order to maintain a stable and reliable detector operation, the mechanical conformity and the electrical stability of the gas gaps have to be guaranteed in the production phase. In addition, the preservation of the initial detector characteristics for the long term CMS operation was also an important factor to be considered for the preparation of the detector production facilities.

The main production chain has been already successfully implemented [82] during the production of the RE4 chambers at the KODEL laboratory. The same production technologies and facilities will be used for the new RPC chambers (RE3/1 and RE4/1).

HPL panels are produced, cut and cleaned by italian industrial companies and then delivered to KODEL. Thin semi-conductive graphite layers of a mean surface resistivity of about 100 Ω·cm on both the high voltage and ground sides of the gaps are coated by a silk screen

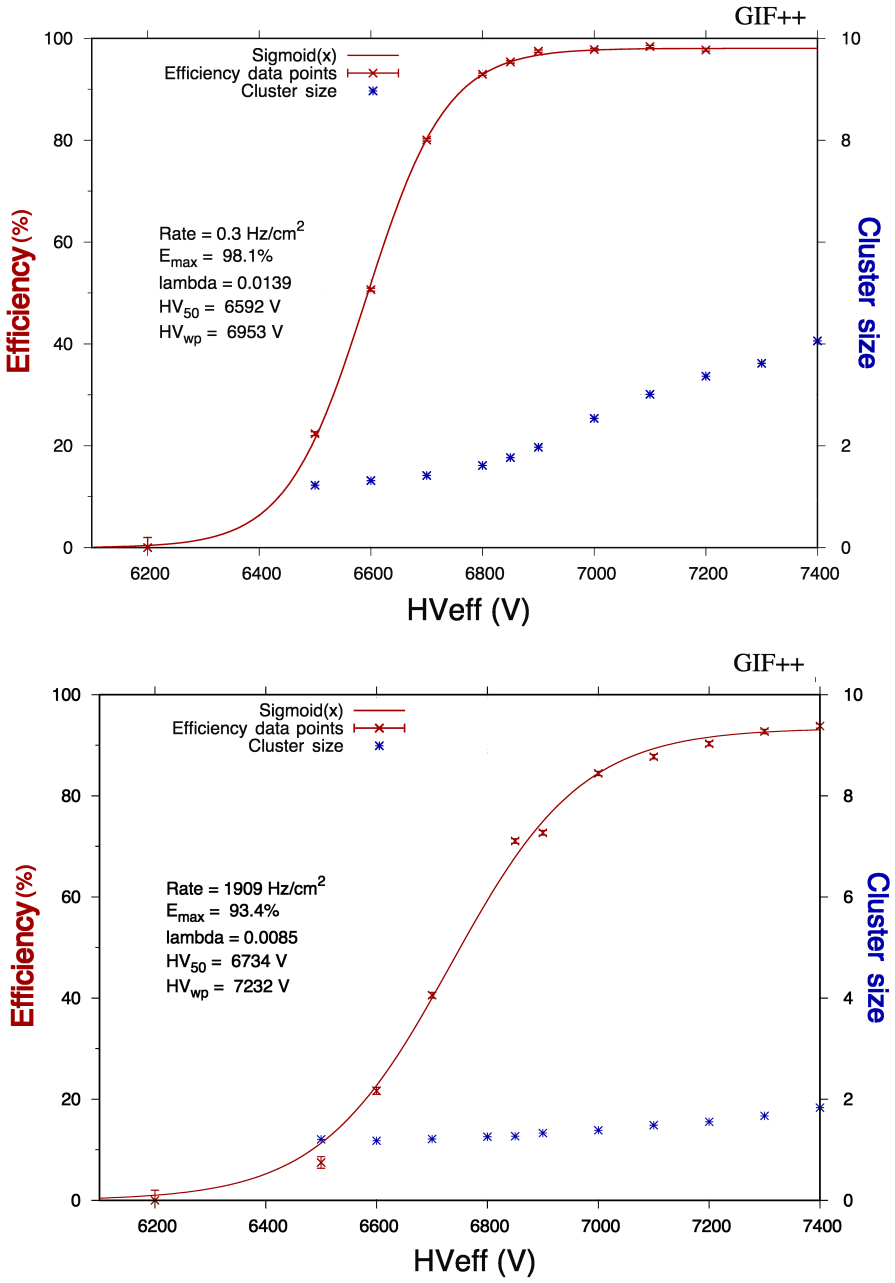

Figure 5.20: Efficiency and average cluster size of a 1.4 mm double-gap RPC large size chamber as a function of the effective voltage, tested without gamma background (top) and under a gamma background rate of 1.91 kHz/cm^2 (bottom). The data were measured at the fixed threshold of 300 μV and fitted with a sigmoidal function.

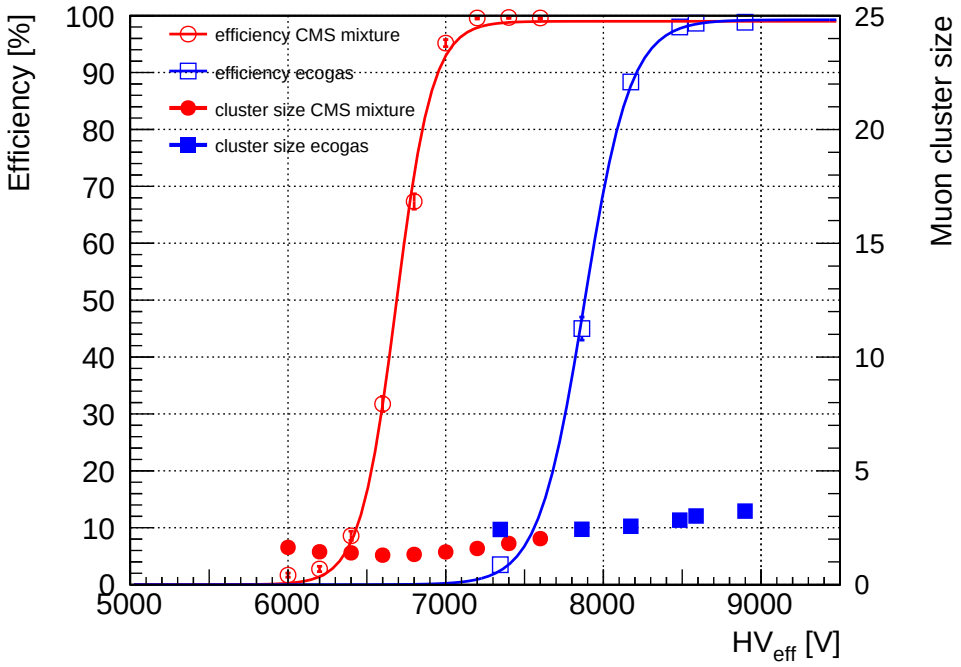

Figure 5.21: Efficiency and Cluster size vs. effective voltage for the CMS gas mixture and an ecological gas mixture.

method. Both sides are then electrically protected by a 190 mm thick polyester (PET) sheet. The thickness of gas gaps is maintained by gluing circular spacers and peripheral edges on the inner surface of the electrodes surface. Finally the sealed gap is oiled using linseed oil to guarantee the smoothness of its surface.

Figure 5.22 shows a silk-screen table for the graphite coating (top left), an electrically controlled device for the PET insulation (top right), optical tables and multi-layered air-pressing tubes ($\sim$ 20 hPa) for the formation of gas gaps (bottom left), and the oil tanks and a pressing device for the oiling procedure (bottom right).

5.5.5 Quality assurance and quality control of iRPCs

The Quality Assurance (QA) and Quality Control (QC) of iRPCs will follow a similar scheme as for the RE4 production. The HPL panels will be produced in Riva Laminati (Milan, Italy), and the gaps in KODEL. The chamber construction and QC tests will be performed in two assembly sites (currently 3 sites are under evaluation). The final chamber certification will be carried out at CERN.

The QC protocols have been standardized and documented since 2010 when the RE4 production was planned [83]. Four levels of QC will be applied: chamber components, HPL gaps, chamber assembly and cosmic test validation at the construction site, chamber long-term performance validation at CERN before installation. For each of them precise acceptance protocols have been defined and will be applied in all sites during mass production [83]. All collected data will be recorded in the RPC construction database.

- QC1 level will be applied to basic chamber components: on-detector electronics, HPL electrodes batch production with control on resistivity level, selection of gas

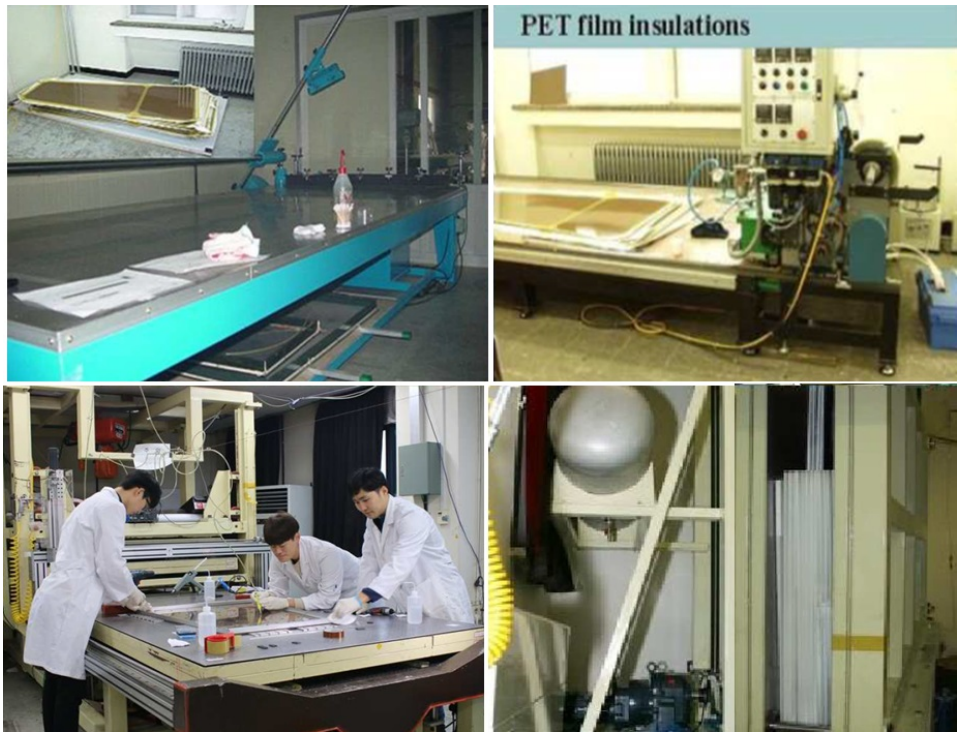

Figure 5.22: iRPC production: a silk-screen table for the graphite coating (top left), a device for the PET insulation (top right), optical tables and multi-layered air-pressing tubes for the composition of gas gaps (bottom left), and oil tanks and a pressing device for the oiling procedure (bottom right).

pipes, unions, HV/LV/signal connectors/cables, cooling pipes/elements. For HPL a visual inspection will be performed and the level and uniformity of resistivity will be controlled in the production site. For all the other components there will be a visual inspection and the production parameters will be recorded in the construction database.

- QC2 level will be applied to chamber elements: RPC gaps and cooling circuit. For RPC gaps several parameters will be recorded during and after the mass production: visual inspection results, gas tightness and spacer gluing, resistivity and dark current. Detailed descriptions on procedures and quality assurance applied in the RE4 gap production at KODEL can be found in Ref. [84]. For cooling circuits a pressure test will be performed with defined maximum leak rate, as pre-agreed with the CMS Cooling team.
- QC3 level will be applied to full chambers soon after production, in two steps. Assembled chambers will be tested for cooling circuit tightness and front-end board electronics functionality. Then longer test with cosmic rays will be performed to monitor dark current (in first 24h, at different HV) and chamber performance. Detailed descriptions on RE4 chamber assembly and quality assurance can be found in Ref. [83].
- QC4 level is based on a final validation test performed in the CERN laboratory in building 904 to ensure that no damage was inflicted during the transport, and to validate the chamber long term performance. Two levels of QC will be applied. Final

Chamber tests: electrical, leak (gas/cooling) and dark current tests; long-term stability tests: dark current monitoring for about one month at operating voltage. Detailed descriptions on chamber test procedures and results are presented in Ref. [85].

There are few differences compared to the previous RPC production for Endcap and Barrel: the iRPCs are very similar to the old chambers, except for the new HPL panel thickness (1.4 mm instead of 2.0 mm previously) and the type of strips and electronics. The reduced HPL panel thickness will demand additional care in manufacturing of HPL panels and gaps. The strips and electronics will follow specific quality criteria as used in previous chamber productions. No change will be applied in terms of gas piping inside the chamber wrt previous CMS endcap RPC chambers, so a similar performance in terms of gas leaks is expected (leaks negligible), following a similar gas leak test protocol.

The RPCs suffering severe gas leaks in CMS are those in the barrel. These chambers have significantly larger dimensions wrt the endcap ones. By splitting the gap for the same layer into two or three elements additional link gas pipe elements and additional T shape connectors were needed, resulting in a higher leak vulnerability for the barrel RPC chambers. Those components are *not* needed/present in the CMS RPC endcap chambers and will *not* be used in the iRPC chambers.

5.5.6 Front-end electronics and DAQ for new iRPC detectors

5.5.6.1 Requirements

The new iRPC chambers are conceived such that the amount of deposited charge associated to the passage of charged particles is reduced with respect to the present CMS RPCs. In order to detect the lower charges without affecting the detector performance, it is not possible to operate with the same front-end boards developed for the present system. A new front-end board equipped with low noise front-end electronics based on the latest available technology, and a new off-detector DAQ system are being developed.

The front-end electronics has to be able to detect signals with a charge as low as 10 fC and needs also to be fast and reliable, and it must sustain the high irradiation environment that will prevail in RE3/1 and RE4/1 during the HL-LHC phase. The latest available technologies that minimize the chip size are proposed.

5.5.6.2 Front-end electronics

The front-end electronics of the *i*RPCs is based on the PETIROC ASIC (Fig. 5.23) and is called CMS RPCROC. It is a 32-channel ASIC using a broad band fast pre-amplifier and a fast discriminator in SiGe technology. Its overall bandwidth is 1 GHz with a gain of 25. Each channel provides a charge measurement and a trigger output that can be used to measure the signal arrival time. Thanks to its low-jitter pre-amplifier, the ASIC jitter is lower than that of the present system, about 20 ps for charges above 300 fC and in the absence of internal clocks as can be seen in Fig. 5.24. To equalize the 32 channels response, the ASIC has two adjustment systems. A common 10-bit DAC ensures the trigger level adjustment in the dynamic range. An individual 6-bit DAC is used in each channel to achieve similar response of the ASIC's channels.

Although this ASIC was not originally developed for CMS, the new chip has been modified to better fulfill the CMS RPC specifications and is a suitable choice for the *i*RPC needs. The charge is roughly estimated using the TimeOverThreshold technique since the PETIROC ASIC allows the time measurements on both rising and falling edges. The lower value of the ASIC dynamic range is also decreased to allow triggering on signals down to 10 fC. The 350 nm SiGe

technology used in the PETIROC will be replaced by the Taiwan Semiconductor Manufacturing Company (TSMC) 130 nm CMOS one, to increase its radiation tolerance. The number of channels is increased from 32 to 64.

The ASICs is hosted on the Front-End (FE) board that is attached on the RPC detector. On the same board it is also present an FPGA device running a TDC for the time measurement. To connect the strip's ends to an ASIC channel a coaxial cable with the same strip impedance is used. It is soldered on one end to the strips and on the other end to a termination board to be plugged on the FE board. This board hosts, for each of the connected cables, a dedicated circuit to match the ASIC input entry impedance of about 200 Ω. On the same FE board a GBT link ensures the communication between the RPCROCs and the TDCs on one hand, and the off-detector RPC DAQ board on the other hand. Thanks to the TDC time precision of the order of 50–100 ps, the information of signal arrival time from the strip's two ends will provide the hit coordinate along the strip length with a resolution of the order of a few centimeters. In summary every front-end board house three RPCROC Asics and three TDC FPGAs each with 64 channels.

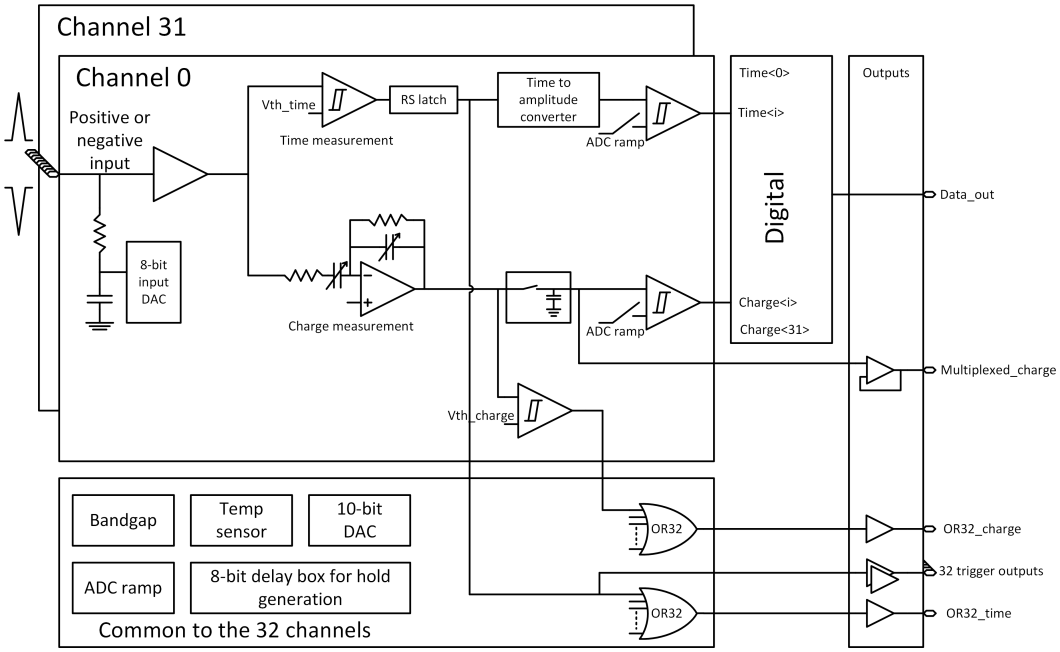

Figure 5.23: The PETIROC schematics.

A small board hosting 32 strips, 50 cm long and 4 mm pitch was designed and produced to test the readout from both edges of the strips as shown in Fig. 5.25. The board hosts two 32-channel PETIROC ASICs as well as two TDCs implemented on a FPGA. The TDC, developed by the Tsinghua University, uses delay-path based techniques. The TDC was adapted to have 32 independent channels that each receive the trigger output of one of the 32 PETIROC channels. The same FPGA used to host the TDC is used to configure the ASICs using a dedicated firmware providing also the needed state machines that enable recorded data to be correctly ordered in time. First tests on the board have shown that a timing as good as 30–35 ps can be achieved by measuring the difference of arrival time of the signal on two of the TDC channels associated to the two ends of the same strip after an injection of a 10 pC charge signal (Fig. 5.26). We obtained 100 ps resolution when 2 pC of charge are injected.

To get the same response from the different ASIC channels to the same injected charge, the

individual threshold of each of the channels was fixed in such a way that their pedestals have similar values. This results in similar *S-curves* which represent the efficiency as a function of the threshold for a given injected charge (Fig. 5.27).

To validate the new readout scheme on a real chamber, a small iRPC prototype (50 cm×50 cm) has been equipped and tested with muon beams at the H4 line of the CERN-SPS. The detector was installed on a X–Y moving table allowing a horizontal and vertical scan. A trigger system made of four fixed scintillator-PMT devices (two upstream and two downstream) was used to tag the muons. The arrival time of the signal detected on each strip end was recorded as well as the one corresponding to the trigger one. The latter was measured with an additional TDC

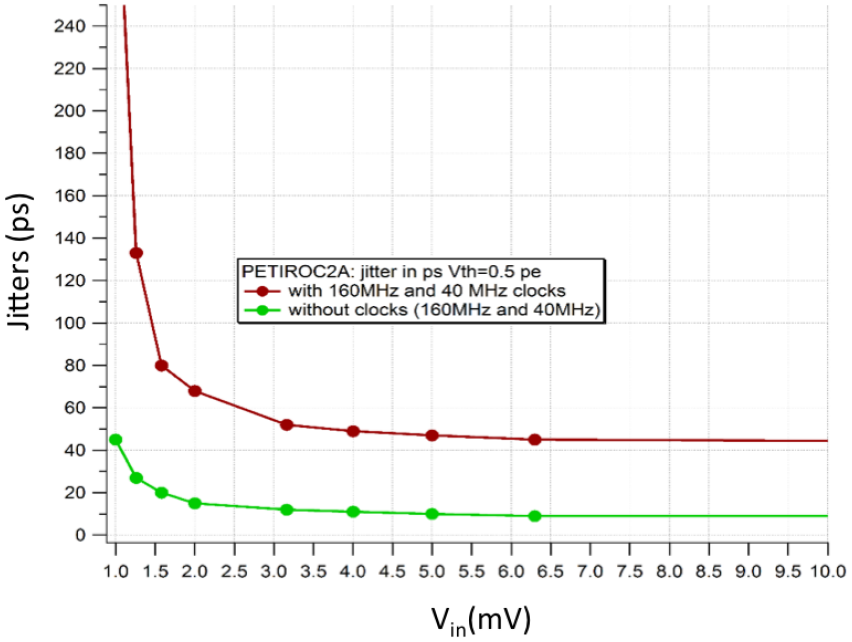

Figure 5.24: The PETIROC time jitter as a function of the input signal amplitude, measured with and without internal clocks.

Figure 5.25: Picture of the preliminary version of the ASU with the final version of the FE board embedded on it, used to test the new readout schema. Pickup strips are placed in the middle.

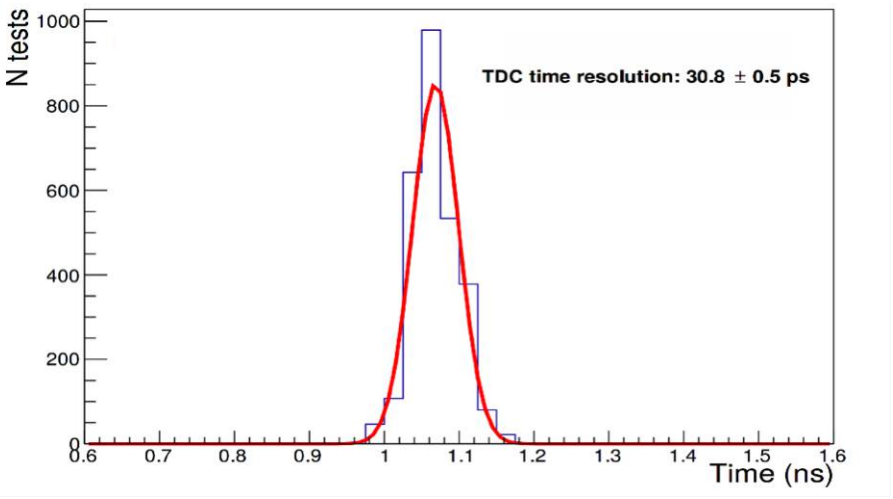

Figure 5.26: Time resolution of the arrival time difference, at the two edges of the strips, when a signal of 10 pC is injected on one of the ASU's strips.

channel. A scan on Y was used to determine the muon impact on the fired strips using time information from both ends of the strip according to the following formula:

$$Y = L/2 - V(T_2 - T_1)/2. \tag{5.1}$$

Here T_1 is the arrival time on one strip end and T_2 is that associated to the other one. V is the signal propagation velocity and L is the total strip length. Figure 5.28 (left) shows $T_2 - T_1$ as a function of the moving table Y position. The linear behavior allows a fit of V. The propagation velocity was found to be 18 cm/ns in good agreement with the expected theoretical value. The resolution on Y is estimated and found to be about 1.8 cm. Taking into account the measured cluster size ($\approx$ 2) associated to the passage of one muon, one can conclude that a position resolution of 1.3 cm is achievable since the same measurement of Y can be repeated on all the strips of the cluster.

The average time difference between the signal arrival associated to each of the strips ends and the one of the trigger signal (T_0) is also measured. Figure 5.28 (right) shows the distribution of the difference of the signal arrival time between the first end of one fired strip and that of the

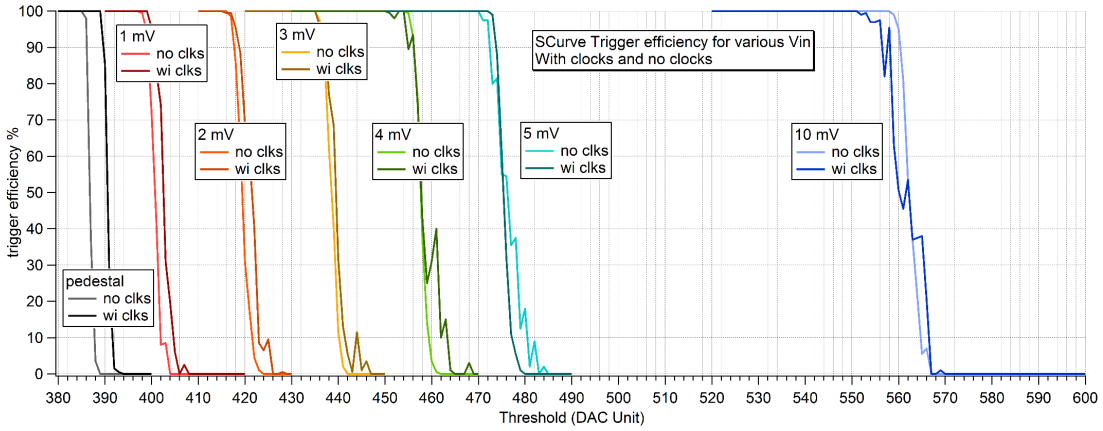

Figure 5.27: S-curves of a typical PETIROC channel.

trigger ($T_1 - T_0$). A time resolution of ≈ 2 ns is observed. The time resolution of the trigger has not been removed so a resolution well below 2 ns is expected when such effect is taken into account. Moreover, the use of the time information from both sides of the strip and of all the strips inside the cluster will reduce the jitter due to the electronics and this has not been accounted for the present results.

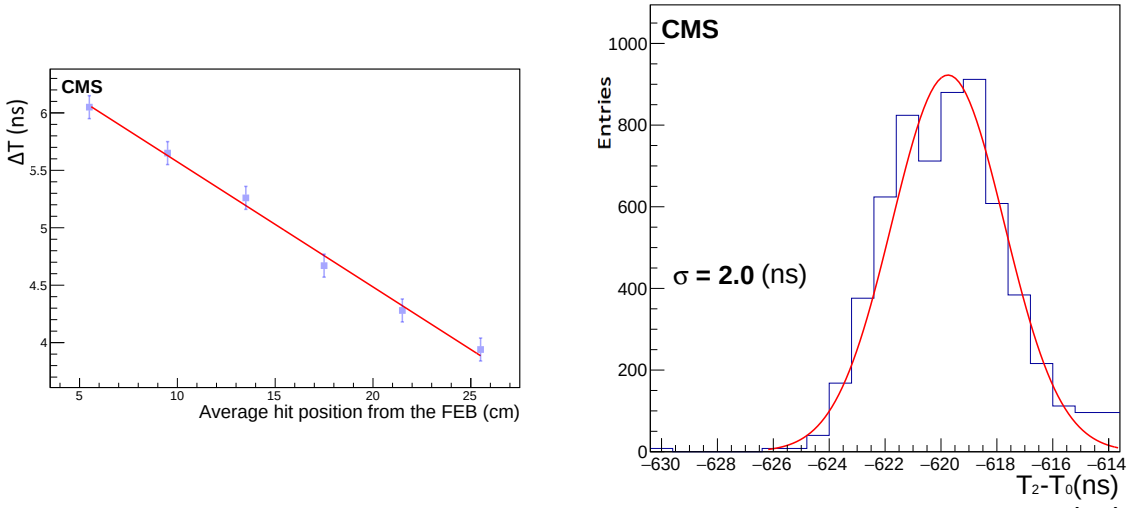

Figure 5.28: Left: Measured time difference of the signal arrival time of each of the two fired strip ends $T_2 - T_1$ as a function of the Y position of the scintillator-PM system center with respect to the RPC. Arbitrary origin of the Y axis is used. Right: Time difference of the time arrival between the first strip end and that of the trigger $T_1 - T_0$.

5.5.6.3 Data Acquisition System

Each of the two stations RE3/1 and RE4/1 is made of 18 detectors (20° span). As mentioned above, each strip will be read out by two channels associated to the two ends of the strip. Signals above a given threshold will be recorded and their arrival time will be measured by the TDC.

To read the strips of one detector on both edges 2×96 channels (3 ASICs of 64 channels) are needed, leading to 3456 channels for each station. Each detector will be equipped with a FE board that collects the data coming from one detector and then transmits it to the off-detector board. Figure 5.29 represents the schematics of the expected DAQ structure.

The data to be transmitted include a header that contains the station information (RE3/1 or RE4/1, 1 bit), the detector number (from 1 to 18, encoded in 5 bits), that of the front-end ASIC (1 to 3, encoded in 2 bits) and the channel number (1 to 64, 6 bits) to determine the position of each strip and which readout end. The header is followed by the information of the time of the detected signal for each channel. The time is coded in 14 bits. As the plan is to save both the falling and the rising time signal in order to use the time over threshold information, 28 bits will be needed for each channel. In total the full information per channel will be packed in 6 Bytes.

We expect at most 2 kHz/cm^2 (it is 600 Hz/cm^2 but we take a safety factor of three). This leads to 1.44×10^{-2} hits/channel every 25 ns (taking into account an average cluster size of two). This results in about $1.44 \times 10^{-2} \times (6 \text{ Bytes}) \times 3456 \leq 0.3$ kByte every 25 ns to be transmitted

by each station (or 12 GByte/s). For the 72 chambers of the 4 stations this amounts to a total of about 48 GBytes/s of data rate to be transmitted, for all RE3/1 and RE4/1 chambers.

5.5.7 Installation and integration

The RE3/1 chambers will be mounted on the YE3 iron disk, as shown in Fig. 5.14. They will partially cover the circular neutron shielding attached to the inner part of YE3 and reach the cylindrical neutron shielding surrounding the collar that separates the yokes YE2 and YE3. The chambers will be mounted directly on the yoke, using the foreseen mounting points threaded into the yoke steel. Allowance for sagitta in the yoke when the magnetic field is applied will be made using simplified kinematic mounts. The screws and washers securing the neutron shielding will be modified to make them flush with the outer lead part of the shield so increasing the available space in z. The CSC alignment system will be decommissioned to give space for the chambers over the neutron shielding.

For RE4/1 the mounting is quite different as they mount to the same side of YE3 as the ME4s taking advantage of the CSC mounting posts, which will be extended with large studding (see Fig. 5.30. On these supports a thin light weight frame made from aluminum alloy 8 mm thick, will be built. The chambers are then screwed to this frame. This configuration is similar to that used for RE4/2 and RE4/3 but the smaller frames and chambers are mounted separately.

5.5.7.1 Power system

The RE3/1 and RE4/1 HV power system will be accommodated in the actual RPC HV power system, occupying 10 racks located in the underground service cavern (USC), therefore no new branches and mainframes will be required. The new system will be distributed in four existing racks following the same regional power collection scheme as of the present endcap detector. The same type of CAEN A3512N 6-channel HV boards, supplying up to 12 kV negative polar-

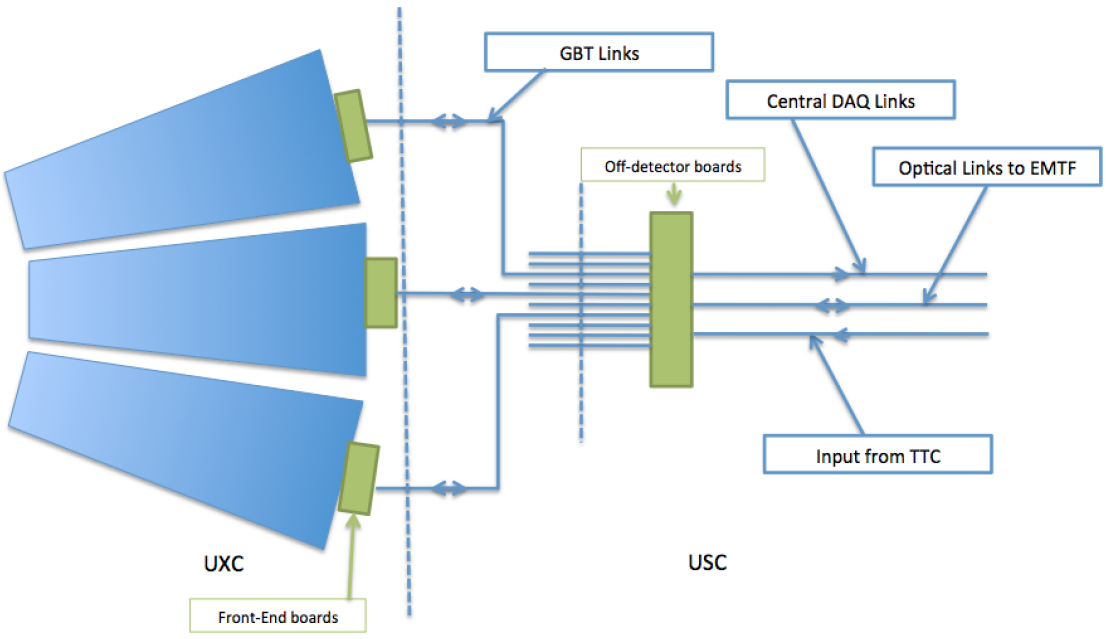

Figure 5.29: A detailed scheme of the new high η RPC DAQ system.

ity, will be used.

Unlike the present RPC Endcap HV system, one upgrade RE3/1 or RE4/1 chamber will be connected to one HV channel, therefore 72 channels or 12 HV boards, distributed equally in four Easy3000 crates, will be needed. Eight HV Distribution boards, with 9 active and 1 spare channel each, will be used to split the power of each HV channel into two lines supplying power to the Top and Bottom chamber HV layers. Eight umbilical cables with 10 two-core cables inside will be needed to bridge the detector HV Patch Panel (YE1 PP) located in UXC. The US-UX connection for the upgrade chambers at the YE1 PP was already foreseen in the initial PP design. From there, single channel HV cables will go through the mini Cable Chains (mCC) to reach the YE3, where they will be redistributed around the peripheral cable trays. Table 5.4 shows the quantities of the power system components.

The RE3/1 and RE4/1 LV power system will be an extension of the present RPC LV system, located mainly in UXC, powered, and controlled through CAEN A1676A branches from the USC. However, for cost and rack space optimization, the powering schema of the upgrade chambers will differ from the one of the actual detector. To supply the LV power to the front-end electronics we will replace the 12-channel, 8 V/45 W per channel, CAEN A3009 boards with 6-channel, 8 V/90 W per channel, CAEN A3016 LV boards. In addition, two A3016 channels will power three 20° chambers, instead of two 10° chambers as at present two CAEN A3009 channels do, in an optimal regime of operation of about ∼70% of maximum power. This will provide excellent segmentation as one A3016 LV board will power 180° in ϕ coverage, therefore 2 boards per end and station or 8 boards in total will be needed. Those boards would require four new Easy3000S crates to be installed at the four corner towers of the endcap detector (positive near, positive far, negative near, negative far) and additional two branches in the Endcap LV mainframe to control the newly installed equipment on the upgrade chambers (see Table 5.5).

Lack of rack space and optimization of costs may dictate that the very same racks and easy crates of the present RPC LV system will be used to power the new chambers. This implies a redesign of the entire LV system by regrouping the existing LV power cables into a smaller quantity of A3009 LV channels to liberate slots for two A3016 boards per crate to fully accommodate the entire RPC LV system.

As already described in Section 5.2, many of the components of the A3009 and A3512N are

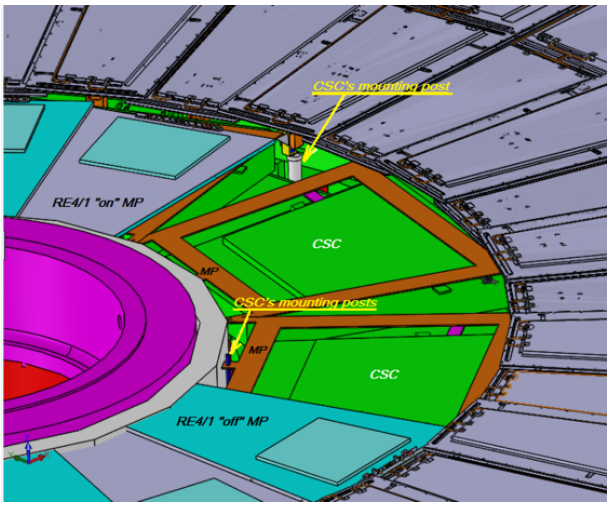

Figure 5.30: Schematic view of the mounting of RE4/1 chambers on the YE3 steel plate.

already obsolete, so if new boards will be produced in time they will be considered also for the RE3/1 and RE4/1 extension.

Table 5.4: HV system equipment for the RE3/1 and RE4/1 project.

Equipment	Quantity
CAEN easy3000 crates	4
48V service cables	8
Anderson connectors for service power	32
CAEN A3512N HV boards per crate	3
Total number of CAEN A3512N HV boards	12
HV cables	152
HV distribution boards	8
HV juppiter connectors	1024
Umbilical cables	8

Table 5.5: LV system equipment for the RE3/1 and RE4/1 project.

Equipment	Quantity
CAEN EASY3000S crate	4
CAEN A1676A branch controller	2
CAEN A3016 board per create	2
Total number of CAEN A3016 board	8

5.5.7.2 Cable routing

Services will transit through the gap formed by the RE3 rear face and the YE3. Trials have been performed to validate this option which is preferable to installing services over the top of the presently installed RE3/2 and RE3/3 chambers as this would hinder their access and removal. Running the services behind the chambers will require their installation prior to the chambers, meaning that installation should be done during LS2, prior to chamber installation in the following end of the year technical stop (2021–22 and 2022–23).

The services are planned to be placed in ducts between the RE4 chambers and ME4s. They will be fed through the ample gap from the inner radius of RE4/2 towards the peripheral cable trays. This scenario will be facilitated and quickened if it remains scheduled to coincide with the change of the front-end electronics on the CSCs. Concerns of induced noise in the CSCs from the RPC services will be dealt with by joint CSC/RPC discussions and appropriate remedial action taken, such as specific cable specification. Figure 5.31 shows the space available for RPC services between CSCs and RE4s chambers.

Although the mini cable chains are quite full, the near side (+X) chain has sufficient space for the HV and fiber optic services. The eight umbilical HV cables and fiber optics will fit in the four main cable chains. Optical fibres will go through the two transfer channels, between the USC and UXC, leading to the base of the main cable chains in the UXC.

5.5.7.3 Gas system

At the moment the baseline is to use the same gas mixture as the present system. The only modification will be downstream of the UXC distribution racks. New piping and bulkheads will have to be installed around the yoke on the opposite side, with respect to interaction point, of the yoke for RE4/1. The presently installed piping foreseen for the original RE3/1 will have to be modified as it occupied all 12 channels on the rack. The bulkheads are placed on the

yoke periphery. Their mapping will need to be modified. All piping from bulkheads to the chambers will be required. Impedences, as used in the RE4 system, will be installed on the peripheral structure to ensure a parallel flow to each chamber.

Table 5.6 shows the gas volumes and flow rates for the RE3/1 and RE4/1 chambers.

Table 5.6: Expected gas volumes and rates for the new RE3/1 and RE4/1 chambers.

Endcap	Volume [l]	Exchange rate/hour per sector	Chambers per channel [l/h]	Flow rates
RE3/1	4.5	1	3	13.5
RE4/1	3.5	1	3	10.5
RE3/1 station	81	1	3	81
RE4/1 station	63	1	3	63
Rack				144
Total	288			288

5.5.7.4 Cooling system

The specification of the cooling system is a function of the electrical power distributed into the UXC cavern. Technical Coordination requested that all electrical load be cooled, to mimimise the heat load lost into the cavern. The chamber loads are significantly less than in the previous RPC chambers. Nonetheless the chambers and rack elements will be cooled by circulating water from the Endcap cooling circuit. The relatively small load can be accommodated by an extension of the present system.

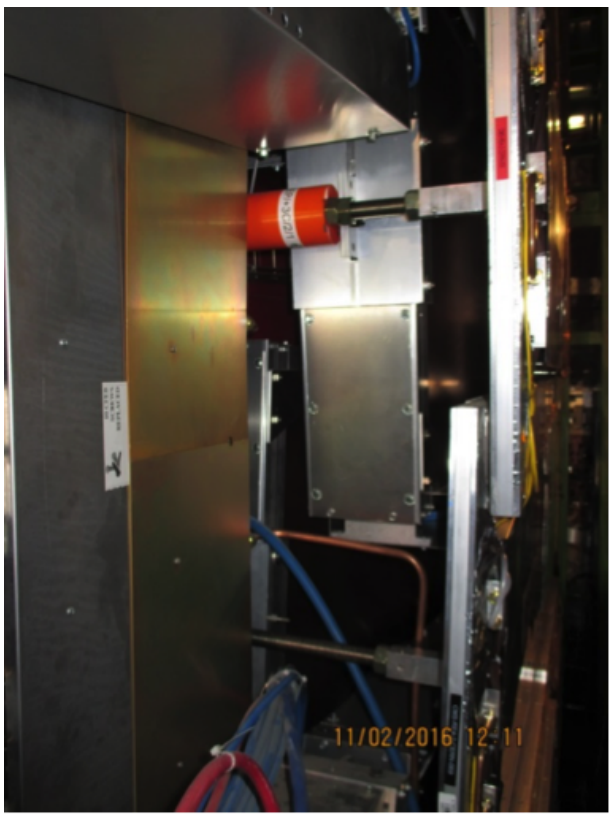

Figure 5.31: Picture showing the available space for RPC services between the CSC and RE4 chambers.

Table 5.7 shows the expected power dissipation for the RPCROC electronics with TDC integrated. The total expected power dissipation for the RPCROC electronics with TDC integrated is about 1700 W.

Table 5.7: Expected power dissipation for RPCROC with integrated TDC for RE3/1 and RE4/1 Chambers.

Unit	Power [W]
Channel	0.083
Chamber (192 channels)	15.94
Station (18 chambers)	287
Full system (4 stations)	1148
Rack Power	592
Total	1740

This value of dissipated power is approx. 10% of the total power dissipated on both YE3s. This power should increase the coolant temperature by approx. 0.1 °C. Given the fragility of the cooling circuits on the RE4 SM, separate cooling circuits will be taken off the present *mini manifold* using tee connections and flow restrictors to equalize the flow in these parallel circuits.

The RE3/1 chambers will be cooled by extending the RE3/2 chamber cooling piping.

5.6 Cost, schedule and institutional responsibilities

The current estimates of the CORE costs of the RPC upgrade are shown in Table 5.8. The CORE costs include the price of all items needed for the upgrade of the RPC system, plus few needed in test stands at CERN. Operational spares are not listed in the CORE costs, but extra modules are included where production is expected to result in some fraction of faulty components that can not be used for commissioning. The CORE costs are all converted to kCHF using 2016 exchange rate.

As the construction of the RE3/1 and RE4/1, for the Phase-2 upgrade, is very similar to the RE4/2–3 station, installed in 2013–2014, the estimates in few cases are based on the production costs of the RE4/2–3 chambers. For the electronics recent vendor quotate or catalog price are used. The distribution of the quality factors for the costs is shown in Fig. 5.32 (left), where (1) is based on a vendor quote or catalog price, (2) is based on a recent similar part or purchase, (3) is based on engineering seeding where sub-components are known, and (4) is based on conceptual design or scaled from similar systems. The expected time profile for the costs is shown in Fig. 5.32 (right).

The institutions expected to contribute to the RPC Phase-2 upgrade are in Table 5.9. Many of these institutions have been associated with the RPC system since its initial construction, others from the Phase-1 upgrade, this provides a strong continuity and expertise.

The schedule for prototyping, production, testing, and installation of the Phase-2 RPC upgrade is implemented and tracked with a MERLIN schedule that is common to all muon subsystems. The RPC project contains approximately 230 individual tasks that are linked with causal dependencies. The higher level summary tasks from the period leading to and following the Electronics Systems Reviews are reported in Figs. 5.33 and 5.34 respectively. Some of the milestones are reported in Table 5.10.

Table 5.8: Summary of estimated CORE costs for the RPC Phase-2 Upgrade. All costs are scaled for 2016 kCHF.

Item number	Item name	Estimated Cost *KCHF*, 2016
2.4	**RPC TOTAL**	**3633.92**
2.4.1	***RE41 & RE31 TOTAL***	***2253.88***
2.4.1.1	**CHAMBER COMPONENTS**	**763.89**
2.4.1.1.1	HPL Electrodes	96.90
2.4.1.1.2	Chamber Mechanics	200.47
2.4.1.1.3	Gap Production	276.25
2.4.1.1.4	Chamber Cooling Circuit	85.93
2.4.1.1.5	Chamber Assembly Components	55.33
2.4.1.7.3	Quality Control Test	50.00
2.4.1.2	**FE ELECTRONICS**	**714.02**
2.4.1.2.1	ASICs	143.14
2.4.1.2.2	PCB	276.25
2.4.1.2.3	FEB & cabling	103.82
2.4.1.2.5	TDC	89.56
2.4.1.2.6	FPGA	101.26
2.4.1.4	**Cables**	**34.65**
2.4.1.5	**Power Sytem**	**335.73**
	Power system HV	*192.22*
2.4.1.5.1	HV crates	15.27
2.4.1.5.4	HV board	119.65
2.4.1.5.5	HV distribution board	0.45
2.4.1.5.2,3,6-13	Connectors and Cables	56.85
	Power System LV	*143.51*
2.4.1.5.13	LV board	68.11
2.4.1.5.14	LV crates	15.27
2.4.1.5.15	LV branch	3.2
2.4.1.5.16	LV power cables	18.53
2.4.1.5.18	Cable Connectorization	12.67
2.4.1.5.19	LV mainframes	25.72
2.4.1.6	**Services**	**45.58**
2.4.1.6.1	Cooling System	14.55
2.4.1.6.2	Gas System: Infrastructure on disks	13.36
2.4.1.5.3	Temperature Sensor (DCS)	17.68
2.4.1.7	**Chamber Assembly and QC**	**140.00**
2.4.1.7.1	Component for assembling	35.00
2.4.1.7.2	Components for Testing	50.00
2.4.1.7.4	Shipment sites	55.00
2.4.1.8	**LOGISTIC & INSTALLATION**	**220.00**
2.4.1.8.1	Consumables for Installations	60.00
2.4.1.8.2	Mechanics for Logistics	60.00
2.4.1.8.3	Cable and Services Installation	100.00
2.4.2	***RPC Trigger Link System***	***1380.04***
2.4.2.1	RPC Link System Master	417.79
2.4.2.2	RPC Link System Slave	723.34
2.4.2.3	RPC Link System Control Board	164.45
2.4.2.4	RPC Link System Front-Plante	74.46

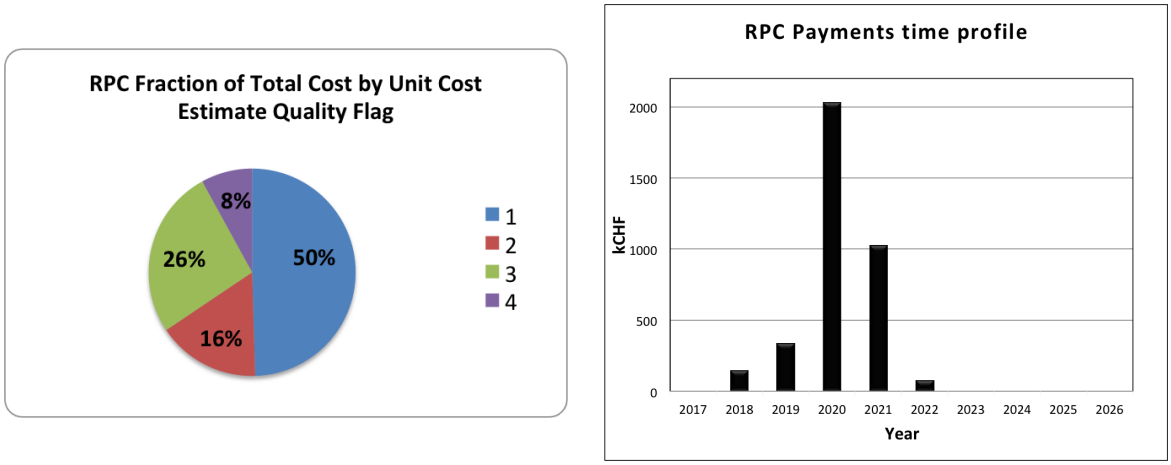

Figure 5.32: Left: Distribution of the project cost by the quality flag attributed to each individual item estimate. Right: Expected time profile for expenditures for the RPC upgrade expressed in 2016 kCHF.

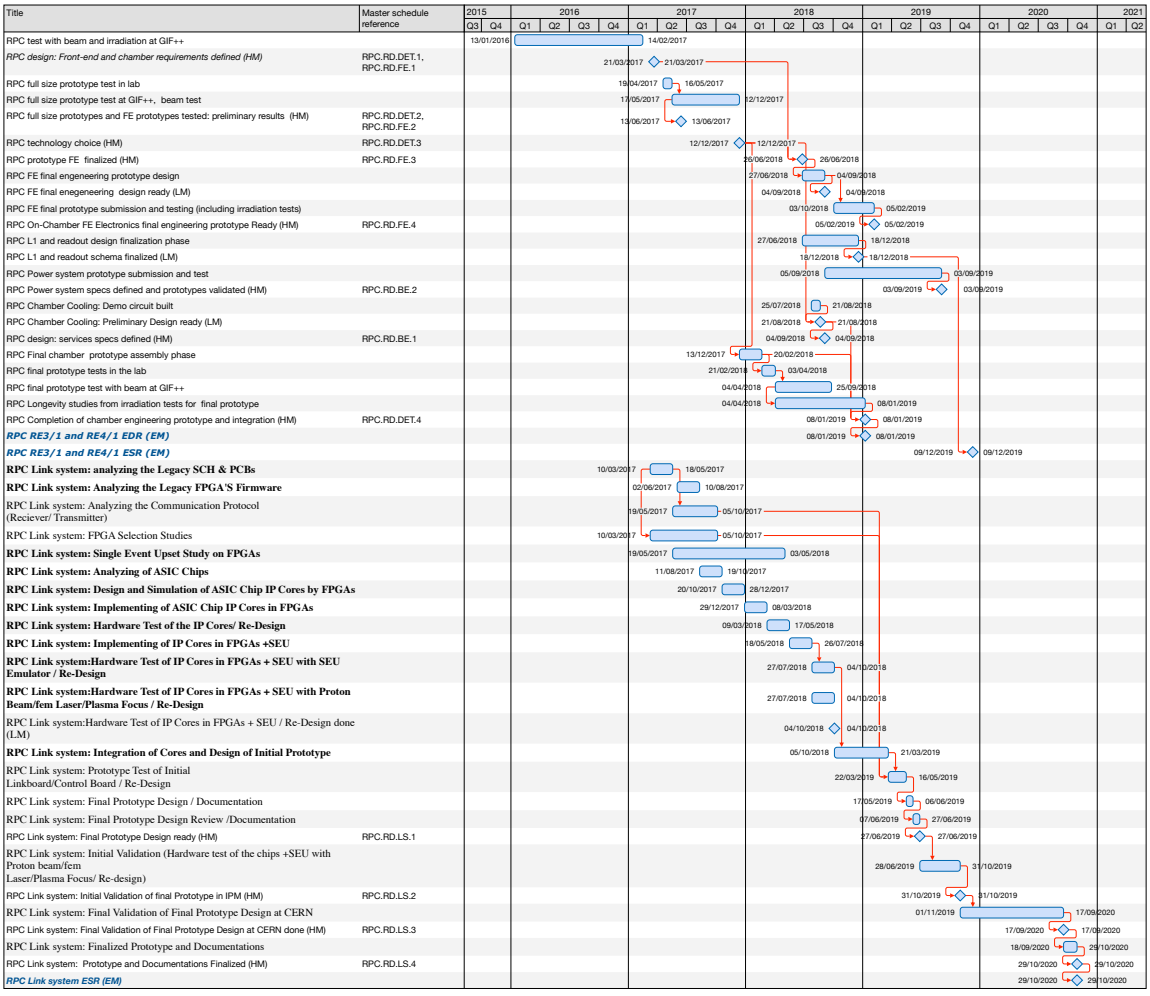

Figure 5.33: The highlights of the RPC upgrade schedule from the period leading to the Electronics Systems Reviews.

Table 5.9: Institutional responsibilities.

Institute	Country	RE3/1 and RE4/1										
		longevity and eco-Gas	Production and QC	Front end	DAQ	LV	HV	link system	integra-tion	Instal-lation	Commis-sioning	Online
Ghent Univ.	Belgium (FWO)	X	X						X	X	X	
Sofia Inst. Nuc. Res. & Nuc. Energy INRNE	Bulgaria	X	X						X		X	X
Sofia U.	Bulgaria								X	X	X	
Tsinghua Univ.	China		X	X								
Universidad de los Andes Bogota Colombia	Colombia					X					X	X
Academy of Scientific Research and Technology	Egypt		X						X	X		
Universite Claude Bernard Lyon	France			X	X				X		X	
Tibilisi-IHEPI	Georgia		X							X		
INFN-Bari	Italy	X	X							X	X	
Laboratori Nazionali Frascati INFN	Italy	X	X							X		
INFN-Napoli	Italy		X				X					X
INFN-Pavia	Italy	X										
Korea U.	Korea		X								X	
Hanyang University	Korea		X								X	
Sungkyunkwan Univ.	Korea		X								X	
Autonomous Univ. of Puebla	Mexico	X	X			X	X		X	X	X	
CINVESTAV	Mexico	X	X			X	X			X		
Universidad Iberoamericana Mexico	Mexico	X	X			X	X		X	X		
Nat. Center for Physics (NCP), Islamabad	Pakistan								X	X		
IPM	Iran							X			X	

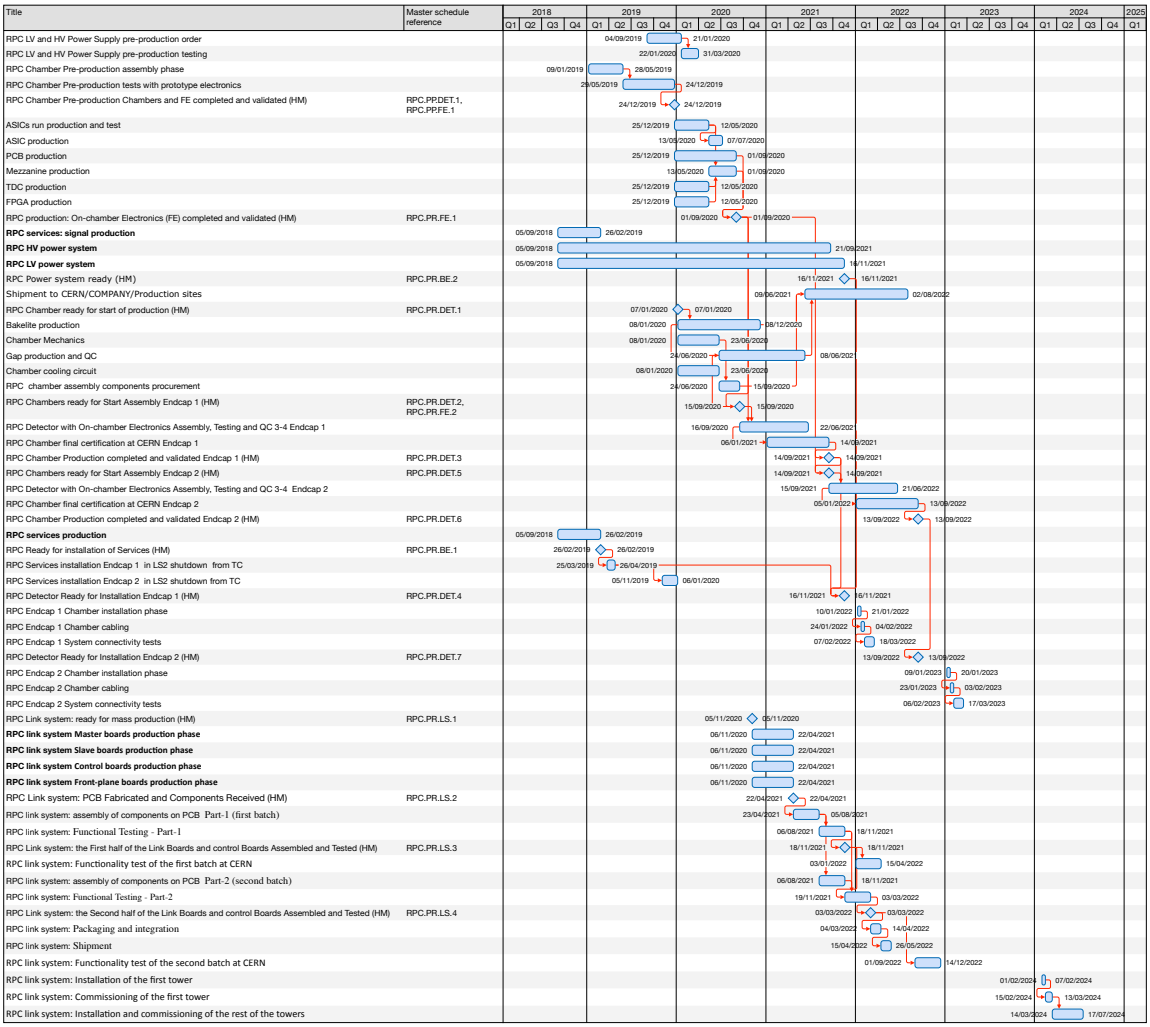

Figure 5.34: The highlights of the RPC upgrade schedule from the period following the Electronics Systems Reviews.

Table 5.10: High Level and External Milestones (HM and EM, respectively) for the RPC upgrade.

	ID	Milestone title	Date
Design	RPC.RD.DET.1, RPC.RD.FE.1	RPC front-end and detector requirements finalized (HM)	21.Mar.2017
	RPC.RD.BE.1	RPC services specs defined (HM)	4.Sept.2018
	RPC.RD.LS.1	Link system: Final prototype design ready (HM)	27.Jun.2019
Prototyping	RPC.RD.DET.2, RPC.RD.FE.2	RPC full size prototypes and FE prototypes tested: preliminary results (HM)	13.Jun.2017
	RPC.RD.DET.3	RPC technology choice (HM)	12.Dec.2017
	RPC.RD.FE.3	RPC prototype FE finalized (HM)	26.Jun.2018
	RPC.RD.FE.4	on-chamber FE electronics final engineering prototype Ready (HM)	5.Feb.2019
	RPC.RD.DET.4	completion of chamber engineering prototype and integration (HM)	8.Jan.2019
	RPC.RD.BE.2	RPC power system specs defined and prototypes validated (HM)	3.Sept.2019
	RPC.RD.LS.2	RPC link system: Initial validation of final prototype in IPM (HM)	31.Oct.2019
	RPC.RD.LS.3	RPC link system: Final validation of final prototype design At CERN	17.Sept.2020
	RPC.RD.LS.4	RPC link system: prototype and documentations finalized (HM)	29.Oct.2020
	RPC EDR (EM)		8.Jan.2019
	RPC ESR (EM)		9.Dec.2019
	RPC link System ESR (EM)		29.Oct.2020
Production	RPC.PR.BE.1	RPC Ready for installation of Services (HM)	26.Feb.2019
	RPC.PP.DET.1, RPC.PP.FE.1	chamber pre-production chambers and FE completed and validated (HM)	24.Dec.2019
	RPC.PR.DET.1	chamber ready for start of production (HM)	7.Jan.2020
	RPC.PR.FE.1	on-chamber Electronics (FE) completed and validated (HM)	1.Sept.2020
	RPC.PR.DET.2, RPC.PR.FE.2	chambers ready for start assembly Endcap 1 (HM)	15.Sept.2020
	RPC.PR.LS.1	RPC link system: ready for mass production (HM)	5.Nov.2020
	RPC.PR.LS.2	RPC link system: PCB fabricated and components received (HM)	22.Apr.2021
	RPC.PR.DET.3	chamber production completed and validated Endcap 1 (HM)	14.Sept.2021
	RPC.PR.DET.5	chambers ready for start assembly Endcap 2 (HM)	14.Sept.2021
	RPC.PR.DET.4	RPC detector ready for installation Endcap 1 (HM)	16.Nov.2021
	RPC.PR.BE.2	RPC power system ready (HM)	16.Nov.2021
	RPC.PR.LS.3	RPC link system: the first half of the Link Boards and Control Boards assembled and tested (HM)	18.Nov.2021
	RPC.PR.LS.4	RPC link system: the second half of the Link Boards and Control Boards assembled and tested (HM)	3.Mar.2022
	RPC.PR.DET.6	RPC chamber production completed and validated Endcap 2 (HM)	13.Sept.2022
	RPC.PR.DET.7	RPC detector ready for installation Endcap 2 (HM)	13.Sept.2022

Chapter 6

New GEM detectors

For Phase-2, the CMS plans include the installation of three new detectors, GE1/1, GE2/1 and ME0, utilizing the Gas Electron Multiplication (GEM) technology. GE1/1 and GE2/1 systems cover the forward peudorapidity range $1.6 < |\eta| < 2.4$ (2.15 for GE1/1) and are designed to improve forward muon triggering capabilities in this challenging region. The ME0 detector aims to take advantage of the extension of the CMS inner tracking capabilities in order to extend efficient muon identification and triggering capabilities up to $|\eta| \sim 2.8$. The GE1/1 system is proposed for early Phase-2 installation in the Long Shutdown 2 and the Technical Design Report for the GE1/1 detector system is available elsewhere [7]. While this chapter describes the technical design for the GE2/1 and ME0 detector systems, the baseline detector technology for all three detectors is identical and therefore many of the measurements related to basic detector capabilities and characteristics presented in this chapter have been performed with the GE1/1 detectors. These measurements have been updated when warranted by, e.g., the different environment or operational conditions.

To form the GE2/1 detector system, in each muon endcap large trapezoidal triple-GEM chambers are arranged in a wide planar ring with inner radius $\approx$ 1.5 m and outer radius $\approx$ 3.2 m, centered on the beamline. Each ring comprises two layers with 18 chambers per layer, 36 chambers per endcap. The rings will be installed on the backsides of the YE$\pm$1 yokes facing the ME$\pm$2/1 CSC chambers mounted on the YE$\pm$2 yokes. In analogy with the ME2/1 label, the label "GE2/1" uses 'G' for GEMs; 'E' for endcap; '2' for the second muon station from the IP, and '1' for an inner ring. Given its large size, each chamber is composed of four individual trapezoidal modules M1-M4 that increase in size with increasing radius.

To form the ME0 detector system, in each muon endcap the trapezoidal stacks of triple-GEM modules are arranged in a wide planar ring with inner radius $\approx$ 0.6 m and outer radius $\approx$ 1.5 m, centered on the beamline. Each ring comprises 18 stacks with six layers of modules per stack. The rings will be mounted in the endcap nose directly behind the new High-Granularity Calorimeter (HGCAL) that upgrades the endcap calorimeter system. The label "ME0" uses 'ME' to indicate a muon endcap system and '0' to indicate that this new muon station is located in front of the original muon endcap system, i.e. closer to the IP than any other muon detector in the endcap.

6.1 Overview and motivation

In the high luminosity operating regime, CMS capabilities in muon triggering and identification will continue playing a critical role for the success of the CMS physics program. Compared to other systems, massive shielding of the muon detectors makes it less affected by the increase in the level of pile-up as the majority of the particles produced in soft interactions remain in-

capable of reaching muon detectors. While both physics considerations and the limitations of the technologies available during the original CMS construction require an upgrade of the CMS muon system, the advantageous situation allows preserving and maintaining excellent performance of the CMS muon detection with relatively modest improvements to the existing system. Furthermore, they make it relatively straightforward to take advantage of the planned extension of the CMS tracking capabilities into the forward region, to simultaneously expand the CMS muon coverage extending the CMS physics reach.

Despite the advantages of good shielding, muon systems are not immune to the effects of increasing luminosity. One particular challenge is the high rate of the incident particles in the most forward region of the CMS detector. These rates approach and in some cases exceed the capabilities of the traditional gaseous detectors, such as the original CMS CSC and RPC detectors, while large areas of muon detectors make other technologies such as silicon tracking impractically expensive. Fortunately, the introduction of the new generation of micro-pattern gaseous detectors (MPGD) capable of operating in substantially higher rates has provided new opportunities for developing cost efficient muon detectors suitable for deployment in the most forward region of the CMS detector. One class of these new detectors utilizes the Gas Electron Multiplication (GEM) principle [86]. CMS has already adopted the plan to install a new muon station GE1/1, comprising 144 triple-GEM modules, as part of the early CMS Phase-2 muon system upgrade. GE1/1 has been scheduled for installation in the Long Shutdown 2. It is also important to note that a major advantage of the GEM detectors is their compact size, which is important given the very limited space available within the current mechanical structures of the CMS detector.

6.1.1 Maintaining existing trigger capabilities

Among the challenges associated with the forward region of the muon system, maintaining an efficient and reliable triggering is the most difficult one. With no upgrades, the muon trigger rates would increase significantly at the HL-LHC luminosities, particularly in the region $|\eta| > 1.6$. High muon trigger rates in the forward part of the detector are driven by the fast drop in the magnetic field towards high $|\eta|$, which results in a decreased bending of muon trajectories as they traverse the CMS muon system. As the measurement of muon transverse momentum by the Level-1 muon trigger is based on the observed bending of muon trajectories, the degradation of transverse momentum resolution in the forward region leads to a high trigger rate due to the increased probability of low transverse momentum particles being reconstructed as high transverse momentum muons.

The planned deployment of the CMS Level-1 tracking trigger enables a high precision measurement of muon candidate momenta using the tracking measurement. It has been demonstrated that an efficient low rate muon trigger can be designed by matching L1 track candidates (L1Trk) with loose standalone muons (L1Mu), as the presence of a reconstructed standalone muon candidate (L1Mu) ensures strong discrimination against non-muon backgrounds while the good transverse momentum measurement of the tracking trigger eliminates mismeasurements that drive the high trigger rate. Figure 6.1 (left) shows the turn-on curve of such a combined trigger, while Fig. 6.1 (right) shows the efficiency of the L1Mu component of the combined trigger as a function of pseudorapidity.

While having an excellent transverse momentum resolution, the L1 tracking trigger reconstruction is inefficient for tracks with impact parameter d_{xy} exceeding a few mm. The L1Trk+L1Mu trigger would therefore be inefficient for triggering on muons produced in decays of long-lived particles, predicted in various extensions of the SM, which requires the full Phase-2 muon trig-

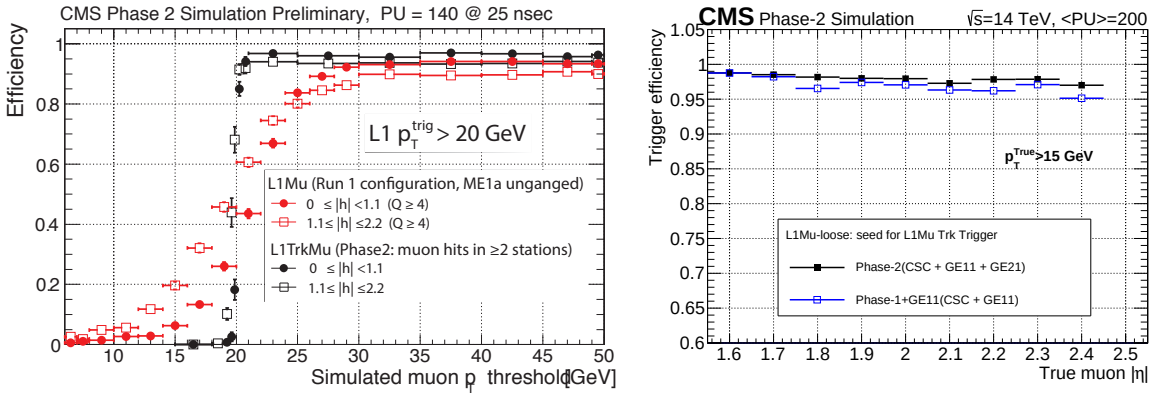

Figure 6.1: Left: Efficiency of the combined L1Trk+L1Mu trigger as a function of true muon p_T showing a large improvement in momentum resolution [24]. Right: Efficiency of the L1Mu component of the combined trigger as a function of η. Note that current trigger algorithms do not use ME0 segments at the track building stage, which leads to an underestimate of the efficiency in the region above $|\eta| > 2.1$.

ger system to rely on more than a single reconstruction technique. This implies the extension of the capabilities of the existing Level-1 standalone muon triggering (L1Mu), which is highly efficient for triggering on muons with d_{xy} up to 10–15 cm. The standalone L1Mu trigger also provides an important complementarity as it can reconstruct muons with momenta below the L1Trk cut-off threshold of $\sim$ 3 GeV, which is especially important for the scenarios of new physics involving forward production where momentum is much higher than the transverse momentum, e.g. $\tau \to 3\mu$. It is therefore planned that the Phase-2 muon trigger design will utilize both L1Trk and L1Mu capabilities in designing specific trigger paths to maximize the CMS physics reach and ensure adequate redundancy in case of unavoidable operational inefficiencies or reduction in performance due to aging or radiation damage.

One major improvement of the CMS L1 standalone muon triggering is expected to arrive from the improved measurement and utilization of the muon candidate directions within single stations. A good example of potential improvement is the new muon station GE1/1 based on triple GEM detectors currently under construction. The measurement of the candidates direction in station 1 using the new GE1/1 and existing CSC ME1/1 chambers allows efficient rejection of the mismeasured muon backgrounds that dominate the Level-1 muon trigger rate, as it is illustrated in Fig. 6.2 (left). With the GE1/1 installation, muon direction is measured using hit positions in the adjacent GEM GE1/1 and CSC ME1/1 chambers. Good position resolution of both detectors and an increased lever arm formed by the two detectors allow for a good direction measurement.

The new GE2/1 detector to be installed next to the CSC ME2/1 chambers provides redundancy by enabling a second muon direction measurement by the GE2/1-ME2/1 chamber pairs. Availability of a second measurement of the muon direction further improves the efficiency and increases the resilience and stability of the trigger in practical operations. While the direction measurement effectiveness decreases with distance from the interaction point, see Fig. 6.2 (right), the bending of muon trajectories in the second station remains substantial. Similarly to the case of GE1/1, the combined reconstruction of trigger stubs using both CSC and GEM hits enables a significant improvement of the efficiency of local stub reconstruction as illustrated in Fig. 6.3 (left) and dramatically improves CMS ability to measure muon direction in the second station using CSC ME2/1 and GEM GE2/1 chamber pairs, see Fig. 6.3 (right). The improved efficiency and precision of the direction measurement in the second station adds an impor-

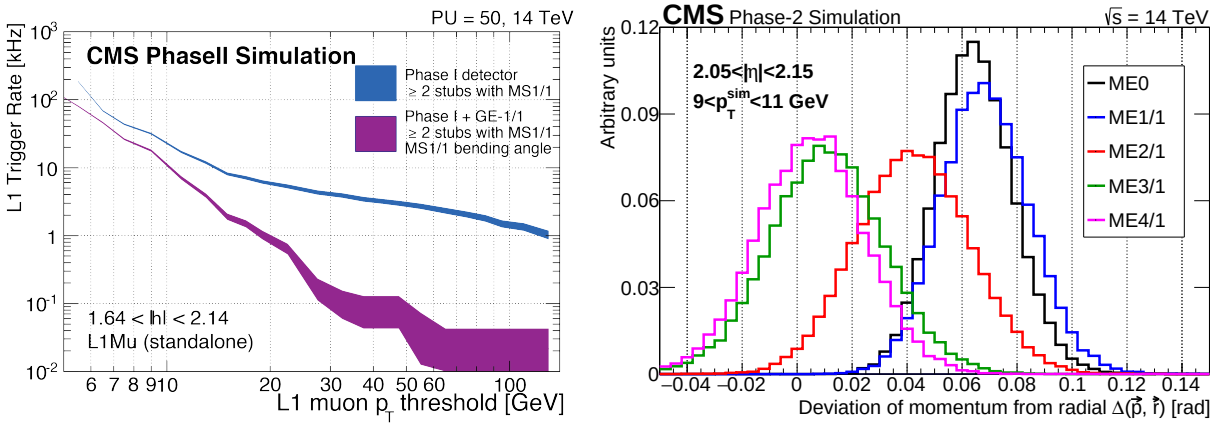

Figure 6.2: Left: Trigger rate reduction with the deployment of muon direction measurement using GEM GE1/1 and CSC ME1/1 chambers [7]. Right: The distribution of local directions for muons with $p_T = 10$ GeV in each of the four muon stations shows that the use of directions in the first two stations can be effective in rejecting low transverse momentum muons [24]. In far stations, the "unbending" of muons due to the radial component of the magnetic field and substantial multiple scattering reduce effectiveness of the direction measurement for rejection of low transverse momentum muon candidates.

tant redundancy needed for robust trigger performance. Because the L1 trigger rate reduction achievable with the installation of the GE1/1 detector is so large, even a modest inefficiency in hit reconstruction by either the GE1/1 or ME1/1 chambers making the measurement of the muon direction unavailable, can lead to a large increase in the trigger rate in the affected parts of the detector. Figure 7.11 shows that installation of GE2/1 allows maintaining good trigger performance even in scenarios with a severe degradation of the ME1/1 system capabilities due to aging or radiation damage.

As the new GE1/1 detector can only extend to $\eta \sim 2.15$, the region $2.1 < |\eta| < 2.4$ of the current muon detector coverage is left out. The new ME0 detector positioned behind the new endcap calorimeter consists of six layers of triple-GEM modules capable of high precision direction measurement and effectively serves as the fifth station in this most difficult region. Installation of GE2/1 and ME0 allows avoiding large trigger rate increases and minimizes efficiency losses, as illustrated in Figs. 6.4 and 7.12, which show efficiency and trigger rate of the standalone muon trigger vs. muon transverse momenta.

The availability of direction measurements in two stations allows deploying a new algorithm for trigger reconstruction and momentum measurement for muons produced with a large impact parameter. The algorithm compares measurements of muon candidate directions and then checks for compatibility with the measured muon candidate positions in the stations it traversed. The two direction measurements are provided by ME1/1-GE1/1 and ME2/1-GE2/1 pairs in the region $1.6 < |\eta| < 2.1$ and by ME0-ME1/1 and ME2/1-GE2/1 pairs in the region $2.1 < |\eta| < 2.4$. The requirement that displaced muon candidates are to be incompatible with any of the L1 tracking trigger candidates allows a further large reduction in the trigger rate. Figure 6.5 shows the efficiency and the trigger rate for a displaced muon trigger. The rate reduction due to the track trigger veto ranges from three to eight depending on the working point and the muon candidate η. Figure 7.15 shows trigger efficiency and rate as a function of the transverse momenta.

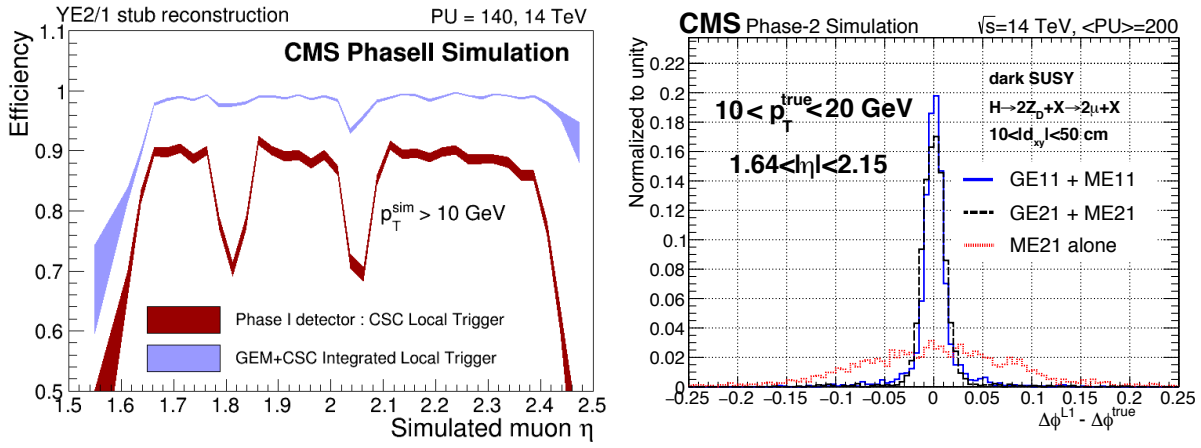

Figure 6.3: Left: Efficiency of reconstructing a L1 trigger segment as a function of muon η using the CSC only (lower curve) or both the CSC and GEM hits (upper curve) [24]. Right: Resolution of the muon direction measurement $\Delta\phi$ in the second station using the CSC only (the dotted line) compared to that using the joint ME2/1-GE2/1 reconstruction (dashed) and with the resolution of a similar measurement in the first station using ME1/1-GE1/1 chamber pairs (solid line).

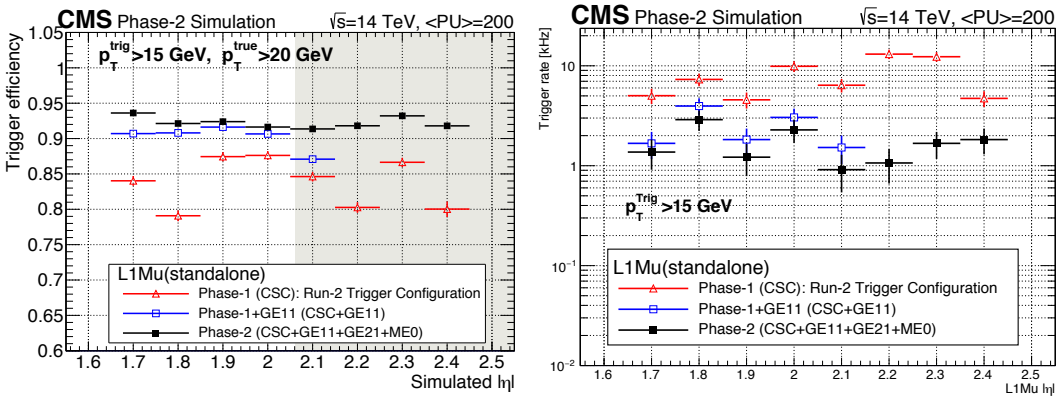

Figure 6.4: Efficiency and the rate of the standalone muon (L1Mu) trigger shows that the muon system upgrades allow avoiding large increases in the trigger rate and minimize trigger inefficiency in the high luminosity operating regime.

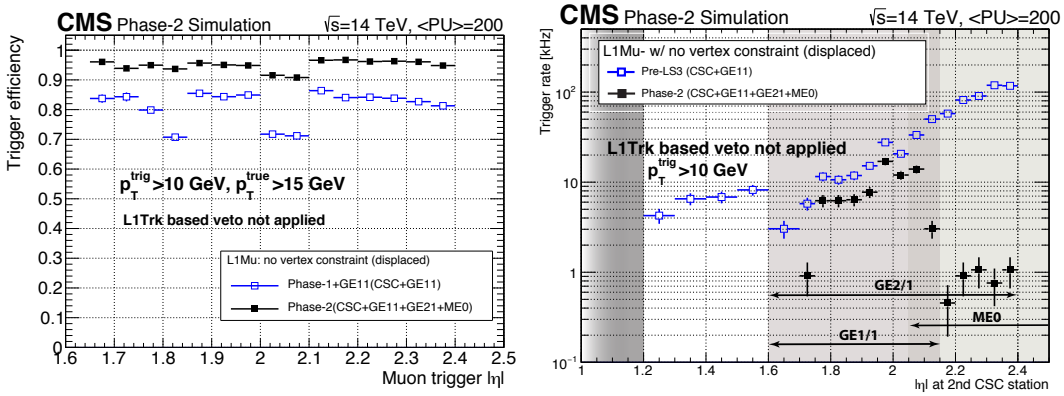

Figure 6.5: Efficiency (left) and trigger rate (right) for the displaced muon candidates. The rates do not include the effect of the L1Trk veto, which, depending on the working point, provides a factor of 3–8 reduction in the trigger rate at the cost of a 3–10% loss in efficiency.

6.1.2 Muon identification and triggering in the very forward region $|\eta| > 2.4$

The baseline design of the ME0 detector consists of six layers of triple-GEM chambers each covering $\Delta\phi = 20^\circ$, divided into 384 radial strips, and $\Delta\eta = 0.8$, divided into eight partitions. Its deployment will reinforce the muon trigger in $2.0 < |\eta| < 2.4$ and extend current muon coverage into the region $2.4 < |\eta| < 2.8$, thereby reducing the uninstrumented area behind HGCAL. The primary challenge of designing ME0 is efficiently identifying muons low in transverse momentum (but large in momentum) while maintaining a low rate of background mis-identified as muons in the harsh HL-LHC conditions. A key feature of the ME0 design is multi-layer detection of charged particle trajectories with excellent ϕ resolution. This allows for the combination of a high precision ϕ trajectory measurement with a less precise η position measurement into a coarse estimate of particle transverse momentum. The quantity $\Delta\phi$, defined as the fitted ϕ position of a ME0 segment at the first detector layer subtracted from its fitted ϕ position at the last layer, is a powerful variable for identifying segments as likely originating from high transverse momentum particles. The current benchmark for optimizing ME0 reconstruction is identifying muons with transverse momentum greater than 3 GeV ($p \gtrsim 15$ GeV) at an efficiency of $\sim$ 95%, resulting in $\sim$ 20% acceptance gain for $H \to ZZ^*(4\mu)$. As the detector is effective in measuring momentum, it is capable of reconstructing segments with lower transverse momentum, which is important for certain physics signatures such as the lepton flavor violation decay $\tau \to 3\mu$.

In this harsh environment there are two distinct sources of background mis-identified as muons, the first being charged particles produced in PU interactions. Baseline ME0 performance is evaluated at 200 PU interactions per BX, resulting in $\sim$ 1000 pixel tracks ($p_T > 0.5$ GeV) per BX in ME0 acceptance. This large pixel track density can potentially lead to the reconstruction of misidentified muon candidates arising from the high combinatorics of background pixel tracks and ME0 segments. The granularity of the ME0 design allows for the association of pixel tracks to the correct ME0 segment by matching in η position, ϕ position, particle transverse momentum, and particle charge. The precision of both the reconstructed segment η position and $\Delta\phi$ is compared to the precision of these quantities obtained from the pixel track projection onto the surface of ME0, accounting for multiple scattering in the calorimeter between them, in Fig. 6.6. The matching in $\Delta\phi$ is limited by multiple scattering for muons with transverse momentum lower than 20 GeV while the precision in the segment η position is similar to that of the pixel measurement for low transverse momentum muons. While ME0 is shielded and placed behind HGCAL, the PU particle density is so large that approximately $\sim$ 12 real muons (dominated by decay-in-flight muons from pile-up interactions) and $\sim$ 50 electrons or hadrons (which either escape HGCAL or are produced through interactions in front of ME0) produce hits in the ME0 detector (including both endcaps) every BX. These low transverse momentum particles are a potentially large source of background segments. The left plot of Fig. 6.7 shows that the segments produced by these particles can be reduced by $\sim$ 30% by requiring that segments contain hits in at least four layers. The right plot shows that they can be further reduced by a factor of $\sim$ 10 by requiring that they have a $\Delta\phi$ consistent with $p_T > 3$ GeV particles ($|\Delta\phi| < 0.013$).

The second source of background mis-identified as muons is long lived neutrons and their byproducts. These particles are estimated to induce $\sim$ 1000 ME0 hits per BX, which due to the large combinatorics can be a potentially large source of background ME0 segments. The number of segments produced by the clustering of random neutron background hits per event is shown in Fig. 6.8 for different neutron background luminosity scales, where the nominal luminosity is 7.5×10^{34} cm^{-2}s^{-1}. At the nominal luminosity scale this background is reduced to a negligible level by requiring that segments contain hits in at least four layers. Because ME0 is designed to consist of six layers, requiring four layers results in a sub-percent loss of muon

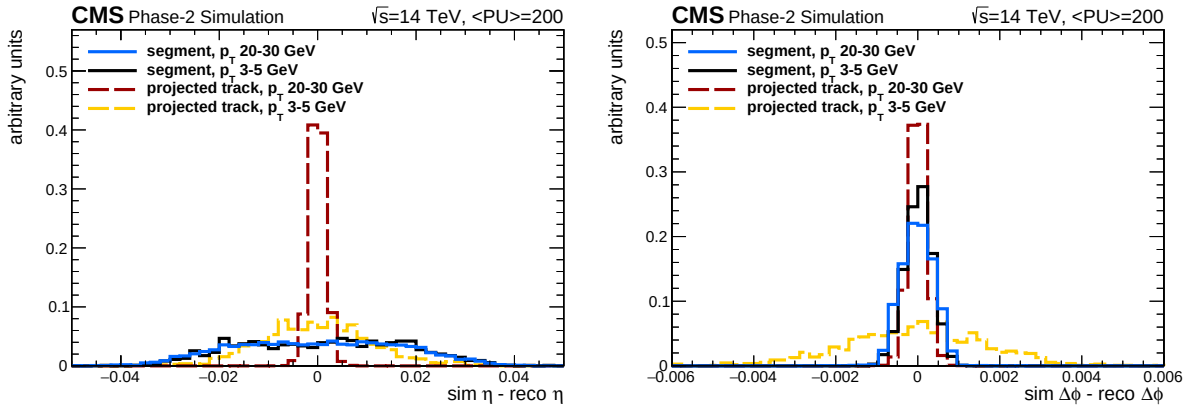

Figure 6.6: Reconstructed quantities, η of the particle at the center of ME0 on the left and $\Delta\phi$ on the right, compared to their generated values for different muon transverse momentum ranges. The quantities obtained by projecting the pixel track onto the ME0 surface are denoted "projected track" and those obtained from reconstructed ME0 segments are labeled "segment". The generated quantities are obtained from the simulated hits on the ME0 detector layers and include the effect of multiple scattering. For "projected track" the primary source of difference from the generated values is multiple scattering through the calorimeter while for "segment" it is the ME0 granularity.

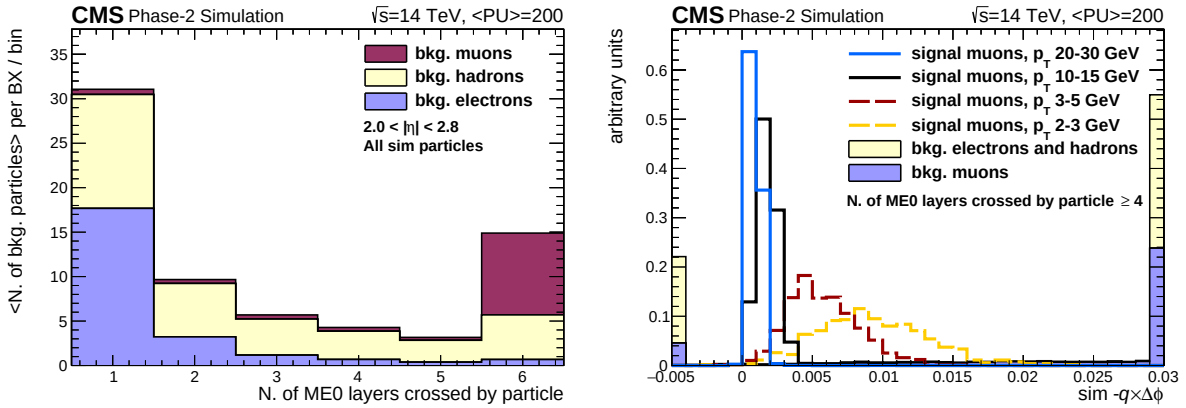

Figure 6.7: Properties of both generated muon and PU particle trajectories in ME0. They are obtained from the simulated hits on the ME0 detector layers and include the effect of multiple scattering. Left: The distribution of the number of ME0 layers crossed by each PU particle, normalized by the total number of generated events. The colors of the stacked histograms denote the type of particle. The category labeled "muons" is primarily comprised of particles originating from light hadron decay. The other categories include particles that escape HGCAL and those that are produced through interactions in front of ME0. Right: The $\Delta\phi$ distribution for generated muons and PU particles for those particles that cross at least four ME0 layers. The distributions for the PU particles are shown in the stacked histograms, in which the colors denote the particle type. The distributions for generated muons are shown in the non-stacked histograms, for which different colors refer to different muon of the particle at the center of ME0 ranges.

segment reconstruction efficiency. However, the neutron induced background estimation has many sources of uncertainty and is sensitive to small changes in beampipe and calorimeter design. Therefore if the neutron induced hit rate is higher than expected, this layer requirement can be increased to five layers for a percent level efficiency loss in order to maintain a negligible neutron induced segment level.

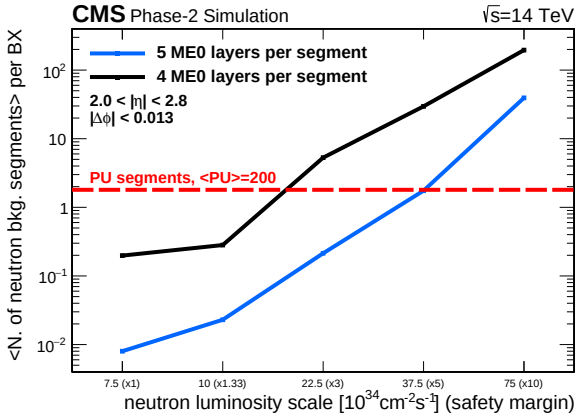

Figure 6.8: The average number of background ME0 segments (including both endcaps) per event from neutron induced background sources as a function of neutron background luminosity scale. The two lines indicate the background level for different layer requirements in segment reconstruction.

The inclusion of ME0 will also extend the range of muon triggering to the $2.4 < |\eta| < 2.8$ region. The average number of background segments per event (for all of ME0) is shown in the left plot of Fig. 6.9. This background multiplicity is too high for using ME0 to increase the single muon trigger coverage. However, the segment position and transverse momentum measurements can be used in conjunction with other L1-trigger objects in multi-object triggers. For example, triggers targeting multi-muon signatures, such as $\tau \to 3\mu$, can include the additional requirement of a ME0 segment in a ϕ slice of one endcap for a factor of ~ 10 rate reduction. The second category of identification is offline reconstruction, in which pixel tracks are matched to ME0 segments, also in the HLT trigger. The matching of track position, charge and, transverse momentum to ME0 segments allows for a background reduction by an order of magnitude. This is shown in the right plot of Fig. 6.9, in which the number of pixel tracks matched to ME0 segments is displayed as a function of pixel track $|\eta|$. ME0 capabilities allow building an effective trigger path extending from Level-1 into the HLT, in which Level-1 selections are followed by the early stages of HLT, where ME0 candidates are first reconstructed at full granularity (L1 uses twice lower granularity), which are used to seed fast local tracking reconstruction in the forward pixel detector, muon-pixel track matching and near-offline selections already at the early stages of the HLT. The high resolution of the upgraded endcap calorimeter system is expected to allow an additional improvement of the offline muon identification and rejection of non-muon backgrounds based on the amount of energy associated with a candidate using the high granularity calorimetry information.

6.2 Common features of CMS GEM detector systems

Triple-GEM detectors have been successfully operated long-term in several major high energy and nuclear physics experiments, i.e. COMPASS, PHENIX, STAR, TOTEM, and LHCb. They have also been adopted by CMS for the GE1/1 station [7]. At the time of the submission of this TDR, CMS has gained first operational experience with ten GE1/1 Triple-GEM chambers under

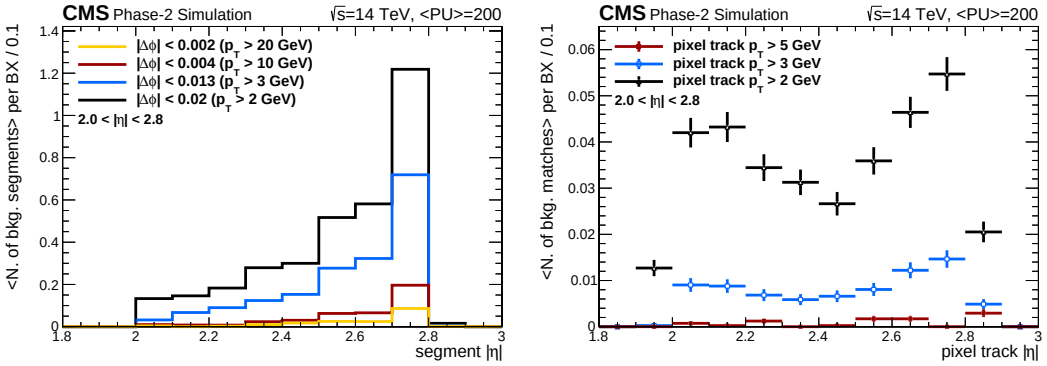

Figure 6.9: Average number of reconstructed ME0 objects per event as a function of $|\eta|$ in events with neutron background simulation and 200 PU interactions per BX. The averages are of all objects reconstructed in both endcaps. Left: The average number of reconstructed ME0 segments per event. The colors indicate the multiplicity after different $\Delta\phi$ selections. Right: The average number of pixel tracks matched to ME0 segments per event. The colors indicate the multiplicity for different pixel track transverse momentum ranges.

LHC conditions [87]. The strong track record for GEMs in high-rate applications demonstrates that GEMs are a mature and robust technology for high-rate experiments. In this section, we present aspects and features that are common to both new GEM detector systems, i.e. GEM foils, Triple-GEM detectors and their performance characteristics, electronics and data acquisition, power systems, and gas infrastructure.

6.2.1 CMS triple-GEM detectors

6.2.1.1 GEM foils

A GEM [86] is a thin metal-clad polymer foil chemically perforated by a high density of microscopic holes. The polyimide (Kapton by DuPont Co. or Apical by Kaneka Co.) used as the bulk material of the foil is 50 μm thick and has a dielectric constant of 3.5. It is clad on both sides with 5 μm of copper. As shown in Fig. 6.10 (left), the GEM holes are truncated double cones with the larger (outer) diameters around 70 μm and the smaller (inner) diameter around 50 μm; they are spaced with a pitch of 140 μm in a hexagonal pattern.

The trapezoidal GEM foils used in a particular CMS triple-GEM module are basically identical so that only one type of GEM foil is required per module. The GEM foil surfaces oriented towards the readout board are a single contiguous conductor whereas the GEM foil surfaces oriented towards the drift board are segmented into numerous HV sectors. The sectors run across the width of the trapezoid (see Fig. 6.11). Their width narrows when going from the short end of the trapezoid to the wide end so that each strip has an approximately equal area of about 100 cm^2. This segmentation restricts the amount of charge that can flow from one foil during a discharge to about 2 μC and, consequently, limits the total energy of a discharge to less than 0.5 mJ. This protects the GEM foil against destruction due to discharges, which are inevitable even if they occur at low rates under standard operating conditions. In the worst case, if a destructive discharge were to occur in an HV sector, it would disable only that one HV sector permanently instead of rendering the entire chamber unusable. To reduce the amount of dead area generated by the 200 micron thicks separation lines between the HV sectors, an additional left/right partition is introduced for the wide GE2/1 foils, which reduces the total number of separation lines by a factor two.

This design requires that each of the HV segments is supplied individually with HV. This is

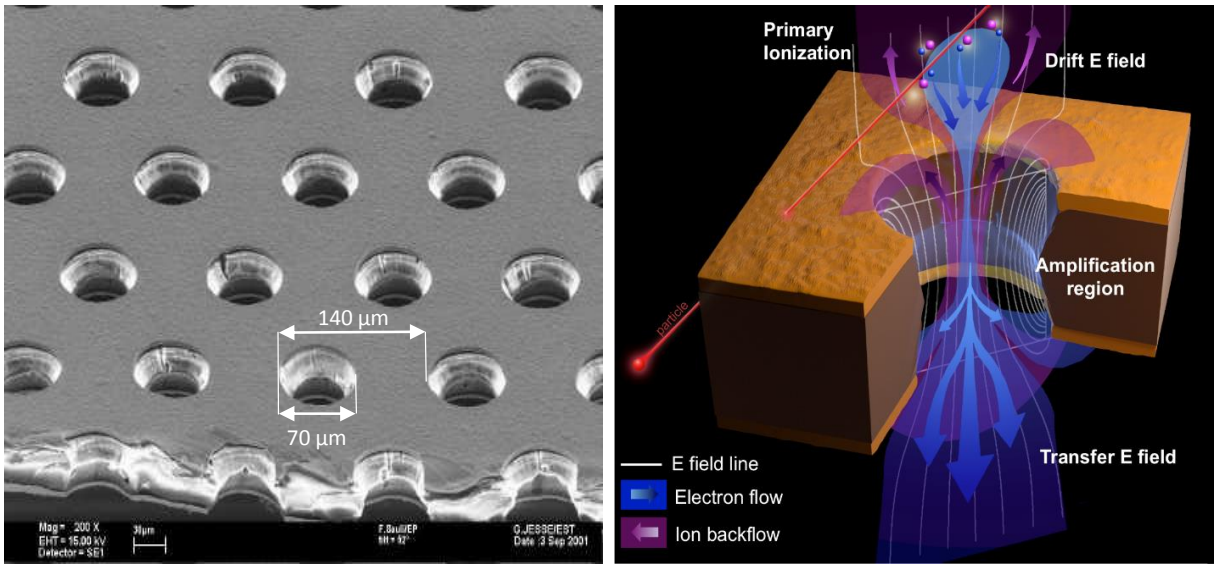

Figure 6.10: Scanning Electron Microscope (SEM) picture of a GEM foil (left) and schematic view (right) of the electric field lines (white), electron flow (blue), and ion flow (purple) through a bi-conical GEM hole (right). The outer diameter of the hole is 70 μm and the inner diameter is 50 μm; the hole pitch is 140 μm.

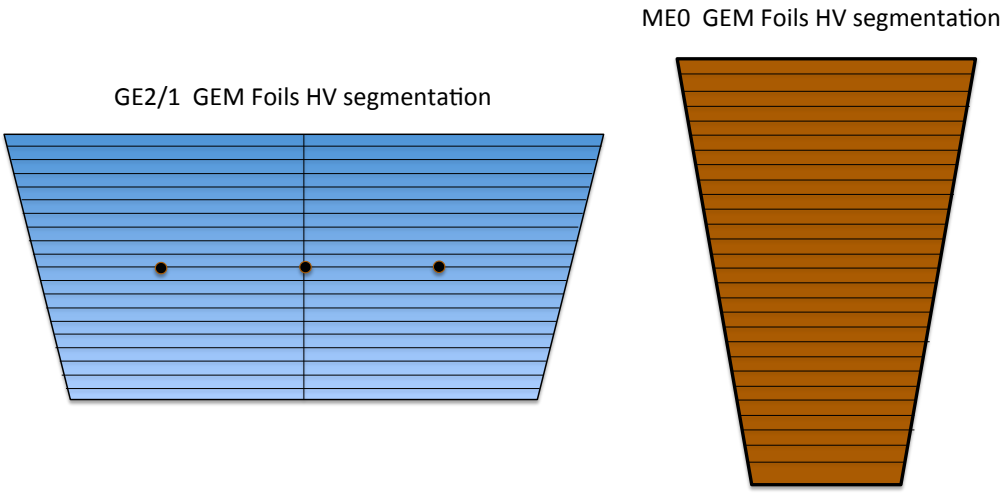

Figure 6.11: Schematic HV segmentation of GE2/1 (M4 module) and ME0 GEM foils into strips on the foil sides that face the drift board. Note that for GE2/1 only the largest module M4 requires a division into left and right segements. Segments in modules M1-3 are not divided.

done by routing a trace around the edge of the GEM foil from a common connection point where the external HV potential is applied to the foil (see Fig. 6.12). The HV trace is connected through 10 MΩ surface-mounted protection resistors to each HV segment (see Fig. 6.12). The potential of the other side of the foil is provided by a single connection point. The common connection points are located at the wide end of the foil (see Fig. 6.12).

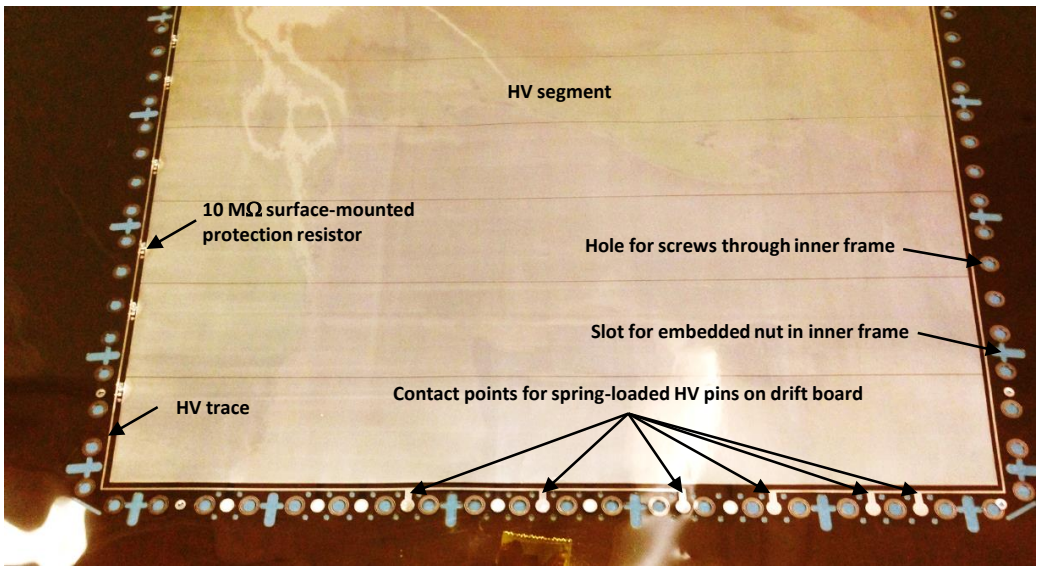

Figure 6.12: GEM foil with traces along the active area that route HV to the HV segments via 10 MΩ protection resistors.

The production of GEM foils is based on photolithographic techniques commonly used by the printed circuit industry. The same technique as for the mass production of GE1/1 foils will be employed. For details we refer the reader to the GE1/1 TDR [7].

6.2.1.2 GEM module design and assembly

A triple-GEM chamber consists of a stack of three GEM foils placed at a relative distance of a few mm and immersed in a counting gas mixture. The voltage applied between the two copper-clad surfaces of a foil produces an electric field as high as ~ 80 kV/cm in the GEM hole as seen in Fig. 6.10 (right). The electrons produced by a charged particle passing through the chamber due to ionization of the counting gas drift towards the holes and once they start to experience the very intense electric field in the holes, they acquire enough kinetic energy to produce secondary ionization in the gas. This produces an electron avalanche process, which induces an electrical signal on the readout strips. A schematic view of this operation principle is given in Fig. 6.13, which also defines the drift region, two transfer regions, and induction region within the triple-GEM chamber.

The dimensions of the different regions in the CMS triple-GEM detectors are: drift region of 3 mm between drift cathode and first GEM, spaces of 1 mm and 2 mm in the electron transfer gaps between GEM foils, and a 1 mm space in the signal induction region (see Fig. 6.13). The baseline gas mixture for operating the CMS triple-GEM detector is Ar/CO_2 70:30.

The foils in the triple-GEM stacks are tensioned and made taut by uniformly pulling the stack outward against stainless steel pull-outs that are affixed to drift and readout PCBs (Fig. 6.14 left). This is achieved by manually tightening the screws that go through the holes in the pull-outs (Fig. 6.14 right) and that are countered by nuts embedded in the inner frame that surrounds the GEM stack. The screws are tightened to a torque of at least 7 cNm. This results

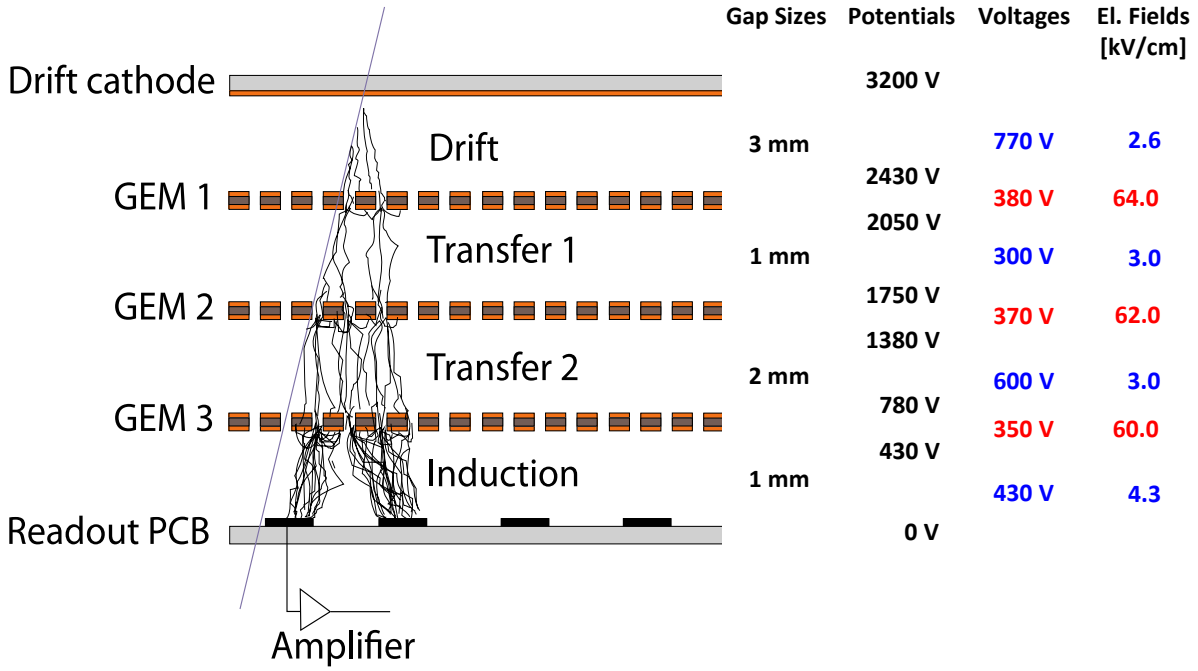

Figure 6.13: Principle of operation of a generic triple-GEM chamber and definition of drift, transfer, and signal induction gap regions within the detector [86]. The columns on the right give the actual gap sizes in the detector. They also list typical values for electric potentials on the seven electrodes and typical values for voltages and electric fields across the four gaps (blue) and the three foils (red) if the nominal potential of 3200 V in Ar/CO_2 70:30 is applied to the drift cathode, i.e. for operation at the start of the efficiency plateau.

in tautly stretched GEM foils closely surrounded by the outer gas frame.

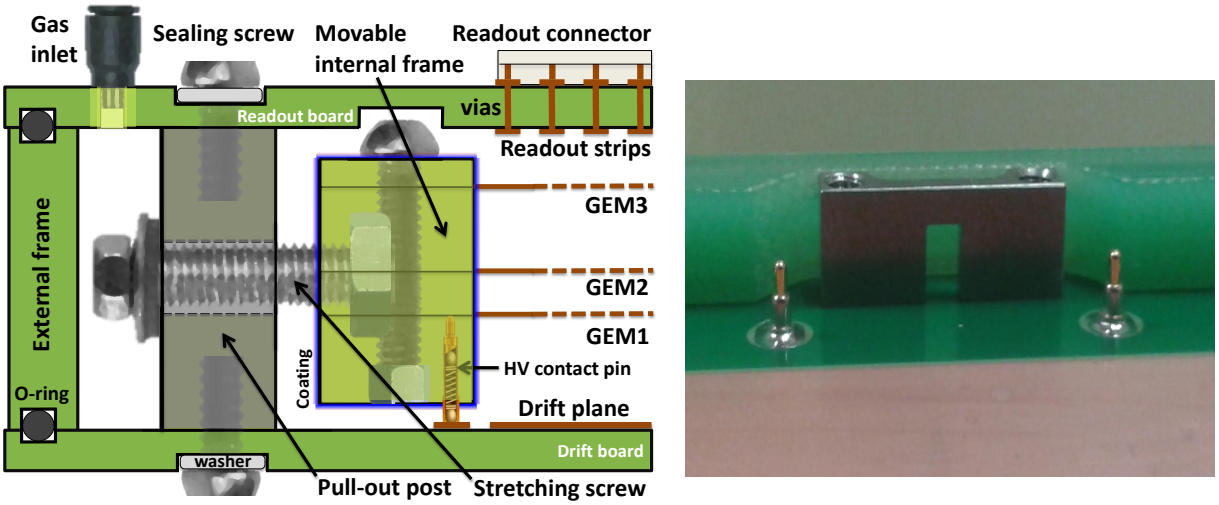

Figure 6.14: Left: Cross-section through inner and outer module frames and GEM foils that shows how the GEM foils are mounted within a CMS triple-GEM module so that they can be mechanically tensioned against the pull-out posts without deforming the drift or readout boards. Right: Stainless steel pull-out post and spring-loaded pins that are soldered to the drift board for making electrical HV connections to corresponding contact pads on the GEM foils.

The GE2/1 and ME0 chamber materials are the same as used in the GE1/1 chambers, which were extensively validated with respect to harmful outgassing [7]. Consequently, no further validation of materials is needed. The three GEM foils are sandwiched at their edges between four layers of a thin internal frame (Fig. 6.15 right) made from halogen-free glass epoxy (ISOLA DE156) that is composed of 8 individual pieces per layer. The thicknesses of the different frame layers define the spacings between GEM foils as well as between GEM foils and drift/readout boards as follows: Drift gap / GEM1-GEM2 transfer gap / GEM2-GEM3 transfer gap / induction gap: 3/1/2/1 mm. The stack is held together by numerous small M2 $\times$ 6 stainless steel screws with T6 Torx heads. They penetrate all frame layers and foils about every centimeter and are tightened against small threaded M2 brass inserts (Fig. 6.15 right center). Using inserts to counter the screws avoids loosening macroscopic and microscopic glass epoxy particulates from the frames as was observed in earlier prototypes where screws were threaded directly into the frame material. Frame pieces are coated with Nuvovern polyurethane varnish before assembly. Both those measures ensure that no glass epoxy particulates detach from the frames during assembly, fall onto GEM foils, and potentially produce electrical shorts in the GEM holes. The screw heads are conical with flat outer surfaces and are sunk into counterbores in the frames that surround the through-holes during tightening (Fig. 6.15 right top). Similarly, the nuts are sunk into counterbores on the frames (Fig. 6.15 right center), so that the screws and nuts are flush with the top and bottom surfaces of the inner frame after the stack is assembled.

Additional square stainless steel nuts are embedded into the frames every few centimeters with the axes of their threaded holes oriented perpendicular to the inner frame and GEM foil surfaces (Figs. 6.12, 6.15 right bottom). These nuts counter M2.5 $\times$ 8 stainless steel screws with T8 Torx heads that are inserted into small stainless steel posts, so-called "pull-outs", which are located within the gas volume. When the pull-out screws are tightened manually, the GEM foils in the stack are tensioned as the inner frame is being pulled outwards towards the pull-outs. Due to the large number of screws, the modules can be assembled with good manual control over the GEM tension so that the foils can be tensioned as uniformly as possible. The

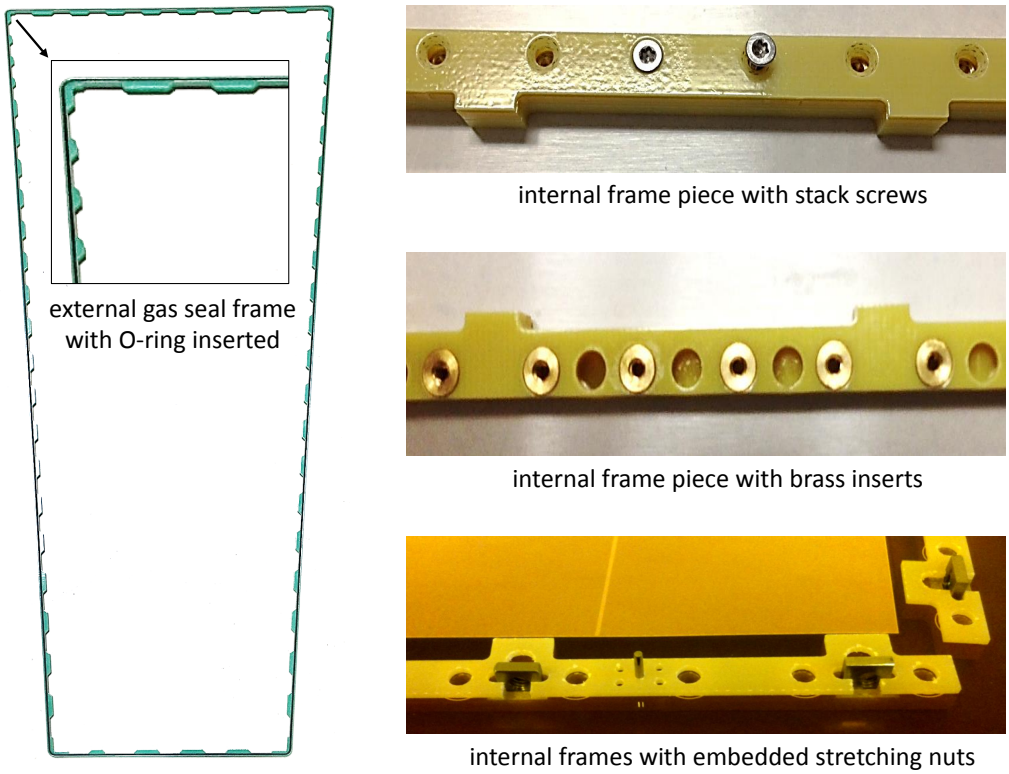

Figure 6.15: Frames used in the assembly of a CMS triple-GEM module. Left: External gas frame made from a single solid piece of halogen-free glass epoxy (ISOLA DE156) with O-ring inserted. Right: Section of the internal frame of a GEM stack with stainless steel screws and counterbores on one side (top) and embedded countering brass nuts on the other (center). The shiny frame surface (top) is due to its coating with Nuvovern polyurethane varnish to prevent fiberglass dust. Square nuts are embedded in the tabs on the frame (bottom) for tensioning the GEM stack against pull-outs with tensioning screws.

relative large size of the square nuts and their large number ensure that the force on the frame at each pull-out is kept as low as possible to avoid any long-term local deformations of the frame due to the stress. The pull-outs are in turn bolted down onto the PCB that provides the drift cathode with two stainless steel M3 $\times$ 6 screws with T10 Torx heads that are sealed with polyamide washers against the drift board.

A large outer glass-epoxy frame machined from a single piece and placed around the tensioned GEM stack and the brass pull-outs provides the border of the gas volume (Fig. 6.15 left). The frame has numerous wide notches to accomodate the brass pull-outs. It is also coated with Nuvovern polyurethane varnish before assembly to seal in particulates. On both sides of the outer frame, a Viton O-ring is placed into a groove that runs around the entire outer frame to seal it. The anode readout board is placed on top of this outer frame and attached to the stainless steel pull-outs with A4 stainless steel M3 $\times$ 6/$\times$ 10 screws which are sealed with polyamide washers against the readout board in the same way as the drift board screws. This sandwiches the outer frame tightly between the drift board and readout board and holds it in place essentially by friction. It provides a solid gas barrier that is only penetrated by two small holes in diagonally opposed corners of the readout PCB to provide the gas inlet and outlet for the chamber.

The electrical HV connections to the GEM foils are made via spring-loaded pins (Fig. 6.14) that are soldered onto the drift board and that push against corresponding connection pads on the

GEM foils. For the HV pins to reach GEM foils 2 and 3, the corresponding connection pads are cut out of GEM foils 1 and 2 during assembly. The drift electrode is powered directly off of the HV line that enters the drift board. The required potentials are brought on individual HV lines to the drift board and routed on-board to the pins that connect to the GEM foils.

An HV short in a GEM foil can only be fixed by extracting the module from CMS, opening the module, and replacing the GEM foil. This requires opening of CMS in case of GE2/1 and de-installation of the new calorimeter endcap in case of ME0, which are major operations. These constraints impose two important requirements on the HV supply system. In case of a short in one HV segment of a GEM foil, the HV supply system must be able to sustain the voltage across that foil and simultaneously provide the current that is then flowing through the 10 MΩ protection resistor on the shorted HV sector. This will allow continued operation of the chamber despite the presence of a short in one (or more) sector(s). The second requirement is that the ramping (up or down) of the potentials on the two sides of all GEM foils that are now provided independently by different HV channels is very well synchronized, monitored, and safe-guarded so that the voltages across the GEM foils can never exceed a maximum given value (about 500V) – even for a very short time. Otherwise, even a brief temporary overvoltage could lead to sparking across the GEM foils that could destroy them. Designs of the HV supply and distribution system that address these concerns are discussed below in the Section 6.2.5 on power systems.

The gas distribution inside the detector should not give rise to areas with very low gas flow that could result in pockets or regions where potentially harmful gas contaminants can accumulate. This was studied for GE1/1 with a finite-element simulation and it was found to be satisfactory to supply the gas to a GE1/1 chamber in the simplest possible manner with one gas inlet and one gas outlet at diametrically opposed corners of the chamber [7]. The same scheme is adopted for GE2/1 modules and ME0 chambers.

Even though the shapes of GE2/1 and ME0 modules are somewhat different, the sizes are comparable so that the assembly techniques and quality control procedures will be identical. They will follow those established for the GE1/1 mass production effort at the various production sites.

Module assembly An overview of the mechanical design of a single trapezoidal CMS triple-GEM module is shown in Fig. 6.16. The main components and materials of a single CMS triple-GEM module are listed in Table 6.1. The assembly and sealing of the detector are entirely mechanical. No glue is applied during assembly, which makes it possible to open a detector again for repairs if needed. It also speeds up the assembly of the module since there are no wait times due to curing of glue.

The drift board features a single drift cathode on its inner side and a solid ground plane on the outside of the module for RF shielding purposes. It provides connections to external high voltage supply lines via HV noise filtering circuitry. The drift board routes a total of seven different potentials to the various GEM electrodes and to the drift cathode.

The readout board has high-density header connectors on its outside to interface the radial readout strips on the inside to the VFAT3 hybrids that plug into the readout board from the outside. The connection is made with vias in the readout board that are sealed with an insulating coverlay (AKAFLEX KDF HT 0/25/25 produced by Krempel corporation).

The VFAT3 hybrids also plug into a second full-size PCB, the GEM Electronics Board (GEB), that is attached directly on top of the readout PCB. The GEB carries the digital output signals from all VFAT3 hybrids to the wide end of the module for processing and transporting to the

Table 6.1: Summary of layer structure and materials of a single CMS triple-GEM module.

Layer	Material	Thickness [mm]
Protective cover	Al	1.0
Cooling pipe	Cu (filled with H_2O)	8 external ⌀, 6 inner ⌀
Cooling pads	Cu	1.0
GEB board	Cu/FR4	0.140/0.856
Readout board	Cu/FR4/Cu	0.035/3.2/0.035
Induction gap	Ar/CO_2	1.0
GEM 3	Cu/polyimide/Cu	0.005/0.050/0.005
Transfer gap 2	Ar/CO_2	2.0
GEM 2	Cu/polyimide/Cu	0.005/0.050/0.005
Transfer gap 1	Ar/CO_2	1.0
GEM 1	Cu/polyimide/Cu	0.005/0.050/0.005
Drift gap	Ar/CO_2	3.0
Drift board	Cu/FR4/Cu	0.035/3.2/0.035

Trigger/DAQ as described in detail in the chapter on electronics and DAQ. The GEB has cut-outs that allow the connectors on the readout board to reach through. Copper pipes are routed on top of the GEB to provide coolant to the VFAT3 hybrids.

Finally, an aluminium frame is mounted on the drift board all around the outer edge (see Fig. 6.16). An aluminium sheet with a thin central chimney along the long axis of the module is attached to that aluminium frame to cover the entire assembly from the readout side. Together, frame and cover provide solid protection for the on-module electronics and utilities.

Drift board design A close-up view (see Fig. 6.17) of the wide end of the drift board side that faces the module interior shows details of the on-board HV circuit traces for the HV noise filtering section, pads for a HV divider, and pads for the spring-loaded pins that make the electrical connections to the GEM foils. The design is asymmetric because the central section of the module needs to accomodate the on-module readout electronics.

Readout board design The inner side of the readout (RO) board, i.e. the side that faces GEM3, features truly radial readout strips arranged in eight η-sectors.The vertex of the strips coincides with the beam line. The strips change width along the RO board increasing in size from high eta to lower eta. The baseline design for the strip material is gold-plated copper produced in an electroless nickel immersion gold (ENIG) process that is standard for PCBs. Figure 6.18 shows a close-up of the design of the short end of the readout board on that side. The smallest sector, i.e. η-sector 1, and a portion of η-sector 2 are shown. The view on the right of Fig. 6.18 zooms in on the center of the strips in sector 1, where the vias are located that connect the strips to the outside of the readout board. On that outer side, traces are routed from the vias to connectors that the front-end VFAT3 hybrids plug into (see Fig. 6.19). Two of the pins on each connector are connected to module common while the other 128 pins are connected to readout strips. The tabs on the edges of the two long sides of the board allow attaching the GEB to the readout board after the module has been closed without compromising the active gas volume of the detector.

Based on the experience acquired during the GE1/1 mass production, the yields for most of the components needed for the assembly of the new modules are estimated to be 95–98% with respect to custom-manufactured pieces and 98% for standard off-the-shelf commercial components and the GEM foils produced at CERN.

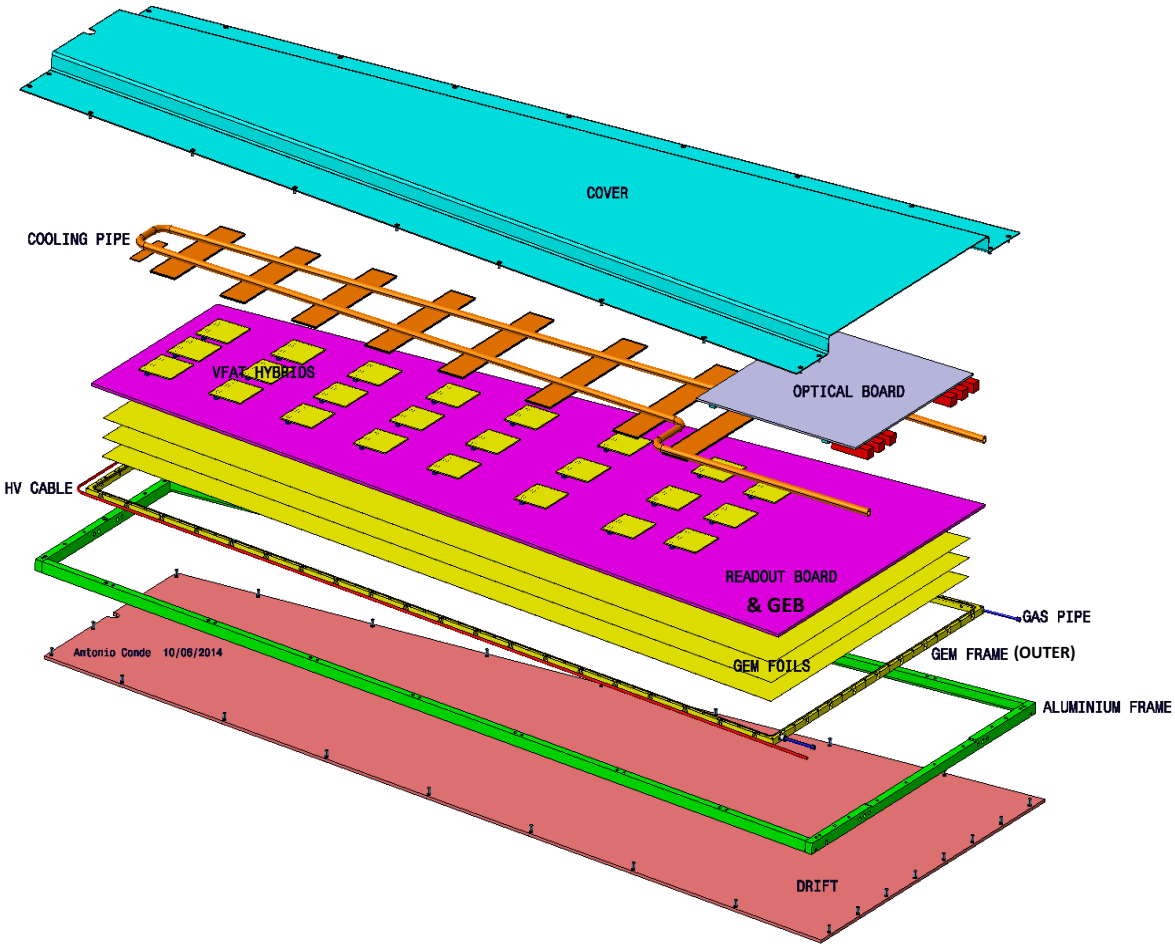

Figure 6.16: Exploded view of the mechanical design of a single CMS triple-GEM module.

Technological and organizational aspects of detector production stages The GE2/1 and ME0 mass production will benefit from the experience and the technical solutions adopted for the GE1/1 chamber mass production. All GE2/1 modules M1-M4 and ME0 modules can be assembled and qualified independently. The assembly techniques and quality control stages for the modules do not differ from those defined for the GE1/1 chambers and described in Sections 5.2 and 5.3.3 of the GE1/1 TDR [7]. The production sites already involved in the assembly and qualification of the GE1/1 chambers automatically qualify for the assembly and production of the new modules.

Modules assembled and qualified at the production sites are delivered to CERN where they are coupled together to form the final GE2/1 chambers or ME0 stacks and then integrated with the readout and cooling systems. Complete chambers and stacks are finally fully characterized and qualified with cosmic ray muons before their integration into the CMS experiment. CERN will act as pivot point of the production; single components will be collected and qualified at CERN before being distributed to the production sites, which will then return qualified modules to CERN.

In the case of the GE1/1 detectors, production uniformity is ensured by a very detailed three-stage qualification process [7] that each production site has to pass successfully before becoming an accepted production site. This comprises construction and full quality control (QC) of prototype detectors, hands-on training by external personnel at the central CERN site, visits

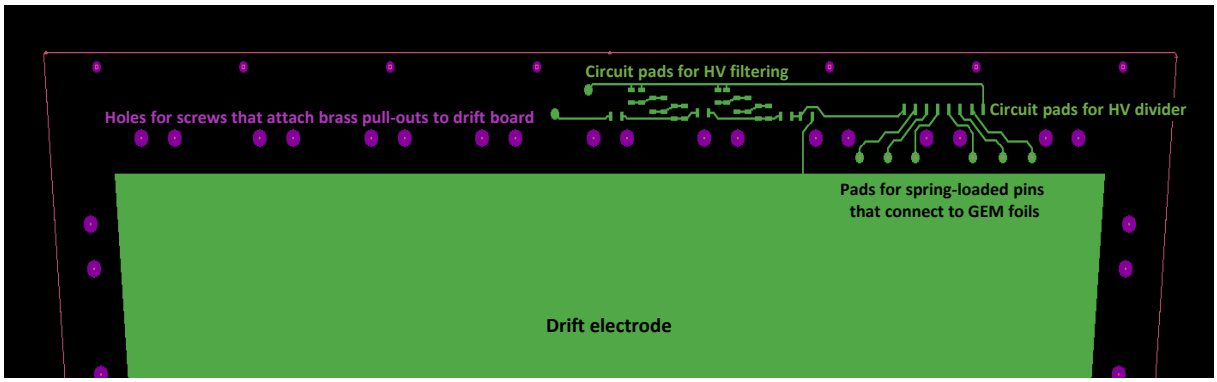

Figure 6.17: Close-up of the wide end of a CMS triple-GEM drift board design with HV circuit traces.

by CERN personnel to all sites to ensure that all required tools, standards, and procedures are completely in place, and finally construction and full quality control of one production detector. That detector is to be returned to CERN for a final check before the site can proceed to full mass production.

All assembly and QC procedures are standardized and documented to a very high level of detail. All performed assembly and QC has to be documented by each site using standardized documents that are submitted to a common data base. All production sites are required to report regularly on their progress and status in ELOG and in bi-weekly working group meetings; the reports are reviewed regularly by the central CERN personnel. Each site has a responsible who is accountable to GEM management. Only once a site has completed this entire process,

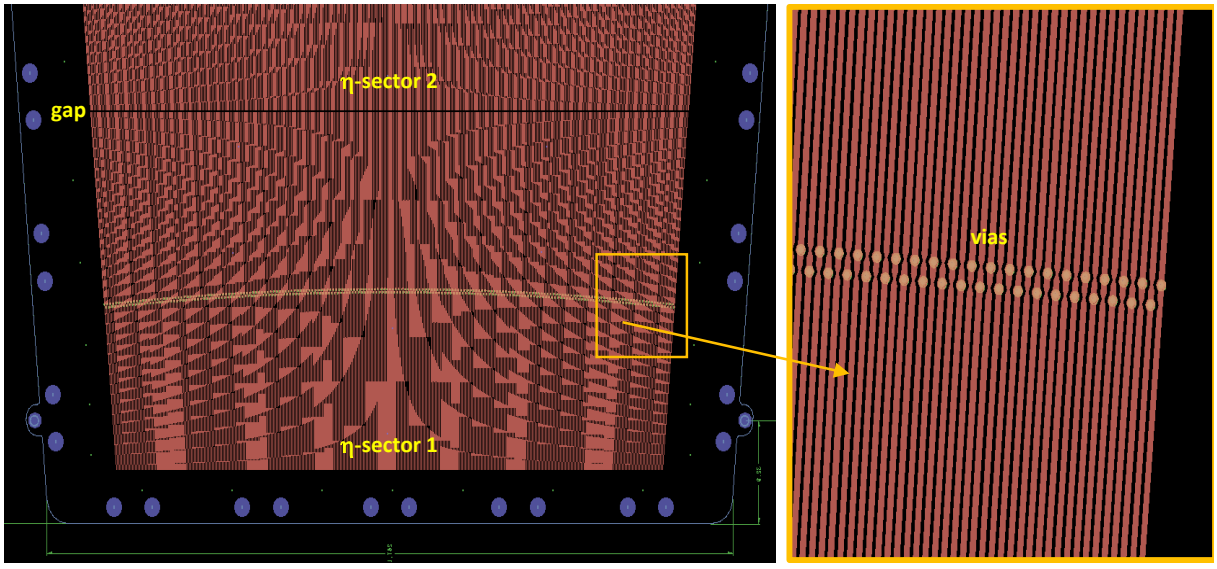

Figure 6.18: Design of the readout board for a CMS triple-GEM module (left). Shown is the inner side that faces into the gas volume opposite GEM3 at the short end of the board. Due to the high density of strips (384 readout strips in each sector), individual strips are not visible at this resolution. Note that the "hyperbolic" geometric pattern is an artifact of the display on a screen. Strips are visible when zooming in (right). The circular structures on each strip are vias that connect the strips to the outside of the board. The blue circles around the edge indicate positions of holes for screws that attach the readout board to the brass pull-outs.

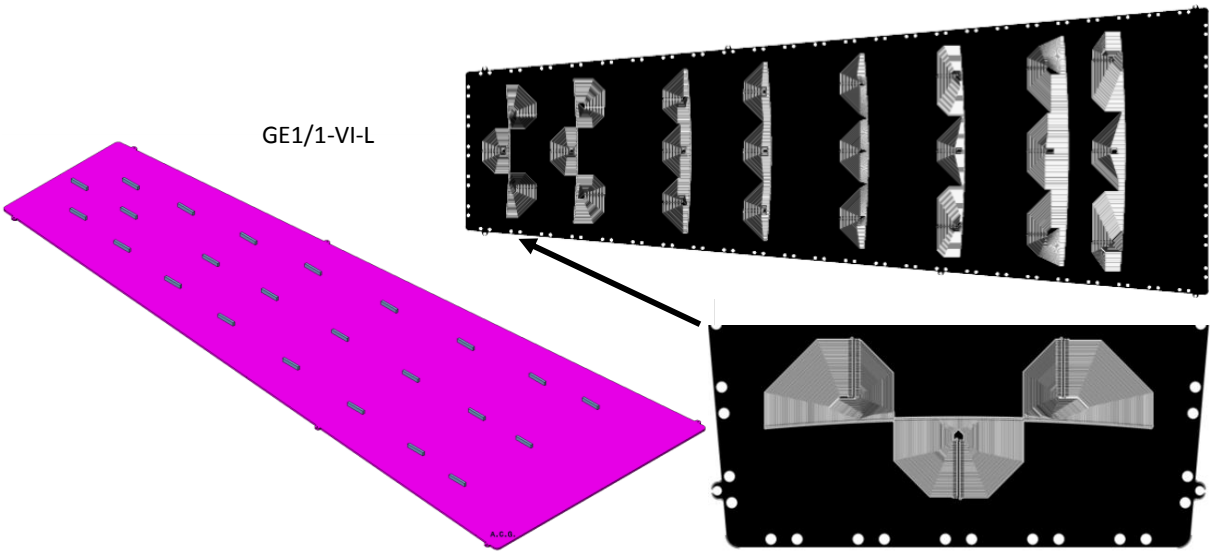

Figure 6.19: Design of the outer side of the readout board for a CMS triple-GEM module showing connectors for VFAT3 hybrids (left) and traces from vias to connectors (right).

which typically takes well over a year, is the site authorized to begin mass production. The GEM group has already proven in the last year that this coordination approach is indeed feasible and appropriate as several production sites are in the very last phase of the qualification process at the time of the writing of this report.

The above approach mitigates the risk of non-uniform production for GE1/1 detectors as much as possible. In addition to risk mitigation, there are also substantial rewards associated with a multi-site production model. There is large redundancy built into the approach. If one site goes down for an extended time period for any reason, e.g. radiation spill, X-ray source failure, cleanroom failure, or personnel changes, then the other sites can compensate collectively so that the schedule is preserved. If such a problem were to occur in a production model with a single site, the production schedule would be immediately in jeopardy. The instrumentation and expert base is also much enlarged. Instead of just a few overloaded experts at CERN working with only two production lines, there is a much deeper pool of 10-20 experts within the GEM group that can apply their expertise directly to production lines at their home institutions. An example of the power of this approach was a problem with the mechanical tolerance of one of the industrially produced detector components (outer frames), which was missed at CERN, but spotted by three of the external sites. This led to the immediate rectification of this problem. The three external sites have built GE1/1 production chambers by the time of the writing of this report and demonstrated high-quality products as proven by their QC results. This shows that the site qualification protocol as described above works as planned.

The situation in Phase 2 for GE2/1 and ME0 production will be much more straight-forward as most GE1/1 production sites are expected to continue directly with GE2/1 and ME0 production. By the time GE2/1 production is to start, it will be very clear from the full GE1/1 production experience which sites can deliver high-quality detectors on time. New production sites, which intend to participate in the GE2/1 and ME0 mass production, will go through the same qualification procedure as the GE1/1 production sites.

6.2.2 Performance requirements

The desired tracking and physics performances of the GE2/1 and ME0 detectors outlined in the introduction and detailed in Section 6.1 impose the following basic requirements on the detection performances of the CMS triple-GEM detectors:

- Maximum geometric acceptance
- Single-chamber efficiency of 97% or better for detecting minimum ionizing particles.
- Rate capability of at least 2.1 kHz/cm^2 for a GE2/1 module and 150 kHz/cm^2 for a ME0 module.
- Angular resolution of 500 μrad or better.
- Timing resolution of 8–10 ns for a single chamber.
- Gain uniformity of 15% or better across a module and between modules.
- No gain loss due to aging effects after 9 mC/cm^2 of integrated charge for GE2/1 and 840 mC/cm^2 for ME0.
- A discharge rate that does not impede performance or operation.

We briefly review the rationale for these requirements. Clearly, maximum acceptance will yield maximum physics yield. For a detector realized with only two layers, such as the GE2/1, high single-chamber efficiency is mandatory to assure good overall muon detection efficiency and reliability. With 97.0% individual module efficiency, an ME0 stack with six modules will have a 98.8% efficiency for providing at least five hits for stub reconstruction based on combinatorics. The maximum expected hit rate within the GE2/1 (ME0) acceptance is about 0.7 (50) kHz/cm^2 for HL-LHC running at 14 TeV and 5 $\times 10^{34}$ cm^{-2}s^{-1}. Multiplying with a safety factor of three gives a required hit-rate cabability of 2.1 (150) kHz/cm^2. A hit precision of 500 μrad will give sufficiently precise stub directions for stub matching to tracker tracks and CSC stubs; see Section 6.1. As the GEM detectors will provide primitives to the trigger, a time resolution of 8–10 ns is required for a single chamber when running with a 25 ns bunch crossing time at the HL-LHC in order to match the correct bunch crossing. A uniform module response will ensure that there are no geometrical reconstruction biases. The gain of a single GEM foil typically varies across the foil surface by 5–8% due to intrinsic variations in hole diameters that stem from the production process.The corresponding typical gain variation in a triple-GEM detector is $\sqrt{3}$ times larger, i.e. about 10–15%. The modules should not incur significant additional response non-uniformities due to any other factors. The charge expected to be integrated (see Appendix B of Ref. [7]) in the ME0 sector at highest η over 20 years of operation at the HL-LHC is about 280 mC/cm^2. The ME0 modules must be able to integrate a charge of 840 mC/cm^2 over their lifetime without any gain loss or other loss in reponse which includes a safety factor of three. The requirement for the GE2/1 chambers is much less stringent; they must be able to integrate a charge of 9 mC/cm^2 over their lifetime without any gain loss or other loss in reponse.

Since the triple-GEM design of the new modules follows very closely that of the GE1/1 triple-GEM chambers, many of the prototype results of the 8-year R&D program that led to the GE1/1 system can directly apply to the new modules (see Section 6.2.3). As the GE1/1 triple-GEMs satisfy the detector requirements on gain, uniformity, efficiencies, and resolutions, this also holds for the new triple-GEM modules; the reader is again referred to the GE1/1 TDR [7] for details. Specifically, with respect to triple-GEM rate capability, we showed that the gas gain is observed to be constant as a function of incident particle rate up to a few MHz/cm^2. This result confirms that the modules will easily operate in the forward muon region of CMS, where a maximum rate on the order of 50 kHz/cm^2 is expected. Discharge probability and expected rates as well as aging aspects are discussed in detail in Sections 6.2.3 and 6.3 which describe the

operational capabilities and longevity of GEM technology.

In addition, several specific technical constraints and requirements need to be taken into account in the module design. As a baseline, it must be possible to operate the modules using only counting gases that have low global warming impact while fulfilling the above performance requirements. Due to the large size of the GE2/1 chamber it must be assembled from four independent triple-GEM modules, which we label M1 through M4. The material budget must be low enough so that multiple scattering within the modules themselves will not affect the use of muon stubs in the trigger and offline reconstruction. Sufficiently small readout segmentation in η, i.e. along the readout strips, is needed so that the rate of multiple hits on the same strip that can lead to ghost stubs is well controlled. The modules must be designed so that chambers and stacks will easily fit into their designated locations in the muon endcap.

6.2.3 Operational capabilities

The development of GEM detector technology specifically for CMS has spanned eight years that have seen continual improvements to the design and performance of the detector modules. These efforts have led to a final detector technology and design for the CMS GEM modules that is shared between the GE1/1, GE2/1, and ME0 systems. In this section we first briefly summarize the results from triple-GEM performance studies that led to the GE1/1 TDR. Details of these experimental and simulation results from these studies can be found in Ref. [7]. We then discuss more recent studies geared mainly towards the GE2/1 and ME0 detector systems.

6.2.3.1 Gain, rate capability, charge, efficiency, resolutions, and response uniformity

While the final design of the CMS GEM detector system will feature a digital readout with the dedicated VFAT3 ASIC chip developed by CMS, many of the intrinsic detector characteristics and performance results were obtained with an analog readout system [88, 89] developed by the RD51 collaboration that uses the APV25 front-end chips [90] and provides full pulse height information for each readout strip. The performances of the different generations of triple-GEM prototypes were studied in a series of beam tests at CERN in 2010 [91], 2011 [92], and 2012 [93], and at Fermilab in 2013 [94]; in particular in the Fermilab beam test the chambers were operated with Ar/CO_2 70:30% and read out with the analog APV25 front-end chips [90]. The GEM collaboration also performed extensive simulations of CMS triple-GEMs.

Gas gains are observed to follow an exponential dependence on applied drift voltage over three orders of magnitude as expected for a gaseous detector. The gas gain for a fixed drift voltage is observed to be constant up to a few MHz/cm^2 of incident particle rate. This demonstrates that the triple-GEM chambers have a high rate capability and will easily operate in the forward muon region of CMS, where a maximum rate on the order of 150 kHz/cm^2 (ME0 at $|\eta| = 2.8$) is expected. When a CMS triple-GEM is operated 50 V above the start of the efficiency plateau in an Ar/CO_2 70:30% gas mixture, the most probable value, mean value, and 99th percentile value of the Landau distribution of the charge induced on a single strip are found to be 4 fC, 11 fC, and 115 fC, respectively [95]. When offline cuts are placed on the strip charge measured by the APV25 to emulate anticipated VFAT3 thresholds, the plateau efficiency is 97%. The angular resolution for triple-GEM prototypes with an angular strip pitch of 455 μrad and binary signal readout is measured to be 137 ± 1 μrad. On the efficiency plateau, the CMS triple-GEM detector operated with Ar/CO_2 70:30% has a timing resolution of 7–8 ns.

The response uniformity of CMS triple-GEM detectors has been extensively studied in high-granularity pulse height measurements using an X-ray generator with a silver target positioned such that the entire active area of the detector is simultaneously illuminated. Photons interact-

ing in the detector gas volume are a combination of predominantly X-ray fluorescence from the copper in the detector materials, electron bremsstrahlung continuum, and a small fraction of unconverted silver K_α and K_β lines (Fig. 6.20).

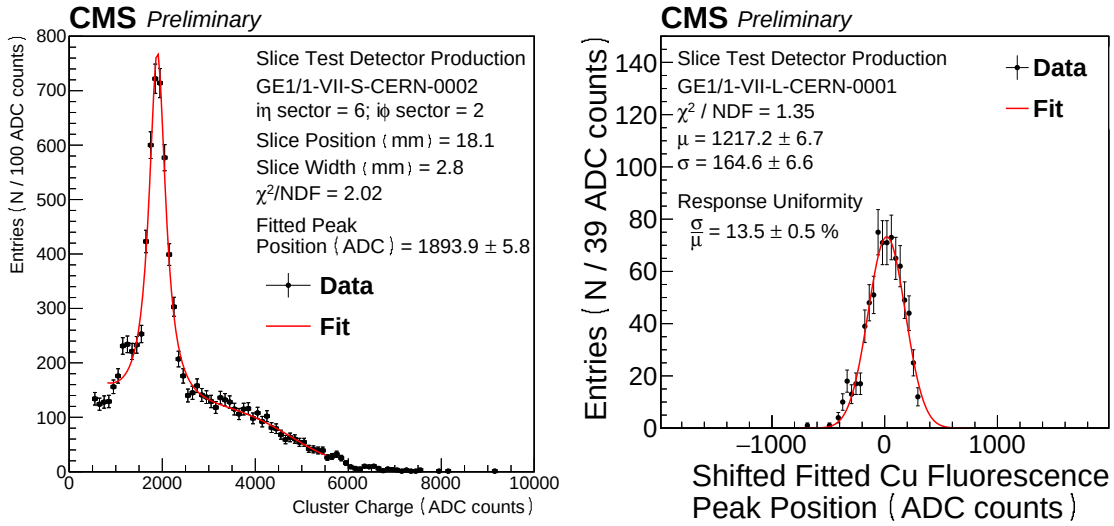

Figure 6.20: Left: Example energy spectrum from approximately four strips of a GE1/1 slice test detector operated at an average gain around 530 with Ar/CO_2 70:30% fully illuminated by a silver X-ray generator. The solid line represents a fit to the experimental data using a Cauchy distribution to model the copper photopeak on top of a fifth order polynomial that models the background. Right: Distribution of fitted photopeak positions obtained from GE1/1 slice test detector GE1/1-VII-L-CERN-0001. The points represent each photopeak position and the solid line is a Gaussian fit to the data. The bulk response uniformity for this detector is $(13.5 \pm 0.5)\%$ based on the Gaussian width.

The detector readout is logically partitioned into radial slices and for each slice a cluster charge ADC spectrum is obtained and fitted to extract the position of the copper fluorescence photopeak. The fit of the spectrum involves a Cauchy distribution to model the photopeak plus a fifth order polynomial to model the combination of electron bremsstrahlung continuum background and a small amount of unconverted silver K_α and K_β lines. Figure 6.21 (left) shows a map of the normalized photopeak energy across a GE1/1 slice test module, where for the purposes of smoother visualization a Delaunay triangulation is used to interpolate the photopeak energies. As Fig. 6.21 (right) shows, it is possible to build large-area triple-GEM detectors with bulk response uniformities of 15%.

6.2.3.2 Performance in magnetic field

Figure 6.22 shows a map of the magnetic field expected in the CMS muon endcap region during LHC Phase-2. In the location of the ME0, we expect a fairly uniform magnetic field with a field strength of about 3 T and a maximum polar angle Θ_B of 5° between the magnetic field lines and the CMS z-coordinate, which is also the direction of the internal electric field lines in the drift region of the ME0. This demonstrates that the ME0 will be operated in a substantial but fairly uniform magnetic field.

At the location of the GE2/1, the magnetic field is weaker with a field strength of about 1 T and a polar angle Θ_B that varies across the chamber and exceeds 15° in the outer radial half of the chamber. The GE2/1 will have to be operated with a substantial angle between the magnetic field and the electric drift and transfer fields within the triple-GEM.

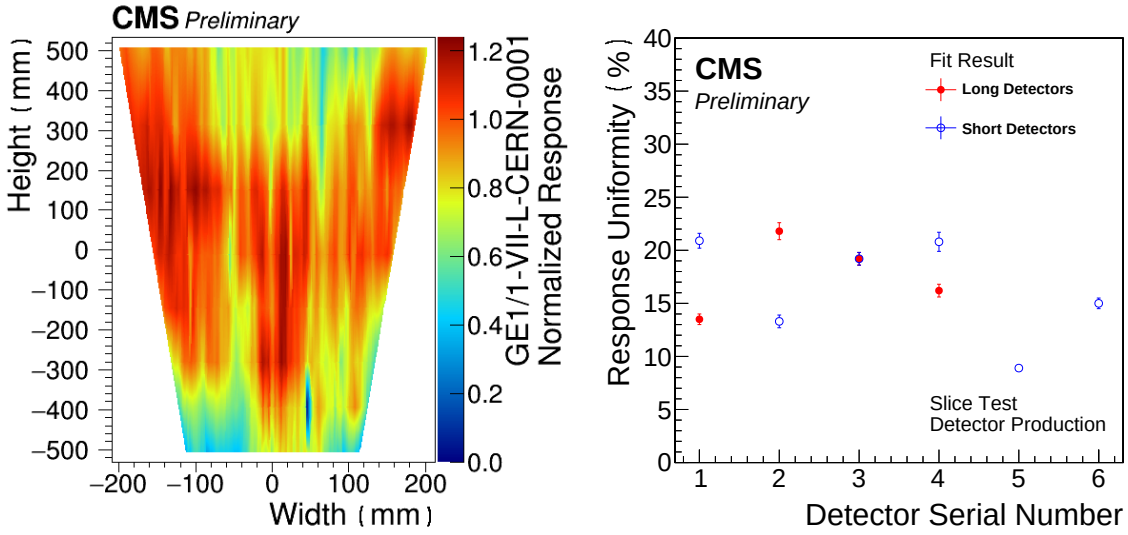

Figure 6.21: Left: Map of the detector response, i.e. the normalized photopeak energy, across a GE1/1 slice test module using Delaunary triangulation. Right: Bulk response uniformity values for triple-GEM detectors installed during the GE1/1 slice test.

During a test with 150 GeV muon and pion beams in the SPS H2 beam line at CERN, a CMS triple-GEM chamber (GE1/1-II prototype) was operated in a magnetic field up to 1.5 T provided by the CMS M1 superconducting magnet [92, 96]. The chamber was placed between the two magnet coils to validate the detector performance in a magnetic environment similar to that in the high-η region of the CMS muon endcap. The Lorentz angle for the drifting electrons at 1.5 T and an extreme angle $\angle(\vec{E},\vec{B}) = 90°$ as applied in the test is somewhat larger than the Lorentz angles expected in GE2/1 and comparable to the Lorentz angle at 3.8 T and $\angle(\vec{E},\vec{B}) = 5°$ that will be encountered by ME0 in CMS (see Fig. 6.22).

Figure 6.23 shows the mean strip multiplicity of strip clusters and the cluster displacements as a function of magnetic field up to 1.5 T. The cluster size does not appear to be affected much by the magnetic field while the cluster position is displaced due to the presence of the magnetic field. The measurement of this displacement is in good agreement with simulations performed with GARFIELD. The overall conclusion from these tests is that the magnetic field does not influence the performance of the ME0 and GE2/1 detectors in any way that would invalidate the conclusions from the measurements without field.

6.2.3.3 Neutron sensitivity

The forward muon region of CMS is exposed to a large photon and neutron flux. The neutron flux is smaller than the photon flux, but the processes that give rise to hits in a GEM detector due to neutrons are more complex and consequently less well understood. Nuclear interactions of neutrons in the material surrounding the chambers and in the material of the chambers themselves (predominantly outer frames and surfaces) lead to the production of photons and electrons that are capable of generating hits in the GEM chambers. Our method for estimating the resulting background rates treats these two contributions separately. An important input parameter for correctly evaluating the overall expected background hit rate in a CMS GEM detector is the sensitivity of a triple-GEM to neutrons. This is defined as the average probability that an impinging neutron interacts with the material of the GEM detector to create ionization that then produces a signal above threshold in the detector. This probability of course depends on the energy spectrum of the incident neutrons.

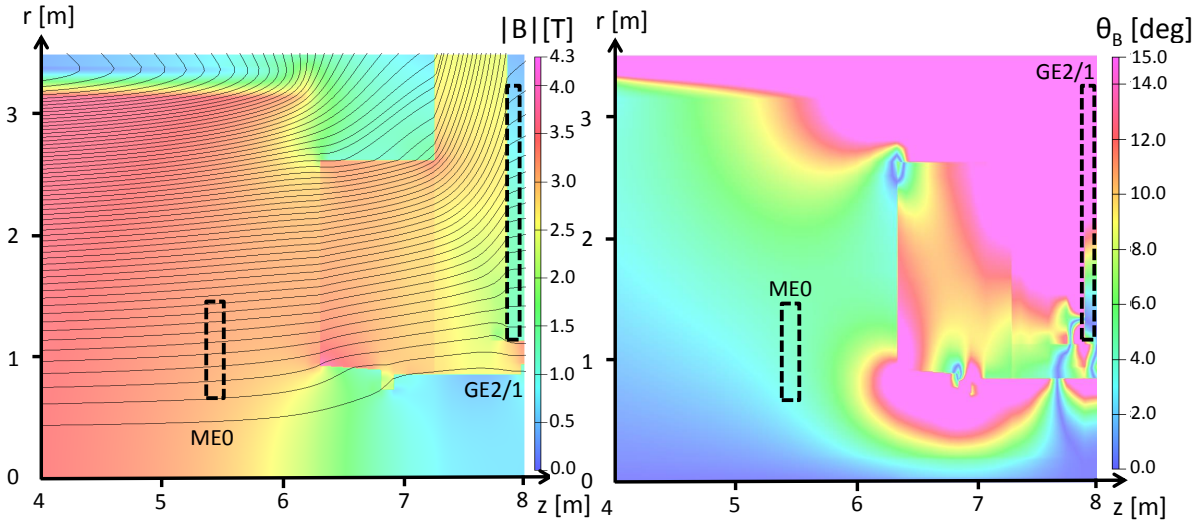

Figure 6.22: Map of the magnetic field expected in the CMS muon endcap region near the solenoid in LHC Phase-2 produced by OPERA simulation. Shown are field strength and field lines (left) and polar angle θ_B of the magnetic field vector (right), i.e. the angle between magnetic field and the z-axis of CMS. The dashed rectangles indicate the locations of ME0 and GE2/1. Regions with $\theta_B > 15^o$ are colored pink.

Due to the complexity of the neutron interactions with the GEM detectors and the dearth of experimental studies on this topic, a dedicated test was done at the CERN High-energy AcceleRator Mixed field (CHARM) facility to measure the neutron sensitivity of triple-GEM detectors directly. At this facility, a 24 GeV proton beam extracted from the CERN PS is used to create a heavy irradiation environment after hitting a copper target inside the facility. The energy spectrum of produced neutrons is similar to that of the neutron background in CMS and ranges from 0.1 eV up to 1 GeV. A small 10×10 cm^2 triple-GEM detector was placed into the radiation field and the resulting high energy particle spectrum was tuned with movable iron and concrete filters to reach the desired dose rate at the position of the test detector. It was exposed to a neutron fluence of about 2.5×10^8 cm^{-2} during the test. Since charged hadrons, electrons, and other particles are also present in this mixed radiation field, neutron signals were selected in the GEM detector by requiring hits with large charge using an appropriate discriminator threshold. From the ratio of measured counts above threshold and incident neutron fluence, the neutron sensitivity for the triple-GEM was measured to be 7.5×10^{-4}.

6.2.4 GE2/1 and ME0 data acquisition systems

While both systems have differences in the implementation of the corresponding DAQ system, there are many commonalities and significant unification of the components used. The general concept of the GE2/1 and ME0 DAQ system is shown in Fig. 6.24.

The signals induced on the strips of the Readout Boards of the GEM modules are directed to the front-end ASIC chip called VFAT3. This chip is the next generation of VFAT2 chip with extended capabilities for operations in high rate and increased latency environment. Digital signals from the VFAT3 chips are routed over another PCB board referred to as GEM Electronics Board (GEB) to an Optohybrid Board (OH). The Optohybrid board has an onboard FPGA to process, compress and transfer the data to the backend electronics located off-detector. The designs (including size of the boards, the number of channels and ASIC chips involved) of these elements are different for the two systems, but functionality is in all cases similar. The

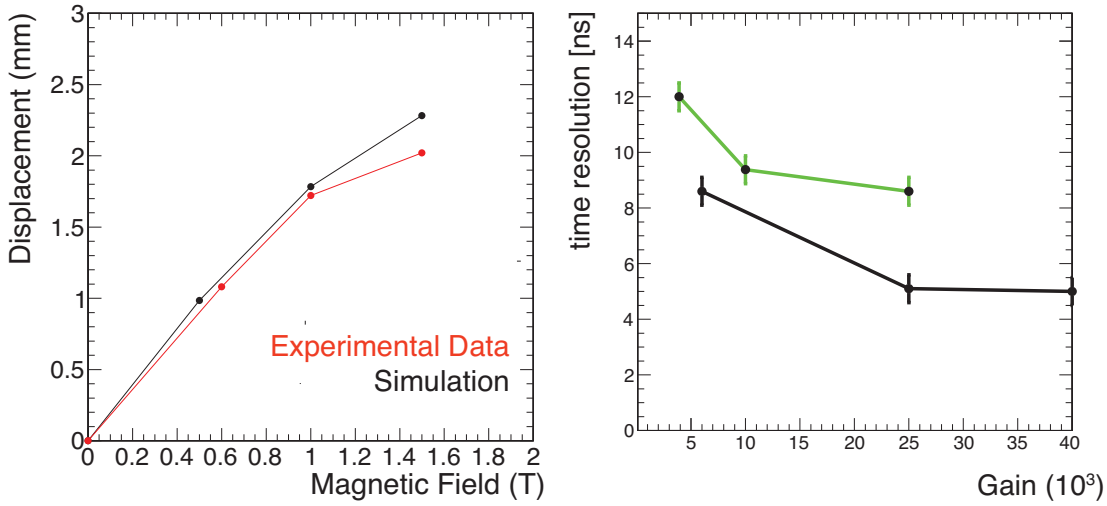

Figure 6.23: CMS triple-GEM (GE1/1-II prototype) performance in a magnetic field. Left: Strip cluster displacement due to the Lorentz force acting on drifting electrons in a magnetic field. Right: Detector time resolution as a function of gas gain in a 1.5 T magnetic field. The green curve is for a CMS triple-GEM (GE1/1-II prototype) while the black curve is for a small prototype.

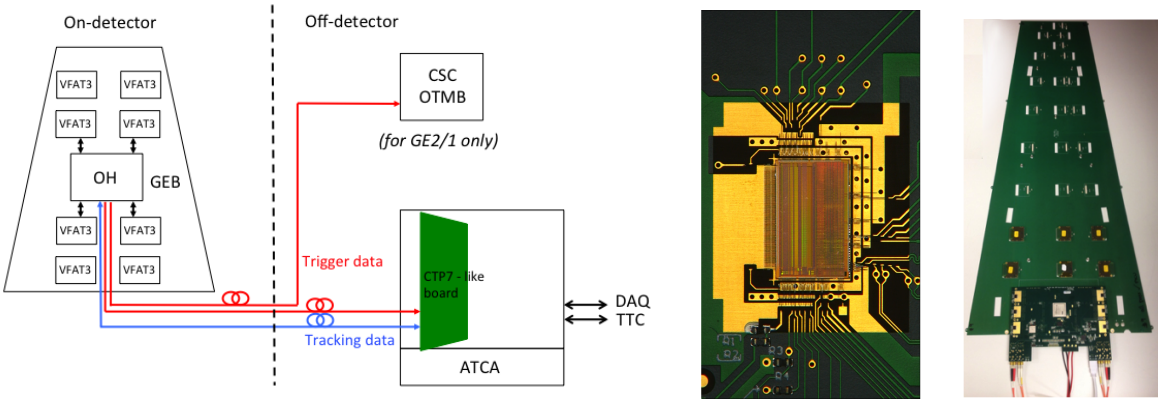

Figure 6.24: Left: The overall principle schema showing main components and communication paths shared by the GE2/1 and ME0 DAQ systems. Center: Photo showing the VFAT3 ASIC chip. Right: Prototype of 1 m-long GEB with Optohybrid board

communication of the on-chamber electronics and the off-chamber electronics as well as the control of the on-chamber electronics is performed over a radiation hard optical link based on the LpGBT technology developed by CERN. The backend electronics consists of processing boards that are hosted in crates and responsible for further processing of the trigger and data streams as well as for the control of the on-chamber electronics. Each crate has a dedicated card to enable communications with the standard clock and control components of the central CMS DAQ.

6.2.4.1 On-chamber electronics

The VFAT3 chip has been developed for use on the GE1/1 chambers, which are scheduled to be installed in the Long Shutdown 2. The chip inputs are the analog signals driven from the strips on the readout board of a triple-GEM module with each chip being capable of handling 128 channels. The output of the VFAT3 ASIC is digital data arranged in two paths: the fixed

latency path to provide trigger signals and a variable latency path to send the full granularity data, also called tracking data. The trigger data is defined as a logical OR of pairs of consecutive channels, e.g. strips 0 and 1, 2 and 3 etc. The ASIC also allows a special mode of operation, in which the trigger data is sent at full granularity using DDR outputs. The VFAT3 ASIC has built-in calibration and monitoring functions and is compatible with the CERN GBT radiation hard link. The ASIC is resistant to doses up to 100 MRad and exceeds the requirements for the expected CMS Level-1 latency (12.5 μs) and frequency (up to 1 MHz). The main specifications of the analog front-end are shown in Table 6.2.

Table 6.2: Main specifications of the analog VFAT-3 front-end ASIC chip.

Key parameter	Comment
Detector charge polarity	Positive and Negative
Detector capacitance range	5 - 80 pF
Peaking times (T_p)	25, 50, 75, 100, 200 ns
Programmable gain	1.25 to 50 mV/fC
Max dynamic range (DR)	Up to 200 fC
Linearity	$<$ 1% of DR
Power consumption	2 mW/ch
Power supply	1.5 V
ENC	$\approx 1100e$ (with T_p=100 ns, $C_d = 30$ pF)
Technology	130 nm CMOS

The VFAT3 chips are to be mounted on the GEM Boards (GEBs), the PCBs responsible for routing signals to the Optohybrid board, which routes and processes signals before they are sent to the backend electronics for further processing. Figure 6.24 (center) and (right) show respectively the VFAT3 ASIC and the GEB on the example of the board designed and built for the GE1/1 detector system. GE2/1 and ME0 detectors systems follow the same principal design for the path from the readout strips on the Readout Board to VFAT3 and then to the Optohybrid board over GEB, but have different segmentation of the ASICs per GEB boards, layout and the size of the boards. For the GE1/1 system, packaged VFAT3 chips can be mounted on small hybrid boards (a 5×5 cm^2 multi-layer PCB) that connect to the GEB and to the Readout Board using dedicated connectors. The GE2/1 and ME0 baseline designs use VFAT3 chips soldered directly onto the GEB boards, which optimizes digital signal quality and simplifies the manufacturing process. To route analogue signals to the front-end chips, a set of short (a few cm long) FlexPCB will connect to the Readout Board and to the GEB. Signals arriving over the FlexPCB to the GEB are then routed over the GEB to the VFAT3 chips.

The Optohybrid board is a multi-layer PCB board with an onboard FPGA and the GBT chipset (GE2/1 and ME0 will use LpGBT) and optical modules for communicating with the backend electronics. The VFAT3 data readout and control functions are performed over a single radiation hard 10.24 Gbps bi-directional link using the GBT protocol. The link includes two fibers, a radiation hard VTRx transmitter/receiver device and a single LpGBTX chip. The OH board also includes a radiation hard SCA chip that enables control of the OH FPGA from the GBT link. In addition to the data/control path, the trigger data readout uses one pair of optical fibers along with the radiation hard VTTx device. No LpGBTX is used for the trigger path. In the case of the GE2/1 detector, the Optohybrid board also transmits trigger information to the ME2/1 OTMB boards, which are part of the CSC trigger electronics for integrated GEM-CSC reconstruction. Links with the CSC OTMB use a pair of optical fibers along with the VTTx device. Size and positioning of the Optohybrid is different for GE2/1 and ME0 detectors, as dictated by spatial constraints and the optimization of the detectors segmentation. Further

details are provided in the corresponding sections.

6.2.4.2 The backend electronics

The backend electronics is planned to be based on the common CMS Phase-2 platform, most likely the ATCA format. While the GE1/1 backend has been based on the earlier μTCA format, the overall schema of the backend electronics setup remains unchanged compared to the GE1/1 DAQ system. It will include processing modules hosted in crates, each processing module receiving data from the OH boards and transmitting time and control data to the on-chamber electronics over optical fibers. This functionality is similar to that provided by the CTP7 μTCA boards that have been adapted for the GE1/1 DAQ system. Each backend crate also hosts a standard CMS "communications" board responsible for common clock and control, as well as communications with the central CMS DAQ and Trigger systems. The backend electronics will be located off-detector and is subject to much less stringent requirements on radiation hardness. The backend system also includes links to the Endcap Muon Track Finder system, which is also undergoing its upgrade. While the GE2/1 and ME0 systems use the same standard components, the number of processing boards is in each case determined by the segmentation of the detectors and the data rates and are described in detail in the corresponding sections.

6.2.4.3 DAQ firmware and software development, control, and data formats

The LpGBT-based bi-directional link enables control of the on-chamber electronics, including the VFAT3 ASICs, by the xTCA backend electronics. The same link is used to transmit tracking data from the on-chamber electronics to the backend system. The xTCA firmware will be responsible of the transmission to the VFAT3s of the fast commands, the slow control, the calibration routines and of the trigger and tracking data acquisition. The OH FPGA is responsible to gather, parse and transmit the trigger data to the xTCA backend and the CSC OTMB (in the case of GE2/1).

We expect that the next generation common CMS processing board will have capabilities similar and exceeding that of the CTP7 board deployed for the GE1/1 backend. The CTP7 features an on-board Zynq controller, a Xilinx produced Linux based System-on-Chip computer with integrated FPGA, which allows for additional flexibility in designing the control firmware, optimal sharing of the processing tasks for the control, the monitoring, the calibrations, etc., between the FPGA and the controller, simplifying the firmware developments and the data processing.

6.2.4.4 Electronics Production Process, Quality Assurance and Control

The plan for design, manufacturing, testing and integration of the components of the DAQ system largely follows the plan developed as part of the ongoing GE1/1 construction project. This includes production of additional quantities of the ASIC chips, manufacturing of the custom electronics, e.g. the GEB and the OH boards, off-the-shelf elements, as well as the CMS-wide standard electronics components (backend processor boards). While only a fraction of the overall system is custom manufactured, every component of the system is expected to undergo rigorous testing as part of the overall quality assurance and quality control program.

The goal of the QA/QC program, details of which are being developed and documented, focuses on steps to avoid or minimize the occurrence of quality issues in the first place as well as procedures designed for early identification of potential problems when they occur. While these procedures are expected to be continuously revised and improved, they are based on the experience of the ongoing GE1/1 construction project as well as previous experience of the

CSC electronics upgrades.

The key elements of this strategy include the following:

- Early prototyping, which includes rigorous testing, including radiation hardness qualification of the components, system integration and torture tests, performed at several R&D test stands at participating institutions in the US and Europe, including the main test-stand at CERN, to assess performance of the components and the system as a whole against a set of parameters devised from the upgrade design requirements;
- In addition to testing the soundness of the designs, the R&D efforts are used to assess the quality and uniformity of the performance of the components used, availability of alternative components, and qualification of vendors, all of which reduce the risk that a significant quality issue is discovered further down the line, thus minimizing the potential impact on the project costs and schedule;
- Quality assurance and quality control focus on early detection of potential problems, and these include manufacturing and testing of smaller quantities of electronics elements (boards) manufactured as part of the production process before full production is released
- Components and parts that are susceptible to batch-to-batch variations due to differences in technological processes deployed at different manufacturing sites are retested before installation on the electronics boards;
- All electronics components undergo testing at the participating institutions as they arrive from the manufacturer following a carefully defined set of standard testing procedures, which range from direct electrical connectivity tests using dedicated firmware and software, functionality and performance testing;
- Each electronics component is individually labeled and tracked for its life cycle using a dedicated database, which includes results of the standard quality control and performance tests for that individual component;
- All components undergo additional testing as they arrive to CERN prior to installation;
- Performance of the on-chamber electronics components is tested again once the electronics is installed on the chamber as part of the chamber assembly quality control, which includes a variety of measurements including connectivity tests, noise levels, communication/bit errors etc. Further, as part of the final certification process, all assembled chambers with final electronics undergo a several week-long period of live testing and data collection at the cosmic test-stand at CERN, the data is analyzed to ensure chambers perform according to specifications, which includes quality control of the electronics components of the readout system.
- Upon re-testing of the backend electronics components on arrival at CERN, these components will be continuously tested as part of the integration tests and activities, including integration with the software and firmware.

6.2.5 Power system design

The power systems for the two detectors rely on the same basic components and modules, which allows us to re-use development and operational experience and simplify future maintenance of the power systems.

6.2.5.1 The high voltage system

To power a triple-GEM, a total of seven different high-voltage potentials have to be applied to its layers. During the R&D phase, these voltages were achieved with a single supply channel using an on-chamber resistive divider circuit. This does not allow for per-channel current measurements or working point optimisation however, and if an HV segment is shorted, the current through the 10 MΩ protection resistor introduces a bias in the operating voltages. Moreover, the divider constitutes a significant local heat load inside the closed volume of the chamber.

To overcome these issues, the seven channels will be powered individually using the CAEN A1515TG multi-channel HV power supply [97] (Fig. 6.25), specifically designed for triple-GEM detectors. This board was developed through a collaboration of CAEN and INFN Napoli, based on the experience in LHCb with a triple-GEM multi-channel high-voltage power supply [98]. One A1515TG board provides 14 floating HV channels, grouped in two complex channels.

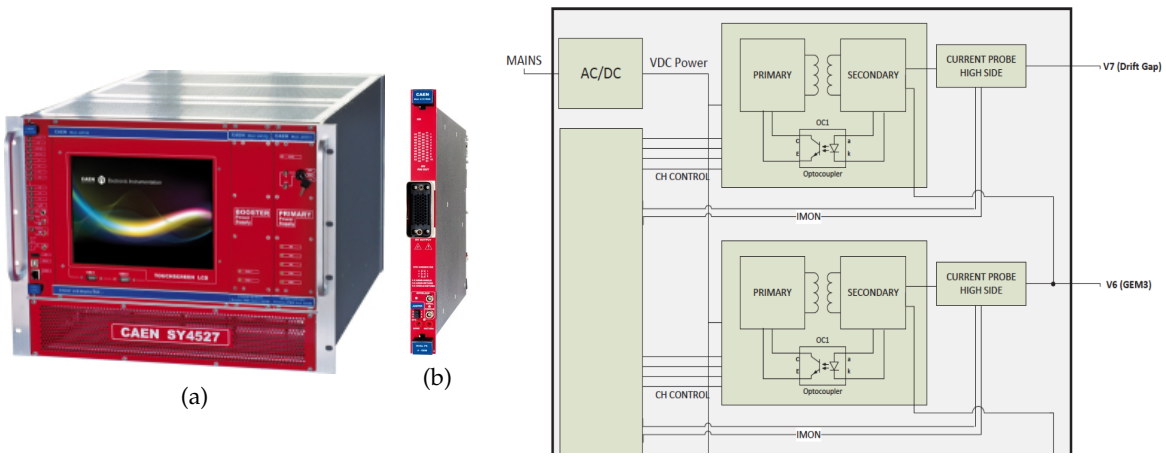

Figure 6.25: The SY4527 mainframe [99] can house up to 16 A1515TG boards [97]. Each A1515TG board provides two complex channels, consisting of 7 floating high-voltage channels each. The SY4527 follows the line of SY*527 mainframes in use in CMS since the start of the LHC operation. The channels in the A1515TG are truly floating with respect to each other as illustrated in the schematic representation (c), and an on-board microcontroller (left) allows for prompt protective responses.

The seven channels within a complex channel can be configured individually. The floating design assures that the failure of one channel does not introduce an increased potential on the neighboring layer. A complex channel can furthermore be configured to act as one. In this mode, the constituting channels are switched on and off together in the desired order. As confirmed by lab measurements (Fig. 6.26), they react on overcurrent and over/undervoltage conditions collectively without software intervention within ∼50 ms, addressing the requirements defined for the trip conditions.

Other important protections implemented in the on-board firmware include overheating detection, an external hardware interlock and a maximum voltage setting to protect the detector against human errors. The A1515TG module is also hot-pluggable, enabling safe, prompt interventions in case of failure.

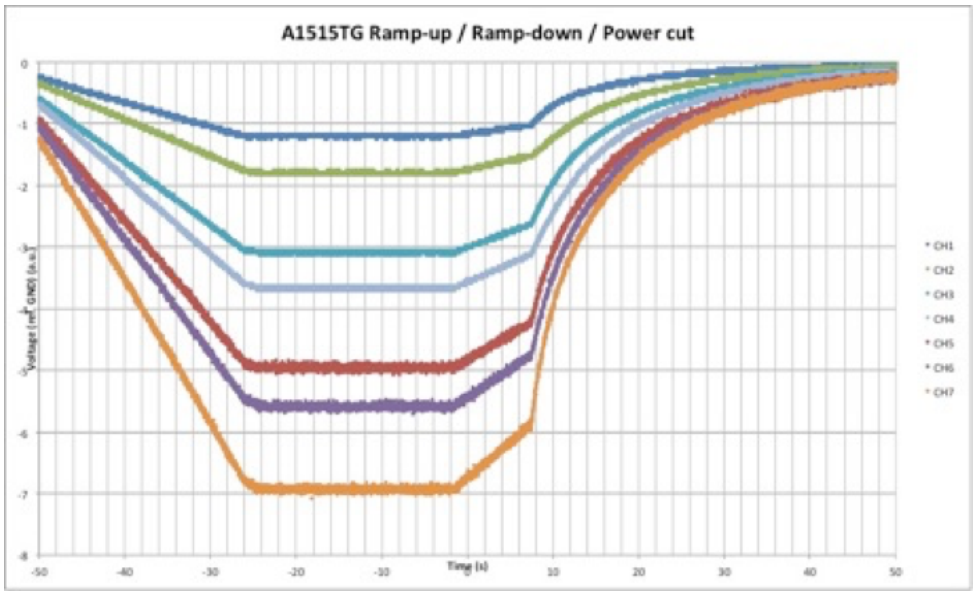

Figure 6.26: Common ramping up of the A1515TG complex channel's HV channels measured in the lab.

Table 6.3: The set of the high voltage working points used in the GE1/1 current cosmic stand is provides as a reference. The final working points are determined as part of the detector QC procedure.

Channel	Drift	GEM 1	Transfer 1	GEM 2	Transfer 2	GEM 3	Induction
Voltage (V)	787.5	394.1	306.6	385.0	612.5	367.5	437.5

The A1515TG module allows for 1 kV and 1 mA per channel, with a limit of 0.7 W, matching detector requirements in Table 6.3. This allows for a total of 8 shorted high-voltage segments while keeping the rest of detector fully operational. The voltage for each channel can be set and read with a 20 mV resolution, and an accuracy of $0.2\% \pm 0.2\,\mathrm{V} \pm 50\,\mathrm{ppm}/^{\circ}\mathrm{C}$, and current limits are set with a 20 nA resolution. Below 100 μA, the current can be monitored with a resolution of 100 pA, and in the range of 100 μA to 1 mA, the resolution becomes 1 nA with accuracy $0.5\% \pm 5\,\mathrm{nA} \pm 50\,\mathrm{ppm}/^{\circ}\mathrm{C}$. The ramping speed can be adjusted from 1 V/s to 100 V/s in steps of 1 V, and reaction to an overcurrent (trip time) can be delayed from 0 s to 1000 s in steps of 0.1 s.

The parameters reported in the datasheet have been verified in lab-conditions by both INFN Naples and RD51 at CERN.

The module has been used for several steps in the production and quality-control of GE1/1 slice-test chambers, and showed compatible detector behaviour with the divider-setup. It also allowed to locate and understand issues more trivially. One super-chamber in the 2017 GE1/1 slice-test has also been installed in CMS equipped with an A1515TG HV supply chain for further long-term-operation validation.

Given the sensitivity of the detector and readout electronics to the noise on the high voltage, an on-detector per-channel low-pass filter (cutoff frequency at 7.2 kHz) reduces noise injected by the module (typically < 10 mV common mode, < 5 mV differential mode for the A1515TG, with main components at 312 kHz, 160 kHz and 80 kHz) or induced along the path to the detector. The necessary HV SMD components have been identified, tested, and operational filters have been installed on the GE1/1 chambers installed in CMS for the 2017–2018 slice-test. The

ultimate filters to be deployed for the GE2/1 and ME0 systems are planned to be similar to the ones deployed for the GE1/1 Slice Test.

To validate the A1515TG modules and the on-detector filters before installation, and to aid in the production and commissioning phases, a seven-channel HV current and voltage monitor is under development with high resolution (10–100 pA, 1 V) and higher rate with respect to the A1515TG (20 Hz). The use of the same HV connectors as the final system allows it to be inserted where necessary.

The A1515TG module fits in the CAEN power mainframes used for several CMS subdetectors since the first LHC collisions, namely the SY*527 series mainframes. This implies that the mainframe, the corresponding OPC server and the WinCC frameworks are mature technologies and the experience is present to implement reliable DCS and DSS systems. Furthermore, it matches the architecture of the LV power supplies, seamlessly unifying software development and detector operation for the full power system. The details of each of the layouts of the High Voltage System for each of the two detectors are provided in the corresponding detector sections.

6.2.5.2 The low voltage system

The main power source for the on-detector electronics is located in the experimental cavern, close to the chambers. That sets additional requirements on the electronics in terms of radiation hardness and operation in the presence of magnetic fields. The baseline LV system for GE2/1 and ME0 rely on the EASY3000 family of boards manufactured by CAEN. The layout of the EASY3000 system is shown in Fig. 6.27. The architecture on the right side of the figure is the mainframe with the A1676A branch controllers, and is located in the USC on the S4 level. Each of these branch controllers can have up to six EASY3000 crates connected. The controllers enable communications between the power modules and the control and monitoring software. The A1676A branch controllers also provide 48V service power to the main A3486 AC-DC converter which powers the EASY3000 crate. The communication goes through cable B, shown in Fig. 6.27, and the services power goes through cable C. Both cables are approximately 200 m long and run between the USC S4 level to the UXC. Both cables must be halogen-free and have good electrical parameters in order to avoid losses. Also located in the UXC is the main A3486 AC-DC converter which transforms the three-phase 230V from its AC power phases to two 48V 2kW channels. Thus one A3486 converter can have up to 2 EASY3000 crates. Cable E, as seen in Fig. 6.27, is the main 48V input power to the crate and cable F, which is part of the communication chain. The services power for the EASY3000 crate is provided by the short cable D which connects the input power to the service power leads. All power connectors are from the Anderson power pole family and have proven to be very rigid in the previous CMS installations.

The GEM LV design uses the A3016 LV modules, which are mounted in the EASY3000 crate. This power module has 6 LV output channels and can provide up to 90 W for each. The GEM chambers are integrated with built-in FEAST DC-DC converters which can adjust the input LV power of the detector to the different levels needed for the on-detector electronics. This is a good approach to eliminate the power loss through the cables, to be more cost-effective, and to use less space for the EASY300 system in the UXC. Thus for each single GEM chamber we will have only one LV channel. The operational voltage is foreseen to be no more than 10 V with maximum current of 15 A. This results in 75 W of maximum power for each of the A3016 output channels. The EASY3000 system with the A3016 module hardware is widely used in CMS. While it provides a reliable and well understood baseline, alternative solutions are being considered, including a next generation CAEN power supply board, which could

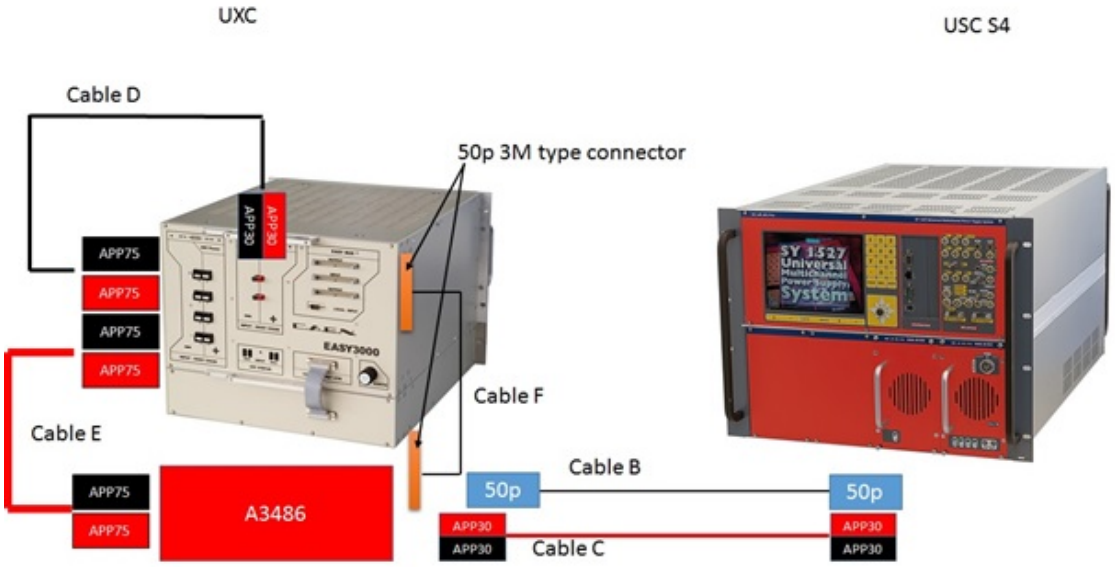

Figure 6.27: Overview of the Low Voltage system for the GEM project

offer advantages in terms of long term system support and maintenance.

6.2.5.3 Quality Assurance and Control

While the design of the GE2/1 and ME0 power systems nearly exclusively relies on commercial components, development and production of the system components will be governed by a rigorous quality assurance and quality contol procedures similar to those developed for the components of the data acquisition system. The QA/QC program will focus on prevention and, when quality issues do occur, on early identification of potential problems to minimize their impact on the project's cost and schedule. The ongoing R&D efforts, which include assessment of components, vendor qualification, smaller scale demonstrator testing and integration tests, focus on prevention of issues. As part of the construction project activities, the focus of the QA/QC program will shift to early identification of problems, tracking of individual components using a dedicated databases, thorough testing of the components arriving from the vendors, testing on delivery and integration testing at participating institutions and at CERN.

6.2.6 Detector devices, monitoring and control systems

6.2.6.1 Gas system

All GEM detectors use Ar/CO_2 70:30% as their standard gas mixture. The requirement is to provide each GEM module with a gas flow of about 5 liters per hour. Based on operational experience with the CSC ME1/1 station, the leakage rate can be expected to be less than 0.6 l/h per module, so we expect system input flow and output flow to differ no more than 10% due to chamber leaks. Since no flammable gases or fluorinated greenhouse gases are used, the GEM gas systems are simple open-loop systems. Figure 6.28 shows an overview of a GEM gas distribution system. It consists of several open-loop circuits, where each circuit covers a 60° detector sector. The same type of gas mixer as used for GE1/1 will be used for all GEM gas systems. It is located in the gas building on the P5 surface level along with the supply cylinders. The Ar/CO_2 mixture flows from the gas building to the detector cavern through a 254 m long transfer pipe made of 30 mm stainless steel, which runs in the PM54 shaft to the gas racks in USC55. Located there is the distributor and mass flow controller which provides the gas to the

UXC via the pipes installed in the cable gallery between USC and UXC. Installation of backup gas pipes from USC to UXC is being planned in consultation with the CERN gas group. The GEM gas distribution racks are located in YE-1 and YE+1 on the X2 far sides. Each is equipped with six flowcells for supply flow and six flowcells for return flow.

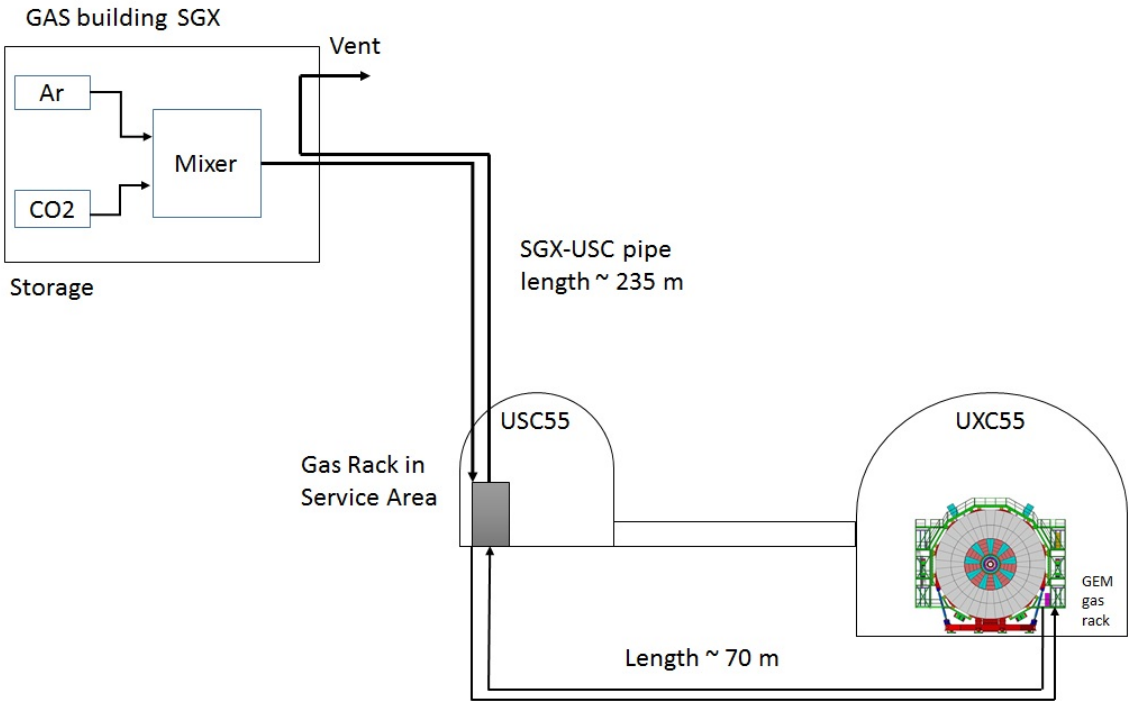

Figure 6.28: Overview of the GEM gas system.

6.2.6.2 Cooling system

The typical temperature of the detector environments in CMS is 22–24 ºC with the maximum temperature not expected to exceed 27 ºC. The humidity remains continuously stable in the cavern with a dew point below 14 ºC. There are no dedicated humidity sensor planned for the GEM detectors as there is already a CMS humidity detection system for all subsystems.

The cooling for all CMS GEM detectors is based on water coolant. The cooling circuit on each individual GEM module is a copper pipe formed into a U-shape and soldered onto copper plates (Fig. 6.29). The plates transport heat from the heated electronics components to the pipe. As all GEM detectors are physically located on the YE1 endcaps, their water coolant is taken from the YE1 water manifolds. The supply water has a temperature of 18 °C and flows at a rate of 2 liters per minute at a maximum pressure of 11 bar. The cooling pipes must have at least 6 mm internal diameter. In the cooling system infrastructure, they are flexible hoses from Swagelok, which are widely used in CMS and proven to be robust and stable over time. Before installation in CMS all cooling circuits must pass a QC test with compressed Argon up to 20 bars. A test with pressurized water is done as the last installation step at P5. In order to ensure safe operation in both closed and open states, we place all the start/stop valves at the periphery of the disk so that in case of a water leak a cooling loop can be easily isolated from the rest of the system during a short access to manipulate these valves.

6.2.6.3 Optical sensors for GEM temperature monitoring

The local temperature of GEM modules will be monitored by fiber-optic sensors (FOS) installed in each module between GEB and readout board. Two FOSs are connected in series along one

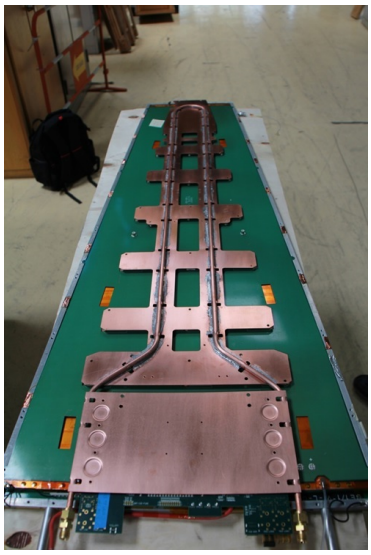

Figure 6.29: U-shaped cooling circuit on GEM modules with plates that make contact with the electronics.

fiber; the two ends of the fiber are terminated on a duplex connector on the patch panel of the chamber. The sensors of all modules in one endcap are daisy-chained by short-length fiber patchcords running from one chamber to the next. If there were a failure on one of the points in the daisy chain, the sensors could be read from the other side of the circle. This system is based on a similar one that has been working very stably in the RPC system since 2007. Long-length fiber patchcords connect the two end chambers of the chain to a fiber that connects to a subrack in a tower rack on each endcap. The rack is connected via fiber to a subrack in the FOS rack in UXC, which in turn is connected via a fiber to a subrack in the FOS rack in USC (Fig. 6.30).

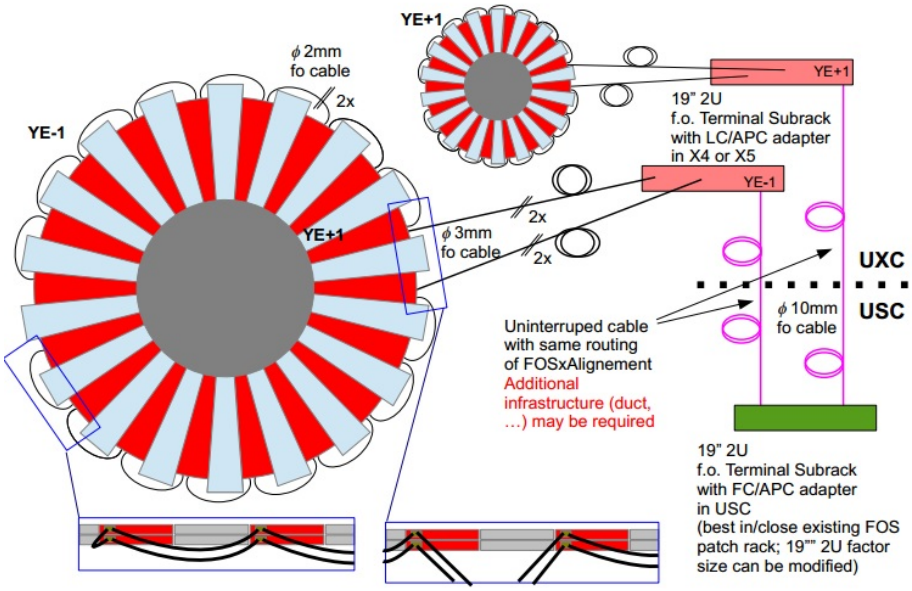

Figure 6.30: Cabling layout of fiber optic system for reading out temperature sensors in GEM modules.

6.2.6.4 Detector control system

The GEM Detector Control System (DCS) is based on the SIMATIC WinCC Open Architecture SCADA software that is already in use for the entire CMS DCS. It controls and monitors the high voltage, low voltage, and gas system and monitors environmental parameters such as temperature and radiation levels independent of the main CMS DAQ system. The HV and LV controls are active sections, in the sense that the operator is able to send commands to the modules and change the set values. The gas and environmental sections allow only continuous monitoring of the sytem status. The gas system is controlled by the CERN gas group. The integration of the GEM DCS into the CMS DCS is done via the use of a Finite State Machine (FSM), which includes the definition of the states that the GEM system can be in and of the actions can be taken. The use of the FSM allows the central DCS shifter to see a single state that summarizes the entire GEM system status and to control it as a whole with a single action.

6.2.6.5 Alignment

The determination of the GEM chamber positions in the CMS coordinate system comprises the location of the chamber positions within the coordinate system of the disk and the location of that disk within the global CMS coordinate system. The chambers themselves will be considered as known rigid bodies guaranteed by construction and optical surveys of the readout boards inside the chamber. Specifically, the alignment procedure entails the following steps:

1. The optical surveys of the readout board segments and the transfer of readout strip information to the outer surface of the boards will be done using the same method and instruments developed for the GE1/1 chambers, i.e. using an optical scanning table and coordinate measuring machine described in detail in Ref. [7].

2. The positions of superchambers or stacks relative to each other wihin a ring can be determined from tracks that cross the overlap region of adjacent superchambers or stacks.

3. The internally aligned disk is connected to the overall muon system via track-based alignment.

6.3 GEM detector longevity

This section describes the study of long-term radiation damage effects on the GEM detectors after long sustained operation in a high-rate environment. These so-called aging issues have been investigated since 2012 to cover the CMS GEM projects GE1/1, GE2/1, and ME0. It includes the understanding of the classical aging processes described in Section 2.2, investigations of possible outgassing of the elements that compose the GEM detectors, the probability of discharges in the detectors as well as the effect of such discharges on the detector operation.

6.3.1 Expected background environment in GE1/1, GE2/1, and ME0 positions

The background in the GEM regions of CMS has been computed using the CMS-FLUKA simulation tool, including the latest CMS geometry, the future detector upgrades, and the new beam pipe geometry. Additionally, the sensitivity of triple-GEM detectors to the different background contributions and energies has been modelled with the GEANT4 framework. The results of the simulation, shown in Table 6.4, indicate that the background hit rate is dominated by photons with an energy around 1 MeV.

Table 6.4: Expected background components and their corresponding hit rates in the GE1/1, GE2/1, and ME0 regions. The total accumulated charge is calculated from the total hit rate at a typical detector gain of 2×10^4.

GEM Station	Max. neutron flux [MHz/cm^2]	Max. neutron induced hit rate [Hz/cm^2]	Max. photon hit rate [Hz/cm^2]	Max. e^+/e^- hit rate [Hz/cm^2]	Max. total hit rate [Hz/cm^2]	Total acc. charge after 10 HL-LHC years [mC/cm^2 - no safety factor]
GE1/1	0.277	499	847	123	1469	6
GE2/1	0.191	343	273	56	672	3
ME0	3.28	5910	33900	7700	47510	283

6.3.2 Classical aging effects

As for all gaseous detectors, the triple-GEM technology might be subject to classical aging due to polymer depositions when operating in a high-rate environment. The aging of GEM-based detectors was extensively studied in the last decade for different sizes, geometries, and configurations (see Refs. [100–102]), which confirm that the GEM technology is particularly resistant to classical aging.

The goal of the CMS GEM aging test campaign [103] is to reproduce ten years of operation at HL-LHC, with a minimum safety factor of three. In order to ensure realistic aging conditions and not to bias the possible aging processes, the aging acceleration factors were kept around 30, as suggested in Refs. [104] and [105]. The study took place at the GIF++ (see Section 2.5). The detector under test is a GE1/1 chamber placed at 50 cm from the 14 TBq ^{137}Cs source and operating at the nominal gain of 2×10^4 in Ar/CO_2 70:30.

The possible aging effects are monitored by continuously measuring the effective gain, which reflects all the aspects of the detector that can be affected by the aging processes: the geometry of the GEM holes, the electric field configuration, and the gas composition. Additionally, the measurement of the energy spectrum at different accumulated charges can indicate a general deterioration of the chamber behaviour and the onset of classical aging. Finally, the constant monitoring of the high voltage and current drawn by the detector can reveal immediately the appearance of dark currents, e.g. due to the onset of Malter effects, shorts in the GEM foils, and sustained discharging.

None of these effects have been observed during the aging test campaign. After twelve months of continuous operation, the detector accumulated a total charge of 110 mC/cm^2, which represents ten years of GE1/1 operation at the HL-LHC with a safety factor 18, ten years of GE2/1 operation with a safety factor 37, and 39% of the total ME0 operation. The result for the effective gain (corrected for pressure and temperature variations) shown in Fig. 6.31 indicates that the CMS Triple-GEM detector does not suffer from any kind of aging effects or long-term degradation.

This test will continue at the GIF++ under the same conditions until the detector accumulates a total charge equivalent to ten HL-LHC years in the ME0 environment (Table 6.4). This will take another 2-3 years of exposure because of the duty factor of the GIF++ and its concurrent use by other experiments. Given this time scale, an additional, faster aging test was mounted in summer 2017 that exposes a GE1/1 chamber to X-rays from an X-ray source with Ag target at a higher rate. At the time of the finalization of this report, 460 mC/cm^2 have been accumulated in one sector of this chamber and smaller amounts in two other sectors. No gain drop has been observed in any of the exposed sectors up to that point. This aging test will continue under the same conditions until the detector accumulates a total charge equivalent to ten HL-LHC years

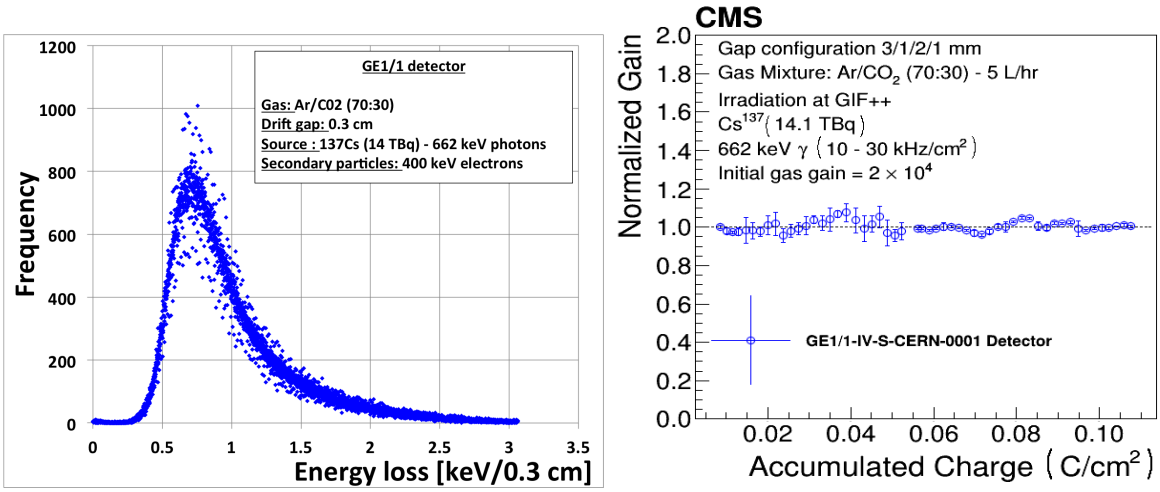

Figure 6.31: Left: Typical energy spectrum from the ^{137}Cs source. Right: Result of the GEM aging test at GIF and GIF++ showing the normalized effective gain as a function of the accumulated charge. The detector under test is a GE1/1 chamber operating in Ar/CO_2 70:30 at an initial gas gain of 2×10^4.

in the ME0 environment with safety factor three. It is expected to be completed by May 2018.

6.3.3 Material outgassing

Past studies have shown that even a small concentration of contaminants in the gas mixture can react with the gas molecules during detector operation, trigger polymerization and cause premature aging [106, 107]. The GEM group investigated the outgassing property of all materials present in the GE1/1, GE2/1, and ME0 chambers to ensure that none of them release pollutants during their lifetime in CMS.

The outgassing test stand consists of a stainless steel cylinder that contains the material under test. The cylinder is flushed with the CMS gas mixture and wrapped with heating tape to control the temperature of the sample and enhance its outgassing rate. The gas with the possible contaminants is then sent to a gaseous detector that is continuously irradiated by a radioactive source. Because the triple-GEM detectors are known to be aging resistant, the gaseous detector is a simple wire chamber operating at a gas gain of 2×10^4 in order to increase the sensitivity of the test. A schematic of the outgassing setup is shown in Fig. 6.32.

In case of material outgassing, the contaminants released in the gas will enter the active volume of the wire chamber. If the contaminants react with the gas and trigger polymerization, the gain of the chamber will immediately drop. The list of all tested materials and their corresponding outgassing test results are given in Table 6.5. Only one material, the polyurethane (PU) CellPack, provoked aging of the wire chamber. It was initially used to coat the internal frame of the GEM detectors. This material has been replaced with another type of PU, NUVOVERN LW, which was tested under the same conditions and did not cause any detector degradations.

6.3.4 Discharge probability

The triple-GEM technology has two main benefits regarding the discharge probability. Firstly, because of the multiple amplification layers, it is possible to achieve gas gains as high as 10^5 without approaching the electrical breakdown of a single GEM foil. Secondly, since the amplification is taking place several millimeters away from the readout structure, it is possible to stop the propagation of a discharge before it reaches the readout electronics. Detailed studies on the

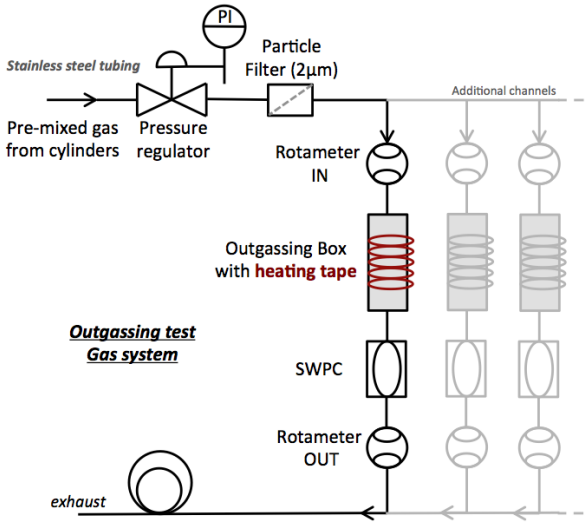

Figure 6.32: Overview of the outgassing test setup showing the outgassing cylinder that contains the material sample and the Single Wire Proportional Counter (SWPC) placed downstream.

Table 6.5: Results of the outgassing test campaign showing the list of the materials under test, their role in the detector, and the effect of their presence on the irradiated wire chamber.

Triple-GEM element	Material	Aging	Comments
O-rings	VITON	No	Baked two hours in vacuum
PU layer	CellPack Nr. 124017	Yes	20% gain drop due to Si deposits
PU layer	NUVOVERN LW	No	
Soldering mask	Elpemer 2467	No	
Sealing coverlay	Krempel AKAFLEX KDF HT	No	
Silver glue	MSDS-Polytec-EC	No	
Washer	Polyamide	No	
Tape	Kapton	No	Energy resolution worsens by 4%
Gas sealing tape	Teflon	No	

discharge probability of GEM-based chambers have been conducted since 2000, which provide a set of recommendations to reduce the discharge probability [108]. These recommendations, adopted in the CMS GEM chambers, include the sectorization of the GEM foils as described above and the use of protection resistors to limit the energy available in case of a discharge, and the asymmetric distribution of charge-amplifying electric fields over the three GEM foils.

6.3.4.1 Measurement of the discharge probability

Several measurements of the discharge probability have been performed to confirm the robustness of the CMS Triple-GEM, estimate the total number of discharges seen by the detectors, and evaluate the effect of discharges on the long-term chamber operation.

In 2014, a CMS triple-GEM detector was irradiated by a 5.5 MeV alpha source to reproduce the heavily ionizing particles (HIPs) induced by the high-energy neutron background in CMS. The discharges were identified via the transient fluctuations of the high voltage and anode current and by recording the number of high-charge signals collected on the readout electrode. Because the discharge probability was expected to be on the order of 10^{-9} – 10^{-10} at nominal gain, the detector under test was set to an extreme gain of 5–6 $\times$ 10^5 in order to measure a sufficient number of discharges in a reasonable time. Then the data were extrapolated to obtain the discharge probability at lower gains. The results indicate that the discharge probability for a triple-GEM detector operating in the CMS configuration is on the order of 10^{-10}/HIP.

More recently, the GEM group has conducted a series of tests in the harsh radiation fields available at the CHARM facility [53] at CERN to measure the discharge probability in more realistic conditions. A triple-GEM detector in CMS configuration was placed near the CHARM target and was irradiated to reach a neutron fluence close to 2.5×10^8/cm^2 and a dose of about 9.4 Gy. The detector was operated at a gas gain of 3.5×10^4 in Ar/CO_2 70:30. The GEM foils were powered independently with a multi-channel power supply in order to monitor the current induced on each electrode and to detect possible discharge signals. Additionally, the signals induced on the bottom electrode of GEM 3 were used to count the total number of particles crossing the detector and to identify the high-charge signals induced by HIPs. A pico-ammeter connected to the readout electrode also measured the total charge generated in the GEM detector.

No trips of the power supply or disruptive events were recorded during the entire test. As a results, considering the average interaction rate at the CHARM facility, we find a preliminary upper limit for the discharge probability of 2.85×10^{-9}/neutron at 95% CL, which is fully compatible with the previous observation with alphas. The discharge study at CHARM facility will continue in 2017 in order to increase the statistics of the measurement, improve the upper limit, and get a more precise estimation of the discharge probability.

6.3.4.2 Expected number of discharges during detector operation

Based on the neutron hit flux presented in Section 6.3.2, we can estimate the total number of discharges per detector after ten HL-LHC years. However, only neutrons with an energy above 1 MeV are expected to produce HIPs and possibly trigger discharges, i.e. about 20% of the total neutron spectrum. Table 6.6 shows the expected number of discharges per cm^2 after ten years of operation, taking into account the discharge probabilities obtained both with the alphas source and with neutrons at the CHARM facility. Due to the high rate in ME0, the largest number of discharges is expected in that system, about 225 per cm^2. This number is to be compared against a discharge test in which 450 discharges per cm^2 were observed. Those discharges did neither damage the foils, nor did they degrade the detector characteristics or performance as detailed in the next section.

Table 6.6: Expected number of discharges seen in GE1/1, GE2/1, and ME0 detectors after ten years of HL-LHC operation. The calculations use the maximum neutron fluence in the hottest region of the detector and we assume that all neutrons with energy higher than 1 MeV can induce heavily ionising particles.

GEM Station	Expected number of discharges (using P = 10^{-10} from test with alphas) [1/cm^2]	Expected number of discharges (using the preliminary upper limit 2.85×10^{-9} measured at CHARM) [1/cm^2]
GE1/1	0.6	17.0
GE2/1	0.4	11.7
ME0	7.9	224.8

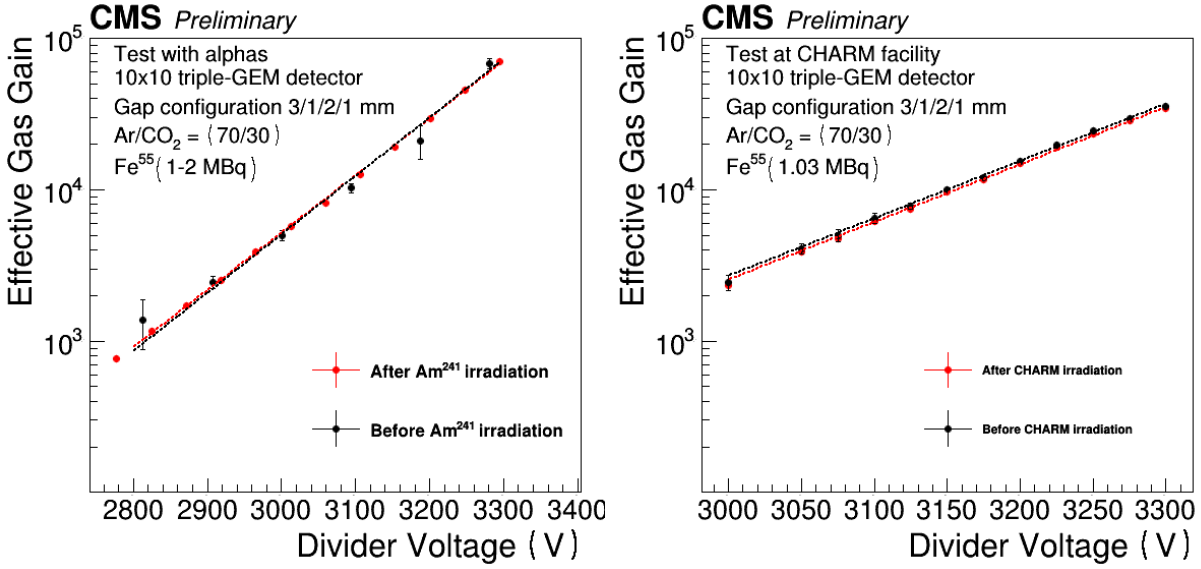

(a) (b)

Figure 6.33: Comparison of the effective gas gain of triple-GEM detectors before and after the intense irradiation with HIPs at CHARM facility (a) and with the alpha source (b).

6.3.4.3 Effects of discharges on the detector operation

Neither during the discharge study with alpha particles, nor during the neutron irradiation at CHARM was any performance degradation or unstable operation observed even though during the measurement the detectors accumulated 450 and 24 discharges, respectively. Figure 6.33 shows the comparison of effective gains of the detectors under test with alpha particles and at the CHARM facility. We do not observe any significant gain differences before and after the intense irradiations.

An SEM analysis of the GEM foils from the GE1/1 chamber irradiated at GIF++ (see Section 6.3.2) also indicated the occurrence of several discharges during the intense irradiation with gammas. After six months of continuous operation, not more than 5–10 discharges per 100 cm^2 of foils have been identified, and all locations show a similar light polymer deposition around groups of 2–3 holes. Figure 6.34 shows examples of polymer deposits and copper vaporisation caused by discharges in GE1/1. It has been established that one of the GE1/1 ma-

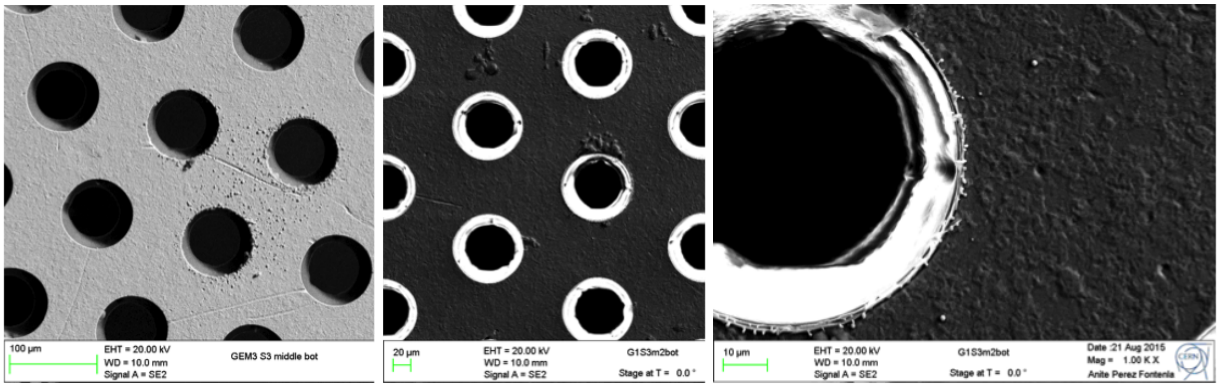

(a) (b) (c)

Figure 6.34: Two examples of polymer deposits after a discharge in a GE1/1 detector irradiated for six months at GIF++ (a and b). Close view of the bottom rim of a GEM hole after a discharge showing a slight vaporisation of the copper (c).

terials was responsible for the presence of contaminants in the gas volume (see Section 6.3.3), which, associated with the energy released by a discharge, could lead to the local production of polymers. The material has been banned from the latter generations of GEM detectors. In addition, the SEM reveals metallic splatters in the vicinity of the copper rim of the GEM hole where the discharge occurred, which certainly results from the vaporization of the copper during the discharge. However, the size of the splatters appears to be limited to 200–500 nm, i.e. negligible compared to the GEM hole size.

Together with the post-irradiation reference measurements in the laboratory, the SEM clearly indicates that the effects of discharges are not strong enough to affect significantly or permanently the operation of a CMS triple-GEM structure or the performance of the detectors. In summary, considering the very small discharge probability and their negligible effect on the detector operation, it has been established that with respect to discharges the triple-GEM technology can operate long-term without losing performance in the GE2/1 and ME0 radiation environments.

6.3.5 Electronics longevity

The radiation environment has been a major consideration in the DAQ electronics system design. The electronics components placed in the CMS experimental cavern, and in particular those located on the detectors, will be exposed to ionising radiation composed mainly of thermal neutrons. Particle flux as well as the total ionizing doze (TID) that various electronics components will see over the HL-LHC runing period vary significantly as a function of pseudorapidity and are summarized in Section 1. GE2/1 electronics is expected to see substantially lower radiation levels compared to the ME0 and the GE1/1 system.

For the ME0 detector, the highest radiation levels are reached at the high η area occupied by the VFAT3 ASICs. The low η sides of the modules, which are farther away from the beam-line and where the Optohybrid boards are located, will see substantially lower radiation levels. The VFAT3 chip is manufactured using the 130 nm CMOS technology and is designed to sustain doses up to 100 MRad, which substantially exceeds the TID to be accumulated by the chips. All the on-detector electronic devices are to be powered by the radiation-hard FEAST DC/DC converters developed by CERN. All the optical communications controlling the front-end electronics use the radiation hard GBT protocol and the GBTx chipset (GE2/1 and ME0 detectors will used the low power LpGBT chips that are an update of the original GBTx chip deployed

on GE1/1). The Virtex-6 OH FPGAs have been tested up to a dose of 80 kRad [109] for the GE1/1 project, and up to 100 kRad as part of recent CSC radiation hardness studies, which exceeds the expected HL-LHC TID. Other authors [110] report the Virtex-6 FPGA to survive up to 380 kRad. The Optohybrid board is designed so that the FPGA can be programmed by the backend processing boards loading the FPGA firmware directly over the optical links. This allows avoiding the use of EEPROMs and is one example of mitigating risks associated with the electronics being damaged by radiation.

During summer 2017 several VFAT3 chips are to be irradiated with high-rate of X-rays at CERN and with heavy ion beams at Louvain-la-Neuve (Belgium) Cyclotron to explicitly evaluate its radiation hardness properties. Additional studies are planned as part of the irradiation campaign foreseen in the Fall of 2017. These studies will also focus on the effects related to single event upsets (SEUs) in relation with the operational requirements and quantifying impact of the SEU mitigation techniques that are planned to be deployed. Examples of the latter include triple logic redundancy features for the firmware and Xilinx Soft Error Mitigation (SEM) core.

6.4 GE2/1 detector system

6.4.1 GE2/1 detector design

6.4.1.1 Design specifications

The basic parameters and specifications for the construction of the GE2/1 triple-GEM chambers and their operation in CMS are compiled in Table 6.7. With these design parameters, the requirements that are outlined in Section 6.2.2 can be satisfied.

Table 6.7: Main specifications and parameters for the design and operation of the GE2/1 chambers.

Specification / Parameter	GE2/1
Detector technology	Gaseous detector; micro-pattern gas detector (MPGD)
Charge amplification element	GEM foil (triple, cascaded, tensioned at $\approx$ 5 N/cm)
Number of chambers in overall system	72 [36 (2×18) in each endcap]
Chamber shape (active readout area)	Trapezoidal, assembled from 4 modules M1-M4; opening angle 20°
Active area overlap in adjacent chambers	15.2 mrad (corresponds to 32 readout strip pitches)
Chamber dimensions (active vol.)	L: 183.3 cm (center line), W: (53.3–117.4) cm, H: 0.72 cm
Total chamber thickness	H: 36.6 mm
Active readout area	1.45 m^2
Active chamber volume	10.4 liters
Radial distance from beam line	1365.5 mm (at inner edge of active readout area)
Geometric acceptance in $\lvert\eta\rvert$	1.62–2.43
Signal readout structure	Truly radial readout strips
Readout strip dimensions	474 μrad angular pitch
Number of η-segments in readout	8
Number of readout strips per η-segment	768
Number of readout strips per chamber	6144
Counting gas mixtures	Ar/CO_2 70:30
Nominal operational gas flow	1 chamber volume per hour
Number of gas inlets	4 (one per module)
Number of gas outlets	4 (one per module)
Nominal HV applied to drift electrode	3200 V (Ar/CO_2)
Nominal operational gas gain	1–2 $\times$ 10^4
Demonstrated rate capability	few MHz/cm^2

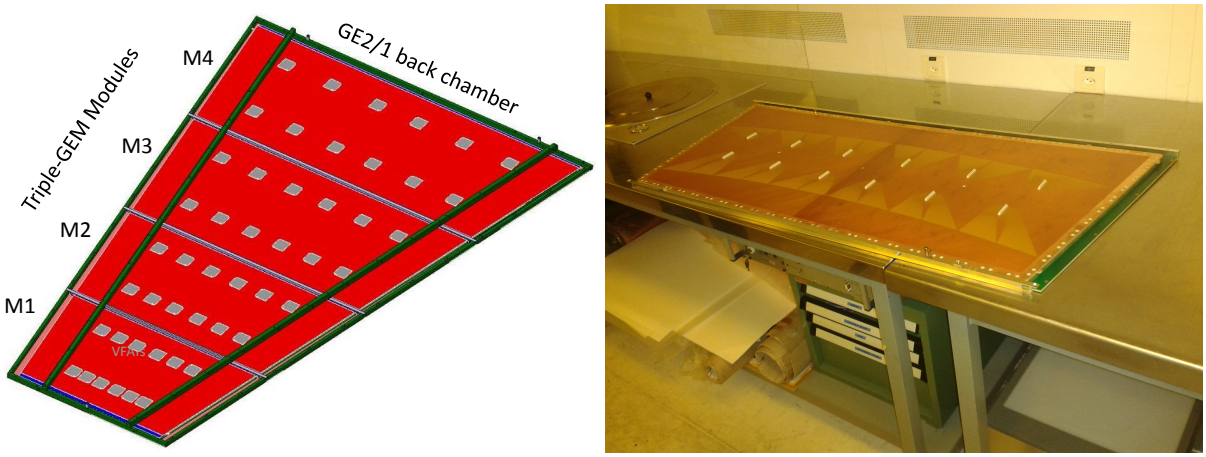

Figure 6.35: Left: GE2/1 back chamber composed of four modules M1-M4. Right: The first M4 prototype produced in the CMS GEM lab at CERN.

6.4.1.2 GE2/1 detector

The GE2/1 baseline detector consists of 20-degree triple-GEM chambers arranged in two layers in each of the CMS endcaps. We refer to the layer closer to the interaction point as the GE2/1 "front" layer consisting of front chambers made from front modules and the other layer as the GE2/1 "back" layer consisting of back chambers made from back modules. For convenience, a pair of GE2/1 chambers covering the same region of space is referred to as a super-chamber although each chamber is completely independent of the other chamber in the superchamber including independent installation. Each GE2/1 chamber consists of four modules M1-M4, each being a single CMS triple-GEM detector. The full system consists of 72 GE2/1 chambers (36 per endcap), which corresponds to 288 basic GE2/1 modules. Figure 6.35 shows the layout of one full GE2/1 chamber and a photograph of the first prototype for a GE2/1 M4 module.

Each module is assembled from a drift and a readout PCB, external and internal frames, and sets of GEM foils specific for each module. The assembly and qualification of the modules can be done independently from the other chamber components. Each single module is segmented into two partitions along the η-direction and 768 strips along the ϕ-direction. Strips that belong to the same η-partition are routed to the readout connectors in groups of 128 strips to match the granularity of the front-end electronics. With this segmentation, each module is partitioned into 12 strip groups (2 η $\times$ 6 ϕ) for a total of 48 strip groups (8 η $\times$ 6 ϕ) in a single GE2/1 chamber.

Modules are distinguished from each other by numbering them along decreasing η starting from the back chamber as shown in Fig. 6.37. The modules differ from each other only with respect to their dimensions; number and type of components are very similar for all eight module types. The unavoidable non-active gap between two adjacent modules in one GE2/1 chamber is 35.5 mm wide in this design. To avoid an overlap between the gaps of two chamber layers within the superchamber that would project back to the interaction point and create a gap in the GE2/1 acceptance, corresponding front and back modules in the two layers have slightly different sizes.

The modules are coupled together to form a GE2/1 chamber with aluminum profiles which are located at the edges of the chamber. To provide mechanical stability to the chamber, three aluminum stiffeners placed between the modules and two radial aluminum bars, which are fixed onto the frame and the stiffeners, run below a protective aluminum chimney that closes the chamber. Figure 6.35 shows the first prototype of this GE2/1 chamber structure; the first GE2/1

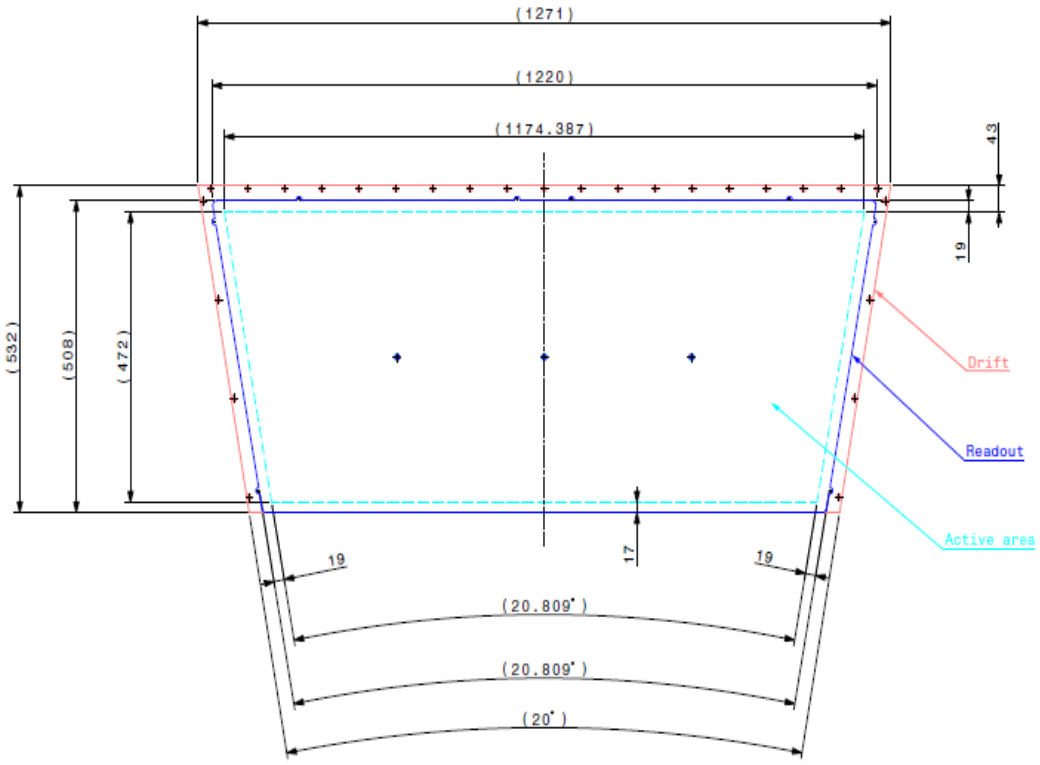

Figure 6.36: Dimensions of the drift and readout PCBs for the GE2/1 M4 back module.

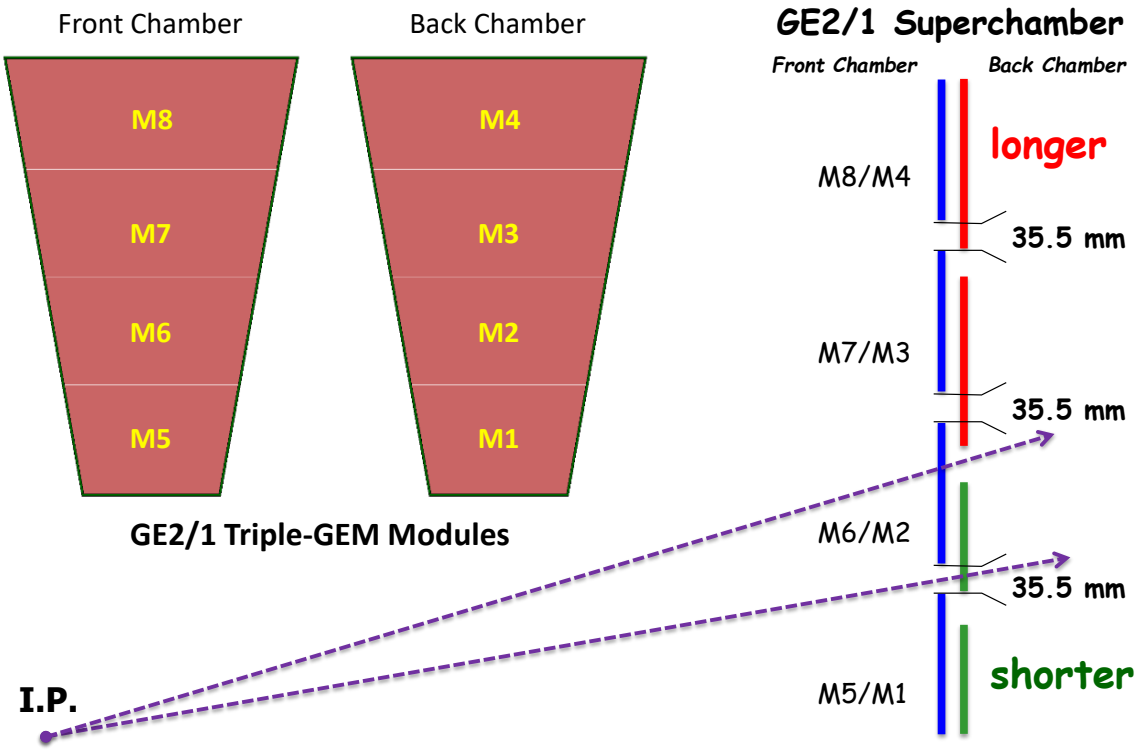

Figure 6.37: GE2/1 triple-GEM module numbering (left) and the overlap of the active areas of the modules between the front and back chambers (right) that minimizes gaps in the acceptance.

Figure 6.38: Prototype of GE2/1 aluminum coupling frame; the M4 prototype module is fixed on the structure in its final position.

M4 module prototype is mounted in this structure. The staggered module design, adopted to preserve full coverage, generates two different "families" of coupling structures, one for the front chambers and one for the back chambers. The copper-pipe cooling system for the electronics will be located under the chimney as for the GE1/1 chambers. Again, the cooling system will be slightly different for the front and back chambers. Each chamber will be equipped with its own service panel for the connection of the chambers to all the services and readout systems (HV, LV, gas, cooling, etc.); identical service panels will be used for front and back chambers.

6.4.2 GE2/1 electronics system

6.4.2.1 GE2/1 electronics design

A block diagram of the main system components in the GE2/1 signal/control electronics is shown in Fig. 6.39. The diagram illustrates the main components for the readout of a single GEM chamber; visible in the on-detector part is the segmentation of the GEM chamber. Each chamber is divided into 4 modules. Each module is equipped with a GEB board segmented into 12 sectors (6 columns in ϕ and 2 partitions in η), each containing 128 strips readout by a single front-end ASIC VFAT3 chip. The GEB boards vary in size, but all are smaller than the GEB boards that have been built for the GE1/1 Slice Test chambers and the manufacturing process for these large PCB boards is well understood.

While the baseline design assumes that each chamber will use four GEB boards, the two modules at the wide side of the chamber are fairly large and there could be advantages in replacing it with two smaller boards. Mechanical considerations, shipping and manufacturing costs, as well as vendor availability are some of the factor being considered. The two modules at the high-η side are made of a single medium-size GEB PCB board.

The pairs of modules are each equipped with a single OH board serving 24 VFAT3 chips (12 in each module). The front-end VFAT3 ASIC converts analog signals delivered by the readout

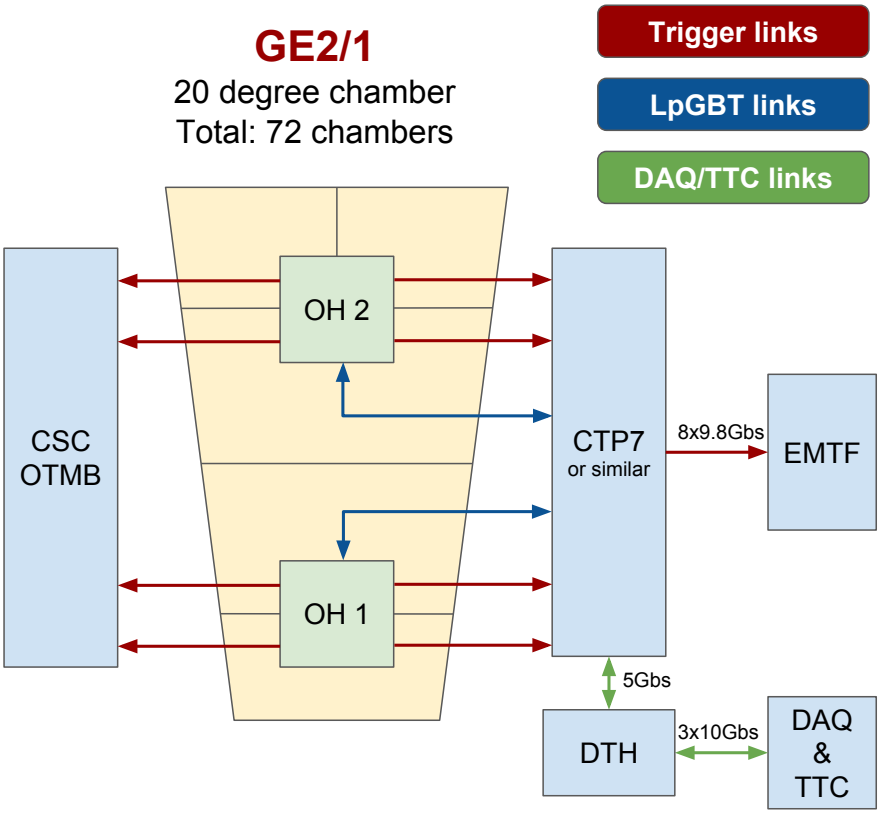

Figure 6.39: A diagram of the GE2/1 electronics readout system for CMS. The vertical line in the center of the top module indicates that the GEB is split into two sections for this module.

PCB board into digital signals containing tracking and trigger data that is communicated to the Optohybrid board, which concentrates and sends the data to the backend electronics. The VFAT3 chip designed for the GE1/1 detector system exceeds the operational requirements for all GEM detectors during the HL-LHC phase in terms of radiation hardness, rate capability, output bandwidth and the Level-1 trigger latency. The main specifications of the analog front-end are shown in Table 6.2 in Section 6.2.4.1.

The GE1/1 VFAT3 chip has been optimized for the range of capacitances of the GE1/1 detector (primarily determined by the area of the readout strips), and these ranges are different than the range of capacitances of the GE2/1 detector. This can lead to a reduced signal to noise ratio for for the GE2/1 and ME0 detectors. These effects are currently being evaluated. While it is expected that the reduction in performance will have little impact on physics performance, the impact and response to this potential risk is well understood. Should the design adjustments to the VFAT3 ASIC be deemed necessary, the manufacturing process will require an additional engineering run to produce a modified variety of the VFAT3 chips.

For each Optohybrid, the data readout and control functions are performed over a single radiation hard 10.24 Gbps bi-directional GBT link connecting the OH with the backend electronics. In addition to the data/control path, the GE2/1 trigger data readout uses two pairs of optical fibers running at 3.2 Gbps. The first pair connects the OH to the GE2/1 backend electronics while the second pair connects it to the CSC OTMB board, which is part of the CSC DAQ/trigger system, for joint processing of the GEM and CSC trigger data.

The Table 6.8 summarizes the information on the number of components per 20 degree GE2/1 chamber and per entire system consisting 72 chambers (two endcaps).

Table 6.8: Breakdown of the GE2/1 electronics DAQ components.

System Component	Number per chamber	Number per system
Front-end		
VFAT3	chips 48	3456
DAQ electronics		
GEB Boards (incl. split GEBs)	4	288
Optohybrid board (incl. GBT SCA)	2	144
Bi-directional Links:	2	144
VTRx devices	2	144
LpGBTX chip	2	144
Optical Fibers	4	288
Uni-directional Link Pairs	2	144
connecting OH & Backend:		
VTTx devices	2	144
Optical Fibers	4	288
Uni-directional Link Pairs	2	144
connecting OH & CSC OTMB:		
VTTx device	2	144
Optical Fibers	4	288
Backend electronics:		
xTCA processor boards		8
xTCA crates		2
xTCA DAQ Link Cards		2

Performance requirements that define the proposed electronics design parameters are primar-

ily defined by the detector hit rates and the bandwidth required to readout the trigger (a synchronous path) and tracking (asynchronous path) data. Simulations show that with 140 PU, the mean GE2/1 cluster occupancy amounts to 0.09 and that the probability to have more than 8 clusters in a GE2/1 module amounts to 1.2×10^{-5}. The bandwidth available at trigger level on each module, that is 2 $\times$ 3.2 Gbps, allows to transmit data for up to 8 clusters (including cluster local coordinates, cluster size as well as a marker for BC0 and overflow) to the back-end. Similar to the GE1/1 system, the latency for the GEM trigger data to be available in the CSC OTMB is around 17–18 bunch crossings. For the tracking data (typically 192 bits of data + 128 bits of headers/trailers per VFAT recording at least one hit), one 10.24 Gbps GBT link is sufficient to transmit the zero-suppressed data from 24 VFAT3s linked to one Optohybrid with a L1A rate of 750 kHz. As noted, the total integrated dose in GE2/1 will be smaller than within GE1/1, that is well below 10 krad for an integrated luminosity of 3000 fb^{-1}. The GE2/1 OH will be equipped with the same Virtex-6 FPGA as the GE1/1 DAQ system and it has been tested to doses up to 100 kRad [109] as part of the CMS GEM and CSC R&D studies and the literature describes testing this type FPGA to doses in excess of 300 kRad without observed damage. To mitigate the SEU events, firmware mitigation techniques will be embedded in the OH FPGA, including logic triplication and Xilinx Soft Error Mitigation (SEM) core. As noted earlier, the GE2/1 OH has been designed to allow programming of the FPGA over the optical link, thus bypassing the EEPROM. This solution is part of the mitigation strategy for long-term electronics survival risks.

Planning and organization of activities related to production of the GE2/1 electronics components, testing and integration follows those deployed for the construction of the GE1/1 electronics. While there are differences in the design of the boards to accommodate for the geometry of the GE2/1 chambers, there are no significant differences in the architecture of technology of the electronics elements. GE2/1 system uses the same or updated versions of existing components: VFAT3, Virtex-6 FPGA, GBTs or LpGBTs, FEAST DC-DC converters, etc. Manufacturing process for the GEB boards, which are a somewhat non-standard element due to the large size of these boards, has been well understood during several iterations of the GE1/1 GEB board prototyping, which included manufacturing of up to 1.2 m-long 6-layer PCBs, which is larger than the GE2/1 GEB boards.

6.4.3 GE2/1 power system

6.4.3.1 GE2/1 high voltage power system

The HV power supplies will be installed in the USC to enable access to the main hardware components for maintenance and repairs during the LHC operations. The multiplexing approach described earlier allows reducing the number of required power supply modules without compromising the current requirements. Figure 6.40 shows the diagram of the power connection scheme for the GE2/1 detector. A 40-conductor cable produced by Novacavi [111] will run from the distributor in the USC to a patch panel in the UXC (X1), each 26 AWG conductor rated at 5 kV. To limit noise induction, the full cable is shielded, and an additional shielding is present for every 10 conductors to match each complex channel and its spare conductors. From the patch panel, a 20-conductor cable with the same properties continues to the detector. This patchpanel gives the possibility to separate problems in the long USC-UXC cable from those in the shorter patch panel-chamber cable.

The current baseline design uses Radiall multi-pin high-voltage connectors [112, 113], including the connection to the A1515TG module, but other solutions are under investigation as well.

Table 6.9 provides a list of components comprising the full GE2/1 high voltage system.

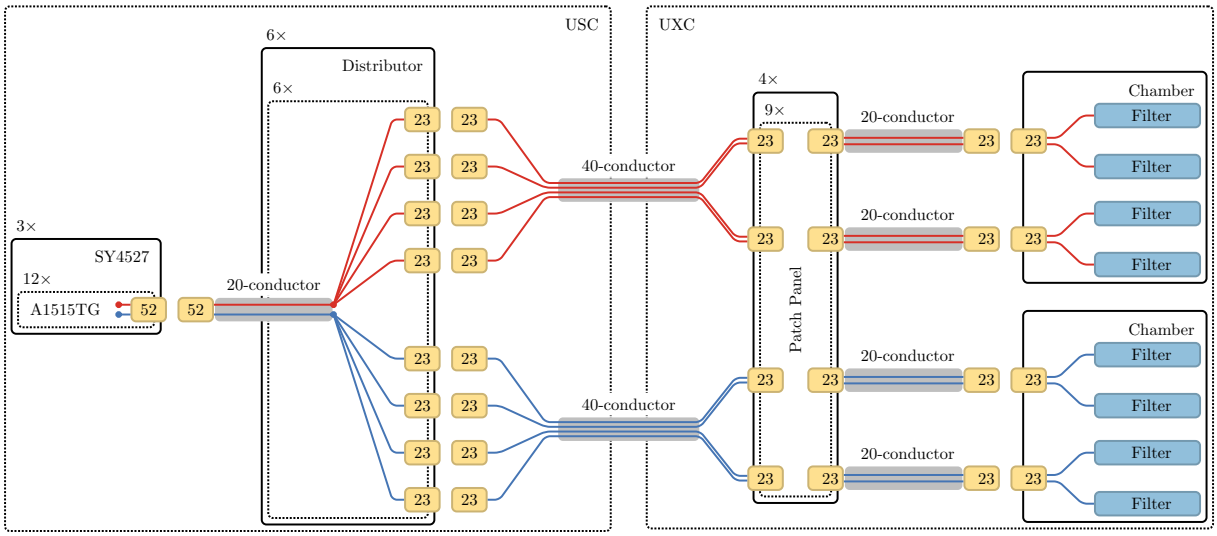

Figure 6.40: Layout of the HV System for GE21, following a single A1515TG and its two complex channels (red and blue). In yellow, the n-pin connectors are indicated.

6.4.3.2 GE2/1 low voltage power system

The GE2/1 LV system follows the generic design described earlier (see Fig. 6.27). Table 6.10 provides specific power requirements for the GE2/1 chambers and superchambers.

Each GE2/1 superchamber has four low voltage channels to power the on-detector electronics (including built-in DC-DC converters), and thus requires two low voltage cables which must be capable of providing 18 A of current on 5 V of voltage. Each disk will consist of 18 superchambers, and thus 72 low voltage channels. In order to accommodate this, we will require three EASY 3000 crates with a total of twelve A3016 low voltage modules spread across the three crates. Currently, space is being reserved for these modules in the X2V33 rack, though additional space considerations will need to be taken into account moving forward. Three EASY 3000 crates require four branch controllers, which will be located in the main GEM communication mainframe in the S4F03 rack in USC-4. For the GE2/1 detectors, we will pull 50-pin DCS cables and 48 V service power cables from the S4F03 rack to the EASY 3000 crates in UXC55, each of which is approximately 200 m long. Power for the 48 V service power cables will be provided from the branch controllers, and go through two A3486 AC-DC converters located in UXC55.

6.4.4 GE2/1 integration, installation, and commissioning

6.4.4.1 Installation procedures and tools

The GE2/1 detectors will be installed on the back of the YE1 disks. The space between the YE1 disk and the ME2/1 detectors on the YE2 disks is 154 mm in total, 65 mm of which is taken up by the shielding of the Y1 disk, leaving 88 mm for the GE2/1 superchambers. The width of a GE2/1 superchamber stack is 74 mm, leaving exactly 14 mm clearance once the GE2/1 detectors are mounted on top of the YE1 shield. These remaining 14 mm must be respected as they are necessary for safely closing the endcaps. For the installation of the GE2/1 chambers, the crane in the UXC must be used due to the size and 40 kg mass of a single GE2/1 chamber. We will first install all GE2/1 back chambers which are close to the yoke and then the off-yoke front chambers to form the GE2/1 superchambers.

Table 6.9: Components needed for the GE2/1 HV System layout.

System Component	Module	Chamber	Disk	System
USC				
HV Mainframe: SY4527 (16 slots)				3
HV Board: A1515TG			18	36
20-conductor cable Board to Distributor			18	36
52-pin connector F			18	36
Distributor			3	6
23-pin connector M	1	4	144	288
40-conductor cable USC to UXC		1	36	72
23-pin connector F	1	4	144	288
23-pin connector M		2	72	144
UXC				
Patch Panel (PP)			2	4
20-conductor cable PP to Chamber		2	72	144
23-pin connector F		2	72	144
23-pin connector M		2	72	144
On-Detector				
23-pin connector F		2	72	144
Filter	1	4	144	288

Table 6.10: LV power requirements for a single GE2/1 chamber (consists of four modules) and a GE1/1 superchamber.

	Voltage	Current consumption for single GE2/1 Chamber	Current consumption for GE1/1 superchamber
VFAT	3.3 V	8 A	16 A
Optohybrid	4 V	6 A	12 A
DC-DC Converter	1.7 V	4 A	8 A

6.4.4.2 Services

All services needed to power and run a single GE2/1 detector are shown in Fig. 6.41. They consist of one LV cable with two LV channels to power the electronics for the 4 GE2/1 modules, two 20-conductor HV cables to power the four GEM modules, fiber patch cords for the readout and control with eight fibers running from the optohybrids to USC55 and four fibers running to the ME2/1 OTMB, and finally pipes for gas and cooling supply and return. At present, there are no readily installed services or infrastructures on the YE1 yokes that can be used for GE2/1. The LS3 period will focus on activities for the barrel and the nose regions without any access to the backside of YE1. Consequently, we plan to install all GE2/1 services already during the LS2 period.

GE2/1 LV infrastructure A total of 72 LV power channels are needed per endcap, i.e. two per chamber. One A3016 channel can power three GE2/1 chambers. As each A3016 module has six channels, twelve modules are required per endcap or 24 modules for the full system. Since one single EASY3000 crate can host up to five A3016 modules, three crates are needed per endcap with two A3486 converters. In terms of U-rack space, 30U each are needed in YE+1 and YE-1 in order to place the three EASY3000 crates and the two A3486 modules. The 30U space should not be allocated in one single rack per endcap in order to avoid concentration of all the LV cables in a single point. Instead, the ideal solution is to spread the modules diamet-

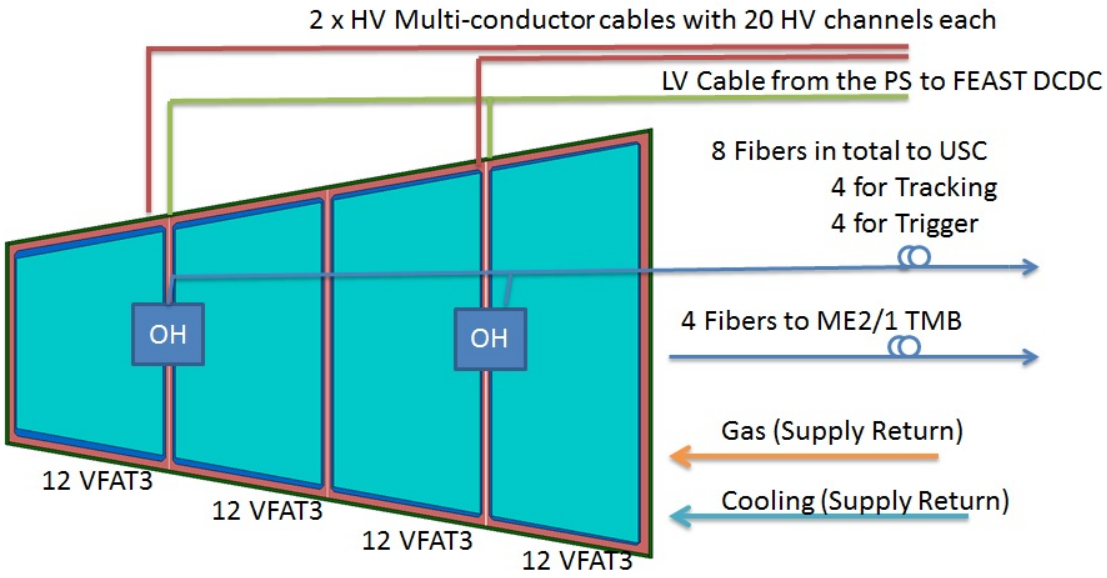

Figure 6.41: Overview of the GE2/1 detector services.

rically along the disk periphery, which may include using left-over space from the GE1/1 LV powering system. Table 6.11 summarizes the LV modules required for the GE2/1 system.

Table 6.11: Summary of LV modules and rack space required in UXC and USC for the GE2/1 system.

Modules in UXC	Modules in USC
A3016 - 24 pcs	Main Frame SY4527 - 1 pc., available from GE1/1
EASY3000 crates - 6 pcs.	A1676A - 2 pcs.
A3486 AC-DC converters - 4 pcs.	
UXC rack space needed - 30U per endcap	USC rack space needed - 0U

6.4.4.3 GE2/1 cooling

The power consumption of a GE2/1 superchamber including a 10% margin is detailed in Table 6.12. The UXC LV rack heating power is estimated by assuming 85% efficieny of the CAEN LV modules, i.e. a total of 6352 W input power consumption and 953 W heat radiated power per endcap. For the full GE2/1 system, a total of 12704 W input power consumption and 1906 W radiated heat is obtained. The GE2/1 cooling system will use water from the YE1 manifolds. Each cooling loop supplies one superchamber, i.e. two single chambers are connected in series. In total there will be 18 cooling loops per endcap for GE2/1, which have to be connected to the YE1 manifolds as described in Section 6.2.6.2.

Table 6.12: Power consumption of the GE2/1 on-detector electronics minus radiated heat.

GE2/1 detector unit	Power consumption
Single chamber	150 W
Superchamber	300 W
Endcap disk	5400 W
Full installation	10800 W

6.4.4.4 GE2/1 temperature monitoring

For the full GE2/1 fiber optic system 72 short and four long patchcords are needed. The installation of the FOS infrastructure is proven to be relatively easy and fast. In case of a fiber failure somewhere in the chain, one can reorganize the system such that it can be fed with light from the other end via the second long patchcord from the UXC rack interrogator.

6.4.4.5 GE2/1 gas system

Table 6.13 shows the basic parameters of the GE2/1 gas system. In the existing gas panel there is a set of twelve flowcells originally allocated to the frozen RE2/1 project, which can be recalibrated and used for the GE2/1 chambers instead. The only additional service installation that needs to be done during LS2 is to pull Cu pipes from the bulkhead boxes on the periphery of the disk to the GE2/1 detector patch panels. The main gas pipe which connects the two endcaps of CMS with the gas distribution rack in USC55 is already in place and available for use for the GE2/1 system. The connections between the gas distribution rack in the far side of UXC-X2 and the GE2/1 detector installation slots currently do not exist. They will have to be made during a technical stop and/or long shutdown.

Table 6.13: Basic specifications of the GE2/1 gas system.

GE2/1 detector unit	Volume [cm^3]	Gas flow [l/h]
Single chamber	10 400	5
Superchamber	20 800	5
Endcap disk	374 400	60
Full installation	748 800	120

6.4.4.6 GE2/1 cable routing

LV cables from USC to UXC A total of four type B and four type C cables, as shown in Fig. 6.27 and described in Section 6.2.5.2, are required, i.e. two type B and two type C for YE-1 and two type B and two type C for YE+1.

Fibers from USC to UXC The GE2/1 chambers require optical fibers for data flow and control as described in Section 6.4.2. Since each chamber requires twelve optical fibers, the full GE2/1 system requires a total of 864 fibers, not including spares. These fibers are classified according to their routing. The uni-directional link pairs that run from the optohybrids to the ME2/1 OTMB require 288 fibers. Another 586 fibers run from UXC55 to USC55, which include 288 fibers for the unidirectional trigger link pairs between the optohybrid and the backend electronics and 288 fibers in the bi-directional data/control links. The exact routing paths of these fibers from the disk onwards are yet to be determined.

Routing on the YE1 yoke On the YE1 yoke, the ring of GE2/1 detectors is surrounded by the central RE2/2 ring and the outer RE2/3 ring. The cables and services for the GE2/1 detectors must be routed between the RE2/2 and RE2/3 rings and the endcap disk. Currently, there is a gap of approximately 30 mm between the RPCs and the disk. Should this space not be large enough for the routing of all necessary cables and pipes, they must instead be routed on top of the RE2/2 and RE2/3 chambers.

6.5 ME0 detector system

6.5.1 ME0 detector design

6.5.1.1 Module design

The basic parameters and specifications for the construction of the ME0 triple-GEM modules and their operation in CMS are compiled in Table 6.14. With these design parameters, the requirements that are outlined in Section 6.2.2 can be satisfied. Figure 6.42 shows the mechanical design and dimensions of the drift boards, readout boards, and active area of an ME0 module; the segmentation of the strips along η are also indicated.

Table 6.14: Main specifications and parameters for the design and operation of the ME0 modules.

Specification / Parameter	ME0
Detector technology	Gaseous detector; micro-pattern gas detector (MPGD)
Charge amplification element	GEM foil (triple, cascaded, tensioned at $\approx$ 6 cN/cm)
Number of modules in overall system	216 (108 in each endcap)
Chamber shape (active readout area)	Trapezoidal; opening angle 20^o
Chamber dimensions (active vol.)	L: 78.8 cm (center line), W: (23.6–51.4) cm, H: 1.8 cm
Total module thickness	H: 3.34 cm
Active readout area	0.296 m^2
Active module volume	2.1 liters
Radial distance from beam line	63 cm (at inner edge of active readout area)
Geometric acceptance in $\lvert\eta\rvert$	2.03–2.8
Signal readout structure	Truly radial readout strips
Readout strip dimensions	0.94 mrad angular pitch
Number of η-segments in readout	8
Number of readout strips per η-segment	384
Number of readout strips per module	3072
Counting gas mixtures	Ar/CO_2 70:30
Nominal operational gas flow	1 module volume per hour
Number of gas inlets	1
Number of gas outlets	1
Nominal HV applied to drift electrode	3200 V (Ar/CO_2)
Nominal operational gas gain	1–2 $\times$ 10^4
Demonstrated rate capability	100 MHz/cm^2

Module cooling The cooling concept is based on the use of a U-shaped, 6 mm inner diameter Cu pipe that is routed across the GEB. The thermal contacts between the pipe and the heat sources are made with Cu strip plates of 1 mm thickness. Every ME0 module will be connected to the Y1 cooling manifold. This design successful passed a cooling test during the commissioning of the five superchambers for the GE1/1 slice test in CMS. The design of the ME0 cooling system is based on power dissipation estimates shown for all heat sources on the detector side, i.e. VFAT3 boards, FEAST DC-DC converters, and Optohybrid as listed in Table 6.15.

6.5.1.2 Six-module stack design

The ME0 detector station comprises 36 module stacks (18 per endcap), each composed of six ME0 modules. Each stack is mounted on a 15 mm thick aluminum plate which supports the stack mechanically (Fig. 1.18). This creates an independently working complete unit, which will allow testing and qualifying of individual ME0 stacks before their installation in the CMS endcap nose. The aluminum plate is itself installed on a rail so that the stack can slide into

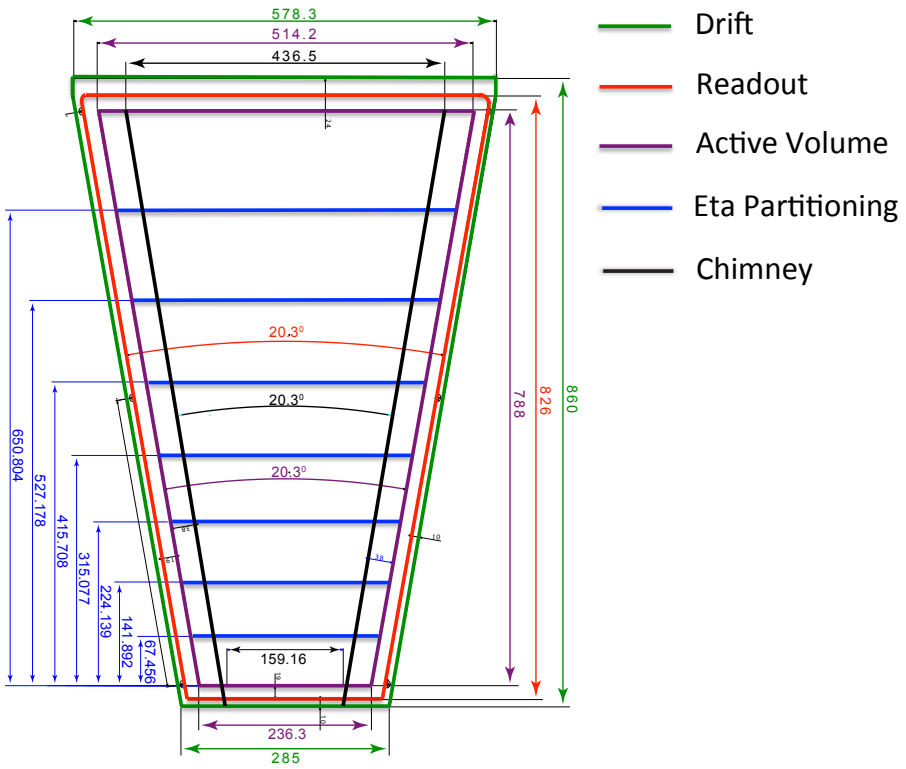

Figure 6.42: Design and dimensions of the drift and readout boards and the active area for the ME0 module. The positions and dimensions of the η-partitions are indicated.

Table 6.15: Expected power consumption for ME0.

	Six-module stack	Endcap	Total
VFAT boards	86 W	1548 W	3096 W
FEAST DC-DC converters	180 W	3240 W	6480 W
Optohybrid v.3	180 W	3240 W	6480 W
Total	446 W	8028 W	16056 W

its final position and so that modules in adjacent stacks can overlap for maximum coverage. Fig. 6.43 shows the ME0 stacks being inserted into the endcap. The modules in each stack are oriented upside-down with respect to the modules in the two adjacent stacks to allow for overlap of modules and maximum coverage.

The thickness of each single ME0 module is constrained by the total space of 238 mm in the z-direction (beam direction) that is available for an ME0 stack. This space needs to accomodate the modules, the aluminum support, and various clearances (Fig. 6.44). Clearances of at least 1.6 mm between overlapping modules in adjacent stacks are needed to allow for comfortable stack insertion. An additional clearance at the top of the stack will avoid any damage to the modules due to the expected 10 mm of maximum deformation of the endcap nose in the magnetic field.

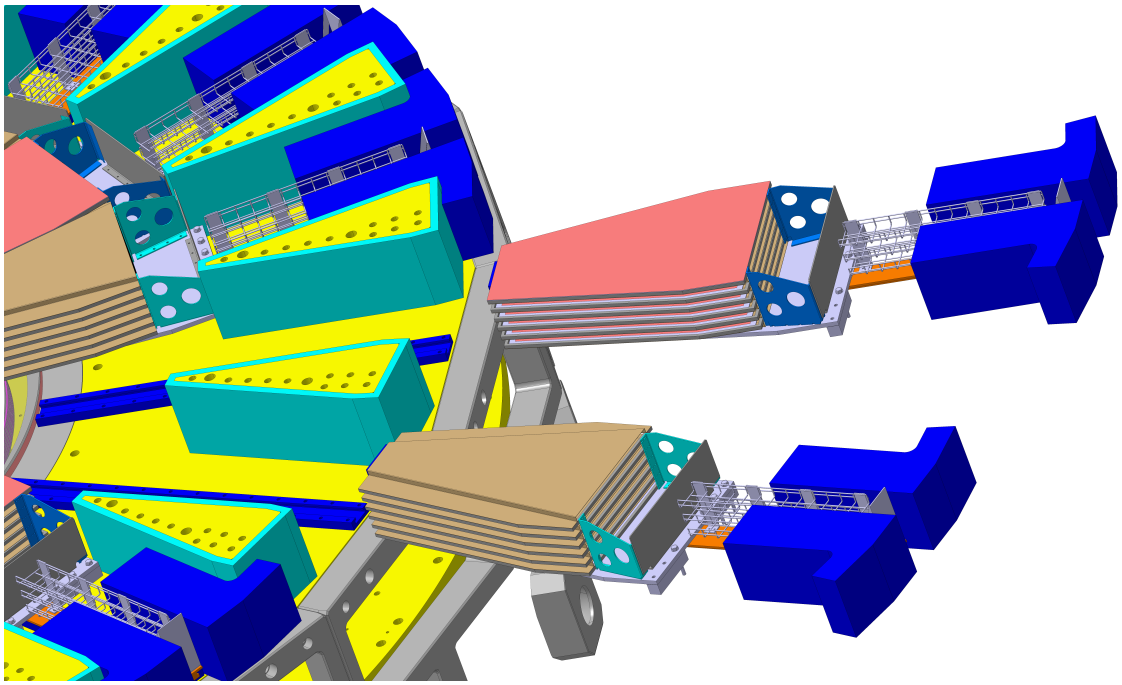

Figure 6.43: 3D drawing of the insertion of two adjacent stacks of six ME0 modules (pink/brown) into the endcap nose. The rails for sliding the stacks into the endcap are visible both on the nose (blue) and on the stack (orange). Note the alternating orientation of modules in the stacks.

6.5.2 ME0 DAQ electronics system

6.5.2.1 ME0 electronics design

The ME0 baseline detector consists of 20 degree stacks each consisting of 6 triple GEM modules. The full system consists of 36 stacks (18 per endcap), which corresponds to 216 ME0 modules. Each module uses a single GEB PCB board. The module readout plane consists of 24 sectors 6 columns in ϕ and 4 partitions in η, each containing 128 strips read-out by a single VFAT3 chip. The 24 chips are placed on the GEB PCB board and the signals are routed to a single Optohybrid (OH) board. A diagram of the ME0 electronics readout system is shown in Fig. 6.45.

For each Optohybrid, the data readout and control functions are performed over a single radiation hard 10.24 Gbps bi-directional GBT link. In addition to the data/control path, the ME0 trigger data readout uses two optical fibers running at 9.6 Gbps (and utilizes two LpGBT chips). All the fibers are connected to the xTCA backend electronics. Table 6.16 summarizes the information on the number of components per 20 degree ME0 module and per entire system consisting of 216 modules.

The electronics performance requirements that define the ME0 electronics system design are again driven by the detector hit rates and the electronics ability to readout the data with minimal losses. In the ME0 case, the very high background hit rates set important requirements on the capabilities of the on-chamber system, specifcially the VFAT3-LpGBT eLinks. The required bandwidth has been estimated using simulation with 240 pile-up interactions per bunch-crossing and using a three-fold the expected neutron background. With these assumptions, the average data rate from the VFAT3 closest to the beam pipe amounts to 275 Mbps, without zero suppression. That is lower than the 320 Mbps bandwidth of the VFAT3-

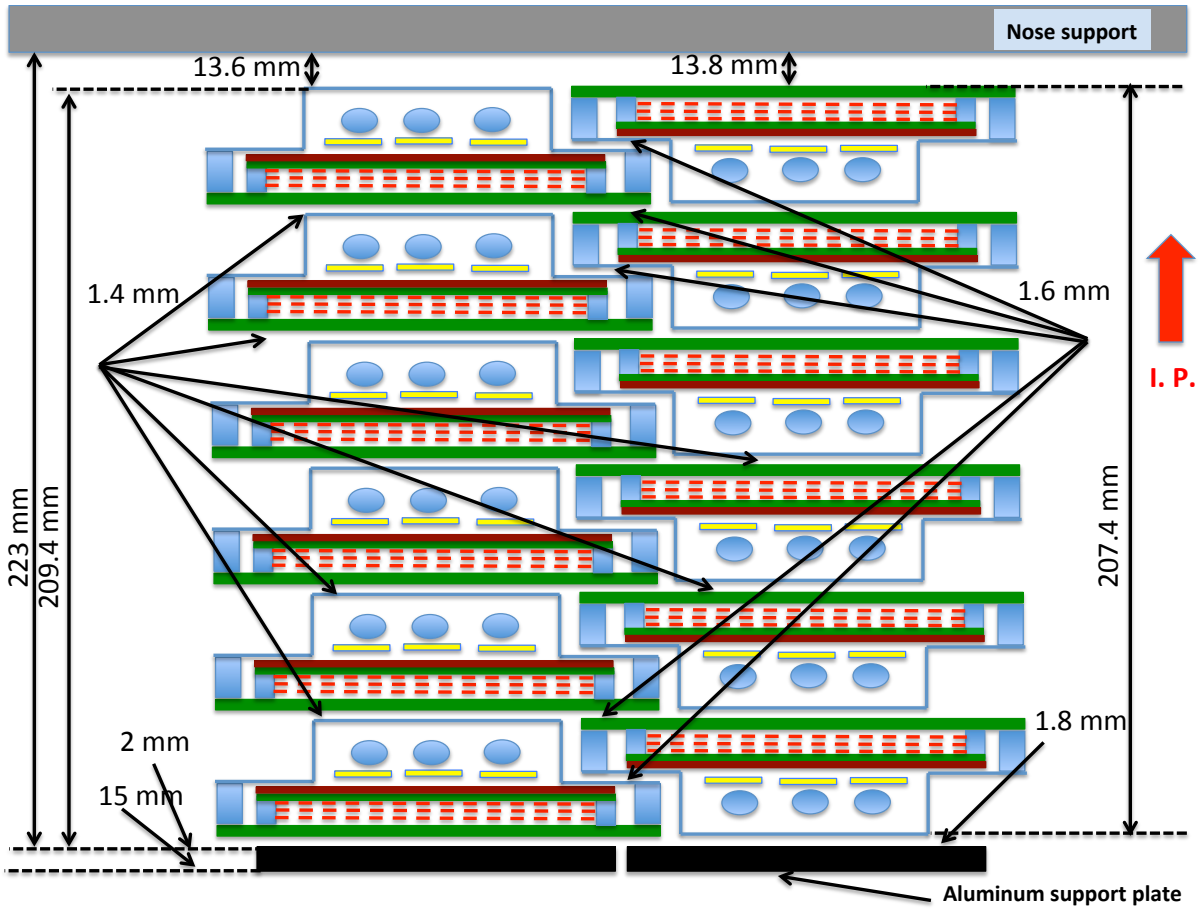

Figure 6.44: Cross-sections (not to scale) of two adjacent stacks after insertion into the nose. The stacks are fixed on the aluminum support plate (black). The total thickness of the stacks, required clearances, and overall available space are shown. The location of the interaction point with respect to this cross-section is towards the top of the figure.

LpGBT eLink. Each xTCA board handles 3 ME0 super-chambers, that is eighteen 10.24 Gbps LpGBT links, for the tracking data and control, and thirtysix 8b10b links for trigger data. In the above scenario, the bandwidth required from one xTCA board to the DTH (the successor of the AMC13) amounts to 120 Gbps, which exceeds the μTCA standard, but enabling the zero-suppressed data format on the VFAT3 and conditioning the readout of a stack (six modules) on a requirement of a loose trigger "stub", similar to the readout of the CSC detectors, reduces the data volume by one order of magnitude. In this case, the rates are well within the operational range of the μTCA at a modest cost in performance. Another alternative is to readout the data either directly from the processing modules to the central CMS DAQ or to a single processing module re-purposed for data concentration and transmission to the CMS DAQ. For the trigger data, each cluster would be identified by 14 bits (11 bits for the position and 3 bits for the cluster size). The two 9.6 Gbps 8b10b optical links per ME0 chamber allow to transmit up to 24 clusters. In the conservative scenario described above, the probability to have more than 24 clusters would amount to 1.3×10^{-3}. This probability decreases to 1.9×10^{-4} at PU = 200.

For an integrated luminosity of 3000 fb^{-1} the total integrated dose in ME0 will be close to 100 times larger than within GE1/1, that is around 1.5 MRad at the highest eta region and less than 30 kRad at the lowest eta region where the OH is located. The specific Virtex-6 FPGA has been tested up to a dose of 80 kRad [109] and more recently 100 kRad as part of the CSC

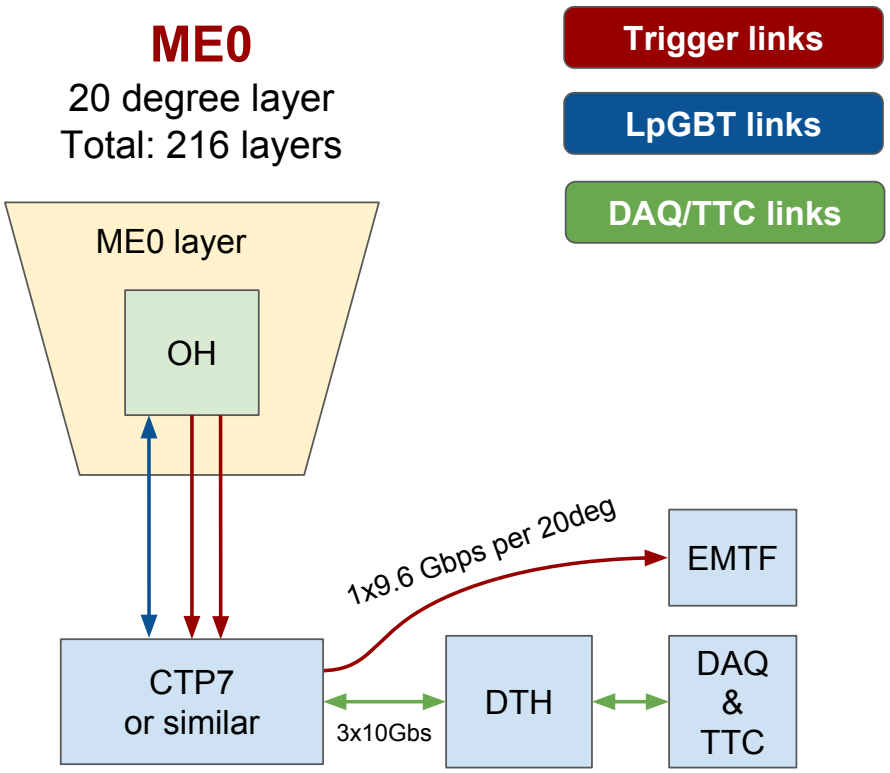

Figure 6.45: Diagram of the ME0 electronics readout system.

Table 6.16: Breakdown of the ME0 electronics DAQ components.

System Component	Number per module	Number per system
Front-end:		
VFAT3 chips	24	5184
DAQ electronics:		
GEB boards	1	216
Optohybrid boards (incl. GBT SCA)	1	
Bi-directional Links:	1	216
VTRx devices	1	216
LpGBTX chips	3	216
Optical Fibers	2	432
Uni-directional Link Pairs:	1	216
VTTx devices	1	216
Optical Fibers	2	432
Backend electronics:		
xTCA processor boards		12
xTCA crates		2
xTCA DAQ Link Cards		2

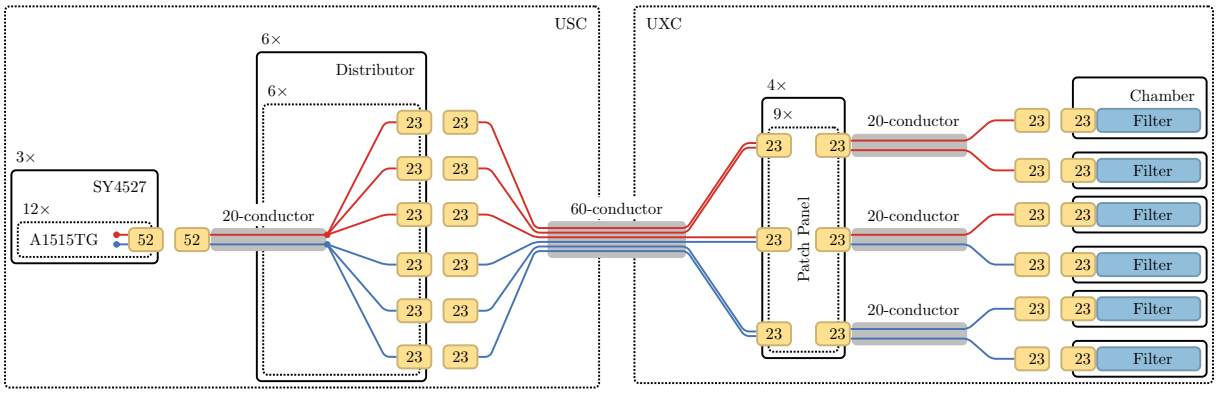

Figure 6.46: Layout of the HV system for ME0, following a single A1515TG and its two complex channels (red and blue). The n-pin connectors are indicated in yellow.

R&D studies, which is a factor of three higher than the expected TID. As mentioned earlier, literature [110] reports studies showing this specific FPGA type capable of surviving TID up to 380 kRad. The 2017 irradiation campaign foreseen in the Fall of 2017 will provide additional measurements and will also quantify the operational effects of the SEUs and the power of the planned mitigation techniques.

The ME0 DAQ electronics system is essentially identical to that of the GE1/1 and GE2/1 detectors and the manufacturing process of the custom boards, selection of components, and vendor qualifications are well understood. The ME0 GEB PCBs have size similar to that of the GEBs deployed for the GE1/1 Slice Test chambers, where the manufacturing process has been well understood. The baseline design relies on electronics components that either exist (Virtex-6 FPGA, FEAST DC-DC converters, etc.) or are updated versions of these components, like the LpGBT chips.

6.5.3 ME0 power system

6.5.3.1 ME0 high voltage power system

The High Voltage power supply layout follows that of the GE2/1 detector, optimized for the 6-chamber wedge layout, see Fig. 6.46 and Table 6.17. Compared to the GE2/1 HV system layout, the 40-conductor cables are therefore replaced with 60-conductor cables, and the distribution is replaced with a one-to-three complex channel fanout.

6.5.3.2 ME0 low voltage power system

Similar to GE2/1, the ME0 LV power system for ME0 will be based on the EASY 3000 crates with A3016 LV modules (see Fig. 6.27 and Section 6.2.5.2). In order to power the ME0 detectors, for each layer we intend to use a single cable with six LV power channels between the ME0 modules and the A3016 module. As a result, in total we will require eighteen A3016 modules per endcap, and four EASY crates per endcap to hold them. In order to power these EASY crates, two A3486 AC-DC converters will be required per endcap, along with one branch controller per endcap. The two system branch controllers will be located in the USC55 S4 level and can be inserted into the already-existing GE1/1 LV mainframe. On the ME0 side, the LV cable will have connectors of 3W3-type, and on the A3016 side the cable will have connectors of APP30-type. For DCS communication and 48 V service power to the AC-DC converters, four cables will run from the mainframe in S4 to the endcaps. These are new cables, and care is being taken to account for the space they will require.

Table 6.17: Components needed for the ME0 HV System layout.

System Component	Chamber	Disk	System
USC			
HV Mainframe: SY4527 (16 slots)			3
HV Board: A1515TG		18	36
20-conductor cable Board to Distributor		18	36
52-pin connector F		18	36
Distributor		3	6
23-pin connector M	1	108	216
60-conductor cable USC to UXC	1	18	36
23-pin connector F	1	108	216
23-pin connector M	1/2	54	108
UXC			
Patch Panel (PP)		2	4
20-conductor cable PP to Chamber	1/2	54	108
23-pin connector F	1/2	54	108
23-pin connector M	1	108	216
On-Detector			
23-pin connector F	1	108	216
Filter	1	108	216

6.5.4 ME0 integration, installation, and commissioning

6.5.4.1 Installation procedures and tools

The ME0 detectors are located on the back flange of the new endcap nose. In the current nose design, the total clearance behind the HGCAL is 274 mm with 205 mm available in the z-direction for the ME0 detector stack and services (Fig. 6.47). The preferred ME0 installation option is to install the detectors prior to the insertion of the endcap nose into CMS. The ME0 detector including all services would be assembled and commissioned together with the HGCAL in the lab. Figure 6.48 shows a sketch of the process for ME0 insertion into the nose, which requires the use of a lifting device, i.e. a small crane. This assembly scenario requires a dedicated heavy transport of the fully assembled nose to P5 and careful handling during its installation in CMS.

6.5.4.2 Services

The required services to power and run a single ME0 stack consist of three LV cables with two LV channels per cable to power the electronics of six ME0 chambers, three 20-conductor HV cables to power six triple-GEMs, 24 optical fibers including one bi-directional link and one uni-directional link pair (four fibers) per module, and pipes for the gas and cooling supply and return lines.

ME0 LV infrastructure The LV power system for ME0 will be based on the EASY 3000 crates with A3016 LV modules. For each layer we intend to use a single cable with six LV power channels between the ME0 modules and the A3016 module. As a result, in total we will require 18 A3016 modules per endcap, and four EASY crates per endcap to hold them. In order to power these EASY crates, two A3486 AC-DC converters will be required per endcap, along with one branch controller per endcap. The two system branch controllers will be located in

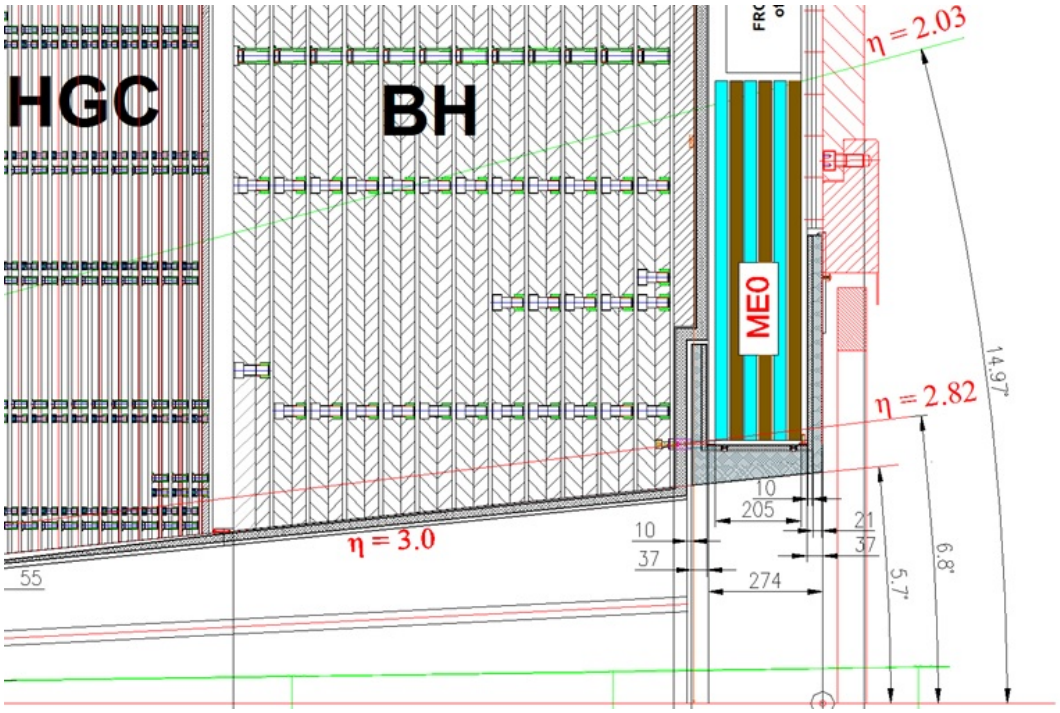

Figure 6.47: Geometry and space constraints for the ME0 detectors in the new endcap nose.

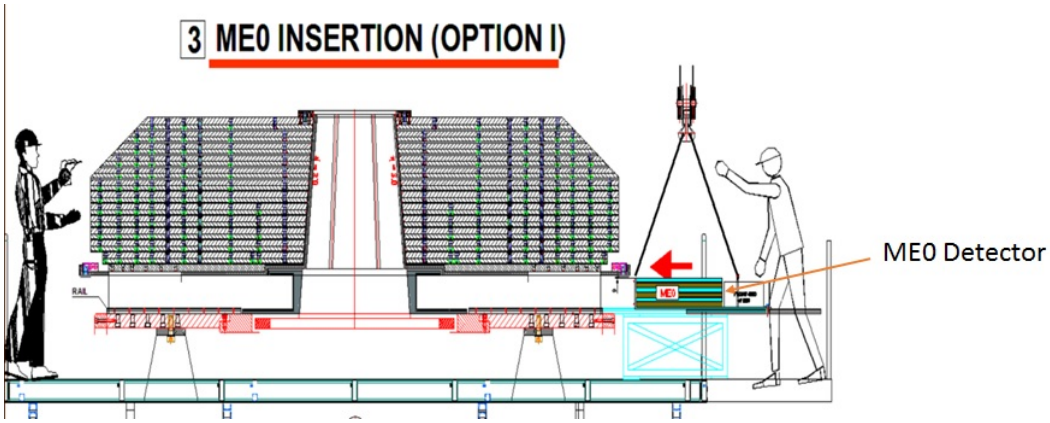

Figure 6.48: Insertion of a ME0 detector stack into the endcap nose before its installation in CMS.

the USC55 S4 level and can be inserted into the already existing GEM LV mainframe. On the ME0 side, the LV cable will have connectors of 3W3-type while on the A3016 side it will have connectors of APP30-type. Table 6.18 summarizes the LV system requirements.

6.5.4.3 ME0 cooling

Tab. 6.19 details the total power consumption of the VFAT3 chip, optohybrid board, and FEAST DC-DC converters for a single ME0 module and for the 18 ME0 stacks per disk; the total power consumption per disk is about 8 kW. Similar to all other GEM detectors, the ME0 cooling system will be based on water cooling. Each cooling loop will supply one ME0 module. The inlet and outlet pipes of every ME0 module have to be connected to their own supply and return points on the YE1 manifold. Consequently, each endcap will require a total of eighteen cooling loops. The specific locations from where the cooling water will be taken are still under discussion.

Table 6.18: Summary of LV modules and rack space required in UXC and USC for the ME0 system.

Modules in UXC	Modules in USC
A3016 - 36 pcs.	Main Frame SY4527 - 1 pc., available from GE1/1
EASY3000 crates - 8 pcs.	A1676A - 2 pcs.
A3486 AC-DC converters - 4 pcs.	
UXC rack space needed - 60U per endcap	USC rack space needed - 0U

Table 6.19: Calculated power consumption for ME0 on-module electronics components.

	Power consumption for ME0			
	Single module	Six-chamber stack	Endcap	Total
VFAT boards	14 W	86 W	1548 W	3096 W
Optohybrid	30 W	180 W	3240 W	6480 W
FEAST DC-DC converters	30 W	180 W	3240 W	6480 W
Total	74 W	446 W	8028 W	16056 W

6.5.4.4 ME0 temperature monitoring

The ME0 detector will also use FOS temperature monitoring. All ME0 modules will be interconnected with short fiber patch cords. The link to the GEM interrogator will be done again with two long patchcords connecting the ME0 circle to the UXC FOS rack (Fig. 6.30). In case of a failure within the ME0 FOS fiber chain, one can power the system from the other end via the second long patchcord.

6.5.4.5 ME0 gas system

Table 6.20 shows the basic parameters of the ME0 gas system. The same Ar/CO_2 gas mixing system that is used for GE1/1 and GE2/1 will be used also for ME0. The gas infrastructure that still needs to be installed during an upcoming technical stop and/or long shutdown are distribution racks in UXC55, supply and return gas pipes between the gas racks in USC55 and the distribution racks in UXC55, and the gas pipes from the UXC55 distribution racks to the ME0 detectors. Each six-module ME0 stack requires its own unique gas loop including supply and return lines. The gas will flow serially through the six modules within a stack. Consequently, 18 loops are needed per endcap, or 36 loops for the entire system. The distribution rack in each endcap should comprise 18 supply and return flow cells.

Table 6.20: Basic specifications of the ME0 gas system.

ME0 detector unit	Volume [cm^3]	Gas flow [l/h]
Module	2 100	5
Stack	12 600	5
Endcap disk	226 800	90
Full installation	453 600	180

6.5.4.6 ME0 radiation monitoring

The baseline design includes a radiation monitoring system utilizing CERN RADMON dosimeters. RADMONs are solid state dosimeters that can provide a quantitative measurement of the deposited dose and the exposed particle fluence in semiconductor devices. One RADMON comprises four detectors, i.e. two Radiation-sensitive Field Effect Transistors (RadFETs) for

photon dosimetry and two p-i-n silicon diodes for neutron and hadron dosimetry. For the RadFETs the allowed range of the dose is 0.001 Gy to tens of kGy depending on required sensitivity. For p-i-n silicon diodes, the generally allowed fluence range is $10^8 - 2\times10^{12}$ cm^{-2} (all fluences are quoted in terms of 1 MeVeq) and for fast hadrons (E $>$ 100 keV) and high-energy neutrons (E $>$ 1 MeV) it is $2 \times 10^{12} - 4 \times 10^{14}$ cm^{-2} as per CERN sensor catalogue - TS-Note-2005-002. This matches the expected high-energy neutron fluence of 2.2×10^{14} cm^{-2} for ME0 well (see Table 1.4). The proposed setup is six RADMONs per ME0 disk that communicate with the CMS DCS.

6.5.4.7 ME0 cable routing

The full package of services for each ME0 stack has to be arranged within a cable tray that is 110 mm wide and 200 mm tall (Fig. 1.18). After insertion of the ME0 detector into the nose, the inner patch-panel will be inaccessible. This means that all the connectivity and operational tests must be done before the ME0 insertion process. The routing needs to be done very carefully with a high packing factor of all cables and pipes. In the current design, the area around the service path is surrounded by HGCAL DC-DC converters and any physical contact with that HGCAL hardware has to be avoided.

LV cables from USC to UXC A total of four type B and four type C cables, as shown in Fig. 6.27 and described in Section 6.2.5.2, need to be installed, i.e. two type B and two type C each for YE-1 and YE+1.

Fibers from UXC to USC The fibers from the ME0 modules have to be patched and combined in trunk cables which will go to the readout system in USC. One feasible paths to the USC is trough the available CMS trigger tunnels. The patching of the 432 fiber links per endcap will require space of 20U in the UXC and USC racks.

Routing on the YE1 nose and disk The routing of services in the new YE1 nose has to be planned in advance together with the neighboring subsystems. For the ME0 detector a dedicated routing path on the nose is being planned. A critical part in the routing is the breaking point between the nose and the disk. Here eighteen areas have to be identified where the ME0 services can pass trough the inflatable seal of the CMS endcap. The exact arrival points of the services, the positions of the LV racks, fiber patch panels, gas distribution rack, and outlets for the cooling water are yet to be specified.

6.6 Cost, schedule and institutional responsibilities

The breakdown of the cost is summarized in Tables 6.21 and 6.22 for the GE2/1 and the ME0 upgrade projects. These estimates include the CORE costs, which incorporate the production costs of all components that are needed for the CMS experiment itself, plus any needed in test stands at CERN, as well as extra components in cases where the production is expected to result in some fraction of faulty components that cannot be used for commissioning. Operational spares are not included in the CORE costs.

The planned schedule and the main groups of activities for each of the two projects is illustrated in Figs. 6.49 and 6.50. The schedule assumes an early installation of the GE2/1 detectors in two consecutive year end technical stops preceding the LS-3 shutdown. Such early installation is consistent with the expected project development schedule and has been deemed highly advantageous in terms of streamlining the schedule of installation activities planned for the LS-3. Institutional responsibilities are summarized in Table 6.23.

Table 6.21: GE2/1 Detector system CORE cost estimate.

WBS	Item	Cost (kCHF)
2.5.2	**GE2/1 Detector System:**	**4 095**
2.5.2.1	*GE2/1 Detectors*	*1 606*
2.5.2.1.1	GE2/1 Detector Components & Assembly	1548
2.5.2.1.1.1	Readout PCB Boards	168
2.5.2.1.1.2	Drift PCB Boards	124
2.5.2.1.1.3	GEM Foil Kits	799
2.5.2.1.1.4	Cooling Circles	116
2.5.2.1.1.5	Module Assembly Components	303
2.5.2.1.1.6	Chamber Assembly Components	36
2.5.2.1.3	Shipping	58
2.5.2.2	*GE2/1 DAQ System*	*1 099*
2.5.2.2.1	GE2/1 FE Readout Electronics	267
2.5.2.2.2.1	GEB Boards	330
2.5.2.2.2.2	OptoHybrid Boards	247
2.5.2.2.2.3	Backend Electronics	150
2.5.2.2.2.4	Optical Links (incl. TRXMM/GBT)	106
2.5.2.3	*GE2/1 Power System*	*920*
2.5.2.3.1	Mainframes (HV & LV)	19
2.5.2.3.2.1	HV Supply Boards	243
2.5.2.3.2.2	HV feet panels & splitter panels	7
2.5.2.3.2.3	HV Cables	119
2.5.2.3.2.4	HV Connectors & Filter Cards	133
2.5.2.3.3.1	LV AC/DC converters	56
2.5.2.3.3.2	LV supply Boards	182
2.5.2.3.3.3	LV Easy crates	18
2.5.2.3.3.4	LV Cables & connectors	139
2.5.2.3.3.5	LV Controllers	3
2.5.2.4	*GE2/1 Services*	*215*
2.5.2.4.1	DCS system	45
2.5.2.4.2	Gas system	56
2.5.2.4.3	Cooling	28
2.5.2.4.4	Alignment	87
2.5.2.5	*GE2/1 Integration*	*140*
2.5.2.5.1	insertion tooling	20
2.5.2.5.2	infrastructure for detector storage	20
2.5.2.5.3	Cable/Services Installation	100
2.5.2.6	*GE2/1 Test bench (2 chambers)*	*115*
2.5.2.6.1	Detector Components & Assembly	41
2.5.2.6.2	DAQ System	56
2.5.2.6.3	Power System	17

Table 6.22: ME0 Detector system CORE cost estimate.

WBS	Item	Cost (kCHF)
2.5.3	**ME0 Detector System:**	**4 241**
2.5.3.1	*ME0 Detectors*	*1,336*
2.5.3.1.1	ME0 Detector Components & Assembly	1 289
2.5.3.1.1.1	Readout PCB Boards	165
2.5.3.1.1.2	Drift PCB Boards	98
2.5.3.1.1.3	GEM Foil Kits	624
2.5.3.1.1.4	Cooling Circles	146
2.5.3.1.1.5	Module Assembly Components	213
2.5.3.1.1.6	Chamber (Stack) Assembly Components	44
2.5.3.1.3	Shipping	47
2.5.3.2	*ME0 DAQ System*	*1 343*
2.5.3.2.1	ME0 FE Readout Electronics	408
2.5.3.2.2.1	GEB Boards	235
2.5.3.2.2.2	OptoHybrid Boards	363
2.5.3.2.2.3	Backend Electronics	226
2.5.3.2.2.4	Optical Links (incl. TRXMM/GBT)	112
2.5.3.3	*ME0 Power System*	*1 106*
2.5.3.3.1	Mainframes (HV & LV)	19
2.5.3.3.2.1	HV Supply Boards	243
2.5.3.3.2.2	HV feet panels & splitter panels	7
2.5.3.3.2.3	HV Cables	100
2.5.3.3.2.4	HV Connectors & Filter Cards	103
2.5.3.3.3.1	LV AC/DC converters	56
2.5.3.3.3.2	LV supply Boards	272
2.5.3.3.3.3	LV Easy crates	24
2.5.3.3.3.4	LV Cables & connectors	277
2.5.3.3.3.5	LV Controllers	3
2.5.3.4	*ME0 Services*	*229*
2.5.3.4.1	DCS system	54
2.5.3.4.2	Gas system	132
2.5.3.4.3	Cooling	37
2.5.3.4.4	Alignment	6
2.5.3.5	*ME0 Integration*	*148*
2.5.3.5.1	insertion tooling	20
2.5.3.5.2	infrastructure for detector storage	20
2.5.3.5.3	Cable/Services Installation	100
2.5.3.5.4	Cable Tray Support Structure	8
2.5.3.6	*ME0 Test bench (3 modules)*	*79*
2.5.3.6.1	Detector Components & Assembly	19
2.5.3.6.2	DAQ System	27
2.5.3.6.3	Power System	33

Table 6.23: GE2/1 and ME0 Institutional Responsibilities

Institution	Country (FA)	Chamber production	Electronics/ DAQ	Power system	Services	Integration
Univ. Libre de Bruxelles	Belgium (FNRS)		X			
Ghent Univ.	Belgium (FWO)	X				
Katholieke Universiteit Leuven	Belgium (FWO)		X			
Inst. for Nucl. Research & Nucl. Energy	Bulgaria	X	X	X		
Sofia Univ.	Bulgaria	X	X			
Peking Univ. (Bejing)	China	X	X			
Bejhang Univ.	China	X				
Sun Yat-sen Univ.	China		X			
Univ. de Los Andes Bogota	Colombia		X		X	
Univ. de Antioquia	Colombia		X		X	
ASRT - ENHEP	Egypt	X		X		
Lappeenranta Univ. of Technology	Finland		X			
RWTH Aachen Univ.	Germany (BMBF)	X				
Inst. for Nuclear Research ATOMKI	Hungary				X	
Panjab Univ. (Chandigarh)	India	X		X		X
Univ. of Delhi	India	X		X	X	X
Saha Inst. of Nuclear Physics	India	X				
Bhabha Atomic Research Center	India	X	X			
INFN Sez. Bari, Univ. of Bari, and Polytechnic of Bari	Italy	X	X			
INFN Sez. Bologna and Univ. of Bologna	Italy	X				
INFN National Laboratory of Frascati	Italy	X			X	
INFN Sez. Napoli, Univ. of Napoli	Italy			X	X	
INFN Sez. Pavia, Univ. of Pavia	Italy	X	X			
Sungkyunkwan Univ.	Korea	X			X	X
Seoul National Univ.	Korea	X			X	X
Korea Univ.	Korea	X			X	X
Univ. of Seoul	Korea	X		X	X	X

Continued...

Table 6.23: Continued

Institution	Country (FA)	Chamber production	Electronics/ DAQ	Power system	Services	Integration
American Univ. of Middle East	Kuwait				X	
Vilnius Univ.	Lithuania		X			
National Center for Physics, Quaid-I-Azam Univ.	Pakistan	X	X	X	X	
Texas A&M Univ. - Qatar	Qatar		X			
CERN	Switzerland	X	X	X	X	X
Florida Inst. of Technology	USA (NSF)	X	X			
Rice Univ.	USA (NSF)		X			
Texas A&M Univ.	USA (NSF)		X			
Univ. of California, Davis	USA (NSF)		X			
Univ. of California, Los Angeles	USA (NSF)		X			
Wayne State University	USA (NSF)		X			

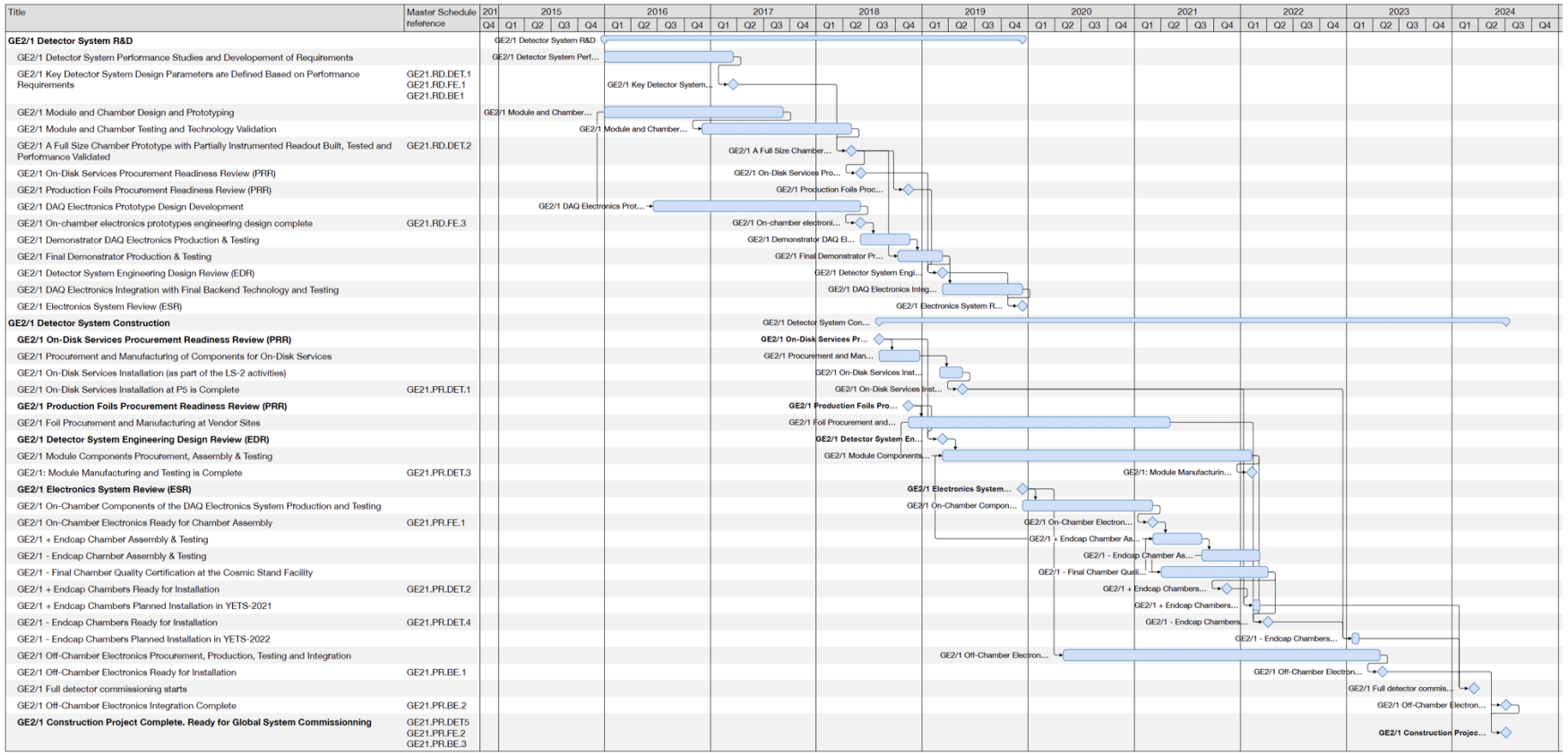

Figure 6.49: Highlights of the schedule of the GE2/1 detector system construction schedule along with the main phases of the preceding R&D activities.

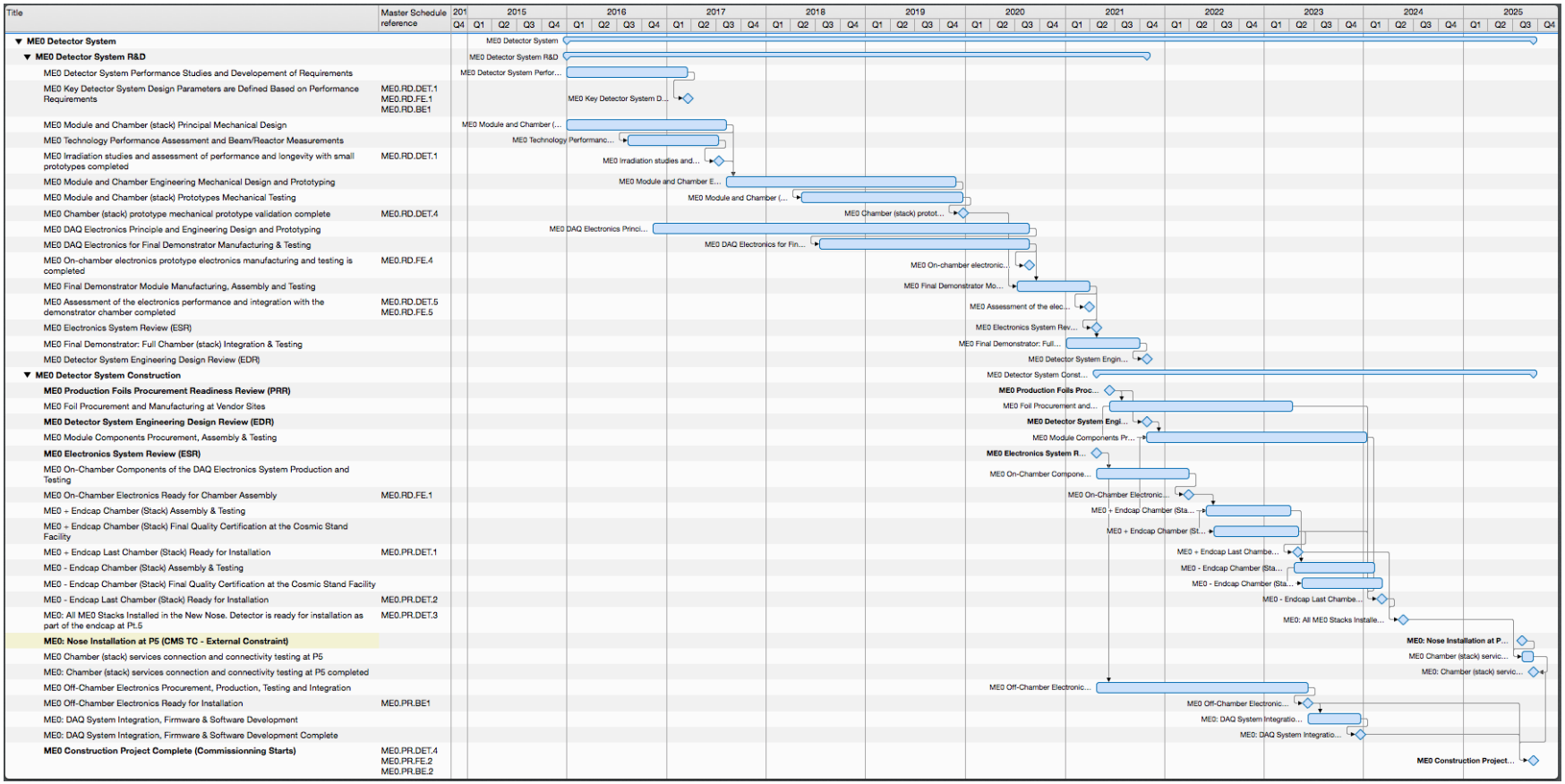

Figure 6.50: Highlights of the schedule of the ME0 detector system construction schedule along with the main phases of the preceding R&D activities.

Tables 6.24 and 6.25 list the main milestones for the GE2/1 and ME0 R&D and construction stages. The time profile of the expected construction project expenditures and the quality of the cost estimates are shown in Figs. 6.51 and 6.52 for the GE2/1 and for ME0 upgrade projects, respectively.

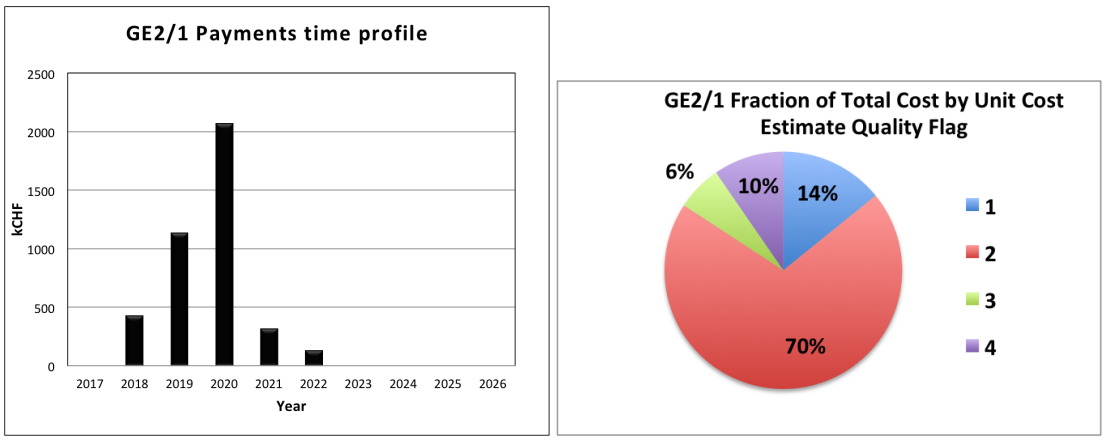

Figure 6.51: Left: The expected time profile for expenditures in the Phase-2 upgrade of the GE2/1 Upgrade. Right: The distribution of costs for the GE2/1 upgrade by cost estimate quality flag, where (1) is based on an vendor quote or catalog price, (2) is based on a recent similar part, (3) is based on engineering seeding where sub-components are known, and (4) is based on a conceptual design of scaled from similar systems.

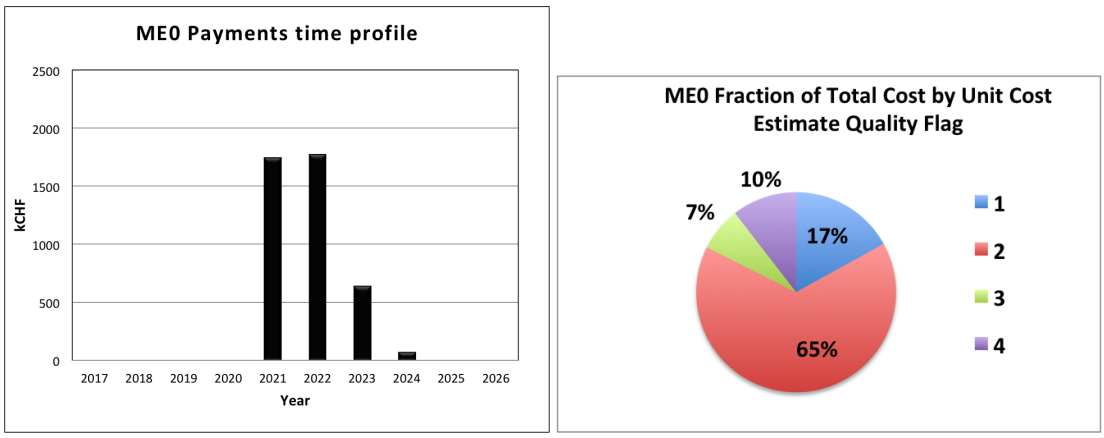

Figure 6.52: Left: The expected time profile for expenditures in the Phase-2 upgrade of the ME0 Upgrade. Right: The distribution of costs for the ME0 upgrade by cost estimate quality flag, where (1) is based on an vendor quote or catalog price, (2) is based on a recent similar part, (3) is based on engineering seeding where sub-components are known, and (4) is based on a conceptual design of scaled from similar systems.

Table 6.24: Summary of most important milestones for the GE2/1 upgrade.

	ID	Milestone title	Date
Design	GE21.RD.DET.1 GE21.RD.FE.1 GE21.RD.BE.1	GE2/1 R&D: Key detector system design parameters are defined based on performance requirements	21.Mar.17
	GE21.RD.FE.2	GE2/1 R&D: On-chamber electronics preliminary design completed and interfaces defined	19.Jun.17
	GE21.RD.BE.2	GE2/1 R&D: Off-chamber electronics preliminary design completed and interfaces defined	12.Mar.18
	GE21.RD.DET.2	GE2/1 R&D: A full size chamber prototype with partially instrumented readout built, tested and performance validated	1.May.18
	GE21.RD.DET.3	GE2/1 R&D: Detector design parameters optimization completed, final chamber design is selected for the demonstrator	8.May.18
	GE21.RD.FE.3	GE2/1 R&D: On-chamber electronics prototypes engineering design complete	1.Jun.18
Prototyping	GE21.RD.FE.4	GE2/1 R&D: On-chamber electronics prototype electronics manufacturing and testing is complete	9.Oct.18
	GE21.RD.DET.4	GE2/1 R&D: Performance of the demonstrator chamber with prototype electronics is validated	12.Mar.19
	GE21.RD.FE.5 GE21.RD.BE.3	GE2/1 R&D: On-chamber and off-chamber prototype electronics integration and performance studies completed	12.Dec.19
		GE2/1 PRR for the On-Detector Services	3.Aug.2018
		GE2/1 PRR for the Foil Production	13.Nov.2018
		GE2/1 Detector EDR	12.Mar.2019
		GE2/1 ESR	12.Dec.2019
Production	GE21.PR.DET.1	GE2/1 On-Disk Services Installation Complete	20.May.2019
	GE21.PR.FE.1	GE2/1 On-Chamber Electronics Manufacturing and Testing is Completed	3.Mar.2021
	GE21.PR.DET.2	GE2/1 Chambers for Disk-1 are assembled, tested, and ready for installation	16.Nov.2021
	GE21.PR.DET.3	GE2/1 Module manufacturing and testing is complete	8.Feb.2022
	GE21.PR.DET.4	GE2/1 Chambers for Disk-2 are assembled, tested, and ready for installation	5.Apr.2022
	GE21.PR.BE.1	GE2/1 Off-Chamber Electronics Manufacturing & Testing completed and ready for installation	5.May.2023
		GE2/1 Full Detector Commissioning Starts	15.Mar.2024

Table 6.25: Summary of most important milestones for the ME0 upgrade.

	ID	Milestone title	Date
Design	ME0.RD.DET.1 ME0.RD.FE.1 ME0.RD.BE.1	ME0 R&D: Key detector system design parameters are defined based on performance requirements	21.Mar.17
	ME0.RD.DET.2	ME0 R&D: Irradiation studies and assessment of performance and longevity with small prototypes completed	11.Jul.2017
	ME0.RD.FE.2 ME0.RD.BE.2	ME0 R&D: On-chamber & off-chamber electronics preliminary principal design complete and interfaces defined	25.Jul.17
	ME0.RD.DET.3	ME0 R&D: Chamber (stack) prototype mechanical design completed	18.Dec.2018
	ME0.RD.FE.3	ME0 R&D: On-chamber electronics engineering design completed and validated	23.Aug.2019
Prototyping	ME0.RD.DET.4	ME0 R&D: Chamber (stack) prototype mechanical prototype testing and validation complete	24.Dec.2019
	ME0.RD.FE.4	ME0 R&D: On-chamber electronics prototype electronics manufacturing and testing is complete	21.Aug.2020
	ME0.RD.BE.3	ME0 R&D: Integration of the on-chamber and off-chamber electronics and performance assessment complete	8.Jan.2021
	ME0.RD.DET.5 ME0.RD.FE.5	ME0 R&D: Assessment of the electronics performance and integration with the demonstrator chamber completed	30.Mar.2021
	ME0.RD.DET.6	ME0 R&D: Beams and Cosmics testing of the demonstrator chamber and performance qualification completed	31.Aug.2021
		ME0 PRR for the Foil Production	14.Jun.2021
		ME0 ESR	27.Apr.2021
		ME0 Detector EDR	28.Oct.2021
Production	ME0.PR.FE.1	ME0 On-Chamber Electronics Manufacturing and Testing complete, ready for chamber (stack) assembly	29.Mar.2022
	ME0.PR.DET.1	ME0 Chambers for Disk-1 are assembled, tested, and ready for installation	4.May.2023
	ME0.PR.BE.1	ME0 Off-Chamber Electronics Manufacturing & Testing complete	8.June.2023
	ME0.PR.DET.2	ME0 Chambers for Disk-2 are assembled, tested, and ready for installation	7.Mar.2024
	ME0.PR.DET.3	All ME0 Stacks Installed in the New Nose. Detector is ready for installation as part of the endcap at Pt. 5	23.May.2024
	ME0.PR.DET.4 ME0.PR.FE.2 ME0.PR.BE.2	Construction Project Complete. Ready for Global System Commissioning	12.Sep.2025

Chapter 7

Muon trigger and reconstruction

7.1 The L1 muon trigger

Up to Phase-2, the CMS L1 muon trigger identifies "standalone" muon candidates using only muon system trigger information. Muon trigger primitives (TP) consist of electronic encoding of the parameters of a segment (in DT or CSC) or a hit (in RPC), from each muon station. Appropriate coincidences between muon trigger primitives in the L1 trigger track finders define standalone L1 muon tracks with the required 20-30% momentum resolution (largely limited by multiple scattering in the calorimeters and the iron return yoke).

The CMS muon trigger was originally designed to find muon tracks using DT trigger primitives in the barrel region, CSC trigger primitives in the endcap region beyond DT coverage, and a combination of CSC and DT trigger primitives in the overlap region of pseudorapidity. Additionally and independently, RPC chamber hits were linked into tracks in both barrel and endcap regions up to $|\eta| < 1.6$, and the resulting RPC tracks were merged with DT and CSC tracks in the Global Muon Trigger (see Chapter 8 in Ref. [1]) when corresponding to the same physical muon.

With the Phase-1 upgrade of the CMS muon trigger, implemented in Run 2, the RPC hits were integrated with DT and CSC trigger primitives before the track-finding stage, both in the barrel and endcap regions, respectively, and the previously independent RPC track finding was decommissioned. In both cases, this improved the efficiency of trigger primitives, and in the barrel the RPC information was used to improve their timing. In the overlap region, $0.9 < |\eta| < 1.2$, trigger primitives from all three subsystems are used in the L1 track finding.

For Phase-2, the overall CMS trigger architecture will remain the same, with a hardware L1 and a Higher-Level Trigger (HLT) that is implemented in software. The maximum L1 rate will be increased from the current 100 kHz to 750 kHz, and the front-end data buffers will be made sufficiently deep to capture the data with an L1 trigger latency increased from the current 3.6 μs to 12.5 μs.

The challenges and requirements for the Phase-2 standalone muon L1 trigger are the following:

- To keep the rates of prompt muon triggers under control, allowing single muon L1 standalone p_{T} thresholds as low as (or lower than) currently, around 20–25 GeV, even at the maximum HL-LHC luminosity;
- To provide spatial resolution sufficient for efficient and pure matching with the Track Trigger, as well as continued use of standalone muon triggers for ultimate efficiency of ultra-high momentum muons;
- To provide standalone muon trigger capabilities for triggering on interesting event topologies not covered by the Track Trigger system, such as displaced tracks and

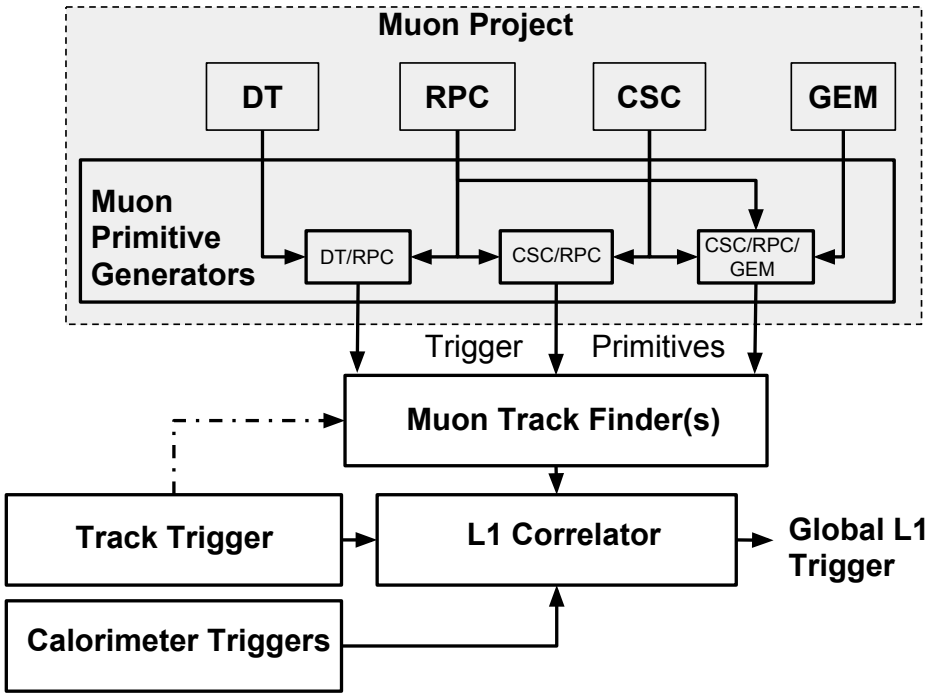

Figure 7.1: Block diagram of the Phase-2 L1 muon trigger data flow.

slow-moving particles.

- These capabilities need to be maintained with additional redundancy in order to compensate for temporal failures and radiation aging of the current muon detectors and their associated electronics.

The architecture of the L1 muon trigger in Phase-2 is shown in Fig. 7.1. TPs from different muon subdetectors will be combined in a similar fashion as in Phase-1, with additional capabilities afforded by the addition of GEM and RPC forward chambers and improved timing for DT and RPC, as previously described in Chapters 3 and 5, respectively. Hits from new GEM chambers will be combined at an early stage with trigger primitives from the nearby CSC chambers in order to improve on efficiency and to provide a measurement of the local muon direction and position. Standalone muon candidates will still be made by Track Finders as described in Ref. [18]. Details on each of the track finders and the composed muon primitives are described in the following sections.

The momentum resolution of the L1 muon trigger for muons coming from the primary vertex will be greatly improved by adding information from the "Track Trigger", a capability that is integral to the design of the new silicon Outer Tracker. While many track candidates are found in each HL-LHC bunch crossing, a spatial coincidence with the L1 standalone muon candidates will provide well-identified muons with well-measured momentum. The improvement in momentum resolution for an L1 trigger threshold of 20 GeV can be seen in Fig. 6.1. The Track Trigger can also be directly combined with trigger primitives at the first stage of the muon track finder electronics; this would mirror the offline reconstruction of "Tracker Muons" which improve the efficiency for very low p_{T} muons, especially in the barrel region [21].

The combination of the L1 Global Muon Trigger candidate with the L1 Tracker Track candidates will be done by a correlator that is currently under development. Phase-1 HLT muon candidates can serve as a good proxy for Phase-2 L1 standalone Muons. Figure 7.2 illustrates the HLT muon performance [22].

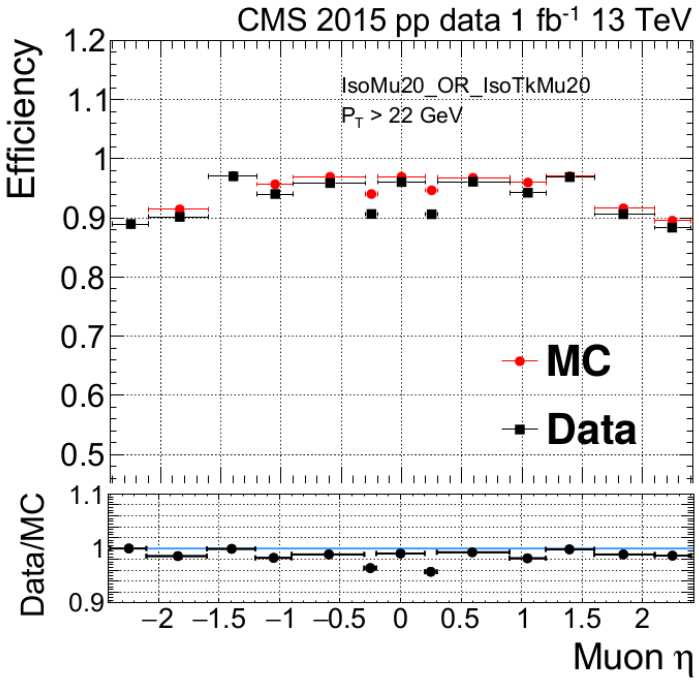

Figure 7.2: Tag-and-probe efficiency for the single-muon HLT trigger in 2015 data (black) and in simulation (red) as a function of offline η. The high level trigger objects in Phase-1 are a good proxy for the level 1 objects in Phase-2. The drops in efficiency for the high eta region will be recovered with the new GEM and iRPC detectors.

In the following sections we discuss separately the barrel, endcap, and overlap regions. For each, we first describe the algorithms for processing single subsystem information, then we outline the capabilities of algorithms combining all available information into a single muon trigger candidate. Displaced leptons and slow moving Heavy Stable Charged Particles are promising physics channels for the HL-LHC. The upgrade of the muon system in Phase-2 will provide the necessary information to assure that CMS will not miss new physics with these final states for the duration of the HL-LHC program. Details about these new triggers are discussed in sections 7.1.4.1 and 7.1.4.2.

7.1.1 Barrel region

In Phase-2, no new muon detectors will be installed in the Barrel region, but significant upgrades of the electronics of present DT and RPC detectors will be implemented. The RPC modules performing the signal digitization will be replaced, improving the time resolution. In the DT system the on-detector electronics will be replaced, including the trigger primitive generator, with a new Time-to-Digital-Converter (TDC) system that will stream hits directly to the backend. More details are given in Chapters 3 and 5, and in the following sections.

There will be no on-detector trigger logic, and the same backend will receive detector data from DT and RPC. The combination of DT and RPC information will give large benefits: already in Phase-1 this allowed an optimization of the trigger objects by improving the BX identification of the DT low quality primitives, giving an increase in the efficiency in the gaps between the wheels, utilizing the extra information that boosts the quality of the original primitive [114]. Also, in the event of reduced DT single hit efficiency due to longevity issues, the availability of RPC hits in track segment building will allow the current trigger efficiency to be maintained.

While the best performance will be achieved when information from both subsystems will be available, it will be important to maintain the capability to generate trigger primitives in a given station, from DT or RPC alone, to ensure the operation of the muon trigger in case of malfunctions of either of the two systems.

In the following sections, more details about DT trigger primitive generation, RPC upgrade and DT+RPC combination in Phase-2 are given.

7.1.1.1 DT local trigger primitives

There are two main algorithmic challenges for Phase-2 DT Trigger Primitive (TP) generation:

- First, the new on-detector electronics will stream cell number and time-stamp information for each hit, and one goal of the early design effort is to demonstrate the capability to arrange hits for pattern recognition and BX identification in this scenario.
- Second, the aging of the detector will reduce the single hit efficiency. The present BTI (Bunch and Track Identifier, the ASIC device connected to the DT frontend), operates at the level of a single superlayer (SL), a block of four DT layers: such approach would develop inefficiencies due to missing hits. Hence, the Phase2 TP generator will have to be based on a larger number of layers.

The final decision concerning the ultimate L1 trigger algorithm will be taken by the time of the Trigger TDR in 2019, once the full trigger chain architecture is defined. At present, design activities are ongoing to provide proof of BX identification and multi-superlayer track fitting in the Phase-2 environment, and are being tested in the SX5 demonstrator (see Chapter 3).

The first design challenge is investigated by an emulation software, written in C++ but designed using a multi-thread pipelined processing approach, with memory buffers (FIFO, ring-buffers, etc) as storage for data between consecutive processes. Therefore, porting to firmware is rather straightforward. The algorithm contains a first stage, called *time window discriminator*, which simulates possible system overflows due to noise and programmable system dead time. Next, there is a channel splitter that classifies the hits from the region of the chamber from which they originated, and a multi-channel data mixer, that selects the time stamps to build 4-cell groups of hits compatible with a muon trajectory. Then the BX identification follows the present mean-timer paradigm technique: equations for every laterality combination are solved and the BX is obtained, together with the position of the track inside the SL and the impact angle. Using real collision data, reformatted as expected in Phase-2, a BX identification performance compatible to what is achieved in the present system was demonstrated.

In order to develop an approach capable of going beyond the SL and optimizing the hardware resources, an histogram-based mean-timer technique (called Majority Mean Timer, MMT) for the bunch crossing identification, plus a chamber level track segment fitting based on a Compact Hough Transform (CHT) [115], were developed.

Due to the geometry of the DT layers, drift times of any triplet of hits caused by a track in three different layers satisfy a linear equation that includes the maximum cell drift time. Thus, the crossing time can be calculated. In MMT, all meaningful patterns in a set of pre-clustered channels are used to compute the crossing time, and the most voted result is chosen. Then the TDC times are converted into pairs of reconstructed positions (each member of the pair corresponding to the hypothesis the hit was either at the left or at the right side of the corresponding wire). Such a technique is fully efficient within impact angles of about 40°.

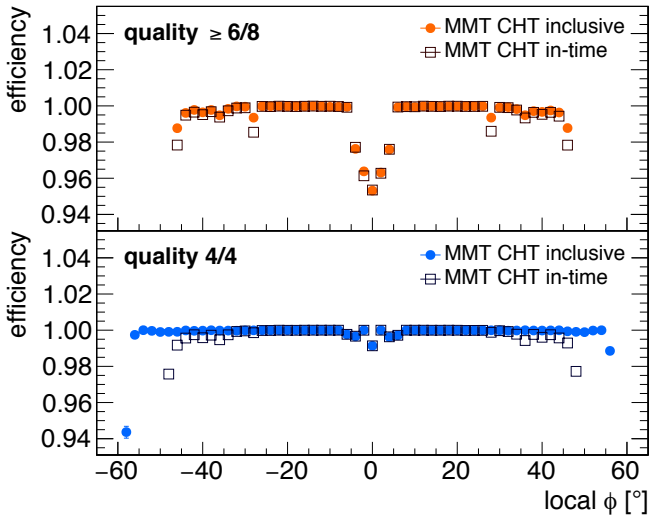

Figure 7.3: Evaluation of the algorithmic efficiency for Phase-2 trigger primitives on a simulated sample of 2×10^6 muon tracks, for segments obtained from both SuperLayers (quality $\geq$ 6/8) and from only one SuperLayer (quality = 4/4); the fraction of candidate tracks with correct time identification is shown in open squares.

The CHT algorithm provides track identification [116, 117]. Instead of Hough-transforming one measurement at a time, the CHT exploits the transformation of N-tuples of measurements. The corresponding reduction in the number of parameters to be assigned, together with he optimization in dimensioning the HT histograms, achieves a significant reduction of the complexity of the computations and of the resources needed in hardware. Subsets from the array of available hit positions are processed in parallel, computing the track slope resulting from pairs of measurements from different layers. Three CHT histograms are filled in parallel, one for each ϕ-SL and one combining the two SuperLayers together, and the resulting hypotheses for the track slope are combined. The track intercept is then calculated.

Both the MMT and CHT algorithms feature corrections for non-linearities of the drift field. The resulting figures are better than for the current system [20] in terms of efficiency (higher than 98%, see Fig. 7.3); angular resolution (down to 3 mrad for high quality segments) and position resolution (1.4 mm), see Fig. 7.4.

In the present DT trigger, the BX identification is obtained from a single SL or from the two ϕ-SLs of one chamber. Such an approach suffers from degraded performance if detector inefficiencies will develop, as expected in Phase-2. This is particularly true for the longitudinal ($r-\theta$) view, where only one SL per chamber is available. The three θ-SLs available along the muon trajectory, which is approximately a straight line in the longitudinal projection, can be used for a relatively simple approach for multi-chamber BX identification and track fitting, with full chamber resolution (less than one mm - while the resolution in the longitudinal view is limited to $\sim$32 cm in the present system). Tracks identified in the longitudinal view can then be used for seeding the reconstruction of TPs in the transverse view, which can also take advantage of multichamber combinations. These mechanisms reduce the sensitivity to detector inefficiencies and improve the overall spatial resolution.

Each TP will also carry as a payload the position of the hits contributing to the track for further track fitting to be performed downstream at the Barrel Track Finder, obtaining a better

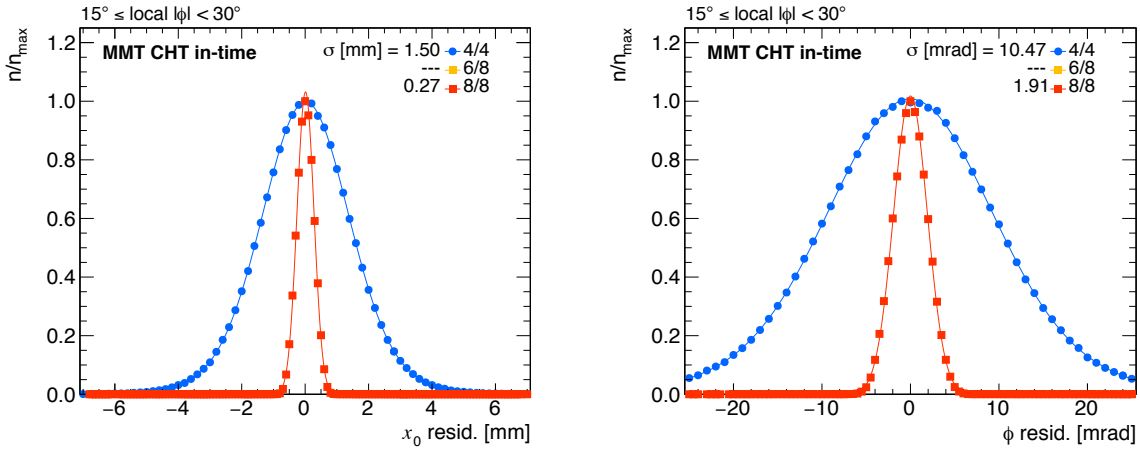

Figure 7.4: Expected resolution of reconstructed track position (left) and angle (right) from correct time identification with 8 aligned hits in both SuperLayers (8/8) and with 4 aligned hits in only one SuperLayer (4/4). The contribution of intermediate quality tracks (6 aligned hits) is negligible in the angular range shown. The preliminary version of the MMT employed for this evaluation results in a fraction of off-time track segments of about 1%, mostly at large angles $|\phi| > 40°$. This is compatible with the current DT trigger, and has a limited impact on the resolution.

momentum estimate and a more precise extrapolation of the track to the reference surface used by the global trigger logic. Cancellation of duplicates, sorting, reformatting, etc. will also be needed. Depending on the final algorithm implementation, FPGA resources will be shared among different parts of the processing chain.

7.1.1.2 Combining RPC and DT for better time measurement and redundancy

The Phase-2 upgrade in the RPC barrel region includes the replacement of the Link Board System (see Section 5.5.6.2) that changes the sampling time of RPC chamber signals from 25 ns to 1.56 ns. This will help to suppress the neutron-induced random hits in RPCs and improve the BX identification capability. It is even possible that RPC hits could be used as seeds for the DT BX identification, provided that the DT algorithm could also work efficiently without the RPC detector input for redundancy considerations. The use of RPC hits together with DT hits in the track fitting stage will also improve the robustness and quality of the parameter assignment, in particular in case of missing DT hits due to inefficiency, malfunctions or limited acceptance.

The improved time information available from the two systems will also be used to build triggers for new exotic particles (see Section 8.2.2).

In Phase-2, RPC detectors can be considered as an extra layer of the DT chambers and the time resolution of the RPC system is used to improve the time resolution of the L1 primitives in the barrel. Composed primitives will be more robust than traditional DT-segments or RPC-only-segments because the RPC layers are considered as extra layer(s) in the fit of a local DT segment. All information available in a given station will be packed in this new proposed object.

The fact that there are up to three RPC rolls just beside the DT chambers will provide extra η information to the super-segment, recovering r-θ information that will be missed when aging affects two cells in the same r-θ DT Super Layer.

7.1.2 Endcap region

The current Endcap Muon Track Finder (EMTF) is an improvement of the original CSC muon track-finder (CSCTF). This upgraded electronics system adds inputs for RPC hits, and allows for a more sophisticated algorithm with faster processing and increased memory resources.

The inputs of the EMTF algorithm are the RPC clusters/strips and the raw input data from the Cathode Strip Chambers (CSC), called local charged tracks (LCTs), which contain various parameters indicating the position and timing of the electronic signal.

A coarse description of where a signal originates is given by the endcap, station, sector, and chamber numbers. In each of the two endcaps there are four stations along the z-direction, as shown in Fig. 1.4, and six sectors which cover the full range of 2π in ϕ, the azimuthal angle. In each sector there are nine chambers which can each record a total of two LCTs. Each LCT has a corresponding strip and wire number; they encapsulate information about the position in ϕ and θ relative to the chamber which detected it. In addition, the relative angle with which the muon passed through the chamber is quantified in a LCT pattern shape. Finally, there is a bunch crossing (BX) indicator which is a measure of the timing of a signal relative to others in the same event. Using the LCTs from a given event, the EMTF algorithm performs its logic to determine a specific set of outputs. These outputs, per found track, are the precise position relative to a sector in ϕ and θ, the deflection angles between stations $\Delta\phi$ and $\Delta\theta$, a quality code, a list of the associated LCTs which the track is comprised of, and an estimation of the charge and p_{T}.

The current method uses LCTs to form so-called extrapolation pairs. In the case of a missing LCT, an RPC hit is used to produce such a pair. Using their associated three-dimensional spatial information, the pairs are tested for compatibility with a muon originating from the primary vertex. These extrapolation pairs are then matched together to form a track. The novel algorithm for the upgraded system is able to analyze all 18 possible LCTs/RPC hits from all four stations simultaneously to form a track via pattern recognition logic.

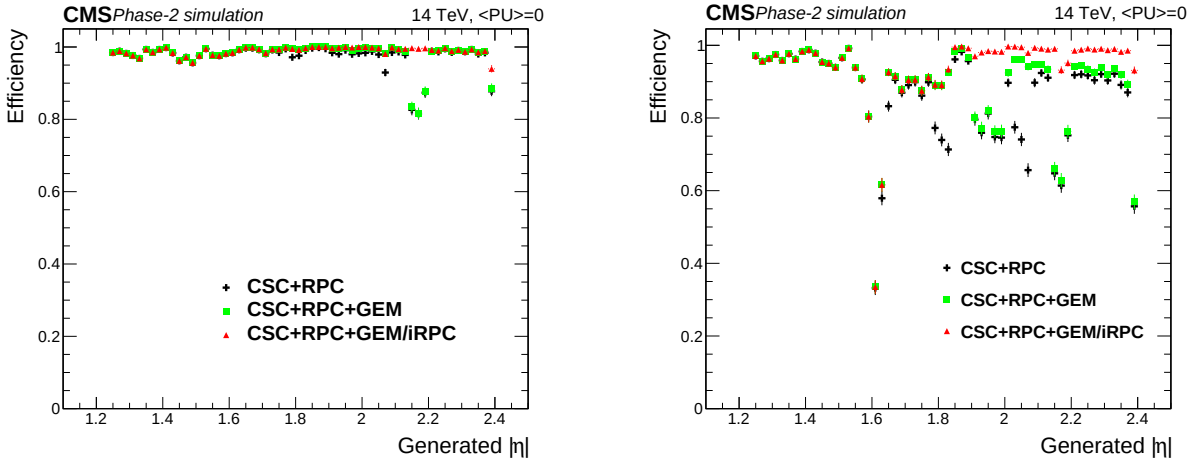

Figure 7.5: The single muon standalone L1 trigger efficiency in the endcap region with and without the Phase-2 upgrade, where CSC/RPC/GEM hits are required in at least two stations (left) or in all four stations (right). The drops in efficiency are expected and are due to the gaps in between rings; when the muon selection is tighter the drops in efficiency are deeper.

The EMTF will benefit from the addition of new detectors in the high η region, the improved RPCs (Chapter 5) and GEMs (Chapter 6). The additional hits provided by these detectors will recover the efficiency losses due to acceptance gaps in this region. Details are shown in the

following sections. Figure 7.5 shows that muons can be identified with a considerably higher efficiency in comparison to a L1 trigger based on CSC detectors alone. The effect is especially pronounced for high quality muons with hits identified in all four muon stations.

The EMTF algorithm for Phase-2 will be improved using the time information from the new RPC link system and the iRPCs. Details on the Phase-2 algorithm and the performance improvements on trigger rate and p_{T} assignment for the Phase-2 EMTF will be shown in the L1 TDR.

7.1.2.1 CSC trigger primitives

Each trigger primitive, or Local Charged Track (LCT), is formed from the coincidence of an anode local charged track (ALCT) and a cathode local charged track (CLCT). Each CSC can provide up to two LCT segments per BX to the Level-1 muon trigger logic. The CLCT data contains information on the azimuthal position of the segment, the bend angle, and the pattern of cathode half strips with hits in a chamber. The ALCT data contains information on the radial position from the beamline of the segment, and the pattern of anode wires with hits in a chamber. The timing information from anodes is used to define the time of the combined LCT.

CLCTs are based the comparator readout of the cathode strips, which identifies the position of each hit to the nearest half strip. The CLCT algorithm looks for suitable patterns in the half strips of the six layers of the CSC chamber corresponding to track segments. The algorithm has several configurable parameters, including the minimum number of layers hit (currently four out of six) and the set of patterns used. The current settings include patterns with near normal incidence, as expected from high-momentum muons, and more inclined patterns to accommodate muons with lower momenta.

ALCTs are formed from the signals from anode wires in CSC, which are hardwired together at the readout end in groups of 10–15 wires in order to reduce the channel count. The ALCT algorithm identifies the bunch crossing and to finds patterns of wire group hits in the six layers that are consistent with track segments. For each spatial pattern of anode hits, a lower coincidence level, typically three or more layers, is used to establish optimal timing, whereas a higher coincidence level, typically four layers, is used to verify the existence of a muon track.

The LCTs formed from the coincidence of the CLCTs and ALCTs are passed on to the EMTF where information from RPCs is matched to the CSCs primitives to provide more robust primitives per station.

The planned upgrades to the HL-LHC do not alter the general scheme for creating trigger primitives. In ME2/1, ME3/1, and ME4/1, the new boards in which the CLCT and ALCT algorithms are executed (OTMB boards and ALCT Mezzanine cards, see Section 4.2), will contain more powerful FPGAs than those of the boards they replace. These allow for more sophisticated algorithms to be implemented for forming LCTs from these chambers. In stations 3 and 4 the new iRPC chambers will be added to the EMTF algorithm following the same scheme of the current RPC chambers. And the use of more precise timing from the RPCs in their full η range (including the rings 2 and 3) will be also combined in the EMTF algorithm.

7.1.2.2 Combining CSC and RPC for higher efficiency

The upgrade of the RPC Link Board System in the endcap includes the improvement of the signal sampling time from 25 ns to 1.56 ns for the existing chambers (as in the barrel). This excellent time resolution will allow the construction of better trigger primitives when combined with the CSC information in all four muon endcap stations. This added information will ensure

the redundancy of the CMS Muon system, and will mitigate the effects of the high hit rate expected in this high η region at HL-LHC.

The simultaneous analysis of CSC and RPC hits by the EMTF will improve the standalone muon L1 trigger efficiency for Phase-2 as is shown in Fig. 7.5. This gain comes from the improvement in recognizing muon segments/hits in muon stations 3 and 4, as shown in Fig. 5.12. The improved RPC timing is not yet included in the Phase-2 EMTF algorithm.

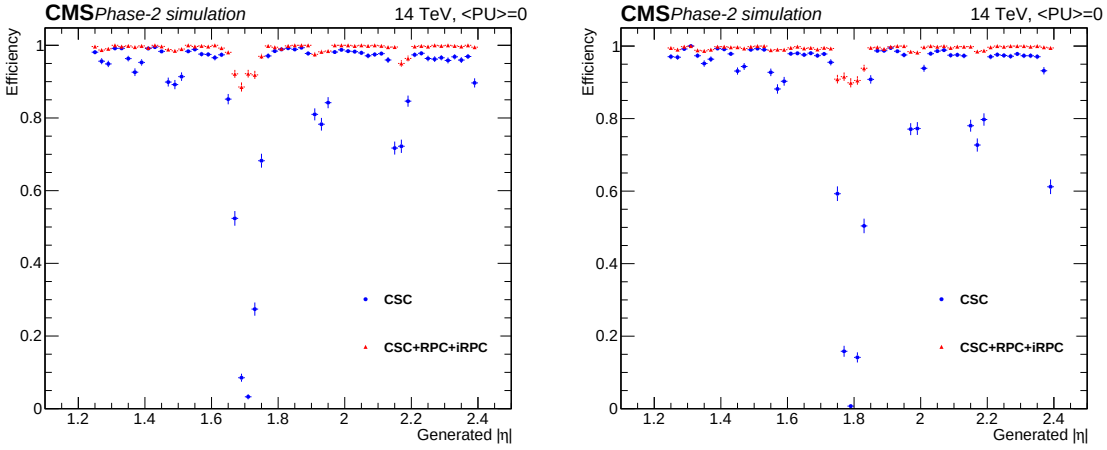

Figure 7.6: Efficiency of identifying muon segments/hits in muon stations 3 (left) and 4 (right) by the EMTF with and without RPC/iRPC detectors.

7.1.2.3 Combining CSC and RPC for lower rate

If two muons cross the same CSC chamber within ± 1 BX with respect to each other, the CSC local (X, Y) measurement is ambiguous as shown in Fig. 7.7. Instead of two muon 2D LCTs (Local Charged Tracks), one has to consider four. This may promote low p_{T} muons to high p_{T} L1 candidates, thus increasing the L1 muon rate. In order to quantify the effect, we used data (minimum bias 2016) to measure the average number of CSCs with at least one LCT vs. the instantaneous luminosity, as shown in Fig. 7.8. A linear projection toward the HL-LHC luminosity (L = $5\times10^{34}\,\mathrm{cm}^{-2}\,\mathrm{s}^{-1}$) predicts that the probability per BX to find an LCT in any given ME3(4)/1 chambers is 0.8/36 = 2.2%. Since the Endcap Muon Track Finder searches for L1 muon candidates using the LCTs from 3 consecutive BXs, the probability to have an extra track in either ME3/1 or ME4/1 chamber already crossed by a true muon is then $(0.8/36) \times 3 \times 2 = 13\%$. The iRPC detectors, with two-sided strip readout, will allow one to resolve the combinatorial background in most of such events. Using a MC model based on the measured CSC background hit counting/rate (as shown Fig. 7.9), we estimated that iRPCs operating at the 95% efficiency working point and with a 2-sided readout strip readout ($\sigma_{\mathrm{Y}} \approx 2\,\mathrm{cm}$) will resolve the combinatorial background in 99.7% of all ambiguous events. In the case of one-sided strip readout with 5 pseudorapidity partitions (corresponding to approximately a 10 cm Y-coordinate resolution), the efficiency of resolving combinatorial background is only 91%.

7.1.2.4 Combining GEM and CSC for higher efficiency and lower rate

From the trigger performance perspective, addition of the GEM detectors and integration of GEM data with the CSC measurements achieves two important goals. First, it allows a substantial improvement in standalone muon momentum resolution using measurements of muon directions in the muon stations closest to the interaction point, where the bending of muons in the magnetic field is sufficiently large and remains unobscured by multiple scattering effects.

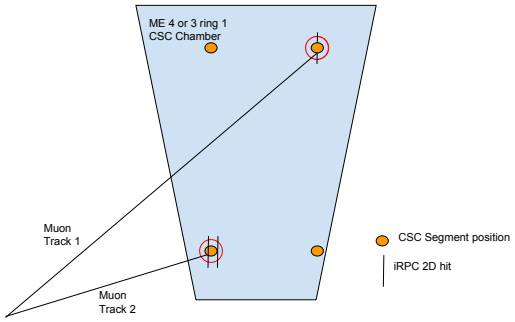

Figure 7.7: CSC and iRPC readout sketch when two muon/LCT cross the same chamber in the same readout window. Two pairs of hits are possible with only one of them being ”real”.

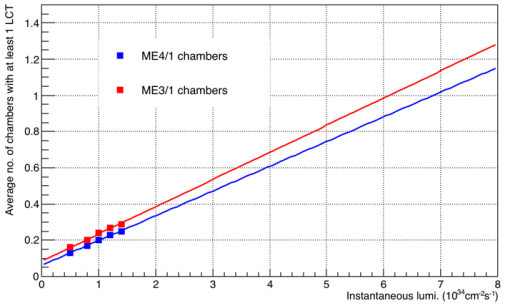

Figure 7.8: Average number of chambers with at least one LCT segment as a function of the instantaneous luminosity. With a linear extrapolation to the HL-LHC region.

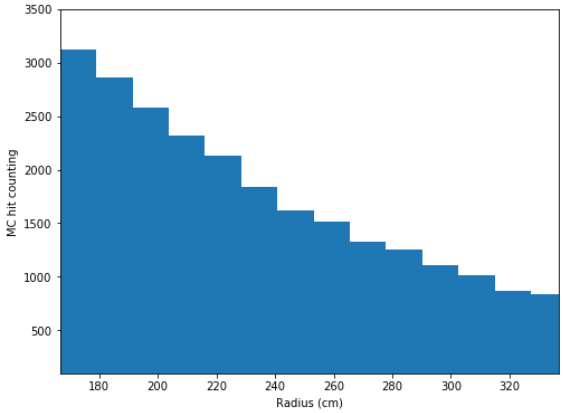

Figure 7.9: Rate of segments (arbitrary units) reconstructed in CSCs as a function of segment distance R from the beam line (simulation). The rate of segments increase closer to the LHC beam pipe at lower R.

The improvement in momentum resolution propagates in very large reductions in the trigger rate compared to the existing system, which is especially important in the very forward region that otherwise would dominates the overall muon trigger rate. Second, combining GEM and CSC measurements reduces inefficiencies in muon hit reconstruction in the stations closest to the interaction point, which in addition to improving the overall efficiency of the trigger reconstruction, also improves momentum resolution by decreasing the fraction of muon candidates with unreconstructed hits in the near stations that drive the resolution of the current momentum reconstruction algorithm based on sagitta measurements.

Deployment of GE1/1, the first CMS GEM detector that is currently under construction, during the LS-2 shutdown allows taking advantage of these improvements early. However, these benefits are limited to the first station and, furthermore, because of mechanical constraints GE1/1 only covers the region up to $|\eta| \sim 2.15$. The new GE2/1 and ME0 systems extend the availability of the direction measurements to the second station and complete the missing coverage in the first station.

Implementation of the GEM-CSC Integrated Triggering

The implementation of the integrated GE2/1-ME2/1 triggering follows the same schema as for GE1/1-ME1/1 [24]. The upgraded CSC Optical Trigger MotherBoard (OTMB) board will receive trigger data from each of the two layers of GE2/1. Super-primitives containing both GEM and CSC information will be formed by matching GEM and CSC trigger primitives in space and time (see Ref. [24] for details). The optical trigger motherboard output data maintains the same size (32 bits) and bandwidth. The format is expected to be reconfigured slightly to include the presence of GEM information.

GEM hit data are sent at the pads granularity (pads are defined as pairs of adjacent GEM strips) to the OTMB and first matched spatially to form "coincidence pads." Anode (ALCT) and cathode (CLCT) trigger primitives are constructed from wire group and comparator hits respectively. The requirements on the number of layers to build ALCT and CLCT trigger primitives are both reduced from four (default) to three. Integrated GEM-CSC trigger primitives are constructed by combining the ALCT and CLCT primitives matched either to a single GEM pad or a coincidence of GEM pads in space and time. Integrated trigger primitives can also be built from either an ALCT or CLCT plus a GEM coincidence pad. The best two trigger primitives per chamber are sent to the EMTF via the Muon Port Card, to be used in track-building.

The legacy TMB board to be replaced with the OTMB utilizes the algorithm that has a dead time and performs less efficiently at increasing hit rate and has significant local efficiency losses at the boundaries of the CSC wire plane HV partitions. Combination of GEM and CSC information allows recovery of the hit information that would have otherwise be lost, which allows for a high trigger efficiency of the order of 98% at 140 PU, as illustrated in Fig. 6.3 (left). The plateau efficiency is expected to further increase with the algorithm improvements.

The efficiency improvements of the local trigger in stations 1 and 2 increase the muon reconstruction efficiency to $\geq$ 90% at 200 PU, as can be seen in Fig. 6.4 (left). In the region $2.0 < |\eta| < 2.4$ only GEM hits in GE2/1 are currently used to build tracks. It is expected that including the ME0 stub in the L1 muon reconstruction will further improve muon trigger efficiency.

Muon Direction Measurement Using GEM and CSC Detector

The direction of the muon as it passes through the endcap is determined by two factors: (1) the magnetic field strength and (2) multiple scattering. The inner stations (ME0, ME1/1, ME2/1)

benefit from a large ($>$ 3 T) to moderate ($>$ 2 T) magnetic field causing muons to bend. Muons in the outer stations (ME3/1, M4/1) bend hardly at all, because of the diminished magnetic field and the multiple scattering caused by the massive steel return yokes in the endcap (Fig. 6.2 (right)).

The instrumental resolution — on top of the bending and multiple scattering — comes into play to measure the muon direction. The presence of high-resolution multi-layer gaseous detectors in several stations allow to measure muon direction with good precision and with high efficiency. Presently, the forward endcap system is only instrumented with CSCs. The CSCs will see improvements with the upgrade of the off-chamber electronics — optical trigger motherboard (OTMB). CSC stubs will be produced with an algorithm in fast programmable logic that is optimized for high pileup. Additionally, their position resolution is expected to improve by up to a factor of 2 (compared to Run-2) by implementing a straight line fit to the positions of the comparator digis assigned to a stub instead of taking the measurement at one of the layers, as it is currently done.

Installation of GE2/1 and ME0 detectors allows one to improve the muon direction resolution in the inner endcap stations. GEM and CSC hits will combine at the level of the OTMB so that GEM-CSC integrated stubs are produced in station 1 (GE1/1-ME1/1) and in station 2 (GE2/1-ME2/1). Stubs produced in multi-layer ME0 chambers are not sent to the ME1/1 OTMBs. Instead, they will combine with ME1/1 stubs at the level of the muon track-finder (ME0-ME1/1).

Figure 7.10 compares the direction resolutions for different stub combinations with ME0, GEM and CSC in the region $2.05 < |\eta| < 2.15$ for displaced muons with an impact parameter $10 < |d_{xy}| < 50$ cm. The left plot makes use of integrated stubs, while the plot on the right shows the best case scenario of what could be achievable with the CSCs alone. The latter uses an offline fit of the information sent to the FPGA in the CSC OTMB board by the front-end DCFEB boards. Clearly, the presence of ME0 and GEMs enhances the muon direction resolution in the region $2.05 < |\eta| < 2.15$. The ME0-ME1/1 combination is comparable to GE1/1-ME1/1. This is because ME0 benefits from a large magnetic field due to its proximity to the interaction point, despite being located closer to the beampipe. The improvement from GE2/1-ME2/1 is smaller due to a reduced magnetic field and multiple scattering in the first endcap yoke.

Impact on the Performance of the Level-1 Muon Trigger

The installation of GE2/1 extends the muon direction measurement capabilities onto the second station and allows both the independent use of the direction measurement in the second station as well as correlation of the direction measurements in the first and second stations. Because GE1/1 and ME0 detectors provide complementary coverage in the first station, illustrating impact of each detector system requires splitting the region of interest into two sub-regions: $1.65 < |\eta| < 2.15$, where directions in the first station are measured using GE1/1-ME1/1 chamber pairs, and $2.15 < |\eta| < 2.4$, where the measurement in the first station uses ME0 and ME1/1 detectors.

For the lower pseudorapidity sub-region $1.65 < |\eta| < 2.15$, addition of GE2/1 reduces the single muon trigger rate by a factor of two, as illustrated in Fig. 7.11 and increases its efficiency by about 4%. Furthermore, the addition of GE2/1 improves the dynamic control and a significantly improved resilience to operational or aging effects of CSC and GE1/1. Figure 7.11 also shows the effect on the rate, if the bending angle in station 1 cannot be measured for 20% of muons due to a combination of GEM/CSC operational and/or aging inefficiencies in station 1.

In the forward sub-region $2.15 < |\eta| < 2.4$, the inclusion of ME0 in the L1 standalone trigger

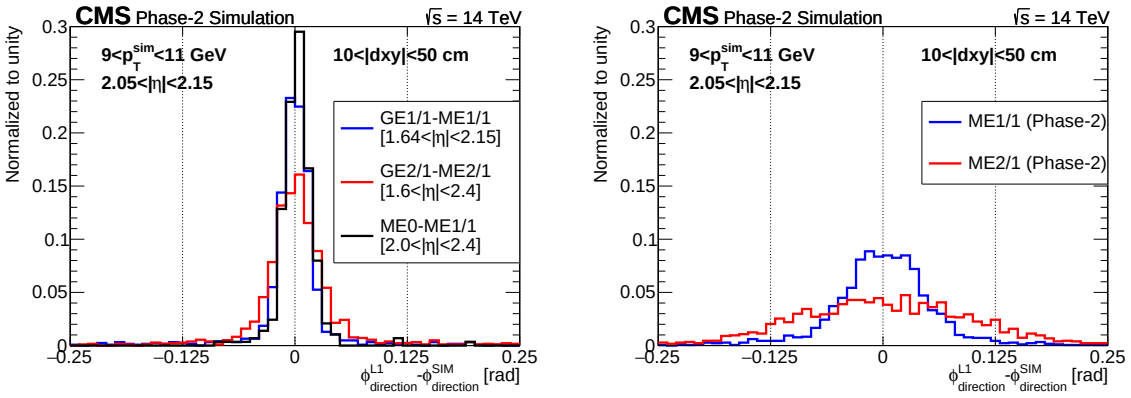

Figure 7.10: Muon direction resolution in the region $2.05 < |\eta| < 2.15$ using phase-2 integrated stubs from different chamber combinations (left) and using only CSCs with phase-2 upgraded electronics (right). The true muon direction is taken from the muon simulated hits, while the measured direction is calculated from the positions of the L1-muon stubs. The coverage of each pair of GEM-CSC detectors that provides the muon direction measurement is given in square brackets in (left). No corresponding direction measurement exists in station-0 without ME0 in (right). Muon direction resolutions are not shown for the outer stations (ME3/1, ME4/1), where muon bending is too small to do a reliable measurement within a single station.

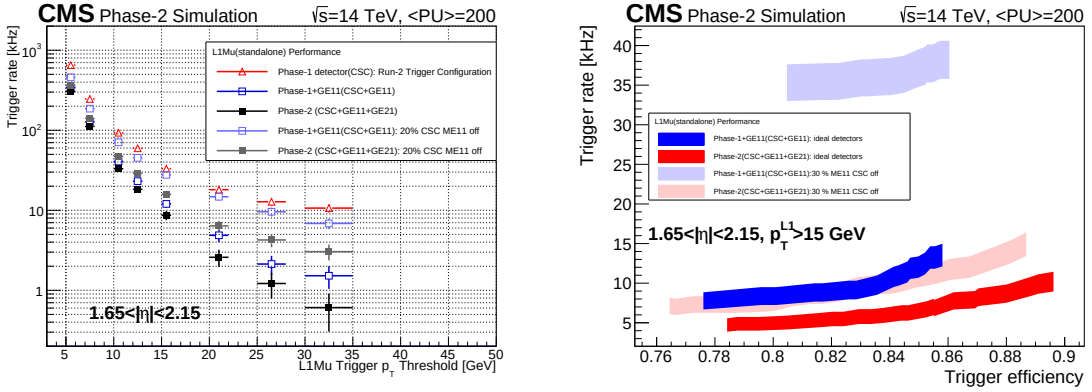

Figure 7.11: Left: Comparison of the L1 standalone muon trigger rate versus p_T in the region $1.65 < |\eta| < 2.15$ covered by GE1/1 and GE2/1, for several scenarios. With the addition of GE2/1, the trigger rate is reduced by about a factor of two, whether the ME1/1 performance is degraded or not. Right: L1 standalone muon trigger rate versus the plateau efficiency, for a L1 standalone muon p_T threshold of 15 GeV in the region $1.65 < |\eta| < 2.15$ covered by GE1/1 and GE2/1, under several scenarios. The plateau efficiencies include contributions from the L1 momentum measurement and an additional GEM-CSC bending angle requirement.

in the region $2.0 < |\eta| < 2.4$ has a similar impact to that of adding GE1/1 detector in the lower eta sub-region. The effect is further amplified as the addition of ME0 provides an extra point for the sagitta-based momentum measurement, leading to an even stronger trigger rate suppression, as shown in Fig. 7.12.

7.1.3 Overlap region

The overlap region is defined as the η slice where DT, RPC and CSCs overlap, $0.83 < |\eta| < 1.24$. The orientation of the muon detectors with respect to the muon trajectory is not uniform and the magnetic field in this region is not homogeneous. These two effects combined pose a

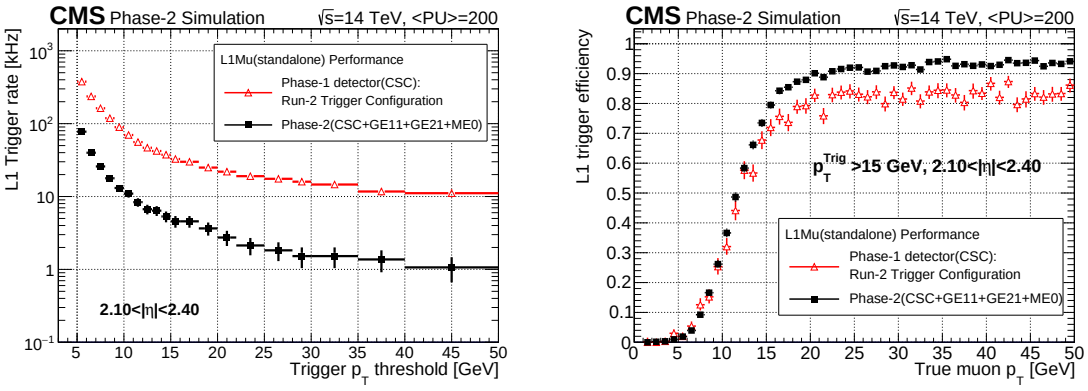

Figure 7.12: L1 standalone muon trigger rate (left) and efficiency (right) for the prompt muon algorithm, with and without GEM chambers included, as a function of the true muon p_T in the region $2.1 < |\eta| < 2.4$.

challenge for the muon trigger and reconstruction.

For the Phase-1 upgrade, a dedicated Muon Track Finder partition was built and a special algorithm dedicated to this region has been developed. The algorithm combines information from 18 separate detectors: six types of DT detectors (three providing θ-position and three giving ϕ-measurements), eight RPC detector types (5 in the barrel and 3 in the endcap), and four CSC detector types.

For Phase-2, there are various options as to the location of the necessary track finder processor boards—they could be separate from barrel and endcap track finders, or be incorporated in one of the two. This is still to be determined. However, the improvements previously discussed in the barrel section of this chapter, such as finer DT spatial resolution and better combination with the fine timing of the RPC; and many of the improvements described in the endcap section of this chapter, such as CSC-RPC coincidence for better efficiency; pertain to the overlap region, and will be implemented there as well.

7.1.4 Special BSM muon triggers

Two classes of triggerable events from beyond-standard model physics require standalone muon trigger capabilities not covered by the Track Trigger system [16]. The first class of events contains high-momentum muons or other penetrating tracks that are significantly displaced from the proton-proton collision point, much more than is expected from beauty or charm quark decays to muons. The second class of events contains semi-stable slow-moving particles generically known as heavy stable charged particles (HSCP) that are penetrating, as predicted for example in SUSY models in which the stau is the next-to-lightest SUSY particle. The plans for using the CMS muon system to trigger on these events in Phase-2 are discussed in Sections 7.1.4.1 and 7.1.4.2, respectively.

7.1.4.1 Trigger algorithm for displaced muons

The prompt muon trigger in the Phase-2 era will match standalone muon objects to L1 Track Trigger objects. The superior tracker momentum resolution replaces the standalone muon momentum measurement. The performance of the combined tracker and muon system momentum resolution was shown in the CMS Phase-2 Technical Proposal [24]. However, the L1 Track Trigger is inefficient for displaced tracks. Many new physics models predict the existence of long-lived bosons. Such long-lived bosons, when coupled to standard model particles, can produce displaced signatures in the CMS detector. For example, when the new bosons are

light, they are expected to decay primarily to pairs of electrons/muons, resulting in displaced lepton signatures. A simplified model (dark SUSY) was used to evaluate the performance of displaced muon triggers. A dark Z boson, Z_d, is produced in the decay of a standard model Higgs boson (e.g., $H \rightarrow Z_d Z_d + X$) and then decays with a delay driven by its long lifetime to a pair of muons. While the decay to a pair of muons may not be the only decay channel, it can be the most triggerable. Achieving good coverage of the range of potential signatures requires a family of displaced muon triggers. High momentum muon signatures (from heavy particle decays) can use a single displaced muon trigger. A significant fraction of the acceptance is in the barrel region. Low momentum muon signatures (from decays of lighter particles, which are produced dominantly in forward direction) will require a displaced dimuon trigger to get low enough thresholds. Here, the endcap region becomes important. This is illustrated in Fig. 7.13.

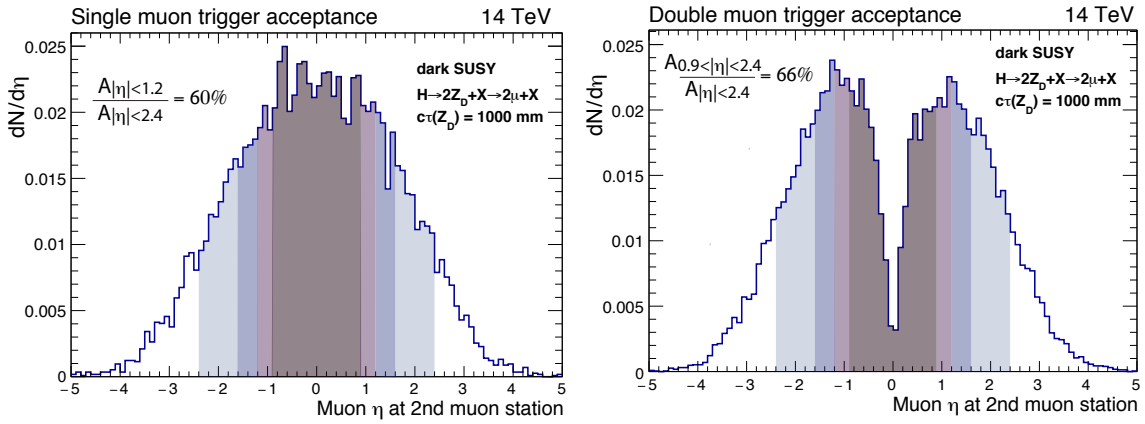

Figure 7.13: Muon pseudorapidity distributions obtained from the simulation of dark SUSY events, generated by Madgraph, in which a Higgs boson decays to two dark photons, one dark photon decays to 2 muons, while the other decays to 2 pions. Left: The barrel region is important for signatures with high p_T muon pairs that require a single muon trigger. The acceptance of a single 30 GeV/c muon trigger is shown as function of eta at the second muon station of the leading muon. Right: The forward region is important for signatures with muon pairs of modest p_T that require a double muon trigger. The acceptance of a double 10 GeV/c muon trigger is shown as function of eta at the second muon station of the most forward muon.

The current muon system is able to reconstruct muons with a displacement transverse to the beam spot, L_{xy}, up to $\sim$ 350 cm and with a transverse impact parameter, d_{xy}, up to $\sim$ 100 cm. This is in strong contrast to the L1 Track Trigger which can reconstruct only prompt muons. The L1 muon p_T reconstruction assumes that muons come from the interaction point. Dropping this constraint reduces resolution and increases rate. Therefore, new handles are needed. Measurements of muon direction within a single station have to be optimized in the L1 Muon trigger.

The conceptual design of the p_T assignment algorithms all rely on the measurement of the bending angle in at least two stations. In the barrel a fairly simplistic algorithm was implemented. It shows good performance for displaced muons: reasonably high efficiency and a trigger rate for single muon trigger around 10 kHz at HL-LHC conditions, as can be seen in Fig. 7.14. While this is good enough as a proof of concept, the final algorithm will need further optimization to cope with high pileup conditions.

In the endcap, the situation is substantially more challenging. CSCs are much thinner than DT chambers; although a L1 trigger measurement of stub directions is available, it is coarse. In addition, the magnetic field is much weaker, especially in the very forward region.

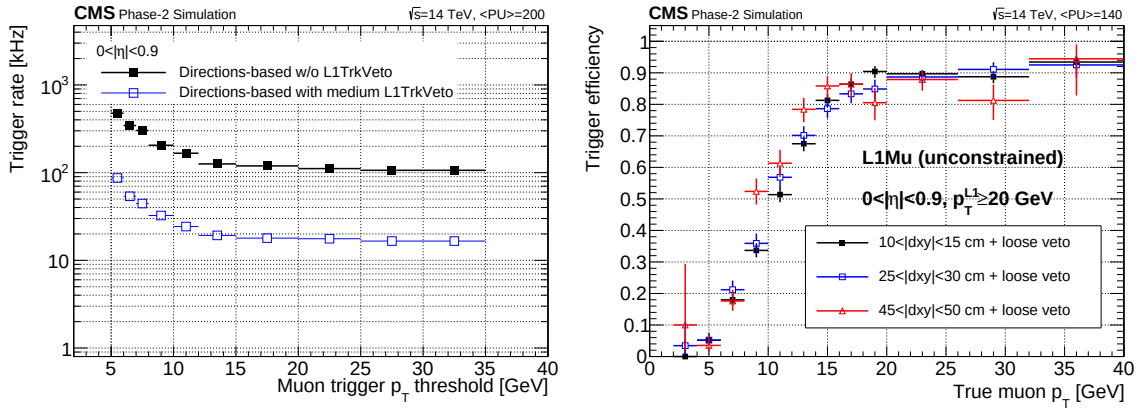

Figure 7.14: L1 Muon trigger rate versus muon p_T threshold (left) and efficiency versus true muon p_T (right) for the barrel displaced muon algorithm.

With the current detectors (including GE1/1), only one direction is well measured, namely GE1/1-ME1/1. At least two are required for a suitable trigger. An endcap trigger on displaced muons has been implemented; it relies on

- inclusion of the GE2/1 detectors to form the second good measurement of muon direction, and
- an improved CSC L1 stub position and direction measurement from slight firmware modifications,
- a hybrid algorithm which combines the power of the direction- and position-based p_T measurements,
- a L1 track trigger veto, if a L1 track is in a cone of $\Delta R = 0.12$ around the muon candidate evaluated at the second muon station.

Figure 7.15 (top) shows the performance of the endcap displaced muon algorithm in $1.65 < |\eta| < 2.10$ without (blue) and with GE2/1 (black). With the addition of GE2/1, the trigger rate is reduced by a factor of two at $p_T = 10$ GeV before application of the track veto. The performance of the position-based algorithm (blue) and of the hybrid algorithm with GE2/1 and ME0 (black) in the region $2.1 < |\eta| < 2.4$ before application of the track veto is shown in Fig. 7.15 (bottom). In the very forward region the direction measured in the ME0 station is essential to reduce the trigger rate to a reasonable level. By applying a loose track-veto the displaced muon trigger rate reduces further to $\sim$ 10 kHz at 10 GeV threshold, which is a reasonable target, while reducing the efficiency by only $\sim$ 5%. A tight L1 track trigger veto ($p_T > 2$ GeV) allows further reduction, but at a cost to efficiency. Further algorithm improvements will allow for a better rate control.

The studies show that the currently developed algorithms for triggering at L1 on displaced muons have high efficiency and the trigger rate is within the acceptable range. The results suggest the following design of the HL-LHC L1 muon trigger:

- A standalone L1Muon generates two p_T measurements for each muon, prompt and non-prompt.
- L1 muons are matched with tracks:
  - If the track match is successful, the L1 track trigger p_T is used and a prompt candidate is formed.
  - If the match is unsuccessful and the muon is not vetoed by L1 tracks, the

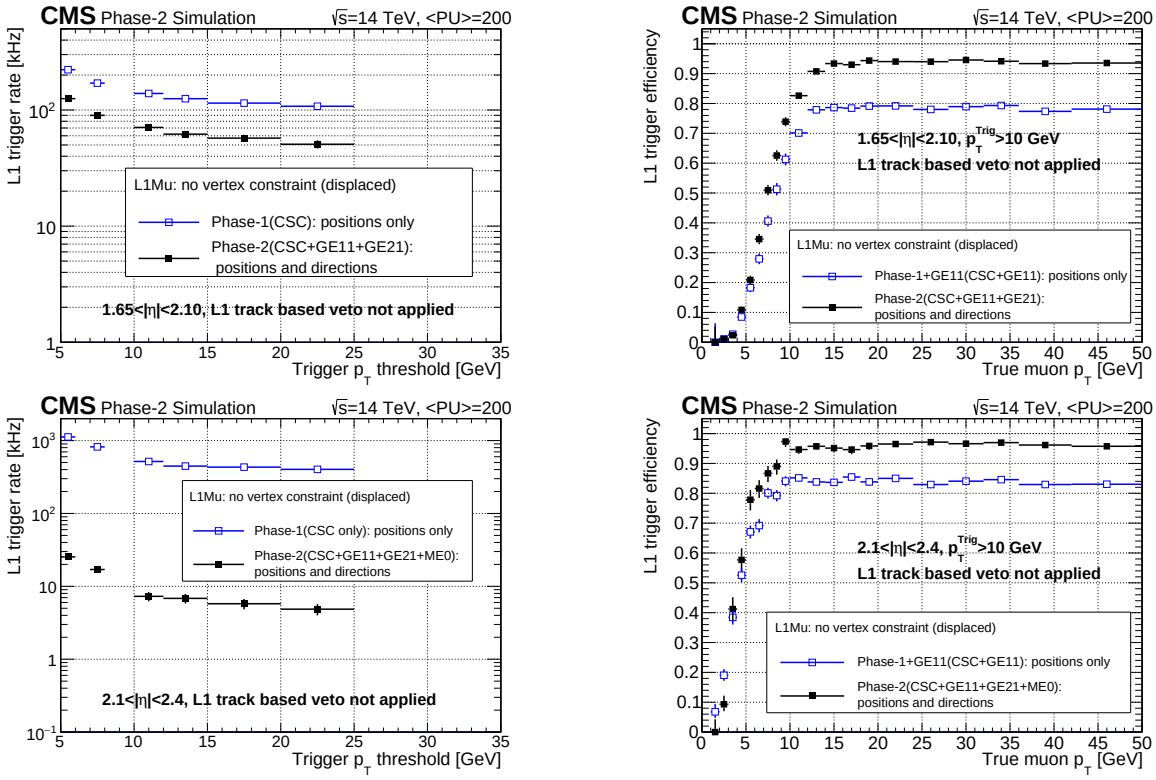

Figure 7.15: L1 muon trigger rate vs trigger p_{T} threshold (left) and trigger efficiency vs. true muon p_{T} (right) for the endcap displaced muon algorithm in the region $1.65 < |\eta| < 2.1$ (top) and $2.1 < |\eta| < 2.4$ (bottom). The track veto is not applied here yet.

non-prompt L1Mu p_{T} is used to form a displaced muon candidate.

Such a scheme is fully compatible with the proposed L1 trigger architecture, and yields good results for both prompt and non-prompt muons.

7.1.4.2 Trigger algorithm for muon-like HSCPs

The upgrade of the RPC system will allow the trigger and identification of slowly moving particles by measuring their time of flight to each RPC station with a resolution of $\mathcal{O}(1)$ ns, as described in Chapter 5. The speed of muon-like particles and the time (bunch crossing) of their origin will be computed with a fast algorithm to be implemented in the Phase-2 Level 1 trigger.

The RPC detectors are synchronized to register muons moving at the speed of light with a local time equal to zero with respect to the collision event that produced the trigger. Slow-moving particles, as HSCPs, will arrive with a delay depending on their speed as shown in Fig. 7.16. This time delay measured by each RPC layer crossed by the HSCP is exploited in order to trigger on and reconstruct such particles.

The principles of the proposed HSCP trigger algorithm are illustrated in Fig. 7.17. In this figure, the vertical axis is the time of signals in RPC chambers, as synchronized so that muons moving nearly at the speed of light from a particular collision are measured at the time of the collision. The horizontal axis is the distance from the collision point to the position of the RPC at which the time is measured. The diagram shows three successive bunch crossings, two of which contain muons represented at horizontal lines. The diagram also shows the RPC time measurements from two HSCPs having slopes different from zero due to their traveling signif-

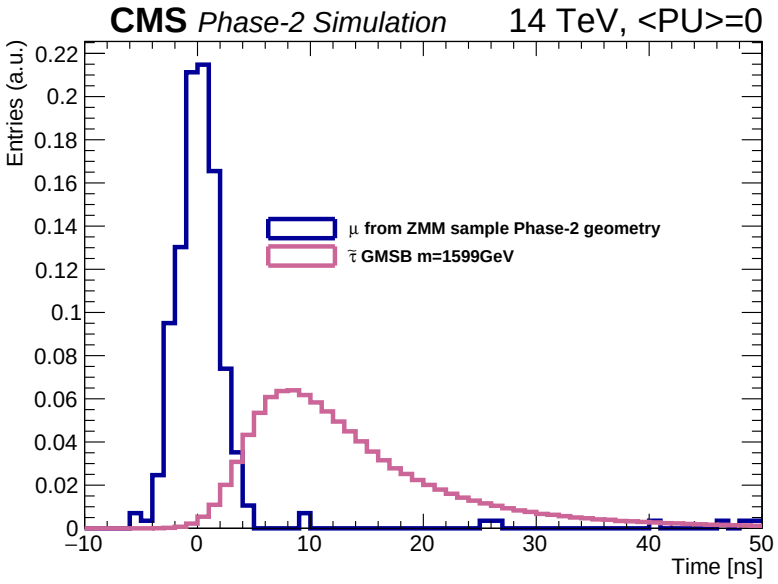

Figure 7.16: RPC hit time measurement distribution for muons from $Z \to \mu\mu$ events and for semi-stable $\tilde{\tau}$'s with m≈1600 GeV, produced in pp $\to \tilde{\tau}\tilde{\tau}$ processes.

icantly slower than the speed of light. The time delay Δt is related to the speed v of an HSCP via the following equation:

$$\Delta t = d\left(\frac{1}{v} - \frac{1}{c}\right), \tag{7.1}$$

where d is the distance between the IP and the point where an HSCP crosses an RPC. For RE4/1 chambers and $\beta = v/c = 0.2$, the delay time is > 6 BXs $= 150$ ns.

A penetrating charge particle leaves a trail of hits in RPC chambers along its trajectory. The time of flight can be computed in each RPC station with respect to a number of BX hypotheses. Should there be a common velocity solution, derived from Eq. (7.1), with $\beta < 0.6$, a trigger is formed. For $\beta > 0.6$, the delays are small and can be handled by the Phase-1 trigger. The performance of this algorithm has been studied in CMS full simulation. All the detector effects (electronics jitter, signal time propagation along strips) are taken into account. A particle speed measurement resolution is shown in Fig. 7.18 (right) for the case of 25 ns signal sampling time (Phase-1) and 1.56 ns sampling time provided with the upgraded RPC Link Board System.

The efficiency of the RPC-HSCP algorithm as a function of β is studied and compared with the standard L1 muon trigger. The results are shown in Fig. 7.18 (right). The current CMS-HSCP Phase-1 trigger performs well down to $\beta \approx 0.75$. The upgraded RPC Link Board System will allow us to trigger, at the correct BX, HSCPs with velocities as low as $\beta \sim 0.25$.

Possible improvements for this trigger proposal in the β measurement could be achieved by matching the Tracker Track trigger to the HSCP muon trigger. The uncertainty coming from the propagation time along RPC strips can be reduced if the hit position is known along the local y coordinate, or the global η. This correction is not needed for the iRPCs thanks to the two-end strip readout for these new detectors as explained in Chapter 5.

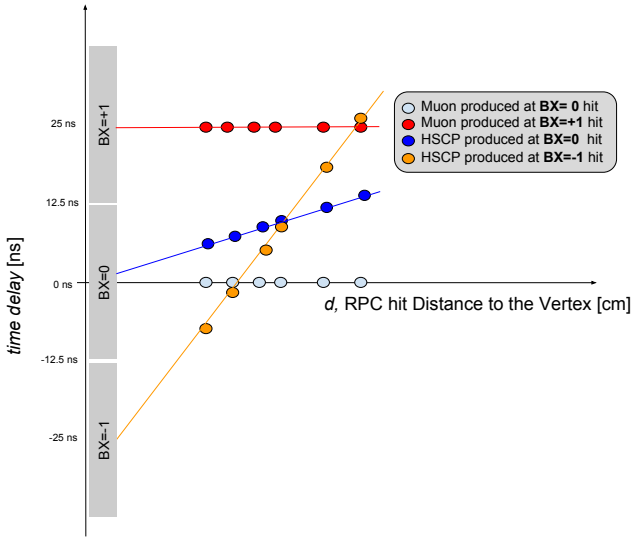

Figure 7.17: Diagram showing times measured at different RPC stations for particles originating at different BXs with different velocities. The x-axis represents the distances from IP to RPC detectors, while y-axis corresponds to time. Clock at all RPC stations is tuned so that particles moving with the speed of light are registered with the exact same "local" times. Hence, relativistic particles are represented by horizontal lines on this diagram.

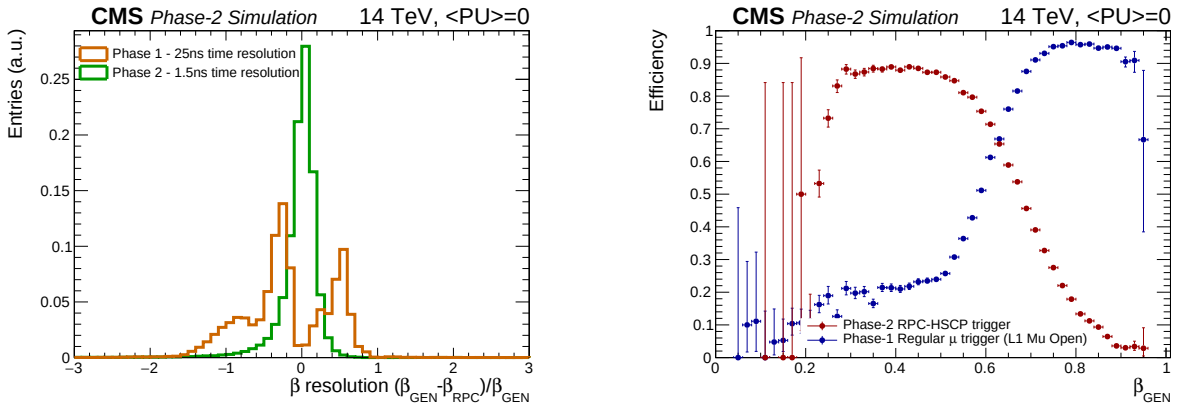

Figure 7.18: (Left) Resolution of a particle speed measurement at L1 trigger level with Phase-1 and upgraded RPC Link Board System. (Right) The efficiency as a function of β of the standard L1 muon trigger without any p_{T} threshold, and the RPC-HSCP Phase-2 trigger with 1.56 ns sampling time.

7.2 Muon reconstruction and identification

For the measurement of muons, the single most important aspect is the 3.8 T solenoidal magnet, with inner diameter of 6 m and length of 13 m. The magnetic flux generated by the strong central field is large enough to saturate the steel in the return yoke. The standard Muon reconstruction is performed using the all-silicon inner tracker at the center of the detector and up to four stations of gas-ionization muon detectors installed outside the solenoid and sandwiched between the layers of the steel return yoke. This provides two measurements of the trajectory of each muon, resulting in a good level of redundancy and excellent momentum resolution, varying from one to few percent at 100 GeV, depending on $|\eta|$, without making stringent demands on spatial resolution and the alignment of muon chambers. The present detector and the favorable length to radius ratio allows efficient muon measurement up to a pseudorapidity of $|\eta| < 2.4$. The strong magnetic field also enables an efficient first-level trigger with an acceptable rate.

While all the muon detectors will undergo improvements to maintain performance throughout the HL-LHC era, the main effort will be to preserve the performance of the endcap muon system, increasing the coverage of detector layers for the $|\eta| > 1.6$ region, since this system experiences the highest particle fluxes and suffers the most from pileup. A second goal is to extend the muon detection coverage to higher η. The present inner tracker is composed of a pixel detector and a silicon strip tracker and measures charged-particle trajectories in the pseudorapidity range $|\eta| < 2.5$. The Phase-2 tracker will cover the pseudorapity rage up to $|\eta| < 4$ and will provide L1 trigger information up to $|\eta| < 2.4$ [16]. The present muon system covers the pseudorapidity range $|\eta| < 2.4$ and performs three main tasks: triggering on muons, identifying muons, and improving the momentum measurement and charge determination of high-p_T muons. With the addition of the ME0 station, the coverage will be extended to $|\eta| < 2.8$ in Phase-2.

The simulations shown in this section are based on Drell–Yan dimuon production to measure signal efficiency, on $t\bar{t}$ events to measure background muon yields, and on QCD muon enriched events for the isolation studies. All the samples have been studied in several pileup scenarios as well as using the Phase-1 detector geometry. For the simulation of the Phase-2 detector, two main scenarios have been considered. The first one assumes that the present DT, CSC, and RPC detectors operate at the same efficiency as for the Phase-1 detector. The second one includes the effects due to aging from radiation damage, extrapolated from the present operational experience and on the basis of irradiation tests performed at the GIF++ facility (see Section 2.2). In the scenario including aging, also the effect of increased neutron background has been considered and included in the simulation (see Section 2.1).

7.2.1 Muon reconstruction

In the standard CMS reconstruction for pp collisions [118, 119], tracks from muons are reconstructed both in the inner tracker (*tracker track*) and in the muon system (*standalone-muon track*).

The standalone muon reconstruction starts from building track segments within individual muon chambers using a linear fit to the positions of the hits reconstructed in each of the 8–12 (in case of DT) or 6 (in case of CSC) layers of the chamber. The new detectors proposed for the Phase-2 upgrade introduce additional hits to the reconstruction. In particular for the GE1/1 and GE2/1 detectors in almost all the cases muons leave two hits. In the ME0 detector the presence of six layers allows to use the segment reconstruction algorithm currently in use for the CSC[120] (properly modified to match the ME0 features) for building segments. All the segments coming from the existing muon detectors are used to generate "seeds" consisting

of position and direction vectors and an initial estimate of the muon transverse momentum. The seeds serve as starting points for the track fits in the muon system, which are performed using segments and hits from DTs, CSCs, RPCs, GEMs and are based on the Kalman-filter technique [121]. To improve the momentum resolution, a beam-spot constraint is applied in the fit for beam collision data. Details about the track reconstruction in the Phase-2 tilted tracker can be found elsewhere [16].

Based on these objects, two reconstruction approaches are used in CMS:

- *Global Muon reconstruction (outside-in).* For each standalone-muon track, a matching tracker track is found by comparing parameters of the two tracks propagated onto a common surface. A *global-muon track* is then fitted combining hits from the tracker track and standalone-muon track, using the Kalman-filter technique [121]. At large transverse momenta, $p_{\mathrm{T}} \gtrsim 200\,\mathrm{GeV}$, the global-muon fit (as well as a set of dedicated *high-*p_{T} refits combining information from tracker and muon chambers with different logics) can improve the momentum resolution compared to the tracker-only fit [21, 119]. As mentioned, the standalone muon reconstruction algorithm has been updated to use also the hits coming from all the new forward muon detectors (GEM and iRPC). Consequently also the Global Muon reconstruction includes those hits.
- *Tracker Muon reconstruction (inside-out).* In this approach, all tracker tracks with $p_{\mathrm{T}} > 0.5\,\mathrm{GeV}$ and total momentum $p > 2.5\,\mathrm{GeV}$ are considered as possible muon candidates and are extrapolated to the muon system taking into account the magnetic field, the average expected energy losses, and multiple Coulomb scattering in the detector material. If at least one muon segment matches the extrapolated track, the corresponding tracker track qualifies as a Tracker Muon. For the Phase-2 era the Tracker Muon algorithm is used to match the tracker tracks also to the new segments provided by the GEM subsystem. This has several benefits: it improves the Tracker Muon performance in the overlap region with the existing muon subdetectors ($1.6 < |\eta| < 2.4$) from the point of view of the fake rejection and redundancy of the muon system. Moreover, it allows also to extended the eta coverage up to $|\eta| = 2.8$. Track-to-segment matching is performed in a local (chamber) coordinate system, where local x is the best-measured coordinate (in the r-ϕ plane) and local y is the coordinate orthogonal to it for DT and CSC. Within ME0 the matching is performed in global ϕ and η coordinates. This is important for ME0 as the η granularity is much coarser than the ϕ granularity. Using local-x matching would result in a lots of mixing from the much less precise η measurements. Moreover, since ME0 provides a bending angle measurement, a track-segment match in p_T is required. All the matching criteria in ME0 become tighter with increasing muon momentum.

Tracker Muon reconstruction is more efficient than the Global Muon reconstruction at low momenta, $p \lesssim 5\,\mathrm{GeV}$, because it requires only a single muon segment in the muon system, whereas Global Muon reconstruction is designed to have high efficiency for muons penetrating through more than one muon station and typically requires segments in at least two muon stations.

Owing to the high efficiency of the tracker-track reconstruction [122] and the very high efficiency for reconstructing segments in the muon system, about 99% of the muons produced in pp collisions within the geometrical acceptance of the muon system (and having sufficiently high momentum) are reconstructed either as a Global Muon or a Tracker Muon, and very often as both.

7.2.2 Muon identification definition and efficiency

The combination of different approaches provides robust and efficient muon reconstruction. Physics analysis can set the desired balance between identification efficiency and purity by applying further selections based on various muon identification variables. The selection criteria used during Run 2 have been updated to exploit the information coming from the new forward detectors, and are optimized for the conditions expected in the HL-LHC era. The performance of the following two basic muon identification algorithms is presented:

- *Loose Muon selection.* The candidate is required to be reconstructed either by the Tracker Muon or the Global Muon algorithm. In addition, the candidate must satisfy the selection criteria of the Particle Flow Muon algorithm [123, 124]. In order to extend the pseudorapidity acceptance the muon candidate is required also to be loosely identified in the ME0 detector with a selection on the track-segment matching in global η, global ϕ and in the bending angle tuned for muons of p_{T} between 2 and 4 GeV. Finally, the candidate must have a transverse impact parameter $|d_{xy}| < 2$ mm and a longitudinal impact parameter $|d_z| < 5$ mm with respect to the primary vertex in the event.
- *Tight Muon selection.* For this selection, the candidate must be reconstructed both as a Global Muon and a Tracker Muon. It also needs to satisfy the PF muon algorithm selection. The Global-Muon track fit must have a $\chi^2/d.o.f.$ less than 10 and must include measurements in more than five inner-tracker layers, including at least one pixel hit, and at least one muon chamber hit. In addition, the Tracker Muon algorithm must find matching segments in at least two muon stations. Finally, the candidate must have a transverse impact parameter $|d_{xy}| < 2$ mm and a longitudinal impact parameter $|d_z| < 5$ mm with respect to the primary vertex in the event (closest to the simulated primary vertex). With this selection, the rate of muons from decays in flight is significantly reduced, at the price of a few percent loss in efficiency for prompt muons, such as those from W and Z decays. In order to extend the $|\eta|$ acceptance the muon candidate is required also to be clearly identified in the ME0 detector with a selection on the track-segment matching in global η, global ϕ and in the bending angle tuned for muons with p_{T} between 3 and 5 GeV.

The primary vertex identification algorithm [16] has been found to be inefficient for $Z/\gamma^* \to \mu\mu$ events in Phase-2 pileup conditions. Hence, the reconstructed vertex closest to the simulated primary vertex is used for the calculation of the impact parameters. This allows us to estimate the muon performance independently of the primary vertex identification efficiency, under the assumption that specific, more efficient, vertexing algorithms may be developed at analysis level.

The muon reconstruction and identification efficiency is calculated as the fraction of simulated muons that are associated to a reconstructed muon passing a given identification selection criteria. The association between simulated and reconstructed muons is performed by matching the simulated signals on each detector layer to the corresponding reconstructed hits, used to fit the muon track.

Figures 7.19 and 7.20 show the identification efficiency of Loose and Tight Muons in different PU scenarios under ideal conditions, that is without taking into account muon system aging and the additional hits coming from the induced neutron background. Figure 7.21 shows instead the identification efficiency of Loose and Tight Muons at pileup 200 when the muon system degradation and the neutron background hits are both simulated. The upgraded detector allows for the identification of muons at high pileup with the same efficiency as the Phase-1

detector with lower pileup. The aged detector shows a drop in efficiency of approximately from 5 to 15%. The impact of the new muon detectors in the forward region is clearly visible, up to the $|\eta|$ coverage provided by ME.

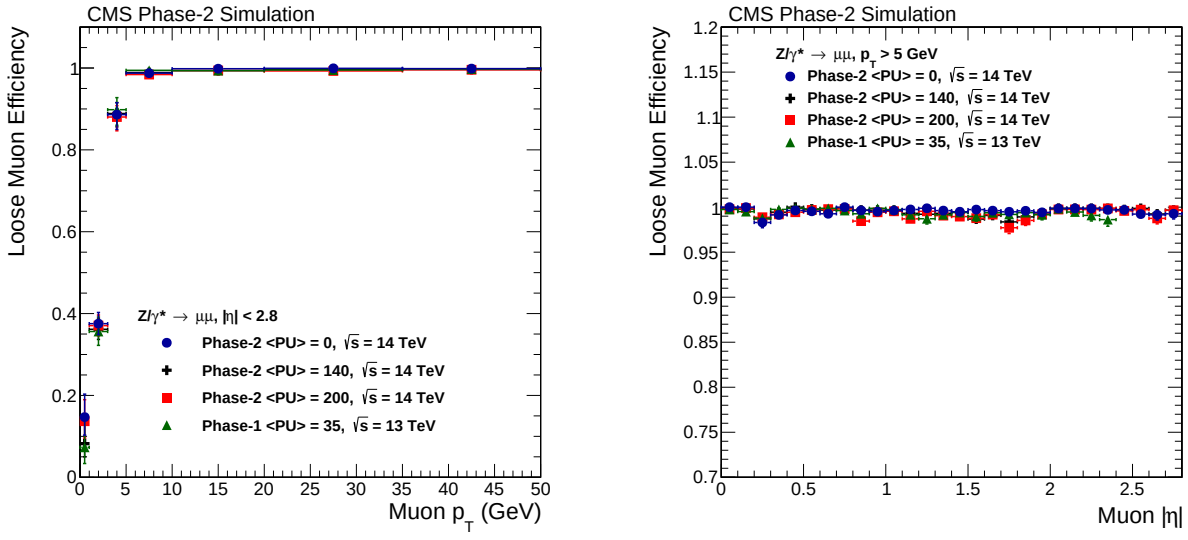

Figure 7.19: Loose Muon reconstruction and identification efficiency in DY events as a function of the simulated muon p_T (left) and $|\eta|$ (right), for the Phase-2 detector in three pileup scenarios, compared to the performance of the Phase-1 detector. The results are obtained in ideal conditions, that is without taking into account the aging of present muon detectors and effects due to neutron background.

7.2.3 Background muon multiplicity

Background muons are defined as all the reconstructed and identified muon candidates that are not matched to a simulated muon from the main "hard" interaction. Background muons originate from various sources: muons from heavy-flavor and light-flavor hadron decays; fake muons from hadron punch-through; random matching of tracker tracks with standalone tracks (or segments) in the muon spectrometer; and duplicates of the same muon.

The background muon multiplicity is defined as the ratio between the reconstructed and identified muons that are not matched to a simulated muon and the total number of processed events. Results are obtained using $t\bar{t}$ events and presented as a function of the transverse momentum and pseudorapidity of the reconstructed muons.

In Fig. 7.22 the average background-muon multiplicity per event plotted versus the muon p_T (left) and the muon η for the Loose Muon identification is shown. The background multiplicity is maximum at low muon transverse momentum, where there is the highest pileup contribution, and does not depend significantly on the multiplicity and on the kinematics of the signal sample. In addition, the background rate is under control with respect to the increase of pileup in the different scenarios shown.

Similar conclusions are obtained when comparing the background multiplicity of Tight Muons in different scenarios, Fig. 7.23. In that case, however, the level of background muons is further reduced with respect to the observation for Loose Muons. A reduction factor between one and two orders of magnitude is found. As an example, the background muon multiplicity for Tight Muons of $p_T < 5$ GeV is below 5×10^{-2} for all considered scenarios. In addition, no significant variation is observed with increasing pileup. The background multiplicity also does not show

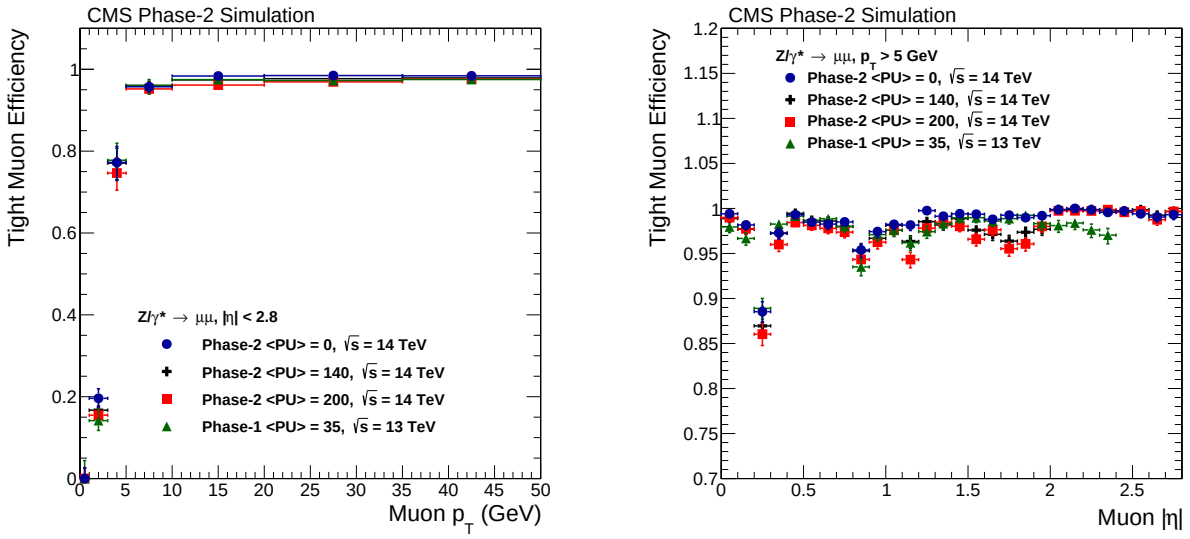

Figure 7.20: Tight Muon reconstruction and identification efficiency in DY events as a function of the simulated muon p_{T} (left) and $|\eta|$ (right), for the Phase-2 detector in three pileup scenarios, compared to the performance of the Phase-1 detector. The results are obtained in ideal conditions, that is without taking into account the aging of present muon detectors and effects due to neutron background.

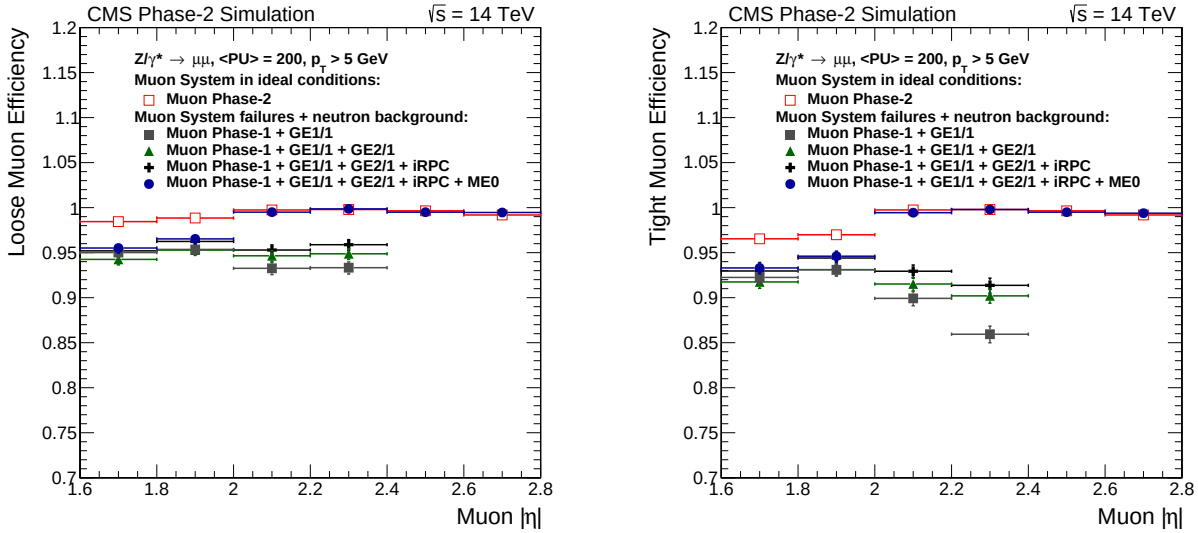

Figure 7.21: Loose (left) and Tight (right) Muon reconstruction and identification efficiency in DY events as a function of the simulated muon $|\eta|$, at pileup 200, obtained including the simulation of muon system aging and neutron background. The performance is measured applying several upgrade scenarios incrementally, from the Phase-1 detector (with the addition of GE1/1) to the full scope of the muon system upgrade.

any particular increase when including the muon system failures and the neutron background simulation.

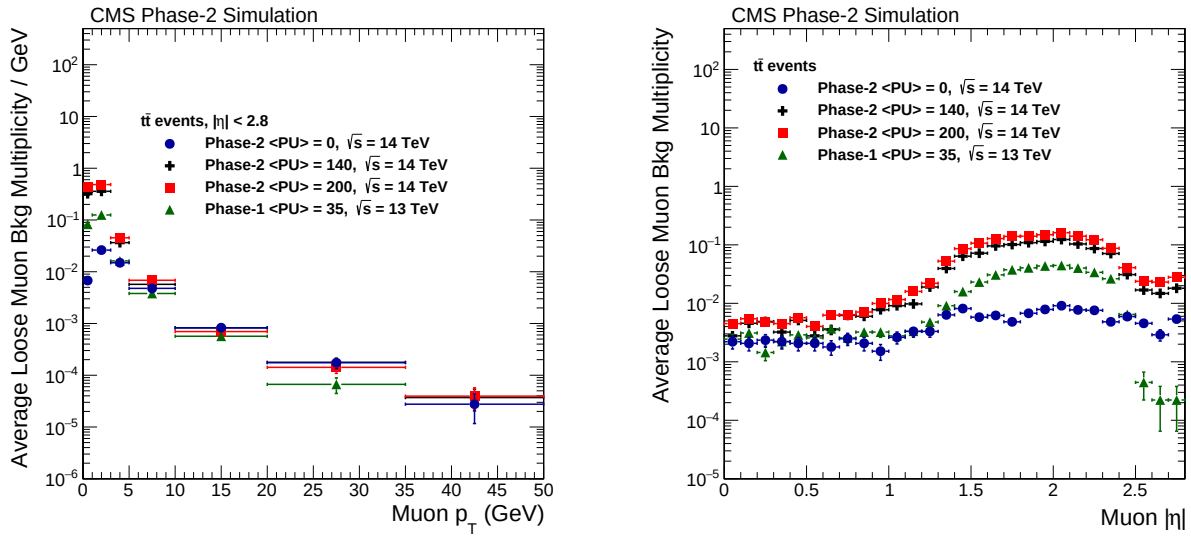

Figure 7.22: Average background-muon multiplicity for the Loose Muon identification as a function of muon p_{T} (left) and $|\eta|$ (right) for the Phase-2 detector in three pileup scenarios, compared to the performance of the Phase-1 detector. The results are obtained in ideal conditions, that is without taking into account the aging of present muon detectors and effects due to neutron background.

7.2.4 Offline displaced standalone muon reconstruction

A special standalone muon reconstruction algorithm was developed in CMS for the reconstruction of highly displaced muons [125]. The displaced standalone (DSA) tracks are reconstructed using only hits in the muon chambers. The reconstructed segments are not required to point towards the event vertex, and the DSA tracks have no constraints to the beam spot.

Since the offline DSA muon reconstruction relies on the standard standalone muon reconstruction, it benefits from the additional hits coming from the Phase-2 muon system forward upgrade. The performance of the DSA reconstruction has been studied in the context of the Phase-2 muon system upgrade by using simulated muons distributed flat in the transverse impact parameter (0–50 cm) and flat in transverse momentum (2–50 GeV). Only the simulated muons originating before the Muon System (with a displacement $L_{xy} < 350$ cm in the transverse plane and $L_z < 500$ cm along the z axis) are considered in the study. Moreover the reconstructed muons are selected by requiring high purity (i.e. percentage of matched rechits with respect to the total number or rechits used for the muon reconstruction $> 75\%$) and a valid hit in at least two different muon stations, in order to ensure a decent transverse momentum estimation. The results of the study are shown in Fig. 7.24. The efficiency of the DSA muon reconstruction is decreased of $\sim$5% by the pileup conditions espected in the Phase-2 era with respect to that in Run 2, nonetheless the reconstruction remains efficient also for big displacements, as can be seen in Fig. 7.24 (b). The background multiplicity increases with pileup as expected, but it is kept under control up to pileup 200, as can be seen in Fig. 7.24 (d). The transverse momentum resolution in the Phase-2 pileup conditions is preserved with respect to the Run 2 conditions and it slightly increases with the displacement ($\sim$5%), as can be seen in Fig. 7.24 (c).

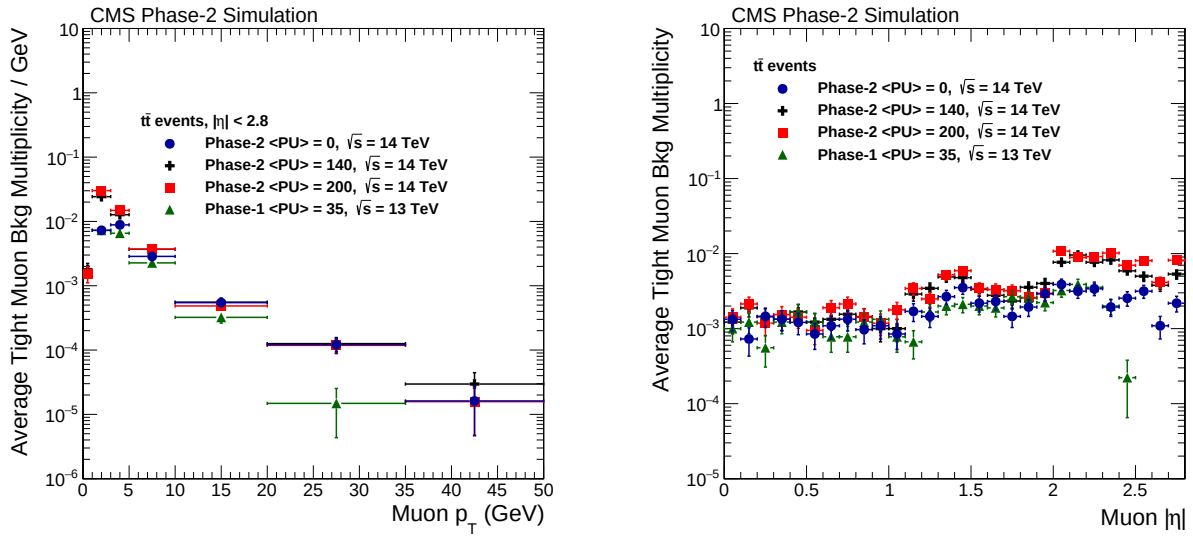

Figure 7.23: Average background-muon multiplicity for the Tight Muon identification as a function of muon p_T (left) and $|\eta|$ (right) for the Phase-2 detector in three pileup scenarios, compared to the performance of the Phase-1 detector. The results are obtained in ideal conditions, that is without taking into account the aging of present muon detectors and effects due to neutron background.

7.3 Muon isolation

Muon isolation is used to distinguish prompt muons from the muons embedded within jets. Muon isolation is typically calculated by the transverse momentum sum of reconstructed objects within a cone around the muon candidate. The Phase-2 luminosity presents a challenge for isolation as the expected pileup of 200 will increase the particle density within the CMS detector, thus increasing the average muon isolation value. For the Phase-1 detector, two isolation methods have been used to reject the non-prompt muons; the tracker based isolation and particle flow based isolation. The tracker based isolation method uses only tracker tracks originating from the primary vertex and takes the p_T sum of these tracks within a cone size of $\delta R = 0.3$ of the muon candidate. Then the isolation value is normalized with the muon p_T. The particle flow based isolation method uses all particle flow candidates within a cone size of $\delta R = 0.3$ of the muon candidate and separates the particle flow objects into four categories; charged hadrons from the primary vertex, neutral hadrons, photons and pileup (charged hadrons not from the primary vertex). Each of the four components are p_T summed and combined using the following equation:

$$\mathrm{Iso_{PF}} = \frac{\sum_{\Delta R<R_0} p_T^{\mathrm{CH}} + \max(0, \sum_{\Delta R<R_0} p_T^{\mathrm{NH}} + \sum_{\Delta R<R_0} p_T^{\mathrm{Photon}} - 0.5 \times \sum_{\Delta R<R_0} p_T^{\mathrm{PU}})}{p_T \text{ of muon}}, \qquad (7.2)$$

where CH, NH, PH and PU denote the charged hadron, neutral hadron, photon and pileup contributions respectively, and R_0 is the size of the cone around the muon candidate. In this equation, half of the charged momentum from pileup is taken as a mean value estimate of the neutral hadron momentum expected from pileup within the cone that should be subtracted from the second term in the numerator.

For the Phase-2 luminosity, this method no longer performs well due to the overabundance of pileup. To reduce the pileup contribution from the charged hadron component, a minimum p_T

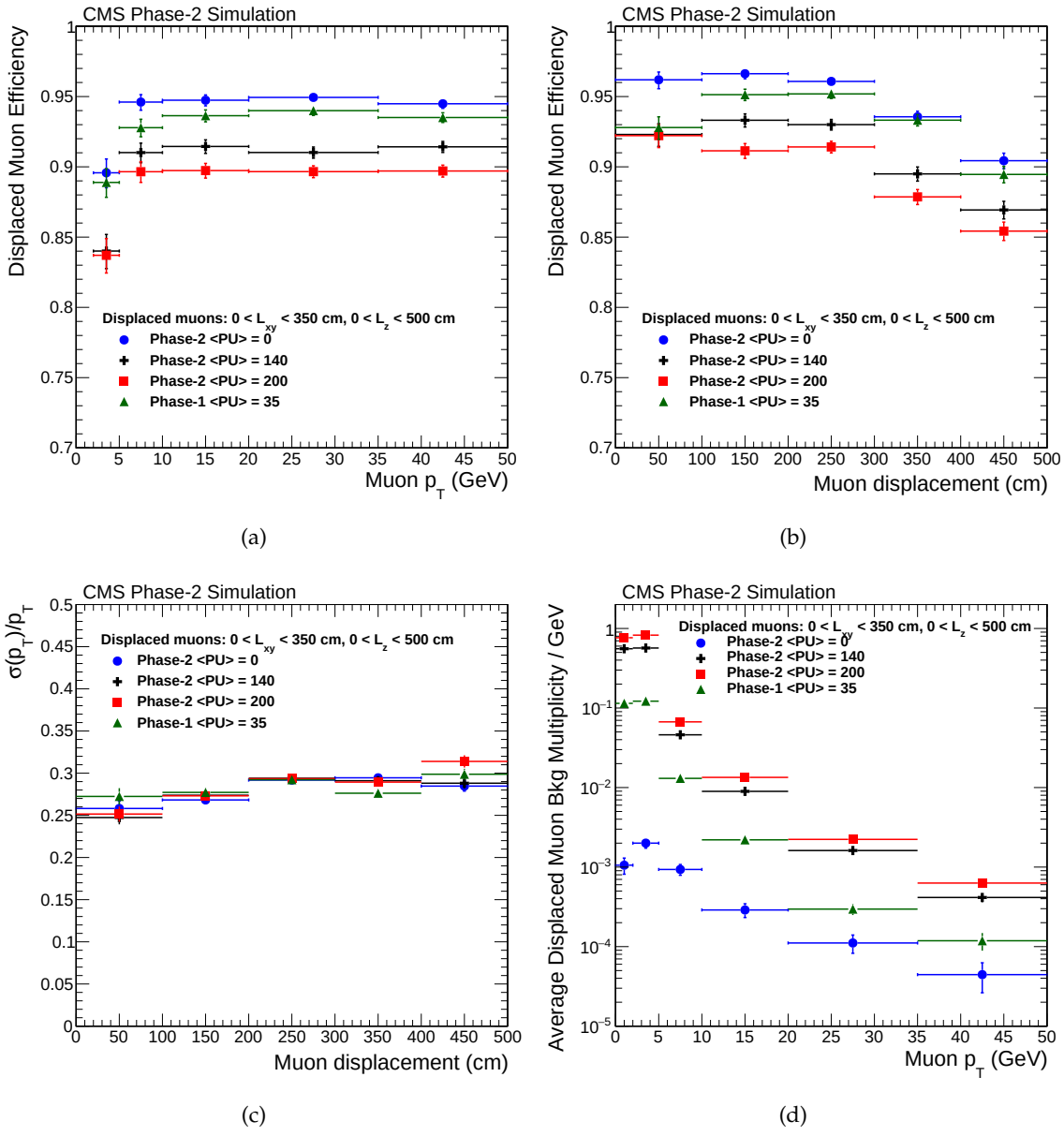

Figure 7.24: Displaced standalone muon reconstruction efficiency as a function of the simulated muon transverse momentum (a) and muon displacement (b), for the Phase-2 detector in three pileup scenarios, compared to the performance of the Phase-1 detector. The transverse momentum resolution of the displaced standalone muon is shown in (c) as a function of the displacement, while the multiplicity of the background muons per event versus the simulated muon transverse momentum is shown in (d). The results are obtained in ideal conditions, that is without taking into account the aging of the present muon detectors and the effects due to neutron background.

requirement of 0.4 GeV is introduced. Then the relative isolations of each of the components are used independently. Figure 7.25 compares the performance of the tracker based isolation and particle flow based isolation methods. A Drell–Yan sample is used for the signal, and a muon enriched QCD sample is used to estimate the average number of background muons per event. We see that isolation can be a very powerful tool to reduce the background rate of Loose Muons even at the highest PU values expected, and even at the high $|\eta|$ region covered by ME0.

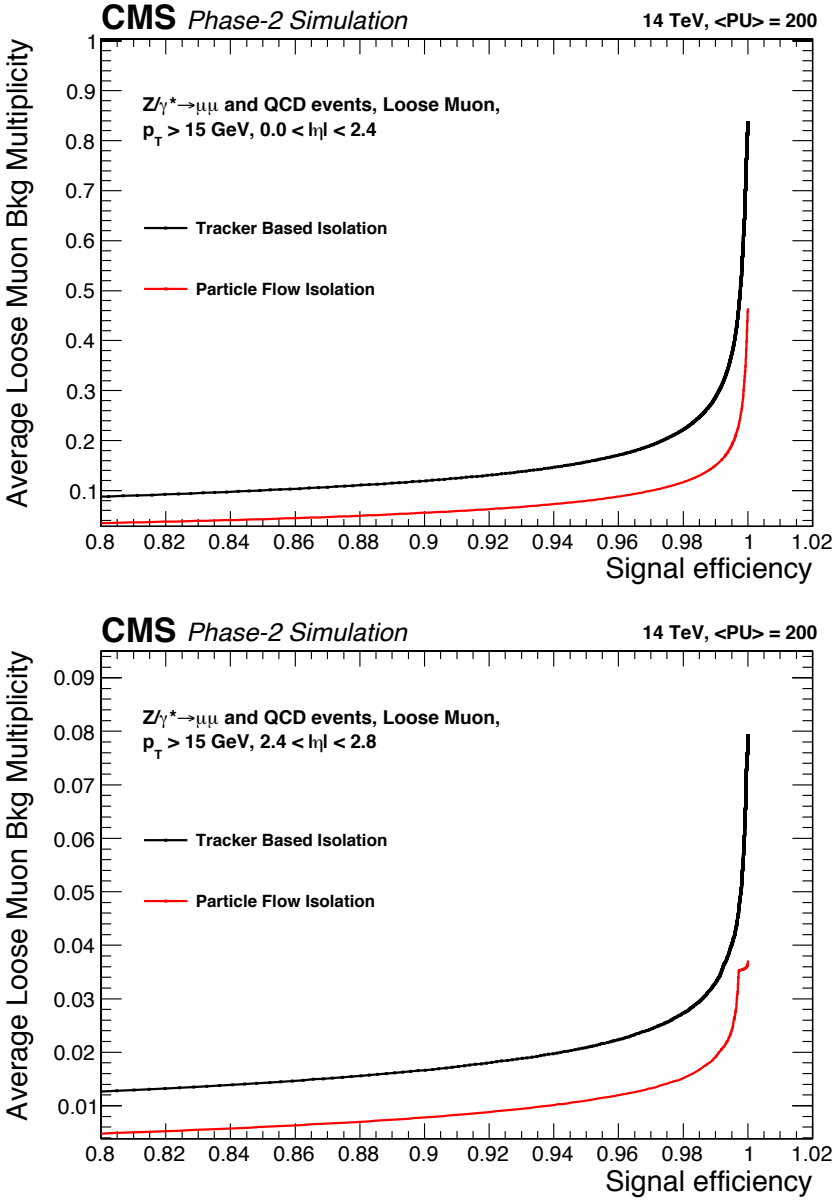

Figure 7.25: Loose muon isolation background rates as a function of efficiency at pileup 200 for tracker and particle flow for 2 η regions; top: $|\eta| < 2.4$, bottom: $2.4 < |\eta| < 2.8$.

Chapter 8

Physics performance

The standard model (SM) of particle physics, the framework developed for the description of fundamental particles and their interactions, is known to be an incomplete theory. There are open fundamental questions and physics phenomena observed in nature that the SM does not adequately explain. In most extensions to the SM, new particles are expected at the TeV scale. However, to date, no such particles have been observed. This implies that their mass is too high, or that their production cross sections are too low, or that their experimental signatures are very difficult to observe.

Therefore the experimental strategy is to perform both direct searches for new physics and precision measurements of SM phenomena. At the HL-LHC the parameter space tested is increased significantly in mass reach and in coupling strength. To fully explore the data delivered by the HL-LHC, it is crucial to maintain or improve the excellent detector performance in a very high pileup environment throughout the lifetime of the experiment.

In this Chapter, we present several example of improvements that are made possible by the proposed upgrades of the CMS muon detector. These are: the new electronics for the existing DT, CSC, and RPC systems, which will allow CMS to maintain its present excellent performance under the harsh HL-LHC conditions through improved triggering, reconstruction, and identification capabilities; the addition of new GEM and iRPC detectors in the endcap stations, which will improve muon momentum measurement and background rejection; and the addition of the ME0 station, which will extend the pseudorapidity coverage of the muon system.

We begin by discussing some measurements that benefit from the extended muon coverage. First, the study of the Higgs boson decay via ZZ into a four-muon final state is a golden channel that allows a complete reconstruction of the Higgs boson decays and has very small expected background. We estimate the additional yield provided by the new ME0 detector. Second, we discuss the measurement of double parton scattering using same sign W boson pair production, where the extended pseudorapidity coverage may provide evidence favoring one of two competing hypotheses: the complete factorization or the nonfactorization of double parton scattering. Third, the search for the lepton-flavor-violating decay of the τ-lepton into three muons. These muons tend to be soft and forward and this search will benefit from the improved trigger and reconstruction performance for low transverse momentum muons in the ME0 region. Fourth, in this category of measurements we demonstrate, using the example of a supersymmetry (SUSY) search, that the additional muon acceptance will also help in rejecting backgrounds for signatures with same sign leptons. Finally, we show that the measurement of the muon forward-backward asymmetry in the extended pseudorapidity range will provide a measurement of $\sin^2\theta^{\text{lept}}_{\text{eff}}$ with greatly improved precision.

The second category of measurements focuses on the new capabilities afforded by the muon system upgrade. We present a study of long lived objects as predicted in SUSY models that

decay into muons. The addition of the GEM detectors and the new trigger electronics will increase the capability of the muon system to trigger on and efficiently reconstruct tracks from their displaced vertices. Then, we discuss the possibilities offered by the improved timing capability of the upgraded muon system in the search for heavy stable charged particles using the time-of-flight technique. Finally, we discuss a measurement of the top quark mass using only measurements of leptons. This is based on top quark decays in which a b quark hadron decays into a J/ψ that decays to muons.

Previous physics sensitivity projections [24, 126–129] were derived by extrapolating from existing Run-1 or Run-2 analyses or from parametrized detector simulations [130]. The results quoted in the following are based on a full simulation of the upgraded tracker, the barrel calorimeters, and the muon system. They confirm that the upgraded detector maintains the performance of the current detector at the much higher pileup rates expected at the HL-LHC, which had been assumed for the previous projections. The results quoted below quantify the achieved detector performance, but mostly stop short of complete physics sensitivity projections, because this would require a complete detector reconstruction, including all subdetector upgrades, which is not yet available.

8.1 Impact of extended coverage of the muon detector upgrade

8.1.1 $H \to ZZ \to 4\mu$

Due to the presence of four muons in the final state, measurements using the decay mode $H \to ZZ \to 4\mu$ will crucially rely on the muon system, and, hence, present an important benchmark for the proposed upgrades, and, in particular, the increase in muon pseudorapidity acceptance from $|\eta| < 2.4$ to $|\eta| < 2.8$ made possible by the ME0 upgrade.

Any increase in acceptance in the forward region greatly benefits the $H \to ZZ \to 4\mu$ analysis [24, 126], since it requires all four muons to be detected, identified, and measured. Triggering is straightforward, as the final state includes four isolated leptons. However, a very high multiplicity of tracks from pileup events expected at the HL-LHC may hinder signal reconstruction and lead to higher background rates.

The four muon signal (gluon-gluon fusion, vector boson fusion, and associated production), irreducible background (the standard model process $ZZ \to 4\mu$), and the main reducible background ($Z(\mu^+\mu^-)$ + jets, referred to as $Z + X$, in which two extra muons come either from heavy flavor decay or from light jet mis-identification) are simulated with an average pileup of 200.

Muons are selected in two ways based on their pseudorapidities. In the region $|\eta| < 2.4$, loose identification criteria are applied to isolated muons with $p_T > 5$ GeV to select high quality muon tracks that have been reconstructed in both the tracker and the muon system.

In the region $2.4 < |\eta| < 2.8$, muons are selected with $p > 5$ GeV and required to pass loose identification criteria with high quality tracks both in the tracker and the ME0 detector. Figure 8.1 shows the muon ID efficiency as a function of muon p_T and η.

The isolation of individual muons is measured relative to their transverse momentum by summing p_T of all the tracks reconstructed within a cone of $\Delta R < 0.4$ around the lepton direction. Figure 8.2 (a, b) shows the isolation distributions for signal and background muons in pseudorapidity ranges $|\eta| < 2.4$ and $2.4 < |\eta| < 2.8$. The signal-vs.-background efficiency ROC (Receiver Operating Characteristics) curve as a function of isolation is shown in Fig. 8.2 (c).

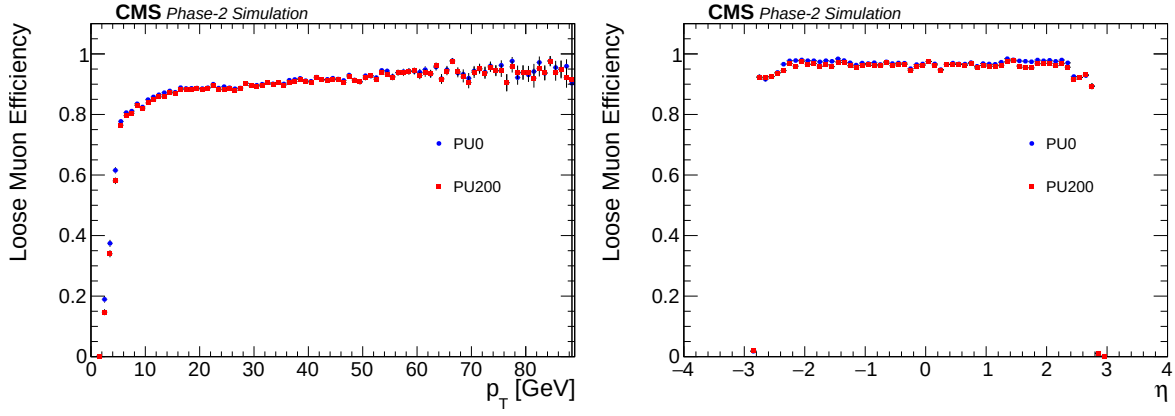

(a) (b)

Figure 8.1: Muon identification efficiency in $H \rightarrow ZZ \rightarrow 4\mu$ events as a function of muon transverse momentum (a) and pseudorapidity (b).

Isolation thresholds used in this analysis depend on the muon pseudorapidity and the pileup conditions; they ensure that 90% of signal events are retained.

A sample of Z+jets events is used to estimate the reducible background.

First, we select a subset of three lepton events that are expected to be completely dominated by final states which include a Z boson and a fake lepton (defined as a lepton that passes the p_{T} and muon ID used for the analysis, and a relaxed isolation requirement). Fake leptons from these events are used to measure probability that such leptons pass the full analysis selection. This probability is then applied in dedicated control samples dominated by Z+jets and $t\bar{t}$ events in order to estimate the contribution of the reducible background in the signal region (see Ref. [131] for details).

The event selection is designed to extract signal candidates from events containing at least four well-identified and isolated leptons, each originating from the primary vertex. Starting from all same flavor, oppositely charged isolated lepton pairs, the one with the invariant mass closest

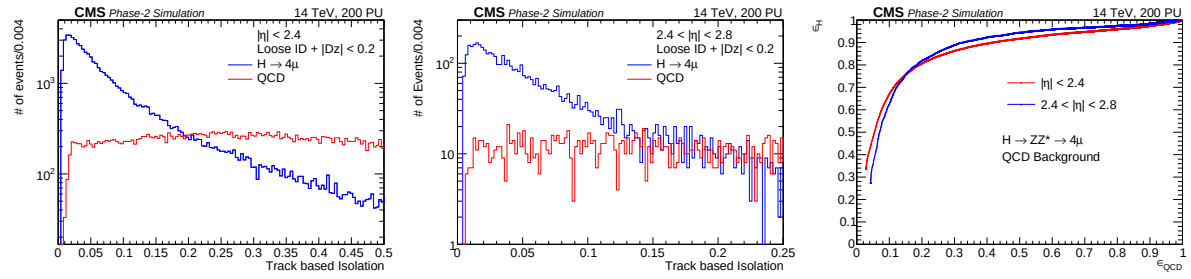

(a) (b) (c)

Figure 8.2: Muon isolation distribution (a) in the $|\eta| < 2.4$ region and (b) in the $2.4 < |\eta| < 2.8$ region for signal and background muons. Background muons are from a general QCD process simulation sample. (c) The ROC curves shows the isolation selection efficiency for identified muons in the Higgs signal sample versus the isolation selection efficiency for identified muons in a QCD sample. Along the ROC curve, the isolation cut runs from from 0 to 10.

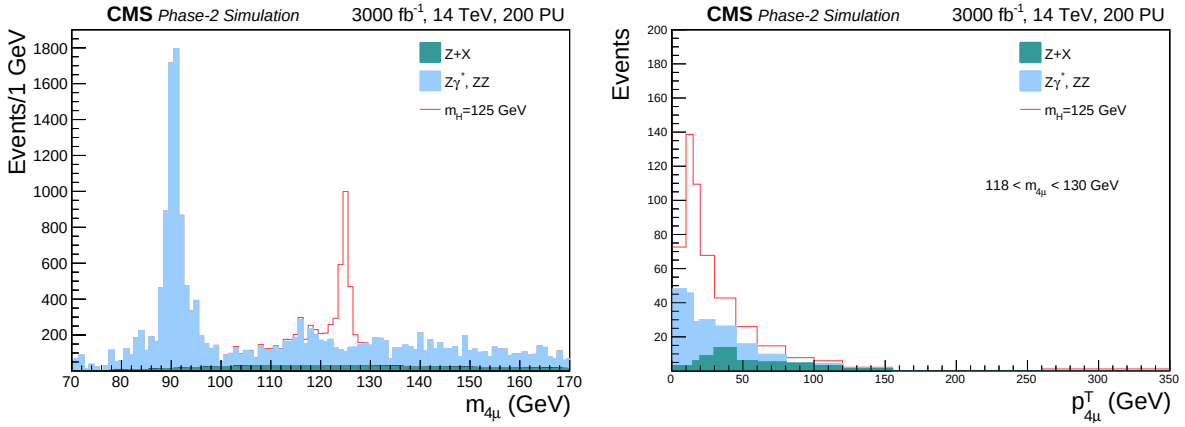

Figure 8.3: (a) Four-muon invariant mass distribution, and (b) four-muon transverse momentum distribution in the mass window 118 $<m_{4\mu} <$ 130 GeV, for the signal, the irreducible ZZ background, and the reducible $Z + X$ background. Both plots assume the acceptance extension from $|\eta| < 2.4$ to 2.8, 200 pileup events, and an integrated luminosity of 3000 fb^{-1}.

to the nominal Z boson mass is selected as the "on-shell" Z boson. Then, from all remaining pairs, the highest p_T pair is selected to reconstruct the other Z boson.

Figure 8.3 (a) shows the four-lepton invariant mass distribution for selected events in the signal and background samples. The resolution of the four-lepton invariant mass in the endcap corresponds to 1.5 GeV in the region where the most forward muon is within $1.2 < |\eta| < 2.4$ (as in Run 2), and increases only by 500 MeV requiring the most forward muon to be in the extended pseudorapidity range, $2.4 < |\eta| < 2.8$. Figure 8.3 (b) shows the transverse momentum of the four lepton system. This illustrates that if a good detector performance is maintained at the HL-LHC we will have an ability to probe the processes in which the Higgs boson is produced with high p_T ($p_T > 100$ GeV). This is of particular interest as the yield and distribution of events in that range is sensitive to BSM physics that may be contributing to the Higgs boson production (e.g., via additional particles in the loop-induced $gg \to H$ process).

Figure 8.4 shows the percentage of events passing each step of the analysis for the two detector configurations, with and without the acceptance extension afforded by the ME0 detectors. Table 8.1 shows the number of $H \to ZZ \to 4\mu$ events and estimated backgrounds after the final selection, normalized to an integrated luminosity of 3000 fb^{-1} and the average pileup 200, with and without the acceptance extension, in two different mass ranges. The Z+X estimates are computed using MC samples with very limited statistics and only conservative upper bounds are quoted.

Two important conclusions can be derived from these results. First, the muon system acceptance extension increases the signal acceptance by 17%. Second, the signal acceptance remains nearly immune to the high pileup conditions. Even though irreducible background increases at higher pace, by 24%, the precision of measuring the overall signal strength improves by 7%, as shown in Table 8.2.

8.1.2 Double parton scattering to WW

Events in which two hard parton-parton interactions occur within one proton-proton collision have been discussed theoretically since the introduction of the parton model and have gathered experimental interest since the advent of the first hadron colliders [132–134]. Analyses of such events in hadron collider data advance the study of transverse and longitudinal parton

Table 8.1: The number of $H \to ZZ \to 4\mu$ and estimated backgrounds, normalized to an integrated luminosity of 3000 fb^{-1}, for the Phase-2 detector with an average pileup of 200, without ($|\eta| < 2.4$) or with ($|\eta| < 2.8$) the ME0 subdetector. Two mass ranges are considered: $70 < m_{4\mu} < 170$ GeV and $118 < m_{4\mu} < 130$ GeV. The Z+X estimate is given as an upper limit due to the limited MC statistics. The systematic uncertainty on Z+X estimate is of the order of 40%.

3000 fb^{-1}@ 14 TeV, PU = 200				
	$70 < m_{4\mu} < 170$ GeV		$118 < m_{4\mu} < 130$ GeV	
	$\|\eta\| < 2.4$	$\eta < 2.8$	$\|\eta\| < 2.4$	$\eta < 2.8$
H $\to$ ZZ $\to 4\mu$, $m_H = 125$ GeV	2029 ± 22	2366 ± 24	1858 ± 21	2164 ± 23
ZZ background	12500 ± 404	16226 ± 464	1177 ± 125	1465 ± 142
Z+X background	< 2800		< 700	

correlations within the proton [135, 136]. Double parton scattering is a background for several new physics searches and a better understanding of this background is critical when studying processes with smaller and smaller cross sections.

Under the assumption of transverse and longitudinal factorization of the two single parton interactions, the cross section of a double parton scattering process can be factorized into the cross sections for the two single partonic processes and a factor σ_{eff} related to the extent of the parton distribution in the plane orthogonal to the direction of motion of the protons.

A particularly accessible channel for studying parton-correlation effects is double parton scattering resulting in two W bosons with the same charge. With subsequent W$\to \mu\nu$ decays, this process provides a very clean signature of exactly two muons of the same charge. The absence of additional jets allows for a good separation with respect to single parton scattering WW boson production. The correlation factor σ_{eff} is often assumed to be a constant. However, recent calculations imply a dependence on the event kinematics, in particular on the product of the pseudorapidities of the two muons, $\eta_1 \cdot \eta_2$ [137]. Measurements of inclusive WW production via double parton scattering have been performed [138, 139]. The large data set expected from

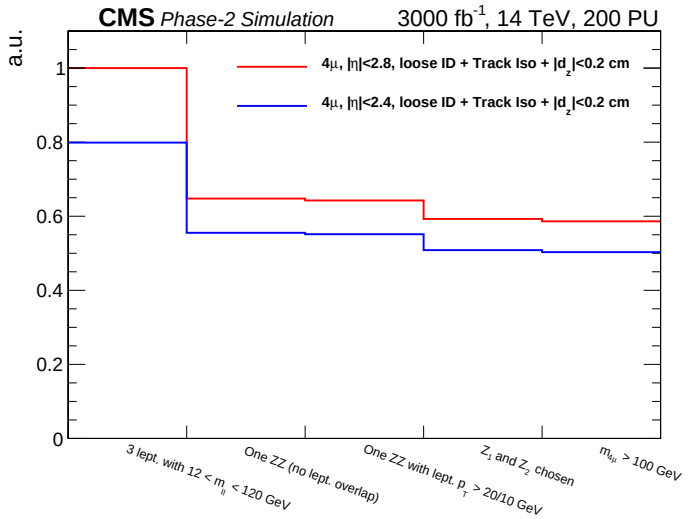

Figure 8.4: The effect of adding the ME0 subdetector for various acceptance choices on the signal with a pileup of 200 events.

Table 8.2: Effect of the ME0 extension on the statistical uncertainty of measuring the signal strength for the $H \to ZZ \to 4\mu$ analysis with the data set corresponding to an integrated luminosity of 3000 fb^{-1}, for the Phase-2 detector with an average pileup of 200.

	$\lvert\eta\rvert$ <2.4	at least one μ within $2.4 < \lvert\eta\rvert < 2.8$
Per category	3.0%	7.8%
Combined	2.8%	

HL-LHC will allow the measurement of the differential cross section in $\eta_1 \cdot \eta_2$. The extended pseudorapidity coverage of the upgraded CMS muon system will increase the sensitivity to the η-dependent observable.

To estimate the sensitivity for this process, the inclusive cross section analysis at 13 TeV is extrapolated to the HL-LHC conditions and the Phase-2 CMS detector. The production cross sections are scaled according to the increase in $\sqrt{s}$, and the statistical uncertainties are scaled by the change in integrated luminosity from 36 fb^{-1} to 3000 fb^{-1}. The effect of the extended coverage in η and the selection and identification efficiencies for the signal and the dominant background process ($WZ \to 3\ell\nu$) are estimated using a full simulation of the Phase-2 CMS detector. In this projection no improvements have been included from the better background rejection for misidentified tri-lepton events enabled by the extended η coverage (Section 8.1.4). An uncertainty below 10% in the measured inclusive double parton scattering cross section can be expected, which is more than a factor of seven improvement compared to the Run 2 result.

Under the hypothesis of nonfactorization of the double parton scattering process, the final-state kinematics of the W decay products depend on each other. In particular, σ_{eff} becomes an almost linear function of $\eta_1 \cdot \eta_2$ with strongest sensitivity at high values for $\eta_1 \cdot \eta_2$. To measure this effect, two complementary approaches are studied: the cross section ratio for double parton scattering in regions with $\eta_1 \cdot \eta_2 > 0$ and $\eta_1 \cdot \eta_2 < 0$, and a differential cross section measurement of σ_{eff} as a function of $\eta_1 \cdot \eta_2$.

The differential cross section measurement gives a direct handle on the impact of the acceptance increase at high η on the expected sensitivity. The results are shown in Fig. 8.5 (left) alongside with two predictions assuming either constant or $\eta_1 \cdot \eta_2$ dependent σ_{eff}. Only statistical uncertainties are considered for this illustration. The extrapolation of statistical uncertainties is based on the acceptance and efficiencies determined from a full simulation of the Phase-2 CMS detector. The shown central values of the measurements are made to be consistent with the prediction of the "nonfactorized" model. The measurements performed within muon coverage $\lvert\eta\rvert < 2.4$ (black points) are compared with the expected results with the muon system extended up to $\lvert\eta\rvert = 2.8$ (blue points). There are two observations to note: (1) measurements in the first and last bins, which have a particularly high weight in the slope fit, are accessible only with the extended muon system; (2) for the intermediate bins, the statistical uncertainties are smaller for the measurements obtained with the extended muon system. Overall, the fit uncertainties on the cross section slope versus $\eta_1 \cdot \eta_2$ are 75% and 50% for the muon system with coverage $\lvert\eta\rvert < 2.4$ and $\lvert\eta\rvert < 2.8$, respectively. The improvement in the slope uncertainty by a factor of 1.5 corresponds to an effective gain in integrated luminosity by a factor of $\sim (1.5)^2 \sim 2$, which would be equivalent to gaining an additional 3000 fb^{-1}.

The measurement of the cross section ratio for double parton scattering in regions with $\eta_1 \cdot \eta_2 > 0$ and $\eta_1 \cdot \eta_2 < 0$ is shown in Fig. 8.5 (right). This technique has the advantage that many systematic uncertainties cancel in the ratio. The systematic uncertainty in the ratio is estimated based on the previous inclusive measurement [139]. A conservative scenario is considered,

assuming a correlation of systematic uncertainties between $\eta_1 \cdot \eta_2 > 0$ and $\eta_1 \cdot \eta_2 < 0$ of 0.8. Larger correlation coefficients do not change the sensitivity. It is reasonable to assume a strong correlation since most systematic uncertainties are symmetric in lepton η. The only source of uncorrelated components are uncertainties that have a different effect depending on the sign of $\eta_1 \cdot \eta_2$. As shown in Fig. 8.5 (right), the measurement at the HL-LHC could provide discrimination between constant and nonfactorizable σ_{eff}. If the ratio was measured to be above 1.08, the factorization hypothesis could be excluded at 95% CL. When restricting the muons to $|\eta| < 2.4$, only a measured ratio above 1.1 could exclude a constant σ_{eff}.

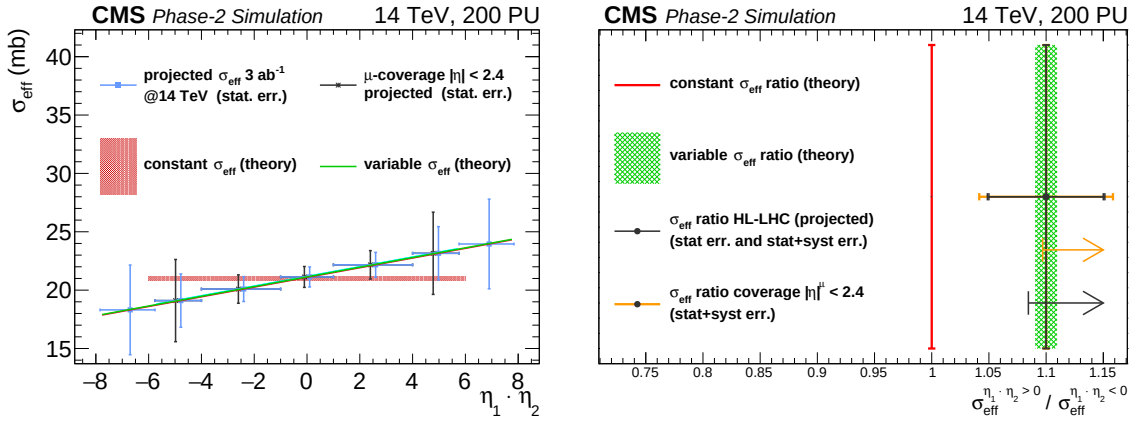

Figure 8.5: Left: Predicted dependence of σ_{eff} on $\eta_1 \cdot \eta_2$ for the cases of complete factorization and non-factorization compared to the projected differential cross section measurement. The black and blue symbols indicate the expected sensitivity of the measurement; their central values are set to the prediction for nonfactorizable σ_{eff}. The black symbols show the expected measurements with muon system coverage up to $|\eta| = 2.8$, the blue symbols up to $|\eta| = 2.4$. Right: Ratio of cross sections σ_{eff} for $\eta_1 \cdot \eta_2 > 0$ and $\eta_1 \cdot \eta_2 < 0$. The inner error bars represent the statistical uncertainty, the outer error bars include systematic uncertainties assuming a conservative correlation of 0.8 between them for $\eta_1 \cdot \eta_2 > 0$ and $\eta_1 \cdot \eta_2 < 0$. The case of complete factorization of the partons is indicated by a red line, and the case of nonfactorization by a green shaded band. The arrows indicate the lowest measured value that would allow for an exclusion of the factorization hypothesis at 95% CL.

8.1.3 Search for lepton flavor violating decays $\tau \to 3\mu$

There are no known symmetries that strictly forbid lepton-flavor violating (LFV) decays, such as $\ell \to \ell'\gamma$, $\ell \to 3\ell'$. In the standard model, due to neutrino oscillations, such decays are possible, albeit with extraordinarily small branching fractions. At the LHC, the $\tau \to 3\mu$ decay is one of the "cleanest" LFV decay channel. The currently best experimental upper limit, set by Belle [33], is $\mathcal{B}(\tau \to 3\mu) < 2.1 \times 10^{-8}$ at 90% CL.

On the order of 10^{15} τ leptons will be produced over the lifetime of HL-LHC, which is a compelling reason to assess the $\tau \to 3\mu$ decay search feasibility. The main source of τ leptons in pp collisions is $D_s \to \tau\nu$ decays. However, such τ leptons, and, hence, muons from $\tau \to 3\mu$ decays, have very low momenta and are significantly boosted in the forward direction. Only about $\sim$ 1.3% of signal events have all three muons with $p > 2.5$ GeV, approximately the energy a muon would need to be measured in the muon subdetectors, and $|\eta| < 2.4$, the current CMS muon system acceptance.

The ME0 chambers, a part of the muon system upgrade, extend the CMS muon coverage in the first muon station from $|\eta| < 2.4$ to 2.82, which increases the signal fiducial acceptance by a fac-

tor of 2.0. Moreover, reconstruction of muon hits in GEM-CSC tandems (GE1/1-ME1/1, ME0-ME1/1, GE2/1-ME2/1) allows one to measure the muon momentum within a single muon station due to a large lever arm formed by the GEM-CSC detector pairs. This will substantially improve purity of reconstructed low momentum muons, which are typically identified as a track matched to a stub in the first muon station. In this analysis, we take advantage of the presence of ME0 chambers, but cannot yet exploit the full potential of the improved muon reconstruction coming from correlation of muon hits in the GEM and CSC detectors,since the software is still under development.

Figure 8.6 (left) shows number of reconstructed $\tau \to 3\mu$ events as a function of pseudorapidity of the most forward muon. Indeed, with the help of the ME0 detectors, one expects to more than double the number of reconstructed signal events although not all of them will pass the final selection. As expected, the additional events with muons at high $|\eta|$ have worse trimuon mass resolution (see Fig. 8.6 (right)). Hence, we introduce two event categories: Category 1 for events with all three muons reconstructed only with the Phase-1 detectors, and Category 2 for events with at least one "ME0-type" muon.

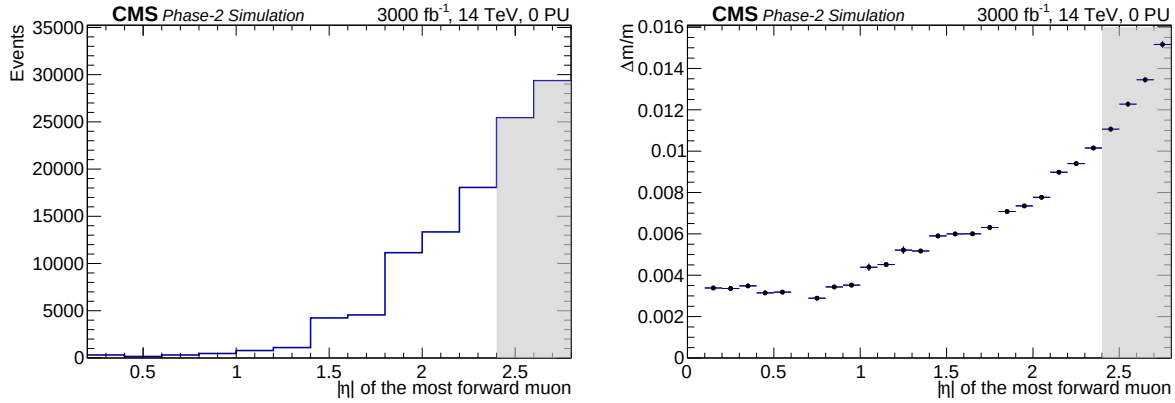

Figure 8.6: Left: Pseudorapidity distribution of most forward muon in reconstructed $\tau \to 3\mu$ events (pseudorapidity is for GEN-level muon). The shaded area corresponds the pseudorapidity range covered by ME0 chambers only. Right: Average trimuon invariant mass resolution as a function of pseudorapidity of the most forward muon.

To select events, we employ a special "Tau3mu" muon identification targeting very low momentum muons, which is further augmented with three additional constraints on trimuon variables: trimuon vertex fit χ^2/dof, transverse displacement of the trimuon vertex, and maximum ΔR distance among three pairs of muons. These three topological cuts help mitigate background associated with the high pileup conditions. The selection has about 30% efficiency for signal events and practically eliminates the pileup contamination.

An analysis of a minbias QCD sample shows that more than 90% of the background is due to events with B mesons, in which two muons come from B-D cascade decays (i.e. $B \to \mu\nu D + X$, followed by $D \to \mu\nu + X$). The third reconstructed muon arises from a π/K decay-in-flight or from an accidental alignment of a charged hadron track with a muon stub in the first muon station.

In this search, there are no sufficiently powerful discriminating observables that could be used as constraints. Therefore, we opt for building a discriminant Q as a product of ratios of 1D signal and background probability density functions for more than a dozen observables, the most discriminating among which are:

- χ^2/dof of the tri-muon vertex,
- transverse displacement of tri-muon vertex with respect to the primary interaction,
- angle between τ lepton (trimuon) direction and the line connecting the primary interaction and the tri-muon vertex,
- minimum ΔR distance among three pairs of muons in a trimuon event candidate,
- the highest and lowest momenta among three muons in a trimuon event candidate,
- number of b quark jets.

A dedicated L1 trigger is designed to be efficient for events passing the final selection and have an acceptable rate. For Category 1, the L1 trigger requires two tracker muons ($p_T > 2$ GeV, $\delta p_T/p_T < 3\%$) and one GEM-CSC segment in the first muon endcap station ($\delta p_T/p_T \sim 20\%$). For Category 2, the trigger requires one tracker muon and two segments in the first muon endcap station, allowing for ME0 segments in the $\eta = 2.4$–2.8 range ($\delta p_T/p_T \sim 40\%$). In each case, a trimuon candidate must have invariant mass $m_{3\mu} < 3$ GeV to pass the trigger. Signal efficiencies of these triggers are about 80% (50%) for events in Category 1 (2).

Figure 8.7 (top) shows the signal and background distributions of discriminant Q for events with trimuon mass in the range 1.55–2.00 GeV in Category 1 (left) and Category 2 (right). We select events with $\ln Q > 6$ (5) in Category 1 (2). The efficiency to select signal events is about 30% in each category.

Figure 8.7 (bottom) shows the trimuon mass distribution for signal and background for the selected events. Table 8.3 shows the numbers of selected signal and background events in the mass window 1.55–2.00 GeV, trimuon mass resolutions, and the expected search sensitivities.

Table 8.3: The expected numbers of signal and background events in mass window 1.55–2.00 GeV for integrated luminosity L = 3000 fb^{-1} (for signal, $B(\tau \to 3\mu) = 2 \times 10^{-8}$ is assumed). In absence of a signal, the projected limits on $B(\tau \to 3\mu)$ are for 90% CL, which are obtained using the standard CL_s methodology [140–142].

	Category 1	Category 2
Number of background events	2.4×10^6	2.6×10^6
Number of signal events	4 580	3 640
Trimuon mass resolution	18 MeV	31 MeV
$B(\tau \to 3\mu)$ limit per event category	4.3×10^{-9}	7.0×10^{-9}
$B(\tau \to 3\mu)$ 90%C.L. limit	3.7×10^{-9}	
$B(\tau \to 3\mu)$ for 3σ-evidence	6.7×10^{-9}	
$B(\tau \to 3\mu)$ for 5σ-observation	1.1×10^{-8}	

A fit for a signal peak over the continuum background constrained by the sidebands can be used to asses a number of signal events (or an upper limit on the number of signal events). To get results in terms of the $\mathcal{B}(\tau \to 3\mu)$ branching fraction, one needs to know the number of τ leptons produced. Since most of τ leptons come from decays of D_s mesons, one can use $D_s \to \phi\pi \to \mu\mu\pi$ decays to derive the normalization directly from data. Production cross section for D mesons have been measured with 10% systematic uncertainties [143], hence we assign the same uncertainty in this analysis (it makes only a small impact on the search sensitivity). Systematic uncertainties associated with background shape are found to have a negligible effect.

With the full HL-LHC dataset (14 TeV, 3000 fb^{-1}), the projected exclusion limit on $\mathcal{B}(\tau \to 3\mu)$ is 3.7×10^{-9} at 90% CL, and 4.3×10^{-9} without ME0 chambers. The difference in the two results

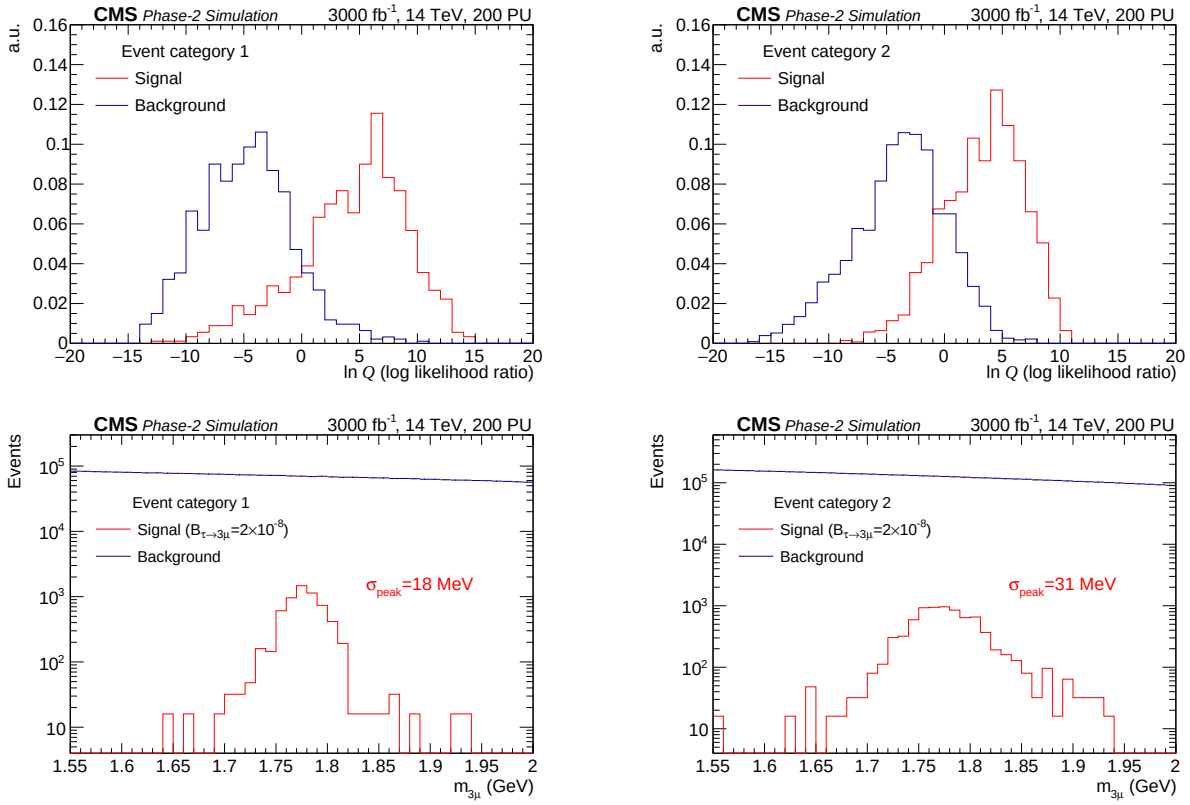

Figure 8.7: (Top) Signal (red) and background (blue) distributions, normalized to unity, for the final observable $\ln Q$. (Bottom) The expected trimuon mass distribution for signal (red) and background (blue) events after the requirement on the $\ln Q$ observable indicated on the top plots. The assumed $\tau \to 3\mu$ branching fraction is $\mathcal{B}(\tau \to 3\mu) = 2 \times 10^{-8}$. Background event fluctuations, nearly invisible, in the bottom plots are emulated for the statistics of events expected with the full HL-LHC dataset. The left plots are for Category 1 events, the right plots are for Category 2.

can be re-interpreted as an effective gain in integrated luminosity $(4.3/3.7)^2 \sim 1.35$, i.e. from 3000 to $\sim$ 4000 fb^{-1}. The 5σ-observation sensitivity projected for $\mathcal{B}(\tau \to 3\mu)$ is 1.1×10^{-8}. Should the observed background be different from the present simulation predicts by a factor k, the stated sensitivities would change by factor a $\sqrt{k}$. Once the muon reconstruction in GEM-CSC tandems becomes available, further improvements of the search sensitivity are expected.

8.1.4 Impact of detector acceptance on background determination in searches

Many new particle search signatures at the HL-LHC can be characterized by the presence of low momentum and forward leptons. This corner of phase space is also dominated by standard model backgrounds and will be further complicated by the presence of an average of 200 pileup events. We illustrate the impact of the muon detector acceptance increase in pseudorapidity on the understanding of these challenging backgrounds in the context of searches for SUSY signatures with multi-leptons.

Historically, SUSY has been considered one of the most compelling solutions for the hierarchy problem. Recently, the focus has moved to natural scenarios, that are not strongly impacted by the exclusion limits set on coloured sparticles. In natural scenarios with gauge coupling unification, the higgsino, bino, and wino are at a few hundred GeV scale or below. A typical spectrum

would be characterized by almost mass degenerate $\tilde{\chi}_1^0$, $\tilde{\chi}_2^0$, $\tilde{\chi}_1^\pm$ (higgsinos-like), followed by a heavier bino-like $\tilde{\chi}_3^0$, and by wino-like $\tilde{\chi}_2^\pm$ and $\tilde{\chi}_4^0$. The latter states have masses roughly twice as large as that of the $\tilde{\chi}_3^0$. The associated production cross sections of the charginos and neutralinos depend on the nature of the particle (whether it is a mixed or pure state) but they are nevertheless expected to be smaller than a few picobarns. Such processes can only be studied with the high luminosity of Phase-2 operation. Among all electroweak pair production processes, the $\tilde{\chi}_1^0$ $\tilde{\chi}_2^0$ exhibits the highest cross section for the spectra described above. However, since the $\tilde{\chi}_1^0$,$\tilde{\chi}_2^0$,$\tilde{\chi}_1^\pm$ are almost mass degenerate in the higgsino scenario, the final states are characterized by the presence of very low p_T standard model particles making the search experimentally challenging. As documented in Ref. [144], the next largest visible cross section is that of the wino-like $\tilde{\chi}_2^\pm$ and $\tilde{\chi}_4^0$. The search for wino pair production of $\tilde{\chi}_2^\pm$ and $\tilde{\chi}_4^0$, depicted in Fig. 8.8 (left), can be carried out using a novel signature with two W bosons of the same electrical charge, large missing transverse energy (MET), and modest jet activity. This background-free final state has an excellent potential offering sensitivities to winos up to the TeV scale.

Requiring two similarly charged leptons ensures a nearly background-free signal. One of the dominant backgrounds is due to SM WZ production where only two leptons with the same electrical charge are reconstructed and the third lepton is lost (a "lost lepton" background). Efficient suppression of this background is essential for the sensitivity to this process. The fraction of correctly identified background events increases with the pseudorapidity coverage of the detector. The analysis is performed using DELPHES [130] and a scenario with an average of 200 pileup events.

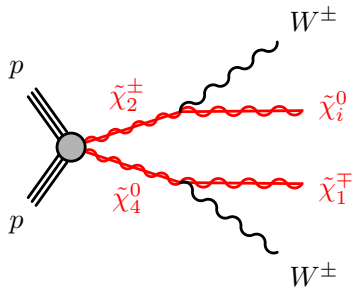

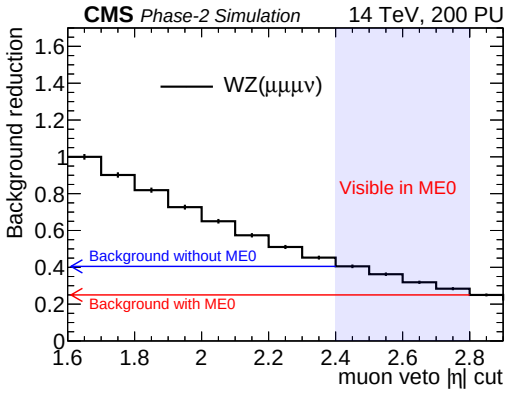

Figure 8.8: Left: Example signal process which yields two same-sign leptons and large MET in the final state. Right: Distribution of generator-level η of unreconstructed muons in WZ background events after selection of exactly two same-sign signal muons with $|\eta| < 1.6$. The event numbers are for 3000 fb^{-1}.

To study the impact of the upgraded muon detectors, events with two muons of equal charge within $|\eta| < 1.6$ are selected and the generator-level η of the third non-reconstructed muon is shown in Fig. 8.8 (right). It is apparent that the extended coverage up to 2.8 in η allows a more efficient veto of WZ$\rightarrow$ $\mu\mu\mu$ decays. If the coverage is extended from $|\eta| < 1.6$ to $|\eta| < 2.8$, the WZ background in the selected mode decreases by a factor four. If the coverage can be exploited for $|\eta| < 2.4$ the background decreases by only a factor two, relative to the background for $|\eta| < 1.6$. In this forward region, additional hits are beneficial to reconstructing muons in the high pileup environment.

As an illustration, we compute the impact of extending $|\eta|$ from 2.4 to 2.8, because of ME0, on

the upper limit on the production cross-section of pair produced $\tilde{\chi}_2^{\pm}$, $\tilde{\chi}_4^0$ decaying into a final state with two same-charge W bosons. For a representative benchmark point ($m_{\tilde{\chi}_2^{\pm}}$ = 400 GeV and $\mu = 150$ GeV), the results indicate an improvement in the expected upper limits on the BSM process cross section by 15%. This can be represented as an effective gain of a factor $\sim (1.15)^2 \sim 1.3$ in integrated luminosity, which is equivalent to gaining an additional 1000 fb^{-1} of data. The improved detector acceptance will lead to reduced backgrounds and improved sensitivities in many new physics searches in which a muon veto is required.

8.1.5 Prospects for measuring the weak mixing angle with the forward-backward asymmetry of Drell–Yan events at the HL-LHC

We report on a proposal for the measurement of the effective weak mixing angle using the forward-backward asymmetry, A_{FB}, in Drell–Yan $\mu\mu$ events at the HL-LHC at CMS. The proposal is based on techniques used in Ref. [35] for such a measurement at $\sqrt{s} = 8$ TeV.

In leading order, dileptons are produced through the annihilation of a quark and antiquark via the exchange of a Z boson or a virtual photon: $\text{q}\bar{\text{q}} \to Z/\gamma^* \to \ell^+\ell^-$. The definition of A_{FB}, based on the angle θ^* of the lepton (ℓ^-) in the Collins–Soper [145] frame of the dilepton system, is as follows:

$$A_{\text{FB}} = \frac{\sigma_{\text{F}} - \sigma_{\text{B}}}{\sigma_{\text{F}} + \sigma_{\text{B}}}, \tag{8.1}$$

where σ_{F} and σ_{B} are the cross sections in the forward ($\cos\theta^* > 0$) and backward ($\cos\theta^* < 0$) hemispheres, respectively.

In this analysis we measure the leptonic effective weak mixing angle ($\sin^2\theta_{\text{eff}}^{\text{lept}}$) by fitting the mass and rapidity dependence of the observed A_{FB} in dilepton events. The most precise previous measurements of $\sin^2\theta_{\text{eff}}^{\text{lept}}$ were performed by the LEP and SLD experiments [38]. There is, however, a known tension of about 3 standard deviations between the two most precise measurements. Measurements of $\sin^2\theta_{\text{eff}}^{\text{lept}}$ were also reported by the LHC and Tevatron experiments [34, 36, 37, 146–148]. The latest and the most precise LHC measurement was done by CMS [35], and its machinery is used in this analysis. The best published LHC results have an absolute uncertainty in $\delta\sin^2\theta_{\text{eff}}^{\text{lept}}$ of about 10^{-3} [34, 36, 37], while the most recent preliminary measurement from CMS [35] reached a precision of 5×10^{-4}, similar to that obtained in Tevatron experiments [146–148].

The analysis is based on samples of pp collisions simulated at $\sqrt{s} = 8$ and 14 TeV with next-to-leading order (NLO) matrix element implemented in the POWHEG event generator [149–152] using the NNPDF3.0 [153] PDFs and interfaced with PYTHIA 8 [154] with CUETP8M1* [155] underlying event tune for parton showering and hadronization and electromagnetic final-state radiation (FSR). The template variations for different values of $\sin^2\theta_{\text{eff}}^{\text{lept}}$ and PDFs are modeled using the POWHEG MC generator that provides matrix-element based event-by-event weights for each variation. The samples are normalized to the integrated luminosities of 19 fb^{-1} for $\sqrt{s} = 8$ TeV and to 10 – 3000 fb^{-1} for $\sqrt{s} = 14$ TeV samples. The analysis is done at the generator level, so the smearing due to detector effects is not taken into account, but comparison of 8 TeV predictions and measured values suggests that this effect is not significant. Moreover since the results are presented as comparison of 8 and 14 TeV measurements they can be directly applied to the measured 8 TeV results with real data.

The HL-LHC CMS detector extends the pseudorapidity, η, coverage for the muon reconstruction from current configuration of 2.4 to 2.8. In this analysis an event is selected if there are

at least two muons with $|\eta| < 2.8$ and with the leading (i.e. having the largest transverse momentum p_T) muon $p_T > 25\,\text{GeV}$ and the second leading muon $p_T > 15\,\text{GeV}$.

We extract $\sin^2\theta^{\text{lept}}_{\text{eff}}$ by minimizing the χ^2 value between the simulated data and template A_{FB} distributions in 72 dilepton mass and rapidity bins. Figure 8.9 shows the A_{FB} distributions in bins of dimuon mass and rapidity for different energies and pseudorapidity acceptances. As expected, at higher center-of-mass energies the observed A_{FB} is smaller because the interacting partons have smaller x-values which results in a smaller fraction of dimuon events produced by the valence quarks, which also means more dilution. The simulated data are shown for $\sqrt{s} = 8\,\text{TeV}$ and $\sqrt{s} = 14\,\text{TeV}$ for two different selection requirements, $|\eta| < 2.4$ and 2.8. Extending the pseudorapidity acceptance significantly increases the coverage for larger x-values in the production and reduces both the statistical and PDF uncertainties, as shown below.

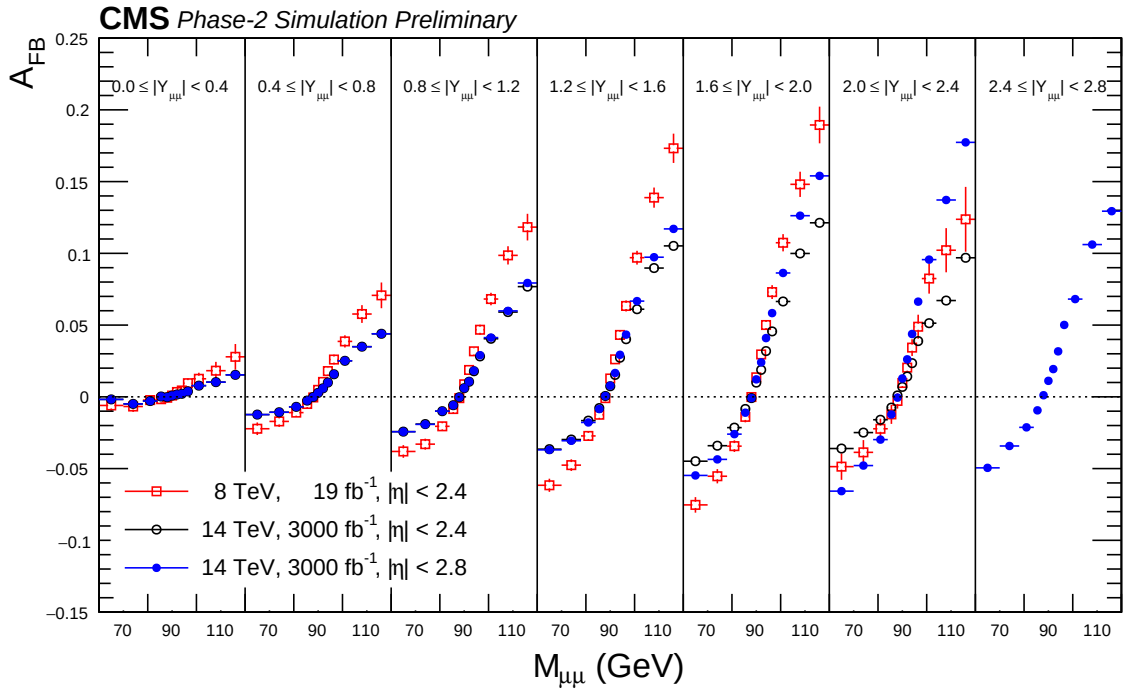

Figure 8.9: Forward-backward asymmetry distribution, $A_{\text{FB}}(M_{\mu\mu}, Y_{\mu\mu})$, in dimuon events at $\sqrt{s} = 8\,\text{TeV}$ and 14 TeV. The distributions are made with POWHEG event generator using NNPDF3.0 PDFs and interfaced with PYTHIA 8 for parton-showering, QED final-state radiation (FSR) and hadronization. Following acceptance selections are applied to the generated muons after FSR: $|\eta| < 2.4$ (or $|\eta| < 2.8$), $p_T^{\text{lead}} > 25\,\text{GeV}$, $p_T^{\text{trail}} > 15\,\text{GeV}$. The error bars represent the statistical uncertainties for the integrated luminosities corresponding to $19\,\text{fb}^{-1}$ at $\sqrt{s} = 8\,\text{TeV}$ and $3000\,\text{fb}^{-1}$ at $\sqrt{s} = 14\,\text{TeV}$.

The observed A_{FB} values depend on the size of the dilution effect, as well as on the relative contributions from u and d valence quarks to the total dilepton production cross section. Therefore, the PDF uncertainties translate into sizable variations in the observed A_{FB} values. However, changes in PDFs affect the $A_{\text{FB}}(M_{\ell\ell}, Y_{\ell\ell})$ distribution in a different way from changes in $\sin^2\theta^{\text{lept}}_{\text{eff}}$. Changes in PDFs result in changes in A_{FB}'s in regions where the absolute values of A_{FB} is large, i.e. at high and low dilepton masses. On the contrary, the effect of changes in $\sin^2\theta^{\text{lept}}_{\text{eff}}$ are largest near the Z-peak and are significantly smaller at high and low masses. Because of this behavior, which is illustrated in Fig. 8.10, we apply the Bayesian χ^2 reweighting method to constrain the PDF uncertainties [156–158] and reduce the PDF errors in the extracted

value of $\sin^2\theta^{\text{lept}}_{\text{eff}}$.

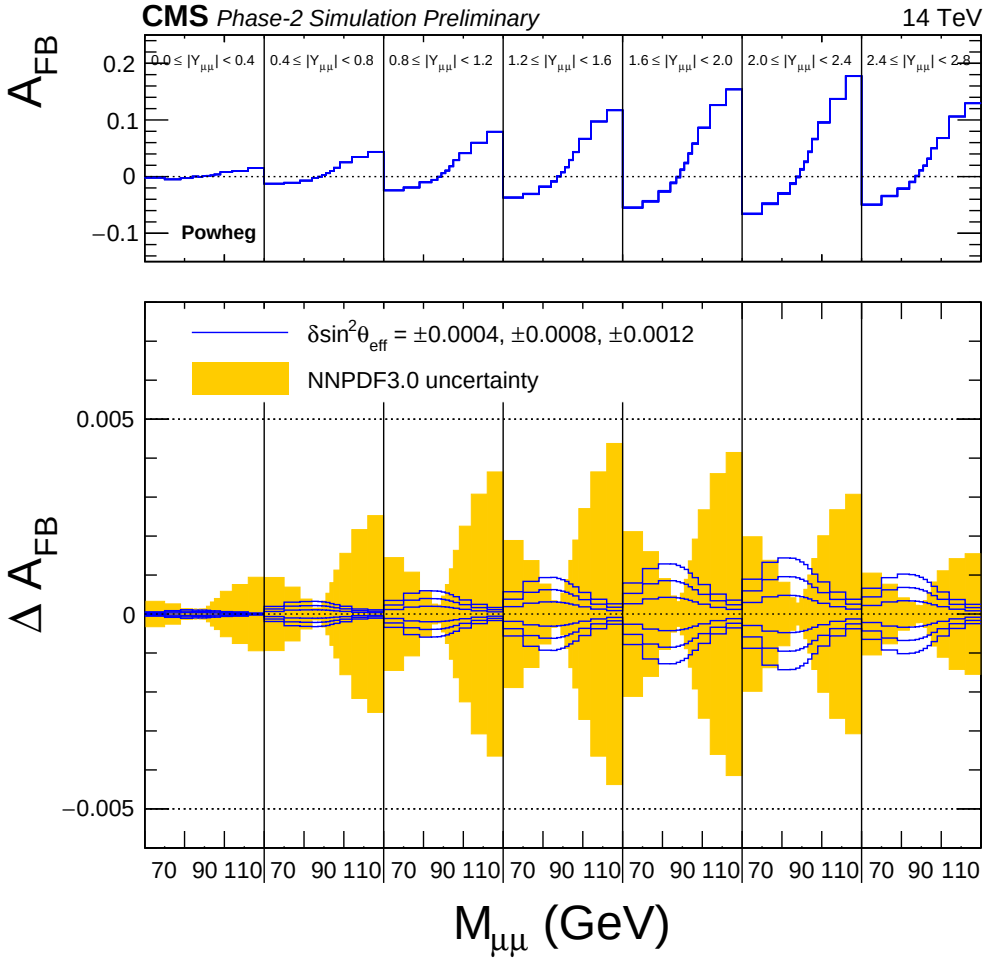

Figure 8.10: Forward-backward asymmetry distribution, $A_{\text{FB}}(M_{\mu\mu}, Y_{\mu\mu})$, in dimuon events at $\sqrt{s} = 14\,\text{TeV}$. The distributions are made with POWHEG event generator using NNPDF3.0 PDFs and interfaced with PYTHIA 8 for parton-showering, QED final-state radiation (FSR) and hadronization. Following acceptance selections are applied to the generated muons after FSR: $|\eta| < 2.8$, $p_{\text{T}}^{\text{lead}} > 25\,\text{GeV}$, $p_{\text{T}}^{\text{trail}} > 15\,\text{GeV}$. The solid lines in the bottom panel correspond to six variations of $\sin^2\theta^{\text{lept}}_{\text{eff}}$ around the central value: ± 0.0004, ± 0.0008, and ± 0.0012. The shaded band shows the standard deviation over the 100 NNPDF3.0 replicas.

As a baseline, we use the NLO NNPDF3.0 set. In the Bayesian χ^2 reweighting method, PDF replicas that better describe the observed A_{FB} distribution are assigned larger weights, and PDF replicas that poorly describe the A_{FB} are assigned smaller weights. Each weight factor is based on the best-fit χ^2-value obtained with a given PDF replica i used in the templates,

$$w_i = \frac{\exp\left(-\frac{\chi^2_{\text{min}}}{2}\right)}{\frac{1}{N}\sum_{i=1}^{N}\exp\left(-\frac{\chi^2_{\text{min}}}{2}\right)}, \tag{8.2}$$

where N is the number of replicas in a PDF set. The final result is then calculated as a weighted average over the PDF replicas: $\sin^2\theta^{\text{lept}}_{\text{eff}} = \sum_{i=1}^{N} w_i s_i / N$, where s_i is the best-fit $\sin^2\theta^{\text{lept}}_{\text{eff}}$ value obtained for i-th PDF replica.

In the case of the 14 TeV analysis with large number of events (> 200 fb^{-1}), the pseudo-data are too precise to estimate the PDF uncertainties with the Bayesian reweighting approach because the replica distributions are too sparse compared to the statistical uncertainties. Therefore, the PDF uncertainties after the Bayesian reweighting is estimated by extrapolating from the lower values of integrated luminosities as illustrated in Fig. 8.11. The corresponding values for various luminosities are summarized in Table 8.4. One can see from the Table that with the extended pseudorapidity coverage of $|\eta| < 2.8$, the statistical uncertainties are reduced by about 30% and the PDF uncertainties are reduced by about 20%, compared to $|\eta| < 2.4$ regardless of the target integrated luminosity and for both nominal and constrained PDF uncertainties.

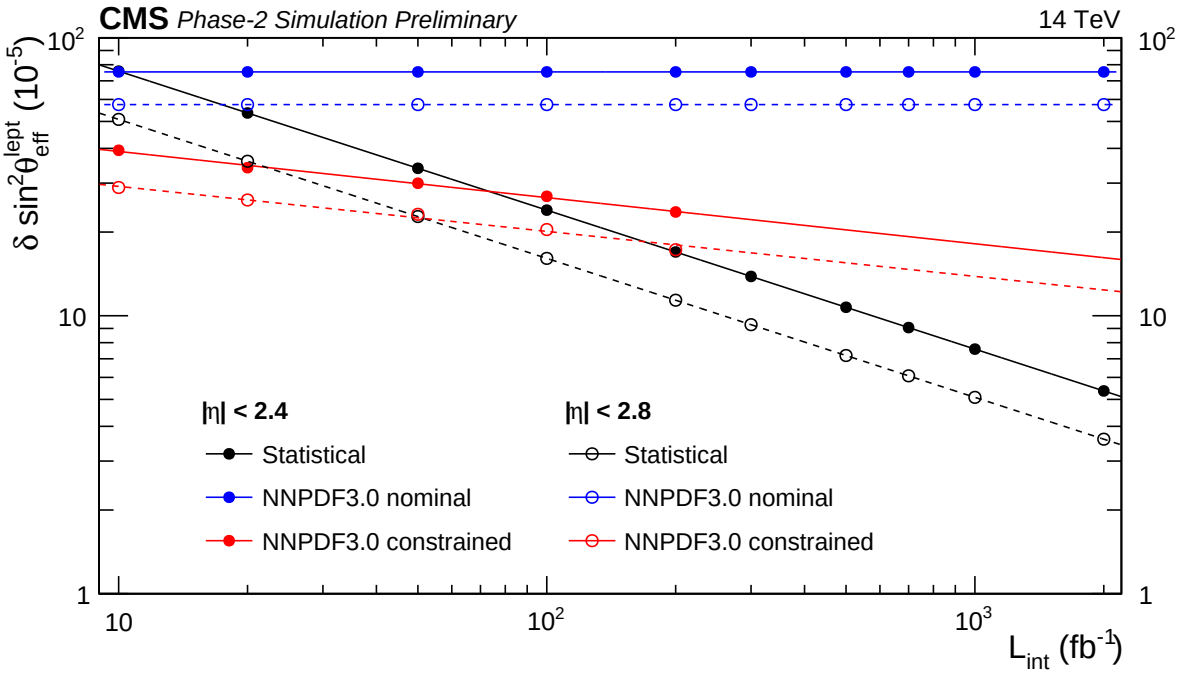

Figure 8.11: Projected statistical, nominal PDF and constrained PDF uncertainties in $\sin^2\theta^{\text{lept}}_{\text{eff}}$ extracted by fitting $A_{\text{FB}}(m_{\mu\mu}, y_{\mu\mu})$ distributions at $\sqrt{s} = 14$ TeV with different values of integrated luminosities and for $|\eta| < 2.4$ and $|\eta| < 2.8$ acceptance selections for the muons. The nominal NNPDF3.0 uncertainty is calculated as a standard deviation of the extracted $\sin^2\theta^{\text{lept}}_{\text{eff}}$ over the 100 NNPDF3.0 replicas. To calculate the constrained NNPDF3.0 uncertainty, each replica is weighted by $\exp(-\chi^2_{\text{min}}/2)$, where χ^2_{min} is the best-fit χ^2 obtained with this replica.

8.1.6 Summary of sensitivity gains

Table 8.5 summarizes the sensitivity gains in the five presented analyses due to the pseudorapidity acceptance extension provided by the ME0 chambers.

8.2 Impact of new capabilities of the muon detector upgrade

8.2.1 Displaced signatures in new physics searches

Future searches at the HL-LHC should cover a large phase space and, ideally, should not be driven by strict model assumptions. An important class of new physics models predict long-lived particles. The existence of such particles would potentially lead to displaced signatures. For particles of a few hundred GeV mass, impact parameters $|d_0|$ can reach up to approximately

Table 8.4: Statistical, nominal NNPDF3.0, and constrained NNPDF3.0 uncertainties of extracted $\sin^2\theta^{\text{lept}}_{\text{eff}}$ at 14 TeV for muon acceptance of $|\eta| < 2.4$ and $|\eta| < 2.8$ and for the different values of integrated luminosity. For comparison, results of the 8 TeV estimate of this analysis are compared to the results obtained from 8 TeV measurement [35].

L_{int}	$\delta_{\text{stat}}[10^{-5}]$		$\delta^{\text{nominal}}_{\text{NNPDF3.0}}[10^{-5}]$		$\delta^{\text{constrained}}_{\text{NNPDF3.0}}[10^{-5}]$	
(fb^{-1})	$\|\eta\| < 2.4$	$\|\eta\| < 2.8$	$\|\eta\| < 2.4$	$\|\eta\| < 2.8$	$\|\eta\| < 2.4$	$\|\eta\| < 2.8$
10	76	51	75	57	39	29
100	24	16	75	57	27	20
500	11	7	75	57	20	16
1000	8	5	75	57	18	14
3000	4	3	75	57	15	12
19	43		49		27	
19 (from [35])	44		54		32	

Table 8.5: Sensitivity gains due to extending the muon pseudorapidity coverage from 2.4 to 2.8 provided by the ME0 chambers.

analysis topic	parameter of interest (POI)	sensitivity gain in POI
$H \to ZZ \to 4\mu$	signal strength	7 %
Double-parton scattering	slope of $\mathrm{d}\sigma/\mathrm{d}(\eta_1\eta_2)$	factor 1.5
$\tau \to 3\,\mu$	$B(\tau \to 3\mu)$	17 % (limit)
BSM same-sign dilepton search	BSM cross section	15 % (limit)
Drell–Yan FB asymmetry	$\sin^2\theta^{\text{lept}}_{\text{eff}}$	factor 1.3

one meter (or longer) for sufficiently large lifetimes as shown in Fig. 8.12 (left). Triggering on and reconstructing muons with such decay length is challenging. Triggers and reconstruction algorithms that use the position of the primary vertex will not be very efficient in reconstructing tracks with large impact parameters. If the particle is sufficiently boosted, the transverse impact parameter is small(er) but the decay may still occur well outside the tracker volume. In both cases, the stand-alone capabilities of the muon system constitute the only possibility for detection.

Section 7.1.4.1 demonstrates that the additional hits in the new endcap muon stations, in combination with improved algorithms, permit efficient triggering on displaced muon tracks. In the following, we discuss the impact on the reconstruction and the physics sensitivity in searches for displaced muons in the context of the HL-LHC.

A dedicated muon reconstruction algorithm was designed for non prompt muons that leave hits only in the muon system. This displaced stand-alone (DSA) algorithm is seeded by groups of track segments in the muon chambers. For each seed, a muon track is reconstructed with the same Kalman-filter technique as for the standard stand-alone (SA) muon reconstruction algorithm, but without constraining the interaction point. The DSA algorithm improves the transverse impact parameter resolution for displaced muons compared to the SA muons. Figure 8.12 (middle) shows the reconstruction efficiency as a function of the transverse impact parameter for the DSA and SA algorithms. For the latter, the efficiency drops to ≈15% at $|d_0| = 300$ cm. With the DSA algorithm, the reconstruction efficiency is around 50–60% and nearly independent of the impact parameter. Figure 8.12 (right) shows the distribution of the number of hits in the Run 2 and Phase-2 detectors for displaced muons. The impact of the new stations is clearly visible. The charge misidentification probability is expected to further

decrease with the additional hits.

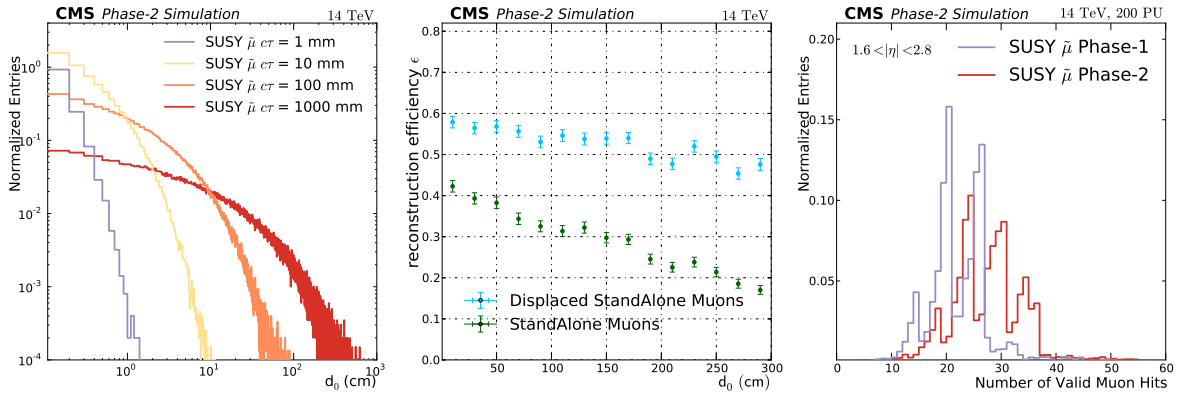

Figure 8.12: Left: The transverse imparameter, d_0, for several simulated decay lengths, $c\tau$, before reconstruction. Middle: Efficiency to reconstruct displaced muons from decays of long-lived particles as a function of the generated impact parameter $|d_0|$ using the dedicated DSA algorithm and the standard SA algorithm which includes a vertex constraint. Right: Distribution of the minimum number of valid hits in the muon system for a SUSY $\tilde{\mu}$ (M = 500 GeV and τ = 1000 mm) for Run 2 (blue) and Phase-2 (red) detectors.

To study the impact on physics sensitivity, a particular SUSY model is selected where the displaced signature consists of a dimuon final state emerging from the decay of heavy sparticles (smuons). This signal serves as a proxy for any long-lived particle. Searches for the direct production of heavy sparticles with long lifetimes are difficult in the present LHC runs, owing to small cross sections and limited integrated luminosity, and will only become possible at the HL-LHC. In gauge-mediated SUSY breaking models, smuons can be (co-)NLSPs (next to lightest supersymmetric particles) and decay to a muon and a gravitino [159]. This decay can either be prompt or the slepton can have a significant lifetime: the final state signature is then given by two displaced oppositely charged muons and significant missing transverse energy. The smuon pair production has the advantage that it can be characterized by a very clean final-state topology and we will therefore focus on the process $q\bar{q} \rightarrow \tilde{\mu}\tilde{\mu}$, where the two smuons decay far from the primary interaction vertex with $c\tau = 10, 100, 1000$ mm and with several mass hypotheses (0.2, 0.5, 1 TeV). The final state contains two oppositely charged muons and MET.

The main background for this search comes from multi-jet production (QCD), $t\bar{t}$ production, and Z/DY $\rightarrow \ell\ell$ events where large impact parameters are (mis)reconstructed. Cosmic ray muons have been studied in Run 2 and are independent of the instantaneous luminosity. In the barrel they are efficiently rejected by the timing of the hits in the upper leg. Cosmic ray muons do not originate at the vertex and therefore pass the upper barrel sectors in reverse direction from outside in. The fraction of cosmic ray muons in the endcaps is negligible. Given the very low cross section of this process, it is essential to reduce the background efficiently. The best background discriminator is the impact parameter significance $d_0/\sigma(d_0) \geq 10$. Given the signal kinematics, the muons should move in roughly opposite directions and MET should be larger than 50 GeV to account for the two gravitinos. After this selection the signal efficiency is about 4–5% for $c\tau$ = 1000 mm, nearly independent of the smuon mass, and 10^{-5} – 10^{-4} for QCD, $t\bar{t}$, and DY backgrounds.

Figure 8.13 shows expected exclusion limits for the gauge-mediated SUSY breaking model with the smuon being a (co-)NLSP for the predicted cross section as well as for a factor 100 larger

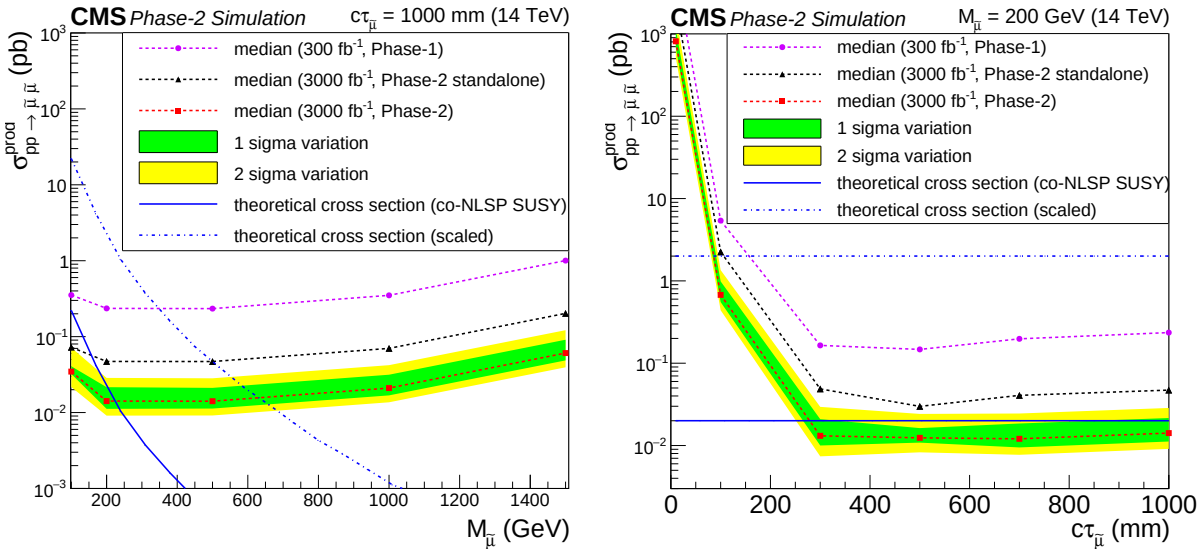

Figure 8.13: The 95% CL upper limits on $q\bar{q} \to \tilde{\mu}\tilde{\mu}$ for various mass hypotheses and $c\tau$ = 1 m (left) and as a function of the decay length for M = 200 GeV (right). In both panels, the theoretical cross section for the specific model is represented by the blue solid line. For different SUSY breaking scales, tan β or otherwise modified parameters, the cross sections may be 100 times larger, reflected by the blue dash-dotted line. Green (yellow) shaded bands show the one (two) sigma range of variation of the expected 95% CL limits. Phase-2 results with an average 200 pileup events and an integrated luminosity of 3000 fb^{-1} are compared to results obtained with 300 fb^{-1}. The black line shows the sensitivity without the DSA algorithm, which reduces the reconstruction efficiency by a factor three.

cross section. The exclusion limits are shown as functions of smuon mass in Fig. 8.13 (left) and decay length in Fig. 8.13 (right). The sensitivity depends on $c\tau$ because shorter decay lengths shift the signal closer to background. Figure 8.12 (right) shows the resulting physics sensitivities in terms of production cross section for HL-LHC, normalized to 3000 fb^{-1}, for the dedicated reconstruction of displaced muons and for the standard reconstruction. Also shown is the expected sensitivity at the end of Phase-1. Systematic uncertainties for the Phase-1 scenario are taken from current Run 2 analyses: for HL-LHC they are guided by the assumptions of reduced systematics from Ref. [128]. Clearly, only the HL-LHC will allow this process to be studied. A 2-dimensional representation of the production cross section as a function of smuon mass and decay length $c\tau$ is depicted in Fig. 8.14. The expected exclusion limit is around 200 GeV for $c\tau = 1000$ mm with 3000 fb^{-1}. For the same mass, a discovery sensitivity of 3σ significance can be reached. This also illustrates the importance of keeping lepton trigger thresholds at a few times 10 GeV, even in the environment of 200 pileup interactions.

8.2.2 Heavy stable charged particles with the time of flight technique

Several extensions of the standard model, most notably Split SUSY [160, 161], predict the existence of new heavy particles with long lifetimes. Such particles have been extensively studied in the context of SUSY models as the next-lightest SUSY particle (NLSP) by choice of theoretical parameters. If the NLSP has a lifetime larger than a few nanoseconds, it can travel through the majority of the detector before decaying and therefore appear as stable. In this section, we consider particles with non zero electric charge which are referred to as heavy stable charged particles (HSCPs). We concentrate on the performance in terms of specific HSCP parameters in a model-independent way rather than providing an interpretation in a dedicated model. Given

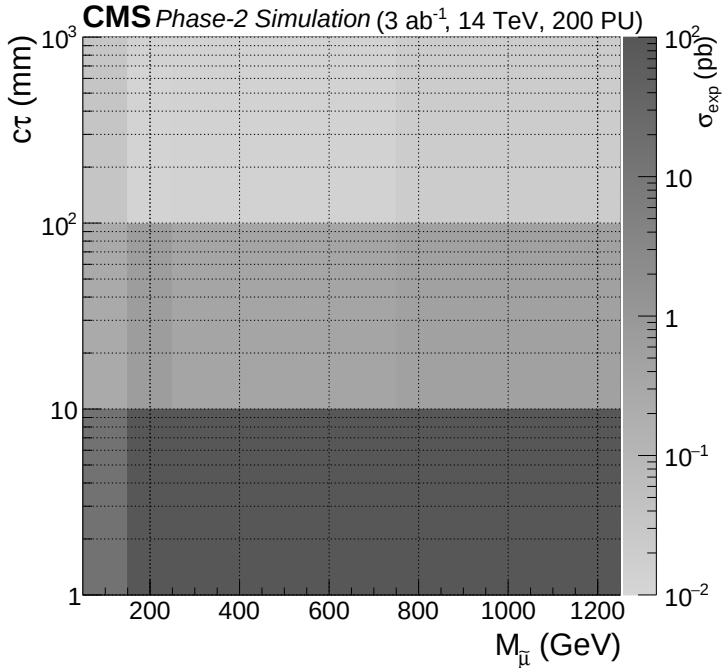

Figure 8.14: 2D representation of the expected limits in production cross section as a function of smuon mass and decay length $c\tau$. The simulated masses of 0.1, 0.2, 0.5, and 1 TeV are shown on the x-axis in the center of each colored area. For the decay length (y-axis in the plot), values of $c\tau = 10, 100, 1000$ mm were used. The z-axis (density of gray) represents the reach in production cross section.

the wide range of new models, it is important to stay sensitive to a wide range of unusual signatures such as very slowly moving particles.

HSCPs will leave a direct signal in the tracker and muon systems of CMS and can be reconstructed similarly to muons. Depending on their mass, HSCPs can potentially move much more slowly than muons, which are typically traveling nearly at the speed of light ($\beta \approx 1$). Therefore, HSCPs can be identified using their time-of-flight (TOF) from the center of CMS to the muon systems. This is illustrated in Fig. 8.15 for a slowly moving HSCP in comparison to relativistic muons, here from the decay of Z bosons. The latter are centered around zero time with respect to their uniquely identified bunch crossing. More slowly moving particles will also lose more energy per unit path length ($\mathrm{d}E/\mathrm{d}x$) through ionization in the CMS tracker. Searches for HSCPs have been performed at CMS and ATLAS using both the TOF and $\mathrm{d}E/\mathrm{d}x$ techniques [162].

This study builds on the improvements from the upgrade of the RPC link boards in the barrel and endcaps as discussed in Section 7.1.4.2. While the time resolution of the present RPC system is around 25 ns, the upgraded link board systems are expected to reach resolutions near 1 ns for the entire RPC system. This upgrade enables new analysis strategies at both the trigger and offline levels.

An HSCP trajectory is reconstructed as a slowly moving muon introducing the parameter β quantifying the (non)-relativistic velocity of the particle. The velocity may be computed by measuring the time of flight in muon sub detectors at large distances from the collision point. Particles moving slowly through the muon systems leave hits with a linear pattern in hit-position versus time. The hits can be spread across several bunch crossings. Therefore, muon

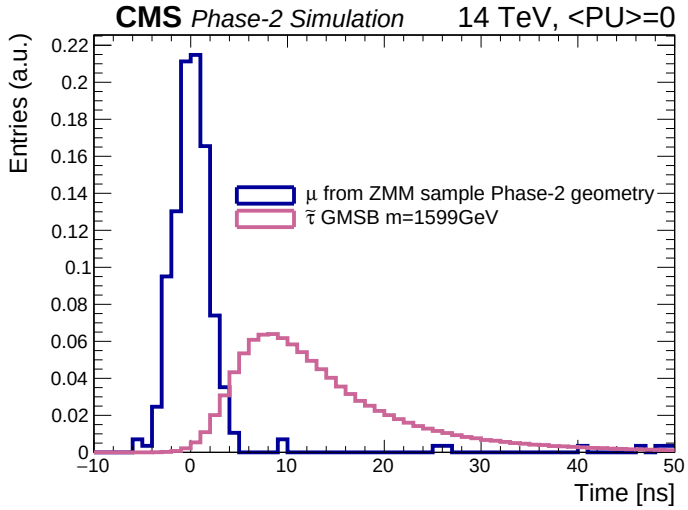

Figure 8.15: Measured time for a particle to traverse CMS with respect to the transit time of a particle traveling at the speed of light. Muons from the decay of Z bosons are relativistic ($\beta = 1$) and HSCPs are slower.

detectors with precise timing can provide important information for the HSCP signal searches.

Figure 8.16 (left) shows the achievable mass resolution for a supersymmetric $\tilde{\tau}$ lepton of 1.6 TeV mass. The resolution for the HSCP mass obtained for Phase-2 at the trigger level is comparable to that realized in Run 2 studies based on offline time-of-flight information (using the DTs and CSCs). The information provided by the RPC trigger can be used as an independent cross check of the reconstructed mass.

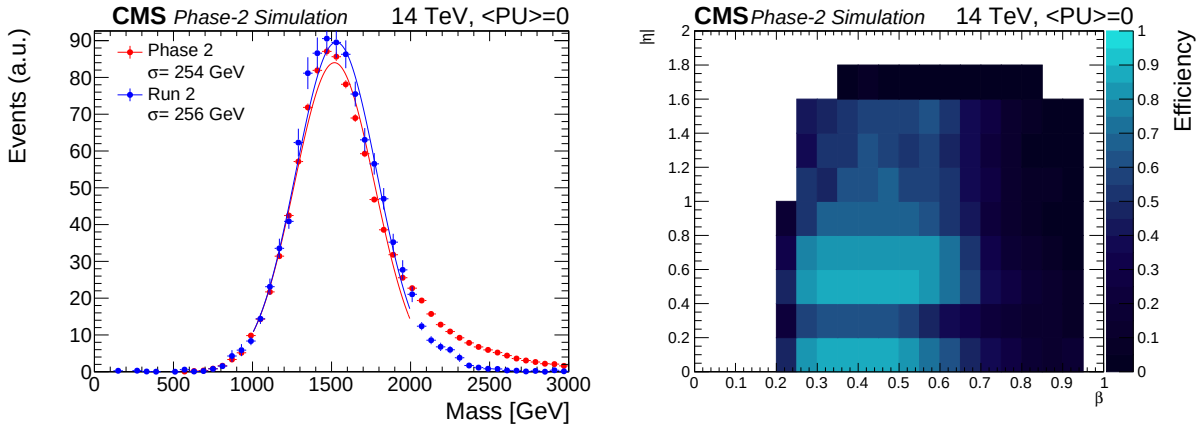

Figure 8.16: Left: Comparison of mass resolution for a 1.6 TeV stau. In Run 2 the shown resolution can only be achieved offline, while the upgraded RPC link-boards in Phase-2 provide a similar mass resolution already at trigger level. Right: Efficiency of β reconstruction as function of β and η. With the Phase-2 upgrade events with $\beta < 0.5$ can be triggered with nearly 90% efficiency for $\eta < 1.4$. The z-axis indicates the efficiency by the color code.

Figure 8.16 (right) illustrates the expected reconstruction efficiency as a function of η and β. For $\eta < 1.5$, an efficiency of about 90% can be reached for values of $\beta > 0.25$. In Run 2, the trigger is highly efficient between $0.6 < \beta < 1$, but only about 20% efficient for $\beta < 0.5$ [162, 163]. Similar 2D plots for the 8 TeV analysis can be found in Ref [163]. The large gain in efficiency for very slowly moving particles in Phase-2 enabled by the upgrade of the RPC trigger can be exploited in a model independent HSCP search.

8.2.3 Top quark mass reconstruction using J/ψ events

The top quark mass (m_t) is a fundamental parameter of the standard model and has unique implications for electroweak precision fits [164] and the stability of the electroweak vacuum [165, 166], as well as for cosmological models [167, 168]. Existing precision measurements of m_t rely at least on a partial reconstruction of the top quark system based on b quark jet kinematics, and are thereby affected by the corresponding experimental and modeling uncertainties. The measurement of m_t using B hadron decays to J/ψ with a subsequent decay to leptons avoids these uncertainties. Instead, it is limited by the low branching fraction and uncertainties in the b quark fragmentation modeling. Currently, this measurement is clearly limited by statistical uncertainties of 3 GeV, compared to a total systematic uncertainty of 0.9 GeV [31]. The large amount of integrated luminosity at the HL-LHC will allow a reduction of the statistical uncertainties to about 0.3 GeV, such that they are of the same order as the projected systematic uncertainties [32]. In addition, the HL-LHC will provide an opportunity to perform a dedicated tuning of the b fragmentation, the dominant systematic uncertainty. Therefore, this purely lepton-based extraction of m_t from the invariant mass of the J/ψ and a lepton (electron or muon) can lead to small uncertainties, which are mostly complementary to existing m_t measurements.

Fully simulated $t\bar{t}$ production events at $\sqrt{s} = 14\,\text{TeV}$ are used to evaluate the performance that can be achieved with the upgraded muon detectors with up to 200 pileup interactions. For this study, the trigger efficiency for $t\bar{t}$ with the Phase-2 detector is assumed to be similar to that observed during Run 2 [32]. Muons with $p_T > 5\,\text{GeV}$ and $|\eta| < 2.4$ that pass the same high purity identification criteria used in the analysis at 8 TeV [31] are selected. These muons are then paired to reconstruct the J/ψ meson. A vertex fit is performed for each possible pair, and all pairs consistent with a J/ψ meson decay are kept. An additional isolated high-purity muon with $p_T > 26\,\text{GeV}$ and $|\eta| < 2.8$ is required and combined with the reconstructed J/ψ meson to form $m(\mu + \text{J}/\psi)$, the m_t estimator, shown in Fig. 8.17 (left). The $\mu + \text{J}/\psi$ mass is linearly correlated with the top quark mass. Even with 200 pileup interactions, the estimator is well resolved. A comparison of the resolution achieved with the HL-LHC simulation and with the Run 2 detector is shown in Fig. 8.17 (right). The reconstructed mass resolution is improved significantly with respect to the Run 2 detector. A better $\mu + \text{J}/\psi$ mass resolution results in a reduced statistical uncertainty and a reduced systematic uncertainty from the fit calibration. The measurement is expected to be statistically limited up to an integrated luminosity of 300 fb^{-1}. With 3000 fb^{-1} the expected statistical precision is 0.24 GeV and the systematic uncertainty is 0.53 GeV.

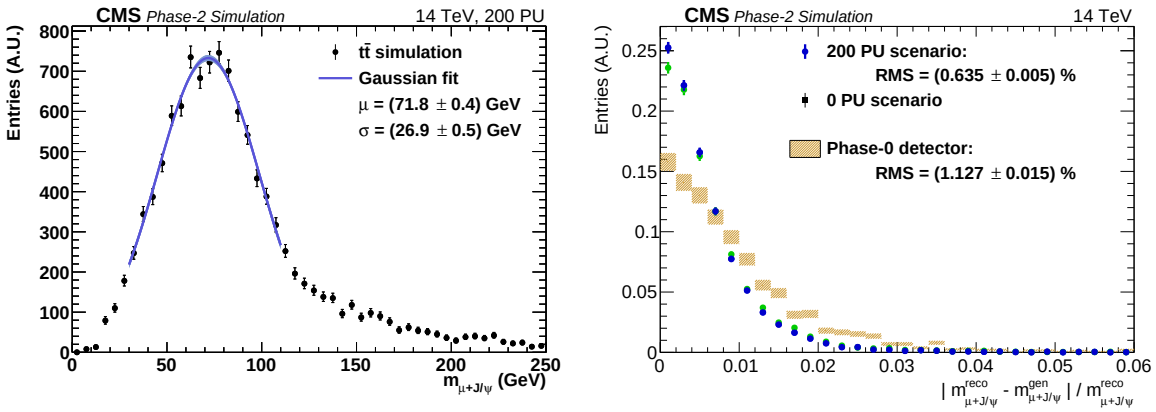

Figure 8.17: Left: Invariant mass $m(\mu + \mathrm{J}/\psi)$ in $\mathrm{t\bar{t}}$ simulation with the Phase-2 upgraded CMS detector with 200 pileup events. Right: The resolution of $m(\mu + \mathrm{J}/\psi)$ for the Phase-2 detector, for the two pileup scenarios, and for the Run 2 detector.

Chapter 9

Organization, schedule, cost

9.1 Participating institutes

The CMS Muon Collaboration is currently comprised of 72 institutions in 23 countries with a total of 212 physicists, 87 engineers, and 106 doctoral students. Most of the institutes participating in the Phase-2 Upgrade project were involved in the construction of the present muon system.

The list of participating institutes follows.

1. RWTH Aachen University, III. Phys. Inst. A, Aachen, Germany
2. Academy of Scientific Research and Technology-Egyptian Network of High Energy Physics, Cairo, Egypt
3. Institute for Nuclear Research ATOMKI of the Hungarian Academy of Sciences, Hungary
4. INFN, University and Politecnico of Bari, Italy
5. Institute of High Energy Physics, Bejing, China
6. INFN and University of Bologna, Italy
7. University Libre de Bruxelles (ULB), Belgium
8. Vrije University Brussel (VUB), Belgium
9. Wigner Research Centre for Physics, Budapest, Hungary
10. Carnegie Mellon University, USA
11. CERN, Switzerland
12. Panjab University, Chandigarh, India
13. University of Debrecen, Institute of Physics, Hungary
14. University of Delhi, India
15. Joint Institute for Nuclear Research, Dubna, Russia
16. FNAL, USA
17. Florida Inst. of Technology, USA

18. University of Florida, USA
19. Laboratori Nazionali Frascati (LNF), INFN, Italy
20. Ghent University, Belgium
21. Saha Institute of Nuclear Physics (HBNI), India
22. Lappeenranta University of Technology (LUT), Finland
23. Katholieke Universiteit Leuven (KU), Belgium
24. Lyon, France
25. CIEMAT, Madrid, Spain
26. Universidad Autonoma de Madrid, Spain
27. National Centre for Particle Physics, University of Malaya, Malaysia
28. Benemerita Universidad Autonoma de Puebla, Mexico
29. Institute for Nuclear Problems (INP), Belarus
30. Bhabha Atomic Research Center Mumbai (BARC), INdia
31. INFN and Università "Federico II" di Napoli, Università della Basilicata and Università G. Marconi, Italy
32. National Center for Physics, Quaid-I-Azam University (NCP), Islamabad, Pakistan
33. National Institute of Science Education and Research (NISER), India
34. Northeastern University, USA
35. The Ohio State University, USA
36. Universidad de Oviedo, Spain
37. INFN and Università di Padova, Italy
38. INFN and Università di Pavia, Italy
39. Bejhang University, China
40. Purdue University, USA
41. Rice University, USA
42. IRFU, CEA, Université Paris-Saclay, France
43. Instituto de Fisica de Cantabria, Universidad de Cantabria, Santander, Spain
44. University of Seoul, South Korea
45. Seoul National University, South Korea
46. Sungkyunkwan University, South Korea
47. Korea University, South Korea

48. Sun Yat-sen University, China
49. American University of Middle East (AUM), Kuwait
50. Institute for Nuclear Research and Nuclear Energy of Bulgaria Academy of Science (INRNE), Bulgaria
51. Sofia University, Bulgaria
52. Electron National Research Institute (St. Petersburg)
53. Institut Pluridisciplinaire Hubert Curien Université de Strasbourg (IPHC), France
54. National Institute of Chemical Physics and Biophysics, Tallinn, Estonia
55. Texas A&M University (TAMU), USA
56. TAMU-Qatar, Qatar
57. INFN and Università di Torino and Università del Piemonte Orientale, Italy
58. Tsinghua University, China
59. University of California, Davis (UCD), USA
60. University of California, Los Angeles (UCLA), USA
61. University of California, Riverside (UCR), USA
62. University of California, Santa Barbara (UCSB), USA
63. Universidad Iberoamericana, Mexico
64. Universidad de los Andes, Bogota, Colombia
65. Universidad de Antioquia, Colombia
66. Vilnius University, Lithuania
67. Wayne State University, USA
68. University of Wisconsin, USA
69. Centro de Investigacion y de Estudios Avanzados del IPN (CINVESTAV), Mexico
70. Hanyang University, South Korea
71. Institute for Research in Fundamental Science (IPM), Iran
72. Tbilisi State University, Georgia

9.2 Muon project organization

The Phase-2 Muon Upgrade project is part of the Muon organization, which also includes the Maintenance and Operation of the present detectors.

The Muon Group follows the organizational scheme of CMS as a whole. It operates under the Muon constitution which sets up a Muon Institution Board as the highest-level decision-making body for the group.

An overview of the CMS Muon project organization is shown in the chart in Fig. 9.1.

The top-level management team is composed of the Muon System Manager (SM) and his or her Deputy, who oversee all the activities. The operation of the detector is handled through internal Subsystems and Offices.

Muon Subsystems are internal collaborations committed to specific parts of the Muon system. Each of the CMS Muon subsystem has its own Project Manager (PM) and a similar project organization. The PMs report to their Subsystem Institution Board.

Offices are coordination bodies for areas that extend across the different Subsystems.

The Muon System Manager is the Chair of the Muon Management Board, composed of the Deputy System Manager, Project Managers and one representative of each Office.

The Muon Conference and Publication Board (MCPB) oversees the preparation of muon-specific papers and participation in conferences.

For what concerns the upgrades, each detector upgrade project is organized and technically managed within the existing subsystem projects. The Upgrade Coordinator Office (UCO) representative reports to the Muon System Manager, to the Muon Managment Board and to the CMS Upgrade Coordinator, who is responsible, on behalf of the CMS Spokesperson, for the overall coordination of the upgrade program. The CMS Upgrade coordinator works closely with the Technical Coordinator, and with Physics and Offline Coordinators to ensure integration of the work on the upgrade program. The CMS Management Board, Finance Board and Collaboration Board oversee the upgrade program along with all other aspects of the experiment, and the CMS Resource Manager oversees the resources.

The Muon Management Board includes a Resource Manager Office representative who maintains detailed records of cost estimates, actual expenditures, and coordinates the assignment of experimental physics responsibilities with the institute representatives.

The overall direction of the Muon project is provided by the Muon Institution Board (Muon IB), composed of representatives from each of the collaborating institutes and led by a chair and deputies. The Muon IB provides a means of communication between the project management and the institutes.

9.2.1 Role of System Manager and Management Board

The Muon Group is led by a Muon System Manager who is the Chair of a Management Board, which is an executive body and is the highest Management Organisation of the Muon Group.

The Muon Management Board is composed of System Manager and Deputy System manager, Subsystem Project Managers and Office Coordinators. It is responsible for the operation, maintenance, and upgrade of the Detector, and defines plans, strategies, and policies. It defines and manages the scope, budget, and milestones of the project, and the sharing of responsibilities among the collaborating institutions.

The System Manager and Project Managers are also responsible for assembling an editorial team and publishing this TDR.

The role of the System Manager is characterized by the following charge and deliverables:

- To lead the Muon Management Board to define and manage the project by fulfilling the upgrade scope, cost and budget for the muon system upgrades, taking into account the LHC shutdowns and schedules, available resources, and interests of the groups involved.
- To lead the Muon Management Board to define a set of project milestones and then steer the project to meet them, assuring the necessary flow of resources and information exchange throughout the project.
- To chair the Muon Managament Board, organize meetings, agendas, objectives and follow-up with reports to the Muon Management Board and the Muon Institution Board.
- To prepare for reviews of important technical, engineering and procurement decisions, normally chaired by CMS Upgrade and Technical Coordination.
- To work closely with Subsystem Project Managers to review technical progress, to manage the planning and strategy, to deal well with problems and opportunities, to establish and maintain appropriate documentation with reliable archiving for all relevant technical specifications of parts and interfaces, to ensure Quality Assurance (QA) procedures and logistics.
- To work in partnership with the CMS Upgrade and Muon teams to assure proper consideration of all decisions, including their impact on the Muon project as a whole, with appropriate preparation of points for endorsement by the Muon IB.
- To work closely with the Resource Manager on all resource-related matters.
- To represent the Muon Upgrade in the CMS Upgrade Steering Group as well as in CMS Management and LHCC meetings.

9.2.2 Muon Upgrade organization and role of the Upgrade Coordination Office

Within each of the four Subsystems, there is an Upgrade Coordinator and Upgrade Deputy coordinator. These eight people together with the overall Muon Upgrade Coordinator form the Muon Upgrade Coordination Office (UCO).

The Muon Upgrade project undergoes right now a transition from the past structure, in which upgrade efforts meant mostly R&D, to a new construction-oriented structure solidly focused on delivering the product on cost and schedule.

For each muon upgrade activity, we have a working group structure which, at the time of writing, is different for each subproject, and each of them is in different stages of this transition, which is expected to be completed by the end of the year 2017. While the upgrade with GEM fall already under the auspices of the Muon upgrade and the organization is a natural extension of the GE1/1 one, for all the other upgrades we have working group structures; as the construction project evolves, individual working groups may split into more specialised ones, or may be added, or dismissed. Working groups corresponding to different activities are materialized in topical meetings, but not always formally established as separate working Groups with coordinators in charge.

For the DT electronics upgrade, the following working groups are currently in place: Electronics, Mechanics, Optical links, Trigger simulation, Integration. For the CSC upgrade, subgroup

coordinators of the CSC upgrade are in charge to supervise the R&D and readiness of the following deliverables: ALCT, DCFEB, High Voltage, Low voltage, ODMB, OTMB, Optical fibers, FED.

For the RPC the following working groups are currently in place: Chamber production, Service and installation, Trigger studies, Detector consolidation, Longevity and eco-gas studies.

In addition we have cross-coordination meetings which allow to exploit commonalities among some deliverables such as: design of electronics (for example synergies are found between RPC link board and OBDT board) and back-end electronics (exploit common muon and CMS standard solutions), phase 2 simulation studies, joint Muon and L1 trigger meeting, infrastructure, services and installation, longevity studies.

It is the responsibility of each subproject management to ensure the coherence of developments of the related upgrade activities, which currently is guaranteed by persons/institutes responsible for the different deliverables.

The Upgrade Coordination Office fulfils the following tasks and takes action collectively:

- Prepare realistic and detailed plans and monitor that the technical progress is consistent with the project milestones, quality objectives, and the estimated budget.
- Adequate resources and supervision are committed to the different activity lines.
- Technical specifications for parts and interfaces between parts of the system are established, well defined, documented and followed.
- Information flows properly within the project, to/from the Muon MB and within the Technical Coordination and Resources Management team. There is a central repository used to organize and archive project documents. The Coordinators convene technical steering groups of experts as necessary.

The Muon Upgrade Coordinator reports to the Muon Management board.

Key decisions are reviewed during meetings organised by the Muon Management board and conducted by UCO and a committee of experts including the CMS Technical coordination team. All milestones are monitored by the Muon Management team on bi-weekly basis. The procedure for dealing with milestone readiness has been formalized and followed by the Muon Management board.

Reporting to CMS management happens typically on a monthly basis.

The Muon Upgrade Coordinator represents, along with the System Manager, the Upgrade of the muon system in the CMS Upgrade Steering Group. Reporting to CMS management happens typically on a monthly basis while reporting to Upgrade Management and Technical Coordination is on a weekly basis in the Upgrade Steering Group meetings and Upgrade Integration meetings. CMS Technical Coordination calls main reviews at the critical steps in the project: Engineering and Electronics Systems Design Reviews before the launch of manufacture, followed by Manufacturing Progress and Installation Readiness Reviews. For any major change in design, an Engineering Change Review is organised (in partnership with Technical Coordination). All of the review sequence organised (and chaired) by CMS Technical Coordination are conducted by a Committee of experts including at least one external expert and result in a written report.

9.2.3 Role of the Muon Technical Coordination Office

The Muon Technical Coordinator Office (TCO) of the Muon system has a specific role in the Phase-2 Upgrade. Working closely with the Muon Upgrade Coordination office and CMS Technical Coordinators, the TCO will:

- Oversee the integration of the different muon projects in CMS, ensuring that the mechanical and environmental interfaces with the neighbouring systems are properly designed and developed. Act as link person towards the CMS Engineering and Integration Office.
- Ensure that the technical choices in the Muon projects are coherent with the other CMS Upgrade projects, maximising synergies wherever possible. The TCO representative acts as link person towards the CMS Technical Coordination.
- Oversee the integration of electronics in the CMS infrastructure, in the services and experimental caverns.

9.2.4 Role of the Muon Detector Performance Coordination Office

The Muon Detector Performance Group coordination Office (DPGO) is organized and reinforced to cope also with the needs of the upgrade project while involved in the activities related to the detector operation and performance studies. This office is responsible for the development of the software algorithms and workflows and for the assessment of their performance. It takes care of the simulation of the background condition of the detectors in the future condition at HL-LHC. Together with the Upgrade Coordination Office, it will develop the simulation and reconstruction algorithms and the data quality monitoring procedures that will be used in the commissioning phase and, eventually, during the HL-LHC data taking. Together with the Muon Physics Object Group (Muon POG) it will contribute to the development of more performant Muon reconstruction algorithms, optimised for the new detector.

9.2.5 Role of the Resource Manager Office

The Coordinator of the Muon Resources Manager Office (RMO) is the Muon Resources Manager in the CMS Finance Board. For what concerns the Upgrade project, the Resource Manager Office of the Muon System has the responsibility of:

- Maintaining and updating the subproject cost-book, starting initially from estimates of costs and funding, and evolving towards a detailed bookkeeping of actual expenses and contributions from the participating FAs.
- Updating the cost time profile and the cost sharing among FAs.
- Taking care, together with the Technical Coordinators office, of procurements for the construction of the upgraded detectors.
- Reporting regularly on construction expenditures to the Muon MB, to the CMS Finance Board (FB), and preparing regular reports for the LHC RRB and the RRB Scrutiny Group as required.

9.3 Project schedule

A simplified view of the project schedule is shown in Fig. 9.2, displaying the main activities, with the major project milestones (represented by diamonds), which are listed separately in Tables 9.1–9.3. The master reference numbers associated to the milestones are taken from the

numbering in the WBS (Work Breakdown Structure) schedule Gantt charts (see Figs. 3.26, 4.17, 4.18, 5.33, 5.34).

Broadly, the development phase can be divided into a design phase, where different technical solutions and design choices are considered and evaluated, and a prototyping phase, where designs are basically finalised, with remaining adjustments largely driven by optimisation of cost and yield in production. Extensive prototyping is instrumental to identify and qualify potential vendors and prepare the participating groups for the production tasks. The Engineering Design Reviews (EDRs) mark the transition from development to production, with an initial period, marked as pre-production, where the throughput is kept low until full confidence is gained in the quality of the components and assembly procedures. The installation dates presented in the muon project schedule are compatible with the current integration sequence of CMS, and the present schedule of the Long Shutdown 2 (LS2), Long Shutdown 3 (LS3) and interleaved Year-End-Technical Stops (YETS). In Fig. 9.2 the different phases of the project are represented in different colours: design (light yellow), prototyping (yellow), pre-production (light salmon), production (dark salmon), installation, integration and commissioning (green).

Several major intervention are foreseen during LS3, mainly focused on the YE 1 noses. The installation schedule in LS3 is currently driven by the replacement of the Tracker and other elements of the CMS central detector such as the ECAL Barrel electronics and DT minicrate electronics. During this work the endcap disks will be moved away from the central detector to the maximum extent, giving no access to the muon stations, except station 1. It appears therefore difficult to schedule long-lasting activities in the barrel and endcaps within the same shutdown period. Therefore, any early installation during LS2 or YETS, whenever compatible with project planning and readiness, would relieve the installation schedule for LS3. A very detailed installation and commissioning plan already includes the installation of GE1/1 and refurbishment of the CSC on-detector electronics during LS2. Also an early installation of the GE2/1, RE3/1 and RE4/1 detectors in the three external rings of each endcap is planned during the two End of Year Technical Stops (YETS), scheduled before LS3. The details of the installation sequence during the YETS will be defined in the next months. The ME0 integration with HGCAL will be done prior to the insertion of the endcap nose into CMS, and the installation will be done in LS3.

9.4 Project cost and resources

9.4.1 Estimated cost

The estimated costs are expressed as CORE cost, according to the definition developed for the CMS Construction Project MoU and LHCC Cost Review Committee. CORE costs are defined as M&S (materials and services) costs for the production phase of the project and include only those items which fall into the allowed expense group according to the following guidelines:

- engineering costs incurred during production at a vendor or contractor, not at a CMS member institution;
- production fabrication and construction costs, including QA and system testing during the assembly process;
- transportation costs;
- integration and installation including costs associated with technical labour supplied at CERN for these purposes.

CORE costs do not include:

Table 9.1: Summary of most important milestones during the design phase.

	ID	Milestone title	Date
Design	DT.RD.BE.1	DT simulation: demonstration of L1 trigger pattern-recognition performance from DT TDC output done	11.Jan.2017
	DT.RD.FE.2, DT.RD.BE.2	DT L1 and Readout System specification defined with demonstrator	7.Jun.2017
	DT.RD.FE.1	DT FPGA demonstrator: firmware implementation of multichannel TDC done	5.Dec.2016
	CSC.RD.FE.1	CSC: Demonstration of readout of upgraded Cathode Front End Board (DCFEB) with present Data Mother Board (DMB)	01.Apr.2016
	CSC.RD.FE.2, CSC.RD.BE.1	CSC Review of electronics design completed	01.Jun.2016
	CSC.RD.FE.3	CSC LV power specifications defined	05.Jan.2017
	CSC.RD.BE.2	CSC FED system preliminary specs assessment	29.Dec.2017
	CSC.RD.BE.3	ODMB optical transmitter and FPGA chosen	1.Jul.2019
	CSC.RD.BE.4	FED architecture chosen	30.Jul.2021
	RPC.RD.DET.1, RPC.RD.FE.1	RPC Front-end and detector requirements finalized	21.Mar.2017
	RPC.RD.BE.1	RPC Services specs defined	4.Sept.2018
	RPC.RD.LS.1	Link system: Final Prototype Design ready	27.Jun.2019
	GE21.RD.DET.1 GE21.RD.FE.1 GE21.RD.BE.1	GE2/1 R&D: Key detector system design parameters are defined based on performance requirements	21.Mar.2017
	GE21.RD.FE.2	GE2/1 R&D: On-chamber electronics preliminary design completed and interfaces defined	19.Jun.2017
	GE21.RD.BE.2	GE2/1 R&D: Off-chamber electronics preliminary design completed and interfaces defined	12.Mar.2018
	GE21.RD.DET.2	GE2/1 R&D: A full size chamber prototype with partially instrumented readout built, tested and performance validated	1.May.2018
	GE21.RD.DET.3	GE2/1 R&D: Detector design parameters optimization completed, final chamber design is selected for the demonstrator	8.May.2018
	GE21.RD.FE.3	GE2/1 R&D: On-chamber electronics prototypes engineering design complete	1.Jun.2018
	ME0.RD.DET.1 ME0.RD.FE.1 ME0.RD.BE.1	ME0 R&D: Key detector system design parameters are defined based on performance requirements	21.Mar.2017
	ME0.RD.DET.2	ME0 R&D: Irradiation studies and assessment of performance and longevity with small prototypes completed	11.Jul.2017
	ME0.RD.FE.2 ME0.RD.BE.2	ME0 R&D: On-chamber & off-chamber electronics preliminary principal design complete and interfaces defined	25.Jul.2017
	ME0.RD.DET.3	ME0 R&D: Chamber (stack) prototype mechanical design completed	18.Dec.2018
	ME0.RD.FE.3	ME0 R&D: On-chamber electronics engineering design completed and validated	23.Aug.2019

Table 9.2: Summary of most important milestones during the prototyping phase.

	ID	Milestone title	Date
Prototyping	DT.RD.FE.3	OBDT demonstrator tested on DT chamber(s) (HM)	5.Mar.2018
	DT.RD.FE.4, DT.RD.BE.3	DT prototype ready for slice test validation at PT5 (HM)	14.Nov.2018
	DT.RD.FE.5, DT.RD.BE.4	DT prototype electronics (MiC2 and back-end) validated (HM)	4.Nov.2019
	CSC.RD.FE.4	CSC LVDB prototype validation completed	2.Apr.2018
	CSC.RD.FE.5	CSC front-end Prototypes validated	1.May.2018
	RPC.RD.DET.2, RPC.RD.FE.2	RPC full size prototypes and FE prototypes tested: preliminary results (HM)	13.Jun.2017
	RPC.RD.DET.3	RPC technology choice (HM)	12.Dec.2017
	RPC.RD.FE.3	RPC prototype FE finalized (HM)	26.Jun.2018
	RPC.RD.FE.4	On-Chamber FE Electronics final engineering prototype Ready	5.Feb.2019
	RPC.RD.DET.4	Completion of chamber engineering prototype and integration	8.Jan.2019
	RPC.RD.BE.2	RPC Power system specs defined and prototypes validated	3.Sept.2019
	RPC.RD.LS.2	RPC Link system: Initial Validation of final Prototype in IPM	31.Oct.2019
	RPC.RD.LS.3	RPC Link system: Final Validation of Final Prototype Design At CERN	17.Sept.2020
	RPC.RD.LS.4	RPC Link system: Prototype and Documentations Finalized (HM)	29.Oct.2020
	GE21.RD.FE.4	GE2/1 R&D: On-chamber electronics prototype electronics manufacturing and testing is complete	9.Oct.2018
	GE21.RD.DET.4	GE2/1 R&D: Performance of the demonstrator chamber with prototype electronics is validated	12.Mar.2019
	GE21.RD.FE.5 GE21.RD.BE.3	GE2/1 R&D: On-chamber and off-chamber prototype electronics integration and performance studies completed	12.Dec.2019
	ME0.RD.DET.4	ME0 R&D: Chamber (stack) prototype mechanical prototype testing and validation complete	24.Dec.2019
	ME0.RD.FE.4	ME0 R&D: On-chamber electronics prototype electronics manufacturing and testing is complete	21.Aug.2020
	ME0.RD.BE.3	ME0 R&D: Integration of the on-chamber and off-chamber electronics and performance assessment complete	8.Jan.2021
	ME0.RD.DET.5 ME0.RD.FE.5	ME0 R&D: Assessment of the electronics performance and integration with the demonstrator chamber completed	30.Mar.2021
	ME0.RD.DET.6	ME0 R&D: Beams and Cosmics testing of the demonstrator chamber and performance qualification completed	31.Aug.2021
EDR and ESR (EM)	DT EDR		1.Jun.20
	CSC on-chamber and trigger electronics EDR		1.Jun.2018
	CSC readout electronics EDR		1.Feb.2023
	RPC EDR		8.Jan.2019
	RPC ESR		9.Dec.2019
	RPC Link System ESR		29.Oct.2020
	GE2/1 EDR		12.Mar.2019
	GE2/1 ESR		12.Dec.2019
	ME0 ESR		27.Apr. 2021
	ME0 EDR		28.Oct.2021

- R&D and prototype costs associated with developing the design;
- costs for purchasing or building infrastructure and facilities at the CMS institutions;

Table 9.3: Summary of most important milestones during the production phase.

	ID	Milestone title	Date
Production	DT.PP.FE.1	DT Final MiC2 pre-production validated	1.Jun.2020
	DT.PR.FE.1	OBDT PCB start of assembly phase	14.Jun.2021
	DT.PP.BE.1	DT Back-end pre-production system validated	6.Jul.2022
	DT.PR.FE.2	DT: MiC2 production ready	22.May.2023
	DT.PR.BE.1	DT Back-end production completed	17.Apr.2024
	DT.PR.FE.3, DT.PR.BE.2	DT ready for installation	17.Apr.2024
	CSC.PR.FE.1	CSC DCFEB ready for production	1.Jun.2018
	CSC.PR.FE.2	CSC DCFEB ready for installation on plus endcap	11.Mar.2019
	CSC.PR.BE.1	CSC ODMB ready for production	6.Jul.2020
	CSC.PR.BE.2	CSC readout electronics ready to install	2.May.2025
	CSC.PR.BE.3	CSC FED ready for installation	2.May.2025
	RPC.PR.BE.1	RPC Ready for installation of Services	26.Feb.2019
	RPC.PP.DET.1, RPC.PP.FE.1	Chamber Pre-production Chambers and FE completed and validated (HM)	24.Dec.2019
	RPC.PR.DET.1	Chamber ready for start of production	7.Jan.2020
	RPC.PR.FE.1	On-chamber Electronics (FE) completed and validated	1.Sept.2020
	RPC.PR.DET.2, RPC.PR.FE.2	Chambers ready for Start Assembly Endcap 1	15.Sept.2020
	RPC.PR.LS.1	RPC Link system: ready for mass production	5.Nov.2020
	RPC.PR.LS.2	RPC Link system: PCB Fabricated and Components Received	22.Apr.2021
	RPC.PR.DET.3, RPC.PR.FE.4	RPC Detector Ready for Installation Endcap 1	16.Nov.2021
	RPC.PR.DET.4	Chamber Production completed and validated Endcap 1	14.Sept.2021
	RPC.PR.DET.5, RPC.PR.FE.5	Chambers ready for Start Assembly Endcap 2	14.Sept.2021
	RPC.PR.BE.2	RPC Power system ready	16.Nov.2021
	RPC.PR.LS.3	RPC Link system: the First half of the Link Boards and control Boards Assembled and Tested	18.Nov.2021
	RPC.PR.LS.4	RPC Link system: the Second half of the Link Boards and control Boards Assembled and Tested	3.Mar.2022
	RPC.PR.DET.6	RPC Chamber Production completed and validated Endcap 2	13.Sept.2022
	RPC.PR.DET.7, RPC.PR.FE.6	RPC Detector Ready for Installation Endcap 2	13.Sept.2022
	GE21.PR.DET.1	GE2/1 On-Disk Services Installation Complete	20.May.2019
	GE21.PR.FE.1	GE2/1 On-Chamber Electronics Manufacturing and Testing is Completed	3.Mar.2021
	GE21.PR.DET.2	GE2/1 Chambers for Disk-1 are assembled, tested, and ready for installation	16.Nov.2021
	GE21.PR.DET.3	GE2/1 Module manufacturing and testing is complete	8.Feb.2022
	GE21.PR.DET.4	GE2/1 Chambers for Disk-2 are assembled, tested, and ready for installation	5.Apr.2022
	GE21.PR.BE.1	GE2/1 Off-Chamber Electronics Manufacturing & Testing completed and ready for installation	5.May.2023
	ME0.PR.FE.1	ME0 On-Chamber Electronics Manufacturing and Testing complete, ready for chamber (stack) assembly	29.Mar.2022
	ME0.PR.DET.1	ME0 Chambers for Disk-1 are assembled, tested, and ready for installation	4.May.2023
	ME0.PR.BE.1	ME0 Off-Chamber Electronics Manufacturing & Testing complete	8.June.2023
	ME0.PR.DET.2	ME0 Chambers for Disk-2 are assembled, tested, and ready for installation	7.Mar.2024
	ME0.PR.DET.3	ME0: Last ME0 stack is inserted into the New Nose	23.May.2024
	ME0.PR.DET.4 ME0.PR.FE.2 ME0.PR.BE.2	ME0: Full Detector commissioning starts at P5	12.Sept.2025

- any labor costs at CMS institutions or support for physicists at CERN;
- travel costs for institution personnel.

The CORE cost estimates do not include contingency, neither for unexpected or unforeseen technical flaws or major accidents, nor for inflation and exchange rate variations.

In addition to the systems installed in the experiment, the estimates include costs for test stands needed for commissioning and firmware development. Spare parts to cover production losses and to ensure successful commissioning are included in the CORE estimates, while spares to support long term maintenance and operation (M&O) are not. In many cases, in order to deliver assembled or produced components of the upgrade with this CORE-value, additional costs are borne by institutions and funding agencies, including (R&D), design engineering and other institution labor. Costs are reported here in 2016 CHF.

A mid-level cost breakdown for each element of the upgrade scope is provided in the preceding sections in Tables 3.5, 4.8, 5.8, 6.21, and 6.22.

A summary of the present cost estimates is presented in Table 9.4, which is also shown in Chapter 1 as Table 1.13.

The total CORE-cost estimate is 25 MCHF. The GE1/1 project has been approved and documented in the corresponding TDR [7] submitted in the year 2015. The overall material cost and infrastructure is estimated to be about 3.75 MCHF. The GE1/1 system is currently undergoing construction.

Table 9.4: CORE cost estimates for the Phase-2 upgrades of the Muon system. The table includes also the GE1/1 system, which is the subject of a separate TDR [7].

Estimated CORE cost in MCHF (2016)		
DT System Upgrade	On-detector electronics	3.289
	Back-end electronics	1.609
	Optical links	0.784
	Total DT Upgrade cost	**5.682**
CSC System Upgrade	On-detector electronics and OTMBs	2.690
	FED system and ODMBs	0.887
	High Voltage modules	0.209
	Total CSC Upgrade cost	**3.785**
RPC System Upgrade	RE3/1 and RE4/1 chambers	0.764
	RE3/1 and RE4/1 power system and on-detector electronics	1.084
	RE3/1 and RE4/1 service and installation	0.406
	Link System Upgrade	1.380
	Total RPC Upgrade cost	**3.634**
GE1/1 System	**Total GE1/1 System cost**	**3.750**
GE2/1 System	Chambers	1.606
	DAQ system	1.099
	Power system	0.920
	Services, installation, test bench	0.470
	Total GE2/1 System cost	**4.095**
ME0 System	Chambers	1.336
	DAQ system	1.343
	Power system	1.106
	Services, installation, test bench	0.456
	Total ME0 System cost	**4.241**
Muon System Upgrade cost (excluding GE1/1)		**21.437**
Total Muon System Upgrade cost (including GE1/1)		**25.187**

All quotes and estimates have been collected from 2014 through 2017 and verified just before the publication of the present TDR. Quotes have been provided in CHF, EUR or USD, depending on the geographical location of institutes, companies, vendors, or suppliers. Engineering estimates performed by members of the CERN group, referring to module parts and to the Common Systems, have been elaborated mostly in CHF. In this TDR, CORE costs are expressed in CHF. The exchange rates used to convert EUR, USD, and YEN to CHF are average values for the calendar year 2016:

- 1 EUR = 1.09 CHF
- 1 USD = 0.98 CHF

The accuracy of the individual item cost estimates range from actual quotes already obtained from vendors and/or companies to educated interpolation of market surveys not yet evolved to the stage of a formal quote. In other cases, careful extrapolations from similar parts of the existing detector were carried out by experts, or groups thereof, who took care of the corresponding parts of existing detectors. Therefore for each unit cost estimate we have associated a quality flag (QF) according to the definition in Table 9.5.

Table 9.5: Quality flags associated to the unit cost estimate of each cost book item.

Flag	Meaning
1	Initial vendor quote or catalog price
2	Estimate based on a recent similar part or purchase
3	Estimate based on engineering seeding where sub-components are known
4	Estimate based on conceptual design or scaled from similar systems

The fraction of total Muon Upgrade cost, with the exception of GE1/1, broken down by unit cost quality flag, is illustrated in the pie chart distribution in Fig. 9.3.

The Muon Upgrade is mostly based on similar and recent upgrades of the muon projects (CSC ME1/1, RE4, GE1/1, DT TwinMux, μROS) and the dominant costs are based on information provided by vendors.

Around 85% of the cost estimate has $QF = 1$ or 2. The fraction of $QF = 1$ is related to the prices of the RPC, GEM and CSC commercial power supplies (2017 store catalogues) and recent quotation of the cost of HPL (bakelite) for the RPC electrodes (recent order). The bulk of the estimates has $QF = 2$:

- recent DT back-end electronics upgrade to the μTCA standard and especially the on-going μROS upgrade;
- the CSC electronics replacement is similar to the upgrade carried out on the inner ring of station 1 (ME1/1) during the Long Shutdown 1, and the costs are taken directly form that upgrade;
- for GEM projects a large fraction of the estimate is based on very recent GE1/1 orders and quotes;

The prices for optical fibers, cables and connectors are generally well known but final mapping and routing still require engineering design ($QF = 3$). In very few cases, corresponding to less than 5% of the overall cost, where the design concepts are not sufficiently advanced, the estimates are based on similar components or purchase of prototypes during the (R&D) phase ($QF = 4$).

9.4.2 Cost sharing and spending profile

Over the last few years, through a series of meetings and discussions of different official managerial boards a responsibility sharing model has been outlined which stems from historical involvements in the construction of the present Muon detector but has expanded into larger communities including new institutes. There is broad engagement of the present muon community in the upgrade program. Deliverying a given part of the detector or contributing to a given operation, rests with the individual institutes, whilst financial responsibilities for the procurement of the parts needed to carry out any construction activity rests with the Funding Agencies, not the individual institutes.

The detailed sharing of responsibilities for delivery of different parts of the detector by collaborating groups at the participating institutes, and the associated financial commitments by the funding agencies supporting those groups, will be formalised in due time, in signed Addenda to the CMS Construction Memorandum of Understanding (MoU), following a general process that the CMS resources manager applies to all CMS Upgrade projects.

For what concern the GE1/1 project it should be noted that total funding has already been accepted and/or approved by the corresponding funding agencies and production is already

started.

For the other projects this exercise has only begun. The full realisation of this planning exercise requires a good knowledge of the payment profile, which is obtained by associating the cost of each component with the estimated delivery sequence of the quantity ordered. We assume that payments of invoices (which for many orders will be partial invoices following delivery of partial quantities) will follow deliveries with a short delay, as is normally the case. The payment profile is presented in Fig. 9.4. The plot does not include the payment related to the GE1/1 project. We will work with CERN and the funding agencies to make ordering of the different parts of the detector possible when needed based on the construction schedule, while accommodating expected funding availability. Any large production and major procurement will be preceded by a dedicated Engineering Design Review (EDR) or Electronics System Review (ESR) and/or Procurement Readiness Review (PRR).

After approval, the integrated total funds available from each of the countries participating in the project will be committed by linking the cost profile to the composite funding profile, as requested by LHCC CORE rules. This is a work in progress and will evolve when the TDR project is approved.

9.4.3 Institution interests

In Figs. 9.5 and 9.6, we provide a synoptic view of the interests expressed at the time of writing by the different participating institutes on specific construction activities. It must be underlined that these interests cannot yet imply a formal commitment to deliver the indicated parts and/or construction operations, as formal commitments can only be taken by the institutes after funding from their respective funding agencies is secured. In addition to the listed construction activities, many institutes are involved in software tasks to which the notion of Materials and Services (M&S) cost does not apply, namely in physics performance studies and simulations.

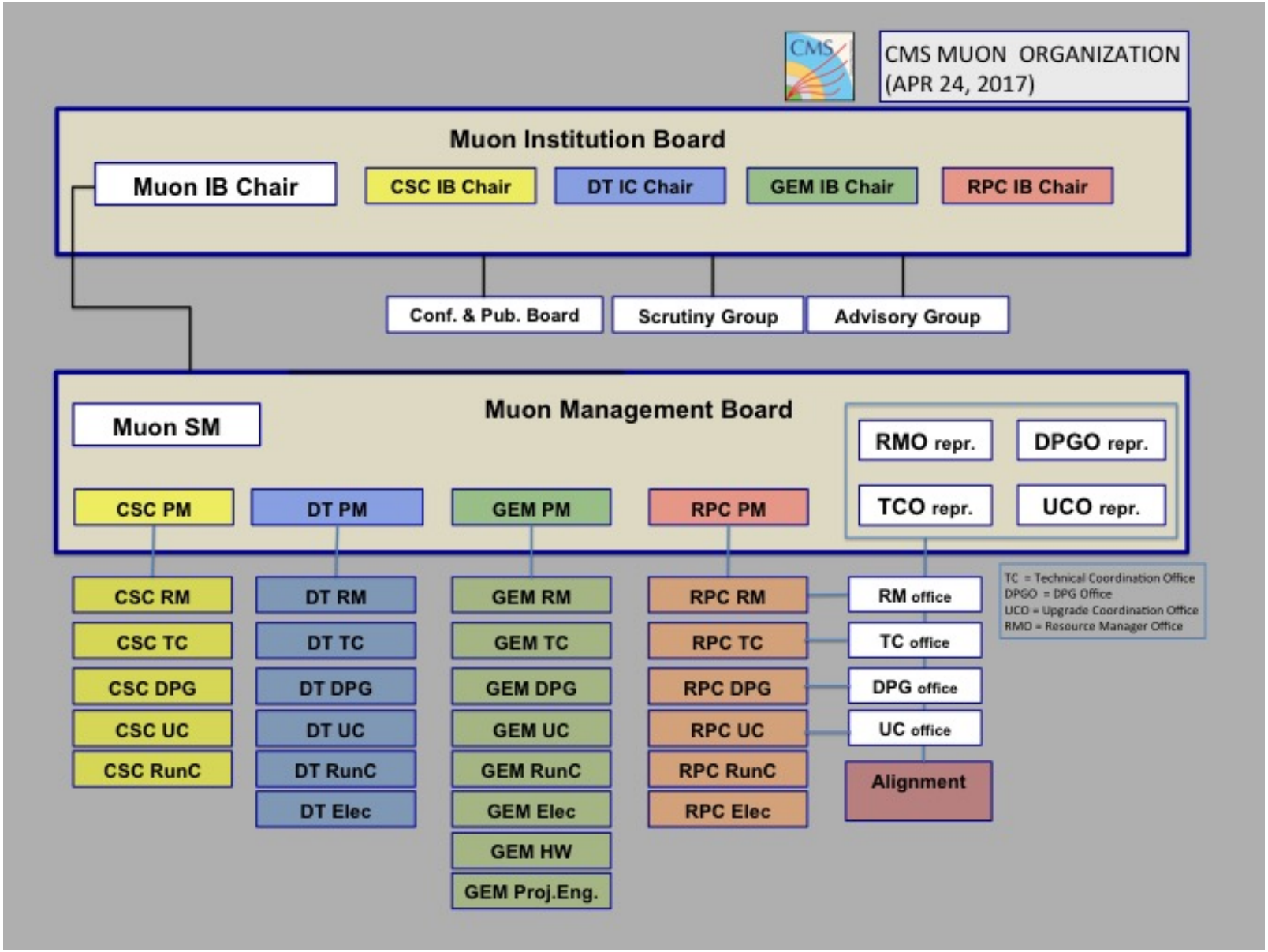

Figure 9.1: Muon Project organization chart, as of 24 April 2017.

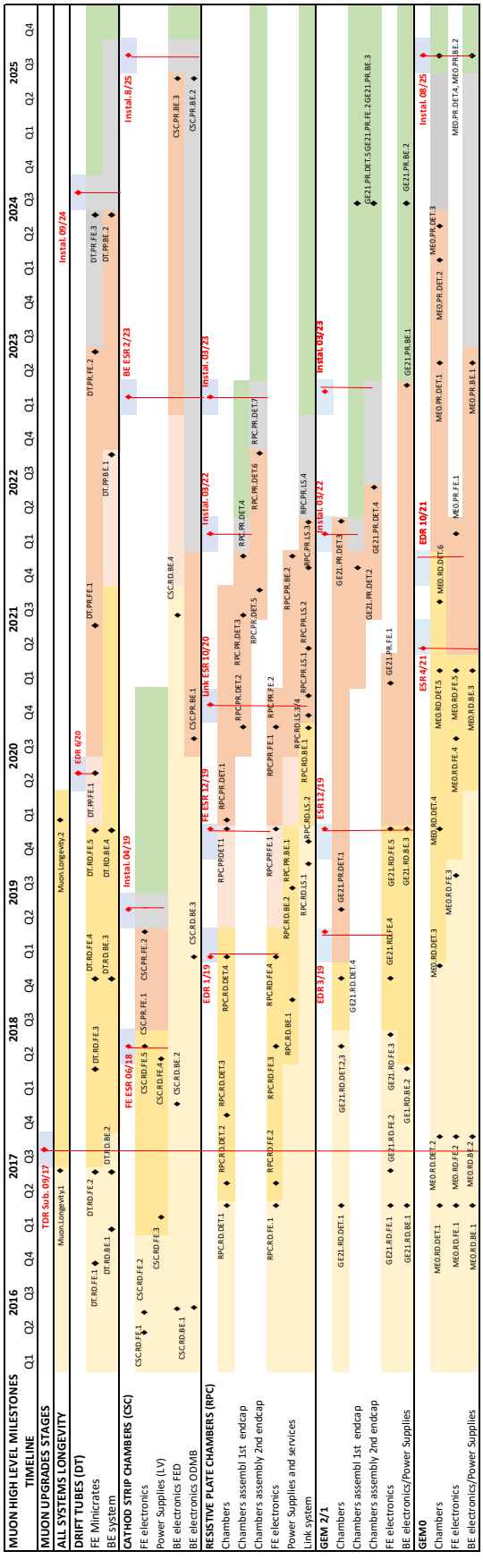

Figure 9.2: Construction schedule for the Phase-2 Muon Upgrade. The milestones shown in the figure are listed in Tables 9.1 and 9.3.

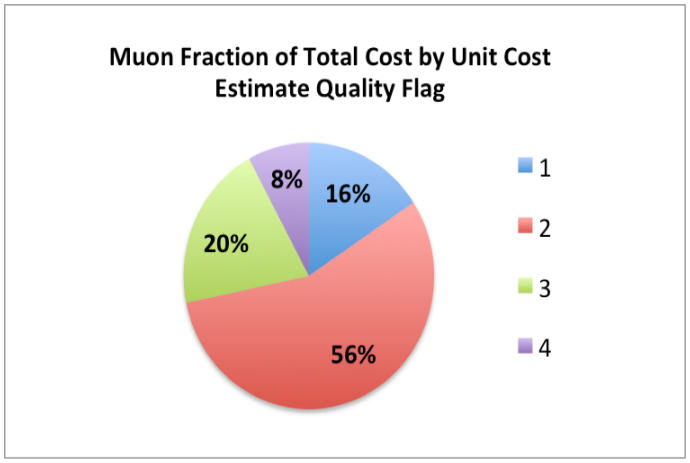

Figure 9.3: Distribution of the project cost by the quality flag attributed to each individual item estimate. Flags are defined in Table 9.5.

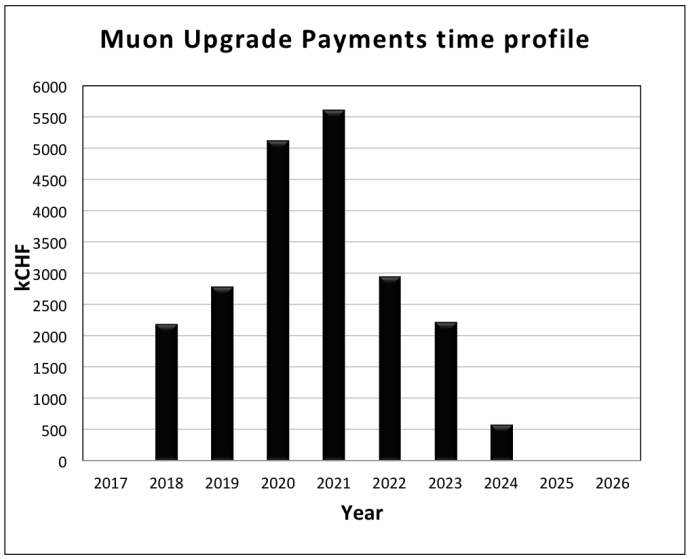

Figure 9.4: Cost time profile, showing the payments to be performed in a given year.

Institution	Country	Longevity				Detector		Electronics				Services				Install. & Comm.			
Institute for Nuclear Problems (INP)	Belarus								CSC										
Vrije University Brussel (VUB)	Belgium																		
University Libre de Bruxelles (ULB)	Belgium										GEM								GEM
Ghent University	Belgium			RPC		RPC	GEM							RPC				RPC	GEM
Katholieke Universiteit Leuven (KU)	Belgium										GEM								GEM
Institute for Nuclear Research and Nuclear Energy of Bulgaria Academy of Science (INRNE)	Bulgaria			RPC		RPC	GEM				GEM			RPC				RPC	GEM
Sofia University	Bulgaria						GEM				GEM			RPC				RPC	GEM
Peking University (Bejing)	China						GEM				GEM								GEM
Bejhang University	China						GEM												GEM
Sun Yat-sen University	China										GEM								GEM
Tsinghua University	China					RPC				RPC									
Universidad de los Andes Bogota	Colombia									RPC	GEM				GEM			RPC	GEM
Univsidad de Antioquia	Colombia										GEM				GEM				GEM
Academy of Scientific Research and Technology-Egyptian Network of High Energy Physics (Cairo)	Egypt					RPC	GEM				GEM							RPC	GEM
National Institute of Chemical Physics and Biophysics (Tallinn)	Estonia																		
Lappeenranta University of Technology (LUT)	Finland										GEM								GEM
Lyon	France									RPC								RPC	
IRFU, CEA, Universitè Paris-Saclay	France																		
Institut Pluridisciplinaire Hubert Curien Universitè de Strasbourg (IPHC)	France																		
Tibilisi State University	Georgia					RPC												RPC	
RWTH Aachen University, III. Phys. Inst. A, Aachen, Germany	Germany	DT					GEM					DT				DT			GEM
Institute for Nuclear Research ATOMKI of the Hungarian Academy of Sciences	Hungary							DT							GEM				GEM
Wigner Research Centre for Physics (Budapest)	Hungary																		
University of Debrecen, Institute of Physics	Hungary																		
Panjab University (Chandigarh)	India						GEM				GEM								GEM
University of Delhi	India						GEM				GEM				GEM				GEM
Saha Inst. Nuc. Physics (HBNI)	India						GEM												GEM
(BARC)	India						GEM				GEM								GEM
Institute for Research in Fundamental Sciences	Iran									RPC								RPC	
INFN, University and Politecnico of Bari	Italy			RPC		RPC	GEM				GEM							RPC	GEM
INFN and University of Bologna	Italy	DT					GEM	DT				DT				DT			GEM
Laboratori Nazionali Frascati (LNF) INFN	Italy			RPC		RPC	GEM								GEM				GEM
INFN and Università "Federico II" di Napoli, Università della Basilicata and Università G. Marconi	Italy					RPC				RPC	GEM				GEM				GEM
INFN and Università di Padova	Italy	DT						DT								DT			
INFN and Università di Pavia	Italy			RPC			GEM				GEM								GEM

Figure 9.5: Preliminary interests of participating institutes on construction deliverables (1/2).

Institution	Country	Longevity				Detector		Electronics				Services				Install. & Comm.			
INFN and Università di Torino and Università del Piemonte Orientale	Italy	DT						DT				DT				DT			
University of Seoul	Korea						GEM				GEM				GEM				GEM
Seoul National University	Korea						GEM								GEM				GEM
Sungkyunkwan University	Korea					RPC	GEM								GEM			RPC	GEM
Korea University	Korea					RPC	GEM								GEM			RPC	GEM
Hanyang University	Korea					RPC												RPC	
American University of Middle East (AUM)	Kuwait														GEM				GEM
Vilnius University	Lithuania										GEM								GEM
of Malaya	Malaysia																		
Benemerita Universidad Autonoma de Puebla	Mexico			RPC		RPC								RPC				RPC	
Universidad Iberoamericana	Mexico			RPC		RPC								RPC				RPC	
Centro de Investigacion y de Estudios Avanzados del IPN (CINVESTAV)	Mexico			RPC		RPC												RPC	
National Center for Physics, Quaid-I-Azam University (NCP), Islamabad	Pakistan						GEM				GEM			RPC	GEM			RPC	GEM
Joint Institute for Nuclear Research (Dubna)	Russia		CSC						CSC				CSC				CSC		
Petersburg Nuclear Physics Institute	Russia		CSC						CSC				CSC				CSC		
CIEMAT (Madrid) & Universidad Autonoma de Madrid (UAM)	Spain	DT						DT				DT				DT			
Universidad de Oviedo	Spain	DT						DT								DT			
Instituto de Fisica de Cantabria, Universidad de Cantabria (Santander)	Spain																		
CERN	Switzerland				GEM		GEM				GEM				GEM				GEM
Carnegie Mellon University	US																		
FNAL	US																		
Florida Inst. of Technology	US				GEM		GEM				GEM								GEM
University of Florida	US		CSC						CSC								CSC		
Northeastern University	US		CSC						CSC				CSC				CSC		
The Ohio State University	US								CSC								CSC		
Purdue University	US																		
Rice University	US								CSC		GEM						CSC		GEM
Texas A&M University (TAMU)	US								CSC		GEM						CSC		GEM
TAMU-Qatar	US										GEM								GEM
University of California Davis	US								CSC		GEM						CSC		GEM
University of California (UCLA)	US		CSC						CSC		GEM						CSC		GEM
University of California Riverside	US		CSC														CSC		
University of California Santa Barbara	US								CSC								CSC		
Wayne State Univiversity	US								CSC		GEM						CSC		GEM
University of Wisconsin	US		CSC						CSC								CSC		

Figure 9.6: Preliminary interests of participating institutes on construction deliverables (2/2).

Glossary of acronyms and technical terms

η = kinematic variable pseudorapidity.
μTCA = Micro Telecommunications Computing Architecture.
μROS = μTCA based Read-Out System, for DT readout.
A1676A = Branch controller for power supply system (from CAEN).
A3009 = LV board (from CAEN).
A3016 = LV board (from CAEN).
A3050 = LV board (from CAEN).
A3486 = AC-DC converter (from CAEN).
A3512N = HV board (from CAEN).
A876 = HV board (from CAEN).
A877 = HV board (from CAEN).
AC = Alternating Current.
ADC = Analog-to-Digital Converter.
AFEB = Anode Front-End Board.
ALCT = Anode Local Charged Track board, CSC system.
AMC = Advanced Mezzanine Card (from the ATCA specification).
AMC13 = A μTCA data concentration and clock distribution card.
APV25 = Analogue Pipeline Voltage, front-end chip.
ASIC = Application-Specific Integrated Circuit.
ATCA = Advanced Telecommunications Computing Architecture.
ATLAS = A Toroidal LHC ApparatuS.
BC0 = Bunch Crossing Zero.
BDT = Boosted Decision Tree, a multivariate analysis method.
Belle = B physics experiment at electron positron collider.
BER = Bit Error Rate.
BGO = control/timing commands in context of LHC.
BMTF = Barrel Muon Track finder.
BRAM = Block RAM.
BSM = Beyond the Standard Model.
BTI = Bunch and Track Identifier.
Building 904 = Building at CERN, Prevessin site, for muon chamber construction.
BX = Bunch crossing.

CB = Control Board.
CCB = Clock and Control Board.
CCS = Clock and Control System.
CCU = Communication and Control Unit.
cDAQ = central Data Acquisition.
CERN = European Organization for Nuclear Research.
CFEB = Cathode Front-End Board, part of the CSC system.
CHARM = CERN High energy AcceleRator Mixed field, measures sensitivity to radiation.
CLCT = Cathode Local Charged Track (cathode view muon stub), part of the CSC system.
CMOS = Complementary Metal-Oxide-Semiconductor.
CMS = Compact Muon Solenoid.
CMSSW = Compact Muon Solenoid Software, the CMS experiment software package.
CORE = CERN COst REview for LHC.
COTS = Commercial Off The Shelf.
CSC = Cathode Strip Chamber.
CTP7 = Calorimeter Trigger Processor 7 card, featuring the Xilinx FPGA Virtex-7 chip.
CuOF = Copper to Optical Fibre translator.
DAC = Digital-to-Analog Converter.
DAQ = Data AcQuisition.
DC = Direct Current.
DC-DC = Devices to convert DC voltage from one level to another.
DCC = Data Concentrator Card.
DCFEB = Digital Cathode Front-End Board, part of the CSC system.
DCS = Detector Control System.
DDR = Double Data Rate.
DDU = Detector Dependent Unit.
DLL = Delay Locked Loop.
DMB = Data acquisition Mother Board, CSC system.
DPS = Double Parton Scattering.
DQM = Data Quality Monitoring, a CMS system that monitors quality of recorded data.
DR = Dynamic Range.
DSA = Displaced StandAlone track, not pointing to event vertex.
DSS = Detector Safety System.
DT = Drift Tubes.
DTC = Data and Trigger Concentrator.
DTH = DAQ ad TTC HUB.
e-link = Electrical link.
EASY = Embedded Assembly SYstem, power supply system (from CAEN).
ECAL = Electromagnetic CALorimeter.

ECC = Error Correction Code.
EDR = Engineering Design Review.
EEPROM = Electrically-Erasable Programmable Read-Only Memory.
EM = ElectroMagnetic.
EMTF = Endcap Muon Track finder.
ENIG = Electroless Nickel Immersion Gold.
EPROM = Erasable Programmable Read-Only Memory.
ESR = Electronics System Review.
F-gas = gas mixture with a fluorine component.
FA = Funding Agency.
FB = Finance Board.
FE = Front End.
FEB = Front End Board.
FEC = Forward Error Correction.
FEC = Front End Controller (an ASIC).
FED = Front End Driver.
FED-Kit = FED-Kit, test bench modules for CMS DAQ.
Fermilab = Fermi National Accelerator Laboratory.
FIFO = First-In First-Out logic device that can be used to store and retrieve data.
FLUKA = FLUktuierende KAskade, particle physics Monte Carlo simulation package.
FMC = FPGA Mezzanine Card.
FPGA = Field Programmable Gate Array.
FR4 = composite material for printed circuit boards.
FSM = Finite State Machine.
GBT = CERN Gigabit Transceiver Project, source of the GBTX and associated chips.
GBTX = Gigabit Transceiver ASIC developed at CERN.
GEB = GEM Electronics Board.
GEM = Gas Electron Multiplier, a type of gaseous ionization detector.
GEn = GEM station in Endcap (n =1,2).
GIF = Gamma Irradiation Facility: area with high-intensity radioactive gamma source.
GIF++ = Gamma Irradiation Facility ++, successor of GIF.
GOL = Gigabit Optical Link.
GTX = a type of high speed electronics link.
GWP = Global Warming Potential.
HCAL = Hadronic CALorimeter.
HEP = High Energy Physics.
HGCAL = High Granularity CALorimeter.
HI = Heavy Ions, at the LHC refers to collisions between lead ions.
HIP = Heavy Ionizing Particle.

HL-LHC = High Luminosity Large Hadron Collider, an upgrade for the LHC machine.
HLT = High Level Trigger, a collection of software trigger algorithms.
HO = HCAL Outer = Outer barrel Hadronic CALorimeter.
HPL = High Pressure Laminate.
HSCP = Heavy Stable Charged Particle.
HTTP = Hypertext Transfer Protocol.
HV = High Voltage.
HVB = High Voltage Board.
I/O = Input/Output.
I2C = Inter-Integrated Circuit chip-to-chip communications protocol.
ID = Identification, algorithm/method to identify particle candidate objects.
IP = Interation Point.
IP = Impact Parameter, minimum distance between a trajectory and a selected vertex.
IPBus = a protocol to control and communicate with Ethernet-attached xTCA hardware.
iRPC = improved RPC.
JTAG = Joint Test Action Group; test and diagnostic bus standard by IEEE1149.1.
KODEL = KOrean DEtector Laboratory.
L1 = Level-1 trigger.
L2 = Level-2 trigger.
L3 = Level-3 trigger.
L1 tracks = Trigger primitives of the Tracker.
L1A = Level-1 trigger Accept.
LAN = Local Area Network.
latency = time neeeded for the level-1 trigger decision.
LB = Link Board.
LCT = Local Charged Track, or muon stub, part of the CSC system.
LHC = Large Hadron Collider.
LHCb = LHC beauty physics experiment.
LHCC = Large Hadron Collider experiments Committee.
LpGBT = Low-power version of the Gigabit transceiver.
LS1 = Long Shutdown 1, first LHC long shutdown from beginning 2013 to end of 2014.
LS2 = Long Shutdown 2, second LHC long shutdown scheduled for 2019-2020.
LS3 = Long Shutdown 3, third LHC long shutdown scheduled for 2024-2026.
LSP = Lightest Supersymmetric Particle.
LV = Low Voltage.
LVDB = Low Voltage Distribution Board, CSC system.
LVDS = Low Voltage Differential Signaling, a specification for differential digital logic.
LVPC = Low Voltage Patch Connector.
MAB = Muon Alignment Barrel.

MAD = Multichannel Amplifier and Discriminator.
MB = Muon Barrel.
MB = Management Board.
MBn = Muon Barrel station (n=1–4, DT).
ME = Muon Endcap.
ME0 = GEM chambers in Muon Endcap, station 0.
MEn = Muon Endcap station (n =1–4, CSC).
MERLIN = Project management software.
MiC = Minicrate electronics for DT system.
MiC1 = Minicrate 1 for DT system (Phase-1).
MiC2 = Minicrate 2 for DT system (Phase-2).
MP7 = Master Processor board, Virtex-7.
MPC = Muon Port Card, part of the CSC system.
mPU = MicroProcessor Unit.
MSSM = Minimal SUSY Standard Model.
MTBF = Mean Time Between Failures.
MTP = Optical fiber connector standard allowing up to 12 fibers in a single connector.
OALCT = Optical Anode Local Charged Track board, CSC system.
OBDT = On-Board Electronics for DT system.
ODMB = Optical Data acquisition Mother Board, CSC system.
OH = Opto-Hybrid board, used for example in the GE2/1 system.
OM3 = a type of optical fiber mostly used for communication over short distances.
OMTF = Overlap region (barrel and endcap) Muon Track finder.
OPC = Object linking and embedding for Process Control.
OTMB = Optical Trigger MotherBoard, part of the CSC system.
P5 = LHC Access Point 5 (location of CMS experiment).
PAC = Pattern Comparator (RPC trigger ASIC).
PCB = Printed Circuit Board.
PETIROC = extended analogue silicon photomultiplier Read-Out Chip.
PF = Particle flow, reconstruction method combining information from different detectors.
Phase-1 = LHC Phase-1, before Long Shutdown LS3.
Phase-2 = LHC Phase-2 = HL-LHC phase, after Long Shutdown LS3.
pileup = Overlapping of multiple soft interactions during a single LHC beam crossing.
PLL = Phase Locked Loop.
PM = Photo Multiplier.
PNPI = Petersburgs Nuclear Physics Institute.
PP = Patch Panel.
PPIB = Patch Panel Interconnecting Board.
PROM = Programmable Read-Only Memory.

PS = Proton Synchrotron at CERN.

PSI = Paul Scherrer Institute.

pseudorapidity $\equiv \eta = -\ln\tan\frac{\theta}{2}$, where θ is the angle of the particle momentum with respect to the anti-clockwise beam direction.

PSU = Power Supply Unit.

p_T = Transverse momentum of a physics object.

PU = Pileup, average quantity of particle collisions per bunch crossing.

PYTHIA = A program to simulate high energy particle interactions.

Q4 = a CMS Barrel Muon Prototype.

QA = Quality Assurance.

QC = Quality Control.

QCD = Quantum Chromodynamics - a theory that describes strong interactions.

QPLL = Quartz Phase Locke Loop.

R134a = tetrafluoroethane.

RD51 = Research and Development collaboration 51 at CERN.

R&D = Research and Development.

RAM = Random Access Memory.

RB = Read-out Board.

RB = RPC Barrel chambers.

RE = RPC Endcap chambers.

RECO = Reconstructed Data, CMS Data tier format.

RMS = Root Mean Square.

RO = Read-Out.

ROB = Read-Out Board.

ROC = Read-Out Chip.

ROC curve = signal efficiency as a function of background efficiency (Receiver Operating Characteristics).

ROS = Read-Out System.

RPC = Resistive Plate Chamber.

RPCROC = RPC Read-Out Chip.

RRB = Resource Review Board.

RTL = Register-Transfer Level.

Run 1 = LHC data taking period before Long Shutdown 1.

Run 2 = LHC data taking period after Long Shutdown 1 and before Long Shutdown 2.

Run 3 = LHC data taking period after Long Shutdown 2 and before Long Shutdown 3.

SB = Server Board.

SCA = Slow Control Adapter.

SCA = Switched Capacitor Array.

SCADA = Supervisory Control And Data Acquisition.

SEE = Single Event Effect, a generic effect of radiation on electronics.

SEL = Single Event Latchup.

SEM = Scanning Electron Microscopy.

SerDes = Serializer/Deserializer.

SET = Single Event Transient.

SEU = Single Event Upset.

SiPM = Silicon Photomulitplier.

SL = SuperLayer (DT system).

SM = Standard Model of Particle Physics, a theory describing electroweak and strong interactions.

Sn = ϕ sector n. Barrel: n=1–12. S4 = top. Endcap: n=1–36. S10 = top.

SPS = Super Proton Synchrotron.

Sp$\bar{p}$S = Super Proton-antiProton Synchrotron.

SRAM = Static Random Access Memory: memory that does not need refresh cycles.

stub = Collection of hits several layers of a particle detector, probably stemming from the same track.

Superchamber = pair of triple-GEM layers as used in GE1/1 and GE2/1.

Superlayer = stack of four staggered DT layers.

SUSY = SUper SYmmetry - an as yet unobserved symmetry between fermions and bosons.

SWPC = Single Wire Proportional Chamber.

SY1527 = power supply mainfraim (from CAEN).

SY4527 = power supply mainfraim (from CAEN).

TC = Technical Coordination.

TCDS = Trigger Control and Distribution System.

TDC = Trigger Data Concentrator card.

TDC = Time-to-Digital Converter.

TDR = Technical Design Report.

TeV = Tera electron Volts = 1000 GeV.

Tevatron = proton antiproton collider with TeV beam energy, at Fermilab.

TF = Track Finder.

TID = Total Ionization Dose.

TMB = Trigger MotherBoard: performs anode-cathode coincidence, CSC system.

TMR = Triple Modular Redundancy, a technique for avoiding errors in electronics circuits.

TP = Technical Proposal.

TPG = Trigger Primitive Generator.

TRACO = TRAck COrrelator.

TRB = Trigger Board.

TriDAS = Trigger and DAQ.

TS = Trigger Server.

TS = Track Segment.

TS = Tigger Supervisor.

TTC = Trigger Timing and Control, a system for distribution of clocking and control.

TTCrx = TTC receiver ASIC.

TwinMux = Twin Multiplexer, data concentrator for muon barrel track finder.

UF = University of Florida.

USC = Underground Service Cavern, where the CMS counting room is located.

UXC = Underground eXperimental Cavern, where the CMS detector is located.

VCC = VME Crate Controller.

Virtex = FPGA (from Xilinx).

VFAT3 = read-out chip (ASIC), used for example for GEM chambers. Original: Very Forward Atlas and Totem.

VHDL = Very-high-speed integrated circuits Hardware Description Language.

VLDB = Virtual Link Development Board.

VME = Versa Module Eurocard bus, an ANSI/IEEE computer hardware bus standard.

VTRX = Versatile Link Transmitter/Receiver, optical transceiver developed by the CERN Versatile Link project.

VTTx = Versatile Link Dual Transmitter, optical transmitter developed by the CERN Versatile Link project.

WBS = Work Breakdown Structure.

WP = Working Point.

xTCA = Telecommunications Computing Architecture, family name.

YB = Yoke Barrel.

YE = Yoke Endcap.

YETS = Year-end Technical Stop of the LHC.

References

[1] CMS Collaboration, "The CMS Experiment at the CERN LHC", *JINST* **3** (2008) S08004, doi:10.1088/1748-0221/3/08/S08004.

[2] ATLAS Collaboration, "Observation of a new particle in the search for the Standard Model Higgs boson with the ATLAS detector at the LHC", *Phys. Lett.* **B716** (2012) 1, doi:10.1016/j.physletb.2012.08.020.

[3] CMS Collaboration, "Observation of a new boson at a mass of 125 GeV with the CMS experiment at the LHC", *Phys. Lett.* **B716** (2012) 30, doi:10.1016/j.physletb.2012.08.021.

[4] CMS Collaboration, "Measurement of the $B_s^0 \to \mu^+\mu^-$ branching fraction and search for $B^0 \to \mu^+\mu^-$ with the CMS experiment", *Phys. Rev. Lett.* **111** (2013) 101804, doi:10.1103/PhysRevLett.111.101804, arXiv:1307.5025.

[5] G. Apollinari et al., "High-Luminosity Large Hadron Collider (HL-LHC): Preliminary Design Report",. CERN-2015-005, FERMILAB-DESIGN-2015-02.

[6] G. Apollinari et al., "High-Luminosity Large Hadron Collider (HL-LHC), Technical Design Report V.0.1",. CERN-2017-007-M.

[7] CMS Collaboration, "CMS Technical Design Report for the Muon Endcap GEM Upgrade", Technical Report CERN-LHCC-2015-012. CMS-TDR-013, CERN, 2015.

[8] O. Brüning et al. (editors), "LHC Design Report". CERN-2004-003, 2016. doi:10.5170/CERN-2004-003-V-1.

[9] UA1 Collaboration, "Experimental Observation of Isolated Large Transverse Energy Electrons with Associated Missing Energy at $\sqrt{s}$ = 540 GeV", *Phys. Lett.* **B122** (1983) 103, doi:10.1016/0370-2693(83)91177-2.

[10] UA2 Collaboration, "Observation of Single Isolated Electrons of High Transverse Momentum in Events with Missing Transverse Energy at the CERN $\bar{\text{p}}$p Collider", *Phys. Lett.* **B122** (1983) 476, doi:10.1016/0370-2693(83)91605-2.

[11] UA1 Collaboration, "Experimental Observation of Lepton Pairs of Invariant Mass Around 95 GeV/c^2 at the CERN SPS Collider", *Phys. Lett.* **B126** (1983) 398, doi:10.1016/0370-2693(83)90188-0.

[12] UA2 Collaboration, "Evidence for $Z^0 \to e^+e^-$ at the CERN $\bar{\text{p}}$p Collider", *Phys. Lett.* **B129** (1983) 130, doi:10.1016/0370-2693(83)90744-X.

[13] CDF Collaboration, "Observation of Top Quark Production in $\bar{p}p$ Collisions with the Collider Detector at Fermilab", *Phys. Rev. Lett.* **74** (1995) 2626, doi:10.1103/PhysRevLett.74.2626.

[14] D0 Collaboration, "Search for High Mass Top Quark Production in $p\bar{p}$ Collisions at $\sqrt{s}$ = 1.8 TeV", *Phys. Rev. Lett.* **74** (1995) 2422, doi:10.1103/PhysRevLett.74.2422.

[15] CMS Collaboration, "The Phase 2 Upgrade of the CMS Endcap Calorimeter", Technical Report CMS-TDR-019, 2017.

[16] CMS Collaboration, "The Phase-2 Upgrade of the CMS Tracker", Technical Report CERN-LHCC-2017-009. CMS-TDR-014, 2017.

[17] CMS Collaboration, "The Phase 2 Upgrade of the CMS Barrel Calorimeter", Technical Report CERN-LHCC-2017-011. CMS-TDR-015, 2017.

[18] CMS Collaboration, "The Phase-2 Upgrade of the CMS Level-1 Trigger - Interim Report to the LHCC", Technical Report CERN-LHCC-2017-013. CMS-TDR-017, 2017.

[19] CMS Collaboration, "The CMS muon project", Technical Report CERN-LHCC-97-032, CERN, 1997.

[20] CMS Collaboration, "The performance of the CMS muon detector in proton-proton collisions at $\sqrt{s} = 7$ TeV at the LHC", *JINST* **8** (2013) P1102, doi:10.1088/1748-0221/8/11/P11002, arXiv:1306.6905.

[21] CMS Collaboration, "Performance of CMS muon reconstruction in pp collision events at $\sqrt{s}$ = 7 TeV", *JINST* **7** (2012) P10002, doi:10.1088/1748-0221/7/10/P10002, arXiv:1206.4071.

[22] CMS Collaboration, "Performance of the CMS muon detector and reconstruction with proton-proton collisions at $\sqrt{s}$ = 13 TeV". To be submitted to JINST.

[23] Buńkowski, K., "Optimization, Synchronization, Calibration and Diagnostic of the RPC PAC Muon Trigger System for the CMS detector". https://cds.cern.ch/record/1308715. Doctoral thesis, Warsaw U., 2009, CERN-THESIS-2009-160.

[24] CMS Collaboration, "Technical Proposal for the Phase-II Upgrade of the CMS Detector", Technical Report CERN-LHCC-2015-010. LHCC-P-008. CMS-TDR-15-02, 2015.

[25] D. Pfeiffer et al., "The Radiation Field in the Gamma Irradiation Facility (GIF++) at CERN", *Nucl. Instrum. Meth.* **A866** (2017) 91, doi:10.1016/j.nima.2017.05.045, arXiv:1611.00299.

[26] S. Agosteo et al., "A facility for the test of large-area muon chambers at high rates", *Nucl. Instrum. Meth.* **A452** (2000) 94, doi:10.1016/S0168-9002(00)00414-9.

[27] The European Parliament and the Council of the European Union, "Regulation (EU) No 517/2014 of 16 April 2014 on fluorinated greenhouse gases", technical report, EU, 2014.

[28] COMPASS Collaboration, "The COMPASS experiment at CERN", *Nucl. Instrum. Meth.* **A577** (2007) 455, doi:10.1016/j.nima.2007.03.026.

[29] A. Cardini, B. Bencivenni, and P. De Simone, "The Operational Experience of the Triple-GEM Detectors of the LHCb Muon System: Summary of 2 Years of Data Taking",. IEEE Nucl. Sci. Symp. Med. Imag. Conf. Rec. (2012) 759.

[30] A. Svetek et al., "The calorimeter trigger processor card: the next generation of high speed algorithmic data processing at CMS", *JINST* **11** (2016) C02011, doi:10.1088/1748-0221/11/02/C02011.

[31] CMS Collaboration, "Measurement of the mass of the top quark in decays with a J/ψ meson in pp collisions at 8 TeV", *JHEP* **12** (2016) 123, doi:10.1007/JHEP12(2016)123, arXiv:1608.03560.

[32] CMS Collaboration, "ECFA 2016: Prospects for selected standard model measurements with the CMS experiment at the High-Luminosity LHC", CMS Physics Analysis Summary CMS-PAS-FTR-16-006, CERN, 2017.

[33] K. Hayasaka et al., "Search for Lepton Flavor Violating Tau Decays into Three Leptons with 719 Million Produced $\tau^+\tau^-$ Pairs", *Phys. Lett.* **B687** (2010) 139, doi:10.1016/j.physletb.2010.03.037, arXiv:1001.3221.

[34] CMS Collaboration, "Measurement of the weak mixing angle with the Drell-Yan process in proton-proton collisions at the LHC", *Phys. Rev. D* **84** (2011) 112002, doi:10.1103/PhysRevD.84.112002, arXiv:1110.2682.

[35] CMS Collaboration, "Measurement of the weak mixing angle with the forward-backward asymmetry of Drell-Yan events at 8 TeV", Technical Report CMS-PAS-SMP-16-007, CERN, Geneva, 2017.

[36] ATLAS Collaboration, "Measurement of the forward-backward asymmetry of electron and muon pair-production in pp collisions at $\sqrt{s} = 7$ TeV with the ATLAS detector", *JHEP* **09** (2015) 049, doi:10.1007/JHEP09(2015)049, arXiv:1503.03709.

[37] LHCb Collaboration, "Measurement of the forward-backward asymmetry in $Z/\gamma^* \to \mu^+\mu^-$ decays and determination of the effective weak mixing angle", *JHEP* **11** (2015) 190, doi:10.1007/JHEP11(2015)190, arXiv:1509.07645.

[38] SLD Electroweak Group, DELPHI, ALEPH, SLD, SLD Heavy Flavour Group, OPAL, LEP Electroweak Working Group, L3 Collaboration, "Precision electroweak measurements on the Z resonance", *Phys. Rept.* **427** (2006) 257, doi:10.1016/j.physrep.2005.12.006, arXiv:hep-ex/0509008.

[39] CMS Collaboration, "CMS Physics : Technical Design Report Volume 1: Detector Performance and Software", Technical Report CERN-LHCC-2006-001, CMS-TDR-8-1, 2006. Section 1.5.9.

[40] E. Conti and F. Gasparini, "Test of the wire ageing induced by radiation for the CMS barrel muon chambers", *Nucl. Instrum. Meth.* **A465** (2001) 472, doi:10.1016/S0168-9002(01)00690-8.

[41] D. Acosta et al., "Aging tests of full scale CMS muon cathode strip chambers", *Nucl. Instrum. Meth.* **A515** (2003) 226, doi:10.1016/j.nima.2003.09.002.

[42] M. Abbrescia et al., "Study of long-term performance of CMS RPC under irradiation at the CERN GIF", *Nucl. Instrum. Meth.* **A533** (2004) 102, doi:10.1016/j.nima.2004.07.009.

[43] H. C. Kim et al., "Quantitative aging study with intense irradiation tests for the CMS forward RPCs", *Nucl. Instrum. Meth.* **A602** (2009) 771, doi:10.1016/j.nima.2008.12.140.

[44] S. Agosteo et al., "Single event effects measurements on the electronics for the CMS muon barrel detector at LHC", *Nucl. Instrum. Meth.* **A489** (2002) 357, doi:10.1016/S0168-9002(02)00791-X.

[45] R. Breedon et al., "Results of radiation test of the cathode front-end board for CMS endcap muon chambers", *Nucl. Instrum. Meth.* **A471** (2001) 340, doi:10.1016/S0168-9002(01)00857-9.

[46] B. Bylsma et al., "Radiation Testing of Electronics for the CMS Endcap Muon System", *Nucl. Instrum. Meth.* **A698** (2013) 242, doi:10.1016/j.nima.2012.09.017, arXiv:1208.4051.

[47] M. Abbrescia et al., "Neutron-induced single event upset on the RPC front-end chips for the CMS experiment", *Nucl. Instrum. Meth.* **A484** (2002) 494, doi:10.1016/S0168-9002(01)01967-2.

[48] J. Va'vra, "Physics and chemistry of aging: Early developments", *Nucl. Instrum. Meth.* **A515** (2003) 1, doi:10.1016/j.nima.2003.08.124.

[49] L. Malter, "Thin Film Field Emission", *Phys. Rev.* **50** (1936) 48, doi:10.1103/PhysRev.50.48.

[50] United Nations, "United Nations Framework Convention on Climate Change: Global Warming Potentials, 2014". http://unfccc.int/ghg_data/items/3825.php. September 1, 2017.

[51] T. Ferguson et al., "Aging studies of CMS muon chamber prototypes", *Nucl. Instrum. Meth.* **A488** (2002) 240, doi:10.1016/S0168-9002(02)00400-X.

[52] J. Mekki et al., "CHARM: A Mixed Field Facility at CERN for Radiation Tests in Ground, Atmospheric, Space and Accelerator Representative Environments", *IEEE Trans. Nucl. Sci.* **63** (2016) 2106, doi:10.1109/TNS.2016.2528289.

[53] CERN, "The CERN High-energy AcceleRator test facility (CHARM)". http://charm.web.cern.ch/CHARM/. September 1, 2017.

[54] M. Matveev et al., "Software Evaluation and Irradiation Test of the SBS Technologies Model 620 PCI-to-VME Bus Adapter", *9th Workshop on Electronics for LHC Experiments* (2003), no. CERN-2003-006, 389, doi:10.5170/CERN-2003-006.389.

[55] G. Altenhöfer et al., "The drift velocity monitoring system of the CMS barrel muon chambers", Technical Report CMS NOTE 2017/007, 2017.

[56] A. Castaneda, "Background modeling for muon stations". https://indico.cern.ch/event/623984/contributions/2518232/attachments/1428898/2193770/BkgSimulation_BrilMeeting_Mar2017_v3.pdf. March 16, 2017.

[57] S. Mallows, "Radiation Simulation Studies for Phase-2 Beampipe - pp collisions". https://indico.cern.ch/event/634730/contributions/2568854/attachments/1478909/2292317/v541beampipeSimulations_PP_14_06.pdf. April 26, 2017.

[58] M. Pegoraro, "Lifetime of FED electronics". https://indico.cern.ch/event/241598/contributions/526765/attachments/409760/569249/fe_life.pdf. May 7, 2013.

[59] I. Gonzalez et al., "Report of the DT Longevity Task Force", Technical Report CMS DN-2017/040, 2017 (in preparation).

[60] G. Mocellin, F. Gonella, F. Gasparini, and A. T. Meneguzzo, "Report on the construction and performances of four drift cells of the muon chambers of CMS for aging effects studies at LNL", Technical Report INFN-LNL-245, 2016.

[61] M. Cerrada et al., "Test Beam Analysis of the First CMS MB2 Drift Tube Muon Chamber", Technical Report CMS NOTE 2003/007, 2003.

[62] E. Conti, "Measurement of the wire gain of cells of the Barrel Muon Drift Chambers", Technical Report CMS NOTE 2002/002, 2002.

[63] F. Gonella and M. Pegoraro, "The MAD, a Full Custom ASIC for the CMS Barrel Muon Chambers Front End Electronics", *7th Workshop on Electronics for LHC Experiments* (2011), no. CERN-LHCC-2001-034,.

[64] CAEN, "Neolite". http://www.caen.it/csite/CaenGeneric.jsp?parent=377&Type=WOCateg. September 1, 2017.

[65] CMS Collaboration, "The TriDAS Project, Volume 1: The Trigger Systems. Chapter 9: The DT Local Trigger". Technical Design Report, CERN-LHCC 2000-038. 2000.

[66] CMS Collaboration, "The Phase-2 Upgrade of the CMS DAQ - Interim Report to the LHCC", Technical Report CERN-LHCC-2017-014. CMS-TDR-018, 2017.

[67] V. Barashko et al, "The Muti-channel High-Voltage System for the CMS Muon Endcap Cathode Strip Chambers". CMS Detector Note DN-2016/015, to be submitted to JINST.

[68] CAEN, "Mod. A1733-A1833-A1733B-A1833B HV Boards". https://www.caen.it/servlet/checkCaenManualFile?Id=9481. March 9, 2013.

[69] V. Thenakis, "Options for abating greenhouse gases from exhaust streams". BNL-52652 Formal Report, https://www.bnl.gov/isd/documents/23784.pdf. December 1, 2001.

[70] F. Ferrarese, "Statistical analysis of Total Ionizing Dose response in 25-nm NAND Flash memory". http://tesi.cab.unipd.it/45696/. PhD thesis, Università degli Studi di Padova, 2014.

[71] S. Durkin, "Modeling the CSC Front End Electronics Rate Limitations". https://twiki.cern.ch/twiki/bin/view/CMS/CSCdescriptionCFEBModels. September 10, 2015.

[72] G. Iles, J. Jones, and A. Rose, "Experience powering Xilinx Virtex-7 FPGAs", *JINST* **8** (2013), no. 12, C12037.

[73] M. Abbrescia et al., "Cosmic ray tests of double-gap resistive plate chambers for the CMS experiment", *Nucl. Instrum. Meth.* **A550** (2005) 116, doi:10.1016/j.nima.2005.06.074.

[74] M. Abbrescia et al., "Preliminary results of Resistive Plate Chambers operated with eco-friendly gas mixtures for application in the CMS experiment", *JINST* **11** (2016) C09018, doi:10.1088/1748-0221/11/09/C09018.

[75] L. Benussi et al., "Properties of potential eco-friendly gas replacements for particle detectors in high-energy physics", (2015). arXiv:1505.00701.

[76] M. Abbrescia et al., "Local and global performance of double-gap resistive plate chambers operated in avalanche mode", *Nucl. Instrum. Meth.* **A434** (1999) 244, doi:10.1016/S0168-9002(99)00534-3.

[77] M. Fras et al., "Use of Triple Modular Redundancy (TMR) technology in FPGAs for the reduction of faults due to radiation in the readout of the ATLAS Monitored Drift Tube (MDT) chambers", *JINST* **5** (2010) C11009, doi:10.1088/1748-0221/5/11/C11009.

[78] G. Aielli et al., "Improving the RPC rate capability", *JINST* **11** (2016) P07014, doi:10.1088/1748-0221/11/07/P07014.

[79] S. K. Park, M. H. Kang, and K. S. Lee, "RPC Gap Production and Performance for CMS RE4 Upgrade", *JINST* **9** (2014) C11009, doi:10.1088/1748-0221/9/11/C11009, arXiv:1408.3720.

[80] K. S. Lee et al., "Radiation tests of real-sized prototype RPCs for the Phase-2 Upgrade of the CMS Muon System", *JINST* **11** (2016) C08008, doi:10.1088/1748-0221/11/08/C08008, arXiv:1605.00440.

[81] R. Cardarelli et al., "Performance of RPCs and diamond detectors using a new very fast low noise preamplifier", *JINST* **8** (2013) P01003, doi:10.1088/1748-0221/8/01/P01003.

[82] S. Park et al., "Production of gas gaps for the Forward RPCs of the CMS experiment", *Nucl. Instrum. Meth.* **A550** (2005) 551, doi:10.1016/j.nima.2005.05.052.

[83] L. Pant et al., "Resistive Plate Chambers for the RE4 upgrade of the CMS endcap system", *JINST* **7** (2012) P10025, doi:10.1088/1748-0221/7/10/P10025.

[84] S. Park et al., "CMS endcap RPC gas gap production for upgrade", *JINST* **7** (2012) P11013, doi:10.1088/1748-0221/7/11/P11013.

[85] S. Colafranceschi et al., "Resistive plate chambers for 2013-2014 muon upgrade in CMS at LHC", *JINST* **9** (2014) C10033, doi:10.1088/1748-0221/9/10/C10033.

[86] F. Sauli, "Gem: A new concept for electron amplification in gas detectors", *Nucl. Instrum. Meth.* **A386** (1997) 531, doi:10.1016/S0168-9002(96)01172-2.

[87] A. Hernandez, "Commissioning and integration testing of the DAQ system for the CMS GEM upgrade", CMS Conference Report CMS-CR-2017-163, 2017.

[88] K. Gnanvo et al., "Detection and Imaging of High-Z Materials with a Muon Tomography Station Using GEM Detectors", *IEEE Nucl. Sci. Symp. Med. Imag. Conf. Rec.* (2010) 552, doi:10.1109/NSSMIC.2010.5873822, arXiv:1011.3231.

[89] S. Martoiu, H. Muller, A. Tarazona, and J. Toledo, "Development of the scalable readout system for micro-pattern gas detectors and other applications", *JINST* **8** (2013) C03015, doi:10.1088/1748-0221/8/03/C03015.

[90] M. French et al., "Design and results from the APV25, a deep sub-micron CMOS front-end chip for the CMS tracker", *Nucl. Instrum. Meth.* **A466** (2001) 359, doi:10.1016/S0168-9002(01)00589-7.

[91] D. Abbaneo et al., "Characterization of GEM Detectors for Application in the CMS Muon Detection System", *IEEE Nucl. Sci. Symp. Med. Imag. Conf. Rec.* (2010) 1416, doi:10.1109/NSSMIC.2010.5874006, arXiv:1012.3675.

[92] D. Abbaneo et al., "Test beam results of the GE1/1 prototype for a future upgrade of the CMS high-η muon system", *IEEE Nucl. Sci. Symp. Med. Imag. Conf. Rec.* (2011) 1806, doi:10.1109/NSSMIC.2011.6154688, arXiv:1111.4883.

[93] D. Abbaneo et al., "Beam Test Results for New Full-scale GEM Prototypes for a Future Upgrade of the CMS High-eta Muon System", *IEEE Nucl. Sci. Symp. Med. Imag. Conf. Rec.* (2012) 1172, doi:10.1109/NSSMIC.2012.6551293, arXiv:1211.3939.

[94] D. Abbaneo et al., "Performance of a Large-Area GEM Detector Prototype for the Upgrade of the CMS Muon Endcap System", *IEEE Nucl. Sci. Symp. Med. Imag. Conf. Rec.* (2014) arXiv:1412.0228.

[95] V. Bhopatkar, M. Hohlmann, A. Zhang, " Measurement of the Charge Induced on the Readout Strips of a GE1/1 Detector Prototype for the CMS Muon Endcap GEM Upgrade", Technical Report CMS IN-2017/001.

[96] M. Tytgat et al., "Construction and Performance of Large-Area Triple-GEM Prototypes for Future Upgrades of the CMS Forward Muon System", *IEEE Nucl. Sci. Symp. Med. Imag. Conf. Rec.* (2011) 1019, doi:10.1109/NSSMIC.2011.6154312, arXiv:1111.7249.

[97] CAEN, "HV module A1515". http://www.caen.it/csite/CaenProd.jsp?parent=20&idmod=960. September 1, 2017.

[98] G. Corradi, F. Murtas, and D. Tagnani, "A novel High-Voltage System for a triple GEM detector", *Nucl. Instrum. Meth.* **A572** (2007) 96, doi:10.1016/j.nima.2006.10.166.

[99] CAEN, "Power supply system SY4527". http://www.caen.it/csite/CaenProd.jsp?idmod=752&parent=20. September 1, 2017.

[100] S. Bachmann et al., "Development and test of large size GEM detectors", *IEEE Trans. Nucl. Sci.* **47** (2000) 1412, doi:10.1109/23.872987.

[101] M. C. Altunbas et al., "Aging measurements with the gas electron multiplier (GEM)", *Nucl. Instrum. Meth.* **A515** (2001) 249, doi:10.1016/j.nima.2003.09.006.

[102] L. Guirl et al., "An aging study of triple GEMs in Ar-CO_2", *Nucl. Instrum. Meth.* **A478** (2002) 263, doi:10.1016/S0168-9002(01)01768-5.

[103] J. A. Merlin, J.-M. Brom, and A. Sharma, "Study of long-term sustained operation of gaseous detectors for the high rate environment in CMS". https://cds.cern.ch/record/2155685. PhD thesis, Strasbourg U., 2016, CERN-THESIS-2016-041.

[104] M. Capeans-Garrido, "Aging and materials: Lessons for detectors and gas systems", *Nucl. Instrum. Meth.* **A515** (2003) 73, doi:10.1016/j.nima.2003.08.134.

[105] J. Wise, "Chemistry of radiation damage to wire chambers". https://cds.cern.ch/record/243580. PhD thesis, Calif. Univ. Berkeley, 1992.

[106] J. A. Kadyk, "Wire chamber aging", *Nucl. Instrum. Meth.* **A300** (1990) 436, doi:10.1016/0168-9002(91)90381-Y.

[107] M. Capeans and J. M. Garabatos Cuadrado, "Estudio del envejecimiento de los detectores gaseosos y soluciones para la utilizacion de MSGCs en experimentos de alta luminosidad". https://cds.cern.ch/record/1331835. PhD thesis, Santiago de Compostela U., 1995, CERN-THESIS-95-004.

[108] S. Bachmann et al., "Discharge studies and prevention in the gas electron multiplier (GEM)", *Nucl. Instrum. Meth.* **A479** (2000) 294, doi:10.1016/S0168-9002(01)00931-7.

[109] T. Lenzi, et al., "A micro-TCA based data acquisition system for the Triple-GEM detectors for the upgrade of the CMS forward muon spectrometer", *JINST* **312** (2017) C01058, doi:10.1088/1748-0221/12/01/C01058.

[110] J. Gebelein, et al., "An approach to system-wide fault tolerance for FPGAs", *http://www.esa.int/Our_Activities/Space_Engineering_Technology/Microelectronics/ESA_Microelectronics_Section* (2009).

[111] "NOVACAVI - Cables for Advanced Technology". http://www.novacavi.it. September 1, 2017.

[112] Radiall, "Company for connectors and associated components". https://www.radiall.com. September 1, 2017.

[113] Radiall, "High Voltage Multipin Connectors". http://www.rojone.com.au/wp-content/uploads/2011/03/radiall-highvoltage-multipin-connectors.pdf. September 1, 2017.

[114] CMS Collaboration, "Performance of the CMS TwinMux algorithm in late 2016 pp collision runs", CMS Detector Performance Summary CMS-DP-2016-074, 2016.

[115] N. Pozzobon, P. Zotto, and F. Montecassiano, "A proposal for the upgrade of the muon drift tubes trigger for the cms experiment at the hl-lhc", 2016. doi:10.1051/epjconf/201612700012.

[116] N. Pozzobon, F. Montecassiano, and P. Zotto, "A novel approach to hough transform for implementation in fast triggers", *Nucl. Instrum. Meth.* **A834** (2016) 81, doi:10.1016/j.nima.2016.07.020.

[117] N. Pozzobon, F. Montecassiano, and P. Zotto, "Design of a Compact Hough Transform for a new L1 Trigger Primitives Generator for the upgrade of the CMS Drift Tubes muon detector at the HL-LHC", *IEEE Transactions on Nuclear Science* **PP** (2017), no. 99, 1474, doi:10.1109/TNS.2017.2691358.

[118] CMS Collaboration, "Performance of CMS muon reconstruction in cosmic-ray events", *JINST* **5** (2010) T03022, doi:10.1088/1748-0221/5/03/T03022, arXiv:0911.4994.

[119] CMS Collaboration, "CMS Physics Technical Design Report, volume I: Detector performance and software", TDR CERN-LHCC-2006-001, CMS-TDR-008-1, CERN, 2006.

[120] I. Golutvin et al., "The new segment building algorithm for the cathode strip chambers in the CMS experiment". https://cds.cern.ch/record/2050723. CMS Conference Report CMS-CR-2015-146 (2015).

[121] R. Frühwirth, "Application of Kalman filtering to track and vertex fitting", *Nucl. Instrum. Meth.* **A262** (1987) 444, doi:10.1016/0168-9002(87)90887-4.

[122] CMS Collaboration, "Measurement of tracking efficiency", CMS Physics Analysis Summary CMS-PAS-TRK-10-002, 2010.

[123] CMS Collaboration, "Particle-flow reconstruction and global event description with the CMS detector", *JINST* **12** (2017) P10003, doi:10.1088/1748-0221/12/10/P10003, arXiv:1706.04965.

[124] CMS Collaboration, "Commissioning of the particle-flow event reconstruction with leptons from J/ψ and W decays at 7 TeV", CMS Physics Analysis Summary CMS-PAS-PFT-10-003, 2010.

[125] CMS Collaboration, "Muon Reconstruction and Identification Improvements for Run-2 and First Results with 2015 Run Data", CMS Detector Performance Summary CMS-DP-2015-015, 2015.

[126] CMS Collaboration, "Studies of the performances of the h zz 4 analysis with the cms phase ii detector upgrade", CMS Physics Analysis Summary CMS-PAS-FTR-13-003, 2013.

[127] CMS Collaboration, "Projected performance of Higgs analyses at the HL-LHC for ECFA 2016", CMS Physics Analysis Summary CMS-PAS-FTR-16-002, CERN, 2017.

[128] CMS Collaboration, "Estimated Sensitivity for New Particle Searches at the HL-LHC", CMS Physics Analysis Summary CMS-PAS-FTR-16-005, 2017.

[129] CMS Collaboration, "ECFA 2016: Prospects for selected standard model measurements with the CMS experiment at the High-Luminosity LHC", CMS Physics Analysis Summary CMS-PAS-FTR-16-006, 2017.

[130] DELPHES 3 Collaboration, "DELPHES 3, A modular framework for fast simulation of a generic collider experiment", *JHEP* **02** (2014) 057, doi:10.1007/JHEP02(2014)057, arXiv:1307.6346.

[131] CMS Collaboration, "Measurements of properties of the Higgs boson decaying into the four-lepton final state in pp collisions at sqrt(s) = 13 TeV", (2017). arXiv:1706.09936. Submitted to JHEP.

[132] C. Goebel, F. Halzen, and D. M. Scott, "Double Drell-Yan Annihilations in Hadron Collisions: Novel Tests of the Constituent Picture", *Phys. Rev.* **D22** (1980) 2789, doi:10.1103/PhysRevD.22.2789.

[133] V. Shelest, A. Snigirev, and G. Zinovjev, "Gazing into the multiparton distribution equations in qcd", *Phys. Lett.* **B113** (1982), no. 4, 325, doi:http://dx.doi.org/10.1016/0370-2693(82)90049-1.

[134] AFS Collaboration, "Double Parton Scattering in p p Collisions at $\sqrt{s} = 63$ GeV", *Z. Phys.* **C34** (1987) 163, doi:10.1007/BF01566757.

[135] M. Diehl, D. Ostermeier, and A. Schafer, "Elements of a theory for multiparton interactions in QCD", *JHEP* **03** (2012) 089, doi:10.1007/JHEP03(2012)089, arXiv:1111.0910.

[136] G. Calucci and D. Treleani, "Disentangling Correlations in Multiple Parton Interactions", *Phys. Rev.* **D83** (2011) 016012, doi:10.1103/PhysRevD.83.016012, arXiv:1009.5881.

[137] F. A. Ceccopieri, M. Rinaldi, and S. Scopetta, "Parton correlations in same-sign W pair production via double parton scattering at the LHC", *Phys. Rev.* **D95** (2017) 114030, doi:10.1103/PhysRevD.95.114030, arXiv:1702.05363.

[138] CMS Collaboration, "Double Parton Scattering cross section limit from same-sign W bosons pair production in di-muon final state at LHC", CMS Physics Analysis Summary CMS-PAS-FSQ-13-001, 2015.

[139] CMS Collaboration, "Measurement of double parton scattering in same-sign WW production in p-p collisions at $\sqrt{s} = 13$ TeV with the CMS experiment", CMS Physics Analysis Summary CMS-PAS-FSQ-16-009, CERN, 2017.

[140] A. L. Read, "Presentation of search results: the CLs technique", *J. Phys.* **G28** (2002) doi:10.1088/0954-3899/28/10/313.

[141] A. L. Read, "Modified frequentist analysis of search results (the CLs method)", Proceedings of the First Workshop on Confidence Limits, CERN, Geneva, Switzerland, CERN-OPEN-2000-205, 2000.

[142] T. Junk, "Confidence level computation for combining searches with small statistics", *Nucl. Instrum. Meth.* **A434** (1999) 435, doi:10.1016/S0168-9002(99)00498-2, arXiv:hep-ex/9902006.

[143] ATLAS Collaboration, "Measurement of $D^{*\pm}$, $D^{\pm}$ and $D_s^{\pm}$ meson production cross sections in pp collisions at $\sqrt{s} = 7$ TeV with the ATLAS detector", *Nucl. Phys.* **B907** (2016) 717, doi:10.1016/j.nuclphysb.2016.04.032, arXiv:1512.02913.

[144] H. Baer et al., "Radiatively-driven natural supersymmetry at the LHC", 2013. doi:10.1007/JHEP12(2013)013.

[145] J. C. Collins and D. E. Soper, "Angular Distribution of Dileptons in High-Energy Hadron Collisions", *Phys. Rev. D* **16** (1977) 2219, doi:10.1103/PhysRevD.16.2219.

[146] CDF Collaboration, "Indirect measurement of $\sin^2\theta_W$ (or M_W) using $\mu^+\mu^-$ pairs from γ^*/Z bosons produced in $p\bar{p}$ collisions at a center-of-momentum energy of 1.96 TeV", *Phys. Rev. D* **89** (2014) 072005, doi:10.1103/PhysRevD.89.072005, arXiv:1402.2239.

[147] CDF Collaboration, "Measurement of $\sin^2\theta_{\rm eff}^{\rm lept}$ using e^+e^- pairs from γ^*/Z bosons produced in $p\bar{p}$ collisions at a center-of-momentum energy of 1.96 TeV", *Phys. Rev. D* **93** (2016) 112016, doi:10.1103/PhysRevD.93.112016, arXiv:1605.02719.

[148] D0 Collaboration, "Measurement of the effective weak mixing angle in $p\bar{p} \to Z/\gamma^* \to e^+e^-$ events", *Phys. Rev. Lett.* **115** (2015) 041801, doi:10.1103/PhysRevLett.115.041801, arXiv:1408.5016.

[149] S. Alioli, P. Nason, C. Oleari, and E. Re, "NLO vector-boson production matched with shower in POWHEG", *JHEP* **07** (2008) 060, doi:10.1088/1126-6708/2008/07/060, arXiv:0805.4802.

[150] P. Nason, "A new method for combining NLO QCD with shower Monte Carlo algorithms", *JHEP* **11** (2004) 040, doi:10.1088/1126-6708/2004/11/040, arXiv:hep-ph/0409146.

[151] S. Frixione, P. Nason, and C. Oleari, "Matching NLO QCD computations with parton shower simulations: the POWHEG method", *JHEP* **11** (2007) 070, doi:10.1088/1126-6708/2007/11/070, arXiv:0709.2092.

[152] S. Alioli, P. Nason, C. Oleari, and E. Re, "A general framework for implementing NLO calculations in shower Monte Carlo programs: the POWHEG BOX", *JHEP* **06** (2010) 043, doi:10.1007/JHEP06(2010)043, arXiv:1002.2581.

[153] NNPDF Collaboration, "Parton distributions for the LHC Run II", *JHEP* **04** (2015) 040, doi:10.1007/JHEP04(2015)040, arXiv:1410.8849.

[154] T. Sjostrand, S. Mrenna, and P. Z. Skands, "A Brief Introduction to PYTHIA 8.1", *Comput. Phys. Commun.* **178** (2008) 852, doi:10.1016/j.cpc.2008.01.036, arXiv:0710.3820.

[155] CMS Collaboration, "Event generator tunes obtained from underlying event and multiparton scattering measurements", *Eur. Phys. J. C* **76** (2016) 155, doi:10.1140/epjc/s10052-016-3988-x, arXiv:1512.00815.

[156] W. T. Giele and S. Keller, "Implications of hadron collider observables on parton distribution function uncertainties", *Phys. Rev. D* **58** (1998) 094023, doi:10.1103/PhysRevD.58.094023, arXiv:hep-ph/9803393.

[157] N. Sato, J. F. Owens, and H. Prosper, "Bayesian Reweighting for Global Fits", *Phys. Rev. D* **89** (2014) 114020, doi:10.1103/PhysRevD.89.114020, arXiv:1310.1089.

[158] A. Bodek, J. Han, A. Khukhunaishvili, and W. Sakumoto, "Using Drell-Yan forward-backward asymmetry to reduce PDF uncertainties in the measurement of electroweak parameters", *Eur. Phys. J. C* **76** (2016) 115, doi:10.1140/epjc/s10052-016-3958-3, arXiv:1507.02470.

[159] J. T. Ruderman and D. Shih, "Slepton co-NLSPs at the Tevatron", *JHEP* **11** (2010) 046, doi:10.1007/JHEP11(2010)046, arXiv:1009.1665.

[160] G. F. Giudice and A. Romanino, "Split supersymmetry", *Nucl. Phys.* **B699** (2004) 65, doi:10.1016/j.nuclphysb.2004.08.001, arXiv:hep-ph/0406088. [Erratum: Nucl. Phys. **B**706 (2005) 487].

[161] N. Arkani-Hamed and S. Dimopoulos, "Supersymmetric unification without low energy supersymmetry and signatures for fine-tuning at the LHC", *JHEP* **06** (2005) 073, doi:10.1088/1126-6708/2005/06/073, arXiv:hep-th/0405159.

[162] CMS Collaboration, "Search for heavy stable charged particles with 12.9 fb^{-1} of 2016 data", CMS Physics Analysis Summary CMS-PAS-EXO-16-036, CERN, 2016.

[163] CMS Collaboration, "Constraints on the pMSSM, AMSB model and on other models from the search for long-lived charged particles in proton-proton collisions at sqrt(s) = 8 TeV", *Eur. Phys. J.* **C75** (2015) 325, doi:10.1140/epjc/s10052-015-3533-3, arXiv:1502.02522.

[164] M. Baak et al., "The electroweak fit of the standard model after the discovery of a new boson at the LHC", *Eur. Phys. J.* **C72** (2012) 2205, doi:10.1140/epjc/s10052-012-2205-9, arXiv:1209.2716. Updates available from http://gfitter.desy.de.

[165] G. Degrassi et al., "Higgs mass and vacuum stability in the standard model at NNLO", *JHEP* **08** (2012) 1, doi:10.1007/JHEP08(2012)098, arXiv:1205.6497.

[166] F. Bezrukov, M. Y. Kalmykov, B. A. Kniehl, and M. Shaposhnikov, "Higgs boson mass and new physics", *JHEP* **10** (2012) 140, doi:10.1007/JHEP10(2012)140, arXiv:1205.2893.

[167] F. Bezrukov and M. Shaposhnikov, "The Standard Model Higgs boson as the inflaton", *Phys. Lett.* **B659** (2008) 703, doi:10.1016/j.physletb.2007.11.072, arXiv:0710.3755.

[168] A. D. Simone, M. P. Herzberg, and F. Wilczek, "Running inflation in the Standard Model", *Phys. Lett.* **B678** (2009) 1, doi:10.1016/j.physletb.2009.05.054, arXiv:0812.4946.

CMS Collaboration

Yerevan Physics Institute, Yerevan, Armenia
A.M. Sirunyan, A. Tumasyan

Institut für Hochenergiephysik, Wien, Austria
W. Adam, F. Ambrogi, E. Asilar, T. Bergauer, J. Brandstetter, E. Brondolin, M. Dragicevic, J. Erö, A. Escalante Del Valle, M. Flechl, M. Friedl, R. Frühwirth[1], V.M. Ghete, J. Grossmann, J. Hrubec, M. Jeitler[1], A. König, N. Krammer, I. Krätschmer, D. Liko, T. Madlener, I. Mikulec, E. Pree, N. Rad, H. Rohringer, J. Schieck[1], R. Schöfbeck, M. Spanring, D. Spitzbart, W. Waltenberger, J. Wittmann, C.-E. Wulz[1], M. Zarucki

Institute for Nuclear Problems, Minsk, Belarus
V. Chekhovsky, V. Mossolov, J. Suarez Gonzalez

Universiteit Antwerpen, Antwerpen, Belgium
E.A. De Wolf, D. Di Croce, X. Janssen, J. Lauwers, M. Van De Klundert, H. Van Haevermaet, P. Van Mechelen, N. Van Remortel

Vrije Universiteit Brussel, Brussel, Belgium
S. Abu Zeid, F. Blekman, J. D'Hondt, I. De Bruyn, J. De Clercq, K. Deroover, G. Flouris, D. Lontkovskyi, S. Lowette, I. Marchesini, S. Moortgat, L. Moreels, Q. Python, K. Skovpen, S. Tavernier, W. Van Doninck, P. Van Mulders, I. Van Parijs

Université Libre de Bruxelles, Bruxelles, Belgium
D. Beghin, B. Bilin, H. Brun, B. Clerbaux, G. De Lentdecker, H. Delannoy, J. Dong, B. Dorney, G. Fasanella, L. Favart, R. Goldouzian, A. Grebenyuk, T. Lenzi, J. Luetic, T. Maerschalk, A. Marinov, S. Rugovac, T. Seva, E. Starling, C. Vander Velde, P. Vanlaer, D. Vannerom, Y. Yang, R. Yonamine, F. Zenoni, F. Zhang[2]

Katholieke Universiteit Leuven, GEEL, Belgium
P. Leroux, F. Tavernier

Ghent University, Ghent, Belgium
T. Cornelis, D. Dobur, A. Fagot, M. Gul, I. Khvastunov[3], D. Poyraz, C. Roskas, S. Salva, M. Tytgat, W. Verbeke, N. Zaganidis

Université Catholique de Louvain, Louvain-la-Neuve, Belgium
H. Bakhshiansohi, O. Bondu, S. Brochet, G. Bruno, C. Caputo, A. Caudron, P. David, S. De Visscher, C. Delaere, M. Delcourt, B. Francois, A. Giammanco, M. Komm, G. Krintiras, V. Lemaitre, A. Magitteri, A. Mertens, M. Musich, K. Piotrzkowski, L. Quertenmont, A. Saggio, M. Vidal Marono, S. Wertz, J. Zobec

Centro Brasileiro de Pesquisas Fisicas, Rio de Janeiro, Brazil
W.L. Aldá Júnior, F.L. Alves, G.A. Alves, L. Brito, M. Correa Martins Junior, C. Hensel, A. Moraes, M.E. Pol, P. Rebello Teles

Universidade do Estado do Rio de Janeiro, Rio de Janeiro, Brazil
E. Belchior Batista Das Chagas, W. Carvalho, J. Chinellato[4], E. Coelho, E.M. Da Costa, G.G. Da Silveira[5], D. De Jesus Damiao, S. Fonseca De Souza, L.M. Huertas Guativa, H. Malbouisson, M. Melo De Almeida, C. Mora Herrera, L. Mundim, H. Nogima, L.J. Sanchez Rosas, A. Santoro, A. Sznajder, M. Thiel, E.J. Tonelli Manganote[4], F. Torres Da Silva De Araujo, A. Vilela Pereira

Universidade Estadual Paulista [a], Universidade Federal do ABC [b], São Paulo, Brazil
S. Ahuja[a], C.A. Bernardes[a], T.R. Fernandez Perez Tomei[a], E.M. Gregores[b], P.G. Mercadante[b], S.F. Novaes[a], Sandra S. Padula[a], D. Romero Abad[b], J.C. Ruiz Vargas[a]

Institute for Nuclear Research and Nuclear Energy, Bulgarian Academy of Sciences, Sofia, Bulgaria
A. Aleksandrov, R. Hadjiiska, P. Iaydjiev, M. Misheva, G. Rashevski, M. Rodozov, M. Shopova, G. Sultanov

University of Sofia, Sofia, Bulgaria
A. Dimitrov, L. Litov, B. Pavlov, P. Petkov

Beihang University, Beijing, China
W. Fang[6], X. Gao[6], L. Yuan

Institute of High Energy Physics, Beijing, China
M. Ahmad, J.G. Bian, G.M. Chen, H.S. Chen, M. Chen, Y. Chen, X. Dong, C.H. Jiang, D. Leggat, H. Liao, Z. Liu, F. Romeo, S.M. Shaheen, A. Spiezia, J. Tao, C. Wang, Z. Wang, E. Yazgan, H. Zhang, S. Zhang, J. Zhao

State Key Laboratory of Nuclear Physics and Technology, Peking University, Beijing, China
Y. Ban, G. Chen, J. Li, Q. Li, S. Liu, Y. Mao, S.J. Qian, D. Wang, Z. Xu

Tsinghua University, Beijing, China
P. Lyu, Y. Wang

Universidad de Los Andes, Bogota, Colombia
C. Avila, A. Cabrera, C.A. Carrillo Montoya, L.F. Chaparro Sierra, C. Florez, C.F. González Hernández, J.D. Ruiz Alvarez, M.A. Segura Delgado

University of Split, Faculty of Electrical Engineering, Mechanical Engineering and Naval Architecture, Split, Croatia
B. Courbon, N. Godinovic, D. Lelas, I. Puljak, P.M. Ribeiro Cipriano, T. Sculac

University of Split, Faculty of Science, Split, Croatia
Z. Antunovic, M. Kovac

Institute Rudjer Boskovic, Zagreb, Croatia
V. Brigljevic, D. Ferencek, K. Kadija, B. Mesic, A. Starodumov[7], T. Susa

University of Cyprus, Nicosia, Cyprus
M.W. Ather, A. Attikis, G. Mavromanolakis, J. Mousa, C. Nicolaou, F. Ptochos, P.A. Razis, H. Rykaczewski

Charles University, Prague, Czech Republic
M. Finger[8], M. Finger Jr.[8]

Universidad San Francisco de Quito, Quito, Ecuador
E. Carrera Jarrin

Academy of Scientific Research and Technology of the Arab Republic of Egypt, Egyptian Network of High Energy Physics, Cairo, Egypt
H. Abdalla[9], A.A. Abdelalim[10,11], Y. Assran[12,13], A. Mohamed[11], S. Mohamed

National Institute of Chemical Physics and Biophysics, Tallinn, Estonia
R.K. Dewanjee, M. Kadastik, L. Perrini, M. Raidal, A. Tiko, C. Veelken

Department of Physics, University of Helsinki, Helsinki, Finland
P. Eerola, H. Kirschenmann, J. Pekkanen, M. Voutilainen

Helsinki Institute of Physics, Helsinki, Finland
J. Havukainen, J.K. Heikkilä, T. Järvinen, V. Karimäki, R. Kinnunen, T. Lampén, K. Lassila-Perini, S. Laurila, S. Lehti, T. Lindén, P. Luukka, H. Siikonen, E. Tuominen, J. Tuominiemi

Lappeenranta University of Technology, Lappeenranta, Finland
T. Tuuva

IRFU, CEA, Université Paris-Saclay, Gif-sur-Yvette, France
M. Besancon, F. Couderc, M. Dejardin, D. Denegri, J.L. Faure, F. Ferri, S. Ganjour, S. Ghosh, P. Gras, G. Hamel de Monchenault, P. Jarry, I. Kucher, C. Leloup, E. Locci, M. Machet, J. Malcles, G. Negro, J. Rander, A. Rosowsky, M.Ö. Sahin, M. Titov

Laboratoire Leprince-Ringuet, Ecole polytechnique, CNRS/IN2P3, Université Paris-Saclay, Palaiseau, France
A. Abdulsalam, C. Amendola, I. Antropov, S. Baffioni, F. Beaudette, P. Busson, L. Cadamuro, C. Charlot, R. Granier de Cassagnac, M. Jo, S. Lisniak, A. Lobanov, J. Martin Blanco, M. Nguyen, C. Ochando, G. Ortona, P. Paganini, P. Pigard, R. Salerno, J.B. Sauvan, Y. Sirois, A.G. Stahl Leiton, T. Strebler, Y. Yilmaz, A. Zabi, A. Zghiche

Université de Strasbourg, CNRS, IPHC UMR 7178, Strasbourg, France
J.-L. Agram[14], J. Andrea, D. Bloch, J.-M. Brom, M. Buttignol, E.C. Chabert, N. Chanon, C. Collard, E. Conte[14], X. Coubez, J.-C. Fontaine[14], D. Gelé, U. Goerlach, M. Jansová, A.-C. Le Bihan, N. Tonon, P. Van Hove

Centre de Calcul de l'Institut National de Physique Nucleaire et de Physique des Particules, CNRS/IN2P3, Villeurbanne, France
S. Gadrat

Université de Lyon, Université Claude Bernard Lyon 1, CNRS-IN2P3, Institut de Physique Nucléaire de Lyon, Villeurbanne, France
S. Beauceron, C. Bernet, G. Boudoul, R. Chierici, C. Combaret, D. Contardo, P. Depasse, H. El Mamouni, J. Fay, L. Finco, S. Gascon, M. Gouzevitch, G. Grenier, B. Ille, F. Lagarde, I.B. Laktineh, M. Lethuillier, H. Mathez, L. Mirabito, A.L. Pequegnot, S. Perries, A. Popov[15], V. Sordini, M. Vander Donckt, S. Viret

Georgian Technical University, Tbilisi, Georgia
I. Lomidze, T. Toriashvili[16]

Tbilisi State University, Tbilisi, Georgia
I. Bagaturia[17], D. Lomidze, Z. Tsamalaidze[8]

RWTH Aachen University, I. Physikalisches Institut, Aachen, Germany
C. Autermann, L. Feld, M.K. Kiesel, K. Klein, M. Lipinski, M. Preuten, C. Schomakers, J. Schulz, M. Teroerde, V. Zhukov[15]

RWTH Aachen University, III. Physikalisches Institut A, Aachen, Germany
A. Albert, E. Dietz-Laursonn, D. Duchardt, M. Endres, M. Erdmann, S. Erdweg, T. Esch, R. Fischer, A. Güth, M. Hamer, T. Hebbeker, C. Heidemann, K. Hoepfner, H. Keller, C. Kilinc, S. Knutzen, D. Louis, M. Merschmeyer, A. Meyer, P. Millet, S. Mukherjee, M. Olschewski, B. Philipps, T. Pook, M. Radziej, H. Reithler, M. Rieger, F. Scheuch, D. Teyssier, S. Thüer, F.P. Zantis

RWTH Aachen University, III. Physikalisches Institut B, Aachen, Germany
G. Flügge, B. Kargoll, T. Kress, A. Künsken, T. Müller, A. Nehrkorn, A. Nowack, C. Pistone, O. Pooth, A. Stahl[18]

Deutsches Elektronen-Synchrotron, Hamburg, Germany
M. Aldaya Martin, T. Arndt, C. Asawatangtrakuldee, K. Beernaert, O. Behnke, U. Behrens, A. Bermúdez Martínez, A.A. Bin Anuar, K. Borras[19], V. Botta, A. Campbell, P. Connor, C. Contreras-Campana, F. Costanza, C. Diez Pardos, G. Eckerlin, D. Eckstein, T. Eichhorn, E. Eren, E. Gallo[20], J. Garay Garcia, A. Geiser, J.M. Grados Luyando, A. Grohsjean, P. Gunnellini, M. Guthoff, A. Harb, J. Hauk, M. Hempel[21], H. Jung, M. Kasemann, J. Keaveney, C. Kleinwort, I. Korol, D. Krücker, W. Lange, A. Lelek, T. Lenz, J. Leonard, K. Lipka, W. Lohmann[21], R. Mankel, I.-A. Melzer-Pellmann, A.B. Meyer, G. Mittag, J. Mnich, A. Mussgiller, E. Ntomari, D. Pitzl, A. Raspereza, M. Savitskyi, P. Saxena, R. Shevchenko, N. Stefaniuk, G.P. Van Onsem, R. Walsh, Y. Wen, K. Wichmann, C. Wissing, O. Zenaiev

University of Hamburg, Hamburg, Germany
R. Aggleton, S. Bein, V. Blobel, M. Centis Vignali, T. Dreyer, E. Garutti, D. Gonzalez, J. Haller, A. Hinzmann, M. Hoffmann, A. Karavdina, R. Klanner, R. Kogler, N. Kovalchuk, S. Kurz, T. Lapsien, D. Marconi, M. Meyer, M. Niedziela, D. Nowatschin, F. Pantaleo[18], T. Peiffer, A. Perieanu, C. Scharf, P. Schleper, A. Schmidt, S. Schumann, J. Schwandt, J. Sonneveld, H. Stadie, G. Steinbrück, F.M. Stober, M. Stöver, H. Tholen, D. Troendle, E. Usai, A. Vanhoefer, B. Vormwald

Institut für Experimentelle Teilchenphysik, Karlsruhe, Germany
S.M. Abbas, M. Akbiyik, C. Barth, M. Baselga, S. Baur, E. Butz, R. Caspart, T. Chwalek, F. Colombo, W. De Boer, A. Dierlamm, N. Faltermann, B. Freund, R. Friese, M. Giffels, M.A. Harrendorf, F. Hartmann[18], S.M. Heindl, U. Husemann, F. Kassel[18], S. Kudella, H. Mildner, M.U. Mozer, Th. Müller, M. Plagge, G. Quast, K. Rabbertz, M. Schröder, I. Shvetsov, G. Sieber, H.J. Simonis, R. Ulrich, S. Wayand, M. Weber, T. Weiler, S. Williamson, C. Wöhrmann, R. Wolf

Institute of Nuclear and Particle Physics (INPP), NCSR Demokritos, Aghia Paraskevi, Greece
G. Anagnostou, G. Daskalakis, T. Geralis, A. Kyriakis, D. Loukas, I. Topsis-Giotis

National and Kapodistrian University of Athens, Athens, Greece
G. Karathanasis, S. Kesisoglou, A. Panagiotou, N. Saoulidou

National Technical University of Athens, Athens, Greece
K. Kousouris

University of Ioánnina, Ioánnina, Greece
I. Evangelou, C. Foudas, P. Gianneios, P. Katsoulis, P. Kokkas, S. Mallios, N. Manthos, I. Papadopoulos, E. Paradas, J. Strologas, F.A. Triantis, D. Tsitsonis

MTA-ELTE Lendület CMS Particle and Nuclear Physics Group, Eötvös Loránd University, Budapest, Hungary
M. Csanad, N. Filipovic, G. Pasztor, O. Surányi, G.I. Veres[22]

Wigner Research Centre for Physics, Budapest, Hungary
G. Bencze, C. Hajdu, D. Horvath[23], Á. Hunyadi, F. Sikler, V. Veszpremi

Institute of Nuclear Research ATOMKI, Debrecen, Hungary
N. Beni, S. Czellar, J. Karancsi[24], A. Makovec, J. Molnar, Z. Szillasi

Institute of Physics, University of Debrecen, Debrecen, Hungary
M. Bartók[22], P. Raics, Z.L. Trocsanyi, B. Ujvari, G. Zilizi

Indian Institute of Science (IISc), Bangalore, India
S. Choudhury, J.R. Komaragiri

National Institute of Science Education and Research, Bhubaneswar, India
S. Bahinipati[25], S. Bhowmik, P. Mal, K. Mandal, A. Nayak[26], D.K. Sahoo[25], N. Sahoo, S.K. Swain

Panjab University, Chandigarh, India
S. Bansal, S.B. Beri, V. Bhatnagar, R. Chawla, N. Dhingra, R. Gupta, A.K. Kalsi, A. Kaur, A. Kaur, M. Kaur, S. Kaur, R. Kumar, P. Kumari, M. Lohan, A. Mehta, J.B. Singh, G. Walia

University of Delhi, Delhi, India
Ashok Kumar, Aashaq Shah, A. Bhardwaj, S. Chauhan, B.C. Choudhary, R.B. Garg, M. Gola, S. Keshri, A. Kumar, S. Malhotra, H. Md, M. Naimuddin, K. Ranjan, R. Sharma

Saha Institute of Nuclear Physics, HBNI, Kolkata, India
R. Bhardwaj, R. Bhattacharya, S. Bhattacharya, U. Bhawandeep, S. Dey, S. Dutt, S. Dutta, S. Ghosh, N. Majumdar, A. Modak, K. Mondal, S. Mukhopadhyay, S. Nandan, A. Purohit, A. Roy, S. Roy Chowdhury, S. Sarkar, M. Sharan, S. Thakur

Indian Institute of Technology Madras, Madras, India
P.K. Behera

Bhabha Atomic Research Centre, Mumbai, India
R. Chudasama, D. Dutta, V. Jha, V. Kumar, A.K. Mohanty[18], P.K. Netrakanti, L.M. Pant, P. Shukla, A. Topkar

Tata Institute of Fundamental Research-A, Mumbai, India
T. Aziz, S. Dugad, B. Mahakud, S. Mitra, G.B. Mohanty, N. Sur, B. Sutar

Tata Institute of Fundamental Research-B, Mumbai, India
S. Banerjee, S. Bhattacharya, S. Chatterjee, P. Das, M. Guchait, Sa. Jain, S. Kumar, M. Maity[27], G. Majumder, K. Mazumdar, T. Sarkar[27], N. Wickramage[28]

Indian Institute of Science Education and Research (IISER), Pune, India
S. Chauhan, S. Dube, V. Hegde, A. Kapoor, K. Kothekar, S. Pandey, A. Rane, S. Sharma

Institute for Research in Fundamental Sciences (IPM), Tehran, Iran
B. Boghrati, S. Chenarani[29], E. Eskandari Tadavani, S.M. Etesami[29], M. Khakzad, M. Mohammadi Najafabadi, M. Naseri, S. Paktinat Mehdiabadi[30], F. Rezaei Hosseinabadi, B. Safarzadeh[31], M. Zeinali

University College Dublin, Dublin, Ireland
M. Felcini, M. Grunewald

INFN Sezione di Bari [a], Università di Bari [b], Politecnico di Bari [c], Bari, Italy
M. Abbrescia[a,b], P.R. Altieri[a,b], C. Calabria[a,b], A. Colaleo[a], S. Costantini[a], D. Creanza[a,c], L. Cristella[a,b], N. De Filippis[a,c], M. De Palma[a,b], G. De Robertis[a], F. Errico[a,b], L. Fiore[a], M. Franco[a], A. Gelmi[a,b], G. Iaselli[a,c], N. Lacalamita[a], S. Lezki[a,b], F. Licciulli, F. Loddo[a], G. Maggi[a,c], M. Maggi[a], G. Miniello[a,b], S. My[a,b], S. Nuzzo[a,b], G. Papagni[a], A. Pompili[a,b], G. Pugliese[a,c], R. Radogna[a],

A. Ranieri[a], G. Selvaggi[a,b], A. Sharma[a], L. Silvestris[a,18], F.M. Simone, E. Soldani[a,b], R. Venditti[a], P. Verwilligen[a]

INFN Sezione di Bologna [a], Università di Bologna [b], Bologna, Italy
G. Abbiendi[a], C. Baldanza[a], C. Battilana[a,b], D. Bonacorsi[a,b], L. Borgonovi[a,b], S. Braibant-Giacomelli[a,b], V.D. Cafaro[a], R. Campanini[a,b], P. Capiluppi[a,b], A. Castro[a,b], F.R. Cavallo[a], S.S. Chhibra[a], G. Codispoti[a,b], M. Cuffiani[a,b], I. D'Antone[a], G.M. Dallavalle[a], F. Fabbri[a], A. Fanfani[a,b], D. Fasanella[a,b], P. Giacomelli[a], V. Giordano[a], C. Grandi[a], M. Guerzoni[a], L. Guiducci[a,b], S. Marcellini[a], G. Masetti[a], A. Montanari[a], F.L. Navarria[a,b], F. Odorici[a], G. Pellegrini[a], A. Perrotta[a], A.M. Rossi[a,b], T. Rovelli[a,b], G.P. Siroli[a,b], G. Torromeo[a], N. Tosi[a]

INFN Sezione di Catania [a], Università di Catania [b], Catania, Italy
S. Albergo[a,b], S. Costa[a,b], A. Di Mattia[a], F. Giordano[a,b], R. Potenza[a,b], A. Tricomi[a,b], C. Tuve[a,b]

INFN Sezione di Firenze [a], Università di Firenze [b], Firenze, Italy
G. Barbagli[a], K. Chatterjee[a,b], V. Ciulli[a,b], C. Civinini[a], R. D'Alessandro[a,b], E. Focardi[a,b], P. Lenzi[a,b], M. Meschini[a], S. Paoletti[a], L. Russo[a,32], G. Sguazzoni[a], D. Strom[a], L. Viliani[a]

INFN Laboratori Nazionali di Frascati, Frascati, Italy
L. Benussi, S. Bianco, M. Caponero[33], F. Fabbri, M. Ferrini, L. Passamonti, D. Piccolo, D. Pierluigi, F. Primavera[18], A. Russo, G. Saviano[34]

INFN Sezione di Genova [a], Università di Genova [b], Genova, Italy
V. Calvelli[a,b], F. Ferro[a], F. Ravera[a,b], E. Robutti[a], S. Tosi[a,b]

INFN Sezione di Milano-Bicocca [a], Università di Milano-Bicocca [b], Milano, Italy
A. Benaglia[a], A. Beschi[b], L. Brianza[a,b], F. Brivio[a,b], V. Ciriolo[a,b,18], M.E. Dinardo[a,b], S. Fiorendi[a,b], S. Gennai[a], A. Ghezzi[a,b], P. Govoni[a,b], M. Malberti[a,b], S. Malvezzi[a], R.A. Manzoni[a,b], D. Menasce[a], L. Moroni[a], M. Paganoni[a,b], K. Pauwels[a,b], D. Pedrini[a], S. Pigazzini[a,b,35], S. Ragazzi[a,b], T. Tabarelli de Fatis[a,b]

INFN Sezione di Napoli [a], Università di Napoli 'Federico II' [b], Napoli, Italy, Università della Basilicata [c], Potenza, Italy, Università G. Marconi [d], Roma, Italy
A. Buonaura[a,b], S. Buontempo[a], F. Cassese, N. Cavallo[a,c], G. De Lellis[a,b], A. Di Crescenzo[a], S. Di Guida[a,d,18], F. Fabozzi[a,c], F. Fienga[a,b], G. Galati[a,b], A.O.M. Iorio[a,b], W.A. Khan[a], L. Lista[a], S. Meola[a,d,18], P. Paolucci[a,18], G. Passeggio[a], C. Sciacca[a,b], F. Thyssen[a], A. Vanzanella[a], E. Voevodina[a,b]

INFN Sezione di Padova [a], Università di Padova [b], Padova, Italy, Università di Trento [c], Trento, Italy
P. Azzi[a], L. Barcellan[a], M. Bellato[a], L. Benato[a,b], M. Benettoni[a], M. Biasotto[a,36], A. Boletti[a,b], R. Carlin[a,b], L. Castellani[a], P. Checchia[a], L. Ciano[a], M. Dall'Osso[a,b], U. Dosselli[a], S. Fantinel[a], F. Fanzago[a], F. Gasparini[a,b], U. Gasparini[a,b], F. Gonella[a], A. Gozzelino[a], M. Gulmini[a,36], R. Isocrate[a], S. Lacaprara[a], I. Lazzizzera[a,c], M. Margoni[a,b], A.T. Meneguzzo[a,b], G. Mocellin, F. Montecassiano[a], M. Passaseo[a], M. Pegoraro[a], N. Pozzobon[a,b], P. Ronchese[a,b], R. Rossin[a,b], M. Sgaravatto[a], F. Simonetto[a,b], N. Toniolo[a], E. Torassa[a], S. Ventura[a], M. Zanetti[a,b], P. Zotto[a,b], G. Zumerle[a,b]

INFN Sezione di Pavia [a], Università di Pavia [b], Pavia, Italy
A. Braghieri[a], A. Magnani[a], P. Montagna[a,b], S.P. Ratti[a,b], V. Re[a], M. Ressegotti[a,b], C. Riccardi[a,b], P. Salvini[a], I. Vai[a,b], P. Vitulo[a,b]

INFN Sezione di Perugia [a], Università di Perugia [b], Perugia, Italy
L. Alunni Solestizi[a,b], M. Biasini[a,b], G.M. Bilei[a], C. Cecchi[a,b], D. Ciangottini[a,b], L. Fanò[a,b], R.

Leonardi[a,b], E. Manoni[a], G. Mantovani[a,b], V. Mariani[a,b], M. Menichelli[a], A. Rossi[a,b], A. Santocchia[a,b], D. Spiga[a]

INFN Sezione di Pisa [a], Università di Pisa [b], Scuola Normale Superiore di Pisa [c], Pisa, Italy
K. Androsov[a], P. Azzurri[a,18], G. Bagliesi[a], T. Boccali[a], L. Borrello, R. Castaldi[a], M.A. Ciocci[a,b], R. Dell'Orso[a], G. Fedi[a], L. Giannini[a,c], A. Giassi[a], M.T. Grippo[a,32], F. Ligabue[a,c], T. Lomtadze[a], E. Manca[a,c], G. Mandorli[a,c], A. Messineo[a,b], F. Palla[a], A. Rizzi[a,b], A. Savoy-Navarro[a,37], P. Spagnolo[a], R. Tenchini[a], G. Tonelli[a,b], A. Venturi[a], P.G. Verdini[a]

INFN Sezione di Roma [a], Sapienza Università di Roma [b], Rome, Italy
L. Barone[a,b], F. Cavallari[a], M. Cipriani[a,b], N. Daci[a], D. Del Re[a,b,18], E. Di Marco[a,b], M. Diemoz[a], S. Gelli[a,b], E. Longo[a,b], F. Margaroli[a,b], B. Marzocchi[a,b], P. Meridiani[a], G. Organtini[a,b], R. Paramatti[a,b], F. Preiato[a,b], S. Rahatlou[a,b], C. Rovelli[a], F. Santanastasio[a,b]

INFN Sezione di Torino [a], Università di Torino [b], Torino, Italy, Università del Piemonte Orientale [c], Novara, Italy
N. Amapane[a,b], R. Arcidiacono[a,c], S. Argiro[a,b], M. Arneodo[a,c], N. Bartosik[a], R. Bellan[a,b], C. Biino[a], N. Cartiglia[a], F. Cenna[a,b], M. Costa[a,b], G. Cotto[a,b], R. Covarelli[a,b], D. Dattola[a], P. De Remigis[a], A. Degano[a,b], G. Dellacasa[a], N. Demaria[a], B. Kiani[a,b], C. Mariotti[a], S. Maselli[a], E. Migliore[a,b], V. Monaco[a,b], E. Monteil[a,b], M. Monteno[a], M.M. Obertino[a,b], L. Pacher[a,b], N. Pastrone[a], M. Pelliccioni[a], G.L. Pinna Angioni[a,b], A. Romero[a,b], F. Rotondo[a], M. Ruspa[a,c], R. Sacchi[a,b], K. Shchelina[a,b], V. Sola[a], A. Solano[a,b], A. Staiano[a], P. Traczyk[a,b]

INFN Sezione di Trieste [a], Università di Trieste [b], Trieste, Italy
S. Belforte[a], M. Casarsa[a], F. Cossutti[a], G. Della Ricca[a,b], A. Zanetti[a]

Kyungpook National University
D.H. Kim, G.N. Kim, M.S. Kim, J. Lee, S. Lee, S.W. Lee, C.S. Moon, Y.D. Oh, S. Sekmen, D.C. Son, Y.C. Yang

Chonbuk National University, Jeonju, Korea
A. Lee

Chonnam National University, Institute for Universe and Elementary Particles, Kwangju, Korea
H. Kim, D.H. Moon, G. Oh

Hanyang University, Seoul, Korea
J.A. Brochero Cifuentes, J. Goh, T.J. Kim

Korea University, Seoul, Korea
S. Cho, S. Choi, Y. Go, D. Gyun, S. Ha, B. Hong, Y. Jo, Y. Jo, M. Kang, Y. Kim, K. Lee, K.S. Lee, S. Lee, J. Lim, S.K. Park, Y. Roh

Seoul National University, Seoul, Korea
J. Almond, J. Kim, J.S. Kim, H. Lee, K. Lee, K. Nam, S.B. Oh, B.C. Radburn-Smith, S.h. Seo, U.K. Yang, H.D. Yoo, G.B. Yu

University of Seoul, Seoul, Korea
H. Kim, J.H. Kim, J.S.H. Lee, I.C. Park

Sungkyunkwan University, Suwon, Korea
Y. Choi, C. Hwang, J. Lee, I. Yu

Vilnius University, Vilnius, Lithuania
V. Dudenas, A. Juodagalvis, J. Vaitkus

National Centre for Particle Physics, Universiti Malaya, Kuala Lumpur, Malaysia
K. Abdul Raman, I. Ahmed, Z.A. Ibrahim, M.A.B. Md Ali[38], M.F.B. Md Halid, F. Mohamad Idris[39], W.A.T. Wan Abdullah, M.N. Yusli, Z. Zolkapli

Centro de Investigacion y de Estudios Avanzados del IPN, Mexico City, Mexico
Reyes-Almanza, R, Ramirez-Sanchez, G., Duran-Osuna, M. C., H. Castilla-Valdez, E. De La Cruz-Burelo, I. Heredia-De La Cruz[40], Rabadan-Trejo, R. I., R. Lopez-Fernandez, J. Mejia Guisao, J.A. Murillo Quijada, A. Sanchez-Hernandez

Universidad Iberoamericana, Mexico City, Mexico
S. Carrillo Moreno, O. Miguel Colin, C. Oropeza Barrera, F. Vazquez Valencia

Benemerita Universidad Autonoma de Puebla, Puebla, Mexico
S. Carpinteyro, J. Eysermans, I. Pedraza, H.A. Salazar Ibarguen, C. Uribe Estrada

Universidad Autónoma de San Luis Potosí, San Luis Potosí, Mexico
A. Morelos Pineda

University of Auckland, Auckland, New Zealand
D. Krofcheck

University of Canterbury, Christchurch, New Zealand
P.H. Butler

National Centre for Physics, Quaid-I-Azam University, Islamabad, Pakistan
A. Ahmad, M. Ahmad, W. Ahmed, I. Ali, M.I. Asghar, M.I.M. Awan, Q. Hassan, H.R. Hoorani, S. Muhammad, M.A. Shah, H. Shahzad, M. Shoaib, A. Sultan, M. Waqas

National Centre for Nuclear Research, Swierk, Poland
H. Bialkowska, M. Bluj, B. Boimska, T. Frueboes, M. Górski, M. Kazana, K. Nawrocki, M. Szleper, P. Zalewski

Institute of Experimental Physics, Faculty of Physics, University of Warsaw, Warsaw, Poland
K. Bunkowski, A. Byszuk[41], K. Doroba, A. Kalinowski, M. Konecki, J. Krolikowski, M. Misiura, M. Olszewski, A. Pyskir, M. Walczak

Laboratório de Instrumentação e Física Experimental de Partículas, Lisboa, Portugal
P. Bargassa, C. Beirão Da Cruz E Silva, A. Di Francesco, P. Faccioli, B. Galinhas, M. Gallinaro, J. Hollar, N. Leonardo, L. Lloret Iglesias, M.V. Nemallapudi, J. Seixas, G. Strong, O. Toldaiev, D. Vadruccio, J. Varela

Joint Institute for Nuclear Research, Dubna, Russia
S. Afanasiev, P. Bunin, M. Gavrilenko, I. Golutvin, I. Gorbunov, A. Kamenev, V. Karjavin, A. Lanev, A. Malakhov, V. Matveev[42,43], V. Palichik, V. Perelygin, S. Shmatov, S. Shulha, N. Skatchkov, V. Smirnov, N. Voytishin, A. Zarubin

Petersburg Nuclear Physics Institute, Gatchina (St. Petersburg), Russia
V. Golovtsov, Y. Ivanov, V. Kim[44], E. Kuznetsova[45], P. Levchenko, V. Murzin, V. Oreshkin, I. Smirnov, D. Sosnov, V. Sulimov, L. Uvarov, S. Vavilov, S. Volkov, A. Vorobyev

Institute for Nuclear Research, Moscow, Russia
Yu. Andreev, A. Dermenev, S. Gninenko, N. Golubev, A. Karneyeu, M. Kirsanov, N. Krasnikov, A. Pashenkov, D. Tlisov, A. Toropin

Institute for Theoretical and Experimental Physics, Moscow, Russia
V. Epshteyn, V. Gavrilov, N. Lychkovskaya, V. Popov, I. Pozdnyakov, G. Safronov, A. Spiridonov, A. Stepennov, M. Toms, E. Vlasov, A. Zhokin

Moscow Institute of Physics and Technology, Moscow, Russia
T. Aushev, A. Bylinkin[43]

P.N. Lebedev Physical Institute, Moscow, Russia
V. Andreev, M. Azarkin[43], I. Dremin[43], M. Kirakosyan[43], A. Terkulov

Skobeltsyn Institute of Nuclear Physics, Lomonosov Moscow State University, Moscow, Russia
A. Baskakov, A. Belyaev, E. Boos, A. Demiyanov, L. Dudko, A. Ershov, A. Gribushin, A. Kaminskiy[46], V. Klyukhin, O. Kodolova, I. Lokhtin, I. Miagkov, S. Obraztsov, S. Petrushanko, V. Savrin

Novosibirsk State University (NSU), Novosibirsk, Russia
V. Blinov[47], D. Shtol[47], Y. Skovpen[47]

State Research Center of Russian Federation, Institute for High Energy Physics of NRC "Kurchatov Institute", Protvino, Russia
I. Azhgirey, I. Bayshev, S. Bitioukov, D. Elumakhov, A. Godizov, V. Kachanov, A. Kalinin, D. Konstantinov, P. Mandrik, V. Petrov, R. Ryutin, A. Sobol, S. Troshin, N. Tyurin, A. Uzunian, A. Volkov

University of Belgrade, Faculty of Physics and Vinca Institute of Nuclear Sciences, Belgrade, Serbia
P. Adzic[48], P. Cirkovic, D. Devetak, M. Dordevic, J. Milosevic, V. Rekovic

Centro de Investigaciones Energéticas Medioambientales y Tecnológicas (CIEMAT), Madrid, Spain
J. Alcaraz Maestre, I. Bachiller, M. Barrio Luna, E. Calvo, J.M. Cela Ruiz, M. Cerrada, N. Colino, B. De La Cruz, A. Delgado Peris, C. Fernandez Bedoya, J.P. Fernández Ramos, J. Flix, M.C. Fouz, D. Francia Ferrero, O. Gonzalez Lopez, S. Goy Lopez, J.M. Hernandez, M.I. Josa, D. Moran, Á. Navarro Tobar, A. Pérez-Calero Yzquierdo, J. Puerta Pelayo, A. Quintario Olmeda, I. Redondo, D.D. Redondo Ferrero, L. Romero, J. Sastre, M.S. Soares, A. Álvarez Fernández

Universidad Autónoma de Madrid, Madrid, Spain
C. Albajar, J.F. de Trocóniz, M. Missiroli

Universidad de Oviedo, Oviedo, Spain
J. Cuevas, C. Erice, J. Fernandez Menendez, I. Gonzalez Caballero, J.R. González Fernández, E. Palencia Cortezon, S. Sanchez Cruz, I. Suárez Andrés, P. Vischia, J.M. Vizan Garcia

Instituto de Física de Cantabria (IFCA), CSIC-Universidad de Cantabria, Santander, Spain
I.J. Cabrillo, A. Calderon, B. Chazin Quero, E. Curras, J. Duarte Campderros, M. Fernandez, J. Garcia-Ferrero, G. Gomez, A. Lopez Virto, J. Marco, C. Martinez Rivero, P. Martinez Ruiz del Arbol, F. Matorras, J. Piedra Gomez, T. Rodrigo, A. Ruiz-Jimeno, L. Scodellaro, N. Trevisani, I. Vila, R. Vilar Cortabitarte

CERN, European Organization for Nuclear Research, Geneva, Switzerland
D. Abbaneo, B. Akgun, P. Aspell, E. Auffray, P. Baillon, A.H. Ball, D. Barney, J. Bendavid, M. Bianco, P. Bloch, A. Bocci, C. Botta, S. Brachet, T. Camporesi, R. Castello, M. Cepeda, G. Cerminara, E. Chapon, Y. Chen, A. Conde Garcia, D. d'Enterria, A. Dabrowski, V. Daponte, A. David, M. De Gruttola, A. De Roeck, N. Deelen, M. Dobson, T. du Pree, M. Dünser, N. Dupont,

A. Elliott-Peisert, P. Everaerts, F. Fallavollita, G. Franzoni, J. Fulcher, W. Funk, D. Gigi, A. Gilbert, K. Gill, F. Glege, M. Gruchala, D. Gulhan, P. Harris, J. Hegeman, V. Innocente, A. Jafari, P. Janot, O. Karacheban[21], J. Kieseler, V. Knünz, A. Kornmayer, M.J. Kortelainen, A. Kotsokechagia, M. Krammer[1], C. Lange, P. Lecoq, C. Lourenço, M.T. Lucchini, L. Malgeri, M. Mannelli, A. Martelli, F. Meijers, J.A. Merlin, S. Mersi, E. Meschi, P. Milenovic[49], F. Moortgat, M. Mulders, H. Neugebauer, J. Ngadiuba, S. Orfanelli, L. Orsini, L. Pape, E. Perez, M. Peruzzi, P. Petiot, A. Petrilli, G. Petrucciani, A. Pfeiffer, M. Pierini, D. Rabady, A. Racz, T. Reis, G. Rolandi[50], M. Rovere, H. Sakulin, C. Schäfer, C. Schwick, M. Seidel, M. Selvaggi, A. Sharma, P. Silva, P. Sphicas[51], A. Stakia, J. Steggemann, M. Stoye, M. Tosi, D. Treille, A. Triossi, A. Tsirou, V. Veckalns[52], M. Verweij, W.D. Zeuner

Paul Scherrer Institut, Villigen, Switzerland
W. Bertl†, L. Caminada[53], K. Deiters, W. Erdmann, R. Horisberger, Q. Ingram, H.C. Kaestli, D. Kotlinski, U. Langenegger, T. Rohe, S.A. Wiederkehr

ETH Zurich - Institute for Particle Physics and Astrophysics (IPA), Zurich, Switzerland
M. Backhaus, L. Bäni, P. Berger, L. Bianchini, B. Casal, G. Dissertori, M. Dittmar, M. Donegà, C. Dorfer, C. Grab, C. Heidegger, D. Hits, J. Hoss, G. Kasieczka, T. Klijnsma, W. Lustermann, B. Mangano, M. Marionneau, M.T. Meinhard, D. Meister, F. Micheli, P. Musella, F. Nessi-Tedaldi, F. Pandolfi, J. Pata, F. Pauss, G. Perrin, L. Perrozzi, M. Quittnat, M. Reichmann, D.A. Sanz Becerra, M. Schönenberger, L. Shchutska, V.R. Tavolaro, K. Theofilatos, M.L. Vesterbacka Olsson, R. Wallny, D.H. Zhu

Universität Zürich, Zurich, Switzerland
T.K. Aarrestad, C. Amsler[54], M.F. Canelli, A. De Cosa, R. Del Burgo, S. Donato, C. Galloni, T. Hreus, B. Kilminster, D. Pinna, G. Rauco, P. Robmann, D. Salerno, K. Schweiger, C. Seitz, Y. Takahashi, A. Zucchetta

National Central University, Chung-Li, Taiwan
V. Candelise, Y.H. Chang, K.y. Cheng, T.H. Doan, Sh. Jain, R. Khurana, C.M. Kuo, W. Lin, A. Pozdnyakov, S.S. Yu

National Taiwan University (NTU), Taipei, Taiwan
Arun Kumar, P. Chang, Y. Chao, K.F. Chen, P.H. Chen, F. Fiori, W.-S. Hou, Y. Hsiung, Y.F. Liu, R.-S. Lu, E. Paganis, A. Psallidas, A. Steen, J.f. Tsai

Chulalongkorn University, Faculty of Science, Department of Physics, Bangkok, Thailand
B. Asavapibhop, K. Kovitanggoon, G. Singh, N. Srimanobhas

Çukurova University, Physics Department, Science and Art Faculty, Adana, Turkey
A. Bat, F. Boran, S. Cerci[55], S. Damarseckin, Z.S. Demiroglu, C. Dozen, I. Dumanoglu, S. Girgis, G. Gokbulut, Y. Guler, I. Hos[56], E.E. Kangal[57], O. Kara, A. Kayis Topaksu, U. Kiminsu, M. Oglakci, G. Onengut[58], K. Ozdemir[59], D. Sunar Cerci[55], B. Tali[55], U.G. Tok, S. Turkcapar, I.S. Zorbakir, C. Zorbilmez

Middle East Technical University, Physics Department, Ankara, Turkey
G. Karapinar[60], K. Ocalan[61], M. Yalvac, M. Zeyrek

Bogazici University, Istanbul, Turkey
E. Gülmez, M. Kaya[62], O. Kaya[63], S. Tekten, E.A. Yetkin[64]

Istanbul Technical University, Istanbul, Turkey
M.N. Agaras, S. Atay, A. Cakir, K. Cankocak, I. Köseoglu

Institute for Scintillation Materials of National Academy of Science of Ukraine, Kharkov, Ukraine
B. Grynyov

National Scientific Center, Kharkov Institute of Physics and Technology, Kharkov, Ukraine
L. Levchuk

University of Bristol, Bristol, United Kingdom
F. Ball, L. Beck, J.J. Brooke, D. Burns, E. Clement, D. Cussans, O. Davignon, H. Flacher, J. Goldstein, G.P. Heath, H.F. Heath, L. Kreczko, D.M. Newbold[65], S. Paramesvaran, T. Sakuma, S. Seif El Nasr-storey, D. Smith, V.J. Smith

Rutherford Appleton Laboratory, Didcot, United Kingdom
K.W. Bell, A. Belyaev[66], C. Brew, R.M. Brown, L. Calligaris, D. Cieri, D.J.A. Cockerill, J.A. Coughlan, K. Harder, S. Harper, J. Linacre, E. Olaiya, D. Petyt, C.H. Shepherd-Themistocleous, A. Thea, I.R. Tomalin, T. Williams

Imperial College, London, United Kingdom
G. Auzinger, R. Bainbridge, J. Borg, S. Breeze, O. Buchmuller, A. Bundock, S. Casasso, M. Citron, D. Colling, L. Corpe, P. Dauncey, G. Davies, A. De Wit, M. Della Negra, R. Di Maria, A. Elwood, Y. Haddad, G. Hall, G. Iles, T. James, R. Lane, C. Laner, L. Lyons, A.-M. Magnan, S. Malik, L. Mastrolorenzo, T. Matsushita, J. Nash, A. Nikitenko[7], V. Palladino, M. Pesaresi, D.M. Raymond, A. Richards, A. Rose, E. Scott, C. Seez, A. Shtipliyski, S. Summers, A. Tapper, K. Uchida, M. Vazquez Acosta[67], T. Virdee[18], N. Wardle, D. Winterbottom, J. Wright, S.C. Zenz

Brunel University, Uxbridge, United Kingdom
J.E. Cole, P.R. Hobson, A. Khan, P. Kyberd, I.D. Reid, L. Teodorescu, S. Zahid

Baylor University, Waco, USA
A. Borzou, K. Call, J. Dittmann, K. Hatakeyama, H. Liu, N. Pastika, C. Smith

Catholic University of America, Washington DC, USA
R. Bartek, A. Dominguez

The University of Alabama, Tuscaloosa, USA
A. Buccilli, S.I. Cooper, C. Henderson, P. Rumerio, C. West

Boston University, Boston, USA
D. Arcaro, A. Avetisyan, T. Bose, D. Gastler, D. Rankin, C. Richardson, J. Rohlf, L. Sulak, D. Zou

Brown University, Providence, USA
G. Benelli, D. Cutts, A. Garabedian, M. Hadley, J. Hakala, U. Heintz, J.M. Hogan, K.H.M. Kwok, E. Laird, G. Landsberg, J. Lee, Z. Mao, M. Narain, J. Pazzini, S. Piperov, S. Sagir, R. Syarif, D. Yu

University of California, Davis, Davis, USA
R. Band, C. Brainerd, R. Breedon, D. Burns, M. Calderon De La Barca Sanchez, M. Chertok, J. Conway, R. Conway, P.T. Cox, R. Erbacher, C. Flores, G. Funk, W. Ko, R. Lander, C. Mclean, M. Mulhearn, D. Pellett, J. Pilot, S. Shalhout, M. Shi, J. Smith, D. Stolp, K. Tos, M. Tripathi, Z. Wang

University of California, Los Angeles, USA
M. Bachtis, C. Bravo, R. Cousins, A. Dasgupta, A. Florent, J. Hauser, M. Ignatenko, N. Mccoll, A. Peck, S. Regnard, D. Saltzberg, C. Schnaible, V. Valuev

University of California, Riverside, Riverside, USA
E. Bouvier, K. Burt, R. Clare, J. Ellison, J.W. Gary, S.M.A. Ghiasi Shirazi, G. Hanson, J. Heilman,

G. Karapostoli, E. Kennedy, F. Lacroix, O.R. Long, M. Olmedo Negrete, M.I. Paneva, W. Si, L. Wang, H. Wei, S. Wimpenny, B. R. Yates

University of California, San Diego, La Jolla, USA
J.G. Branson, S. Cittolin, M. Derdzinski, R. Gerosa, D. Gilbert, B. Hashemi, A. Holzner, D. Klein, G. Kole, V. Krutelyov, J. Letts, M. Masciovecchio, D. Olivito, S. Padhi, M. Pieri, M. Sani, V. Sharma, M. Tadel, A. Vartak, S. Wasserbaech[68], J. Wood, F. Würthwein, A. Yagil, G. Zevi Della Porta

University of California, Santa Barbara - Department of Physics, Santa Barbara, USA
N. Amin, R. Bhandari, J. Bradmiller-Feld, C. Campagnari, A. Dishaw, V. Dutta, M. Franco Sevilla, F. Golf, L. Gouskos, R. Heller, J. Incandela, A. Ovcharova, H. Qu, J. Richman, D. Stuart, I. Suarez, J. Yoo

California Institute of Technology, Pasadena, USA
D. Anderson, A. Bornheim, J.M. Lawhorn, H.B. Newman, T. Nguyen, C. Pena, M. Spiropulu, J.R. Vlimant, S. Xie, Z. Zhang, R.Y. Zhu

Carnegie Mellon University, Pittsburgh, USA
M.B. Andrews, T. Ferguson, T. Mudholkar, M. Paulini, J. Russ, M. Sun, H. Vogel, I. Vorobiev, M. Weinberg

University of Colorado Boulder, Boulder, USA
J.P. Cumalat, W.T. Ford, F. Jensen, A. Johnson, M. Krohn, S. Leontsinis, T. Mulholland, K. Stenson, S.R. Wagner

Cornell University, Ithaca, USA
J. Alexander, J. Chaves, J. Chu, S. Dittmer, K. Mcdermott, N. Mirman, J.R. Patterson, D. Quach, A. Rinkevicius, A. Ryd, L. Skinnari, L. Soffi, S.M. Tan, Z. Tao, J. Thom, J. Tucker, P. Wittich, M. Zientek

Fermi National Accelerator Laboratory, Batavia, USA
S. Abdullin, M. Albrow, M. Alyari, G. Apollinari, A. Apresyan, A. Apyan, S. Banerjee, L.A.T. Bauerdick, A. Beretvas, J. Berryhill, P.C. Bhat, G. Bolla[†], K. Burkett, J.N. Butler, A. Canepa, G.B. Cerati, H.W.K. Cheung, F. Chlebana, M. Cremonesi, J. Duarte, V.D. Elvira, J. Freeman, Z. Gecse, E. Gottschalk, L. Gray, D. Green, S. Grünendahl, O. Gutsche, R.M. Harris, S. Hasegawa, J. Hirschauer, Z. Hu, B. Jayatilaka, S. Jindariani, M. Johnson, U. Joshi, B. Klima, B. Kreis, S. Lammel, D. Lincoln, R. Lipton, M. Liu, T. Liu, R. Lopes De Sá, J. Lykken, K. Maeshima, N. Magini, J.M. Marraffino, D. Mason, P. McBride, P. Merkel, S. Mrenna, S. Nahn, V. O'Dell, K. Pedro, O. Prokofyev, G. Rakness, L. Ristori, B. Schneider, E. Sexton-Kennedy, A. Soha, W.J. Spalding, L. Spiegel, S. Stoynev, J. Strait, N. Strobbe, L. Taylor, S. Tkaczyk, N.V. Tran, L. Uplegger, E.W. Vaandering, C. Vernieri, M. Verzocchi, R. Vidal, M. Wang, H.A. Weber, A. Whitbeck

University of Florida, Gainesville, USA
D. Acosta, P. Avery, V. Barashko, P. Bortignon, D. Bourilkov, A. Brinkerhoff, A. Carnes, M. Carver, D. Curry, R.D. Field, I.K. Furic, S.V. Gleyzer, B.M. Joshi, J. Konigsberg, A. Korytov, K. Kotov, P. Ma, A. Madorsky, K. Matchev, H. Mei, G. Mitselmakher, D. Rosenzweig, K. Shi, D. Sperka, N. Terentyev, L. Thomas, J. Wang, S. Wang, J. Yelton

Florida International University, Miami, USA
Y.R. Joshi, S. Linn, P. Markowitz, J.L. Rodriguez

Florida State University, Tallahassee, USA
A. Ackert, T. Adams, A. Askew, S. Hagopian, V. Hagopian, K.F. Johnson, T. Kolberg, G. Martinez, T. Perry, H. Prosper, A. Saha, A. Santra, V. Sharma, R. Yohay

Florida Institute of Technology, Melbourne, USA
M.M. Baarmand, V. Bhopatkar, S. Colafranceschi, M. Hohlmann, D. Noonan, M. Rahmani, T. Roy, F. Yumiceva

University of Illinois at Chicago (UIC), Chicago, USA
M.R. Adams, L. Apanasevich, D. Berry, R.R. Betts, R. Cavanaugh, X. Chen, O. Evdokimov, C.E. Gerber, D.A. Hangal, D.J. Hofman, K. Jung, J. Kamin, I.D. Sandoval Gonzalez, M.B. Tonjes, H. Trauger, N. Varelas, H. Wang, Z. Wu, J. Zhang

The University of Iowa, Iowa City, USA
B. Bilki[69], W. Clarida, K. Dilsiz[70], S. Durgut, R.P. Gandrajula, M. Haytmyradov, V. Khristenko, J.-P. Merlo, H. Mermerkaya[71], A. Mestvirishvili, A. Moeller, J. Nachtman, H. Ogul[72], Y. Onel, F. Ozok[73], A. Penzo, C. Snyder, E. Tiras, J. Wetzel, K. Yi

Johns Hopkins University, Baltimore, USA
B. Blumenfeld, A. Cocoros, N. Eminizer, D. Fehling, L. Feng, A.V. Gritsan, P. Maksimovic, J. Roskes, U. Sarica, M. Swartz, M. Xiao, C. You

The University of Kansas, Lawrence, USA
A. Al-bataineh, P. Baringer, A. Bean, S. Boren, J. Bowen, J. Castle, S. Khalil, A. Kropivnitskaya, D. Majumder, W. Mcbrayer, M. Murray, C. Royon, S. Sanders, E. Schmitz, J.D. Tapia Takaki, Q. Wang

Kansas State University, Manhattan, USA
A. Ivanov, K. Kaadze, Y. Maravin, A. Mohammadi, L.K. Saini, N. Skhirtladze

Lawrence Livermore National Laboratory, Livermore, USA
F. Rebassoo, D. Wright

University of Maryland, College Park, USA
C. Anelli, A. Baden, O. Baron, A. Belloni, S.C. Eno, Y. Feng, C. Ferraioli, N.J. Hadley, S. Jabeen, G.Y. Jeng, R.G. Kellogg, J. Kunkle, A.C. Mignerey, F. Ricci-Tam, Y.H. Shin, A. Skuja, S.C. Tonwar

Massachusetts Institute of Technology, Cambridge, USA
D. Abercrombie, B. Allen, V. Azzolini, R. Barbieri, A. Baty, R. Bi, S. Brandt, W. Busza, I.A. Cali, M. D'Alfonso, Z. Demiragli, G. Gomez Ceballos, M. Goncharov, D. Hsu, M. Hu, Y. Iiyama, G.M. Innocenti, M. Klute, D. Kovalskyi, Y.-J. Lee, A. Levin, P.D. Luckey, B. Maier, A.C. Marini, C. Mcginn, C. Mironov, S. Narayanan, X. Niu, C. Paus, C. Roland, G. Roland, J. Salfeld-Nebgen, G.S.F. Stephans, K. Tatar, D. Velicanu, J. Wang, T.W. Wang, B. Wyslouch

University of Minnesota, Minneapolis, USA
A.C. Benvenuti, R.M. Chatterjee, A. Evans, P. Hansen, J. Hiltbrand, S. Kalafut, Y. Kubota, Z. Lesko, J. Mans, S. Nourbakhsh, N. Ruckstuhl, R. Rusack, J. Turkewitz, M.A. Wadud

University of Mississippi, Oxford, USA
J.G. Acosta, S. Oliveros

University of Nebraska-Lincoln, Lincoln, USA
E. Avdeeva, K. Bloom, D.R. Claes, C. Fangmeier, R. Gonzalez Suarez, R. Kamalieddin, I. Kravchenko, J. Monroy, J.E. Siado, G.R. Snow, B. Stieger

State University of New York at Buffalo, Buffalo, USA
J. Dolen, A. Godshalk, C. Harrington, I. Iashvili, D. Nguyen, A. Parker, S. Rappoccio, B. Roozbahani

Northeastern University, Boston, USA
G. Alverson, E. Barberis, C. Freer, A. Hortiangtham, A. Massironi, D.M. Morse, T. Orimoto, R. Teixeira De Lima, D. Trocino, T. Wamorkar, B. Wang, A. Wisecarver, D. Wood

Northwestern University, Evanston, USA
S. Bhattacharya, O. Charaf, K.A. Hahn, N. Mucia, N. Odell, M.H. Schmitt, K. Sung, M. Trovato, M. Velasco

University of Notre Dame, Notre Dame, USA
R. Bucci, N. Dev, M. Hildreth, K. Hurtado Anampa, C. Jessop, D.J. Karmgard, N. Kellams, K. Lannon, W. Li, N. Loukas, N. Marinelli, F. Meng, C. Mueller, Y. Musienko[42], M. Planer, A. Reinsvold, R. Ruchti, P. Siddireddy, G. Smith, S. Taroni, M. Wayne, A. Wightman, M. Wolf, A. Woodard

The Ohio State University, Columbus, USA
J. Alimena, L. Antonelli, B. Bylsma, L.S. Durkin, S. Flowers, B. Francis, A. Hart, C. Hill, W. Ji, B. Liu, W. Luo, B.L. Winer, H.W. Wulsin

Princeton University, Princeton, USA
S. Cooperstein, O. Driga, P. Elmer, J. Hardenbrook, P. Hebda, S. Higginbotham, A. Kalogeropoulos, D. Lange, J. Luo, D. Marlow, K. Mei, I. Ojalvo, J. Olsen, C. Palmer, P. Piroué, D. Stickland, C. Tully

University of Puerto Rico, Mayaguez, USA
S. Malik, S. Norberg

Purdue University, West Lafayette, USA
A. Barker, V.E. Barnes, S. Das, S. Folgueras, L. Gutay, M.K. Jha, M. Jones, A.W. Jung, A. Khatiwada, D.H. Miller, N. Neumeister, C.C. Peng, H. Qiu, J.F. Schulte, J. Sun, F. Wang, R. Xiao, W. Xie

Purdue University Northwest, Hammond, USA
T. Cheng, N. Parashar, J. Stupak

Rice University, Houston, USA
Z. Chen, K.M. Ecklund, S. Freed, F.J.M. Geurts, M. Guilbaud, M. Kilpatrick, W. Li, M. Matveev, B. Michlin, B.P. Padley, J. Roberts, J. Rorie, W. Shi, Z. Tu, J. Zabel, A. Zhang

University of Rochester, Rochester, USA
A. Bodek, P. de Barbaro, R. Demina, Y.t. Duh, T. Ferbel, M. Galanti, A. Garcia-Bellido, J. Han, O. Hindrichs, A. Khukhunaishvili, K.H. Lo, P. Tan, M. Verzetti

The Rockefeller University, New York, USA
R. Ciesielski, K. Goulianos, C. Mesropian

Rutgers, The State University of New Jersey, Piscataway, USA
A. Agapitos, J.P. Chou, Y. Gershtein, T.A. Gómez Espinosa, E. Halkiadakis, M. Heindl, E. Hughes, S. Kaplan, R. Kunnawalkam Elayavalli, S. Kyriacou, A. Lath, R. Montalvo, K. Nash, M. Osherson, H. Saka, S. Salur, S. Schnetzer, D. Sheffield, S. Somalwar, R. Stone, S. Thomas, P. Thomassen, M. Walker

University of Tennessee, Knoxville, USA
A.G. Delannoy, J. Heideman, G. Riley, K. Rose, S. Spanier, K. Thapa

Texas A&M University, College Station, USA
O. Bouhali[74], A. Castaneda Hernandez[74], A. Celik, M. Dalchenko, M. De Mattia, A. Delgado,

S. Dildick, J.R. Dimas Valle, R. Eusebi, J. Gilmore, T. Huang, E. Juska, T. Kamon[75], R. King, R. Mueller, Y. Pakhotin, R. Patel, A. Perloff, L. Perniè, D. Rathjens, A. Safonov, A. Tatarinov, K.A. Ulmer

Texas Tech University, Lubbock, USA
N. Akchurin, J. Damgov, F. De Guio, P.R. Dudero, J. Faulkner, E. Gurpinar, S. Kunori, K. Lamichhane, S.W. Lee, T. Libeiro, T. Mengke, S. Muthumuni, T. Peltola, S. Undleeb, I. Volobouev, Z. Wang

Vanderbilt University, Nashville, USA
S. Greene, A. Gurrola, R. Janjam, W. Johns, C. Maguire, A. Melo, H. Ni, K. Padeken, P. Sheldon, S. Tuo, J. Velkovska, Q. Xu

University of Virginia, Charlottesville, USA
M.W. Arenton, P. Barria, B. Cox, R. Hirosky, M. Joyce, A. Ledovskoy, H. Li, C. Neu, T. Sinthuprasith, Y. Wang, E. Wolfe, F. Xia

Wayne State University, Detroit, USA
A. Gutierrez, R. Harr, P.E. Karchin, N. Poudyal, J. Sturdy, P. Thapa, S. Zaleski

University of Wisconsin - Madison, Madison, WI, USA
M. Brodski, J. Buchanan, C. Caillol, I. Crotty[18], S. Dasu, L. Dodd, S. Duric, G. Fetchenhauer, B. Gomber, T. Gorski, M. Grothe, M. Herndon, A. Hervé, U. Hussain, P. Klabbers, A. Lanaro, A. Levine, K. Long, R. Loveless, T. Ruggles, A. Savin, N. Smith, W.H. Smith, D. Taylor, S. Trembath-reichert, D. Wenman, N. Woods

†: Deceased
1: Also at Vienna University of Technology, Vienna, Austria
2: Also at State Key Laboratory of Nuclear Physics and Technology, Peking University, Beijing, China
3: Also at IRFU, CEA, Université Paris-Saclay, Gif-sur-Yvette, France
4: Also at Universidade Estadual de Campinas, Campinas, Brazil
5: Also at Federal University of Rio Grande do Sul, Porto Alegre, Brazil
6: Also at Université Libre de Bruxelles, Bruxelles, Belgium
7: Also at Institute for Theoretical and Experimental Physics, Moscow, Russia
8: Also at Joint Institute for Nuclear Research, Dubna, Russia
9: Also at Cairo University, Cairo, Egypt
10: Also at Helwan University, Cairo, Egypt
11: Now at Zewail City of Science and Technology, Zewail, Egypt
12: Also at Suez University, Suez, Egypt
13: Now at British University in Egypt, Cairo, Egypt
14: Also at Université de Haute Alsace, Mulhouse, France
15: Also at Skobeltsyn Institute of Nuclear Physics, Lomonosov Moscow State University, Moscow, Russia
16: Also at Tbilisi State University, Tbilisi, Georgia
17: Also at Ilia State University, Tbilisi, Georgia
18: Also at CERN, European Organization for Nuclear Research, Geneva, Switzerland
19: Also at RWTH Aachen University, III. Physikalisches Institut A, Aachen, Germany
20: Also at University of Hamburg, Hamburg, Germany
21: Also at Brandenburg University of Technology, Cottbus, Germany
22: Also at MTA-ELTE Lendület CMS Particle and Nuclear Physics Group, Eötvös Loránd University, Budapest, Hungary

23: Also at Institute of Nuclear Research ATOMKI, Debrecen, Hungary
24: Also at Institute of Physics, University of Debrecen, Debrecen, Hungary
25: Also at Indian Institute of Technology Bhubaneswar, Bhubaneswar, India
26: Also at Institute of Physics, Bhubaneswar, India
27: Also at University of Visva-Bharati, Santiniketan, India
28: Also at University of Ruhuna, Matara, Sri Lanka
29: Also at Isfahan University of Technology, Isfahan, Iran
30: Also at Yazd University, Yazd, Iran
31: Also at Plasma Physics Research Center, Science and Research Branch, Islamic Azad University, Tehran, Iran
32: Also at Università degli Studi di Siena, Siena, Italy
33: Also at ENEA - Casaccia Research Center, S. Maria di Galeria, Italy
34: Also at Facoltà Ingegneria, Università di Roma, Roma, Italy
35: Also at INFN Sezione di Milano-Bicocca; Università di Milano-Bicocca, Milano, Italy
36: Also at Laboratori Nazionali di Legnaro dell'INFN, Legnaro, Italy
37: Also at Purdue University, West Lafayette, USA
38: Also at International Islamic University of Malaysia, Kuala Lumpur, Malaysia
39: Also at Malaysian Nuclear Agency, MOSTI, Kajang, Malaysia
40: Also at Consejo Nacional de Ciencia y Tecnología, Mexico city, Mexico
41: Also at Warsaw University of Technology, Institute of Electronic Systems, Warsaw, Poland
42: Also at Institute for Nuclear Research, Moscow, Russia
43: Now at National Research Nuclear University 'Moscow Engineering Physics Institute' (MEPhI), Moscow, Russia
44: Also at St. Petersburg State Polytechnical University, St. Petersburg, Russia
45: Also at University of Florida, Gainesville, USA
46: Also at INFN Sezione di Padova; Università di Padova; Università di Trento (Trento), Padova, Italy
47: Also at Budker Institute of Nuclear Physics, Novosibirsk, Russia
48: Also at Faculty of Physics, University of Belgrade, Belgrade, Serbia
49: Also at University of Belgrade, Faculty of Physics and Vinca Institute of Nuclear Sciences, Belgrade, Serbia
50: Also at Scuola Normale e Sezione dell'INFN, Pisa, Italy
51: Also at National and Kapodistrian University of Athens, Athens, Greece
52: Also at Riga Technical University, Riga, Latvia
53: Also at Universität Zürich, Zurich, Switzerland
54: Also at Stefan Meyer Institute for Subatomic Physics (SMI), Vienna, Austria
55: Also at Adiyaman University, Adiyaman, Turkey
56: Also at Istanbul Aydin University, Istanbul, Turkey
57: Also at Mersin University, Mersin, Turkey
58: Also at Cag University, Mersin, Turkey
59: Also at Piri Reis University, Istanbul, Turkey
60: Also at Izmir Institute of Technology, Izmir, Turkey
61: Also at Necmettin Erbakan University, Konya, Turkey
62: Also at Marmara University, Istanbul, Turkey
63: Also at Kafkas University, Kars, Turkey
64: Also at Istanbul Bilgi University, Istanbul, Turkey
65: Also at Rutherford Appleton Laboratory, Didcot, United Kingdom
66: Also at School of Physics and Astronomy, University of Southampton, Southampton, United Kingdom

67: Also at Instituto de Astrofísica de Canarias, La Laguna, Spain
68: Also at Utah Valley University, Orem, USA
69: Also at Beykent University, Istanbul, Turkey
70: Also at Bingol University, Bingol, Turkey
71: Also at Erzincan University, Erzincan, Turkey
72: Also at Sinop University, Sinop, Turkey
73: Also at Mimar Sinan University, Istanbul, Istanbul, Turkey
74: Also at Texas A&M University at Qatar, Doha, Qatar
75: Also at Kyungpook National University, Daegu, Korea